




2018

NUMERICAL MODELING AND ISOTOPE TRACERS TO INVESTIGATE KARST BIOGEOCHEMISTRY AND TRANSPORT PROCESSES

Admin Husic

University of Kentucky, admin.husic@uky.edu

Author ORCID Identifier:

 <https://orcid.org/0000-0002-4225-2252>

Digital Object Identifier: <https://doi.org/10.13023/etd.2018.322>

[Right click to open a feedback form in a new tab to let us know how this document benefits you.](#)

Recommended Citation

Husic, Admin, "NUMERICAL MODELING AND ISOTOPE TRACERS TO INVESTIGATE KARST BIOGEOCHEMISTRY AND TRANSPORT PROCESSES" (2018). *Theses and Dissertations--Civil Engineering*. 70.

https://uknowledge.uky.edu/ce_etds/70

This Doctoral Dissertation is brought to you for free and open access by the Civil Engineering at UKnowledge. It has been accepted for inclusion in Theses and Dissertations--Civil Engineering by an authorized administrator of UKnowledge. For more information, please contact UKnowledge@lsv.uky.edu.

STUDENT AGREEMENT:

I represent that my thesis or dissertation and abstract are my original work. Proper attribution has been given to all outside sources. I understand that I am solely responsible for obtaining any needed copyright permissions. I have obtained needed written permission statement(s) from the owner(s) of each third-party copyrighted matter to be included in my work, allowing electronic distribution (if such use is not permitted by the fair use doctrine) which will be submitted to UKnowledge as Additional File.

I hereby grant to The University of Kentucky and its agents the irrevocable, non-exclusive, and royalty-free license to archive and make accessible my work in whole or in part in all forms of media, now or hereafter known. I agree that the document mentioned above may be made available immediately for worldwide access unless an embargo applies.

I retain all other ownership rights to the copyright of my work. I also retain the right to use in future works (such as articles or books) all or part of my work. I understand that I am free to register the copyright to my work.

REVIEW, APPROVAL AND ACCEPTANCE

The document mentioned above has been reviewed and accepted by the student's advisor, on behalf of the advisory committee, and by the Director of Graduate Studies (DGS), on behalf of the program; we verify that this is the final, approved version of the student's thesis including all changes required by the advisory committee. The undersigned agree to abide by the statements above.

Admin Husic, Student

Dr. James F. Fox, Major Professor

Dr. Yi-Tin Wang, Director of Graduate Studies

NUMERICAL MODELING AND ISOTOPE TRACERS TO INVESTIGATE KARST
BIOGEOCHEMISTRY AND TRANSPORT PROCESSES

DISSERTATION

A dissertation submitted in partial fulfillment of the
requirements for the degree of Doctor of Philosophy in the
College of Engineering at the University of Kentucky

By

Admin Husic

Lexington, Kentucky

Director: Dr. James F. Fox, Professor of Civil Engineering

Lexington, Kentucky

2018

Copyright © Admin Husic 2018

ABSTRACT OF DISSERTATION

NUMERICAL MODELING AND ISOTOPE TRACERS TO INVESTIGATE KARST BIOGEOCHEMISTRY AND TRANSPORT PROCESSES

This dissertation investigated the physical and biogeochemical processes affecting the source, fate, and transport of sediment, carbon, and nitrogen within a highly-coupled fluviokarst system. Elemental and isotopic datasets were collected at surface and subsurface locations for both dissolved and particulate contaminant phases, new methodology regarding data collection was presented to the karst research community, an in-cave sediment transport model coupling physical transport with elemental and isotopic mass balances of carbon and nitrogen was formulated, pathway and process control on nitrate leaching from agricultural karst watersheds was assessed, and nitrate mobilization and fractionation were modeled using high frequency storm sampling and long-term low-flow sampling. Data and modeling results indicate that phreatic karst conduits are transport-limited during hydrologic events and experience subsurface deposition of labile, storm-injected sediment which is subsequently decomposed by heterotrophic bacteria. An estimated 30% of the organic carbon associated with sediment is decomposed during transport in the subsurface karst. Concentrations of nitrate in subsurface waters are consistently 50% greater than surface inputs suggesting an additional source of subsurface nitrate. Further modeling of nitrate leaching indicates that quick-flow water sources dilute nitrate concentrations and slow-flow (epikarst and phreatic) sources account for approximately 90% of downstream nitrate delivery. Field sampling of extreme events highlights the physical transport and delayed release of high nitrate concentrations by intermediate karst pathways, which is likely associated with a transition from epikarst to soil drainage during storm recession. Modeling of sediment carbon and nitrogen within the karst SFGL supports the idea that the cave sediment bed experiences hot spots and hot moments of biogeochemical activity. Sediment nitrogen tracing data show a significant increase in $\delta^{15}\text{N}_{\text{Sed}}$ at the spring outlet relative to karst inputs indicating the potential for isotope fractionation effects during dissolved N uptake by cave biota. Dissolved nitrogen stable isotopic composition shows a significant downstream decrease in $\delta^{15}\text{N}_{\text{NO}_3}$ within the conduit, likely associated with nitrification. Data and modeling results of sediment, carbon, and nitrogen emphasize the role of multiple pathways, turbulent transport, and in-conduit transformations in controlling contaminant flux from karst watersheds.

Keywords: karst, sediment, carbon, nitrogen, stable isotopes, numerical model

Admin Husic
Student Signature

05/21/2018
Date

NUMERICAL MODELING AND ISOTOPE TRACERS TO INVESTIGATE KARST
BIOGEOCHEMISTRY AND TRANSPORT PROCESSES

By

Admin Husic

Dr. James F. Fox
Director of Dissertation

Dr. Yi-Tin Wang
Director of Graduate Studies

05/21/2018
Date

ACKNOWLEDGEMENTS

This work benefited greatly from the contributions of my dissertation committee, fellow graduate students, and laboratory technicians and staff. First and foremost, I would like to express my great appreciation to my dissertation advisor, Dr. James F. Fox, for his support throughout my studies. I can only hope to emulate the guidance, mentorship, and positive attitude he exhibited, every day, regardless of the challenges faced along the way. I'd also like to thank the other members of my dissertation committee: Dr. Alan Fryar, Dr. Yi-Tin Wang, Dr. Scott Yost, and outside examiner Dr. Carmen Agouridis. Further, I'd like to extend my thanks to the many undergraduate and graduate students who have helped me along the way whether in the laboratory, the field, or at the computer. Numerous laboratories are also to thank for their contributions to my research learning and data analysis. Particularly, I'd like to thank the Kentucky Geological Survey, the University of Arkansas Stable Isotope Lab, and the University of Kentucky Environmental Research and Training Lab.

This dissertation, data collection and analysis, and my graduate studies were financially supported by the University of Kentucky College of Engineering, the Kentucky Water Resources Research Institute, the United States Geological Survey, the Kentucky State Senate, and the National Science Foundation.

Lastly, I'd like to thank my parents, Senahid and Hajrija, as well as my sisters, Senida, Sabina, Adina, and Emina for their unending love and support even during the hectic times when I could hardly reciprocate it. This dissertation is dedicated to them.

TABLE OF CONTENTS

ACKNOWLEDGEMENTS.....	iii
TABLE OF CONTENTS.....	iv
LIST OF TABLES.....	viii
LIST OF FIGURES.....	x
PREFACE.....	xix
Chapter 1: Sediment Carbon Fate in Phreatic Karst (Part 1): Conceptual Model Development.....	1
1.1 ABSTRACT.....	1
1.2 INTRODUCTION.....	2
1.3 METHODS.....	5
1.3.1 Conceptual Model Development.....	5
1.3.2 Methodological Approach.....	6
1.3.3 Continuous Water Sediment Monitoring.....	8
1.3.4 Sediment Carbon Monitoring.....	9
1.4 RESULTS AND DISCUSSION.....	13
1.4.1 Water Conveyance in Phreatic Karst.....	13
1.4.2 Sediment Transport in Phreatic Karst.....	15
1.4.3 Sediment Carbon Fate in Phreatic Karst.....	18
1.4.4 Implications for Carbon in Fluviokarst.....	21
1.5 CONCLUSIONS.....	24
1.6 ACKNOWLEDGEMENTS.....	25
1.7 TABLES AND FIGURES.....	26
Chapter 2: Sediment Carbon Fate in Phreatic Karst (Part 2): Numerical Model Development and Application.....	40
2.1 ABSTRACT.....	40
2.2 INTRODUCTION.....	41
2.3 METHODS.....	43
2.3.1 Model Formulation.....	43

2.3.2 Model Setup and Discretization.....	46
2.4 RESULTS AND DISCUSSION.....	50
2.4.1 Model Evaluation.....	50
2.4.2 Hydrologic Processes in Phreatic Karst.....	51
2.4.3 Phreatic Karst Actively Convey Sediment Carbon.....	55
2.4.4 Advancement in Numerical Modeling of Karst Systems	56
2.5 CONCLUSIONS.....	57
2.6 ACKNOWLEDGEMENTS.....	58
2.7 TABLES AND FIGURES	59
Chapter 3: Nitrate pathways, processes, and timing in an agricultural karst system: development and application of a numerical model.....	66
3.1 ABSTRACT.....	66
3.2 INTRODUCTION	67
3.3 METHODS	69
3.3.1 Numerical model development and application	69
3.3.2 Karst pathways, processes, and timing of N transport.....	78
3.4 RESULTS AND DISCUSSION	80
3.4.1 Numerical model development and application	80
3.4.2 Karst pathways, processes, and timing of N transport.....	84
3.5 CONCLUSIONS.....	89
3.6 ACKNOWLEDGEMENTS.....	90
3.7 TABLES AND FIGURES	91
Chapter 4: Inland impacts of atmospheric river and tropical cyclone extremes on nitrate transport and stable isotope measurements	107
4.1 ABSTRACT.....	107
4.2 INTRODUCTION	108
4.3 THEORETICAL BACKGROUND.....	110
4.4 STUDY SITE AND MATERIALS	112

4.5 METHODS	113
4.5.1 Characterizing extreme events and their hydrographs.....	113
4.5.2 Water quality and environmental tracer data collection	114
4.5.3 Hydrograph and loadograph separation analyses	116
4.5.4 Nutrient lag effect in rivers	117
4.6 RESULTS AND DISCUSSION.....	117
4.6.1 Characterizing extreme events and their hydrographs.....	117
4.6.2 Water quality and environmental tracer analyses	119
4.6.3 Hydrograph and loadograph separation analyses	123
4.6.4 Nutrient lag effect in karst aquifers	126
4.7 CONCLUSIONS.....	128
4.8 ACKNOWLEDGEMENTS	129
4.9 TABLES AND FIGURES	130
Chapter 5: Nitrogen stable isotopes and numerical modeling show hot moments, hot spots, and environmental drivers in a karst surficial fine-grained laminae	142
5.1 ABSTRACT.....	142
5.2 INTRODUCTION	143
5.3 THEORETICAL BACKGROUND.....	145
5.4 STUDY SITE AND MATERIALS	147
5.5 METHODS	150
5.5.1 Karst SFGL data collection and modeling using stable isotopes.....	150
5.5.2 Hot moments in the karst SFGL	156
5.5.3 Hot spots in the karst SFGL.....	156
5.5.4 Environmental drivers impacting the karst SFGL	157
5.6 RESULTS AND DISCUSSION.....	158
5.6.1 Karst SFGL data collection and modeling using stable isotopes.....	158
5.6.2 Hot moments in the karst SFGL	161
5.6.3 Hot spots in the karst SFGL.....	164
5.6.4 Environmental drivers impacting the karst SFGL	166

5.7 CONCLUSIONS.....	167
5.8 TABLES AND FIGURES	169
Chapter 6: Nitrate removal in a phreatic karst conduit: estimating nitrification and denitrification rates by coupling stable isotope data with numerical modeling	186
6.1 ABSTRACT.....	186
6.2 INTRODUCTION	187
6.3 THEORETICAL BACKGROUND.....	189
6.4 STUDY SITE AND MATERIALS	191
6.5 METHODS	193
6.5.1 Collection of ambient stable N isotope data:	193
6.5.2 Isotope-aided numerical modeling of nitrate removal:	194
6.5.3 Nitrate removal in sinking streams:	197
6.6 RESULTS AND DISCUSSION	198
6.6.1 Collection of ambient stable N isotope data:	198
6.6.2 Isotope-aided numerical modeling of nitrate removal:	201
6.6.3 Nitrate removal in sinking streams:	203
6.7 CONCLUSIONS.....	204
6.8 TABLES AND FIGURES	206
APPENDIX.....	217
Quality Assurance Project Plan (QAPP).....	217
REFERENCES	286
VITA.....	310

LIST OF TABLES

CHAPTER 1

Table 1.1 Water budget for coupled surface-subsurface watershed presented in inches of rainfall per year normalized by catchment area. 26

Table 1.2 Dye trace experiment results from an eclipse karst window to the Groundwater Station (1.5 km)..... 27

Table 1.3 Sediment organic carbon source allocation for varying percent algae. Note: urban tributaries contribute no algal load..... 28

CHAPTER 2

Table 2.1 Model inputs, initial conditions, potential calibration parameters in sediment transport model, and calibration parameters in the carbon model. 59

Table 2.2 Conduit bathymetry, swallet density, and land use information for model cells. *P_{swallet}* represents the proportion of swallets in the watershed located within a particular model cell. *P_{urban}* and *P_{ag}* represent the percentage of land used for agricultural and urban purposes, respectively, contributing to a given model cell. 60

CHAPTER 3

Table 3.1 Review table of NO₃⁻ studies conducted in karst watersheds (n = 22) showing study location, the concentration of quickflow NO₃⁻, and the concentration of discharged aquifer NO₃⁻. 18 of 22 (82%) studies reported higher NO₃⁻ concentrations in aquifer water than in quickflow water. 91

Table 3.2 Hydrologic and nitrogen model inputs and parameters. Each input and parameter is presented with a description, measured or calibrated value, units of measurement, and the source material for the value. Hydrologic and nitrogen model parameter values are presented as the median of the posterior distribution for each parameter. 92

Table 3.3 Hydrologic and nitrogen model evaluation results including number of data points within each calibration/validation set; the methodology for selecting calibration/validation subsets; and the mean, min, and max of the Nash-Sutcliffe Efficiency (NSE) statistic. Mean, min, and max values shown are calculated from all accepted hydrologic (n = 3,653) and nitrogen (n = 2,687) model realizations. 93

Table 3.4 Percentages of water and NO₃⁻ yield ($\pm 1\sigma$) from modeled karst pathways during the study period. 94

Table 3.5 (a) NO₃⁻ budget ($\pm 1\sigma$) for the Royal Spring basin showing inputs (infiltration and quickflow recharge) and outputs (spring, stream, and losses such as pumping). (b) Biochemical reactions ($\pm 1\sigma$) shown as the area-normalized annual masses of NO₃⁻ denitrified, NH₄⁺ nitrified, and DON mineralized within each reservoir. 95

CHAPTER 5

Table 5.1 Summary of dominant processes in subsurface karst SFGL. Note: justification for excluding a process is noted by a parenthetical in the process description. 169

Table 5.2 Nitrogen transformations, equations, terms and units, and associated references. 170

Table 5.3 Model inputs, sediment nitrogen and $\delta^{15}\text{N}_{\text{sed}}$ model parameter ranges and calibrated values, and dissolved N model parameter ranges and calibrated values. 171

Table 5.4 a) Relative air temperature shifts (all increases) for 2057 using GCM ensemble results. b) Relative conduit water temperature shifts (all increases) for 2057 using GCM ensemble results. c) Relative mean flow shifts for 2057 using GCM ensemble results. Results for ± 1 standard deviation (σ) from the projected mean are shown. d) Forecasted scenarios for land cover change for 2057..... 172

Table 5.5 Fate of NO_3^- during temporary residence within karst soil, epikarst, matrix, and conduit (SFGL) zones. Soil, epikarst, and matrix results are from Chapter 3. The SFGL zone is further subdivided to highlight seasonality of conduit N transformation. MRT = mean residence time (see Chapter 3 for MRT method and results). 173

CHAPTER 6

Table 6.1 Inputs and calibration parameters for NO_3^- , $\delta^{15}\text{N}_{\text{NO}_3}$, and $\delta^{18}\text{O}_{\text{NO}_3}$ fate and transport model. Input and parameter descriptions, ranges, calibrated values, and units are presented. 206

Table 6.2 Nitrogen transformations, equations, terms and units, and associated references. 207

LIST OF FIGURES

CHAPTER 1

Figure 1.1 Conceptual model of sediment organic carbon (SOC) transport in phreatic karst. Bold text indicates processes..... 29

Figure 1.2 Diagram of the methodological approach for the fluviokarst sediment organic carbon study. 30

Figure 1.3 (a) Cane Run watershed and Royal Spring basin, (b) karst swallet pirating surface flow during low flow, and (c) watershed attributes..... 31

Figure 1.4 Inflows and outflows to the watershed normalized by maximum flow rate at each respective location. 32

Figure 1.5 Temperature fluctuations during a storm at four sampling sites. Discharge shown on figure is from the Surface Outflow site. 33

Figure 1.6 Suspended sediment concentration at tributaries and Groundwater Station on the left. Suspended sediment discharge normalized by maximum sediment discharge at each location on the right. *Gap in Groundwater Station data starting on May 20, 2013 due to instrument failure. 34

Figure 1.7 Particle size distribution at inflows and outflows to the watershed. 35

Figure 1.8 Suspended sediment flux comparison for four characteristic hydrologic events. Note that the y-axis is normalized discharge; the urban tributary discharges a larger magnitude overall..... 36

Figure 1.9 Transport carrying capacity of urban and agricultural tributaries and the conduit normalized by maximum transport carrying capacity at each respective location. 37

Figure 1.10 Organic carbon content and carbon isotope values for inflowing tributary (n = 32) and outflowing spring (n = 18) sediment..... 38

Figure 1.11 Schematic of the fate of sediment organic carbon in the fluvial environment with and without the phreatic karst. (After Fox and Ford, 2016; Marín-Spiotta *et al.*, 2014). 39

CHAPTER 2

Figure 2.1 Fluviokarst sediment and carbon transport modeling framework. STAGE 1: model preparation. Sediment pirated from tributaries (Q_{ss}), conduit flow rate (Q_i), and hydraulic and hydrologic input were calculated for use in model. STAGE 2: Sediment Transport Model (STM). Transport coefficients (C_{tc}) were calibrated to match STM results with TSS data. STAGE 3: Carbon Model (CM). The generalized likelihood uncertainty estimation (GLUE) method was performed to estimate the distribution of results, model domain, and optimal model run for the CM..... 61

Figure 2.2 (a) Sediment model calibration and validation at the Groundwater Station. (b) Probability density functions and (c) cumulative distribution functions of data and model-integrated results. 62

Figure 2.3 (a) Sediment model results at the Groundwater Station, and (b) longitudinal surface fine grained laminae (SFGL) depth changes in conduit. 63

Figure 2.4 (a) Sediment organic carbon flux (Q_{soc}) in the subsurface conduit at the Groundwater Station (GW) compared to Royal Spring (RS) and organic carbon percentage in suspended sediment and bed sediment at GW. (b) Fractioning of carbon pools in conduit bed (SFGL) and suspended sediment (SS) at GW. 64

Figure 2.5 Sediment and SOC budget for the Cane Run watershed. Surface processes shown are tributary sediment production, sediment pirating to the subsurface, in-stream storage, and surface stream sediment yield. Subsurface processes shown are deposition, erosion, mixing (i.e. equilibrium sediment exchange between SFGL and SS), and yield of conduit sediment, as well as decomposition of sediment organic carbon. Sediment flux is represented in tons (t) and Sediment organic carbon flux is represented in tons Carbon (tC). 65

CHAPTER 3

Figure 3.1 Conceptual model of water and NO_3^- pathways in an agricultural karst system. Contaminant provenance includes surface, subsurface, distributed, and point sources and pathways. The accumulation of NO_3^- within the karst aquifer followed by a release to the primary conduit results in NO_3^- leaching losses to downstream waterbodies. 96

Figure 3.2 Model framework for water and nitrogen processes and pathways in a karst aquifer. Recharge (R) of water, NO_3^- , NH_4^+ , and DON is applied as concentrated input to the quickflow reservoir (X) or as distributed input to soil ($I-X$). Distributed recharge of NO_3^- , NH_4^+ , and DON represents bulk infiltration of material (e.g., precipitation, fertilizer, manure and sewage) to the soil. Evapotranspiration (ET_A), flow to surface stream (Q_{stream}) which includes runoff (x_{REC}) and lateral soil flow (x_{SOIL}) fractions, and percolation (Q_{soil}) are outflows from the soil reservoir. Soil field capacity is represented by $V_{S,MIN}$ and saturation conditions by $V_{S,MAX}$. Concentrated recharge to the quickflow reservoir includes sinkholes, swallets, and stream abstractions (dashed line). Outflow from the quickflow reservoir (Q_Q) occurs via shaft, sinkhole, and swallet discharge to the conduit. The epikarst is recharged by soil percolation and discharges water via seepage to the phreatic aquifer (Q_{EL}) or as conduit recharge via larger fractures (Q_E). Direct flow from the epikarst to the conduit occurs when dynamic storage within the epikarst exceeds a threshold ($V_{E,FAST}$). Finally, the phreatic zone is recharged by the epikarst and losses are attributed to diffuse flow (Q_P) and pumping losses (Q_{PUMP}) related to agricultural and other human demands. The level at which baseflow to the spring ceases (i.e., the spring runs dry) is represented by $V_{P,MIN}$, and pumping losses are stopped when drawdown reaches V_{PUMP} 97

- Figure 3.3 Cane Run Watershed and Royal Spring Basin indicating sampling sites, karst holes, and the primary conduit conveyance zone for fluid and nutrients..... 98
- Figure 3.4 Master recession curve (MRC) for Royal Spring using nine events over a decade of flow data. The MRC was decomposed into three constituent reservoirs (quick, epikarst, phreatic) and recession coefficients ($\alpha_1, \alpha_2, \alpha_3$) were fitted to match data results (see Malík and Vojtková, 2012). 99
- Figure 3.5 Framework for evaluating hydrologic and nitrogen model uncertainty in parameters and predictions. Hydrologic model parameters (θ) are sampled from an assumed prior distribution. The parameters are fed into the numerical model, M , and simulated model results (Q) are compared to measured flow data (\tilde{Q}). Only model realizations and parameter sets that satisfy the objective function are retained. Accepted hydrologic parameter sets are fed through to the dissolved nitrogen model where biochemical parameters (x) are sampled and model results (C_{NO_3}) are evaluated against measured spring data (\tilde{C}_{NO_3}). Evaluation statistics for the dissolved nitrogen model include a Nash-Sutcliffe (NSE) function for Spring NO_3^- results and t-tests for modeled vs measured means of Stream NO_3^- , Spring NH_4^+ , and Spring DON. Lastly, accepted hydrologic and biochemical realizations are used to construct posterior parameter distributions and prediction bounds. 100
- Figure 3.6 Concurrently sampled ($n = 99$) surface stream (CRCK) and subsurface phreatic conduit (KYHP) NO_3^- concentrations. 101
- Figure 3.7 (a) Hydrologic model results simulating Royal Spring discharge. (b) Nitrogen model results simulating NO_3^- concentration at Royal Spring. (c) NO_3^- concentration within the four modeled reservoir pathways. Prediction bounds for each pathway include 66% of accepted results – rather than 95% – for visual clarity of the differences in mean pathway concentrations. 102
- Figure 3.8 (a) Prior and posterior distributions of hydrologic model parameters: X (concentrated recharge fraction), k_{soil} (soil discharge coefficient), k_{stream} (stream discharge coefficient), k_{EL} (epikarst seepage discharge coefficient), Q_{PUMP} (aquifer pumping rate), $V_{S,MIN}$ (soil field capacity), $V_{S,MAX}$ (soil saturation), $V_{E,FAST}$ (activation height for fast epikarst pathways), and $V_{P,MIN}$ (height at which aquifer over-extraction causes an end to pumping). (b) Prior and posterior distributions of nitrogen model parameters: denitrification ($k_{S,DEN}$, $k_{E,DEN}$, and $k_{P,DEN}$), nitrification ($k_{S,NITR}$, $k_{E,NITR}$, and $k_{P,NITR}$), and mineralization ($k_{S,MIN}$, $k_{E,MIN}$, and $k_{P,MIN}$) transformation rates for soil, epikarst, and phreatic pathways, respectively. Also shown are the seasonal NO_3^- concentrations for fall ($C_{NO_3(F)}$), winter ($C_{NO_3(W)}$), spring ($C_{NO_3(SP)}$), and summer ($C_{NO_3(SU)}$) recharge. Note: the x-axis for transformation rates is presented as the \log_{10} value of the rate. 103
- Figure 3.9 (a) Modeled mean residence time of spring water decomposed into three karst pathways (results presented are from the optimal simulation). (b) Autocorrelation

	analysis of modeled and measured spring discharge. (c) Cross-covariance analysis of rainfall with modeled and measured spring discharge. Model bounds include 95% of accepted model simulations.	104
Figure 3.10	Nitrate source contribution via multiple karst pathways over a two year period for the optimal model simulation. The top plot shows the fraction of each pathway to the total NO_3^- load. Blank (white) spaces indicate no discharge at the spring. During dry summer periods, particularly when aquifer stores have experienced over-pumping, the spring water level will drop below the weir where flow is recorded. The bottom plot is an area graph and quantifies the NO_3^- load of each pathway as the area between two curves.	105
Figure 3.11	Comparison of Cane Run Creek-Royal Spring (CR+RS) to a neighboring immature karst watershed, South Elkhorn Creek (SE) (Ford <i>et al.</i> , 2017). (a) Area-normalized N load, (b) close-up of six months of N load, and (c) highlighting low-flow N dynamics in CR+RS.	106
CHAPTER 4		
Figure 4.1	(a) Location, names, and generalized orientation of coastal extreme events on the conterminous United States. The Maya Express is an atmospheric river (orange arrow). Hurricanes and Tropical Storms are tropical cyclones (blue arrows). The white star represents the study region located within Kentucky. (b) Trajectory of the Maya Express (Moore et al. 2012). Surface fronts are shown in their standard frontal notation. The orange line represents a stream of dry midlevel air and the blue line represents the atmospheric river. Red lines and the green light shading around the atmospheric river denote streamlines above the atmospheric boundary layer and areas of high water vapor. (c) Trajectory of an inland tropical cyclone (NHC NOAA, 2017). The light orange shading represents areas of tropical-level winds. Red and blue colors indicate hurricane and tropical storm warnings, respectively. The white cone represents probable path of the storm center.	130
Figure 4.2	(a) Pathway diagram showing quickflow, intermediate flow (epikarst + soil), and slow flow (phreatic). (b) An image of a karst swallet in Cane Run Creek, Kentucky (Husic et al. 2017a). (c) Surficial epikarst features in Bowman’s Bend of the Kentucky River (Phillips, 2015). (d) Nutrient lag effect (Clare et al. 2018).	131
Figure 4.3	Cane Run Watershed and Royal Spring Basin indicating drainage basins, primary conduit conveyance zone for flow and nutrients, the three sampling sites (Royal Spring, Phreatic Conduit, and Cane Run Creek), karst holes, surface channels, and the flow direction for surface and subsurface discharges.	132
Figure 4.4	Rainfall intensity for the 2017 calendar year and the timing of two sampled extreme events. Total annual rainfall is 1,249 mm. The two storms approximate	

- winter/spring (Storm #1) and fall (Storm #2) hydrologic events. Rank is determined by the three-day precipitation total of an event..... 133
- Figure 4.5 Precipitation, stream flow, groundwater elevation (above mean sea level), spring discharge, specific conductance, and temperature data results. The dashed horizontal line on the second row represents the elevation. The surface stream discharge peaks quickly to rainfall input relative to spring discharge. The groundwater elevation in the well intersecting the conduit corresponds closely to spring discharge. Specific conductance and temperature of the conduit and spring are largely influenced by the surface creek and are either warmed or cooled depending on season..... 134
- Figure 4.6 NO_3^- , $\delta^{15}\text{N}_{\text{NO}_3}$, and $\delta^{18}\text{O}_{\text{NO}_3}$ signatures of creek, conduit, and spring water during two extreme events. NO_3^- is initially diluted by surface quickflow during both events. The temporal changes in $\delta^{15}\text{N}_{\text{NO}_3}$ and $\delta^{18}\text{O}_{\text{NO}_3}$ in the conduit and at the spring are similar for both storms. 135
- Figure 4.7 $\delta^2\text{H}_{\text{H}_2\text{O}}$, $\delta^{18}\text{O}_{\text{H}_2\text{O}}$, and $\delta^{13}\text{C}_{\text{DIC}}$ signatures of creek, conduit, and spring water during two extreme events. Variability is limited in the $\delta^2\text{H}_{\text{H}_2\text{O}}$ and $\delta^{18}\text{O}_{\text{H}_2\text{O}}$ signatures during Storms 1 and 2, but the fall event caused by Hurricane Nate delivered highly depleted rain water (close to that of sea surface water vapor $\delta^{18}\text{O}_{\text{H}_2\text{O}} \sim -12\text{‰}$). Likewise, $\delta^{13}\text{C}_{\text{DIC}}$ data indicate delivery of highly depleted DIC during Storm 2. 136
- Figure 4.8 (a) $\delta^2\text{H}_{\text{H}_2\text{O}}$ and $\delta^{18}\text{O}_{\text{H}_2\text{O}}$ of all samples collected for the two storm events. (b) Sample sets collected from creek, conduit, and spring in relation to spring hydrograph. (c) Zoom-in on Storm #3 (Hurricane Nate). $\delta^2\text{H}_{\text{H}_2\text{O}}$ and $\delta^{18}\text{O}_{\text{H}_2\text{O}}$ signatures show an appreciable effect of coastal water delivery to inland Kentucky *via* the shift towards lighter isotopes of water during peak event activity. Numbers inset in gray circles in (c) indicate the approximate $\delta^2\text{H}_{\text{H}_2\text{O}}$ and $\delta^{18}\text{O}_{\text{H}_2\text{O}}$ average of creek, conduit, and spring samples in a set. GMWL = global mean water line. 137
- Figure 4.9 Method for hydrograph and loadograph recession analyses and separation of pathways. (a) During the spring event (atmospheric river), quickflow-epikarst and epikarst-phreatic inflection points occur 0.5 and 5.8 days, respectively, after peak of event. (b) During the fall event (tropical cyclone), quickflow-epikarst and epikarst-phreatic inflection points occur 2.5 and 6.3 days, respectively, after peak of event. Note: Abrupt spikes and drops in the recession hydrographs are the result of periodic pumping, by a water treatment plant, directly upstream of the v-notch weir where water depth is gaged. These abstractions were considered when estimating the recession lines. 138
- Figure 4.10 (a) Atmospheric river (spring storm) loadograph results separated into three separate pathways (quickflow, epikarst, and phreatic). The dashed lines direct to the inflection points (quickflow-epikarst and epikarst-phreatic) identified by the

	recession analysis. (b) Same as (a) but for the tropical cyclone event. (c) The fraction of the total event spring discharge and nitrate loading per pathway for the atmospheric river and tropical cyclone events. Note: Abrupt spikes and drops in the loadograph are the result of periodic pumping, by a water treatment plant, directly upstream of the v-notch weir where water depth is gaged.....	139
Figure 4.11	Temporal changes in water quality and isotopes plotted alongside the flow contribution of different pathways during the two extreme events. The left axis corresponds with samples collected at spring, conduit, and creek sites. The right axis is the discharge by each pathway.....	140
Figure 4.12	Conceptualized response of nitrate to extreme events in a mature karst watershed. Prior to a storm event, when the epikarst and soil are disconnected from the spring, nitrate concentrations are constant ($t = 0$). An initial decrease to the nitrate concentration (C_{NO_3}) is caused by dilute storm recharge. Nitrate concentration increases as epikarst flow (Q_{epi}) becomes more dominant ($t = 1$). There is a time lag between peak epikarst discharge and peak nitrate concentration (t_{lag}). This lag occurs as pre-storm epikarst water drains and is recharged by nitrate-rich soil water ($t = 2$). Lastly, as the hydrograph recedes, nitrate concentrations return to phreatic groundwater levels.	141
CHAPTER 5		
Figure 5.1	Lighted photograph of the karst SFGL from an underwater camera placed in a groundwater well that intersects a phreatic conduit 20 meters below the ground surface. SFGL = “surficial fine-grained laminae”.	174
Figure 5.2	(a) Conceptual model of sediment carbon (SOC) and nitrogen (SN) delivery, trapping, and export in fluvio karst system. Emboldened text indicates processes. (b) Transect of a phreatic conduit illustrating dominant processes. Inflow of SOC and SN is supplied by quickflow pathways and inflow of dissolved inorganic N and dissolved organic N is supplied by quickflow, fracture, and matrix pathways. Physical processes include deposition, erosion, and equilibrium mixing. Biochemical processes include N immobilization, mineralization, nitrification, denitrification, anammox, and C decomposition.	175
Figure 5.3	(a) Cane Run watershed and Royal Spring basin, (b) karst swallet pirating surface flow during low flow, and (c) watershed attributes	176
Figure 5.4	Sediment N concentration (C_{SN}), sediment N isotope ($\delta^{15}N_{Sed}$), and nitrate (C_{NO_3}) modeling framework. STAGE 1: Model inputs from previously published water, sediment, and carbon (Husic <i>et al.</i> , 2017a,b), and NO_3^- pathway recharge (Chapter 3) results. STAGE 2: Sediment N and $\delta^{15}N_{Sed}$ modeling. Immobilization and mineralization rates (k_{imm} and k_{min}) of nitrogen pools (i.e., algae, litter, and soil) were calibrated and evaluated using a t-test. STAGE 3: Dissolved nitrogen (NO_3^- , NH_4^+ , and DON) modeling. Sensitive rates (β_{DEN} and k_{nitr}) were calibrated to match model results to C_{NO_3} data.....	177

Figure 5.5 Elemental and isotopic data results for (a) stable nitrogen isotope of sediment ($\delta^{15}N_{Sed}$), and (b) sediment nitrogen (SN) at two surface tributaries (Spindletop and Lexmark) and the conduit discharge point (Royal Spring).	178
Figure 5.6 Modeled results of (a) SOC, (b) SN, (c) $\delta^{13}C_{Sed}$, and (d) $\delta^{15}N_{Sed}$ at Royal Spring. Legend: Blue line indicates composition of suspended sediment, solid black line indicates composition of the SFGL, and dashed black line indicates average composition of pirated surface sediment. Black and red bars represent data and model results with the width of each bar describing the deployment duration of the temporally-integrated sediment trap sample.	179
Figure 5.7 Histogram distribution of data and model results at Royal Spring (n = 18) for (a) SOC, (b) SN, (c) $\delta^{13}C_{Sed}$, and (d) $\delta^{15}N_{Sed}$	180
Figure 5.8 Measured vs modeled NO_3^- concentrations. The model simulates the typical range of observed NO_3^- (0 to 4 mg N L ⁻¹) well. Three data points during disproportionately affect model statistics and are associated with a transient event of high NO_3^- flushing.	181
Figure 5.9 Time-series of modeled NO_3^- concentrations for water recharging the conduit (inflowing) and water discharging at KYHP (outflowing). (a) During the entire study period, (b) zoomed-in view a wet season (net-nitrifying), and (c) zoomed-in view of a dry season (net-denitrifying). Shaded regions indicate dry seasons.	182
Figure 5.10 Mean (i.e. averaged over the entire conduit) transformations and removal of (a) NH_4^+ and (b) NO_3^- over the two-year study period. For example, positive NO_3^- removal values represent NO_3^- losses (e.g. denitrification) whereas negative removal values represent additions to the NO_3^- pool (e.g. nitrification). Spring discharge is shown on the secondary axis. Shaded regions indicate dry seasons.	183
Figure 5.11 (a) Modeled NO_3^- removal and (b) modeled sediment carbon and (c) nitrogen content as they vary spatially within the karst SFGL over the course of the two year study period. Positive NO_3^- removal values represent aggregate NO_3^- losses (e.g. denitrification) whereas negative removal values represent additions to the NO_3^- pool (e.g. nitrification). Results indicate that cells with greater sediment carbon contents remove relatively more NO_3^- during the dry season and contribute relatively less NO_3^- during the wet season. Additionally, upstream cells (spatial steps 1 to 10) are more well-connected to labile organic inputs from the surface than are downstream cells (spatial step 11 to 16). Gaps in continuous modeling indicate that a substrate was exhausted (i.e. complete erosion of SFGL). Shaded regions indicate dry seasons.	184
Figure 5.12 (a) Change in net-nitrate removal in karst SFGL under varying temperature, flow discharge, and land use 2057 scenarios. (b) Percent change in model yields	

and fluxes under varying temperature, flow discharge, and land use 2057 scenarios. 185

CHAPTER 6

Figure 6.1 Conceptual model of physical and biogeochemical carbon and nitrogen processes in a subsurface conduit. Physical processes are shown in black arrows. Biogeochemical processes are shown in orange arrows. Fractionations for each transformation are also identified. 208

Figure 6.2 Cane Run Watershed and Royal Spring Basin indicating the Phreatic Conduit and Royal Spring sites. During low-flow periods, flow between these two points is believed to consist of the same material. Also shown is the location of the surface Cane Run Creek that is activated during moderate to large events. ... 209

Figure 6.3 Daily average air temperature, spring discharge, and precipitation intensity for the 2017 year. High air temperatures coincide with a low spring discharge and limited recharge to the conduit. One such period is identified with a dashed box and serves as the focus of this study. The numbers inset in the dashed box enumerate the low-flow periods of 10 or more consecutive days. 210

Figure 6.4 Model calibration and uncertainty framework for evaluating NO_3^- and $\delta^{15}\text{N}_{\text{NO}_3}$, NH_4^+ , and DON model results. R_{NH_4} represents the ratio of average NH_4^+ into vs out of the conduit. R_{DON} is calculated the same way as R_{NH_4} , but for DON. Modeled R_{NH_4} and R_{DON} were compared to data R_{NH_4} and R_{DON} to constrain uncertainty in NH_4^+ and DON inputs. For a definition of other terms see Table 1. 211

Figure 6.5 Water quality data collected at the subsurface conduit and the primary spring. The top plot shows groundwater elevation (above mean sea level) at the conduit and discharge at the spring. The dashed horizontal line represents the spring elevation. In the bottom plot, water temperature (solid lines) and specific conductivity (dashed lines) at the conduit (black) and spring (blue) sites are shown. Environmental data show that water is cooled and becomes more conductive during transport within the conduit. Areas shaded in gray indicate low-flow periods (defined as 10 or more days with less than $0.3 \text{ m}^3 \text{ s}^{-1}$). 212

Figure 6.6 Elemental and isotopic data collected at the subsurface conduit and the spring. (a) NO_3^- concentration decreases temporally during dry periods, but tends to increase longitudinally from conduit to spring. (b) $\delta^{15}\text{N}_{\text{NO}_3}$ increases temporally, indicating enrichment of NO_3^- , but tends to decrease longitudinally, suggesting an additional mineralization or nitrification source. (c) $\delta^{18}\text{O}_{\text{NO}_3}$ at the two sites is not significantly different ($p = 0.66$), is highly variable, and does not show any discernable trends. Areas shaded in gray indicate low-flow periods (defined as 10 or more days with less than $0.3 \text{ m}^3 \text{ s}^{-1}$). 213

Figure 6.7 $\delta^{18}\text{O}_{\text{NO}_3}$ and $\delta^{15}\text{N}_{\text{NO}_3}$ of collected samples from conduit and spring locations. At first observation, samples collected at the spring outlet could ostensibly indicate

denitrification, but the observed longitudinal trend shows a relatively depleted spring $\delta^{15}\text{N}_{\text{NO}_3}$ relative to the intermediate conduit location, suggesting additional in-conduit biogeochemical cycling (i.e., nitrification). We note a statistically significant ($p < 10^{-5}$) difference in $\delta^{15}\text{N}$ means (spring: $6.48 \pm 1.17\text{‰}$ vs conduit: $7.80 \pm 1.41\text{‰}$), but not in $\delta^{18}\text{O}$ signatures ($p = 0.66$) of the two sites. Approximate NO_3^- sources and their ranges are demarcated (adapted from Kendall *et al.*, 2008). The “Denitrification Trend” is manually drawn through the data with a 1:2 slope (Kendall *et al.*, 2008)..... 214

Figure 6.8 Modeling results of (a) NO_3^- , (b) $\delta^{15}\text{N}_{\text{NO}_3}$, and (c) $\delta^{18}\text{O}_{\text{NO}_3}$ for three low-flow periods contained within the sampling duration. Input concentrations to the study section (gray lines) are interpolated from data (see Figure 4) while outflowing concentrations at the spring (shaded blue area) are continuously simulated. Spring output is presented as the 95% prediction bound from the set of acceptable model simulations. Blue dots represent discrete data points collected at the primary spring. Sub-models were evaluated using the Nash-Sutcliffe Efficiency and the resulting value for the best cumulative run is shown on each graph. Areas shaded in gray indicate low-flow periods (defined as 10 or more days with less than $0.3 \text{ m}^3 \text{ s}^{-1}$). 215

Figure 6.9 Prior (uniform) and posterior histogram densities of model parameters and inputs. Parameters such as the enrichment factors of nitrification (ϵ_{nitr} and ϵ_{IN}) and the recharge concentration of NH_4^+ and signature of $\delta^{15}\text{N}_{\text{NH}_4}$ during event 3 are sensitive while others such as enrichment factor of immobilization (ϵ_{imm}), reaction coefficient for indirect nitrification (β_{IN}), and the recharge signature of $\delta^{15}\text{N}_{\text{DON}}$ are not sensitive..... 216

PREFACE

Chapter	New Dataset	Innovative Method	Main Concluding Results
1	Two years of: <ul style="list-style-type: none"> • Conduit velocity • Sediment concentration and particle size • Sediment organic carbon and $\delta^{13}\text{C}_{\text{Sed}}$ 	Conceptual model of sediment and sediment organic carbon fate and transport in karst.	Sediment transport carrying capacity behavior in karst investigated for first time. Karst pathways act as discontinuities in the fluvial fate of sediment carbon by discharging relatively depleted sediment earlier on in the fluvial continuum.
2	Same as companion chapter 1.	Numerical model for sediment and sediment carbon fate and transport in karst.	Exchange of new and old sediment; residence time of sediment in caves; high C turnover rates relative to surface.
3	4 years of nitrate data in conduit and at surface creek.	Reservoir model applied to karst hydrology for nitrogen model. Uncertainty reduction using nitrogen data.	Coupling water and nitrogen datasets reduces water equifinality by 68%. Slowflow dominates karst N load (over 89% of total load), and is due to leaching from epikarst
4	High-frequency NO_3^- , $\delta^{15}\text{N}_{\text{NO}_3}$, $\delta^{18}\text{O}_{\text{NO}_3}$, $\delta^2\text{H}_{\text{H}_2\text{O}}$, $\delta^{18}\text{O}_{\text{H}_2\text{O}}$, and $\delta^{13}\text{C}_{\text{DIC}}$ during two extreme events (an atmospheric river and tropical cyclone).	Loadograph recession analysis to estimate pathways and transport of NO_3^- during extreme events in karst.	Coastally derived extremes can have varying effects on karst response depending on rainfall intensity and distribution. Peak NO_3^- contamination occurs after peak storm flow. The lag likely occurs as epikarst drains soil-derived water.
5	Two years of: <ul style="list-style-type: none"> • Sediment nitrogen • $\delta^{15}\text{N}_{\text{Sed}}$ 	Numerical model for sediment nitrate fate and transport in karst for hot spots and hot moments. Environmental driver and climate modeling impacts on karst N removal.	Hot spots in karst are related to areas of the karst conduit highly-connected to the surface. Hot moments in karst are related to dry seasons. Both are affected by forecasted climate and land use changes.
6	Long-term (65 consecutive days), paired sampling at two locations within a conduit. <ul style="list-style-type: none"> • NO_3^- • $\delta^{15}\text{N}_{\text{NO}_3}$ • $\delta^{18}\text{O}_{\text{NO}_3}$ 	Nitrogen and oxygen isotope fractionation model developed for a karst conduit. Data method of sampling a conduit control volume during an extended low-flow period.	Nitrification and denitrification rates reported for karst conduits for the first time. Rates are a magnitude greater than porous groundwater media, but a magnitude less than surface water. Isotope-aided modeling helps reduce uncertainty when estimating nitrate removal.

Chapter 1: Sediment Carbon Fate in Phreatic Karst (Part 1): Conceptual Model Development

Adapted with permission from Husic *et al.*, 2017. Sediment Carbon Fate in Phreatic Karst (Part 1): Conceptual Model Development. *Journal of Hydrology* 549, 179-193.

Copyright © 2017 Elsevier

1.1 ABSTRACT

Recent research has paid increased attention to quantifying the fate of carbon pools within fluvial networks, but few, if any, studies consider the fate of sediment organic carbon in fluviokarst systems despite that karst landscapes cover 12% of the earth's land surface. The authors develop a conceptual model of sediment carbon fate in karst terrain with specific emphasis upon phreatic karst conduits, i.e., those located below the groundwater table that have the potential to trap surface-derived sediment and turnover carbon. To assist with their conceptual model development, the authors study a phreatic system and apply a mixture of methods traditional and novel to karst studies, including electrical resistivity imaging, well drilling, instantaneous velocimetry, dye tracing, stage recording, discrete and continuous sediment and water quality sampling, and elemental and stable carbon isotope fingerprinting.

Results show that the sediment transport carrying capacity of the phreatic karst water is orders of magnitude less than surface streams during storm-activated periods promoting deposition of fine sediments in the phreatic karst. However, the sediment transport carrying capacity is sustained long after the hydrologic event has ended leading to sediment resuspension and prolonged transport. The surficial fine-grained laminae occurs in the subsurface karst system; but unlike surface streams, the light-limited conditions of the subsurface karst promotes constant heterotrophy leading to carbon turnover. The coupling of the hydrological processes leads to a conceptual model that frames phreatic karst as a biologically active conveyor of sediment carbon that recharges degraded organic carbon back to surface streams. For example, fluvial sediment is estimated to lose 30% of its organic carbon by mass during a one year temporary residence within the phreatic karst. It is recommended that scientists consider karst pathways when attempting to estimate organic matter stocks and carbon transformation in fluvial networks.

1.2 INTRODUCTION

Fluvial networks are recognized to not only act as conveyors of sediment organic carbon to the ocean, but also to serve as ecosystems that can actively turnover carbon (Battin *et al.*, 2008). Sediment carbon enters the fluvial system via multiple routes which include overland runoff, subsurface flow, mass wasting, and abscission as well as from autochthonous growth within the fluvial system (Ford and Fox, 2014; Hotchkiss and Hall, 2015). It is now recognized that sediment carbon is an important energy source for decomposers and that microbial oxidation results in the production of carbon dioxide and increasingly degraded terrestrially-derived carbon longitudinally in a fluvial system (Swift *et al.*, 1979; Moore *et al.*, 2004). However, the degradation state of sediment carbon and its downstream fate remain highly uncertain with open questions regarding the spatial variability of turnover, temporary burial, and removal of sediment carbon from active carbon cycles (Cole *et al.*, 2007). In this context, one area that has not been well investigated is sediment carbon fate in fluvial systems that drain karst landscapes.

Karst landscapes are typified as solutionally dissolved landscapes that are dominated by secondary and tertiary porosity features (e.g., macropores, fractures, and conduits) that produce low-resistance pathways for water transport (Thraillkill, 1974; Smart and Hobbs, 1986; Pronk *et al.*, 2009b). When coupled to surface streams of the fluvial network, mature karst topography is well-recognized to include subterranean fluid pathways that act as turbulent conduits conveying fluid from surface sinks termed swallets to sources called springs (White, 2002). Karst watersheds often carry high loads of sediment brought in by sinking streams and other karst features (Drysedale *et al.*, 2001). In this manner, karst topography provides subsurface pathways for water, sediment, and carbon transport whereby both terrestrially- and aquatically-derived sediment carbon can be temporarily sequestered and transformed only to resurface further downstream. It is highly reasonable that temporarily stored sediment carbon is oxidized and results in a net production of CO₂ given that bacteria and other microbes within epilithic biofilms in subsurface karst utilize particulate and dissolved organic carbon as an energy source (Chapelle, 2001; Danovaro *et al.* 2001; Simon *et al.*, 2003; Goldscheider *et al.*, 2006; Humphreys, 2006; Simon *et al.*, 2007). Accounting for the spatiotemporal distribution and variability of organic matter inputs, turnover, and fluxes has been identified as one of the

greatest challenges in estimating sediment carbon fate in karst (Simon *et al.*, 2007; Pronk *et al.*, 2009a). Thus, the motivation of this paper is towards elucidating the role of hydrologic processes impacting sediment carbon in fluviokarst landscapes and working towards a conceptual model of sediment carbon fate within fluviokarst systems.

A precursor to a conceptual model of sediment carbon impacted by karst is the non-trivial task of estimating the morphology of karst systems, hydraulics of karst water conveyance, and physics of subsurface sediment transport within karst conduits. The comprehensive review of karst hydrology by White (2002) suggested that sediment transport in karst settings remained one of the most unstudied aspects of karst in need of research. Since that time, a number of groups have investigated the ability of fluviokarst networks to transport sediment and have found that rainfall activated surface tributaries can carry high sediment loads and provide quickflow to the subterranean karst (Hart and Schurger, 2005; Massei *et al.*, 2003); karst drainages entrain and transport sediment loads as function of fluid intensity, similarly to surface streams (Dogwiler and Wicks, 2004); and karst systems store and convey a distribution of sediment under varying ground saturation, moisture, and discharge conditions (Hart and Schurger, 2005; Herman *et al.*, 2008). From recent sediment transport studies, an important feature has been the realization of a sub-classification of karst in phreatic systems. Phreatic conduits are situated below the water table and therefore have a downstream hydraulic control structure, i.e., subterranean dam, or adverse conduit gradient in the streamwise direction that produces saturated flow conditions. In terms of hydraulics, phreatic conduits have an upper limit for their energy gradient and thus upper limit for fluid conveyance due to the existence of the downstream controls. The fluid energy threshold of the phreatic conduits offers the potential to trap sediment either temporarily or permanently (Herman *et al.*, 2008), which highlights the potential for sediment carbon mineralization within the fluviokarst system.

Advancement in our understanding of sediment carbon fate and hydrological processes in karst relies on the application of new or advanced instrumentation within karst systems as well as adopting existing methods from other fluvial settings and applying them to karst. Methods in karst have been greatly advanced in recent years, with a number of methods available for hydrologic analysis. Water conveyance methods generally consist of gaging stations for flow estimation installed at swallow holes and springs (Mahler and

Lynch, 1999; Bonacci, 2001; Reed *et al.*, 2010), piezometers for continuous measurement of the groundwater table (Long and Derickson, 1999), and natural as well as artificial tracers for understanding water origin and connectivity between surface and subsurface pathways (Katz *et al.*, 1997; Perrin *et al.*, 2003; Barbieri *et al.*, 2005). Sediment measurements in karst aquifers are typically performed by scraping cave surfaces, pumping or coring at well sites, automated pump sampling at spring outlets (Mahler *et al.*, 1999; Herman *et al.*, 2008; Reed *et al.*, 2010), and use of sediment fingerprinting techniques for distinguishing sediment sources and estimating residence time (Mahler *et al.*, 1998; Pronk *et al.*, 2006).

In the present paper, the authors apply the above mentioned data collection methods and also work to extend the karst scientific toolbox in order to understand sediment carbon fate. The authors apply carbon stable isotopes for understanding the source of sediment carbon supplied to the karst subsurface *via* swallets and for investigating the fate of carbon within the subsurface. The stable isotopic signature of carbon ($\delta^{13}\text{C}$) is inherently linked to the land use origin of sediment from different plant type and management scenarios (Fox and Papanicolaou, 2008) as well as to the organic matter structure of carbon due to its sensitivity to the level of microbial processing (Acton *et al.*, 2013). Carbon stable isotopes have been previously used in fluvial environments for understanding the source and fate of sediment carbon as well as within sediment fingerprinting (Fox and Papanicolaou, 2007; Fox, 2009; Jacinthe *et al.*, 2009; Mukundan *et al.*, 2010; Ford and Fox, 2015; Fox and Martin, 2015). However, to the authors' knowledge, the method has not been applied in karst settings. In addition to the use of stable isotopes and traditional sampling methods, the authors install several monitoring wells which directly intersect the primary karst at its longitudinal midpoint in order to continuously monitor water and sediment. The authors find few studies in the literature that have continuously collected hydrologic data at karst inlets and outlets as well as from within the primary conduit draining the aquifer.

This study's objectives were to elucidate previously unstudied hydrological processes within phreatic karst and develop a conceptual model of sediment carbon fate within phreatic karst. The conceptual model is discussed in the context of active freshwater carbon cycles. Thereafter, the conceptual model is used as a guide to build a numerical

model in our companion paper (Paper 2: Numerical Model) that immediately follows this article in this journal.

1.3 METHODS

1.3.1 Conceptual Model Development

The authors focus their conceptual model development for sediment carbon in phreatic karst upon hydrologic and landscape features that provides a sub-classification of karst systems (see Figure 1.1). The authors emphasize mature, phreatic karst systems with hydraulically connected surface water and subsurface water. Sinking streams and swallets located in the surface stream corridor are fluviokarst features that can transport stream sediment to subsurface conduits and caves. The authors focus on phreatic karst such that a subsurface hydraulic control has the potential to mediate fluid energy, cause trapping of sediments, and potentially allow for the mineralization of sediment carbon. The authors emphasize karst systems with active subsurface conduit flow that can convey sediment to a springhead. The existence of a springhead allows connectivity of sediment carbon back to the fluvial network, which highlights the broader goal of understanding karst landscapes within the fluvial carbon cycle. Many phreatic karst systems reported upon in the literature can be characterized by the features mentioned above and conceptualized in Figure 1.1 (White, 2002; Drysdale *et al.*, 2001; Massei *et al.*, 2003; Herman *et al.*, 2008), yet sediment carbon fate and transport is understudied in such phreatic systems.

With the mentioned hydrologic and geologic characteristics in mind, the authors chose a mature karst system to assist with the conceptual model development for sediment carbon in phreatic karst. The study site chosen is the coupled Cane Run Creek Watershed and Royal Springs Groundwater Basin located in the Bluegrass Region of central Kentucky, United States. Reasons for choosing the study site for development of our conceptual model were as follows: (1) The surface stream network of Cane Run Creek has high connectivity to the subsurface such that stream sediments can be conveyed to phreatic karst. Fifty seven karst holes (e.g., swallets) have been mapped in and around the surface stream corridor, and many of these features connect surface water and sediment carbon to a primary, phreatic conduit (Taylor, 1992; Paylor and Currens, 2004). (2) The subsurface

karst system consists of a series of anastomosis conduits that converge to the primary, phreatic conduit that transports water and sediment carbon. The phreatic conduit is approximately 20 m below the ground surface, 5.4 m² in cross-sectional area at its longitudinal midpoint, elliptical in cross-section (6 m wide by 0.9 m height), and gains 15 m of elevation from its low point to springhead due to a subsurface hydraulic barrier (Thraikill *et al.*, 1991). The existence of the active conduit allowed the authors to investigate how phreatic karst might convey, trap, and turnover sediment carbon. (3) The phreatic conduit recharges water and sediment at a springhead allowing connectivity of sediment carbon back to the fluvial network. The Royal Spring springhead has the largest baseflow discharge of any spring in the region and conveys perennial flow from the phreatic conduit (Currens *et al.*, 2015). (4) The Cane Run-Royal Springs system was also chosen due to the large amount of previous morphologic and hydrologic study of the basin (Spangler, 1982; Thraikill *et al.*, 1991; Taylor, 1992; Paylor and Currens, 2004; Currens *et al.*, 2015). (5) Finally, the karst system was chosen due to its close proximity of 15 km to the University of Kentucky and Kentucky Geological Survey headquarters allowing researchers to easily access the site throughout the course of this study.

1.3.2 Methodological Approach

The authors' methodological approach for developing a conceptual model for sediment carbon in phreatic karst first relied on mapping the subsurface phreatic karst morphology as well as karst inlets and outlets for the specific system studied. Next, the authors sampled water and sediment carbon within the subsurface phreatic conduit, and the authors sampled water and sediment carbon entering and exiting the subsurface phreatic karst. Thereafter, the authors used analyses of the data streams and data-driven mass balances (see Figure 1.2) to elucidate hydrological processes within the phreatic karst. The authors then infer sediment carbon fate within the study system that might be characteristic of a conceptual model of sediment carbon in phreatic karst more generally.

The authors mapped the subsurface phreatic karst morphology and its connectivity with the surface streams using 37 electrical resistivity profiles analyzed with the dipole-dipole electrode configuration method to estimate the extent of the primary conduit (Zhu *et al.*, 2011). 44 wells were drilled to 20 to 30 m in depth to intersect and map the primary

phreatic conduit, and potentiometric surface mapping was performed to estimate flow direction within the fracture aquifer to the conduit. Field investigation of swallet and springhead morphology was performed to measure inlets and outlets. Underwater camera observation and Doppler sonar techniques were used to estimate the phreatic conduit geometry.

The authors sampled water and sediment carbon within the subsurface phreatic conduit and at subsurface inlets and outlets at the stations shown in Figure 1.3 for the coupled Cane Run Creek Watershed and Royal Springs Groundwater Basin. In the figure, it is shown that surface stream network conveys water and sediment carbon from urban and agricultural land surfaces to Cane Run Creek, which flows in the northwestern direction. The surface water and sediments are pirated via the 57 sinking streams and swallets to the phreatic conduit. The phreatic conduit is north to northwest flowing to Royal Springs, and its groundwater basin is shaded in Figure 1.3. The subsurface phreatic conduit drains the landscape year round while the main stem of Cane Run Creek is only active about 10% of the year. During periods of high intensity or long duration precipitation, surface water and sediments overtop the swallets and continue downstream as surface flow.

The authors used their understanding of the karst system to choose stations for sample collection. Water and sediment carbon entering from the surface streamflow to the subsurface phreatic conduit were monitored at streamflow stations including the Agricultural Surface Flow Station and Urban Surface Flow Station. The streamflow stations were representative of urban and agricultural streamflow, in general, for the basin because: the urban or agriculture land-use dominated the drainage area; and the streams stations were located upstream of the swallets or sinking streams. The Surface Outflow Station was monitored to sample water and sediment carbon that overtops the swallets and sinking streams during high flow events and thus exits the watershed via surface flow. The phreatic karst conduit was directly monitored within the conduit near its longitudinal midpoint at the Groundwater Station and at its springhead at Royal Springs Station. Three wells directly intersected the phreatic conduit at the Groundwater Station, which allowed for sample collection.

1.3.3 Continuous Water Sediment Monitoring

The authors designed continuous water and sediment monitoring with emphasis upon elucidating fluid energy and sediment transport within a conceptual model for sediment carbon in phreatic karst. To do so, the authors carried out continuous flow monitoring at all five sampling stations shown in Figure 1.3 at a 10 minute sampling rate for two years (1 October 2011 to 30 September 2013). Extensive details of the quality assurance protocol for sample collection is provided in Husic (2015), and the primary method applied is included herein. The surface stream stations were instrumented with *in situ* pressure transducers, and velocity measurements were collected at different stages to develop stage-discharge relationships for each station. Instrumentation installed at the Groundwater Station included a permanent Marsh-McBirney 201-D continuous velocity recording device as well as several Telog 2109 Water Level Recorders. The velocimeter was placed at 80% of the height of the conduit to collect the depth average velocity as estimated by the one-seventh power law (De Chant, 2005). At Royal Spring Station, the United States Geological Survey (USGS) operates a v-notch weir and associated staff gage (USGS 03288110). Water discharge estimates were used to calculate a data-driven water budget (Table 1.1) in which the agricultural and urban stream stations were scaled to represent inputs to the basin.

Temperature measurements and dye traces assisted with understanding hydrologic connectivity within the phreatic karst system. Temperature data were recorded with YSI 6920v2 water quality sondes at the sampling stations to monitor the flushing of pre-event conduit water by quickflow from the surface. Quantitative and qualitative dye traces were used to estimate travel time and swallet connectivity to the phreatic conduit. Rhodamine WT and fluorescein were injected into a karst window at a travel distance of approximately 1.5 km upstream from the Groundwater Station following established methods (Smart and Laidlaw, 1977; Wilson *et al.*, 1986). Downstream tracer concentration was measured by collecting water samples every 10 minutes using a Teledyne ISCO 6712 pump sampler. Fluorescein tracer analysis was performed with a Cary Eclipse Varian fluorescence spectrophotometer. The arrival time of the center of mass of the fluorescein was used to estimate the velocity of the flow. Additionally, a conservation of mass approach was

applied to the Rhodamine WT dye trace in order to estimate conduit discharge (Gouzie *et al.*, 2015).

Sediment measurements were coupled with the water measurements to estimate particle size characteristics and sediment discharge at the five stations. Suspended sediment was collected at the sampling stations and analyzed using a LISST-Portable|XR to estimate particle size distribution. The method for estimating sediment transport rates at the stations applied the sediment concentration relationship for tributaries in the region coupled with Einstein's Approach, which integrates the velocity and sediment concentration profiles (e.g., Chang, 1998; Fox and Russo, 2012). Velocity profiles relied on the modified logarithmic law and one-seventh power law for the streams and conduits, respectively (Chang, 1998; De Chant, 2005). The friction velocity in the streams and conduits was estimated using the momentum equation and Darcy-Weisbach equation, respectively (Chang, 1998, pp. 41; Allen *et al.*, 2007; Husic, 2015). Continuous data were input to the sediment discharge formula at 10 minute intervals, and data input included sediment concentration, water depth in the stream, and velocity within the conduit (Husic, 2015). Sediment concentration measurements were measured using water samples collected with Teledyne ISCO 6712 pump samplers, and then continuous estimates were provided by coupling concentration measurements with continuous YSI 6920v2 turbidity probe measurements, which is commonly performed for sediment budget studies (e.g., Walling *et al.*, 2006).

1.3.4 Sediment Carbon Monitoring

The authors designed sediment carbon monitoring with the conceptual model development for sediment carbon in phreatic karst in mind, and specifically focused on carbon sources to the phreatic karst and carbon fate within the phreatic conduit. As a first step, the authors applied sediment carbon concentration and stable carbon isotope ($\delta^{13}\text{C}$) measurements to fingerprint the sources of sediment carbon entering the phreatic conduit. As a second step, the authors applied carbon and $\delta^{13}\text{C}$ measurements to estimate the fate of sediment carbon within the phreatic conduit by analyzing data input from the surface streams and output from the phreatic conduit at the springhead.

The authors considered carbon sources entering the phreatic conduit by recognizing that urban and agricultural surface streams transport sediment carbon derived from terrestrial and aquatic origin within the fluvial load (<53 μm in diameter) (Arango *et al.*, 2007; Cole *et al.*, 2007; Trimmer *et al.*, 2012; Ford and Fox, 2014). Thus, sediment carbon is a mixture of: (i) a terrestrial carbon pool that includes fine-sized litter and newly derived soil carbon from litter or root turnover; (ii) a terrestrial carbon pool of recalcitrant soil carbon that has undergone numerous stages of decomposition; and (iii) an aquatic carbon pool of disaggregated and humified algae produced in the bed of the stream network (Ford *et al.*, 2015). The three carbon sources are worthy of note because they will vary in their recalcitrance (Cambardella and Elliott, 1992; Marwick *et al.*, 2015), and will provide ecosystem energy production, and hence carbon turnover, *via* oxidation by heterotrophic bacteria (Thorp and Delong, 2002). Fine-sized litter is high in carbohydrates with high C:N ratios, whereas older soil carbon has a high contribution of microbial processed and synthesized compounds with smaller C:N ratios (Marin-Spiotta *et al.*, 2014). In turn, more highly bioavailable carbon within labile litter will provide high energy production per unit mass of carbon relative to the older, more recalcitrant pool (Thorp and Delong, 2002). Studies of *in situ* organic matter decomposition in streams suggest that sediment carbon recently derived from leaf litter and detritus has decomposition rates on the order of $1 \times 10^{-3} \text{ d}^{-1}$ while older soil carbon has decomposition rates on the order of $1 \times 10^{-5} \text{ d}^{-1}$ (Webster *et al.*, 1999; Six and Jastrow, 2002; Yoshimura *et al.*, 2008). Algal-derived sediment carbon is recognized as a carbon-rich pool composed of highly labile neutral sugars (Vieira and Myklestad, 1986; Waite *et al.*, 1995; Lane *et al.*, 2013) and, in turn, will have decomposition rates on the order of $1 \times 10^{-3} \text{ d}^{-1}$ or higher (Ford and Fox, 2015).

The authors applied carbon fingerprinting for estimating the contribution of litter, soil, and algal carbon to the phreatic karst using tracer un-mixing (Davis and Fox, 2009) as

$$y^T = \sum_k (x_k^T \times P_k), \quad (1)$$

and

$$\sum_k P_k = 1, \quad (2)$$

where, y is the tracer of sediment carbon collected from the mixture location in the stream, x is the tracer of a carbon source, T designates an index for the tracer being used, k

designates an index for the carbon source, and P is the mass fraction of carbon originating from a particular source. In the present analysis, the stable carbon isotope ($\delta^{13}\text{C}$) of sediment carbon was chosen as the biomarker tracer to un-mix the carbon pools. $\delta^{13}\text{C}$ is inherently linked to the organic matter structure of the carbon pool (Sharp, 2007) and has been found to discriminate terrestrial carbon and aquatic pools so long as the nature of the carbon pool and end-members are properly characterized and $\delta^{13}\text{C}$ is treated as conservative (Ford and Fox, 2015; Fox and Martin, 2015). In the present study, urban tributaries are storm event-activated and do not sustain flow necessary for primary in-stream production hence only two sources (i.e., soil and litter) were considered for tributaries draining urban lands. Sediment carbon fingerprinting from agriculture tributaries contained all three sources.

As mentioned, the second step of the sediment carbon monitoring focused on estimating the fate of carbon within the phreatic conduit. The microbial decomposition of carbon was estimated during temporary storage as

$$SOC_{out} = SOC_{in} - DEC t_R, \quad (3)$$

where Equation (3) is a first-order carbon turnover model commonly applied for carbon cycling in freshwater (Shih *et al.*, 2010; Ford and Fox, 2014). SOC_{in} is the sediment carbon composition of sediment entering the subsurface karst from the surface streams (g C), SOC_{out} is the sediment carbon exiting the subsurface karst at the springhead (g C), DEC is the net microbial decomposition rate that can be estimated when the distribution of carbon sources to the conduit is known or estimated (g C d⁻¹), and t_R is the net residence time of the sediment carbon in the conduit (d). It was recognized that influx of sediment carbon into the karst system is likely episodic and driven by the occurrence of hydrologic events, and, for this reason, the net residence time estimated in Equation (3) assumes equilibrium over several years and relies on repetition of samples to estimate mean sediment carbon concentrations entering and exiting the phreatic karst.

In addition to the net change in sediment carbon concentration within the phreatic conduit, the authors considered the change in the stable carbon isotopic signature of sediment. The authors assumed long term equilibrium and applied a Rayleigh-like fractionation model (Ford and Fox, 2016) as

$$\delta^{13}\text{C}_{out} = \delta^{13}\text{C}_{in} - \epsilon \ln f, \quad (4)$$

where the carbon isotope signature is changed *via* the product of enrichment via fractionation during decomposition, ϵ (‰), and the natural logarithm of the net organic carbon lost during decomposition, f . The enrichment factor associated with decomposition of fine sediment carbon is on the order of 0 to 2‰ (Jacinthe *et al.*, 2009). Equation (4) provides an independent method to assess aerobic microbial decomposition of sediment carbon given carbon concentration and $\delta^{13}\text{C}$ of sediment carbon entering and existing the karst subsurface.

To carry out the sediment carbon source and fate analyses in Equations (1), (3) and (4), transported sediment carbon was collected from the surface flow stations and the springhead station using *in situ* sediment trap samplers over the course of 22 months. The sampling method relied on the use of time-integrated sediment samplers, which have been found to provide a representative, integrated total carbon signature for a stream (Phillips *et al.*, 2000; Fox and Papanicolaou, 2007; Ford and Fox, 2014; Fox *et al.*, 2014). Sediment traps were installed at the sampling stations and samples were collected from the traps on a weekly basis. Samples collected from traps which were clogged and samples with an inadequate sediment mass were not included in the analysis in order to avoid biasing. Samples were processed back in the laboratory following the methods outlined in Ford and Fox (2014) and Husic (2015). In brief, the samples were dewatered and weighed, wet-sieved through a 53 μm sieve, dewatered and weighed again, ground to a fine powder, and acidified repeatedly using 6% sulfurous acid (Verardo *et al.*, 1990). Sediment carbon samples were analyzed for elemental and isotope composition by combusting samples at 980°C on a Costech 4010 Elemental Analyzer, passing the gas stream through a Gas Chromatograph (GC) column (3 m HS-Q) to a Thermo Finnigan Delta-Plus XP Isotope Ratio Mass Spectrometer (IRMS). The carbon elemental signature, C , was reported as a percentage of the mass of carbon relative the mass of sediment. Isotopic results were reported in delta notation as

$$\delta^{13}\text{C} = \left(\frac{R_{\text{Sample}}}{R_{\text{Standard}}} - 1 \right) * 1000 \quad (5)$$

where R_{Sample} is the $^{13}\text{C}/^{12}\text{C}$ ratio of the samples and R_{Standard} is the $^{13}\text{C}/^{12}\text{C}$ ratio of the universal standard, Vienna Pee Dee Belemnite (VPDB). The elemental reference was acetanilide (%C=71.09%), and isotopic references were DORM ($\delta^{13}\text{C}=-19.59$), and CCHIX ($\delta^{13}\text{C}=-16.4$ ‰). Average standard deviations for elemental and isotopic standards

were 0.34% and 0.20‰, respectively. Average standard deviations of replicates were 0.10% and 0.08‰ for carbon concentration and $\delta^{13}C$, respectively.

Carbon isotope signatures applied in Equation (1) were previously collected from litter, soil, and algae stocks in nearby Kentucky watersheds with similar lithologic, soil, C3 plant type, and benthic algae characteristics (Fox *et al.*, 2010; Acton *et al.*, 2013; Ford *et al.*, 2015). Within the carbon fingerprinting analysis, Equations (1) and (2) were underparameterized for the condition of a single tracer, and therefore additional field information was integrated into the analysis. The source fraction of algae contributing to sediment carbon in the surface streams was estimated using the results from nearby streams in the Inner Bluegrass (Ford *et al.*, 2014). The average value of percent algae in these streams was found to be 17.8% (Ford *et al.*, 2014), and the authors in this study varied this range widely from 0 to 40% algae to account for uncertainty within the results.

1.4 RESULTS AND DISCUSSION

As will be shown, the authors used analyses and interpretation of the data streams to elucidate understudied hydrological processes within phreatic karst including the sediment transport carrying capacity of the flow during and after storm events and the functioning of the surficial fine grained laminae. Thereafter, the authors discuss a conceptual model that may be characteristic of sediment carbon in phreatic karst more generally whereby phreatic karst temporarily stores sediment, turns over carbon at higher rates than would be considered otherwise, respire carbon dioxide to the water column, and recharges degraded organic carbon back to the surface stream.

1.4.1 Water Conveyance in Phreatic Karst

Water and its conveyance provides the medium and energy by which sediment carbon is transported, stored, and turned over in phreatic karst. Numerous studies have presented results of water conveyance in phreatic karst. Therefore, the authors recognized the need to measure hydrologic connectivity and response time of their study system to who that it behaves similarly with phreatic karst systems for which the conceptual model of sediment carbon is sought after.

Surface streams in the study area were event activated exhibiting high stormflow and low baseflow periods. The urban stream was generally much more active with regards

to storm flow than the agricultural stream (Figure 1.4), which was attributed to the higher percentage of impervious areas contributing runoff. The Surface Outflow Station displayed a similar behavior as the urban and agricultural streams in that it was active primarily during hydrologic events and had relatively short-lived hydrographs. Peak stormflow in the surface streams was orders of magnitude greater than baseflow (Figure 1.4).

Water conveyance results were quite different for the phreatic conduit in comparison to the surface streams (see Groundwater Station in Figure 1.4). The phreatic conduit exhibited sustained year-round flow, but flow was buffered due to limited conveyance of the subsurface pathway. Well stage data from the conduit and surrounding karst aquifer showed that even during very low flow conditions the conduit remained phreatic; the groundwater table fluctuated 6 to 16 m above the mid-point of the conduit. The mean conduit velocity was 0.12 m s^{-1} and the standard error was small (± 0.11), especially relative to surface streams. Figure 1.4 shows that peak flows in the conduit were limited in their extremes relative to the surface streams. Flow rate in the surface streams was as high as $25 \text{ m}^3 \text{ s}^{-1}$ while flow in the conduit was an order of magnitude lower and never exceeded $3 \text{ m}^3 \text{ s}^{-1}$. The limited water conveyance was attributed to the dimensions of the karst conduit (i.e., $0.9 \text{ m} \times 6 \text{ m}$), the downstream pressure gradient induced by the hydraulic control, and intermittent swallet overflow. The sustained perennial flow of the conduit resulted in 76% of the water that exited the coupled surface-subsurface system occurred via the phreatic conduit.

Water conveyance time-series measurements suggested confidence that the surface streams and phreatic conduit have high hydrologic connectivity that would allow for active sediment carbon delivery to the subsurface karst. Temperature and discharge time series from a storm event in March 2013 show the temperature response of the conduit at the Groundwater Station to quickflow from surface tributaries during the rising limb of the hydrograph (Figure 1.5). Water temperature decreases at the Groundwater Station before flow is recorded at the Surface Outflow Station indicating that initial surface flows are pirated before continuing downstream and reaching the surface outlet. The temperature decrease at each location occurs within the first 18 hours of the event indicating the close coupling of surface streams and phreatic karst. Additional justification for the high

connectivity between the surface and subsurface was provided by the fast travel times within the conduit estimated from dye traces (Table 1.2). The average travel time from the dye traces was scaled to the entire conduit, and it is estimated that fluid travels a distance of 16 km over approximately 22 (± 6.8) hours. Results highlight the relatively high velocity of fluid (20 cm s^{-1}) and hydrologic connectivity of the surface-subsurface system during hydrologic events.

The results of water conveyance in the study system are consistent with the features of phreatic karst for which a conceptual model of sediment carbon is sought after (see Figure 1.1) and agree with phreatic karst hydrology reported in other studies. For example, mature karst morphology is well-recognized to have conduit networks developed along geologic bedding planes with water at velocities orders of magnitude greater than porous media or fracture matrix flows (Atkinson, 1977; White, 2002; Waltham and Fookes, 2003). A number of studies have suggested that recharge occurs to phreatic conduits during stormflow when rainfall activated surface water tributaries carry quickflow *via* swallets to the subterranean karst (Vesper and White, 2004; Massei *et al.*, 2006). The finite water conveyance of karst conduits and caves due to internal energy controls and springhead overflow has long been identified in karst literature (White, 1988; Bonacci, 2001).

1.4.2 Sediment Transport in Phreatic Karst

The hydrologic connectivity of surface streams to swallets to phreatic conduits to springheads back to surface streams coupled with phreatic water conveyance that is buffered during storm events yet sustained perennially suggests a particularly ‘jerky conveyor’ for sediment within phreatic karst (as coined by Ferguson, 1981, for fluvial systems). The sediment residence time in fluvial systems that includes phreatic karst pathways is expected to be increased relative to surface-dominated systems. The authors use their data results and literature comparison in this section to elucidate hydrologic processes in phreatic karst including the role of the sediment transport carrying capacity to induce deposition, temporary storage, and resuspension of sediment carbon as well as the presence of the surficial fine grained laminae. In turn, the results lead to a conceptual model suggesting that phreatic karst turn over carbon at higher rates than would be considered otherwise in fluvial systems.

Sediment discharge results (Figure 1.6) show that sediment transport near the longitudinal center of the phreatic conduit has low sediment transport rates during hydrologic events relative to the surface streams that input sediment to the subsurface. For example, the peak sediment concentration and discharge within the phreatic conduit was 192 mg L^{-1} and 0.27 kg s^{-1} , respectively, which were substantially smaller than the urban surface stream sediment concentration and discharge of $1,584 \text{ mg L}^{-1}$ and 29.73 kg s^{-1} , respectively. The sediment transport rate differences between the phreatic conduit and surface streams are not explainable based on particle size differences. Particle size results suggest that very little sorting occurs during the transport process as the particle size distribution of conduit suspended sediments nearly match the particle size distribution of suspended sediments in the surface streams (Figure 1.7). Rather, the results are explained based on deposition of sediment within the phreatic conduit. The surface streams input water with high sediment concentration directly to the karst swallets, however, results from the Groundwater Station suggest that the majority of the sediment has fallen out of suspension by the time the water reaches the longitudinal center of the conduit. As mentioned, water flow results suggest the water travel time is $22 (\pm 6.8)$ hours, which provides ample time for settling considering the settling velocity and conduit height that provides a deposition time of approximately 0.14 hours ($t = 0.5Hw_s^{-1}$).

Downhole imagery of the phreatic conduit provided justification of pronounced sediment deposition within the phreatic conduit. Fine sediment was present on the conduit bed along with larger limestone rocks that also were covered with a layer of fine sediment. In frames of the video, suspended sediment transport was also visually observed within the conduit moving at relatively high velocities. Blanketing of the cave's floor with a fine sediment layer is consistent with fluvial sediment entering and exiting the conduit and suggests deposition of transported fine sediment. This fine sediment layer in fluvial systems has been termed the surficial fine grained laminae (Droppo and Stone, 1994) and is recognized to be active both physically in terms of deposition and resuspension and biologically in terms of microbial growth and carbon turnover (Russo and Fox, 2012; Ford and Fox, 2014).

While sediment peaks during the hydrologic events are much smaller, sediment data results show that turbidity spikes in the phreatic conduit last through the peak of a

hydrologic event and are maintained for much longer durations in comparison to the surface streams. From analysis of four characteristic hydrologic events, Figure 1.8 shows that elevated sediment discharge in the conduit lasts approximately 2.5 times the duration of peak urban stream transport. The relatively high sediment concentration within the conduit continues to occur after input of sediment from tributaries has ceased. The results highlight that sediment transport occurs after the external sediment source has been cutoff. In this manner, conduit internal sediment deposited during the hydrologic events provides a sustained source in the absence of hydrologic events. The result occurs because water flowrates in the conduit are sustained for days to weeks after the storm event, and in turn the water conveyance provides fluid energy to erode conduit bed material and transport sediment to the springhead.

The deposition of sediment during storm events within the phreatic conduit, presence of the active surficial fine grained laminae, and later resuspension of sediment long after the storm pulse has passed through the surface streams can be well explained by considering the energy of the fluid to carry sediment. The sediment transport carrying capacity (T_C) of the flow was normalized by its maximum (see Figure 1.9) as

$$\frac{T_C}{T_{C\max}} = \frac{k_{tc}V^3}{k_{tc}V_{\max}^3} \quad (6)$$

where, k_{tc} is a transport coefficient and V is the flow velocity (m s^{-1}). Analysis of the ratio of the surface stream transport carrying capacity to that of the conduit shows that during hydrologic events the sediment carrying capacity of the surface streams is many orders of magnitude greater than that of the conduit (i.e., $T_C^{\text{urban stream}}/T_C^{\text{conduit}}=10^3$). The result highlights the reason as to why pronounced deposition occurs in the conduit during hydrologic events and reinforces the limiting of sediment transport by the phreatic conduit. The transport capacity of the conduit is shown to be highly sustained relative to the surface streams (Figure 1.9), which highlights the ability of water conveyed within the conduit to erode and transport sediment long after the surface hydrologic activity has ended. Surface events have short-lived transport capacity peaks with a subsequent return to low- or no-flow. The transport capacity within the karst conduits recedes much more slowly and is maintained for weeks after an event, i.e., water is continually supplied to the conduit by fractures, macropores, and the epikarst allowing for continued subsurface sediment transport. The result diverges the phreatic karst from surface streams and non-phreatic

karst where the energy of the fluid is a function of flow depth. The sustained transport capacity promotes resuspension of fine sediments long after surface events and sediment transport in the phreatic karst is higher than surface streams for most of the year (Figure 1.9).

Hydrologic processes of deposition, temporary storage, and resuspension are discussed or alluded to in other phreatic karst studies and therefore provides further support towards our conceptual model for sediment carbon. For example, the fluid energy threshold of phreatic conduits has been suggested as a means to trap sediment (Herman *et al.*, 2008). Specifically, the buffering and maintaining of the transport capacity resulting in deposition within the subsurface conduit during an event has been an observed phenomena by large sediment pulse deposition in a cave after hydrologic events (Gillieson, 1986), and hourly sampling of large and small hydrologic events showed prolonged high sediment loads at a springhead following a storm (Mahler and Lynch, 1999). Finally, the idea of an active surficial fine grained laminae has been highlighted by the observance of epilithic biofilms in karst streams that have shown active microbial and invertebrate communities that turnover surface-derived organic matter (Simon *et al.*, 2003) and carbon balances have shown the oxidation of sediment organic carbon during transport (Albéric and Lepiller, 1998).

1.4.3 Sediment Carbon Fate in Phreatic Karst

The hydrologic processes identified for phreatic karst point towards a conceptual model for sediment carbon that includes temporary storage, turnover of carbon at higher rates than would be considered otherwise, respiration of carbon dioxide to the water column, and recharge of degraded organic carbon back to the surface fluvial system. Such a conceptual model might be expected for karst that includes hydrologic connectivity and active sediment delivery from surface streams to the subsurface, the presence of phreatic conduits, and active recharge of back to the fluvial network.

Sediment carbon results from the present study support the conceptual model for sediment carbon. Surface stream sediment carbon input to the karst averaged 4.8 (± 1.2) gC 100g⁻¹ sediment while sediment carbon collected from the conduit discharge averaged 3.4 (± 0.5) gC 100g⁻¹ sediment. Some point data overlap existed for sediment carbon

inflowing to and outflowing from the karst conduit (Figure 1.10), which is at least partially attributed to suspended sediment that is flushed through the conduit during a hydrologic event. Carbon inputs and outputs were significantly different (p -value $< 1 \times 10^{-6}$) based on two-tailed statistical t -tests.

On average, results of carbon measurements show a 30% loss of sediment carbon when comparing inputs to the karst conduit with outflowing sediment at the springhead. The carbon density differences suggest that the temporary sediment carbon storage within the bed of the conduit promotes carbon turnover by heterotrophic bacteria. The explanation is reasonable given that the sediment carbon inflowing to the karst subsurface includes labile carbon pools and the karst water in the conduit is oxygenated and maintains a relatively constant water temperature. Sediment carbon within the surface streams that enters to the karst conduit *via* the swallets was found to be a mixture of fine-sized litter carbon, algae-originated carbon, and soil carbon (Table 1.3). Litter and algal carbon are recognized to be fairly labile carbon pools, and the labile pools comprised approximately 50% of the total sediment carbon entering the conduit from urban waters and 50-75% from agricultural waters. Studies of *in situ* organic matter decomposition in streams suggest that particulate organic matter recently derived from leaf litter and algae have decomposition rates on the order of $1 \times 10^{-3} \text{ d}^{-1}$ while the less labile soil carbon pool has decomposition rates on the order of $1 \times 10^{-5} \text{ d}^{-1}$ due to homogenization to low quality, highly recalcitrant carbon compounds (Webster *et al.*, 1999; Six and Jastrow, 2002; Jackson and Vallaire, 2007; Rier *et al.*, 2007; Yoshimura *et al.*, 2008; Venarsky *et al.*, 2012).

Water within the conduit studied was highly oxygenated during the study period with measurements showing levels at or near saturation much of the time, and on average dissolved oxygen was 76% its saturation level. A year-round fish population exists within the conduit, as visualized using downhole video, further supporting the oxygenated conditions. The oxygenated conditions coupled with the presence of the surficial fine grained laminae support the concept of oxidation of labile sediment carbon within the karst conduit as a process for carbon loss in the fluviokarst system. Based on the distribution of carbon pools (Table 1.3) and estimated aerobic decomposition rate of sediment carbon, the net residence time of sediment carbon within the karst conduit was 342 (± 190) days or

nearly one year. This contrasts the water transport, as the karst subsurface water has an average residence time of about one day.

The one year storage of sediment and loss of carbon within the phreatic conduit support the concept that sediment carbon turns over at high rates in the subsurface and recharges degraded organic carbon back to surface streams. The authors further support this concept because alternative explanations for the decreases in carbon density can be marginalized using our other results measured for the conduit and surface streams. The near identical particle size distributions of source sediments from tributaries in the watershed and sediments collected from the karst conduit (Figure 1.7) justify the idea that the same sediments are being studied at both source and sink locations and that additional sediment sources have not been erroneously omitted. Further, $\delta^{13}\text{C}$ of inflowing source sediments and $\delta^{13}\text{C}$ of outflowing conduit sediments were not significantly different (p -value = 0.79) (Figure 1.10). The lack of difference for the carbon isotope signatures suggests again that the same sediments are being studied at both source and sink locations. Heterotrophically-mediated oxidation in oxygenated waters would not be expected to produce a substantial change in $\delta^{13}\text{C}$, as past studies have shown relatively small enrichment ratios and suggest that $\delta^{13}\text{C}$ of sediment carbon pools is fairly conservative (Ford *et al.*, 2015). In the present study, the carbon isotope change can be estimated considering isotope fractionation during the carbon turnover and net loss. Considering the Rayleigh model (Equation 4), isotopic enrichment of temporarily stored karst sediments would result in a conservative estimate of 0 to 0.5‰ change in the sediment carbon pool. As mentioned, data results did not reflect significant changes in $\delta^{13}\text{C}$ when comparing karst inputs ($-26.6 \pm 0.8\text{‰}$) and outputs ($-26.6 \pm 0.9\text{‰}$). While Rayleigh fractionation does not consider variability such as that imposed by transient fractionation (Maggi and Riley, 2009), the result highlights further evidence towards the carbon turnover in the subsurface karst. Further, the lack of isotopic change supports the suggestion of aerobic, as opposed to anaerobic, carbon mineralization due to the fact that anaerobic losses result in pronounced isotope changes for the substrate (e.g., isotopic enrichment on the order of -80‰ during methanogenesis of deposited sediment carbon, Liu *et al.*, 2013).

The data results provide a conceptual model for the behavior of sediment carbon within phreatic karst (Figure 1.1). Strong physical coupling of surface streams with

subsurface karst pathways promotes the pirating of terrestrially-derived sediment carbon to the karst aquifer. The limited, yet sustained, transport carrying capacity of the conduit promotes the deposition of labile carbon to the conduit bed followed by later resuspension of the degraded sediment. Year-round flow within the conduit coupled with the subsequent deposition and resuspension of sediment provide conditions for heterotrophic bacteria to oxidize labile sediment carbon and in turn provide a mechanism for particulate carbon loss. The existence of the loosely compacted surficial fine grained laminae at the floor of the conduit within oxygenated water further supports the phreatic conduits as a biologically-active pathway that degrades sediment carbon. The subterranean biology is unique relative to surface streams because there is a lack of autochthonous growth to offset heterotrophic-respired CO₂ due to the lack of sunlight. For example, the net loss of sediment carbon for the karst conduit contrasts the surface stream in a neighboring watershed where a 50% enrichment in sediment carbon occurred due to the sequestration of humified algal (Ford and Fox, 2015). Further, karst water on average is warmer than water in surface streams in this region, i.e., mean annual temperature is 16.5 and 13.7°C for the karst conduit and a neighboring surface stream (Ford and Fox, 2015), respectively. While the mean water temperatures are just a few degrees different, microbial growth rate increases exponentially with water temperature (White, 1991). For example, deposited sediment carbon experiences winter water temperatures of 9.2°C in the surface stream relative to 15.8°C in the phreatic karst, which more than doubles the bacteria growth rate (White *et al.*, 1991).

1.4.4 Implications for Carbon in Fluviokarst

Given the similarity of water and sediment results in this study with other studies, it is highly conceivable that other phreatic karst systems show a similar behavior in terms of sediment carbon turnover within karst pathways. One implication of biologically-active karst pathways is that karst springheads may produce a low quality sediment carbon source to stream systems. A number of studies have reported the high sediment loads that karst springheads can discharge to surface streams (Mahler and Lynch, 1999; Drysdale *et al.*, 2001; Herman *et al.*, 2008; Reed *et al.*, 2010). Due to carbon turnover within karst pathways, the springheads may provide lower quality sediment carbon than would be expected from the surrounding landscapes, which in turn will impact carbon mineralization

rates controlling CO₂ outgassing from streams and freshwater ecosystem function (Butmam and Raymond, 2011; Raymond *et al.*, 2013). In this manner, the presence of karst pathways should be considered as scientists attempt to estimate organic matter stocks and transformation in streams. Further, in terms of the fluvial system, which transforms carbon en route to the ocean, the phreatic karst pathway is perceived as a discontinuity due to the increased residence time of sediment (Figure 1.11). Discharge has been recognized as the primary driver of differences in organic carbon spiraling lengths in low-order Midwestern agricultural streams (Griffiths *et al.*, 2012) highlighting the potential of karst to increase turnover as a result of limited discharge. The karst pathway would lead to higher net CO₂ respiration rates early on in the fluvial continuum resulting in more highly degraded sediment carbon delivery to the ocean. Findings from our study point towards a perhaps unforeseen discontinuity impacting carbon in the fluvial continuum due to phreatic karst pathways.

A second implication of biologically-active karst pathways is the potential for CO₂ production *via* microbial oxidation to exhibit control upon karst geochemistry within the karst environment. The presence of CO₂ is well recognized to control the rate of dissolution and hence erosion of carbonate rock during karst formation (White, 2002). The source of CO₂ is often a primary question when estimating the rate of development for karst morphology (e.g., surface water, advection of CO₂ in vadose zone, conduit surficial fine grain laminae). Some studies have found an increase of CO₂ concentration with depth in karst aquifers pointing to a potential source from oxidation of surface derived organic carbon (Baldini *et al.*, 2006; Whitaker and Smart, 2007). Baldini *et al.* (2006) noted the importance in spatial variability of CO₂ with higher concentrations at the cave walls where fractures may shelter CO₂ from advection and also higher concentrations near soil accumulation sites such as collapsed cave floors. Albéric and Lepiller (1998) estimated the direct dependence of limestone dissolution on carbon oxidation to be 7-29 mg CaCO₃ L⁻¹. Results of this study suggest that stronger coupling of karst geochemistry with microbial activity associated with sediment carbon mineralization as a driver of the reactions and a consistent source of CO₂ from temporarily trapped labile material.

While the authors suggest the potential for biologically-active karst systems and discuss implications of this idea, we also point out limitations of this research. Features of

this study are characteristic of phreatic pathways with the active input of labile sediment carbon. We speculate that a non-phreatic system where conduits are located in the vadose zone may have higher flow and sediment transport capacities hence reduced deposition. Karst development in these systems could be favored by CO₂ air flow advection or diffusion rather than microbial production (Garcia-Anton *et al.*, 2014). Further, input of geogenic or fossil carbon would be expected to be fairly inert within the karst pathway due to their recalcitrant nature and transformation timescales that are several orders of magnitude smaller than those for sediment carbon. For such non-phreatic systems and systems with varying sediment quality, more research is needed to understand the fate of carbon in karst systems. Nevertheless, the result from this study provides a concept for consideration in future studies.

We offer a final discussion point regarding the advancement of research methods applied in this paper. The progress of karst research calls for continued instrumentation and measurements within karst aquifers and at springheads to estimate hydrologic processes (White, 2002). With this goal in mind, the present study collected numerous water, sediment, and biogeochemical measurements at karst inputs, within the aquifer and at the springheads. The difficulty with investigating processes within phreatic karst systems cannot be overstated, and often research methods that strive to perform tasks as simple as water connectivity rely on postulating assumptions and using all available data to accept or refute the assumption. To this end, the traditional dye trace methods offered important first validation of our understanding of the karst system. Although expensive, drilling 20 m directly into the karst aquifer was an advantage of this study in that we could continuously monitor the fluid velocity and sediment transport by means of sediment concentration at an intermediate phreatic section of the conduit. The internal karst monitoring station allowed us to test assumptions derived from the springheads such as the pressure head during hydrologic events. We also watched hours upon hours of downhole video, which provided further context for scientific discussion among our research group and visualization of sediment deposition. Perhaps the most innovative method of this study was the use of $\delta^{13}\text{C}$ of sediment to assist with discerning carbon source and fate processes. In this study, $\delta^{13}\text{C}$ was useful for understanding the provenience of carbon input to the conduit, which is a contribution that extends recent research in this area (e.g. Fox and

Papanicolaou, 2007; Fox and Martin, 2015) to the karst environment. Further, coupling $\delta^{13}\text{C}$ data with isotope fractionation estimates within the karst conduit allowed further evidence of aerobic mineralization of carbon.

1.5 CONCLUSIONS

Hydrological processes highlighted in this paper include the following:

- The sediment transport carrying capacity of the phreatic karst water is orders of magnitude less than surface streams during storm-activated periods. The relatively buffered fluid energy promotes pronounced deposition of fine sediments to the subsurface phreatic karst.
- The sediment transport carrying capacity is sustained long after storm events have ceased. The result diverges the phreatic karst from surface streams and non-phreatic karst where the energy of the fluid is a power function of the flow depth.
- The surficial fine grained laminae occurs in the subsurface karst system, much like surface streams, and includes deposition of a fine sediment layer coating the cave floor. Unlike surface streams, the light-limited conditions of the subsurface karst promote constant heterotrophy leading to net degradation of sediment organic carbon.

Results of this study help provide a conceptual model for sediment carbon fate in phreatic karst. Karst pathways act as biologically active conveyors of sediment carbon that temporarily stores sediment, turns over carbon at higher rates than would be considered otherwise, respire carbon dioxide to the water column, and recharges degraded organic carbon back to surface streams. Karst morphologic and hydrologic features for which this conceptual model are deemed applicable include hydrologic connectivity of surface streams to subsurface karst such that an active sediment delivery system exists, the presence of a phreatic system that promotes storage and turnover of carbon, and active recharge of sediment back to the fluvial network. In the case of the new data results presented here, the conceptual model is supported by a one-day residence estimated for water within the subsurface karst but nearly a one year residence estimated for sediments. Further, fluvial sediment is estimated to lose 30% of its carbon by mass during temporary residence within the subsurface karst prior to recharge back to the surface streams.

Implications of the conceptual model proposed here are that karst springheads produce low quality sediment carbon source to stream systems, which in turn impacts carbon mineralization rates controlling CO₂ outgassing from streams and freshwater ecosystem function. A second implication of biologically-active karst pathways is the potential for CO₂ production *via* microbial oxidation to exhibit control upon karst geochemistry within the karst environment. It is recommended that scientists consider karst pathways when estimating carbon and carbonate transformation in surface and karst streams.

1.6 ACKNOWLEDGEMENTS

The authors would like to thank the associated editor Nico Goldscheider and anonymous reviewers whose comments helped the authors to greatly improve the quality of this manuscript and its companion. We would like to thank the extended staff at the Kentucky Geological Survey for the extensive research performed in the Cane Run Watershed and Royal Spring Groundwater Basin both prior to and concurrent with this research. We thank Dr. Harry Rowe for analysis of the elemental and carbon data and several undergraduate and graduate research associates that helped with collecting field data and performing laboratory analysis. We thank the University Of Kentucky Department Of Civil Engineering for partial funding of the graduate student during this research study. We also thank the United States Geological Survey for partial funding of this research through the 104b Student Research Enhancement Grant. We also acknowledge funding from the Kentucky Senate Bill 271B Water Quality program.

1.7 TABLES AND FIGURES

Table 1.1 Water budget for coupled surface-subsurface watershed presented in inches of rainfall per year normalized by catchment area.

Input / Output	(cm km ⁻² y ⁻¹)
Agriculture Tributaries	12.2
Urban Tributaries	39.9
Surface Outflow	11.9
Groundwater Station	37.8
Change in Volume	2.4

Table 1.2 Dye trace experiment results from an eclipse karst window to the Groundwater Station (1.5 km)

Date and Time	Dye Spike Velocity (m s^{-1})	Travel Time (hr)
6 Dec 2011 14:50	0.32	1.3
1 Mar 2012 14:00	0.15	2.7
10 Dec 2012 15:40	0.20	2.0
7 Feb 2013 18:00	0.14	2.9
12 Mar 2013 13:20	0.18	2.3
19 Mar 2013 11:35	0.28	1.5
12 Apr 2013 15:30	0.14	2.9
8 Apr 2014 13:00	0.18	2.3
Average	0.20	2.2
Standard Deviation	0.07	0.6

Table 1.3 Sediment organic carbon source allocation for varying percent algae. Note: urban tributaries contribute no algal load.

Agriculture Tributaries (%)			Urban Tributaries (%)		
Algae	Litter	Soil	Algae	Litter	Soil
0.0	78.3	21.7	0.0	48.0	52.0
5.0	63.4	31.6	0.0	50.1	49.9
10.0	46.8	43.2	0.0	51.1	48.9
15.0	36.0	49.0	0.0	52.3	47.7
20.0	31.0	49.0	0.0	53.5	46.5
30.0	27.3	42.7	0.0	53.7	46.3
40.0	24.5	35.5	0.0	52.9	47.1

Figure 1.1 Conceptual model of sediment organic carbon (SOC) transport in phreatic karst. Bold text indicates processes.

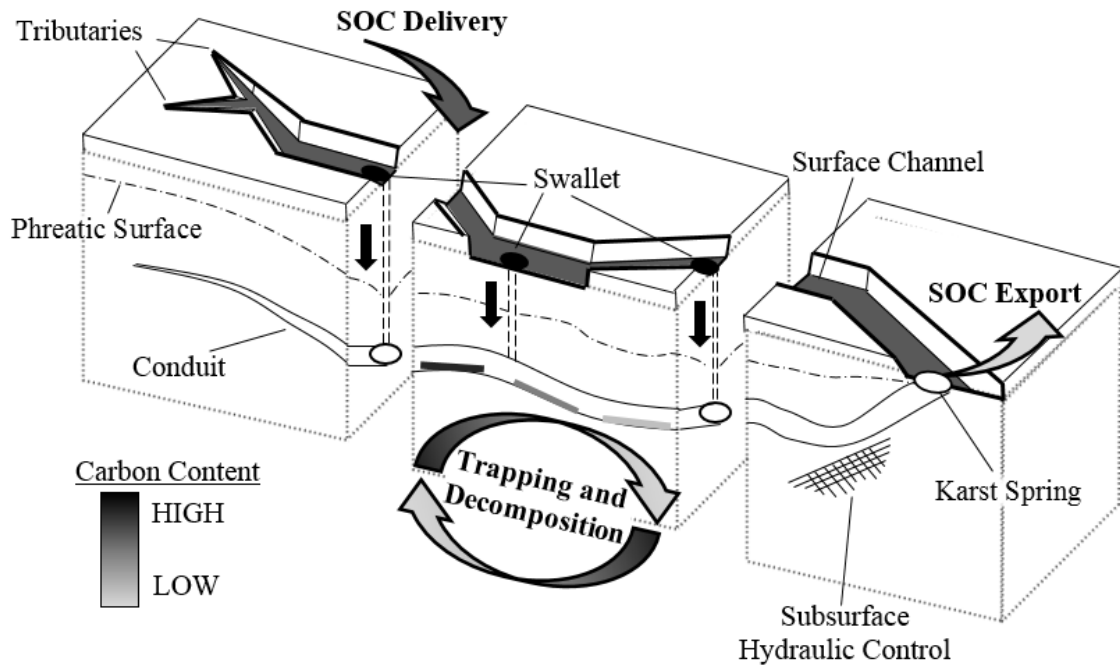


Figure 1.2 Diagram of the methodological approach for the fluvioikarst sediment organic carbon study.

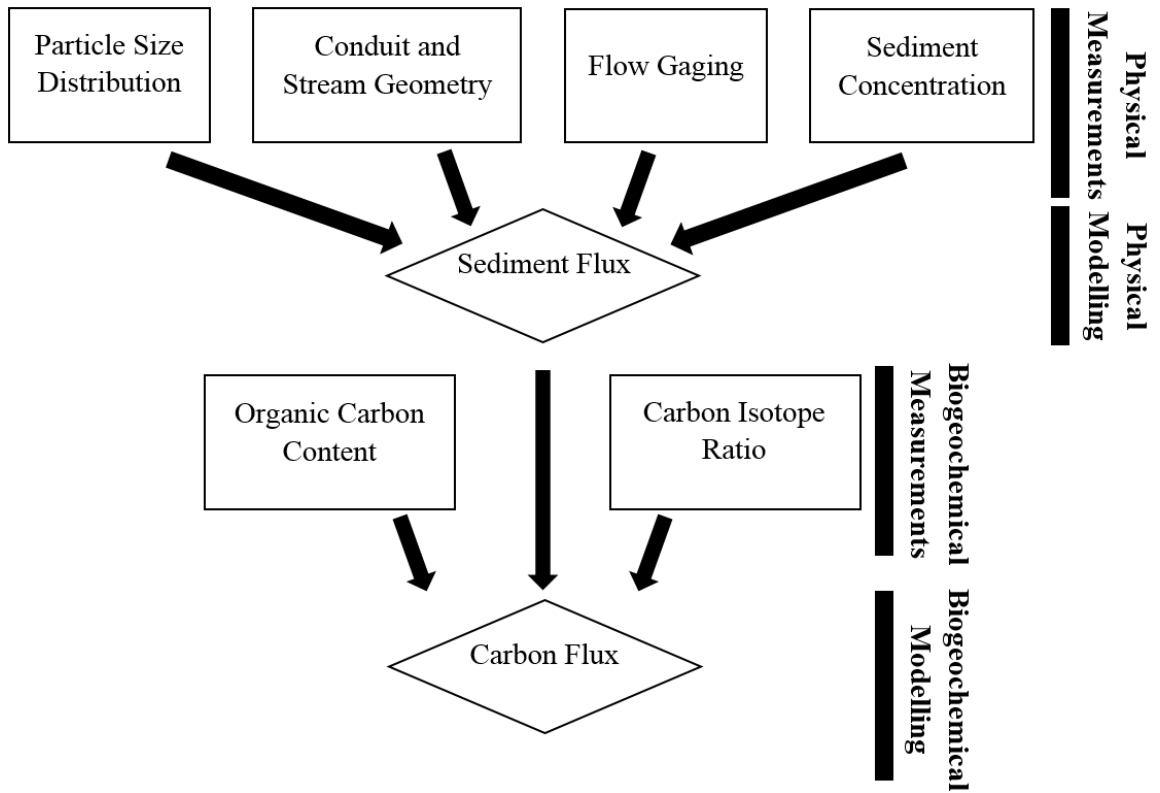
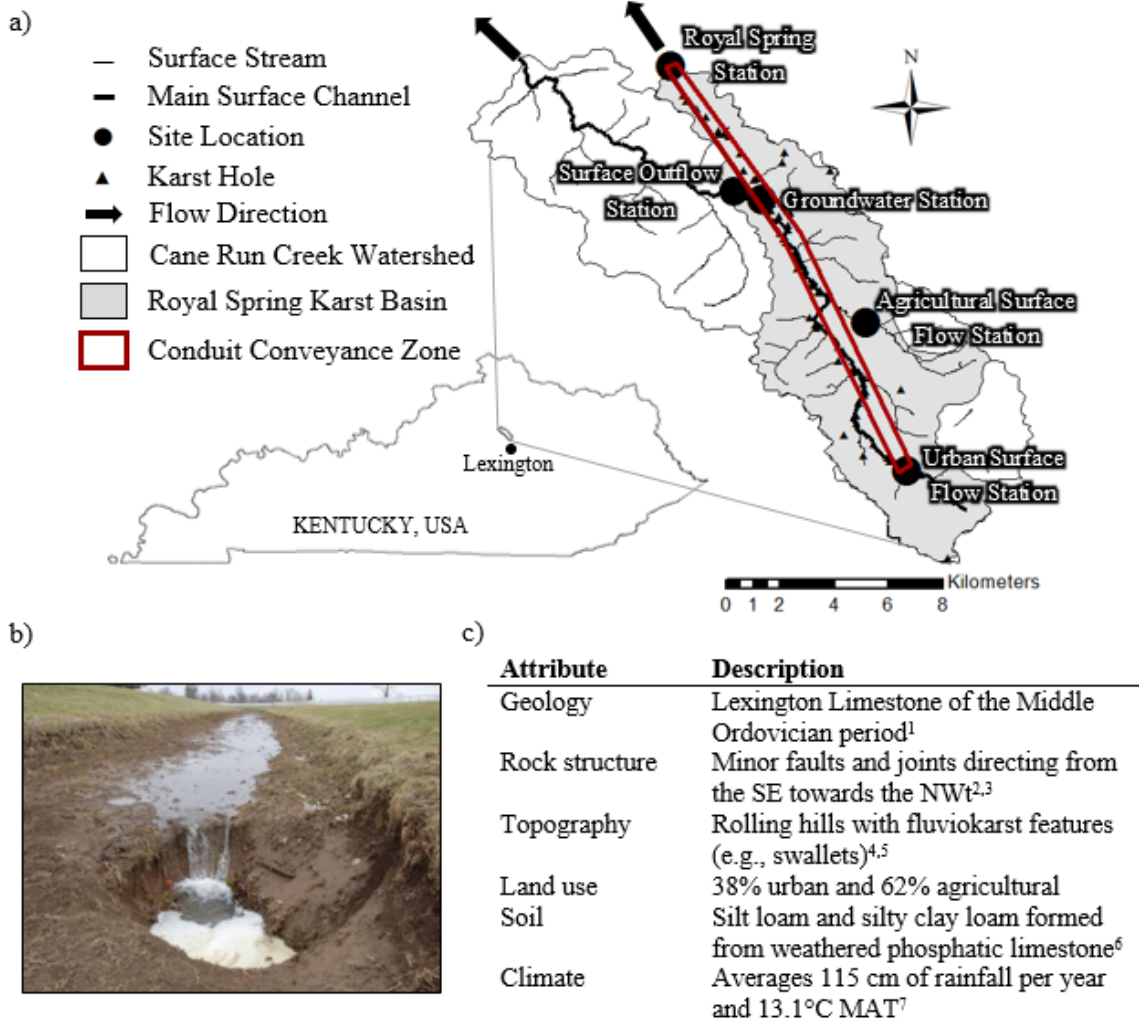


Figure 1.3 (a) Cane Run watershed and Royal Spring basin, (b) karst swallet pirating surface flow during low flow, and (c) watershed attributes.



¹Cressman and Peterson, 1986; ²Drahovzal *et al.*, 1992; ³Drahovzal and Noger, 1995; ⁴Paylor and Currens, 2004; ⁵Husic, 2015; ⁶USDA, 1993; ⁷Bluegrass Regional Airport

Figure 1.4 Inflows and outflows to the watershed normalized by maximum flow rate at each respective location.

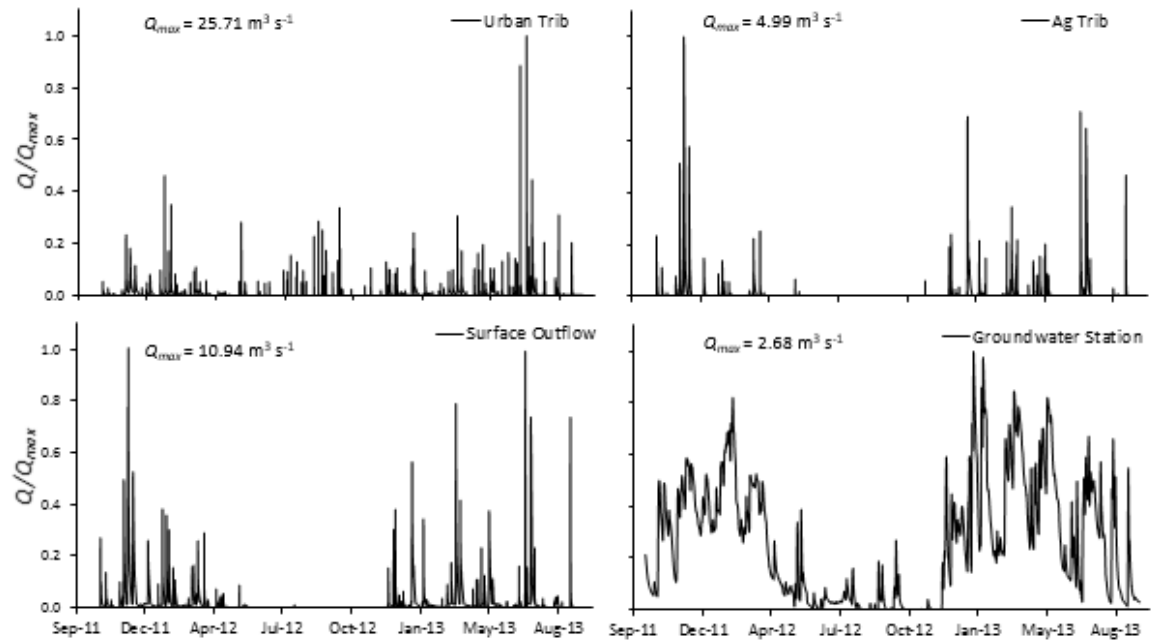


Figure 1.5 Temperature fluctuations during a storm at four sampling sites. Discharge shown on figure is from the Surface Outflow site.

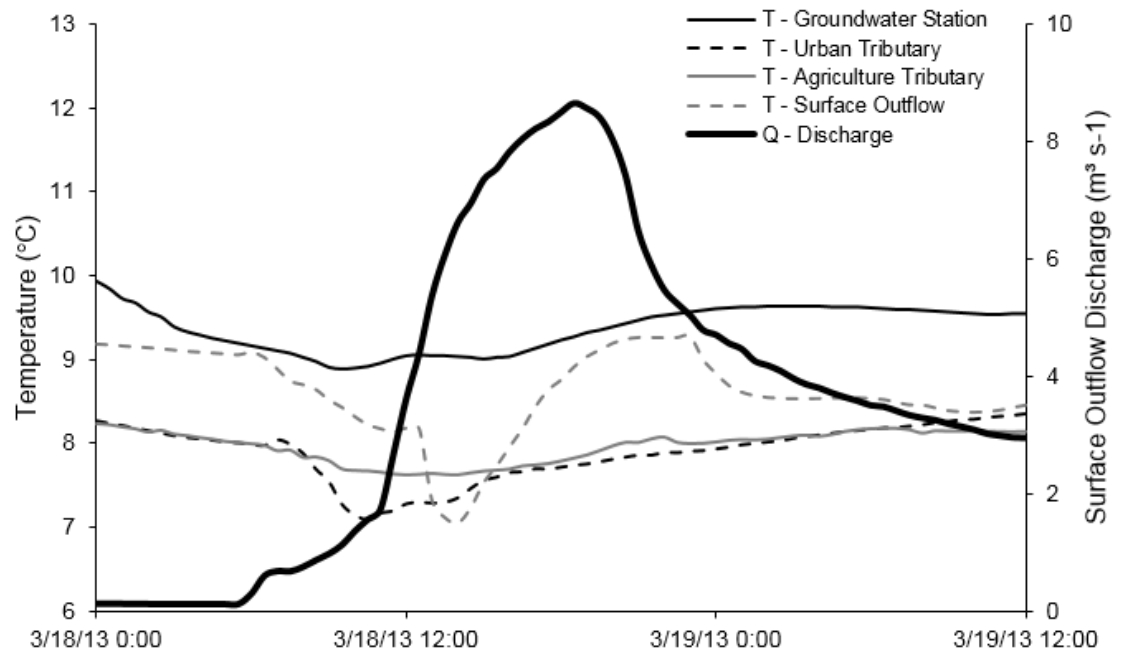


Figure 1.6 Suspended sediment concentration at tributaries and Groundwater Station on the left. Suspended sediment discharge normalized by maximum sediment discharge at each location on the right. *Gap in Groundwater Station data starting on May 20, 2013 due to instrument failure.

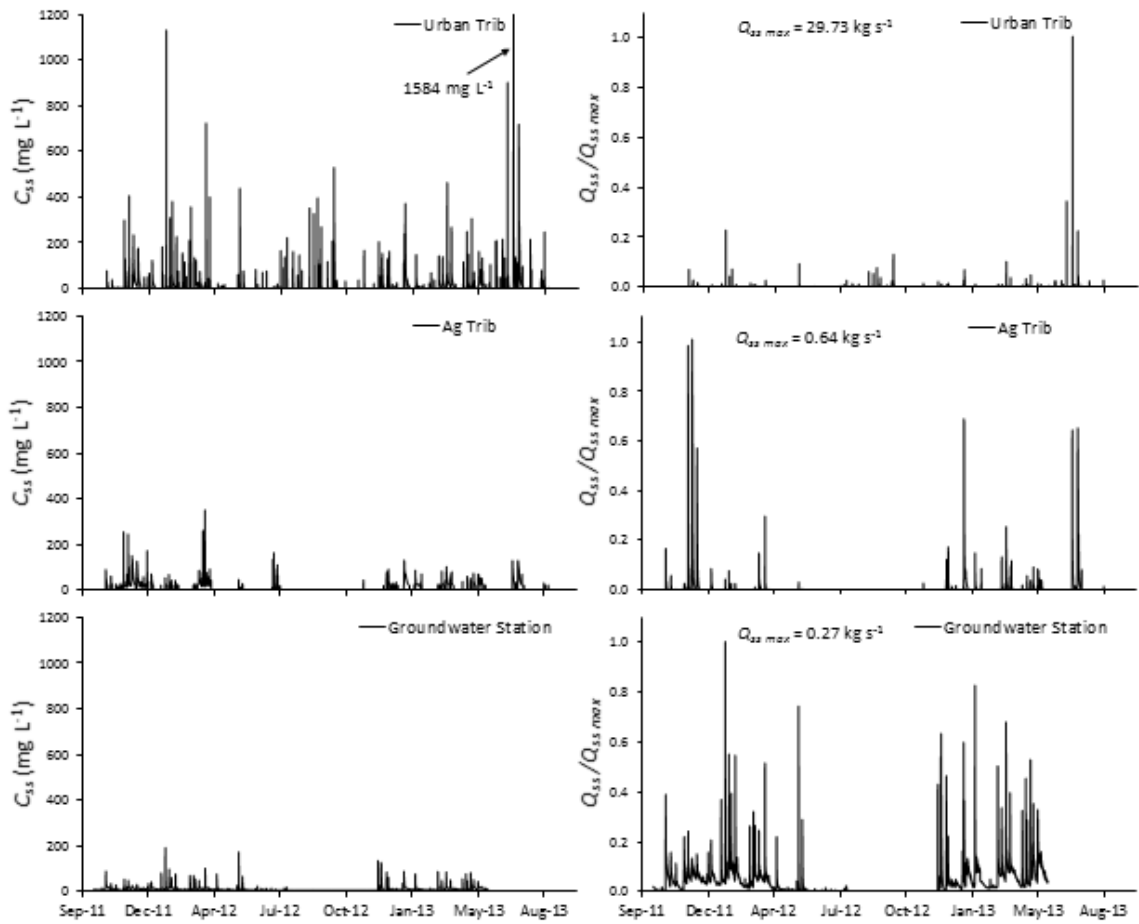


Figure 1.7 Particle size distribution at inflows and outflows to the watershed.

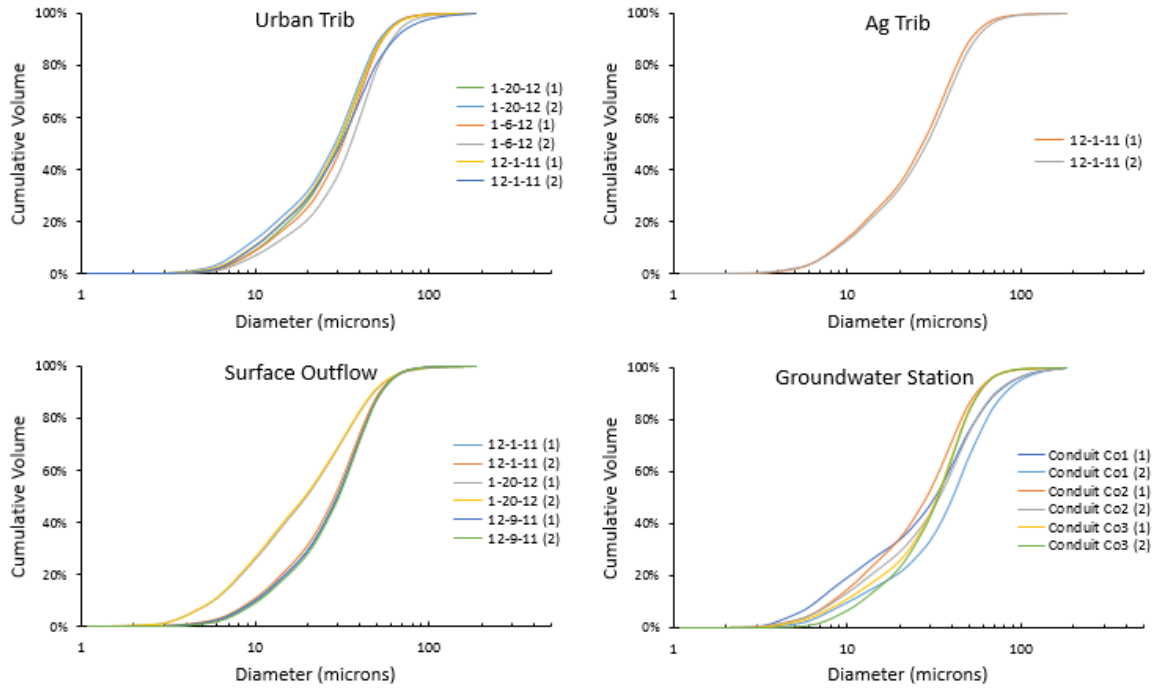


Figure 1.8 Suspended sediment flux comparison for four characteristic hydrologic events. Note that the y-axis is normalized discharge; the urban tributary discharges a larger magnitude overall.

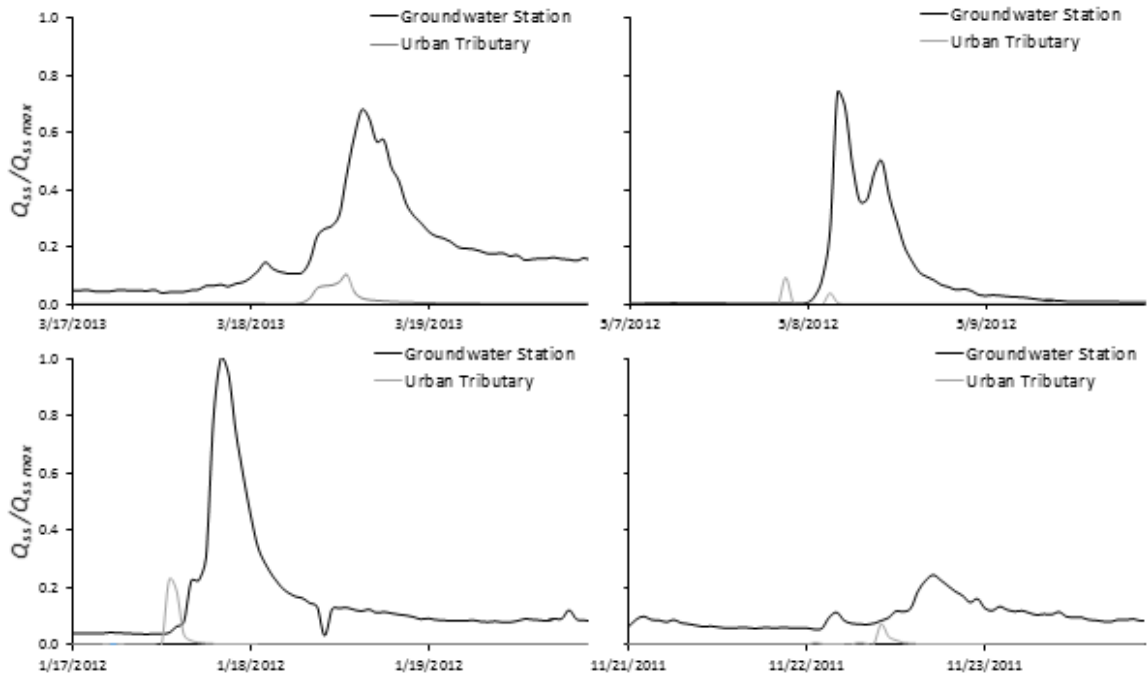


Figure 1.9 Transport carrying capacity of urban and agricultural tributaries and the conduit normalized by maximum transport carrying capacity at each respective location.

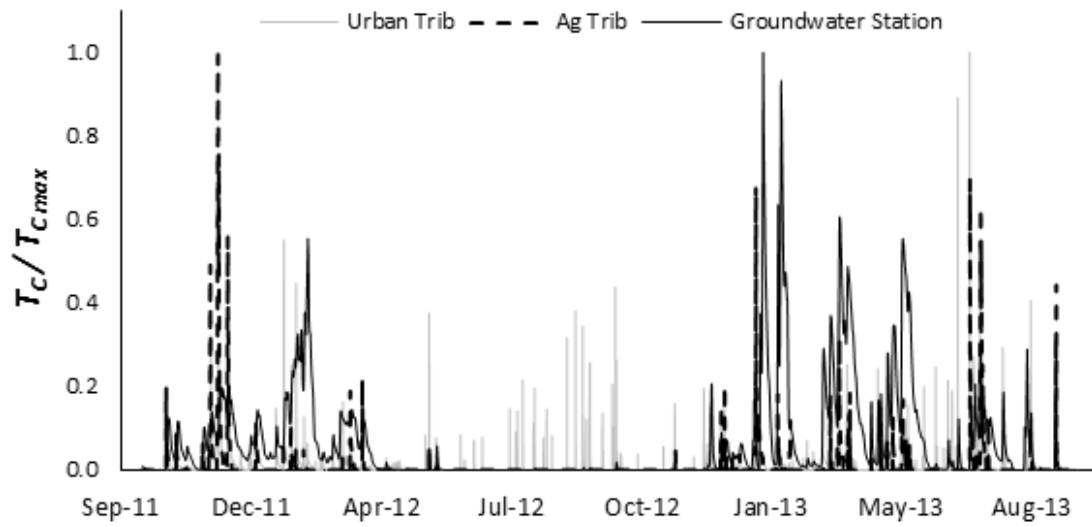


Figure 1.10 Organic carbon content and carbon isotope values for inflowing tributary (n = 32) and outflowing spring (n = 18) sediment

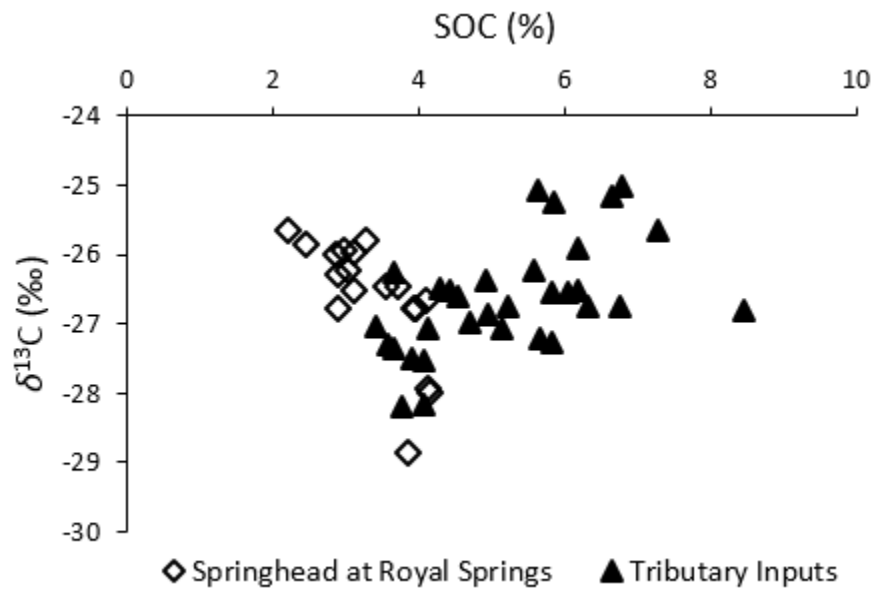
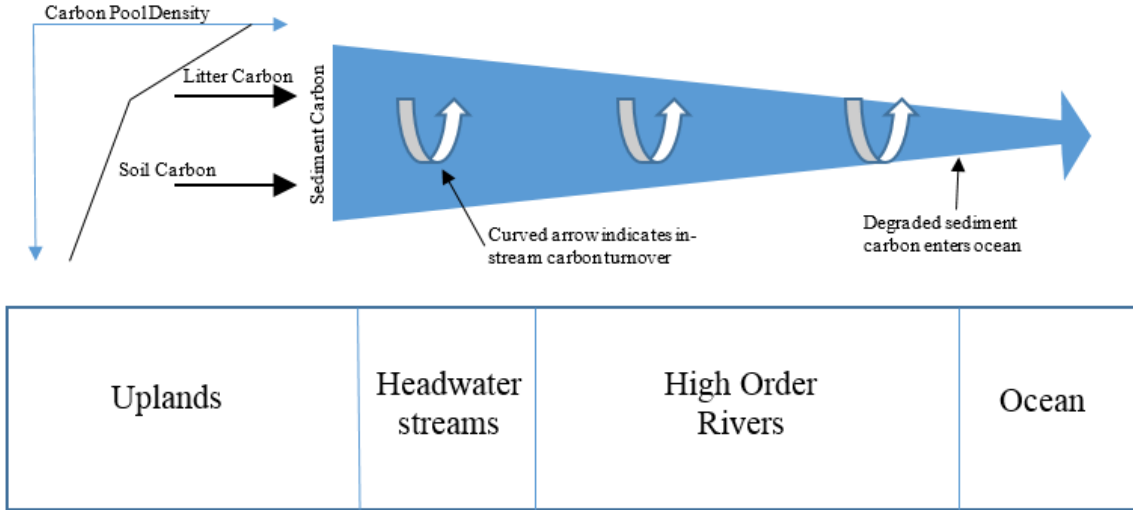
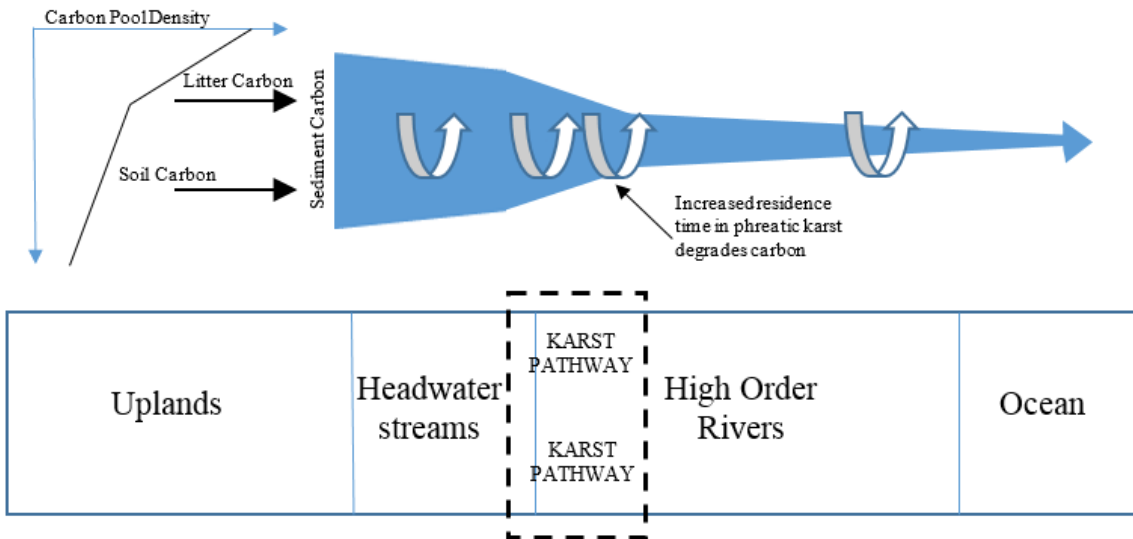


Figure 1.11 Schematic of the fate of sediment organic carbon in the fluvial environment with and without the phreatic karst. (After Fox and Ford, 2016; Marín-Spiotta *et al.*, 2014).

a) FATE OF SEDIMENT CARBON EN ROUTE TO THE OCEAN



b) FATE OF SEDIMENT CARBON EN ROUTE TO THE OCEAN WITH PHREATIC KARST



Chapter 2: Sediment Carbon Fate in Phreatic Karst (Part 2): Numerical Model Development and Application

Adapted with permission from Husic *et al.*, 2017. Sediment Carbon Fate in Phreatic Karst (Part 2): Conceptual Model Development. *Journal of Hydrology* 549, 208-219.

Copyright © 2017 Elsevier

2.1 ABSTRACT

The authors develop a numerical model to elucidate time-distributed processes controlling sediment carbon fate in phreatic karst. Sediment carbon processes simulated in the new numerical model include in-conduit erosion and deposition, sediment carbon transport, surficial fine grained laminae evolution, carbon pool mixing, microbial oxidation, and the understudied process of sediment carbon exchange during equilibrium transport. The authors perform a model evaluation procedure that includes generalized likelihood uncertainty estimation to quantify uncertainty of the model results. Modeling results suggest that phreatic karst conduits sustain sediment transport activity long after surface storm events cease. The sustained sediment transport has the potential to shift the baseflow sediment yield of the phreatic karst to be on par with stormflow sediment yield. The sustained activity is suggested to promote the exchange of sediment carbon between the water column and subsurface karst deposits during equilibrium sediment transport conditions. In turn, the sediment carbon exchange impacts the mixing of new and old carbon pools and the flux of carbon from phreatic karst. Integrated numerical model results from this study support the concept that phreatic karst act as a biologically active conveyor of sediment carbon that temporarily stores sediment, turns over carbon at higher rates than surface streams, and recharges degraded carbon back to the fluvial system. The numerical modeling method adopted in this paper shows the efficacy of coupling carbon isotope fingerprinting with water quality modeling to study sediment carbon in phreatic karst.

2.2 INTRODUCTION

The authors' motivation for Part 2 of these two companion papers was to advance numerical modeling of sediment carbon in phreatic karst. The conceptual model developed in Part 1 was carried forward and further tested with a new numerical simulation. The conceptual model from Part 1 suggests that phreatic karst acts as a biologically active conveyor of sediment carbon that temporarily stores sediment, turns over carbon at higher rates than surface streams, respire carbon dioxide to the water column, and recharges degraded organic carbon back to the fluvial system. Karst morphologic and hydrologic features for which the conceptual model, and hence the numerical model herein, are deemed applicable includes active sediment carbon delivery from surface streams to subsurface karst, the presence of a phreatic system that promotes carbon storage and turnover, and active recharge of sediment back to the fluvial network. The authors' arguments for research that warrants improving numerical modeling of phreatic karst systems is described in the following paragraphs.

Karst terrain covers 12% of the Earth's land surface (Ford and Williams, 2007) underscoring the importance of numerical modeling to better elucidate the role of karst systems within fluvial carbon cycling. Nevertheless, we find that few studies have performed numerical modeling of sediment carbon in karst. A number of authors have performed hydrologic and hydraulic modeling of karst aquifers that has led to the development of many methods to estimate spring discharge such as the application of pipe flow models (Thraillkill, 1974; Jeannin, 2001), watershed modeling tools (Baffaut and Benson, 2009; Palanisamy and Workman, 2014), and equivalent porous media models (Scanlon *et al.*, 2003; Panagopolous, 2012; Hartmann *et al.*, 2014). However, the development of numerical models to estimate sediment transport is a relatively uninvestigated area of karst research save for a recent study that used results of a watershed modeling simulation and sediment measurements at a springhead to indirectly estimate sediment discharge (Nerantzaki *et al.*, 2015). With respect to carbon, Simon and Benfield (2001) modeled stream metabolism and carbon processing in a karst cave and found that rates of benthic organic carbon turnover are high in caves compared to surface streams. However, no studies, to our knowledge, have focused on modelling sediment carbon fate in karst.

The development of numerical modeling tools for sediment has a number of advantages for karst systems. One advantage is that numerical modeling can help to elucidate coupled physical and biological processes that exhibit interdependence and non-linearity and cannot be studied with data alone. The surficial fine grained laminae is a feature of phreatic karst that exhibits such complexity for which numerical modeling is deemed useful. The physically-active surficial fine grained laminae is partially controlled by the sediment transport carrying capacity of the fluid to transport sediment carbon in phreatic karst. Within a numerical model, the transport capacity can be calibrated using sediment measurements (Guo and Jin, 1999; Russo and Fox, 2012). Further, the biologically-active surficial fine grained laminae is partially controlled by the inrush of labile carbon and microbial oxidation. Within a numerical model, carbon source quality that is input to the system can be simulated with carbon fingerprinting while carbon measurements can be used to constrain oxidation (Ford and Fox, 2014; Fox and Ford, 2016). Thereafter, continuous simulation of the processes can be integrated to understand their net influence on phreatic karst.

A second advantage of numerical modeling of sediment carbon in phreatic karst is that processes that cannot feasibly be measured in a phreatic setting can be simulated to appreciate their role, or lack thereof, to carbon fate. Sediment exchange between suspended sediments and bed deposits has long been known to occur in fluvial systems during equilibrium sediment transport (i.e., net-zero erosion/deposition, Chang, 1998), yet rarely has been included in sediment transport modeling because emphasis was on prediction of bed morphology or sediment transport rates. In the case of sediment carbon, sediment exchange from turbulent mixing of bed and suspended sediment has the potential to change the overall carbon makeup of each pool even during equilibrium transport conditions. Numerical modeling of phreatic karst allows explicit consideration of sediment carbon exchange between the water and surficial fine grained laminae during transport.

A third advantage of numerical modeling in karst systems is that model calibration and model-integrated results can provide additional lines of evidence to support the conceptual models that underlie our comprehension of karst systems. While the progress of karst research calls for the use of advanced instrumentation and measurements (White, 2002), emphasis on numerical modeling provides a cost-effective alternative to high

resolution data collection. Numerical modeling allows the researcher to fill in gaps in data streams when instruments malfunction or are under routine maintenance. These continuous estimates of processes are then integrated to provide sediment carbon budgets. Thereafter, numerical modeling results can provide an additional line of evidence to reinforce, or refute, postulations made during conceptual model development. In this context, it will be shown that the numerical model applied in this study gives further evidence to support the concept that karst pathways act as biological conveyors that temporarily trap and release surface-derived sediment (see Paper 1: Conceptual Model).

The authors had the objective to develop and apply a sediment carbon numerical simulation model to phreatic karst. The main contributions of this paper are: (1) advancement of sediment carbon modeling for karst by coupling physical processes, biological processes, and carbon isotope fingerprinting; (2) the use of the numerical model to simulate sediment transport and sediment carbon exchange processes that have not been investigated previously for karst systems; and (3) integrated results of the numerical simulation that provide additional lines of evidence towards a conceptual model of sediment carbon within karst pathways.

2.3 METHODS

2.3.1 Model Formulation

The authors formulate the numerical model by considering the existence of karst morphologic and hydrologic features, including active sediment carbon delivery from the surface to subsurface karst, the presence of a phreatic system that promotes carbon storage and turnover, and active recharge of sediment back to the fluvial network (Atkinson, 1977; Drysdale *et al.*, 2001; White, 2002; Massei *et al.*, 2003; Fleury *et al.*, 2007; Bakalowicz *et al.*, 2008; Herman *et al.*, 2008; Fleury *et al.*, 2013). The authors assume sediment carbon originating from urban/suburban and agricultural landscapes and streams is transported within the fluvial load (<53 μm in diameter) to a phreatic karst conduit. Quick flow from surface streams to a phreatic conduit (i.e., tertiary porosity pathways) are formulated to dominate sediment carbon inputs based on the data results in the companion Paper 1 as well as by the results of others (Ryan and Meiman, 1996; Katz *et al.*, 1998; Mahler and

Lynch, 1999; Pronk *et al.*, 2006; Simon *et al.*, 2007). Based on the potential for a mixture of land uses and stream conditions, the authors consider that sediment carbon can be from a mixture of carbon pools with varying levels of quality (e.g., litter-derived, soil carbon, algae). The authors formulate the model considering that boundary condition measurements of sediment carbon inflowing to a phreatic karst system (i.e., at swallets or sinking streams) and carbon recharged from the phreatic karst (i.e., at springheads) provide information for model inputs and model evaluation, respectively.

The authors formulate the continuity equation to simulate sediment organic carbon (SOC) fate within a phreatic conduit as

$$\frac{d(SS_{SOC})}{dt} = Q_{SOC\ in} - Q_{SOC\ out} + Q_{SOC\ pir} + \sum_{i=1}^{n_d} E_{SOC\ i} - D_{SOC} + X_S - X_{SS} \text{ , and (1)}$$

$$\frac{d(S_{SOC})}{dt} = - \sum_{i=1}^{n_d} E_{SOC\ i} + D_{SOC} - X_S + X_{SS} - DEC_{SOC} \text{ , (2)}$$

where each term has dimensions of mass per time (kg s^{-1}). Equations (1) and (2) represent sediment carbon fate within suspended sediment (SS) and storage (S), respectively, within a phreatic conduit. In Equation (1), suspended sediment carbon may transport into ($Q_{SOC\ in}$) and out of ($Q_{SOC\ out}$) a section of a phreatic conduit or may arrive within the conduit from swallets that pirate sediment carbon from surface streams ($Q_{SOC\ pir}$). Sediment carbon can move between suspended sediment and storage with the surficial fine grained laminae by physical mechanisms, including erosion from surface storage and deep storage (E_{SOC} , where n_d vertical depths of sediment are stored), deposition to the stored sediment carbon (D_{SOC}), and the exchange (X) during equilibrium sediment transport. During storage within the surficial fine grained laminae, sediment carbon can undergo microbial oxidation (DEC_{SOC}), and carbon fingerprinting can be used to discretize incoming labile and recalcitrant pools that can be tracked within a phreatic conduit and simulated using pool-specific oxidation rates.

The authors formulate erosion within a phreatic conduit based on the physical limitations of shear, transport, and supply as

$$E_{SOC} = S_{SOC} S^{-1} \min[a(\tau_o - \tau_{cr})^b \ell B, T_c \ell - SS t^{-1}, St^{-1}] \text{ , (3)}$$

where $S_{SOC} S^{-1}$ is the density of carbon within the stored sediment (gC gSed^{-1}) since the erosion and deposition mechanics are based on both the inorganic and organic portions of the fluvial load, τ_o is the fluid shear stress at the bed of the phreatic conduit (Pa), τ_{cr} is the

critical shear stress of sediment (Pa), a and b are empirical coefficients, ℓ is the bed length (m), B is the bed width (m), T_c is the transport carrying capacity ($\text{kg m}^{-1}\text{s}^{-1}$), and t is the time step (s). The fluid shear stress for conduit flow can be estimated by the Darcy-Weisbach formula as

$$\tau_o = \frac{f\rho V^2}{8}, \quad (4)$$

where, f is the Darcy friction factor (unitless), ρ is the density of water (kg m^{-3}), and V is the velocity of fluid in the conduit (m s^{-1}). The erosion rate in Equation (3) also relies on the excess transport capacity expressed as the difference between the sediment transport carrying capacity of the flow (T_c) and the suspended sediment load per time. T_c ($\text{kg m}^{-1} \text{s}^{-1}$) can be expressed (Julien and Simons, 1985; Hessel and Jetten, 2007) as

$$T_c = C_{tc}\tau_o^{\frac{3}{2}}, \quad (5)$$

where C_{tc} ($\text{m}^{1/2}\text{s}^2 \text{kg}^{-1/2}$) is an empirical coefficient typically calibrated with suspended sediment measurements. The available storage of sediment (kg) within the phreatic conduit is the final erosion rate-limiting process as the surficial fine grained laminae source can be exhausted as a result of erosion.

The authors simulate sediment carbon deposition within the phreatic conduit for hydraulic conditions when excess transport capacity is not met. Deposition of sediment carbon can be expressed using a sediment deposition function (Russo and Fox, 2012) as

$$D = SS_{SOC}SS^{-1} \times \max\left[\frac{w_s}{k_p H} (SSt^{-1} - T_c\ell), 0\right], \quad (6)$$

where $SS_{SOC}SS^{-1}$ is the density of carbon in the suspended sediment (gC gSed^{-1}), w_s is the settling velocity of sediment (m s^{-1}), k_p is the deposition coefficient based on the Rouse concentration profile (unitless), and H is the height of the phreatic conduit (m).

The authors formulate Equations (1) and (2) by accounting for the exchange (X) of sediment carbon during equilibrium sediment transport. It is recognized that during equilibrium sediment transport there is a net-zero effect on the mass of suspended sediment or mass of stored sediment within the conduit bed, however, instantaneous turbulence allows for near-continuous exchange of sediment from the water column to the bed and vice versa (e.g., Chang, 1998). The equilibrium exchange is included to potentially change the overall makeup of carbon quality in the suspended and stored carbon pools as

$$X_{SS} = (e_x SS) \times (SS_{SOC}SS^{-1})t^{-1}, \quad (7)$$

and

$$X_S = (e_x SS) \times (S_{SOC} S^{-1}) t^{-1}, \quad (8)$$

where, e_x is the exchange rate (unitless) between suspended and stored surficial fine grained laminae sediment carbon. The physical mass of sediment mixed ($e_x SS$) is equal (i.e., equilibrium mixing) in Equations (7) and (8), but the quantity of sediment carbon within the water column or bed (i.e., $SS_{SOC} SS^{-1}$ and $S_{SOC} S^{-1}$, respectively) can vary.

The authors formulate sediment carbon fate by considering that temporarily stored carbon within the surficial fine grained laminae of the phreatic conduit undergoes oxidation by heterotrophic bacteria. The authors formulate a first-order decomposition function for each carbon pool

$$DEC_{SOC} = \sum_{j=1}^{n_p} k_j S_{SOC j} \quad (9)$$

where j is an index for carbon pool (i.e., litter, soil, algae), n_p is the total number of carbon pools, k_j is the soil decomposition rate (d^{-1}) of each pool, and $S_{SOC j}$ is the supply of organic carbon associated with each pool in the surficial fine grained laminae (kg).

2.3.2 Model Setup and Discretization

The authors test the sediment carbon numerical formulation in Equations (1) through (9) within the coupled Cane Run Creek Watershed and Royal Spring Groundwater Basin located in the Bluegrass Region of central Kentucky, United States. The reasons for choosing the fluviokarst system and the physiogeographic features of the system are described in Figure (3) and the methods section of our companion Paper 1. In brief, a landscape with urban/suburban and agricultural land uses drains to the Cane Run Creek and its tributaries. The phreatic subsurface conduit is approximately 16 km in length, generally aligned with the main stem of the surface channel of Cane Run, and pirates nearly all surface flow during low to moderate hydrologic conditions. The phreatic conduit is approximately 20 m below the ground surface, is hydraulically controlled by a subsurface dam, and recharges at the Royal Spring springhead, which has the highest average discharge of any perennially spring in the highly karstic region of central Kentucky, USA (Currens *et al.*, 2015).

The authors applied the numerical model for sediment carbon to the primary phreatic conduit, and discretized the model formulation as follows. The authors specified

three sediment carbon pools, including fine-sized litter, recalcitrant soil carbon, and stabilized algae, that can be transported to the phreatic conduit and vary in recalcitrance and microbial oxidation rates (Thorp and Delong, 2002; Marin-Spiotta *et al.*, 2014). The authors specified two vertical depths of sediment carbon in the phreatic conduit including the highly active surficial fine grained laminae and a deeper more consolidated storage with higher critical shear stress (Ford and Fox, 2014). The authors discretized the transport carrying capacity using the residual T_c concept (Chang, 1998) such that the surficial fine grained laminae would be eroded first followed by the deeper, more consolidated stored bed carbon. The authors discretized the transport calibration coefficient to differentiate between baseflow and stormflow transport in the phreatic conduit (Russo and Fox, 2012), which reflects three orders of magnitude difference in fluid energy. The authors discretized the phreatic conduit into sixteen, 1 km in length, spatial cells and simulated the model at a one hour time step. The temporal discretization reflected the authors' confidence in the time series data. The spatial scale was selected in order to satisfy the Courant-Friedrichs-Lewy condition such that the average velocity of suspended sediment carbon within the model is on the same order of magnitude as the downstream transmission of information (Islam and Chaudhry, 1997).

The authors used data, including water, sediment, sediment carbon measurements and carbon fingerprinting results, from surface streams as upstream inputs to the model (see Figure 2.1). The authors solved the numerical model for sediment carbon flux and sediment carbon storage for each spatial cell and time step by estimating erosion and deposition as a function of hydraulic variables and sediment concentration and by performing the calculation steps outlined in Russo and Fox (2012) and Husic (2015). The authors used data, including sediment and sediment carbon measurements, within the conduit at the Groundwater Station (see Paper 1, Figure 1.3) and at the springhead (Royal Spring) as downstream boundary conditions and for model evaluation.

2.3.2.1 Measured Inputs and Parameters

The friction factor was estimated by solving for the conservation of energy from within the conduit to the springhead (see model inputs in Table 2.1). The maximum supply of the surficial fine grained laminae was estimated by assuming that the neutrally buoyant

mixture reaches a maximum depth of 5 mm (Droppo and Stone, 1994; Stone and Droppo, 1994; Droppo and Amos, 2001). The bulk density of the deeper bed sediment is estimated as $1.5 \times 10^3 \text{ kg m}^{-3}$ (Russo and Fox, 2012). The exponent in the erosion calculation (Equation 3), b , is assumed to be 1 for all fluvial erosion sources, which agrees with the concept of erosion being a shear driven process (Hanson and Simon, 2001; Sanford and Maa, 2001; Wynn *et al.*, 2008; Simon *et al.*, 2009). Erodibility and critical shear stress for these equations, a and τ_{cr} , are parameterized uniquely for each erosion source based on literature reported values and equations (Droppo and Amos, 2001; Hanson and Simon, 2001; Sanford and Maa, 2001; Simon and Thomas, 2002; Russo and Fox, 2012). Sediment settling velocity was modeled using Stoke's Law and the settling depth coefficient was estimated based on a uniform concentration profile (Russo and Fox, 2012). The boundary flow rate reflects changes in sediment transport behavior between baseflow and storm flow and is dependent on hydraulic watershed characteristics (Russo and Fox, 2012).

Sediment carbon quality varies within the watershed due to land use. Fingerprinting results (see Table 2.3, companion Paper 1) were used to unmix soil, algal, and litter carbon contributions to urban and agricultural tributaries. The proportion of urban (P_{urban}) and agricultural (P_{ag}) land use in each model cell is shown in Table 2.2. The flux of sediment by surface tributaries into the main Cane Run creek was modeled using Einstein's Approach (Chang, 1998) which integrates the vertical velocity and sediment concentration profiles over the flow depth. Sediment and flow pirating from the surface channel into the subsurface conduit was estimated as a function of swallet density ($P_{swallet}$), surface sediment concentration, and conduit flow rate and satisfied the conservation of mass within each model cell (Husic, 2015). Conduit bathymetry at the Groundwater Station (cell 10) was estimated from the results of multiple quantitative dye, Doppler sonar, and video experiments. The geometry at other cells (see Table 2.2) was estimated by optimizing net dynamic equilibrium of sediment over the simulation period.

Model parameterization ranges that were carried forward to the model evaluation relied on measurements within the study region or ranges reported in the literature for similar systems. The percent algae (P_{algae}) in surface-derived sediment was modeled using a distribution from a nearby agriculturally dominated watershed (Ford *et al.*, 2014, also see

Paper 1). Decomposition rates for soil, litter, and algal carbon were parameterized based on results from literature (Webster *et al.*, 1999; Six and Jastrow, 2002; Ford and Fox, 2014). Liu *et al.* (2010) investigated sediment exchange ratio (e_x) variation using grain-size distributions within an estuary dominated by clayey silt and estimated that the exchange ratio is < 0.10 for unidirectional flows. While the exchange rate is likely to vary with turbulence intensity, mean bursting and sweeping behavior was approximated by a single rate within the model.

2.3.2.2 Model Evaluation

Model evaluation was facilitated using measured datasets detailed in our companion Paper 1. In brief, flow, sediment, and sediment organic carbon data were collected over a two year period to calibrate and validate model results. Flow and turbidity data were sampled at 15 and 10 minute intervals, respectively, and sediment organic carbon samples were collected approximately every fortnight. Surface streams were continuously monitored using staff gages while a Marsh McBirney® 201-D magnetic water flow-meter was deployed in the subsurface conduit to collect continuous velocity data. Depth integrated sediment samples were collected and analyzed for total suspended solids (TSS). Turbidity and TSS were correlated to provide a continuous record of sediment transport. Sediment organic carbon values of the tributaries and outlets were measured using in situ trap samplers (Phillips *et al.*, 2000).

Calibration parameters for the sediment model included the transport capacity coefficients for low and high flows. Regarding calibration, it is well recognized that sediment transport model yields are highly sensitive to the transport capacity terms with negligible sensitivity to other parameters (Ahmandi *et al.*, 2006; Hessel and Jetten, 2007; Yan *et al.*, 2008; Russo and Fox, 2012). Further, note that the two controlling transport capacity coefficients are independent and do not interact since they are used for mutually exclusive hydrologic conditions (i.e., baseflow vs storm flow). Therefore, sediment transport model results were calibrated with the transport capacity coefficients using the collected data at the Groundwater Station (see “Stage 2” Figure 2.1). The Generalized Reduced Gradient method (GRG nonlinear algorithm) was used to optimize sediment transport modeling results (Lasdon *et al.*, 1974). Initial conditions to the algorithm were

selected based on manual calibration and visual assessment of the model and data sediment discharge graphs. Sediment transport model results were evaluated using the Nash-Sutcliffe efficiency (Nash and Sutcliffe, 1970) following the guidelines of Moriasi *et al.* (2007).

Model evaluation parameters for the carbon model included the percent of algae in the carbon load, the decomposition rates of soil, litter, and algae carbon, and the sediment exchange rate. Uncertainty in the carbon model results was performed using a generalized likelihood uncertainty estimation (GLUE) statistical approach which is increasingly utilized in water resources modeling given the potential of equifinality of multivariate parametric models (Bevin and Binley, 1992; Beven, 2006; Dean *et al.*, 2009; Gong *et al.*, 2011; Ford and Fox, 2015). For each model run, a parameter set was randomly generated using a uniform distribution over the min-max range of each parameter. The authors found the response variable to be approximately normally distributed for both data and model results; therefore a t-test ($n < 30$) was used on each set of model outputs to retain likely results and discard statistically different results ($\alpha = 0.05$) (see “Stage 3” Figure 2.1). Twenty-thousand model simulations were performed to estimate uncertainty in carbon model results. Sediment trap carbon samples were compared with model results for $SS_{SOC}SS^{-1}$ ($gC\ gSed^{-1}$) at the Royal Spring from December 2012 through August 2013.

2.4 RESULTS AND DISCUSSION

2.4.1 Model Evaluation

Sediment transport model results from the phreatic conduit agreed well with sediment data observations during calibration and validation periods (Figure 2.2a). Baseflow conditions were reflected well in the model suggesting that the low flow transport capacity coefficient represented the sediment transport dynamics in the conduit adequately. Model results typically underestimated peak sediment discharge: low estimates of peak sediment discharge could arise from heterogeneity of sediment inputs (e.g., swallet geometry, spatial variability, and clogging). The E_{NS} and R^2 statistics for calibration and validation perform satisfactorily when compared to sediment modelling results reported in the literature (Moriasi *et al.*, 2007), especially considering that the model was simulated at

an hourly time step while most literature values are daily or monthly. Yuan *et al.* (2007) showed that statistical evaluation values worsen as time steps are shortened.

Sediment carbon model results from Royal Spring were evaluated using the GLUE methodology by which values for the five carbon model calibration parameters were estimated. Of the 20,000 model simulations, approximately half of the parameter sets were found to meet the specified statistical criteria (t-test, $\alpha = 0.05$). The median parameter values of the acceptable model results showed that the decomposition rate of soil ($k_s = 1.1 \times 10^{-4} \text{ d}^{-1}$) was one order of magnitude smaller than that of the algal ($k_a = 4.0 \times 10^{-3} \text{ d}^{-1}$) and litter ($k_l = 4.5 \times 10^{-3} \text{ d}^{-1}$) carbon pools, but near the maximum end of soil decomposition rates published in other studies (Alvarez and Guerrero, 2000; Ford and Fox, 2014). Model results also showed the exchange rate to be 4.3% and the percent of algae in the carbon load to be 21%. The distribution of model results and data results is approximately normal and the minimum, median, and maximum model outputs are shown in Figure 2.2b. The sediment carbon model under predicts the range of variability exhibited by the sediment carbon data results reflecting the mean representation of erosion and decomposition in the model (e.g., constant rates over grid cells that are approximately one kilometer in length). For example, it is realized that fluvial sediment carbon data can be highly variable (Ford *et al.*, 2014) reflecting episodic transport of eroded sediment (Fox and Papanicolaou, 2008) and the spatial variability of decomposition hot spots in fluvial systems (Battin *et al.*, 2003). Nevertheless, the fact that the data range is on the same order as the model results and is included within the model domain (Figure 2.2c) adds confidence to the results and highlights that the model is able to reflect the mixing of new sediment carbon transported to the subsurface and resuspended sediment carbon that was temporarily stored in the bed.

2.4.2 Hydrologic Processes in Phreatic Karst

Numerical modeling results highlight the impact of sustained fluid energy and equilibrium sediment exchange upon sediment carbon in the phreatic conduit. The fate of pirated sediment provides a depiction of sustained fluid energy's impact on sediment carbon. Sediment is pirated from the surface streams to the phreatic conduit during storm events from September 2011 to April 2012 and from December 2012 to August 2013 while April 2012 to December 2013 is a period of prolonged drought with little to no streamflow

(Figure 2.3a, Q_{ss}). Storage in the surficial fine grained laminae (SFGL in Figure 2.3a) increases during the largest storm events because sediment is deposited as the transport carrying capacity of the fluid decreases in the phreatic conduit relative to the surface streams. However, sustained fluid energy exists in the phreatic conduit long after stormflow has ceased in the surface streams. The sustained transport capacity continues to erode the sediment from the surficial fine grained laminae such that sediment transport rates are non-zero for much of the time during September 2011 to April 2012 and December 2012 to August 2013. The sustained sediment transport results in high yields of sediment during baseflow conditions in the surface streams. For example, integrated model results showed that 46% of the total sediment exported from the phreatic conduit to the springhead occurs during periods of no surface stream activity. The sediment carbon eroded from the surficial fine grained laminae and transported during these baseflow periods is lower than newly pirated sediment carbon (i.e., OC in Figure 2.4a) and highlights the recharge of degraded sediment carbon back to the surface streams.

The longitudinal variability of sediment storage and sediment carbon transport in the conduit highlights the role of equilibrium sediment exchange in phreatic karst. The surficial fine grained laminae's evolution shows the highest variability in the first 10 km of the phreatic conduit (i.e., cells 5 and 10 in Figure 2.3b). The phreatic conduit in this section is near swallets that deliver sediment. The sediment deposits to the surficial fine grained laminae and later erodes as mentioned above. Moving downstream in the conduit from kilometers 11 to 16, much lower variability of the surficial fine grained laminae's depth is shown in time (i.e., cells 13 and 16 in Figure 2.3b). The phreatic conduit does not gain or lose water or sediment through this section and the cross sectional area is fairly uniform. The fluid energy is relatively constant and the mass rate of suspended sediment stays relatively constant spatially through this section.

While fluid and sediment is conveyed at constant rates in the lower reach of the phreatic conduit, sediment carbon transport varies due to equilibrium sediment exchange. Sediment carbon becomes more and more degraded when moving downstream in the conduit (i.e., Q_{SOC} decreases from GW to RS in Figure 2.4a). Suspended sediment instantaneously exchanges more labile suspended sediment carbon with more recalcitrant bed sediment carbon. The organic carbon content of suspended sediment is considerably

higher than that of the surficial fine grained laminae (i.e., OC in Figure 2.4a) due to the fact that heterotrophic bacteria oxidize organic carbon while it is temporarily stored. The sediment exchange during equilibrium sediment transport therefore causes the entrainment of older, more highly decomposed bed sediment and deposition of more labile, newly delivered sediment carbon. The exchange process also impacts the distribution of transported carbon across carbon pools (Figure 2.4b). The proportion of soil carbon increases in the surficial fine grained laminae relative to the suspended sediment and remaining algae and litter carbon decrease due to their order of magnitude higher rates of decomposition. Equilibrium sediment exchange increases the proportion of the degraded soil carbon to the sediment carbon load during conveyance through the phreatic conduit, again highlighting a more degraded sediment carbon that is recharged to surface streams.

The mentioned hydrologic processes, including the sustained fluid energy to transport degraded sediment carbon during low flow and the impact of equilibrium sediment exchange upon transporting degraded carbon, are worthy of discussion. Both processes have the potential to help deliver degraded carbon from phreatic karst to surface streams, and neither process has been mentioned previously in the literature, to the authors' knowledge.

One net effect of sustained fluid energy in phreatic karst is that storm flow deposition coupled together with low to moderate flow erosion results in a near long term equilibrium of the surficial fine grained laminae (Figure 2.3a). The surficial fine grained laminae can therefore continuously harbor and oxidize sediment carbon. Another impact is that the phreatic karst often acts as a constant conveyor of sediment carbon through the system regardless of surface stream conditions (i.e., as mentioned, nearly half of sediment is transported during surface baseflow). The sediment transport activity of the phreatic karst highlights the disconnect between surface and subsurface streams in karst terrain. This is particularly interesting because conventional wisdom, or at least the first rule of thumb, is that fluvial systems transport 90% of their sediment load during 5% of the year (Walling and Webb, 1982; Hossain and Eyre, 2002). The phreatic karst obviously does not conform to this conventional wisdom and in turn continually recharges degraded sediment carbon to surface streams.

The equilibrium sediment exchange extends our knowledge of phreatic karst but also highlights the potential importance of a less studied sediment transport physical process. Sediment transport scientists have long understood that suspended sediments in turbulent flow can actively exchange with stored bed sediments although during equilibrium transport it is recognized that the net exchange is zero (e.g., Chang, 1998). The physics of the sediment exchange process has been more recently justified using advanced visualization techniques and it has been found that sediment erosion and deposition is coupled to flow coherency (Cellino and Lemmin, 2004). Cellino and Lemmin (2004) showed that low momentum zones of coherent fluid that transports settling sediment episodically deposits sediment to the bed while fluid ejections associated with the shedding phenomena at the bed episodically re-suspends bed sediment into the water column. However, sediment exchange processes between the water column and bed during equilibrium transport have been rarely included in sediment transport models. One reason for omitting the equilibrium exchange process from models is a lack of need for such detailed information given that the net results sought after for sediment transport models have been the downstream transport rates distributed over time and the net change in the streambed elevation; estimates of sediment equilibrium exchange does not help this goal. A second reason for omitting the exchange process from sediment transport models has likely been a lack of methods to help parameterize the exchange rate, as studies such as those by Cellino and Lemmin (2004) were experimental in nature and limited to the laboratory scale.

The equilibrium exchange of sediment is potentially of high interest in the recent class of scientific studies that emphasize elucidating the role of carbon processes in the inland freshwater carbon budget (Battin *et al.*, 2008; Regnier *et al.*, 2013). In the case of sediment carbon fate and transport in the phreatic karst studied here, the exchange rate appears important given the potential to exchange labile carbon with recalcitrant carbon. It is likely that the net importance of the equilibrium exchange process upon sediment carbon fate varies in other fluvial systems. For example, storm-activated surface stream equilibrium transport can be of a short duration since bed sediments are eroded to the water column during the rising limb of the hydrograph while sediments originating from upstream are deposited to the bed during the falling limb of the hydrograph. For such

occurrences, the exchange during equilibrium may be marginalized in importance relative to non-equilibrium exchanges. However, highly regulated rivers such as systems with controlled dam release will have fairly constant sediment transport carrying capacity and for such systems the sediment carbon balance might be impacted by equilibrium exchange. With this in mind, it is possible that the phreatic karst conduits represents a class of fluvial systems in which equilibrium exchange is significant due to the fairly limited range of the sediment transport carrying capacity of the flow dictated by an upstream or downstream hydraulic control.

2.4.3 Phreatic Karst Actively Convey Sediment Carbon

Hydrologic processes discussed in companion Paper 1 and this paper allow the authors to justify and further update the conceptual model of sediment carbon in phreatic karst. The biologically active phreatic karst conveyor temporarily stores newly delivered sediment carbon within the surficial fine grained laminae because the sediment transport carrying capacity of phreatic karst water is orders of magnitude less than the surface streams. Labile carbon including algae and litter carbon turnover within the surficial fine grained laminae at higher rates than soil carbon, so degraded soil carbon is sequestered while carbon dioxide is respired to the water column. The sustained fluid energy to transport sediment and equilibrium sediment exchange act to transport more and more highly degraded sediment carbon during low flows and longitudinally in the phreatic karst. In turn, degraded organic carbon is almost continuously recharged back to the fluvial system at perennial springheads.

Integration of the numerical modeling results to estimate a sediment carbon budget (Figure 2.5) further support the conceptual model as the authors are able to estimate the mentioned processes for the phreatic system studied in this paper. Evidence of the ability of the karst conduit to limit transport capacity was shown by the result that sediment deposition within the conduit was similar to the total amount of sediment pirated from surface pathways. In turn, 84% of the pirated sediment carbon was deposited to the surficial fine grained laminae. The biological activity of the surficial fine grained laminae to oxidize sediment carbon is evidenced by the substantial carbon turned over, which is 46% of the carbon recharged to the surface stream. The similarity of net erosion and

deposition in the phreatic conduit highlights the sustained energy of the fluid during low flows. Net deposition of sediment to the surficial fine grained laminae slightly exceeded erosion, which was attributed to the fact that the two years studied contained about 15% more rainfall events than average (e.g., the 2013 hydrologically active summer period was atypical). The potential importance of equilibrium exchange is evidenced by the modeling result that sediment suspended during equilibrium exchange had 29% less carbon than sediment deposited during equilibrium exchange. The recharge of degraded sediment carbon by the phreatic karst to surface streams is highlighted by the modeling results that estimate that recharged sediment carbon is just 57% of pirated sediment carbon.

2.4.4 Advancement in Numerical Modeling of Karst Systems

As one final contribution of this paper, the authors make a note regarding the advancement of water quality modeling that couples the conservation of mass for a system with tracer-based methods. The progressive method adopted in this paper and our companion paper shows how the novel use of stable isotope data can be coupled with more traditional water quality modeling in order to assist with understanding the non-linear behavior of sediment carbon fate in fluviokarst watersheds. The stable carbon isotopic composition of sediment provides an independent method to assist with allocating sources of surface derived sediments to the karst subsurface and justify the consistency of the sediment pool studied in the surface and subsurface environments.

The research method applied here provides another example of a branch of hydrologic modeling that relies on the application of stable carbon isotopes for inputs and verification purposes. The stable carbon isotope composition of sediments has been long used for gaining an understanding of sediment carbon provenance in estuary and marine sciences (e.g., Martinotti *et al.*, 1997). Over the past fifteen years, stable carbon isotopes have been increasingly applied within the sediment fingerprinting methodology in order to understand erosion sources at catchment and watershed scales (Papanicolaou *et al.*, 2003; Bellanger *et al.*, 2004; Fox, 2005, 2009; Fox and Papanicolaou, 2007; Jacinthe *et al.*, 2009; Imberger *et al.*, 2014; Ford *et al.*, 2015).

With the stable carbon isotopes of sediment carbon now as a consistent tool applied within the hydrologic sciences, we expect to see more and more examples of coupling

fingerprinting technology, where stable isotopes are used as tracers, with traditional water quality modeling that simulates sediment and sediment carbon continuity. Ford and Fox (2015) showed the use of the *ISOFLOC* model for such purposes, to simulate algal growth and turnover to sediment carbon; and showed how algal sloughing could be calibrated with stable carbon isotopes in order to help simulate the fluvial organic carbon budget. Fox and Martin (2015) showed how stable isotopes could be used to assist with calibration of model parameters including the sediment delivery ratio and sediment transport capacity with a soil erosion and sediment yield model applicable to watersheds with mixed land uses. Coupling of stable isotopes and water quality modeling is a fairly new class of research, and it is expected that model advancement and lessons learned from the present study as well as the aforementioned studies will assist researchers as they apply the stable isotope tools to assist with reducing numerical model uncertainties.

2.5 CONCLUSIONS

The main conclusions of this paper are as follows:

- Phreatic karst conduits are suggested to sustain sediment transport activity long after surface storm events cease. The sustained sediment transport has the potential to shift the baseflow sediment yield of the phreatic karst to be on par with stormflow sediment yield. For example, in the present study almost 50% of the sediment conveyed by the phreatic conduit was during time periods when no flow existed in the surface streams of the watershed.
- Exchange of sediment carbon between the water column and subsurface karst deposits is suggested to occur during equilibrium sediment transport within phreatic karst. In turn, the sediment carbon exchange impacts the mixing of new and old carbon pools and the flux of carbon from phreatic karst. Phreatic karst provides a hydrologic phenomenon where equilibrium sediment transport is likely sustained for rather long periods of time (see point 1 above). The understudied equilibrium exchange of sediment is potentially of high interest for scientific studies that emphasize elucidating the role of carbon processes in the inland freshwater carbon budget.
- The integrated numerical model results from this study support the conceptual model proposed in Paper 1 of these two companion papers. Phreatic karst are suggested to act

as a biologically active conveyor of sediment carbon that temporarily stores sediment, turns over carbon at higher rates than surface streams, respire carbon dioxide to the water column, and recharges relatively depleted organic carbon back to the fluvial system.

- The method adopted in this paper shows the efficacy of coupling carbon isotope fingerprinting with water quality modeling to study sediment carbon in phreatic karst. It is expected that such methods can be built upon in future research studies.

2.6 ACKNOWLEDGEMENTS

The authors would like to thank the associated editor Nico Goldscheider and anonymous reviewers whose comments helped the authors to greatly improve the quality of this manuscript and its companion. We would like to thank the extended staff at the Kentucky Geological Survey for the extensive research performed in the Cane Run Watershed and Royal Spring Groundwater Basin both prior to and concurrent with this research. We thank Dr. Harry Rowe for analysis of the elemental and carbon data and several undergraduate and graduate research associates that helped with collecting field data and performing laboratory analysis. We thank the University Of Kentucky Department Of Civil Engineering for partial funding of the graduate student during this research study. We also thank the United States Geological Survey for partial funding of this research through the 104b Student Research Enhancement Grant. We also acknowledge funding from the Kentucky Senate Bill 271B Water Quality program.

2.7 TABLES AND FIGURES

Table 2.1 Model inputs, initial conditions, potential calibration parameters in sediment transport model, and calibration parameters in the carbon model.

Symbol	Description	Value	Unit		
MODEL INPUTS					
ΔL	Spatial step	1×10^3	m		
Δt	Temporal step	3600	s		
f	Darcy friction factor	0.3	unitless		
ρ	Density of water	1×10^3	kg m^{-3}		
ρ_{SFGL}	Bulk density of SFGL sediment	1×10^3	kg m^{-3}		
ρ_{BED}	Bulk density of deep bed sediment	1.5×10^3	kg m^{-3}		
d_{max}	Maximum depth of SFGL sediment	5.0×10^{-3}	m		
τ_{cr}^{SFGL}	Critical shear of the SFGL source	0.05	Pa		
τ_{cr}^{BED}	Critical shear of the bed source	1	Pa		
w_s	Mean settling velocity of suspended material	9.2×10^{-4}	m s^{-1}		
k_p	Settling depth coefficient	0.5	unitless		
$Q_{boundary}$	Boundary between low and high flows	1.4	$\text{m}^3 \text{s}^{-1}$		
SOC_{urban}	Carbon content of urban sediment	5.70	$\text{gC } 100\text{gSed}^{-1}$		
SOC_{ag}	Carbon content of agricultural sediment	3.83	$\text{gC } 100\text{gSed}^{-1}$		
MODEL INTIAL CONDITIONS					
$d_{SFGL(0)}$	Initial depth of SFGL sediment in the conduit	2.5×10^{-3}	m		
$S_{SOC(0)}$	Initial organic carbon content of SFGL	2.68	$\text{gC } 100\text{gSed}^{-1}$		
SEDIMENT CALIBRATION PARAMETERS					
		Min	Optimal	Max	
$C_{rc_{low}}$	Transport capacity coefficient for low flows	1.0×10^{-6}	1.2×10^{-5}	4.0×10^{-5}	$\text{m}^{1/2} \cdot \text{s}^2 \text{kg}^{-1/2}$
$C_{rc_{high}}$	Transport capacity coefficient for high flows	3.0×10^{-7}	3.1×10^{-6}	6.0×10^{-6}	$\text{m}^{1/2} \cdot \text{s}^2 \text{kg}^{-1/2}$
CARBON CALIBRATION PARAMETERS					
		Min	Median	Max	
P_{algae}	Percent of algal carbon	0	0.21	0.4	unitless
k_s	Soil carbon decomposition rate	2.6×10^{-6}	1.1×10^{-4}	2.3×10^{-4}	d^{-1}
k_l	Litter carbon decomposition rate	2.3×10^{-4}	4.5×10^{-3}	8.0×10^{-3}	d^{-1}
k_a	Algae carbon decomposition rate	2.3×10^{-4}	4.0×10^{-3}	8.0×10^{-3}	d^{-1}
e_x	Sediment mixing exchange rate	0	0.043	0.10	unitless

Table 2.2 Conduit bathymetry, swallet density, and land use information for model cells. $P_{swallet}$ represents the proportion of swallets in the watershed located within a particular model cell. P_{urban} and P_{ag} represent the percentage of land used for agricultural and urban purposes, respectively, contributing to a given model cell.

Cell	Height (m)	Width (m)	$P_{swallet}$ (%)	P_{urban} (%)	P_{ag} (%)
1	0.45	3.11	9	80	20
2	0.50	3.42	6	75	25
3	0.59	4.04	11	63	37
4	0.65	4.51	10	58	42
5	0.69	4.79	7	52	48
6	0.73	5.04	6	48	52
7	0.77	5.35	10	46	54
8	0.83	5.72	14	43	57
9	0.86	5.97	12	40	60
10*	0.90	6.22	15	38	62
11	0.90	6.22	No surface sediment diverted to the conduit in Cells 11 – 16		
12	0.90	6.22			
13	0.90	6.22			
14	0.90	6.22			
15	0.90	6.22			
16†	0.90	6.22			

* Cell 10 represents the Groundwater Station (GS) site.

† Cell 16 represents the Royal Spring (RS) site.

Figure 2.1 Fluviokarst sediment and carbon transport modeling framework. STAGE 1: model preparation. Sediment pirated from tributaries (Q_{SS}), conduit flow rate (Q_i), and hydraulic and hydrologic input were calculated for use in model. STAGE 2: Sediment Transport Model (STM). Transport coefficients (C_{tc}) were calibrated to match STM results with TSS data. STAGE 3: Carbon Model (CM). The generalized likelihood uncertainty estimation (GLUE) method was performed to estimate the distribution of results, model domain, and optimal model run for the CM.

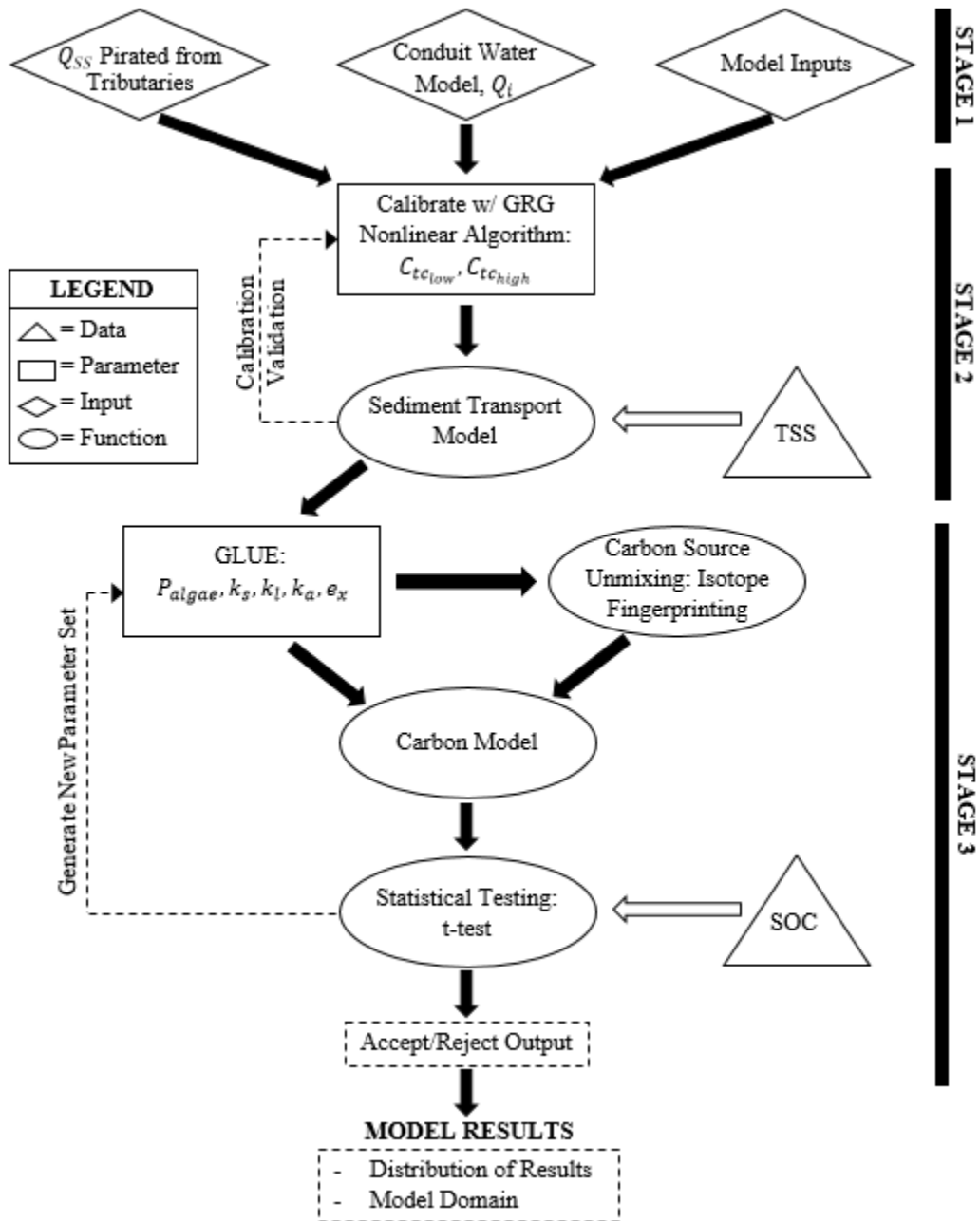


Figure 2.2 (a) Sediment model calibration and validation at the Groundwater Station. (b) Probability density functions and (c) cumulative distribution functions of data and model-integrated results.

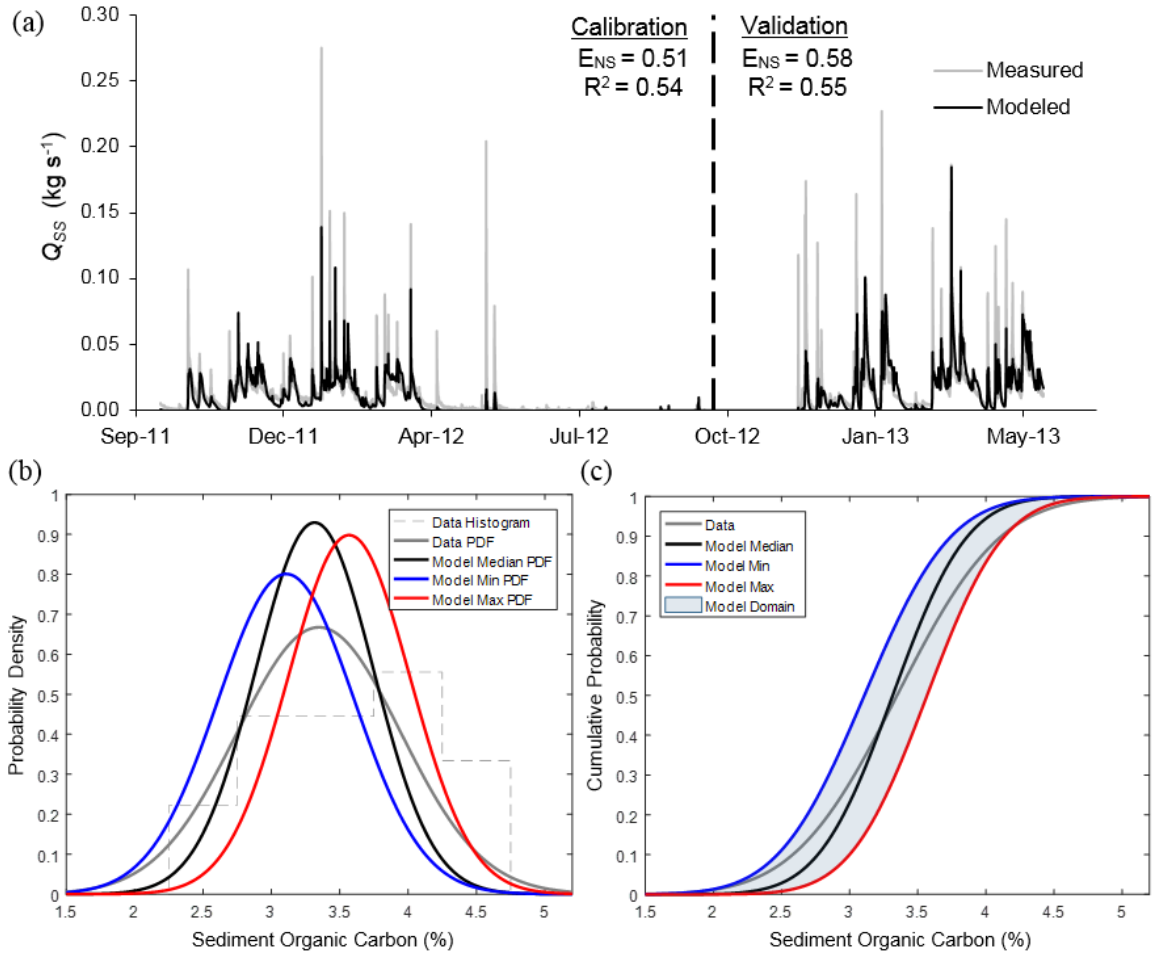


Figure 2.3 (a) Sediment model results at the Groundwater Station, and (b) longitudinal surface fine grained laminae (SFGL) depth changes in conduit.

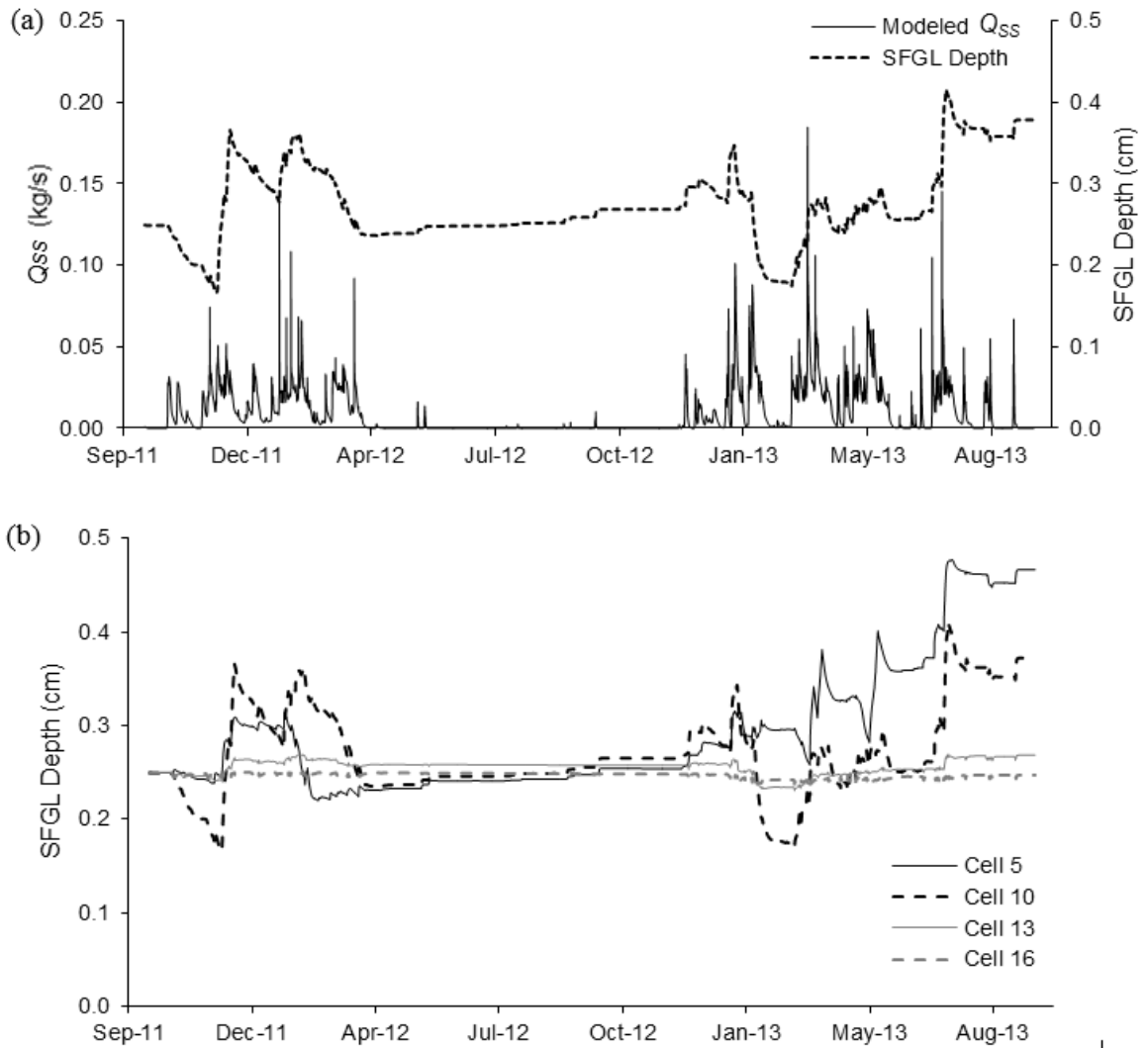


Figure 2.4 (a) Sediment organic carbon flux (Q_{soc}) in the subsurface conduit at the Groundwater Station (GW) compared to Royal Spring (RS) and organic carbon percentage in suspended sediment and bed sediment at GW. (b) Fractioning of carbon pools in conduit bed (SFGL) and suspended sediment (SS) at GW.

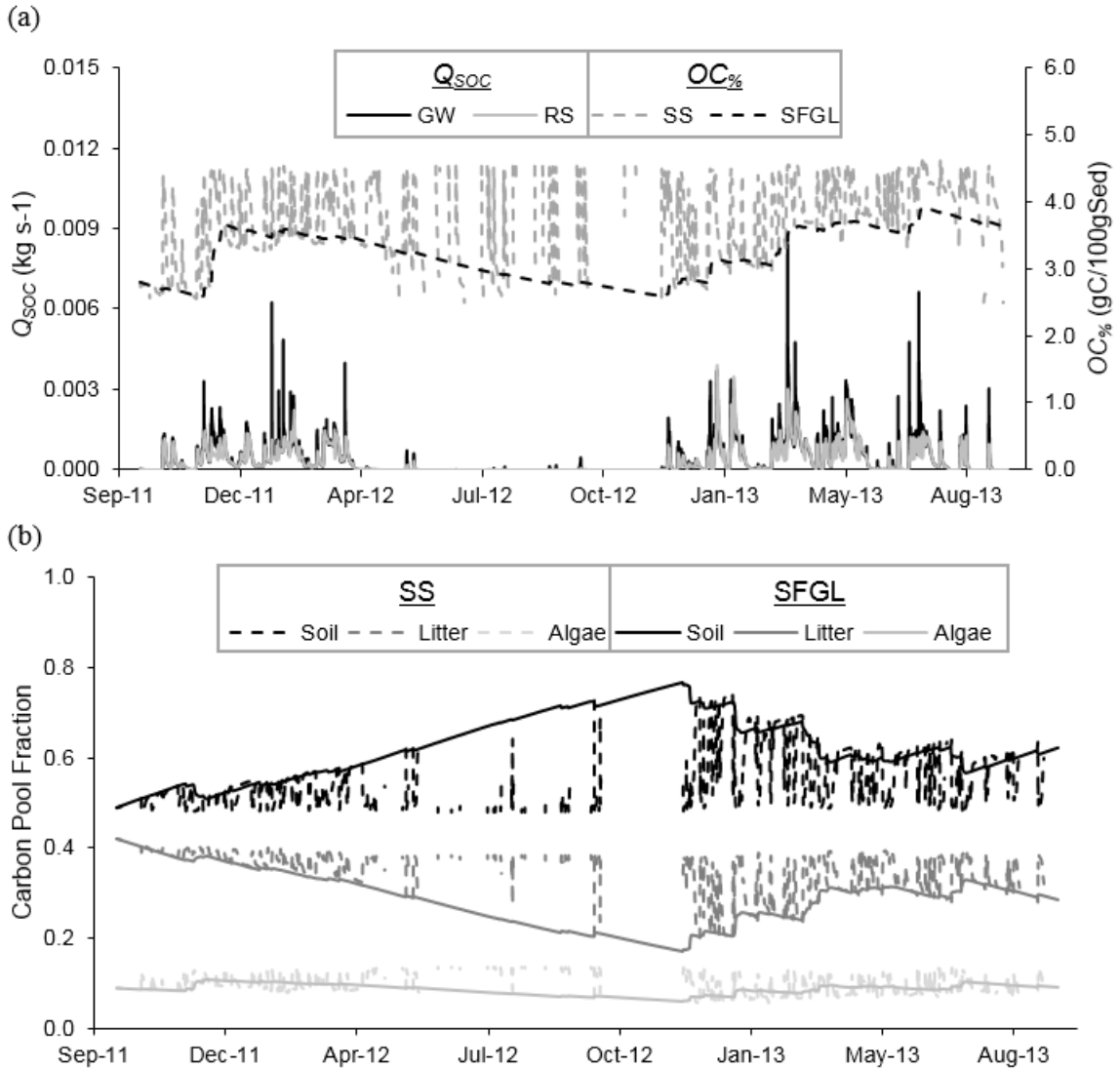
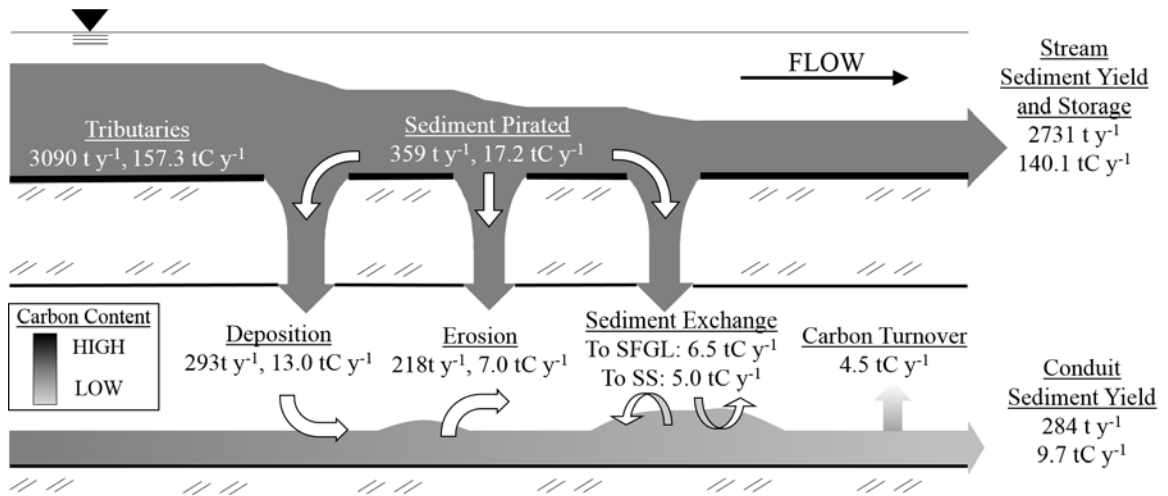


Figure 2.5 Sediment and SOC budget for the Cane Run watershed. Surface processes shown are tributary sediment production, sediment pirating to the subsurface, in-stream storage, and surface stream sediment yield. Subsurface processes shown are deposition, erosion, mixing (i.e. equilibrium sediment exchange between SFGL and SS), and yield of conduit sediment, as well as decomposition of sediment organic carbon. Sediment flux is represented in tons (t) and Sediment organic carbon flux is represented in tons Carbon (tC).



Chapter 3: Nitrate pathways, processes, and timing in an agricultural karst system: development and application of a numerical model

3.1 ABSTRACT

Nitrogen (N) contamination within agricultural-karst landscapes and aquifers is widely reported, however the complex hydrological pathways of karst make N fate difficult to ascertain. We developed a hydrologic and N numerical model for agricultural-karst, including simulation of soil, epikarst, phreatic, and quickflow pathways as well as biochemical processes such as nitrification, mineralization, and denitrification. We tested the model on four years of nitrate (NO_3^-) data collected from a phreatic conduit and an overlying surface channel in the Cane Run watershed, Kentucky, USA. By coupling the hydrologic and NO_3^- models, equifinality in the hydrologic model was reduced by 68%. Model results indicate that slow to moderate flow pathways (phreatic and epikarst) dominate the N load and account for nearly 90% of downstream NO_3^- delivery. Further, quickflow pathways dilute NO_3^- concentrations relative to background aquifer levels. Net denitrification distributed across soil, epikarst, and phreatic water removes approximately 36% of the N inputs to the system at rates comparable to non-karst systems. Evidence is provided by numerical modeling that NO_3^- accumulation via evapotranspiration in the soil followed by leaching through the epikarst acts as a control on spring NO_3^- concentration and loading. Compared to a fluvial-dominated system, mature-karst systems behave as natural detention basins for NO_3^- , temporarily delaying NO_3^- delivery to downstream waters and maintaining elevated NO_3^- concentrations for days to weeks after hydrologic activity ends. This study shows the efficacy of numerical modelling to elucidate complex pathways, processes, and timing of N in karst systems.

3.2 INTRODUCTION

The hydrologic complexity of karst systems has caused our knowledge of N fate and pathways to lag behind that of non-karst systems (Dirnböck *et al.*, 2016; Fenton *et al.*, 2017). Pathways of N transport to agricultural streams in non-karst landscapes include dilute quickflow, concentrated quickflow, and slowflow groundwater (Tesoriero *et al.*, 2013; Miller *et al.*, 2017). In terms of land use, karst systems are expected to receive similar N inputs because karst topography is often gently rolling making it suitable for livestock production and row cropping (Boyer and Pasquarell, 1995). However, N pathways in karst include a quickflow groundwater component (e.g., sinking streams, epikarst fracture networks, and subsurface conduits) (White, 2002; Pronk *et al.*, 2009). A quickflow component to groundwater obscures the timing of surface water and groundwater inputs making N fate difficult to estimate. Our motivation was to develop a numerical model to identify dominant N pathways, processes, and timing in agricultural-karst systems.

Numerical model development for N in karst is warranted because existing tools have several limitations. Off-the-shelf watershed water quality models (e.g., SWAT, HSPF) have been applied to karst nutrient studies with some success (Nikolaidis *et al.*, 2013; Palanisamy and Workman, 2014), however the models tend to be extrapolated beyond their hydrologic structure given the turbulent flow of the karst subsurface requiring empirical augmentation to allow adequate model calibration (Palanisamy and Workman, 2014). Graphical methods to apportion N loads to fast, intermediate, and slow flow pathways are robust (Mellander *et al.*, 2012; Fenton *et al.*, 2017), but limited in that they do not explicitly quantify internal N fate nor do they provide forecasting ability. Other karst-specific nutrient models assume N is conservative (Mahler and Garner, 2009; Mudarra *et al.*, 2014), however we know that N transformation occurs in karst (Panno *et al.*, 2001; Katz *et al.*, 2010).

We argue the reservoir modeling approach provides a suitable choice for N pathway, process, and timing estimates in karst. Reservoir-based models are increasingly used to estimate water transport in karst given their ability to accurately reflect multiple pathways (e.g., Fleury *et al.*, 2007; Tritz *et al.*, 2011; Hartmann *et al.*, 2014). The reservoir approach shown by Fleury *et al.* and others for karst water transport has not yet been widely

applied to the N fate problem, yet the approach is suitable because of advantages associated with (i) simulating non-conservative N in the subsurface; (ii) representing many subsurface pathways as well as surface overflows; (iii) ease of coupling with long-term multi-year data streams; and (iv) including robust uncertainty routines coupled to high performance computing. To that last point, equifinality (defined as the existence of multiple ‘acceptable’ representations of an environmental system) is apparent in all models (Beven, 2006), but can be reduced through coupling multiple data-streams (e.g., Ford *et al.*, 2017). Therefore, we develop the reservoir modeling approach for karst water and N in this paper.

By developing the numerical reservoir model for karst, we can investigate open questions of dominant pathways, processes, and timing that control N fate in agricultural-karst (Jones and Smart, 2005; Yue *et al.*, 2015; Opsahl *et al.*, 2017). N pathway-emphasis has been placed on aquifer contamination via quickflow pathways due in part to the optical nature of entire streams sinking into the subsurface (Mahler and Garner, 2009). However, we hypothesize that slow is the dominant N pathway in agricultural-karst. Two ideas from review of current literature bring us to this hypothesis. First, we analyzed data from 22 karst studies (Table 3.1) reporting N data for quickflow and slowflow NO_3^- pathways, and we found that 18 out of 22 (82%) studies show higher NO_3^- concentrations for slowflow as compared to quickflow. Second, recent water studies in karst discuss large water storage volumes within the epikarst and phreatic reservoirs and their potential to dominate water exports even in karst systems with high surface connectivity (Toran and White, 2005; Aquilina *et al.*, 2006; Williams, 2008; Knierim *et al.*, 2013). High NO_3^- concentrations in slowflow water and the large storage volumes of slowflow reservoirs suggest the potential for their control on net N export from karst aquifers.

Regarding N processes, the control of physical processes versus biogeochemical processes upon N in agricultural-karst is under-reported. Karst research suggests the potential for physical building-up and then leaching of soil nitrate as controlling N transport in agricultural-karst, with one study reporting increased nitrate concentration with percent of agricultural cover (Boyer and Alloush, 2001). However, the longer residence time of slowflow pathways suggest the potential for biogeochemical transformations to augment N contamination (Fenton *et al.*, 2017). We surmised that model development could help us untangle physical and biogeochemical processes controlling N fate and transport.

With regards to N timing, we questioned the time distribution of N export from side-by-side comparisons of a karst-dominated watershed with a fluvial-dominated watershed. Terrain with karst potential experiences competition between karstic and fluvial development (Ghasemizadeh *et al.*, 2012). Further, karst landscape in some regions can be organized into discrete zones dominated by either karst- or fluvial-dominated features, to the near-exclusion of the other (Phillips *et al.*, 2004). Such side-by-site organization allowed us to use our numerical modeling to study how N timing in karst compares to its fluvial counterpart.

Our objectives were to: (1) collect four years of N data, develop a reservoir-based numerical model for N fate and transport, and apply it to an agricultural-karst system, and (2) investigate the pathways controlling N transport, the net effect of physical and biogeochemical processes on N export, and the timing of N exports from agricultural-karst relative to a fluvial-dominated counterpart. The two objectives provide the structural sub-headings for the methods, results and discussion sections of the paper.

3.3 METHODS

3.3.1 Numerical model development and application

Theoretical basis for the model

The theoretical background provides the context behind our conceptual model of pathways and processes impacting N in agricultural-karst (Figure 3.1). Surface to subsurface pathways can most broadly be separated into concentrated or diffuse N recharge (White, 2002). This broad division is further sub-divided considering the three porosities that influence N recharge in karst: primary (matrix), secondary (fracture), and tertiary (conduit) (White, 2002). Quickflow pathways convey concentrated N recharge through tertiary porosity voids such as sinkholes, swallets, and estavelles. As is typical of many karst systems, surface streams are event-activated and run dry for large parts of the year as a result of flow pirating by quickflow pathways karst features (Husic *et al.*, 2017a). Diffuse recharge follows soil, epikarst, and phreatic zone pathways where storage volumes are several orders of magnitude greater than that of the quickflow pathways and have the

potential to retain N (Bottrell and Atkinson, 1992; Williams, 2008). Dynamic soil and epikarst storages provide the potential for N accumulation and leaching processes to act as important mechanisms affecting net NO_3^- exports (Aquilina *et al.*, 2006; Tzoraki and Nikolaidis, 2007). Phreatic pathways are sustained by Darcian groundwater recharge from stored volumes in the aquifer bedrock and are characterized by long residence times of water and N (Ghasemizadeh *et al.*, 2012). Our concept (Figure 3.1) is consistent with numerous studies focused on water movement and N recharge in karst (e.g., Tritz *et al.*, 2011; Hartmann *et al.*, 2016).

We investigate N pathways, processes, and timing with the described conceptual model in mind. We designed a study to sample N from a sinking stream and subsurface conduit, and we use a numerical reservoir model to simulate pathways that cannot be measured directly in the field. We formulated the model using a system of cascading linear reservoirs to represent storage and conveyance zones (i.e., soil, epikarst, phreatic/matrix, and quickflow) (Figure 3.2). The model simulates solute loads at the spring and surface stream and integrates net upstream processes. Our study assumes temperate agricultural surface processes, mature karst subsurface development, coupled surface-subsurface pathways, and daily mixing of solutes after accounting for mass changes.

Numerical model formulation

Numerical model formulation begins with the quickflow and soil reservoirs receiving concentrated and distributed recharge, respectively, which initializes the hierarchical model structure (Figure 3.2). Precipitation input was estimated using the Thiessen polygon method, which calculates an area-weighted average of precipitation given multiple rain gauges (Goovaerts, 2000). Of this area-weighted average, the quickflow reservoir receives an X fraction to represent concentrated recharge via swallets, sinkholes, and stream abstractions. The soil reservoir receives the remaining $1 - X$ fraction as distributed recharge. Due to their proximity to the surface and relative shallowness compared to the rest of the aquifer, several earlier models combine the soil and epikarst storages into a single lumped reservoir (e.g., Tritz *et al.*, 2011), but the two have been separated in this work to highlight evapotranspiration and lateral flow processes that primarily occur within the soil and dynamic storage that occurs in the epikarst (Aquilina *et*

al., 2006; Williams, 2008). Potential evapotranspiration (ET_P) was modeled using the Penman-Montieth method which considers a reference crop type (i.e., grass, as much of the watershed consists of pasture). Actual evapotranspiration (ET_A) was modeled as a function of soil water content and ET_P (mm d^{-1}) as

$$ET_{A(i)} = \min[ET_{P(i)}, ET_{P(i)} \times (V_{S(i)}/V_{S,MAX})] \Delta t, \quad (1)$$

where $V_{S(i)}$ is the volume of water in the soil reservoir at time step i (mm), $V_{S,MAX}$ is the soil saturation depth (mm), and Δt is the model time step (d). This linear formulation of ET_A is consistent with reservoir model applications in other karst environments (e.g., Chang *et al.*, 2017; Hartmann, 2017).

The mass balance of water within the soil reservoir (V_S) was discretized as

$$V_{S(i)} = V_{S(i-1)} + (R_{(i)}(1 - X) - ET_{A(i)} - Q_{stream(i)} - Q_{soil(i)})\Delta t, \quad (2)$$

where $V_{S(i-1)}$ is the volume of water in the soil reservoir at the end of the previous time step (mm), $R_{(i)}$ is the recharge from precipitation input (mm d^{-1}), $1 - X$ is the fraction of total recharge that infiltrates the soil reservoir, $Q_{stream(i)}$ is lateral flow into the surface stream occurring only after soil saturation (mm d^{-1}), and $Q_{soil(i)}$ is soil percolation to the epikarst (mm d^{-1}).

The model utilizes the linear discharge law, which relates discharge (Q) as the product of available head ($V - V_{MIN}$) and a discharge coefficient (α or k). As an example, soil discharge to the surface stream (Q_{stream}), was calculated as

$$Q_{stream(i)} = \max[0, k_{stream}(V_{S(i-1)} - V_{S,MAX})\Delta t], \quad (3)$$

where k_{stream} is the discharge coefficient for runoff and lateral flow to the surface stream (d^{-1}). Analogous relationships were used for the remaining discharges (coefficients) in Figure 3.2: Q_{soil} (k_{soil}), Q_{EL} (k_{EL}), Q_Q (α_1), Q_E (α_2), and Q_P (α_3).

The mass balance of water within the epikarst reservoir (V_E) was modeled as

$$V_{E(i)} = V_{E(i-1)} + (Q_{soil(i)} - Q_{E(i)} - Q_{EL(i)})\Delta t, \quad (4)$$

where $V_{E(i-1)}$ is the volume of water in the epikarst reservoir at the end of the previous time step (mm), $Q_{E(i)}$ is the fast component of epikarst discharge (mm d^{-1}) arising from preferential flow in large fractures that are well-connected to the conduit, and $Q_{EL(i)}$ is the slower percolation of water through the vadose zone to the phreatic zone (mm d^{-1}).

The mass balance of water within the phreatic reservoir (V_P) was represented as

$$V_{P(i)} = V_{P(i-1)} + (Q_{EL(i)} - Q_{PUMP(i)} - Q_{P(i)})\Delta t, \quad (5)$$

where $V_{P(i-1)}$ is the volume of water in the phreatic reservoir at the end of the previous time step (mm), $Q_{PUMP(i)}$ is the pumping rate from the aquifer (mm d⁻¹), and $Q_{P(i)}$ is the phreatic baseflow to the conduit (mm d⁻¹).

The balance of water within the quickflow reservoir (V_Q) has a single input from concentrated recharge and was formulated as

$$V_{Q(i)} = V_{Q(i-1)} + (R_{(i)} \cdot X - Q_{Q(i)})\Delta t, \quad (6)$$

where $V_{Q(i-1)}$ is the volume of water in the quickflow reservoir at the end of the previous step (mm) and $Q_{Q(i)}$ is the discharge from the quickflow reservoir (mm d⁻¹). Lastly, spring discharge (mm d⁻¹) was calculated as the sum of quickflow, epikarst, and phreatic discharge to the conduit/spring:

$$Q_{spring(i)} = Q_{Q(i)} + Q_{E(i)} + Q_{P(i)}, \quad (7)$$

The mass balance of solutes (i.e., NO₃⁻, NH₄⁺, and DON) within the soil reservoir was modeled as

$$M_{S(i)} = M_{S(i-1)} + (C_{R(i)}R_{(i)}(1 - X) - C_{CRCK(i)}Q_{stream(i)} - C_{S(i-1)}Q_{soil(i)} \pm M_{FATE(i)})\Delta t, \quad (8)$$

where $M_{S(i-1)}$ is the mass of solute in the soil reservoir at end of the previous time step (mg), $C_{R(i)}$ is the seasonal concentration recharging the soil (mg L⁻¹) which represents the bulk recharge of many contaminant sources (e.g., precipitation, fertilizer, manure, and sewage), $C_{CRCK(i)}$ is the concentration of the runoff and lateral flow mixture that discharges into the surface stream and is described further in the next paragraph (mg L⁻¹), $C_{S(i-1)}$ is the solute concentration of the soil reservoir at the end of the previous time step (mg L⁻¹), and $M_{FATE(i)}$ represents biogeochemical mass changes (mg d⁻¹) as a function of temperature, a first order rate constant, and mass of solute. The biogeochemical mass changes (i.e., nitrification, mineralization, and denitrification) were modeled as

$$M_{FATE(i)} = M_{S(i-1)} \times k_{ref} \times \theta^{(T_{S(i)} - T_{ref})}, \quad (9)$$

where k_{ref} is a first-order rate constant for a reaction (i.e., k_{DEN} , k_{NITR} , and k_{MIN}) at the reference temperature (d⁻¹), θ is a temperature adjustment coefficient, $T_{S(i)}$ is the soil temperature (°C), and T_{ref} is a reference temperature for the reaction (°C). This formulation is consistent with the influence of temperature on the rates of the biochemical

transformations modeled in this study (Bowie *et al.*, 1985; Reichstein *et al.*, 2000). The epikarst and phreatic zone solute balances are constructed in the same way whereas solutes in the quickflow reservoir were assumed conservative due to their short residence times. Residence time of water within each reservoir was modeled using a mass balance of water age with recharge to the soil providing ‘young’ or ‘new’ water and subsequent discharge exporting well-mixed reservoir water.

Surface stream NO_3^- concentration is considered as a mixture of low concentration runoff (i.e., recent recharge) and high concentration soil water. This end-member mixture is recognized as an important aspect of solute delivery to the in-stream environment (Miller *et al.*, 2017) and was modeled as

$$C_{CRCK(i)} = x_{SOIL}C_{S(i-1)} + x_{REC}C_{R(i)}, \quad (10)$$

where x_{SOIL} is the fraction of stream water of soil origin, $C_{S(i-1)}$ is the soil solute concentration (mg L^{-1}), x_{REC} is the fraction of stream water of runoff origin, and $C_{R(i)}$ is the recharge solute concentration (mg L^{-1}). In the event that the model produces flow in the surface channel, $C_{CRCK(i)}$ is used as the concentration of recharge to the quickflow aquifer (i.e., stream abstraction), otherwise the bulk $C_{R(i)}$ value is used and represents recharge into sinkholes and other upland, non-stream karst features.

Lastly, the concentration of solute at the spring (C_{RYSP}) was modeled as

$$C_{RYSP(i)} = (Q_{Q(i)}C_{Q(i)} + Q_{E(i)}C_{E(i)} + Q_{P(i)}C_{P(i)}) / (Q_{Q(i)} + Q_{E(i)} + Q_{P(i)}), \quad (11)$$

where $C_{Q(i)}$ is the concentration of solute in quickflow (mg L^{-1}), $C_{E(i)}$ is the solute concentration in the epikarst (mg L^{-1}), and $C_{P(i)}$ is the concentration of solute in the phreatic zone (mg L^{-1}).

Model application

The Royal Spring groundwater basin (58 km^2) drains part of the Cane Run watershed (96 km^2) located in the Inner Bluegrass Region of Kentucky, USA (Figure 3.3). The land surface is primarily agricultural in use (60%) with highly urbanized headwaters (40%) and a temperate climate (MAT: $13.0 \pm 0.7 \text{ }^\circ\text{C}$; MAP: $1,170 \pm 200 \text{ mm}$). The land surface is composed of moderately deep, well-drained soils underlain by phosphatic limestone of the Middle Ordovician period. Epikarst features are visible throughout the

watershed both in naturally exposed karren as well as roadcuts. More than fifty swallets, estavelles, and sinks have been identified within Cane Run creek. The creek runs dry for approximately 90% of the year due to flow pirating by the subsurface drainage (Husic *et al.*, 2017a). Anastomosing subsurface conduits converge to a primary phreatic cavern, 20 m below the ground surface, closely aligned with the overlying creek. The phreatic conduit supplies the primary basin outlet, Royal Spring (243 m a.s.l.), with an average perennial discharge of $0.67 \text{ m}^3 \text{ s}^{-1}$. The Royal Spring aquifer supplies water for distilleries, grist mills, horse farms, and crop irrigation, and the main springhead serves as the raw municipal water source for the City of Georgetown, Kentucky. The urbanization of the uplands has resulted in bacteria and nutrient loadings that exceed standards set by the Clean Water Act and Kentucky Division of Water (UKCAFE, 2011). The high surface-subsurface flow path connectivity has been suggested as the primary cause for the deterioration of water quality at the spring (UKCAFE, 2011). The watershed has been a karst research site led by the Kentucky Geological Survey and the University of Kentucky the past 40 years (Spangler, 1982; Thrailkill *et al.*, 1991; Taylor, 1992; Paylor and Currens, 2004; Zhu *et al.*, 2011; Husic *et al.*, 2017a,b).

A sampling station was placed at the spring (“RYSP” in Figure 3.3) providing water outputs from the karst conduit, and is operated by the United States Geological Survey (USGS 03288110). A second sampling station was placed at the Cane Run creek surface water overflow (“CRCK” in Figure 3.3), which became active during high rainfall storm events. A third sampling station was located near the longitudinal midpoint of the primary phreatic conduit where a series of groundwater wells directly intersect the subsurface flow path (“KYHP” in Figure 3.3, Zhu *et al.*, 2013; Husic *et al.*, 2017a). Water data collection and analyses was previously published in Husic *et al.* (2017a,b). Weekly maximum flows at the Phreatic Conduit (PC) and Royal Spring (RS) sites are similar in magnitude ($Q_{RS} = 0.99 \times Q_{PC}$, $R^2 = 0.77$; Husic, 2015) thus we assume few water inputs/outputs along this section. Likewise, NO_3^- sampling at the two sites showed a nearly 1:1 relationship in NO_3^- concentration ($\text{NO}_3^-_{RS} = 1.06 \times \text{NO}_3^-_{PC}$, $R^2 = 0.81$; Kentucky Geological Survey, unpublished data). This result allowed us to use data from the Phreatic Conduit or Royal Spring to assist with calibrating N concentrations for the numerical model. The United States Geological Survey (USGS) operates a flow gage at Royal Spring (USGS 03288110).

Four years (2012 – 2016) of NO_3^- data were collected at the surface stream (CRCK) and subsurface conduit (KYHP) locations. The temporal scale of sampling varied from hourly to biweekly depending on flow conditions (i.e., baseflow vs flood conditions). In the field, surface stream samples were collected using 1L HDPE bottles with either manual collection or an automatic sampler (ISCO 6712) depending on flow conditions. For the subsurface conduit, a bailer with a one-way check valve was used to ensure well samples were collected at the depth of the conduit. The Kentucky Geological Survey laboratory analyzed NO_3^- samples, consistent with US EPA Method 300.0, using a Dionex ICS-3000 Ion Chromatography System featuring a carbonate-bicarbonate eluent generator and Dionex AS4A analytical column. The NO_3^- anion was identified by retention time and the peak area was compared to a calibration curve generated from known standards. QAQC protocol included (i) analyses of NIST secondary source standards before and after each run to verify calibration; (ii) blanks before and after each run to verify lack of carry-over in the column; and (iii) analyses of randomly selected duplicate samples to verify that deviation was less than 10%. Field ($n = 8$) and lab ($n = 49$) duplicates of NO_3^- had a standard deviation of 0.07 and 0.02 mg N L⁻¹, respectively. No field or lab blanks registered above the method detection limit (MDL). Failure of any criteria involved the researchers questioning the protocol and re-running the batch.

Model inputs and parameters are enumerated in Table 3.2. Meteorological data were available from the Bluegrass Airport (NOAA ID: USW00093820) as well as three nearby rain gauges (NOAA IDs: US1KYSC0001, US1KYFY0009, and USC00153194). The gauge stations recorded relative humidity, temperature, solar radiation, and wind speed. Soil temperature was recorded at Spindletop Research Farm near the center of the groundwater basin (UKAg, 2007). Previously collected ammonium (NH_4^+) and dissolved organic N (DON) data were used to estimate NH_4^+ and DON concentrations of recharge to the watershed. The recharge concentration of NH_4^+ ($C_{\text{NH}_4(R)}$) was assumed constant (mean: 0.12 ± 0.19 mg N L⁻¹; $n = 54$) as field-collected data from surface sites in the watershed was highly variable and relatively low in concentration compared to NO_3^- (KWW, 2016). Likewise, the recharge concentration of DON ($C_{\text{DON}(R)}$) was also assumed constant (mean: 0.35 ± 0.07 mg N L⁻¹; $n = 4$) for the same reasons as NH_4^+ (UKCAFE, 2011). Recession coefficients were estimated from a master recession curve constructed

using nine events over a decade (Figure 3.4). The fractions of stream water from soil and runoff origin can vary from event to event, but were selected in this study based on a range of values reported in the literature for karst using isotopic hydrograph separation (Buda and DeWalle, 2009) and two-domain modeling (Long, 2009). Surface events in the Cane Run Watershed are short-lived and often peak and recede within a day (i.e., the time step of the model; Husic *et al.*, 2017a) providing support that an average value for the respective soil and runoff fractions can adequately portray mixing processes. Hydrologic model parameters were evaluated over a wide range of values, and minimum and maximum values represent inferred physical bounds. For example, the soil percolation coefficient is bounded on the high end by the coefficient for quickflow and on the low end by “0” (i.e. no flow). The seasonal NO_3^- concentration of recharge water was varied over the minimum and maximum values of observed stream NO_3^- data. The upper limits for biogeochemical first-order rate reactions in the soil, epikarst, and phreatic reservoirs were estimated using values based on temperature (Table 3.2 for references).

The framework for evaluating model performance includes the generation of model parameters, comparison to measured data, and the evaluation against statistical criteria (Figure 3.5). The calibration objective for the hydrologic model was mean daily spring discharge. On the other hand, the biogeochemical N model had four calibration objectives including spring NO_3^- , stream NO_3^- , spring NH_4^+ , and spring DON concentrations. The hydrologic ($n = 1,461$) and NO_3^- ($n = 162$) datasets were divided into calibration and validation subsets of equal cardinality. Split sample subsets were selected for the hydrologic model evaluation with the first two years used as calibration and the last two years used as validation. Evaluation subsets for the N model were randomly selected for each model realization as the frequency of NO_3^- data collection varied over the four year period and split sampling would have biased the model to time periods with greater density of collected data (Liu *et al.*, 2018). Initial model conditions were selected based on mean model results, but typically initial conditions in karst have little effect on evaluation statistics if the model is initiated during very low water periods and the upper reservoirs are disconnected from the lower (Mazzilli *et al.*, 2012). Both conditions were satisfied in this study.

The Nash-Sutcliffe efficiency (NSE) was selected as the statistical evaluation metric due to its ubiquitous use in hydrologic modeling and established performance guidelines (Moriiasi *et al.*, 2007). The NSE statistic was calculated as

$$NSE = 1 - \frac{\sum_{t=1}^T (N_m^{(t)} - N_o^{(t)})^2}{\sum_{t=1}^T (N_m^{(t)} - \bar{N}_o)^2}, \quad (12)$$

where T is the total number of observations, $N_o^{(t)}$ is the observed value for sample t , $N_m^{(t)}$ is the modeled value for sample t , and \bar{N}_o is the mean of all observed values. The Nash Sutcliffe efficiency ranges from $-\infty$ to 1, with 1 indicating a perfect match of the model to data and 0 indicating the model performs no better than the mean of the data (Moriiasi *et al.*, 2007). Considering the criteria set out by Moriiasi *et al.* (2007), minimum NSE values of 0.5 and 0 were set for spring discharge and spring NO_3^- concentration results, respectively. The use of NO_3^- concentration rather than NO_3^- flux to calibrate the N model is more difficult but was performed for two reasons. First, NO_3^- flux statistics are highly correlated with discharge and lead to biased water quality model performance (Hirsch, 2014). Second, calibrating to concentration rather than flux gives a more accurate description of internal watershed N cycling. The accepted spring NO_3^- solution space was further constrained so that modeled stream NO_3^- , spring NH_4^+ , and spring DON results were not statistically different ($\alpha = 0.05$, using Welch's t-test) from observed stream NO_3^- (mean: 1.92 ± 1.02 mg N L⁻¹; $n = 111$), spring NH_4^+ (mean: 0.07 ± 0.11 mg N L⁻¹; $n = 40$) and spring DON (mean: 0.23 ± 0.14 mg N L⁻¹; $n = 19$) data (KGS, 2018). Only samples collected while water was moving (i.e., no standing water) were included in model evaluation.

Numerical modeling uncertainty analysis was performed on an institutionally shared high performance computing cluster (DLX2/3) with 4800 processor cores, 18TB of RAM, and 1PB of high-speed disk storage. Uncertainty in the hydrologic and N models was assessed with the generalized likelihood uncertainty estimation (GLUE) method (Figure 3.5), which has been applied to water resources modeling to assess the equifinality of model parameter sets (Beven, 2006; Ford *et al.*, 2017). The GLUE methodology is initiated by assuming a prior distribution (e.g., uniform) for model parameters. Parameter sets that satisfy one or more evaluation statistics are retained while sets that fail are discarded. A posterior distribution is then constructed from the collection of acceptable

sets. A prediction bound can also be used to represent water and NO_3^- results that are contained by 95% of accepted simulation results. In this study, several thousand acceptable hydrologic parameter sets were first established requiring millions of simulations. Thereafter, they were randomly fed through to the N model where several more thousand parameter sets were deemed acceptable requiring over ten million more simulations. The final NO_3^- prediction bounds represent both the effects of physical (water) and biochemical (N) uncertainty.

3.3.2 Karst pathways, processes, and timing of N transport

Pathways controlling N transport

Pathways controlling N transport were investigated using residence time and correlation analyses of both data and numerical model results. The autocorrelation function indicates the memory effect of the system, and a pre-determined value of 0.2 is typically used to represent the decorrelation lag time (Mangin, 1984). The autocorrelation function was calculated as

$$R_x(\tau) = \frac{E[(x_t - \mu_x)(x_{t+\tau} - \mu_x)]}{\sigma_x^2}, \quad (13)$$

where E is the expected value operator, x_t is an observation in the time series (e.g., discharge) with mean μ_x and variance σ_x^2 , and τ is the time lag. Well-drained systems typically have an initial steep decline in the autocorrelation function which corresponds to influence by quickflow pathways (Kovačič, 2010). Cross-covariance can indicate the relationship between an uncorrelated cause (e.g., rainfall) and the subsequent effect (e.g., spring discharge). The cross-covariance function was calculated as

$$C_{xy}(\tau) = E[x_t y_{t+\tau}] - E[x_t]E[y_{t+\tau}], \quad (14)$$

where y_t is the causal observation (e.g., precipitation). The time elapsed between a lag of 0 days and the maximum cross-covariance gives an indication of the pressure pulse transfer through an aquifer. Additionally, gently sloping cross-covariance plots imply high storage and a low degree of karstification while well-developed aquifers are characterized by much shorter response times and steeper curves (Kovačič, 2010).

Pathways controlling N transport were also quantified using integration of numerical modeling results. The spring discharge signal can be decomposed into

constituent quickflow, epikarst, and phreatic flow pathways. Each flow path was integrated with a daily time step over the model simulation to estimate total pathway load. Model integrated budgets could be compared across pathways to indicate the relative importance of certain pathways on controlling N transport.

Processes affecting N exports

The physical and biochemical processes impacting N exports from karst were investigated. An N budget of physical processes such as inflows (diffuse infiltration and concentrated recharge) and outflows (karst spring, surface stream, and net aquifer losses such as pumping) was constructed. A similar budget of biogeochemical N processes (denitrification, nitrification, and mineralization) was performed within each reservoir and the watershed as a whole. Physical processes such as soil-epikarst connectivity (depending on field capacity of soil) may act to retain and accumulate NO_3^- in the soil prior to subsequent leaching during hydrologic activity. Other processes such as evapotranspiration affect both the water budget and the N concentration within the soil reservoir. The temporal distribution of these processes was of note considering that they may be impacted by daily or seasonal variations in temperature, humidity, sunlight, N source, soil moisture, and aquifer abstractions. The distribution of these processes across the multiple storage zones was also of interest and solute concentrations were compared across pathways over several years to estimate processes affecting N exports.

Timing of N exports from karst

Timing of N exports from karst was analyzed to assess temporal delivery of NO_3^- to downstream waterbodies. We performed an analysis using results from a recent fluvial-dominated study in Ford *et al.* (2017) to provide comparison with karst-dominated NO_3^- results from the present system. The South Elkhorn watershed studied in the Ford *et al.* work was a fluvial-dominated system in an adjacent watershed. The South Elkhorn (62 km^2) drains southwest Lexington, KY while the Cane Run system (58 km^2) drains the northern portion of the city. The distribution of land uses, soil conditions, and topography are nearly identical in the two systems. However, Cane Run is underlain by mature karst

topography that includes fractures, sinkholes, swallets and conduits forming the Royal Spring groundwater basin whereas the South Elkhorn has weak karst development and perennial surface stream flow (Mahoney *et al.*, 2018). Both systems drain to Elkhorn Creek, and then to the Kentucky, Ohio, and Mississippi Rivers.

Nitrogen loading from the South Elkhorn was produced using results in Ford *et al.* (2017) at the single watershed outlet. Results for N loading from the Cane Run-Royal Spring system was produced by summing loads from both the surface stream and conduit outlets from the watersheds in order to provide an integrated watershed response. The temporal distribution of N loading to downstream waterbodies was then analyzed graphically and comparisons were made between the karst-dominated drainage and the non-karst system.

3.4 RESULTS AND DISCUSSION

3.4.1 Numerical model development and application

Prior to assessing the numerical model, we first investigate trends in collected data. Results of N seasonality in water, comparison of surface and subsurface N concentrations, and N dynamics during storms were generally consistent with existing data. The sinusoidal cycling of NO_3^- concentration at both locations (Figure 3.6) reflects the seasonality of anthropogenic loading, soil processes, and hydrologic mobilization of N. The agricultural land use and temperate climate, including fall and winter application of fertilizer (UKCAFE, 2011), dormancy of vegetation, and hydrologic mobilization, coincides with seasonal N levels. These results are typical of agricultural watersheds where over-application of fertilizer and manure during the fall, coupled with mobilization of accumulated N, can lead to excess runoff and leaching of NO_3^- in winter (Toran and White, 2005; Royer *et al.*, 2006; Ford *et al.*, 2018). Nitrate concentrations of samples collected on the same day at both sites are ~50% greater in the karst conduit than the surface stream (Figure 3.6). Further, 95 of the 99 paired daily-average samples show greater NO_3^- concentrations in the subsurface. This result is consistent with agricultural landscape processes such as soil N accumulation followed by hydrologic N mobilization of highly-concentrated subsurface water (Di and Cameron, 2002). Lastly, the timing of NO_3^-

concentration peaks caused by storm events and seasonality are well-matched by the surface and subsurface pathways (Figure 3.6). The result demonstrates the pressure pulse of storm flow on the karst subsurface that can mirror the temporal response seen in surface streams (Husic *et al.*, 2017a). Further, the multiple inferred pathways (i.e., quickflow, epikarst, and phreatic) introduce wide temporal variability in NO_3^- data results. In many instances, the NO_3^- concentration of samples collected from the spring within days of one another (e.g., see April 2013 in Figure 3.6) can span over 3 mg N L^{-1} (the average NO_3^- concentration of the spring) highlighting the influence of pathway variability on spring NO_3^- concentration. The N export behavior in this karst system tends to agree with the hypothesis that precipitation can dominate interannual variability of downstream N loading (Sinha and Michalak, 2016). Data results of NO_3^- at the surface stream and karst spring provided the basis for our numerical model evaluation.

The water component of the numerical model produced satisfactory results throughout the four year simulation period (Figure 3.7a). Statistical evaluation of water model fit showed agreement between simulated and measured discharge during both calibration and validation time periods (Table 3.3). Peak flows were adequately simulated by the model and represented pulses of discharge occurring primarily *via* quickflow pathways. Baseflow conditions were well-represented by the model during both the active winter and dryer summer periods, which reflects the model's ability to accurately represent subsurface water storage and drainage. The satisfactory simulation of spring flow recession following hydrologic activity provides support for the master recession curve analysis (Figure 3.4) used to estimate recession coefficients. Successful performance of the parent water model gave us confidence in carrying the results forward to the N fate subroutines.

Numerical model results of N fate and transport reflect NO_3^- seasonality and storm event dynamics (Figure 3.7b). The model performed very well with 123 of the 164 NO_3^- data results falling within the modeled prediction bounds. Model bounds are wide as biochemical uncertainty is also affected by hydrologic uncertainty in the parent model. For example, transitions from quickflow to epikarst flow control of spring discharge can substantially impact NO_3^- concentration as the two flow paths may have significantly different solute signatures (Figure 3.7c). Modeled subsurface NO_3^- concentration remains

elevated throughout the spring season despite a decrease in seasonal NO_3^- recharge from the surface indicating storage and release of high concentration NO_3^- (see Figure 3.7c). Our statistical results for N modeling were good (Table 3.3), which offers confidence to the multi-reservoir approach as a tool for modeling NO_3^- . In particular, model performance is impressive given the time-scale and response variable used for model evaluation (i.e., daily N concentration rather than daily, weekly, or monthly N load/yield). Evaluation statistics are recognized to decrease as time frequency of model evaluation increases (Yuan *et al.*, 2001) and when concentration rather than load is used as the response variable (Hirsch, 2014). The N model developed in this study accurately portrays watershed N dynamics and is capable of successfully simulating daily NO_3^- concentration at the primary karst springhead.

Our uncertainty analysis with the high-performance computer was pivotal to constraining and bounding reservoir model results. For the hydrologic model, 1,560,000 model realizations were performed, of which 3,653 were successful. For the N model, 9,600,000 model realizations were performed, of which 2,687 were successful. If the uncertainty analysis were performed on a single machine, it would have taken approximately 200 days in simulation time, but that was cut down to just 1.5 days as the simulations were distributed over 128 cores on the high-performance cluster. A large number of model simulations were necessary for a few reasons: the physical and biochemical parameter bounds were wide to encompass potential equifinality as well as provide a conservative estimate of modeled processes; each biochemical parameter set was generated and then applied randomly to one of the 3,653 accepted hydrologic parameter sets – recognizing the equifinality that may occur not only in one sub-model, but also its parent model; and finally, failure of any one of the multiple calibration objectives resulted in the entire parameter set being discarded (see Figure 3.5). To that last point, the four calibration objectives – Spring NO_3^- , Stream NO_3^- , Spring NH_4^+ , and Spring DON – had success rates of approximately 2%, 20%, 35%, and 30%, respectively, per model realization. Taken together, if the respective success rates are uncorrelated, the composite success rate for any random realization was 0.04%. Thus, to ensure that each randomly selected hydrologic parameter set has enough realizations to generate a single correct N model solution, over 9 million N model simulations ($n = 3,653/0.0004$) had to be

performed. The use of high performance computing was instrumental to running the required number of simulations necessary to build a posterior sample distribution, construct a prediction bound, and evaluate uncertainty within multiple sub-models.

Nitrogen model calibration also decreased equifinality in discharge estimates by reducing the number of acceptable hydrologic parameter sets from 3,653 to 1,164 (a 68% reduction). Despite the considerable number of simulations, some hydrologic parameter sets were incapable of generating an acceptable N model solution set. The reduction in equifinality by including the N model had material effects when inferring water pathway results. For example, from the original 3,653 parameter sets, 46% of the water was discharged by epikarst, 32% by the phreatic zone, and 22% by quickflow. However, by including only hydrologic sets that also produce satisfactory N model results, the remaining sets ($n = 1,164$) indicate that 35% of water is discharged by epikarst, 47% by phreatic zone, and 18% by quickflow. The utility of multiple response variables to reduce equifinality has been noted in other systems such as in surface streams using stable isotopes (Ford and Fox, 2015; Ford *et al.*, 2017), in watershed-scale models using remote-sensing data (Silvestro *et al.*, 2015), and in vegetation zones using carbon data representative of different time scales (Carvalho *et al.*, 2010). We add to this list with an application of equifinality reduction to water flow dynamics in an agricultural karst system using an N dataset and numerical modeling.

Uncertainty analysis indicated that some hydrologic model parameters vary considerably from the assumed uniform prior distribution to the posterior distribution (e.g., k_{soil} and X) (Figure 3.8a). Other parameters were not sensitive (e.g., $V_{S,MIN}$ and $V_{P,MIN}$). The sensitivity of soil discharge coefficient (k_{soil}) is pronounced as soil discharge into the stream was vital in reconstructing the water balance where the two outputs are primarily the stream and subsurface spring. The sensitivity in the fraction of rainfall redirected as concentrated recharge to the conduit (X) was important in simulating peaks in the spring flow hydrograph. Uncertainty analysis for the biochemical transformation rates of NH_4^+ , DON, and NO_3^- (Figure 3.8b) indicates that the soil and phreatic zones are the most sensitive, likely as a result of their large water storage capacities, residence times, and potential impact to net N fate whereas the epikarst acts more as a dynamic transfer zone of soil water to either the conduit or to deep groundwater. While the first order rate constants may vary

over several orders of magnitude, their net impact is dependent on the size of the pool that the reactions occur in. Analysis also indicates that fall and winter have the most concentrated recharge to the watershed while spring and summer have the most dilute recharge.

In summary, consistency of the N dataset with literature and our numerical modeling results gave us confidence in carrying the model forward to assess pathways, processes, and timing of N in karst. We focused heavily on performing robust uncertainty analysis as only 10% of published water quality modelling papers between 1992 and 2010 ($n = 257$) include any uncertainty analysis (Wellen *et al.*, 2015). Our extensive uncertainty analysis was pivotal to gaining confidence in the N results, and our study details a method for karst researchers who aim to assess hydrologic and biochemical uncertainty in their own models.

3.4.2 Karst pathways, processes, and timing of N transport

Pathways controlling N transport

Residence time results provide a first look at karst pathways controlling N transport. The residence time of spring water spans three orders of magnitude (Figure 3.9a). Quickflow water is discharged on the order of a few days, epikarst water is drained within weeks, and phreatic water is typically exported over several months. The maximum cross-covariance occurs on the same day as rainfall and rapidly decreases thereafter, and both data and model results show similar steepness and de-correlation times (Figure 3.9b,c). The result indicates the pressure pulse of fluid through the system during a storm event, which is indicative of high karstification. However, results also indicate that distributed recharge from storms is stored within the aquifer and drained by epikarst and phreatic pathways for months to weeks thereafter. Our residence time results show agreement with water tracing results of others (Bottrell and Atkinson, 1992) and the mean residence time curve agrees with the potential for high volume water storage in the saturated aquifer (e.g., Knierim *et al.*, 2013).

A water and NO_3^- budget over the four-year observation period shows that epikarst and phreatic pathways contribute, on average, 89% of the annual NO_3^- yield (Table 3.4). The percent of NO_3^- exported by each pathway is generally similar to the percent water

discharged, but with increased N contribution by slower pathways. Quickflow in karst aquifers acts to dilute spring NO_3^- concentration with model results indicating that the quickflow pathways compose 18% of total water discharge, but 11% of the NO_3^- load, a one-third reduction. On the other hand, the intermediate pathway (i.e., epikarst) sees an increase in the percentage of NO_3^- exported (40%) compared to water discharged (35%). Lastly, the phreatic pathway has the most similar NO_3^- (47%) and water (49%) yields.

The relative provenance of spring NO_3^- flux from the three contributing reservoirs varies temporally (Figure 3.10). The epikarst N load dominates much of the NO_3^- flux from the spring primarily due to three factors: the epikarst can act as a large storage zone for infiltrated water (Aquilina *et al.*, 2006), the epikarst is well-connected to highly-concentrated soil water (Fretwell *et al.*, 2005), and the epikarst behaves as a dynamic transfer zone that is effective at conveying water to the spring and conduit *via* enlarged fractures (Williams, 2008). This idea tends to be consistent with the fractured network of the Lexington Limestone bedrock (Thraillkill *et al.*, 1991). The quickflow contribution increases at the incidence of hydrologic activity and contributes relatively diluted NO_3^- to the spring flux signal. Lastly, the phreatic fraction is highly affected by seasonal water processes such as pumping from the deep aquifer and loss of epikarst recharge during dry periods. The long residence time of water in phreatic pores could lead to net-denitrification (Heffernan *et al.*, 2012) as pathway results indicate that slightly less N is exported by the phreatic pathway as compared to water discharged. Otherwise, phreatic pathways yield a large volume of NO_3^- during winter and spring periods characterized by frequent hydrologic activity and cooler temperatures.

Our results place emphasis on diffuse (i.e., epikarst and phreatic) pathways when estimating dissolved N fate. Water budget estimates indicate that only 5% of recharge is directed to quickflow pathways (Table 3.5a) reinforcing a need to focus on distributed soil recharge even in watersheds heavily influenced by karst topography. Our results are noteworthy because studies often emphasize quickflow contamination of mature karst aquifers *via* high speed water and contaminant transport through sinking streams, turbulent conduits, and vertical shafts which preclude aquifer bioremediation (Daly *et al.*, 2002). Past emphasis upon quickflow contamination is highly reasonable given the visible nature of sinking streams and their ability to directly convey solid and runoff bound contaminants

to the subsurface (e.g., see Figure 3.1). Quickflow-associated pathways may provide the dominant origin for some contaminants (e.g., sediment-bound contaminants in sinking streams; Husic *et al.*, 2017a,b), however our results suggest slow pathways are most important for dissolved N fate. This result supports our hypothesis from analysis of the literature based on diluted N concentration data from quickflow (Table 3.1). The N results of our study extend the past work in Table 3.1 to show not only is N concentration of the diffuse flow higher (see Figure 3.7c), but also these pathways may dominate the annual N load.

Processes affecting N exports

Evidence is provided that physical processes and biogeochemical processes both have a strong control on N fate in agricultural-karst. We estimate rates of denitrification comparable to other systems, but the governing mechanisms for downstream NO_3^- concentration and loading are associated with N accumulation in soil through evapotranspiration and N leaching via epikarst pathways.

Numerical modeling results reflect net removal of N via denitrification within the subterranean karst system (Table 3.5b). There is approximately a 36% removal of N inputs by denitrification in all reservoirs. The rate of removal in soil is $1.3 \text{ mg N m}^{-2} \text{ d}^{-1}$, and the phreatic and epikarst reservoirs remove approximately $0.5 \text{ mg N m}^{-2} \text{ d}^{-1}$ each. The relatively low residence time of water in karst aquifers limits the ability of subsurface microbes to further denitrify NO_3^- , and subsequent hydrologic activity promotes the mobilization of accumulated NO_3^- to the springhead. The rates estimated by our model are similar to other karst groundwater systems such as in the Upper Florida (USA) Aquifer where Heffernan *et al.* (2012) used N isotopic signatures to estimate 32% removal, on average, of N inputs by denitrification. The rates for the 61 springs analyzed in Heffernan *et al.* (2012) ranged from 0 to $15 \text{ mg N m}^{-2} \text{ d}^{-1}$ showcasing the large degree of variability and uncertainty associated with watershed-scale denitrification estimates in karst – even within the same geologic formation. Our results are also consistent with broader groundwater denitrification removal estimates in non-karst soils ($\sim 5.0 \text{ mg N m}^{-2} \text{ d}^{-1}$) and groundwater ($\sim 1.5 \text{ mg N m}^{-2} \text{ d}^{-1}$) for the Southeastern United States region (Seitzinger *et*

al., 2006). These results provide support for the efficacy of relatively simple reservoir models to provide accurate representation of internal aquifer biogeochemical processes.

However, even in the presence of net-denitrification we observe an increase in NO_3^- concentration of spring discharge relative to water recharging the aquifer. Modeling results suggest that soil-zone processes, particularly during dryer periods, highly control NO_3^- contamination in the karst watershed (see “Soil” in Figure 3.7c). High rates of evapotranspiration during the dry season remove water, but not N, from the soil column resulting in the relative increase in concentration of N species remaining in the soil. The evapotranspirative concentration of NO_3^- can be quite pronounced in temperate climates where 60% of precipitation can be removed as evapotranspiration (Hanson, 1991). It is plausible that the highest NO_3^- concentrations observed during the study period (see winter 2012 in Figure 3.7b) could arise from flushing of highly-concentrated soil-N accumulated over the months-long dry period preceding the first large hydrologic event of the wet season. The initial fall/winter flushing event can infiltrate soil and cause highly soluble soil-attached NO_3^- to become entrained within the water and leached via large fractures in the epikarst. Further model support for this idea is observed by comparing relatively dry periods (see “discharge” in Figure 3.7a) with coinciding periods of higher soil NO_3^- concentration (see “soil” in Figure 3.7c). The impact of this flushing is expected to be temporally limited as greater contribution of fresh recharge dilutes the initially flushed material. Others have observed NO_3^- flushing in karst such as in a chalk (a relatively immature karst) aquifer in Loiret, France (Baran *et al.*, 2008) and a mantled (a karst with a thin surficial sediment deposit) aquifer in Indiana, USA (Wells and Krothe, 1989). Baran *et al.* (2008) attribute the flushing to NO_3^- accumulation via physical concentration whereas Wells and Krothe (1989) attribute the flushing to soil water flow through large epikarst fractures. Likewise, in non-karst systems, evaporation in the vadose zone has been identified – using dual isotopic tracers of NO_3^- ($\delta^{15}\text{N}$ and $\delta^{18}\text{O}$) – as an important mechanism affecting NO_3^- concentration (Yuan *et al.*, 2012; Huang *et al.*, 2013). The authors find relatively little discussion in the literature as to the impact of physical processes leading to concentration and leaching of solutes in karst aquifers. The numerical modeling performed in this study hints to the potential of evapotranspiration to increase observed spring NO_3^- concentrations despite net-denitrifying conditions within the aquifer.

The net N source-sink capacity of karst basin remains an open question with previous karst studies not showing a clear consensus on estimated net nitrification versus net denitrification. Studies such as Vaute *et al.* (1997) have observed nitrification in the soil of a karst aquifer, and Duchaufour (1991) has remarked that limestone environments are “most active” in nitrification. On the other hand, Katz *et al.* (2010) estimated a 25-40% N loss of septic tank effluent during percolation in the unsaturated zone, as stated earlier Heffernan *et al.* (2012) estimates 32% loss of N due to denitrification in the Upper Florida Aquifer, and many other studies using stable isotopes have reported potential denitrification in the aquifer (e.g., Panno *et al.*, 2001; Li *et al.*, 2010). Results in this study show that explicit modeling of both physical and biogeochemical processes may assist with estimating the N source-sink capacity.

Timing of N exports from karst

The timing of N exports from this mature karst basin was compared with the timing of exports from an adjacent immature karst watershed in Ford *et al.* (2017). While the magnitude of flux from South Elkhorn ($2.10 \pm 0.66 \text{ t N km}^{-2} \text{ y}^{-1}$) and Cane Run ($1.83 \pm 0.24 \text{ t N km}^{-2} \text{ y}^{-1}$) are comparable, the dynamics controlling the timing of flux vary considerably. At coarse resolution (Figure 3.11a), the karst-dominated system of this study and fluvial-dominated system in Ford *et al.* (2017) exhibit high similarity in terms of their mean temporal trend. The similarity is reasonable given that the agricultural land surfaces in the two systems apply similar nutrient treatments seasonally and that the two systems experienced the same rainfall distributions. However, closer analyses of the systems (Figure 3.11b) showed the highly dampened nature of N peaks within the karst watershed even when including both surface and subsurface loading from the karst system. Karst N load peaks were typically on the order of 30% of the non-karst systems response to hydrologic events, and the karst system N load was as low as 15% of the non-karst system. N loading during hydrologic recession and baseflow periods (see Figure 3.11c) shows that the karst system consistently produces higher N loads to the downstream water bodies and that it temporally distributes N across active periods more so than the immature karst watershed. Delay of N delivery in karst basins has been discussed in previous work (Croll and Hayes, 1988; Fretwell *et al.*, 2005; Mahler *et al.*, 2008), and the side-by-side

comparison presented here extends this discussion. The results occur because of the karst pathway complexity that in turn impacts timing of N loads.

Taken together, the results in Figure 3.11 highlight the ability of the phreatic karst terrain to act a natural detention basin for NO_3^- that is later received by downstream water bodies. The karst watershed temporally delays the flow of N to downstream waters during hydrologic activity and thereafter exports the N at a more constant rate. Unlike fluvial-dominated systems where over 50% of NO_3^- export may occur during 90th percentile and greater flows (e.g. Royer *et al.*, 2006), modeling results indicate that for our karst-dominated system > 90th percentile flows account for less than 25% of NO_3^- export. The sustained downstream delivery of spring water NO_3^- and reduced flow velocities at karst springs (Husic *et al.*, 2017a,b) could prolong the period of bioavailable nutrients to in-stream growth and reduce shearing potential of streams supplied by karst waters. Both of these factors could potentially lead to the development of harmful algal blooms (Franklin *et al.*, 2008; Paerl *et al.*, 2011). Nutrient management scenarios within karst watersheds should not only consider the N concentration of spring discharge, but also the timing and length of elevated N concentrations.

3.5 CONCLUSIONS

We have demonstrated the utility of a reservoir model to simulate water and NO_3^- dynamics in an agricultural-karst system. Coupling the reservoir-based model with the four years of N field data provided estimates of the internal epikarst and phreatic processes controlling N fate in agricultural-karst. Extensive uncertainty analysis quantified bounds on model outputs and also reduced equifinality in hydrologic predictions by 68%. The numerical modeling approach used herein to estimate water and N fluxes and reduce equifinality has broad applications to other karst modeling studies.

Numerical modeling results also provided insight into the pathways, processes, and timing that control N exports from agricultural-karst systems. Epikarst and phreatic pathways account for nearly 90% of N loading. Further, quickflow pathways dilute downstream NO_3^- contamination. The relative dominance of slowflow in karst is an underdeveloped topic in the water science community. As a second point, evidence is provided that physical processes have a stronger control on N fate in agricultural-karst than

biogeochemical processes. N accumulation and subsequent N leaching in soils and the epikarst, at relatively rapid velocities, govern the N load. N turnover in karst is similar to non-karst systems, but the dominance of physical processes particularly evapotranspiration leads to net increases in NO_3^- concentration in spring water. As a final note, the timing of N exports from the karst-dominated system suggests it behaves as a natural detention basin relative to its fluvial-dominated counterpart. To this end, the karst system temporally delays the flow of NO_3^- to downstream waters during storm events and thereafter exports NO_3^- at a more gradual rate distributed over the flood recession. This work highlights the capability of relatively parsimonious modeling to provide meaningful insights into flow and nutrient dynamics of highly complex systems such as karst watersheds.

3.6 ACKNOWLEDGEMENTS

The authors would like to acknowledge primary funding from the Kentucky Senate Bill 271B Water Quality program. Steve Workman and Charles Taylor are greatly acknowledged for their contributions and support. The researchers and staff at the Kentucky Geological Survey and the extensive field and laboratory work they performed in the Cane Run Watershed were instrumental in the completion of this work. We thank the Department of Civil Engineering at the University of Kentucky for partial funding of the graduate student during this research study. The authors thank University of Kentucky Research Computing for making available the high performance computing resources used to perform uncertainty analysis in this study. Lastly, we gratefully acknowledge financial support of this research under National Science Foundation Award 1632888, which provided partial support for the graduate student and partial support to two of the authors.

3.7 TABLES AND FIGURES

Table 3.1 Review table of NO₃⁻ studies conducted in karst watersheds (n = 22) showing study location, the concentration of quickflow NO₃⁻, and the concentration of discharged aquifer NO₃⁻. 18 of 22 (82%) studies reported higher NO₃⁻ concentrations in aquifer water than in quickflow water.

Study Site / Reference	Location	Quickflow NO ₃ ⁻ (mg N L ⁻¹)*	Aquifer NO ₃ ⁻ (mg N L ⁻¹)**
Royal Spring <i>Present Study</i>	Kentucky, USA	1.92	2.86
Barton Springs <i>Mahler and Garner (2009)</i>	Texas, USA	0.05	0.34
Los Tajos <i>Mudarra et al. (2014)</i>	Malaga, Spain	0.43	2.53
Barton Springs <i>Mahler et al. (2008)</i>	Texas, USA	0.29	1.56
San Antonio Edwards Aquifer <i>Musgrove et al. (2016)</i>	Texas, USA	0.43	1.86
Fountain Creek Watershed <i>Sueber and Criss (2005)</i>	Illinois, USA	2.80	4.20
Wakulla Springs <i>Katz et al. (2004)</i>	Florida, USA	0.02	0.80
Guiyang Basin <i>Liu et al. (2006)</i>	Guizhou, China	2.14	4.15
Stafford Springs <i>Davis et al. (1995); Peterson et al. (2002)</i>	Arkansas, USA	1.50	5.10
Umm Rijam Aquifer <i>Obeidat et al. (2008)</i>	Yarmouk, Jordan	0.61	7.45
Yverdon-les-Bains System <i>Pronk et al. (2009)</i>	Jura, Switzerland	6.75	1.96
Big Spring Basin <i>Rowden et al. (1998, 2001)</i>	Iowa, USA	7.61	9.93
Jiangjia Spring <i>He et al. (2010)</i>	Chongqing, China	0.79	5.01
Spring Creek Watershed <i>Buda and DeWalle (2009)</i>	Pennsylvania, USA	2.80	4.47
Springbrook Creek Watershed <i>Schilling and Helmers (2008)</i>	Iowa, USA	0.10	12.08
Pays de Caux System <i>Fournier et al. (2007)</i>	Norville, France	2.40	4.86
Houzhai Catchment <i>Yue et al. (2015, 2017)</i>	Guizhou, China	2.58	3.62
Vransko Polje <i>Markovic et al. (2006)</i>	Zagreb, Croatia	0.20	2.13
Kestel Polje-Kirkgoz Springs <i>Ekmekci (2005)</i>	Antalya, Turkey	1.20	0.70
Plainview System <i>Moers and Alexander (1994)</i>	Minnesota, USA	16.85	12.90
Jackson and Cleghorn Springs <i>Swanson (2004); Long et al. (2008)</i>	South Dakota, USA	0.10	0.31
Funshion River Watershed <i>Fenton et al. (2017)</i>	Fermoy, Ireland	12.04	11.80

*Mean value shown is that of the surface stream(s) or other quickflow sources (e.g., rain).

**Mean value shown is that of the spring(s) (if available) or other aquifer values (e.g., wells).

Table 3.2 Hydrologic and nitrogen model inputs and parameters. Each input and parameter is presented with a description, measured or calibrated value, units of measurement, and the source material for the value. Hydrologic and nitrogen model parameter values are presented as the median of the posterior distribution for each parameter.

Symbol	Description	Value	Units	Source
MODEL INPUTS				
Δt	Temporal step	1	d	User input
A	Recharge Area	5.8×10^7	m ²	Measured in field
α_1	Recession coefficient for quickflow pathway	0.50	d ⁻¹	Mean Recession Curve
α_2	Recession coefficient for epikarst pathway	0.15	d ⁻¹	Mean Recession Curve
α_3	Recession coefficient for phreatic pathway	0.05	d ⁻¹	Mean Recession Curve
x_{SOIL}	Fraction of stream water of soil origin	0.25	-	Buda and DeWalle, 2009;
x_{REC}	Fraction of stream water of runoff origin	0.75	-	Long, 2009
$C_{NH_4^+(R)}$	NH ₄ ⁺ concentration of recharge	0.12	mg N L ⁻¹	Measured in field
$C_{DON(R)}$	DON concentration of recharge	0.35	mg N L ⁻¹	Measured in field
HYDROLOGIC MODEL PARAMETERS				
X	Fraction of rainfall as concentrated recharge	0.05	-	Minimum and maximum bounds represent inferred (low and high) physical bounds. Median value from GLUE analysis.
k_{soil}	Soil percolation coefficient	0.04	d ⁻¹	
k_{stream}	Soil lateral flow coefficient	1.91	d ⁻¹	
k_{EL}	Epikarst percolation coefficient	0.06	d ⁻¹	
Q_{PUMP}	Aquifer pumping rate	0.66	mm d ⁻¹	
$V_{S,MIN}$	Soil field capacity	53.3	mm	
$V_{S,MAX}$	Soil height to activate lateral flow	130.6	mm	
$V_{E,FAST}$	Height to activate quick epikarst pathways	16.5	mm	
$V_{P,MIN}$	Minimum phreatic water level	55.1	mm	
NITROGEN MODEL PARAMETERS				
$C_{NO_3^-(F)}$	NO ₃ ⁻ concentration of fall recharge	2.69	mg N L ⁻¹	Bound by minimum and maximum values of observed stream data. Median value from GLUE analysis.
$C_{NO_3^-(W)}$	NO ₃ ⁻ concentration of winter recharge	2.46	mg N L ⁻¹	
$C_{NO_3^-(SP)}$	NO ₃ ⁻ concentration of spring recharge	0.69	mg N L ⁻¹	
$C_{NO_3^-(SU)}$	NO ₃ ⁻ concentration of summer recharge	1.01	mg N L ⁻¹	
$k_{S,DEN}$	Soil denitrification first-order rate constant	0.005	d ⁻¹	Minimum and maximum bounds represent (low and high) biochemical rates (Bowie et al., 1985; Zak et al., 1993; Tesoriero and Puckett, 2011). Median value from GLUE analysis.
$k_{S,NITR}$	Soil nitrification first-order rate constant	0.108	d ⁻¹	
$k_{S,MIN}$	Soil mineralization first-order rate constant	0.031	d ⁻¹	
$k_{E,DEN}$	Epikarst denitrification first-order rate constant	0.009	d ⁻¹	
$k_{E,NITR}$	Epikarst nitrification first-order rate constant	0.108	d ⁻¹	
$k_{E,MIN}$	Epikarst mineralization first-order rate constant	0.011	d ⁻¹	
$k_{P,DEN}$	Phreatic denitrification first-order rate constant	0.002	d ⁻¹	
$k_{P,NITR}$	Phreatic nitrification first-order rate constant	0.149	d ⁻¹	
$k_{P,MIN}$	Phreatic mineralization first-order rate constant	0.016	d ⁻¹	

Table 3.3 Hydrologic and nitrogen model evaluation results including number of data points within each calibration/validation set; the methodology for selecting calibration/validation subsets; and the mean, min, and max of the Nash-Sutcliffe Efficiency (NSE) statistic. Mean, min, and max values shown are calculated from all accepted hydrologic (n = 3,653) and nitrogen (n = 2,687) model realizations.

Model	Period	No. of Data Points	Data Split Methodology	NSE		
				Mean	Max.	Min.
Hydrologic	Calibration	730	50:50 Split	0.53	0.65	0.50
	Validation	731	Sampling	0.33	0.56	-0.30
Nitrogen	Calibration	82	50:50 Random	0.07	0.46	0.00
	Validation	82	Sampling	-0.02	0.48	-1.09

Table 3.4 Percentages of water and NO₃⁻ yield ($\pm 1\sigma$) from modeled karst pathways during the study period.

Reservoir	Water Discharged (%)	Nitrate Exported (%)
Quickflow	18 \pm 7	11 \pm 5
Epikarst Flow	35 \pm 22	40 \pm 25
Phreatic Flow	47 \pm 21	49 \pm 25

Table 3.5 (a) NO_3^- budget ($\pm 1\sigma$) for the Royal Spring basin showing inputs (infiltration and quickflow recharge) and outputs (spring, stream, and losses such as pumping). (b) Biochemical reactions ($\pm 1\sigma$) shown as the area-normalized annual masses of NO_3^- denitrified, NH_4^+ nitrified, and DON mineralized within each reservoir.

a) NO_3^- Inputs and Outputs			
Inputs	(t N km ⁻² y ⁻¹)	Outputs	(t N km ⁻² y ⁻¹)
Infiltration	2.15 (0.30)	Karst Spring	1.13 (0.14)
Quickflow	0.11 (0.05)	Surface Stream	0.31 (0.11)
		Net Aquifer Losses	0.39 (0.23)
Total	2.26 (0.32)	Total	1.83 (0.24)

b) Biochemical Reactions			
Reservoir	Denitrification (t N km ⁻² y ⁻¹)	Nitrification (t N km ⁻² y ⁻¹)	Mineralization (t N km ⁻² y ⁻¹)
Soil	0.47 (0.34)	0.26 (0.11)	0.21 (0.10)
Epikarst	0.16 (0.17)	0.05 (0.05)	0.03 (0.04)
Phreatic	0.19 (0.15)	0.11 (0.08)	0.07 (0.07)
Total	0.82 (0.35)	0.42 (0.05)	0.31 (0.04)

Figure 3.1 Conceptual model of water and NO_3^- pathways in an agricultural karst system. Contaminant provenance includes surface, subsurface, distributed, and point sources and pathways. The accumulation of NO_3^- within the karst aquifer followed by a release to the primary conduit results in NO_3^- leaching losses to downstream waterbodies.

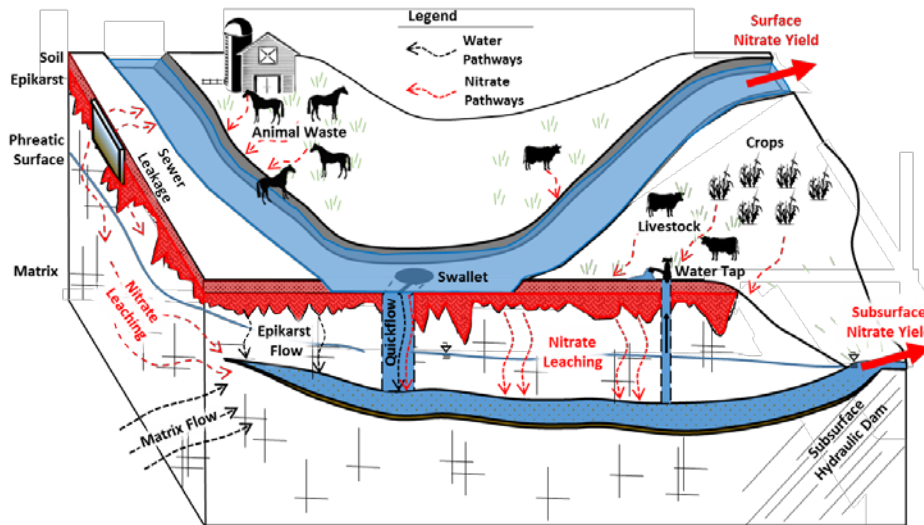


Figure 3.2 Model framework for water and nitrogen processes and pathways in a karst aquifer. Recharge (R) of water, NO_3^- , NH_4^+ , and DON is applied as concentrated input to the quickflow reservoir (X) or as distributed input to soil ($1-X$). Distributed recharge of NO_3^- , NH_4^+ , and DON represents bulk infiltration of material (e.g., precipitation, fertilizer, manure and sewage) to the soil. Evapotranspiration (ET_A), flow to surface stream (Q_{stream}) which includes runoff (x_{REC}) and lateral soil flow (x_{SOIL}) fractions, and percolation (Q_{soil}) are outflows from the soil reservoir. Soil field capacity is represented by $V_{S,MIN}$ and saturation conditions by $V_{S,MAX}$. Concentrated recharge to the quickflow reservoir includes sinkholes, swallets, and stream abstractions (dashed line). Outflow from the quickflow reservoir (Q_Q) occurs via shaft, sinkhole, and swallet discharge to the conduit. The epikarst is recharged by soil percolation and discharges water via seepage to the phreatic aquifer (Q_{EL}) or as conduit recharge via larger fractures (Q_E). Direct flow from the epikarst to the conduit occurs when dynamic storage within the epikarst exceeds a threshold ($V_{E,FAST}$). Finally, the phreatic zone is recharged by the epikarst and losses are attributed to diffuse flow (Q_P) and pumping losses (Q_{PUMP}) related to agricultural and other human demands. The level at which baseflow to the spring ceases (i.e., the spring runs dry) is represented by $V_{P,MIN}$, and pumping losses are stopped when drawdown reaches $V_{P,PUMP}$.

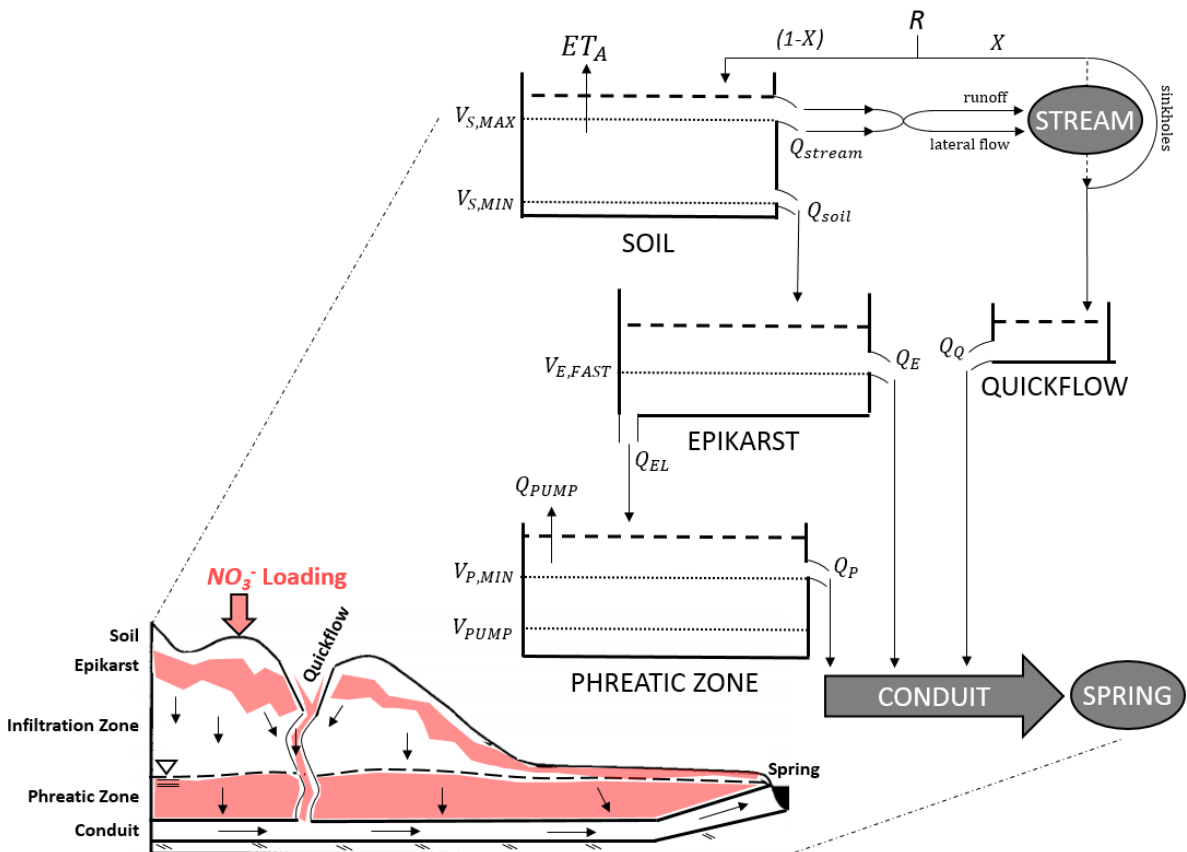


Figure 3.3 Cane Run Watershed and Royal Spring Basin indicating sampling sites, karst holes, and the primary conduit conveyance zone for fluid and nutrients.

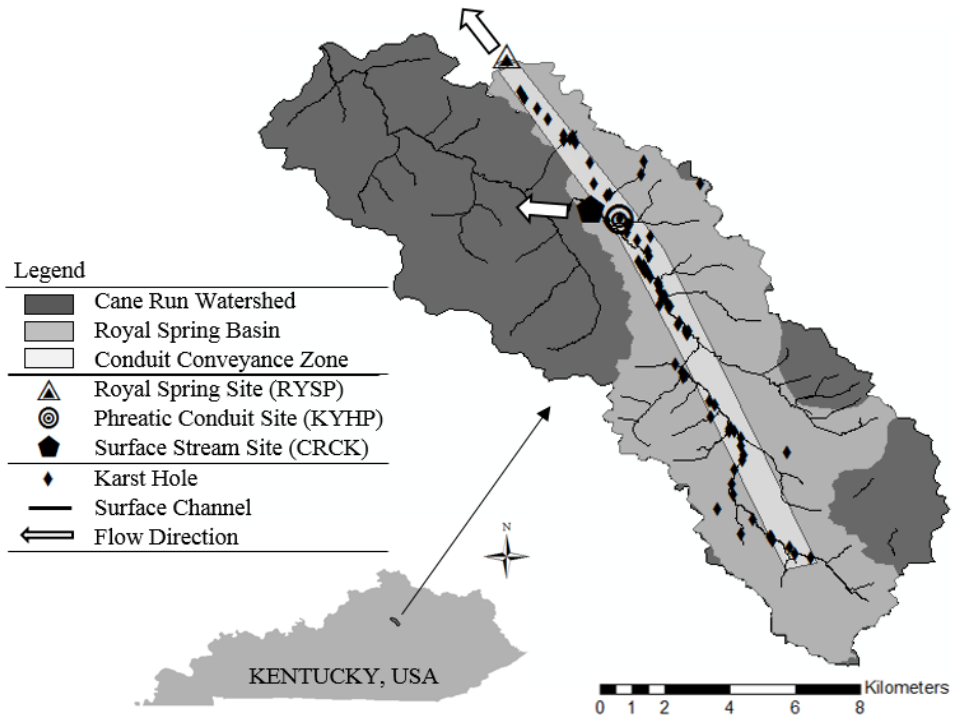


Figure 3.4 Master recession curve (MRC) for Royal Spring using nine events over a decade of flow data. The MRC was decomposed into three constituent reservoirs (quick, epikarst, phreatic) and recession coefficients (α_1 , α_2 , α_3) were fitted to match data results (see Malík and Vojtková, 2012).

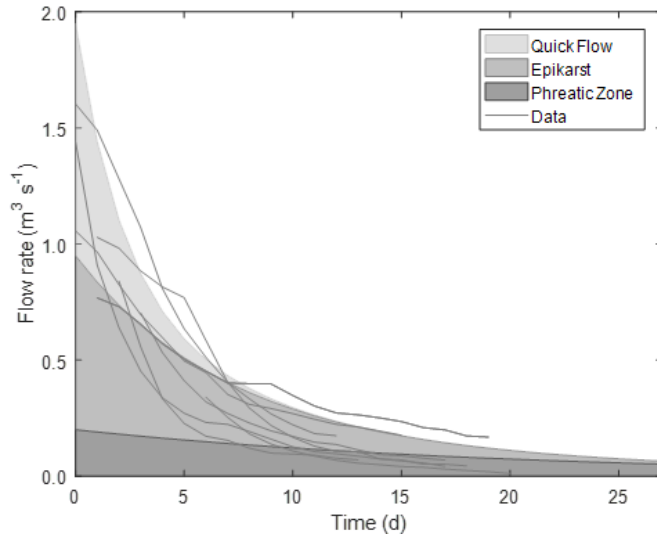


Figure 3.5 Framework for evaluating hydrologic and nitrogen model uncertainty in parameters and predictions. Hydrologic model parameters (θ) are sampled from an assumed prior distribution. The parameters are fed into the numerical model, M , and simulated model results (Q) are compared to measured flow data (\tilde{Q}). Only model realizations and parameter sets that satisfy the objective function are retained. Accepted hydrologic parameter sets are fed through to the dissolved nitrogen model where biochemical parameters (x) are sampled and model results (C_{NO3}) are evaluated against measured spring data (\tilde{C}_{NO3}). Evaluation statistics for the dissolved nitrogen model include a Nash-Sutcliffe (NSE) function for Spring NO_3^- results and t-tests for modeled vs measured means of Stream NO_3^- , Spring NH_4^+ , and Spring DON. Lastly, accepted hydrologic and biochemical realizations are used to construct posterior parameter distributions and prediction bounds.

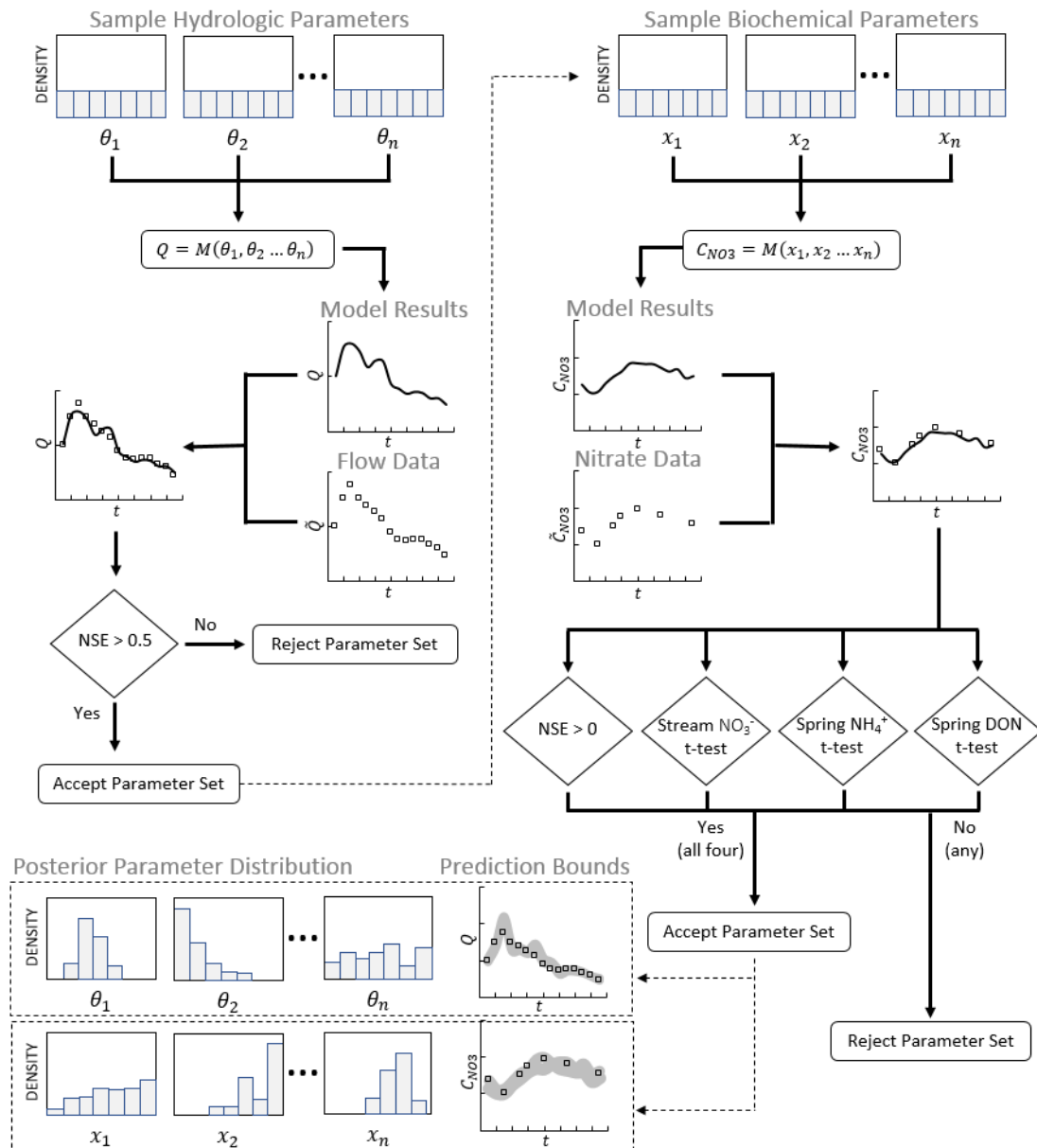


Figure 3.6 Concurrently sampled (n = 99) surface steam (CRCK) and subsurface phreatic conduit (KYHP) NO₃⁻ concentrations.

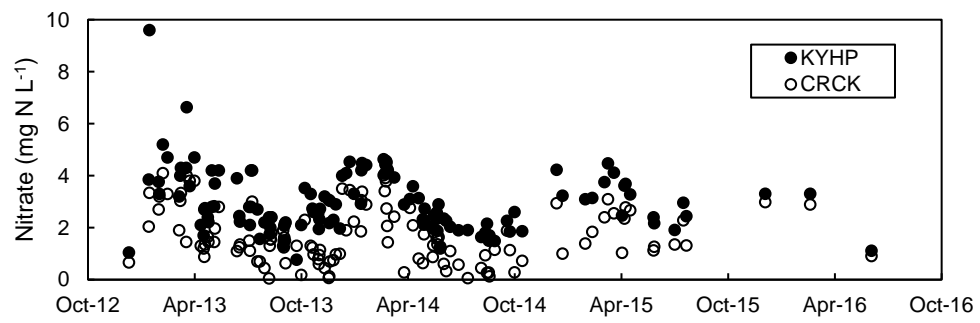


Figure 3.7 (a) Hydrologic model results simulating Royal Spring discharge. (b) Nitrogen model results simulating NO_3^- concentration at Royal Spring. (c) NO_3^- concentration within the four modeled reservoir pathways. Prediction bounds for each pathway include 66% of accepted results – rather than 95% – for visual clarity of the differences in mean pathway concentrations.

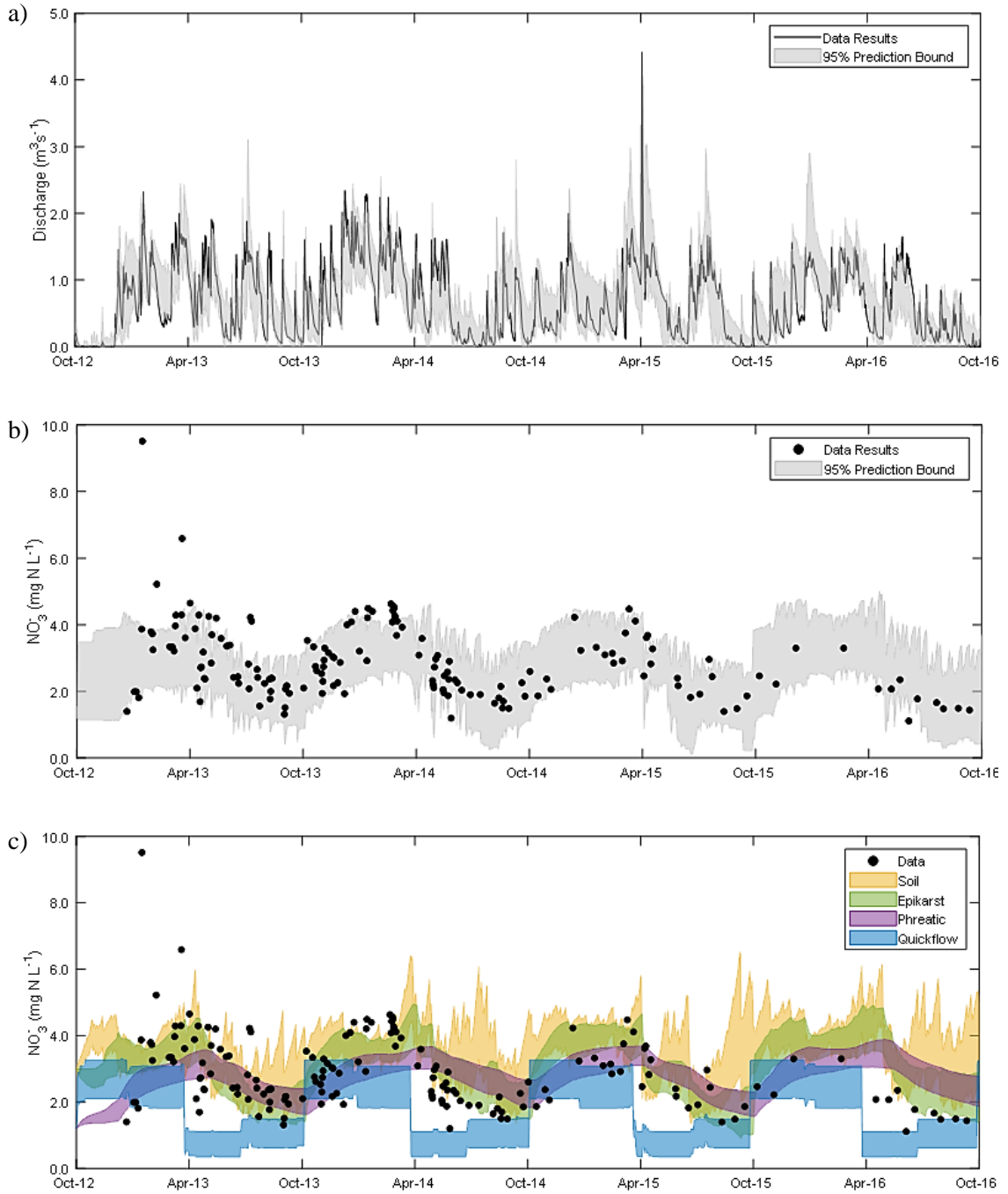


Figure 3.8 (a) Prior and posterior distributions of hydrologic model parameters: X (concentrated recharge fraction), k_{soil} (soil discharge coefficient), k_{stream} (stream discharge coefficient), k_{EL} (epikarst seepage discharge coefficient), Q_{PUMP} (aquifer pumping rate), $V_{S,MIN}$ (soil field capacity), $V_{S,MAX}$ (soil saturation), $V_{E,FAST}$ (activation height for fast epikarst pathways), and $V_{P,MIN}$ (height at which aquifer over-extraction causes an end to pumping). (b) Prior and posterior distributions of nitrogen model parameters: denitrification ($k_{S,DEN}$, $k_{E,DEN}$, and $k_{P,DEN}$), nitrification ($k_{S,NITR}$, $k_{E,NITR}$, and $k_{P,NITR}$), and mineralization ($k_{S,MIN}$, $k_{E,MIN}$, and $k_{P,MIN}$) transformation rates for soil, epikarst, and phreatic pathways, respectively. Also shown are the seasonal NO_3^- concentrations for fall ($C_{NO_3(F)}$), winter ($C_{NO_3(W)}$), spring ($C_{NO_3(SP)}$), and summer ($C_{NO_3(SU)}$) recharge. Note: the x-axis for transformation rates is presented as the \log_{10} value of the rate.

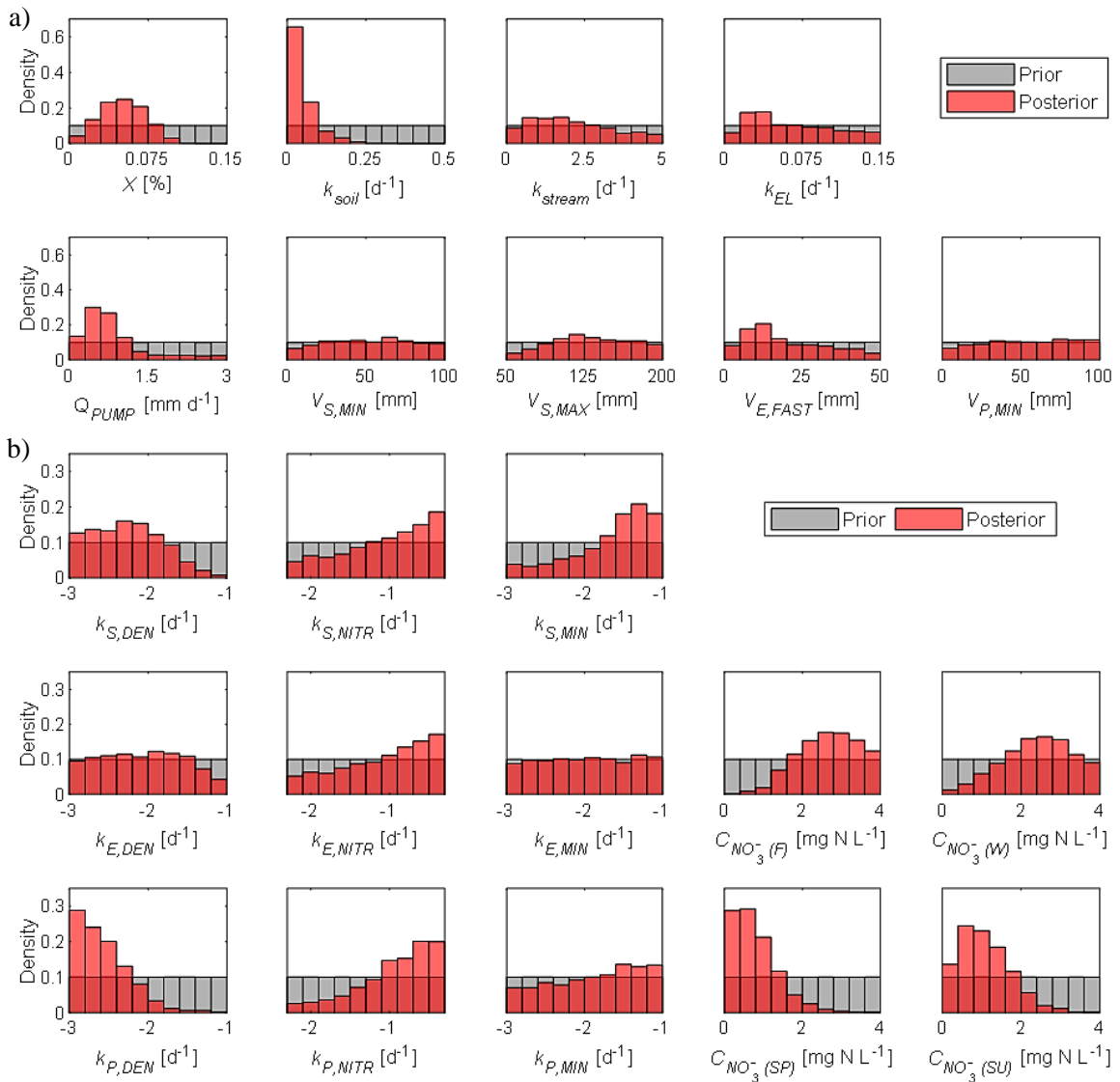


Figure 3.9 (a) Modeled mean residence time of spring water decomposed into three karst pathways (results presented are from the optimal simulation). (b) Autocorrelation analysis of modeled and measured spring discharge. (c) Cross-covariance analysis of rainfall with modeled and measured spring discharge. Model bounds include 95% of accepted model simulations.

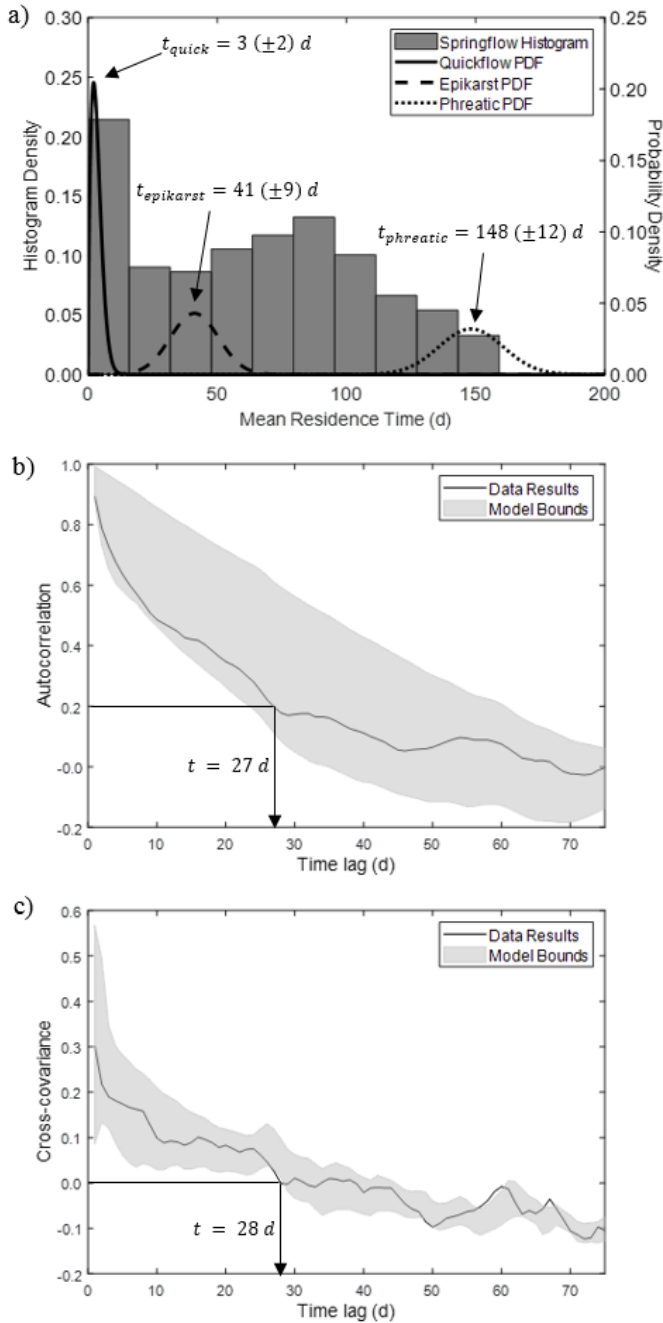


Figure 3.10 Nitrate source contribution via multiple karst pathways over a two year period for the optimal model simulation. The top plot shows the fraction of each pathway to the total NO_3^- load. Blank (white) spaces indicate no discharge at the spring. During dry summer periods, particularly when aquifer stores have experienced over-pumping, the spring water level will drop below the weir where flow is recorded. The bottom plot is an area graph and quantifies the NO_3^- load of each pathway as the area between two curves.

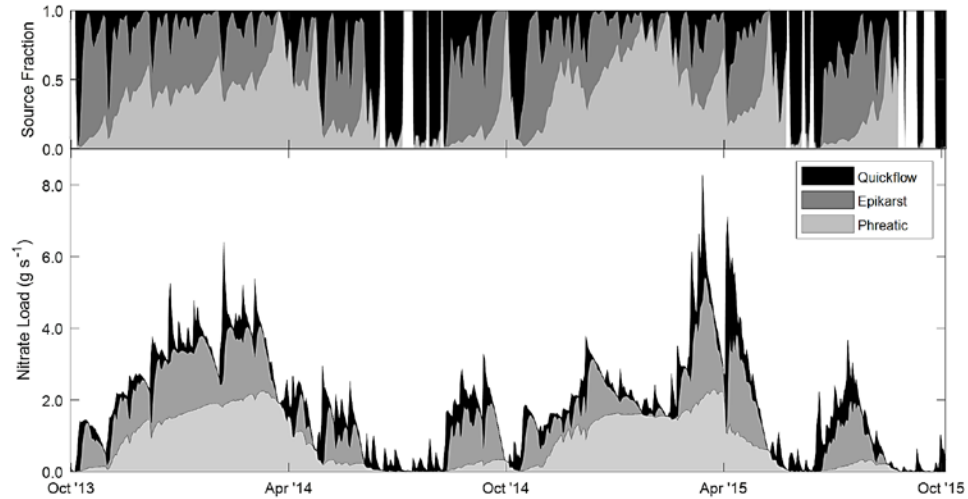
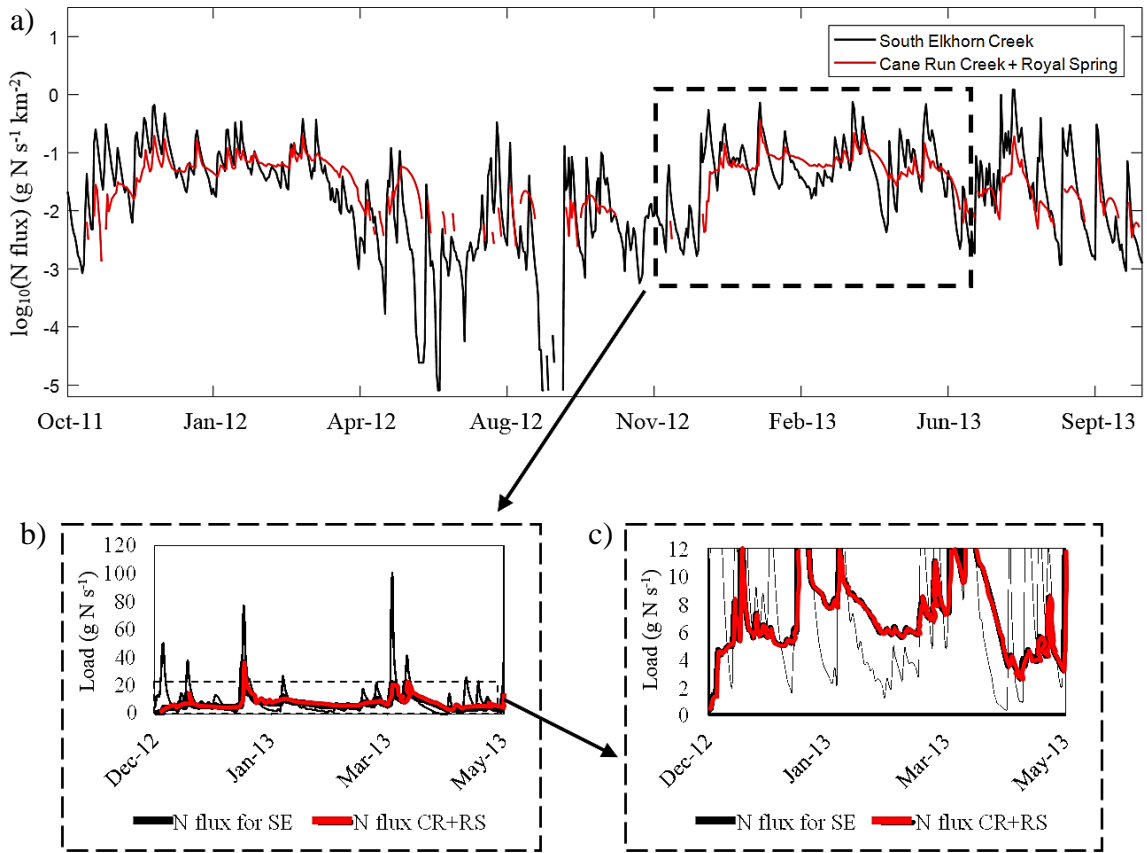


Figure 3.11 Comparison of Cane Run Creek-Royal Spring (CR+RS) to a neighboring immature karst watershed, South Elkhorn Creek (SE) (Ford *et al.*, 2017). (a) Area-normalized N load, (b) close-up of six months of N load, and (c) highlighting low-flow N dynamics in CR+RS.



Chapter 4: Inland impacts of atmospheric river and tropical cyclone extremes on nitrate transport and stable isotope measurements

4.1 ABSTRACT

Atmospheric river and tropical cyclone extremes originate in the tropics and can transport high rainfall amounts to inland temperate regions. The purpose of this study was to investigate the response of nitrate (NO_3^-) pathways, concentration peaks, and stable isotope ($\delta^{15}\text{N}_{\text{NO}_3}$, $\delta^{18}\text{O}_{\text{NO}_3}$, $\delta^2\text{H}_{\text{H}_2\text{O}}$, $\delta^{18}\text{O}_{\text{H}_2\text{O}}$, and $\delta^{13}\text{C}_{\text{DIC}}$) measurements to extreme hydrologic events. Inland impacts of a tropical cyclone and atmospheric river produced the number one and four ranked events, respectively, in 2017 at a Kentucky USA watershed characterized by karst topography. Hydrologic responses from the two extremes were different due to rainfall characteristics, and the tropical cyclone produced a steeper spring hydrograph on the rising limb and greater runoff contribution compared to the atmospheric river. Local extrema of specific conductance, $\delta^2\text{H}_{\text{H}_2\text{O}}$ and $\delta^{18}\text{O}_{\text{H}_2\text{O}}$, and $\delta^{13}\text{C}_{\text{DIC}}$ coincided with hydrograph peaks for both extremes. Extrema of NO_3^- concentration, temperature, $\delta^{15}\text{N}_{\text{NO}_3}$, and $\delta^{18}\text{O}_{\text{NO}_3}$ lagged behind hydrograph peaks for both extreme events, and the values remained impacted by recharge during the storm recession. In general, all stable isotope measurements showed relative decreases in per mil values during quickflow dominance relative to times when the epikarst and phreatic dominate. Loadograph separation showed that quickflow accounts for, on average, less than 20% of the total NO_3^- yield during extreme hydrologic events, and epikarst (30%) and phreatic (50%) compose the remaining load. However, hydrograph separation into quickflow, intermediate (epikarst), and phreatic pathways was not able to predict timing of NO_3^- concentration peaks. Rather, the intermediate flow pathway is conceptualized to experience a shifting porosity, associated with epikarst macropore fissures to soil micropore porosity with the arrival of the latter component at the spring likely causing peak NO_3^- concentration. Our results suggest that a more discretized conceptual model of pathways may be needed to predict peak nutrient concentration in rivers draining karst.

4.2 INTRODUCTION

The inland trajectory of atmospheric river and tropical cyclone extremes can impact the hydrologic cycle thousands of kilometers from coastal landfall (Moore et al. 2012; Lavers and Villarini 2013). Atmospheric rivers are narrow bands of transported moisture that carry water vapor from the tropics to temperate regions (Rutz et al. 2014). Tropical cyclones also originate in the tropics and carry moisture via high-speed cyclonic winds to sub-tropic and temperate regions (Knight and Davis 2009). Tropical storms are highly impactful as they make landfall, endanger human life, and flood manmade infrastructure along coastlines (Lavers et al. 2012; Ralph and Dettinger 2012). In addition, their effects are felt far inland where storm remnants can drive local hydrology. For example, in the southeastern USA, atmospheric rivers can account for over one-third of total annual rainfall (Lavers and Villarini 2013) and tropical cyclones are most likely to produce the largest annual event (Shepherd et al. 2007). The intensity of these extreme events is projected to increase as climate change alters regional hydrology (Lavers and Villarini 2013).

Given the high inland rainfall amounts that fall from these extremes, their impact on mobilizing water contaminants is also of question. During rainfall and immediately thereafter, contaminants can be mobilized from different land surface and subsurface sources via runoff, lateral soil flow, and groundwater flow. Peak contaminant concentrations in river water during or after an event can be detrimental to ecosystems (Cánovas et al. 2008; Jarsjö et al. 2017). For this reason, we were motivated to understand contaminant pathways and concentration peaks and how they are impacted by the inland effects of atmospheric rivers and tropical cyclones.

Nitrate contamination is the focus of this study. Nitrate in rivers is of immediate concern as human activities have increased NO_3^- loading to waterways leading to development of harmful algal blooms and hypoxic zones (Dodds and Smith 2016). Past research provides some hints as to how NO_3^- may be mobilized from pathways during extreme events. Nitrate pathways from the landscape to rivers can be defined to include dilute quickflow from runoff, slowflow of groundwater, and concentrated quickflow (Tesoriero et al. 2013; Miller et al. 2017). The timing and relative NO_3^- contribution of these mobilized pathways is expected to result in a peak concentration of NO_3^- , and the NO_3^- peak during a storm event has often been cited to be delayed (“lagged”) relative to

the hydrograph peak (Koenig et al. 2017). However, the nutrient paradigm remains open-ended with questions regarding both the distribution of pathways throughout a basin and the cause for timing of peak concentrations. The importance of understanding these pathways becomes more apparent as climate change exerts influence on inland hydrology (Al Aamery et al. 2016, 2018) and land management strategies adapt to extreme events (Tomer and Schilling 2009; Lal et al. 2011).

Research tools applied to understand NO_3^- pathways and peaks during extremes include both high resolution sampling routines and quantitative analyses of pathways. Storm event sampling of water, NO_3^- , and its indicators can help resolve mobilization from different pathways. In addition, NO_3^- source and fate can be investigated using its stable isotopes (i.e., $\delta^{15}\text{N}_{\text{NO}_3}$ and $\delta^{18}\text{O}_{\text{NO}_3}$) (Panno et al. 2001; Katz et al. 2010; Yue et al. 2018). Quantitative analysis of NO_3^- pathways can be assessed using loadograph recession analyses (Mellander et al. 2012; Fenton et al. 2017). Inflections in hydrograph and loadograph recessions can be used to quantify pathway contributions of NO_3^- stores in a watershed (Fenton et al. 2017). Assessment of the lag effect corresponding with the relative locations of concentration and hydrograph peaks can be used to infer causes and pathways of contamination (Koenig et al. 2017). Likewise, water and dissolved inorganic (DIC) isotopic composition can assist in identifying pathways (Lee and Krothe 2001). However, there is a lack of relatively high-frequency data collection of stable isotope measurements during extreme events as the events are, by their nature, infrequent and stable isotopes, to characterize response to these events, are an emerging technology.

The 2017 calendar year brought an unusually high number of atmospheric river and tropical cyclone extremes to inland North America. January and February 2017 brought a string of atmospheric rivers to the contiguous United States (US), and June through November 2017 was one of the most active hurricane seasons on record featuring 17 tropical cyclones in the Atlantic and Caribbean (NHC NOAA, 2017). Aftereffects resulted in approximately 1,000 fatalities and damage to infrastructure totaling \$300 billion making 2017 the costliest year on record for natural disasters (NOAA, 2017a). While recognizing the distressing impact to human life, we questioned the inland impacts on NO_3^- contaminant pathways, stable isotope measurements of NO_3^- and water, and peak contaminant concentration in rivers. As the 2017 extremes approached inland Kentucky

USA, our research team carried out an extensive storm event sampling plan to understand their impact on mobilizing NO_3^- in a mature karst watershed.

The study objectives were to (1) characterize the inland impacts of extreme events including their timing, rainfall amounts, intensities, and hydrograph responses for extremes during 2017 in Kentucky USA; (2) collect and analyze water quality and environmental tracer data resulting from the extremes; (3) perform hydrograph and loadograph separation analyses for NO_3^- pathways mobilized from the extremes; and (4) perform nutrient lag effect analyses. The objectives provide the structural sub-headings of the methods and results/discussion sections of this paper.

4.3 THEORETICAL BACKGROUND

The theoretical background allows definition of extremes, NO_3^- pathways, and the NO_3^- lag effect.

Both atmospheric rivers and tropical cyclones can produce high inland rainfall such as in Kentucky USA (Figure 4.1a). A set of atmospheric rivers termed the “Maya Express” transport moisture from the eastern tropical Pacific and Caribbean Sea into the US Midwest and Southeast (Figure 4.1b) (Moore et al. 2012; Debbage et al. 2017). During the wet season, southerly atmospheric rivers can account for 30–50% of rainfall in Kentucky and Tennessee (Lavers and Villarini 2013). The term ‘tropical cyclone’ refers to the warm, tropical sea origin of these extremes and the circular winds round the storms center eye, although far inland aftereffects of the storms typically are associated with high winds and high rainfall intensity (Larson et al. 2005). Tropical cyclones originating in the mid-Atlantic Ocean often make landfall in the Caribbean and Southeast US and a trajectory of an inland tropical cyclone can reach far inland (see Figure 4.1c; NHC NOAA, 2017). In terms of watershed hydrology for inland regions of North America, the seasonality of the extremes allows us to investigate atmospheric rivers and tropical cyclones as two separate classifications of extreme rainfall events. The mid- to late-winter atmospheric rivers bring high rainfall, distributed over days, upon wet soils while the late-summer and early-fall hurricanes bring extreme rainfall upon dry soils. In this manner, we hypothesize that

hydrologic events in the central Kentucky region may be characterized by behavior that falls between the atmospheric river and tropical cyclone end-members.

Pathways of nitrogen (N) transport include a mixture of quickflow, intermediate and slowflow pathways distributed across an extreme storm event. A more refined view of pathways was conceptualized by considering karst-dominated watersheds typical of Kentucky USA (see Figure 4.2a). The Kentucky karst region is characterized by gently rolling terrain caused by the weathering of chemically soluble limestone which in turn produces sinkholes (i.e., dolines), sinking streams, springs, and conduits (Figure 4.2b; Phillips et al. 2004). In highly-karstified systems, direct quickflow recharge into conduit systems dominates the early hydrograph response (Geyer et al. 2007). Diffuse recharge follows soil, epikarst, and phreatic zone pathways where storage volumes are several orders of magnitude greater than that of the quickflow pathways and have the potential to retain N (Williams, 2008) (see Figure 4.2c for epikarst example). We conceptualize the diffuse recharge as two pathways including intermediate (soil and epikarst) and slowflow (phreatic) pathways (Figure 4.2a). Intermediate pathway soil and epikarst storages provide the potential for high N accumulation and subsequent leaching (Tzoraki and Nikolaidis 2007), potentially providing the most concentrated NO_3^- within water. Slowflow pathways reflect phreatic storage sustained by Darcian groundwater recharge from stored volumes in the aquifer bedrock (Ghasemizadeh et al. 2012).

The mentioned pathways mobilize and deliver both dilute and concentrated NO_3^- to rivers. Identifying variability in NO_3^- concentration during storm conditions requires relatively high frequency sampling as lower sampling rates may miss changes in source contribution. For the watershed scale, a lagged N concentration peak has been suggested that involves a sequence of dilute quickflow followed by concentrated intermediate flow and subsequent slowflow from groundwater stores (Miller et al. 2017). As the dilute quickflow recedes and give way to the intermediate and slowflow pathways, a peak NO_3^- concentration will be expected (Figure 4.2d). The terminal NO_3^- concentration is then associated with slow pathways that sustain baseflow (Burns et al. 2016). Additionally, concentration and discharge of nutrients is influenced by biogeochemical activity during low flows and hydrology at high flows (Moatar et al. 2017). Thus, we expect that during high flows in a karst watershed, NO_3^- concentrations will be heavily influenced by

hydrological pathways. The dilution/concentration dynamics discussed in this section relate primarily to dissolved nutrient phases whereas particulate nutrients such as phosphorous are associated more closely with quickflow (Jarvie et al. 2014).

As the inland impacts of 2017 atmospheric river and tropical cyclone extremes approached Kentucky USA, a sampling and analyses plan was carried out to investigate how extreme events mobilize pathways, impact stable isotope measurements, and produce peak N concentrations.

4.4 STUDY SITE AND MATERIALS

The study site, Cane Run watershed (96 km²) and Royal Spring groundwater basin (58 km²), is in the Inner Bluegrass Region of Kentucky USA (Figure 4.3). The inland study basin is located approximately 1,000 km from the Gulf of Mexico, where the atmospheric river and tropical cyclones made landfall in 2017. The study watershed is characterized by rolling hills and mild relief (Paylor and Currens 2004). This topography makes the land surface suitable for agricultural use and much of it is horse farm pasture (UKCAFE, 2011). The geologic medium forming the underlying spring basin is Lexington Limestone of the Middle Ordovician period (Cressman and Peterson, 1986). The hydrogeology of the subsurface follows a series of en echelon minor faults and joints trending from the Southeast to the Northwest (Drahovzal et al. 1992). Surface and subsurface flow pathways are highly connected with over 50 karst features identified in the field (Figure 4.3) (Paylor and Currens, 2004; Husic et al. 2017a). These karst holes are situated in silt loam and silty clay loam formed from the residue of weathered phosphatic limestone (USDA, 1993). Tributary recharge to the primary creek channel is abstracted by swallets to a trunk conduit 20 m below the earth surface (see “Conduit Conveyance Zone” in Figure 4.3). Flow abstraction in Cane Run is so prevalent that the primary creek flows less than 20% of the year, only becoming active during moderate to intense hydrologic activity (Husic et al. 2017a). The mean discharge of the primary spring that drains the aquifer (Royal Spring, 243 m.a.s.l.) is 0.67 m³ s⁻¹. The site has been a karst research site led by the Kentucky Geological Survey and the University of Kentucky the past 40 years (Spangler, 1982;

Thraill et al. 1991; Taylor, 1992; Paylor and Currens, 2004; Zhu et al. 2011; Husic et al. 2017a,b).

Three sampling stations were placed in the basin including: the surface stream that recharges the karst aquifer (Cane Run Creek), the midpoint of the subsurface primary conduit (Phreatic Conduit), and the primary karst spring (Royal Spring) (Figure 4.3). Groundwater wells were drilled at the “Phreatic Conduit” station to sample from within the submerged conduit near its longitudinal midpoint (Zhu et al. 2011; Husic et al. 2017a). The conduit was sampled with a deep well pump (Hallmark Industries MA0414X-7) submerged directly into the primary flow path. The “Cane Run Creek” surface stream station was sampled using a Teledyne ISCO 6712 automated pumping system affixed to the creek streambed. Streamflow in Cane Run Creek was monitored 9 km upstream at Citation Blvd (USGS 03288180) by a gage operated by the United States Geological Survey (USGS). The USGS also operates a gage at Royal Spring (USGS 03288110) where discharge was recorded and grab samples were collected. Rainfall data were available from the Bluegrass Airport gage station (NOAA ID: USW00093820).

4.5 METHODS

4.5.1 Characterizing extreme events and their hydrographs

Storm events were characterized based on the meteorological conditions responsible for rainfall. During 2017, four total events were sampled for the entire suite of water quality and environmental tracer data. Of the four events, two produced enough rainfall to be characterized as ‘extreme’ (i.e., the 95th percentile of rainy days; Gao et al. 2012), and were the subjects of this study. The atmospheric river studied herein made landfall in late February 2017, originated from the Gulf of Mexico, and joined a cold front from the Great Plains and led to the 4th largest rainfall event, in the study watershed, of 2017 (Figure 4.4). The tropical cyclone known as “Hurricane Nate” occurred in early October 2017 and originated from a broad area of low pressure over the southwestern Caribbean. The inland impact of Hurricane Nate produced the largest rainfall event in 2017 for the study site (Figure 4.4). Events were ranked as the three-day sums of recorded precipitation.

Antecedent conditions of the watershed were also of interest to characterizing flow hydrographs. Storms were sampled based on 1) the expected rainfall intensity (to create an appreciable response at the three sampling locations), and 2) antecedent spring conditions (lower initial spring flow allows for attribution of more of the flow to the sampled event rather than pre-event water). Hydrograph shapes were then compared across storm events as the steepness of the rising limb and the slope(s) of the falling limbs can coincide with changes in quickflow and diffuse flow contribution, respectively (Geyer et al. 2007)

4.5.2 Water quality and environmental tracer data collection

Specific conductance, temperature, NO_3^- , $\delta^{15}\text{N}_{\text{NO}_3}$, $\delta^{18}\text{O}_{\text{NO}_3}$, $\delta^2\text{H}_{\text{H}_2\text{O}}$, $\delta^{18}\text{O}_{\text{H}_2\text{O}}$, and $\delta^{13}\text{C}_{\text{DIC}}$ samples were collected to show timing of contaminants and pathways. The temporal sampling strategy included high frequency data collection during various points in a storm hydrograph including: pre-event baseflow, rising limb, peak flow, and the beginning, middle, and end of a recession. Water samples at the spring site were collected directly from the mouth of the spring into sterile 1 L jars (I-Chem 312-0950BPC). At the creek site, if the water level was low, grab samples were collected directly from the stream into 1 L jars. However, during intense storm conditions, water was pumped into the jars using the automated sampler. At the conduit site, a deep well submersible pump extracted water directly from the conduit into sterile 1 L jars. If time did not permit installation of the pump before an event began, samples were collected using a double check valve bailer (AMS 61844). In the subsurface, water depth in a well directly intersecting the conduit was measured with a well-level indicator (Slope 113583) during each sample set. A multi-parameter probe (Horiba U-10) was used to record temperature and specific conductance data for every sample collected at every site. For each set of samples collected during a storm, the time elapsed between the collection of a sample at the first site and the last site was kept to a minimum (< 1 hour).

The Kentucky Geological Survey (KGS) laboratory analyzed NO_3^- samples following US EPA Method 300.0. Analysis was performed using a Dionex ICS-3000 Ion Chromatography System featuring a carbonate-bicarbonate eluent generator and Dionex

AS4A analytical column. Retention time was used to identify the NO_3^- anion and peak areas were compared to calibration curves generated from known standards. Duplicate field samples of NO_3^- showed little variability ($n = 8, \pm 0.07 \text{ mg N L}^{-1}$). Likewise, lab duplicates also showed little variability ($n = 49, \pm 0.02 \text{ mg N L}^{-1}$). No lab, field, or equipment blanks registered above the method detection limit (MDL).

Samples for $\delta^{15}\text{N}_{\text{NO}_3}$, $\delta^{18}\text{O}_{\text{NO}_3}$, $\delta^2\text{H}_{\text{H}_2\text{O}}$, $\delta^{18}\text{O}_{\text{H}_2\text{O}}$, and $\delta^{13}\text{C}_{\text{DIC}}$ analysis were extracted in the field from the bulk 1 L jars using clean 60 mL syringes and filtered through 0.45 μm syringe filters (Whatman 6780-2504) into sterile 40 mL borosilicate vials (I-Chem TB36-0040). Each borosilicate vial came with a permeable 1.5 mm septum; however, use of permeable septum can contaminate $\delta^{13}\text{C}_{\text{DIC}}$ values so dissolved inorganic carbon (DIC) vials were amended with an additional thick butyl rubber septum (St-Jean 2003). Samples were stored in a refrigerated environment without the use of preservatives for less than a week before delivery to the University of Arkansas Stable Isotope Lab (UASIL) for analysis. The isotopic ratio (δ) is reported in units of per mille (‰) and represents the relative abundance of heavy to light isotopes in a sample and was calculated as:

$$\delta = \left(\frac{R_{\text{sample}} - R_{\text{standard}}}{R_{\text{standard}}} \right) \times 1000, \quad (1)$$

where R is the ratio of the abundance of the heavy to light isotopes, *sample* is the field sample, and *standard* is the reference standard of known isotope ratio. The references used for the analysis of N, O and H, and C isotopes are related to AIR, Vienna Standard Ocean Water (VSMOW), and Vienna Pee Dee Belemnite (VPDB), respectively. Isotope data for NO_3^- was produced using the bacterial denitrifier method with a Thermo Scientific GasBench II (Sigman et al. 2001; Casciotti et al. 2002). Isotope data for H_2O was produced using high temperature pyrolysis with a Thermo Scientific TCEA with modified reverse-flow set up (Gehre et al. 2004). Isotope data for DIC was produced by converting DIC to CO_2 through the use of phosphoric acid with a Thermo Scientific GasBench II (Knierim et al. 2013). The isotopic reference materials for NO_3^- were USGS32 ($\delta^{15}\text{N}_{\text{NO}_3} = +180\text{‰}$), USGS34 ($\delta^{15}\text{N}_{\text{NO}_3} = -1.8\text{‰}$, $\delta^{18}\text{O}_{\text{NO}_3} = -27.9\text{‰}$), and USGS35 ($\delta^{18}\text{O}_{\text{NO}_3} = +57.5\text{‰}$). Average standard deviations for the NO_3^- isotopic standards were 2.03‰ for USGS32 for $\delta^{15}\text{N}$; 0.34 and 0.70‰ for USGS34 for $\delta^{15}\text{N}$ and $\delta^{18}\text{O}$, respectively; and 1.00‰ for USGS35 for $\delta^{18}\text{O}$. Duplicates of $\delta^{15}\text{N}_{\text{NO}_3}$ and $\delta^{18}\text{O}_{\text{NO}_3}$ ($n = 5$) had standard deviations of $\pm 0.28\text{‰}$ and $\pm 0.45\text{‰}$, respectively. The isotopic reference material for DIC was NBS 19 ($\delta^{13}\text{C} = +1.95\text{‰}$) and two

house standards (UASIL 22, UASIL23) and average standard deviation for the standards was $\pm 0.09\%$. Duplicates of $\delta^{13}\text{C}_{\text{DIC}}$ ($n = 5$) had a standard deviation of $\pm 0.37\%$. Water hydrogen and oxygen stable isotope samples were normalized to VSMOW using three isotopically distinct standards (USGS47, UASIL_L, and UASIL_R) with a precision of $\pm 1.0\%$ and $\pm 0.2\%$, for H and O, respectively. All detection was accomplished through interfacing with a Thermo Scientific Delta Plus or Delta V Advantage IRMS.

4.5.3 Hydrograph and loadograph separation analyses

The receding limb of the spring hydrograph can be conceptualized as the draining of multiple reservoirs with varying porosities, hydraulic conductivities, and storage volumes. The exponential form of recession is the most common method used in the analysis of karst springs (Fiorillo 2014). We construct a composite exponential recession to represent the drainage of multiple reservoirs. Each linear segment of the log plot of spring discharge represents a different reservoir and each segment was identified graphically using the constant slope method (Fiorillo 2014). In this study, three segments were identified in the spring recession and characterized quickflow, intermediate (epikarst and soil), and slow flow (phreatic) water. The quickflow and intermediate flows were separated by the first inflection point in the recession while the intermediate and slow flows were separated by the second inflection point in the recession.

A loadograph recession analysis was coupled to the hydrograph recession analysis and NO_3^- loads were quantified for each pathway (Fenton et al. 2017). Nitrate load is a product of spring discharge and spring NO_3^- concentration. While discharge data was available continuously (every 15 minutes), NO_3^- data was discretely collected. To develop a continuous loadograph, NO_3^- concentration at the spring was continuously estimated by interpolating between collected samples. The sample collection design for this study justified interpolation as the highest frequency data collection occurred during periods of greatest change at the spring. Thus, the total NO_3^- yield was estimated by integrating under the loadograph over the course of the event. The inflection points identified in the hydrograph analysis were superimposed onto the NO_3^- loadograph (Fenton et al. 2017). Each pathway comprises an area under the loadograph and, by integrating that area, a total

contribution of that pathway to NO_3^- at the spring can be estimated (Mellander et al. 2012). The pathways and methodology used in this study were similar to other karst studies such as Fenton *et al.* (2017) who used continuous sensor N data to estimate conduit, large fissure, medium fissure, and small fissure pathways.

4.5.4 Nutrient lag effect in rivers

Streams act as net-integrators of upstream sources, processes, and their pathways impact the timing and magnitude of solute transport (Koenig et al. 2017). We assessed the nutrient lag effect at Royal Spring by investigating the temporal changes to collected water quality and environmental tracer data. Further, we compared these temporal trends with respect to the discharge by each pathway as determined by composite hydrograph separation. The timing of NO_3^- peak was compared to the timing of maximum flow contribution from quickflow, intermediate flow, and slow flow to identify lags. The extent to which water quality or environmental tracer data lags was used to infer dominant storage and transfer processes impacting contaminant concentrations at karst springs.

4.6 RESULTS AND DISCUSSION

4.6.1 Characterizing extreme events and their hydrographs

The 2017 calendar year was wet (1,249 mm) compared to the historical average annual precipitation of 1,170 (± 200) mm (Figure 4.4). It was also a year characterized by the landfall of many extreme events and the migration of these events far inland from original coastal landfall. The four largest events (in order of occurrence), were an atmospheric river in February which was sampled, Tropical Storm Cindy in June which was not sampled here, a thunderstorm in July not sampled here, and Hurricane Nate in October which was sampled. The four storms together delivered 25% of the annual rainfall.

The atmospheric river occurring in February 2017 provided 54.9 mm of rainfall over the course of three days (Figure 4.5). Rainfall on the first day of the event caused a steep increase in spring discharge (to $2 \text{ m}^3 \text{ s}^{-1}$) followed by a second day of rain and another

increase in discharge (to $4 \text{ m}^3 \text{ s}^{-1}$). Though the event occurred in the late winter/early spring, the initial discharge at Royal Spring was relatively low for this season which highlights the flushing of new water through the system. Discharge in the surface stream initially rose to $4 \text{ m}^3 \text{ s}^{-1}$ on the first day of rainfall and nearly returned to baseflow conditions within a day. The second day of rainfall caused a peak in stream discharge of $6 \text{ m}^3 \text{ s}^{-1}$.

The tropical cyclone (Hurricane Nate) in October 2017 was the largest event of the calendar year with the bulk of precipitation falling in a single day (Figure 4.5). Pre-event conditions were extremely dry with a low flow period of 70 days, many of which had no flow at all, preceding the event. The fall season typically receives the least amount of rainfall of all seasons in Kentucky (NOAA, 2017b) so many extreme events of this type are expected to make landfall on dry soil and aquifer conditions. It is because of these dry conditions that the 103.4 mm of rainfall during the largest event did not increase the spring discharge ($2 \text{ m}^3 \text{ s}^{-1}$) more than the 54.9 mm as seen with the fourth largest event, the atmospheric river ($4 \text{ m}^3 \text{ s}^{-1}$). Additionally, flow in the surface stream during Hurricane Nate approached $12 \text{ m}^3 \text{ s}^{-1}$ (nearly double the max stream discharge for the atmospheric river), but much of this flow simply overtopped in-stream swallets and exited the system via the surface stream rather than subsurface spring.

We find few, if any, studies that directly link hydrologic responses in karst systems to multiple types of extreme events including atmospheric rivers and tropical cyclones. Therefore, we did not have past literature studies for direct comparison to our results. However, our results of tropical extremes impacting inland karst tend to be corroborated by recent study of karst watersheds with highly-connect surface and subsurface flow paths (Martin and Dean 2001; Geyer et al. 2007; Herman et al. 2008; Hartmann et al. 2014). Similarly to the work of others, our results showed that the distribution of rainfall was important to the structure of spring hydrograph (Fiorillo 2014). We observed a larger loss of water to the surface creek as runoff with increased rainfall intensity. This loss could likely be associated with an exceedance of the hydrologic carrying capacity of recharging quickflow features (e.g., sinkholes and swallets). This idea is corroborated by a study in Pennsylvania USA that noted a non-linear relationship between rainfall and spring discharge at during extreme precipitation activity (Herman et al. 2008). Thus, it appears

that karst springs may be limited to the immediate hydrologic impact of extreme events as more water is lost to the surface drainage as rainfall intensity increases. The implication of this result is that flow and contaminants in surface streams of karst systems should be closely monitored during extreme events even in systems where the subsurface discharges the vast majority of flow from the watershed (e.g., over three-quarters in this study watershed; Husic et al. 2017a). Also, the extent of this loss can vary based on pre-event hydrologic conditions and thus extreme events that occur during different seasons (i.e., atmospheric rivers and tropical cyclones) are expected to produce differing responses. Since contaminant transport is heavily influenced by hydrology (Padilla and Vesper 2018), we may expect to see rainfall intensity also impact the loading and timing of NO_3^- delivery to the spring.

4.6.2 Water quality and environmental tracer analyses

Specific conductance varies greatly over the course of the atmospheric river and tropical cyclone events and is impacted by surface stream peaks (Figure 4.5). During the tropical cyclone, specific conductance varied more than it did for the atmospheric river because of 1) the highly conductive antecedent water in the aquifer from an extended dry period and 2) the overloading of the system with an annual-maxima of poorly-conductive rainfall. The conductivities of all three pathways had a similar evolution temporally as the storm progressed. Temperature did not vary significantly during the atmospheric river event even with the influx of stream water as the air temperature during this time was similar to the aquifer water temperature ($\sim 13^\circ\text{C}$). On the other hand, the temperature shift between surface and subsurface pathways was more noticeable in the fall during Hurricane Nate. The significantly warmer surface water abstracted by swallets markedly increased the temperature of subsurface conduit water. During longitudinal transport in the conduit, convective heat losses at the conduit walls cool the water close to that of the background aquifer temperature. During both events, temperature minima and maxima tend to occur early on in the recession rather than at the peak of the event indicating a unique temperature value within the epikarst and soil.

High specific conductance reflects water-rock exchange of solutes and increases with longer water residence time (Winston and Criss 2004). For example, prior to the atmospheric river event, the specific conductance in the creek is also high and is attributed to a several week period without streamflow, which allows adequate time for the limestone bedrock of the stream to exchange solutes with the standing pool of water. In a study comparing conservative and non-conservative tracers in a karst conduit, Luhmann *et al.* (2012) found that the temperature lag is more apparent than the specific conductance lag effect showing agreement with our results. This is associated with thermal losses to the surrounding rock which produced a temperature pulse less than that of the actual groundwater velocity (Molson *et al.* 2007).

The concentration of NO_3^- is consistently higher in the subsurface than it is in the surface creek for both events (Figure 4.6). For the atmospheric river event, surface creek NO_3^- concentration is initially $\sim 1 \text{ mg N L}^{-1}$ and increases thereafter as runoff and lateral soil flow, more concentrated in NO_3^- , contribute to streamflow. An initial decrease in NO_3^- concentration is realized at the conduit and spring sites reflecting the mixing of pre-event water with less-concentrated surface water. Nitrate concentration at all three locations peaks a few days after the event and begins to decline thereafter. The temporal evolution of $\delta^{15}\text{N}_{\text{NO}_3}$ and $\delta^{18}\text{O}_{\text{NO}_3}$ over the course of both events is similar at the conduit and spring sites. During initial event activity, $\delta^{15}\text{N}_{\text{NO}_3}$ and $\delta^{18}\text{O}_{\text{NO}_3}$ values of spring and conduit samples are decreased by surface stream NO_3^- contributions. Thereafter, $\delta^{15}\text{N}_{\text{NO}_3}$ and $\delta^{18}\text{O}_{\text{NO}_3}$ tends to increase during the hydrograph recession of both events.

The discrepancy in NO_3^- concentration between surface and subsurface flow paths may be associated with the leaching of NO_3^- from soil and epikarst pathways. Initially, the NO_3^- concentration is diluted by quickflow and, as the system transitions from quickflow to diffuse flow, the concentration reaches a peak during the time that epikarst and soil pathways supply most of the spring water. Others have also indicated that geochemical time responses in karst tend to be delayed relative to discharge response (e.g., Winston and Criss, 2004). Whereas some researchers have indicated that initial spikes in karst spring NO_3^- concentration can be associated with mobilization of NO_3^- accumulated within the watershed (e.g., Toran and White, 2005; Huebsch *al.*, 2014), our comprehensive data set suggests otherwise. at least in the case of fluviokarst systems. Where there is pronounced

quickflow contribution (i.e. high connectivity between surface and subsurface pathways), an initial dilution (rather than mobilization) is likely to occur as intense rainfall is first routed to large fissures and shafts rather than through soil pores. Thereafter, as connectivity is re-established via wetting of the epikarst, NO_3^- that has accumulated in the soil and vadose zone is introduced to the active subsurface pathways leading to an increase in NO_3^- concentration. Others have noted that when soil moisture is low and soils are well-aerated, nitrification can generate large pools of NO_3^- , which may potentially be flushed during storm events (Christopher et al. 2008; Buda and DeWalle 2009). The connectivity of the epikarst to the larger soil basin may have an analogous effect on NO_3^- delivery within the context of karst: NO_3^- stored within the soil may be higher due to production by nitrification and concentration by evaporation whereas NO_3^- in the water-logged epikarst aquifer may have experienced a degree of denitrification. While the rising limb and peak hydrograph periods are associated with the highest NO_3^- concentrations in some surface streams (Inamdar et al. 2004; Rusjan et al. 2008), the results of this study in a mature fluviokarst system indicate that the highest NO_3^- concentrations in springs may appear days after the storm peak.

Observed $\delta^{15}\text{N}_{\text{NO}_3}$ values at the spring during both events fall within the range of NO_3^- derived from soil mineralization (0 to +9‰), ammonium (NH_4^+) in fertilizer and precipitation (-10 to +5‰), and manure and septic waste (0 to +25‰) (Kendall et al. 2007). The initial decrease in $\delta^{15}\text{N}_{\text{NO}_3}$ and $\delta^{18}\text{O}_{\text{NO}_3}$ at the spring during the rising limb of both events is likely associated with inflowing NO_3^- from NH_4^+ fertilizer, soil, and precipitation sources. The $\delta^{15}\text{N}_{\text{NO}_3}$ and $\delta^{18}\text{O}_{\text{NO}_3}$ values tend to reach stability (4 and 0‰, respectively) a few days after the peak of both events indicating that the source of NO_3^- during spring recession was likely derived from soil mineralization. The observed NO_3^- , $\delta^{15}\text{N}_{\text{NO}_3}$, and $\delta^{18}\text{O}_{\text{NO}_3}$ responses at Royal Spring are indicative of influence from quickflow, epikarst, and phreatic flow paths. The initial decreases in NO_3^- are likely due to dilute quickflow recharge, whereas subsequent increases are associated with epikarst drainage, a peak in NO_3^- is associated with maximum soil-zone flushing, and an ultimate return to baseflow conditions is brought upon by phreatic water.

The $\delta^2\text{H}_{\text{H}_2\text{O}}$ and $\delta^{18}\text{O}_{\text{H}_2\text{O}}$ signatures of the three sampling sites are similar across the entirety of the atmospheric river event with a small peak during maximum discharge

suggesting only slight differences in the origin of water flushing through the system (Figure 4.7). The variability observed in $\delta^{13}\text{C}_{\text{DIC}}$ also indicates a quick response to the relatively depleted $\delta^{13}\text{C}_{\text{DIC}}$ during peak storm conditions and a return to isotopically heavier $\delta^{13}\text{C}_{\text{DIC}}$ during baseflow recession. The $\delta^2\text{H}_{\text{H}_2\text{O}}$, $\delta^{18}\text{O}_{\text{H}_2\text{O}}$, and $\delta^{13}\text{C}_{\text{DIC}}$ signatures of samples collected during the fall event show a stronger flushing of water and DIC through the watershed unique from the observations for the atmospheric river (Figure 4.7). The variability in $\delta^2\text{H}_{\text{H}_2\text{O}}$ and $\delta^{18}\text{O}_{\text{H}_2\text{O}}$ values of water moving through the system was much greater during the tropical cyclone (Figure 4.8a). During the rising limb of the event, signatures at all three locations show a distinct shift towards lighter isotopes of water during peak activity (Figure 4.8b and 4.8c). Subsequent baseflow returns $\delta^2\text{H}_{\text{H}_2\text{O}}$ and $\delta^{18}\text{O}_{\text{H}_2\text{O}}$ values back to their pre-storm conditions (Figure 4.8c).

The observed changes in $\delta^2\text{H}_{\text{H}_2\text{O}}$ and $\delta^{18}\text{O}_{\text{H}_2\text{O}}$ values are consistent with our knowledge of meteorology and karst hydrology. The trend of $\delta^2\text{H}_{\text{H}_2\text{O}}$ and $\delta^{18}\text{O}_{\text{H}_2\text{O}}$ values towards lighter isotopes during extreme events is a process well-documented and termed the “amount effect” or the greater depletion of heavier water molecules in rainfall of regions with high precipitation rates (Lawrence and Gedzelman 1996). Tropical cyclones are efficient precipitation systems which cause precipitation of rainfall with $\delta^{18}\text{O}_{\text{H}_2\text{O}}$ similar to that of sea water vapor (-12.3‰) (Lawrence and Gedzelman 1996). Indeed, $\delta^{18}\text{O}_{\text{H}_2\text{O}}$ during peak flows in Hurricane Nate approached values of -11.0‰, a dramatic shift from the typical value of -5.0‰ (Figure 4.8c). The inland Hurricane Nate (demoted to a tropical storm before reaching central Kentucky) delivered water highly depleted relative to typical rainfall in the region indicating the ability of coastally-derived inland storms to alter local hydrology. Additionally, the observed changes in $\delta^{13}\text{C}_{\text{DIC}}$ signature is consistent with the changing of source waters in a karst watershed (Lee and Krothe 2001). Although no DIC concentration data was collected during this study, the DIC isotope composition can be used as a qualitative indicator of changes to discharging water. $\delta^{13}\text{C}_{\text{DIC}}$ values of DIC generated by biological processes in the soil and epikarst zones tend to be lighter than those of the deeper groundwater caused by dissolution of an inorganic source of carbon (i.e. bedrock) to phreatic waters (Knierim et al. 2013). Thus, it can be inferred that the transition from lighter to heavier $\delta^{13}\text{C}_{\text{DIC}}$ over the hydrograph recession (Figure 4.7) may be indicative of a change from intermediate (soil and epikarst) to slow flow (phreatic) zones.

Our comprehensive water quality and environmental tracer dataset was vital to understanding the physical and biogeochemical processes occurring during two structurally different extreme events. Though environmental isotope tracers have received widespread use in karst (e.g., Lee and Krothe, 2001; Buda and DeWalle, 2009; Albertin et al. 2012; Yue et al. 2018), we provide a dataset with unique components including: high frequency (up to hourly) isotope tracer collection during atmospheric river and tropical cyclone events, longitudinal water quality and isotope tracer data within a karst conduit (i.e., from Phreatic Conduit to Royal Spring), and surface and subsurface event data from a suite of isotopes ($\delta^{15}N_{NO_3}$, $\delta^{18}O_{NO_3}$, $\delta^{13}C_{DIC}$, $\delta^2H_{H_2O}$, and $\delta^{18}O_{H_2O}$). A limitation of this dataset is the number of extreme events included. While our dataset is composed of only two events, the collection of such data is difficult due to the unpredictability of the timing of hydrologic activity, the uncertainty associated with the amount of rainfall and if enough will be generated to be considered ‘extreme’, and the incidence of specific kinds of extreme events that may have recurrence intervals of a year or longer. To the second point, we collected data for four total events, but by the conclusion of the calendar year, some events collected earlier in the year fell out of the 95th percentile (i.e., the threshold definition for ‘extreme’ used in this study). Thus, the dataset is a great contribution as it includes 2 of the 4 largest events (possessing structurally different origins) in the study year and these events occurred during significantly different parts of the year eliciting a varied hydrologic response.

4.6.3 Hydrograph and loadograph separation analyses

Hydrograph recession analysis indicates the presence of two inflection points on the falling limb that segment contributions of quickflow, epikarst, and phreatic pathways (Figure 4.9). The atmospheric river event is characterized by a steeper initial quickflow component and then gradual decreases in slope for epikarst and phreatic components (Figure 4.9a). The quickflow-epikarst inflection point occurs 0.5 days after the peak of the event. The inflection point for epikarst-phreatic flows occurs 5.8 days after the peak of the event. The tropical cyclone event has a more gradual quickflow recession component, followed by a milder epikarst component, and a slightly steeper phreatic component

(Figure 4.9b). The quickflow-epikarst and epikarst-phreatic inflection points occur 2.5 and 6.3 days, respectively, after the peak of the event.

The atmospheric river event storm hydrograph is characterized by a more typical shape with a steep initial recession followed by gradually milder recessions. The fall tropical cyclone event has a less typical hydrograph recession resulting from the large volume of rainfall and infiltration that occurred in a short period of time on dry soils. This type of behavior has been observed during extreme events in other karst studies where hydrographs may potentially diverge from their typical recession behavior with multiple recessions that may alternate in convexity (Herman et al. 2008). This deviation from typical hydrograph behavior is associated with non-linearity induced by drainage from other reservoirs (Herman et al. 2008). The mild slope of the hydrograph recession between the two inflection points likely corresponds to a perched-reservoir condition influenced by the recently wetted epikarst and soil. The perched aquifer may provide a storage volume of water that is highly influenced by the soil but lacks hydrologic connectivity to the primary springhead during hydrologically inactive periods. As the epikarst and soil are reconnected to the aquifer, they provide the opportunity to deliver waters highly concentrated in NO_3^- .

The loadograph results have a similar shape to the hydrograph results (Figure 4.10). The loadograph quickflow ceases at the first inflection point of the recession and epikarst recharge ends at the second inflection point (identified by dashed lines). The loadograph shows that quickflow pathway contributes NO_3^- loads for a longer duration during the tropical cyclone event (Figure 4.10b) than the atmospheric river event (Figure 4.10a). The average NO_3^- loading from the catchment during the atmospheric river and tropical cyclone events was 3.6 and $1.5 \text{ g N ha}^{-1} \text{ hr}^{-1}$, respectively. Nitrate loads were integrated for the duration of both events using the three pathways identified by recession analysis (Figure 4.10c). For the atmospheric river event, the quickflow pathway contributed 10.1%, the epikarst pathway contributed 36.9%, and the phreatic pathway contributed 53.0% of total event NO_3^- . Results for the fall event were more heavily impacted by the high intensity rainfall with 20.7%, 28.7%, and 50.6% of total event NO_3^- attributed to quickflow, epikarst, and phreatic pathways, respectively. The epikarst pathway delivers the highest NO_3^- concentration for both events while the quickflow pathway dilutes the NO_3^- concentration.

Nitrogen loading from our watershed over the course of two events (1.5 to 3.6 g N ha⁻¹ hr⁻¹) is similar to other well-drained ag-impacted watersheds both with karst features (3.13 to 7.60 g N ha⁻¹ h⁻¹) and without karst features (2.64 to 2.81 g N ha⁻¹ h⁻¹) (Mellander et al. 2012; Fenton et al. 2017). Fenton et al. 2017 separated flow into four components (conduit, large fissure, medium fissure, and small fissure), and they note that the proportion of NO₃⁻ discharge increases with storm intensity showing agreement with our results. However, they suggest that the highest flow-weighted means are in the quickflow transfer pathways whereas our results indicate dilution by quickflow and concentration by intermediate pathways (Figure 4.10c). This discrepancy may potentially be due to the difference in watershed characteristics whereby the Fenton *et al.* (2017) study (a dairy farm in Ireland) is recharged primarily by diffuse flow whereas the Cane Run watershed has considerable recharge by dilute streamflow from a surface creek. This result highlights that aquifer pathway connectivity to the surface can influence NO₃⁻ concentrations at the spring.

Integration of the hydrograph and loadograph for each event revealed surprising similarities. First, the maximum percentage of total storm-water conveyed by the quickflow pathway for the two events was only 21% (Figure 4.10c). This result was unexpected as the Cane Run watershed is highly-karstified, pirates all streamflow from the surface for over 80% of the year, and has a hydrologic response time on the same order of magnitude as the surface stream, all indicating a large quickflow influence (Husic et al. 2017a,b). We anticipated that the contribution by quickflow would be considerably greater as the studied events were two of the four largest events of 2017. Rather, it was the intermediate and slow flow pathways which dominated the water and NO₃⁻ loads with approximately 30% and 50% of water and N discharged by epikarst and phreatic pathways, respectively. A second similarity was the NO₃⁻ behavior of pathways for both events. Irrespective of the differences in NO₃⁻ concentration from the atmospheric river to the tropical cyclone, which ranged from a maximum of 3 to 5 mg N L⁻¹ (Figure 4.6), both events were characterized by dilution via quickflow and concentration via epikarst; quickflow discharges relatively less NO₃⁻ than water and epikarst discharges relatively more NO₃⁻ than water (Figure 4.10c). This result suggests that when adequate hydrologic connectivity is established across the various karst pathways (such as in the case of extreme

events), the net contribution of pathways may act predictably regardless of the level or extent of aquifer contamination.

4.6.4 Nutrient lag effect in karst aquifers

We used the recession analysis to separate the hydrograph into its three flow pathways (i.e., quickflow, epikarst, and phreatic) and plotted the pathways against collected water quality and isotopic measurements (Figure 4.11) to investigate temporal changes in data with regard to pathway contribution. For the atmospheric river event, specific conductance, $\delta^{13}C_{DIC}$, δ^2H_{H2O} , and $\delta^{18}O_{H2O}$ have peaks that occur during the influence of quickflow and before peak epikarst flow. Upon passing of the quickflow component, the observed values for each measurement return to pre-storm conditions. NO_3^- , temperature, $\delta^{15}N_{NO3}$, and $\delta^{18}O_{NO3}$ experience a ‘lag effect’ relative to other measurements. The values of NO_3^- , $\delta^{15}N_{NO3}$, and $\delta^{18}O_{NO3}$ continue to increase after quickflow ceases, and even after peak epikarst flow, indicating that intermediate flows can potentially be subdivided into epikarst and soil pathways. The NO_3^- concentration maxima occurred approximately 1.3 days after the flow hydrograph peak and 0.8 days after the transition from quickflow to epikarst flow. The tropical cyclone event experiences similar behavior whereby specific conductance, $\delta^{13}C_{DIC}$, δ^2H_{H2O} , and $\delta^{18}O_{H2O}$ tend to peak around maximum quickflow discharge (Figure 4.11). On the other hand, NO_3^- continues to increase days after peak epikarst flow. The NO_3^- concentration maxima occurred 3.6 days after the peak of the event and 1.1 days after the quickflow-epikarst flow inflection point. $\delta^{15}N_{NO3}$ and $\delta^{18}O_{NO3}$ at the spring have minima located after the NO_3^- maxima.

In the case of both extremes, hydrograph pathway separation alone cannot predict NO_3^- concentration maxima in water. The points of inflection on the hydrograph which separate sources did not coincide with the NO_3^- concentration maxima. The shift from dilute (quickflow) source to concentrated (epikarst) source occurs a few days prior (t_{lag}) to the maximum NO_3^- concentration (Figure 4.12). Rather, an intermediate flow is conceptualized that experiences a shifting porosity, likely associated with epikarst macropore fissures and soil micropore porosity. The delayed arrival of nitrate-laden water from the soil into the epikarst pathways results in a nutrient lag effect whereby maximum

discharge from the epikarst pathway (the most concentrated pathway) does not equal maximum concentration in that pathway (Figure 4.12). This result suggests that epikarst does not have its own constant concentration but rather a relatively dilute component (fissures) and a relatively concentrated component (soil). As transport of N through a watershed is primarily controlled by hydrology (Bauwe et al. 2015; Sinha and Michalak 2016), the accurate discretization of sources is paramount for mitigation efforts. Our results point to a more discretized conceptual model of pathways may be needed to predict peak N concentration in rivers with karst.

While consideration for the soil-derived peak in NO_3^- concentration is a further improvement in our understanding of N pathways, existing literature of soil processes helps provide support for this concept. Accumulation and leaching of NO_3^- from the soil is recognized as a driving factor in the rising concentrations of NO_3^- in surface and subsurface waters draining agricultural systems (Di and Cameron 2002). While discharge may initially dilute the NO_3^- signal (Miller et al. 2017), it also provides the mechanism to activate pathways and transport concentrated NO_3^- (Baran et al. 2008). Studies in tile-drained agricultural systems, which have been likened to karst (Schilling and Helmers 2008), have noted that initial flow may bypass highly concentrated soil zones and, only after significant wetting, is connectivity established between highly concentrated zones and preferential flow paths (Klaus et al. 2013; Ford et al. 2018). Thus, soil water NO_3^- becomes rapidly transported during and after intense storm conditions (Huebsch et al. 2014). The time lag between peak intermediate flow and peak intermediate concentrations of other geochemical pollutants such as pesticides in a chalk aquifer agrees with our results and is associated with a retarding effect of less mobile water within smaller pores (Baran et al. 2008). In the study by Baran *et al.* (2008), a NO_3^- peak is observed after large events which would indicate mobilization by quickflow, but the sampling frequency used in that study was approximately 10 days (over 17 years) which may overlook initial quickflow dilution and subsequent intermediate flow maxima. Long-term studies are useful to assess changing land practices and climate drivers (Xue et al. 2009), but we recommend high-frequency sampling during storm events to de-couple pathways. Given that a shift from fissure-scale porosity in epikarst to pore-scale porosity in soil can impact peak NO_3^-

concentration in spring water, further investigation of this shift is crucial to meeting water quality needs.

4.7 CONCLUSIONS

The conclusions of the paper are as follows:

- Inland impacts of an atmospheric river and tropical cyclone produced the number one and four ranked rainfall events in 2017 for the basin. Hydrologic pathway responses from the two extremes were different due to rainfall characteristics of the storms. The atmospheric river delivered low intensity rainfall on wet soils while the tropical cyclone brought high intensity rainfall on dry soils.
- Water quality and environmental tracer data showed similar responses regardless of event structure (i.e., atmospheric river or tropical cyclone) and antecedent field conditions. In general, all stable isotope measurements, including $\delta^{15}\text{N}_{\text{NO}_3}$, $\delta^{18}\text{O}_{\text{NO}_3}$, $\delta^2\text{H}_{\text{H}_2\text{O}}$, $\delta^{18}\text{O}_{\text{H}_2\text{O}}$, and $\delta^{13}\text{C}_{\text{DIC}}$, showed decreases in per mil values during quickflow dominance relative to times when the epikarst and phreatic dominate. Local extrema of water and DIC isotope compositions as well as specific conductance coincided with hydrograph peaks for both events. Local extrema of NO_3^- concentration and isotopes of NO_3^- lagged behind hydrograph peaks for both events.
- The two extreme events showed similarities in mobilizing quickflow, intermediate-flow (epikarst and soil), and slowflow pathways of water and NO_3^- in the karst basin. Hydrograph and loadograph separation results show quickflow pathways account for less than 20% of transported water and nitrate during two of the year's most extreme events. The remaining water and NO_3^- are divided between the epikarst (~30%) and phreatic (~50%) pathways.
- In the case of both extremes, hydrograph and loadograph pathway separation cannot predict NO_3^- concentration maxima in water. Rather, the intermediate flow is conceptualized to experience a shifting porosity, likely associated with epikarst macropore fissures to the micropore porosity of the soil. Our results point out that a more discretized conceptual model of pathways may be needed to predict peak nutrient concentration in rivers.

4.8 ACKNOWLEDGEMENTS

The authors would like to acknowledge the researchers and staff at the Kentucky Geological Survey, in particular Chuck Taylor and James Currens, and the University of Arkansas Stable Isotope Laboratory. We also thank the Department of Civil Engineering at the University of Kentucky for partial funding of students involved with this research study. We thank Evan Clare for supplying part of the graphics used in Figure 4.2. Lastly, we gratefully acknowledge financial support of this research under National Science Foundation Award 1632888.

4.9 TABLES AND FIGURES

Figure 4.1 (a) Location, names, and generalized orientation of coastal extreme events on the conterminous United States. The Maya Express is an atmospheric river (orange arrow). Hurricanes and Tropical Storms are tropical cyclones (blue arrows). The white star represents the study region located within Kentucky. (b) Trajectory of the Maya Express (Moore et al. 2012). Surface fronts are shown in their standard frontal notation. The orange line represents a stream of dry midlevel air and the blue line represents the atmospheric river. Red lines and the green light shading around the atmospheric river denote streamlines above the atmospheric boundary layer and areas of high water vapor. (c) Trajectory of an inland tropical cyclone (NHC NOAA, 2017). The light orange shading represents areas of tropical-level winds. Red and blue colors indicate hurricane and tropical storm warnings, respectively. The white cone represents probable path of the storm center.

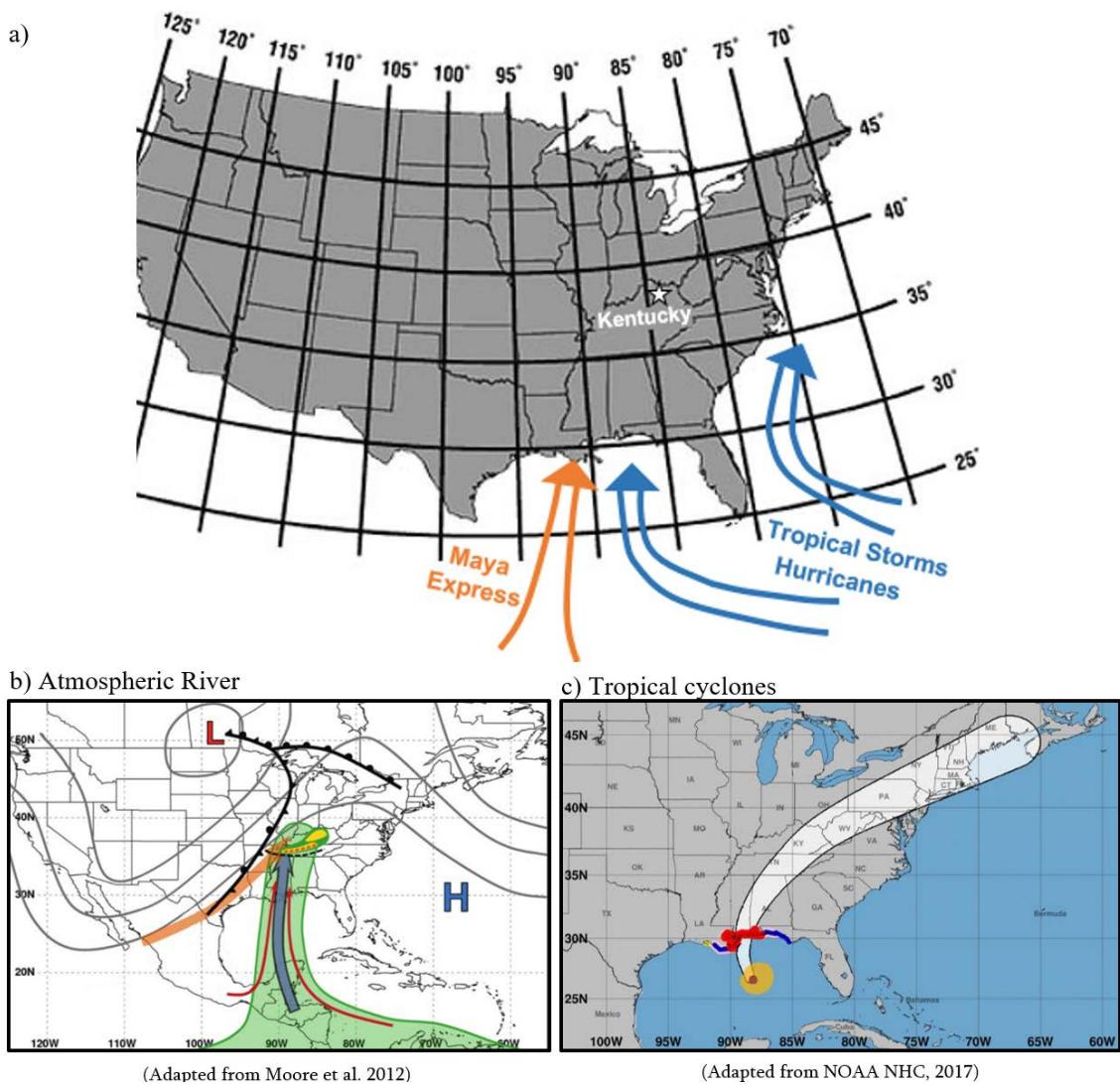
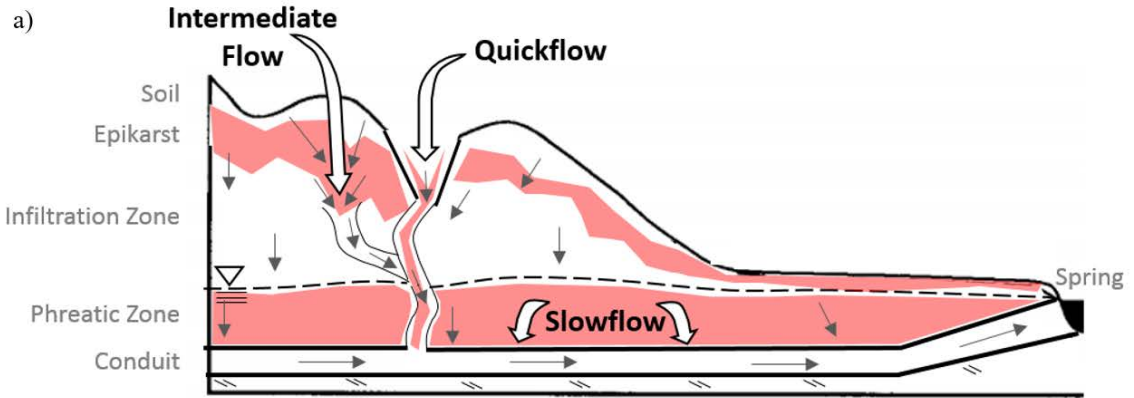


Figure 4.2 (a) Pathway diagram showing quickflow, intermediate flow (epikarst + soil), and slow flow (phreatic). (b) An image of a karst swallet in Cane Run Creek, Kentucky (Husic et al. 2017a). (c) Surficial epikarst features in Bowman’s Bend of the Kentucky River (Phillips, 2015). (d) Nutrient lag effect (Clare et al. 2018).



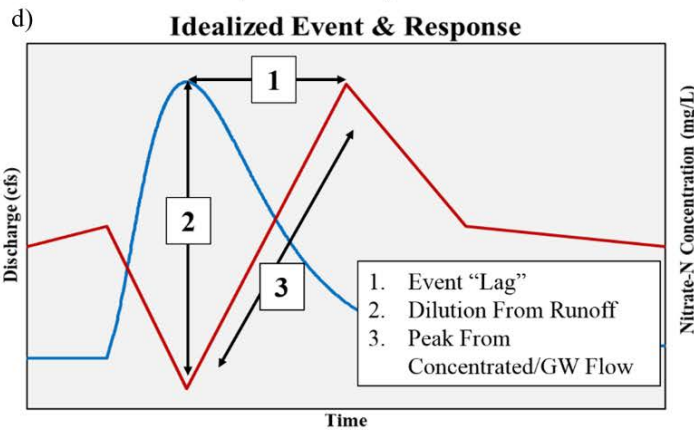
(Adapted from Husic et al., 2018 – Unpublished)



(Husic et al. 2017a)



(Phillips, 2015)



(Clare et al. 2018)

Figure 4.3 Cane Run Watershed and Royal Spring Basin indicating drainage basins, primary conduit conveyance zone for flow and nutrients, the three sampling sites (Royal Spring, Phreatic Conduit, and Cane Run Creek), karst holes, surface channels, and the flow direction for surface and subsurface discharges.

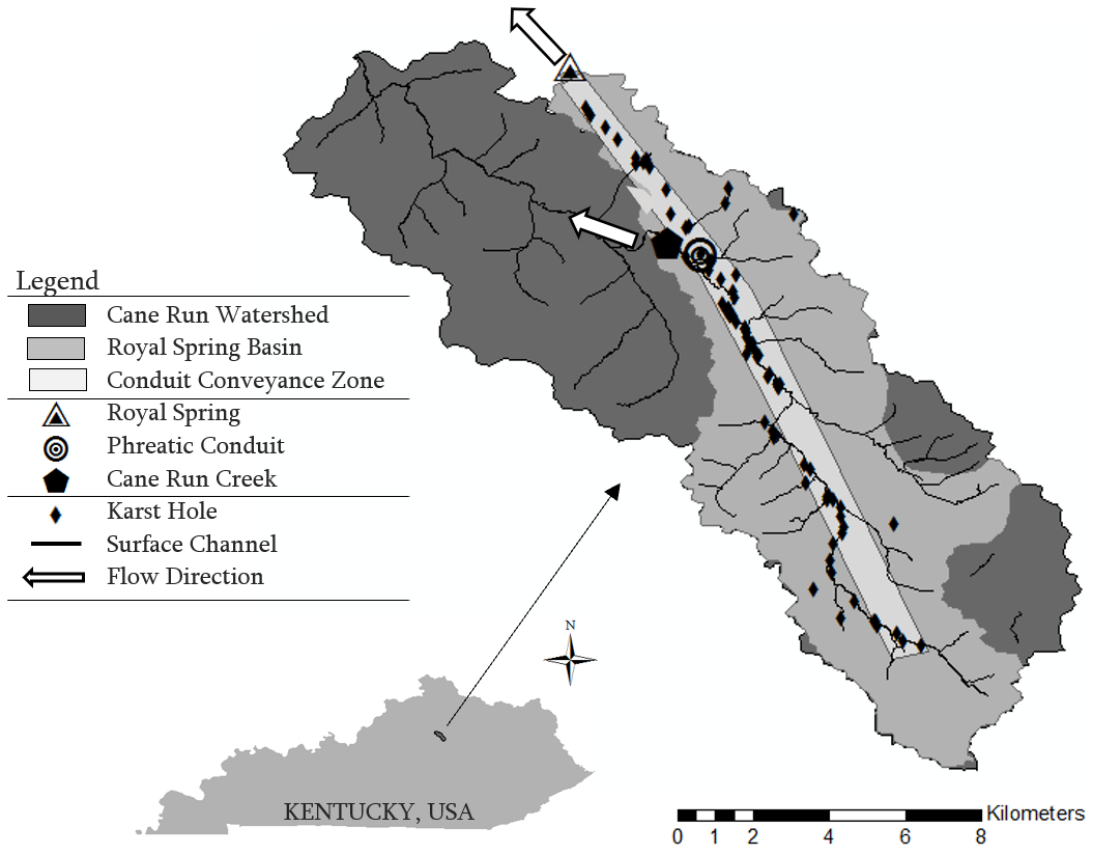
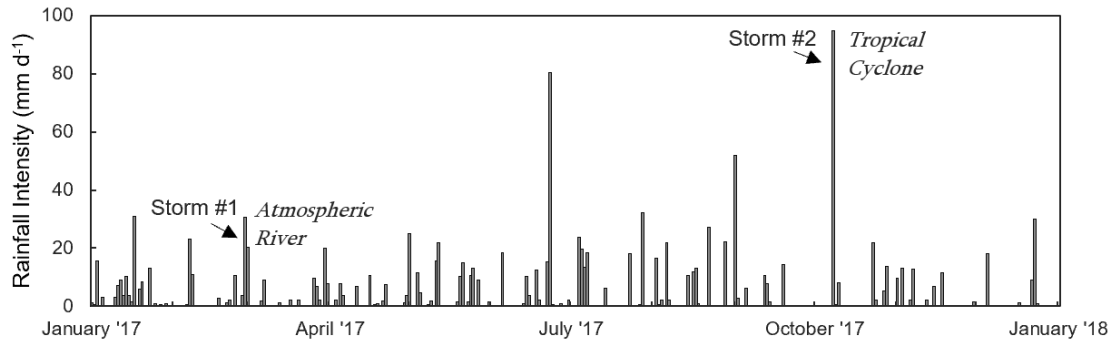


Figure 4.4 Rainfall intensity for the 2017 calendar year and the timing of two sampled extreme events. Total annual rainfall is 1,249 mm. The two storms approximate winter/spring (Storm #1) and fall (Storm #2) hydrologic events. Rank is determined by the three-day precipitation total of an event.



Storm	Date	Season	Description	Rank (in 2017)	Precipitation (mm)
1	Feb 28 '17	Late Winter/Early Spring	Atmospheric River	4	54.9
2	Oct 8, '17	Fall	Tropical Cyclone	1	103.4

Figure 4.5 Precipitation, stream flow, groundwater elevation (above mean sea level), spring discharge, specific conductance, and temperature data results. The dashed horizontal line on the second row represents the elevation. The surface stream discharge peaks quickly to rainfall input relative to spring discharge. The groundwater elevation in the well intersecting the conduit corresponds closely to spring discharge. Specific conductance and temperature of the conduit and spring are largely influenced by the surface creek and are either warmed or cooled depending on season.

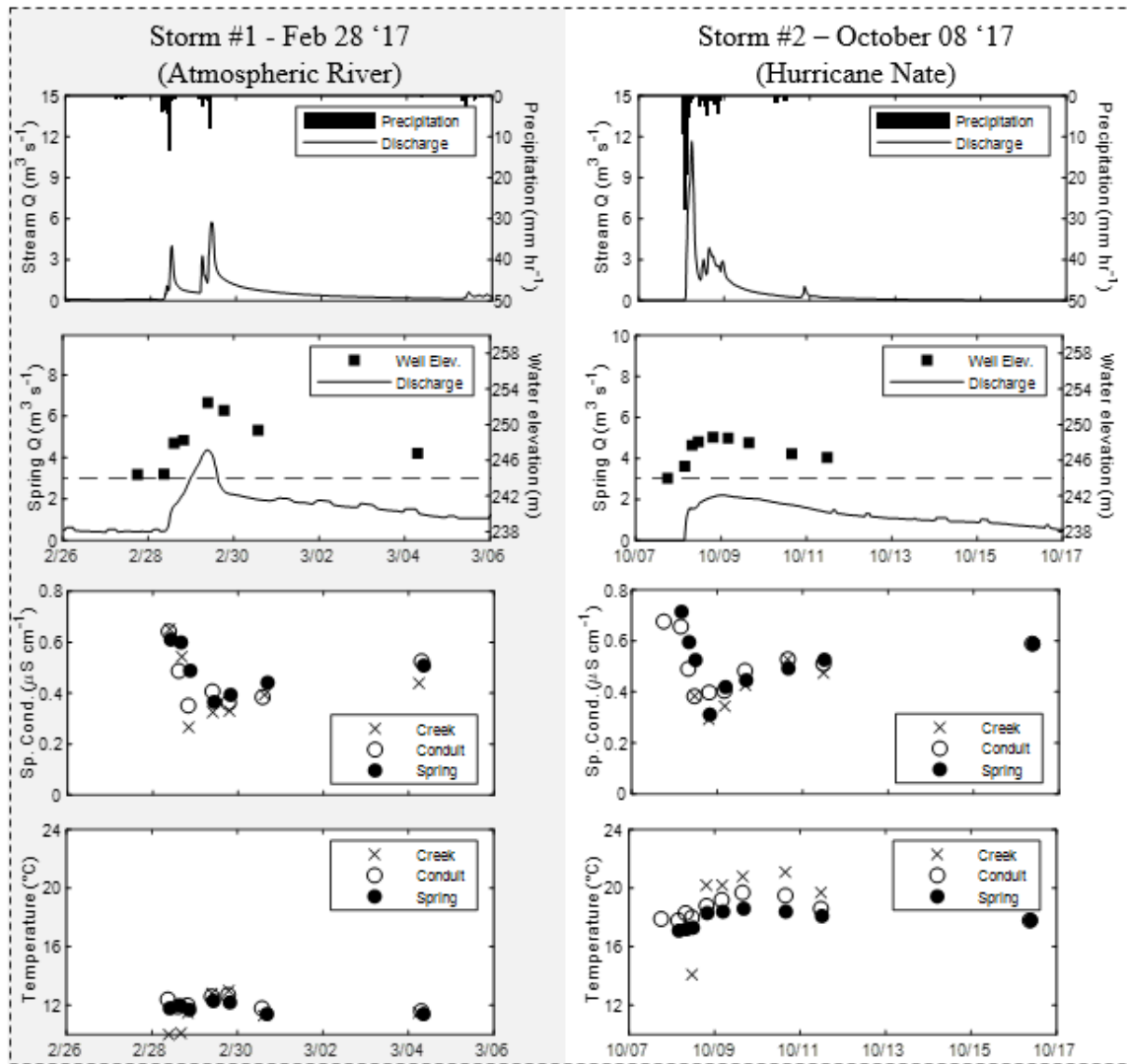


Figure 4.6 NO_3^- , $\delta^{15}\text{N}_{\text{NO}_3}$, and $\delta^{18}\text{O}_{\text{NO}_3}$ signatures of creek, conduit, and spring water during two extreme events. NO_3^- is initially diluted by surface quickflow during both events. The temporal changes in $\delta^{15}\text{N}_{\text{NO}_3}$ and $\delta^{18}\text{O}_{\text{NO}_3}$ in the conduit and at the spring are similar for both storms.

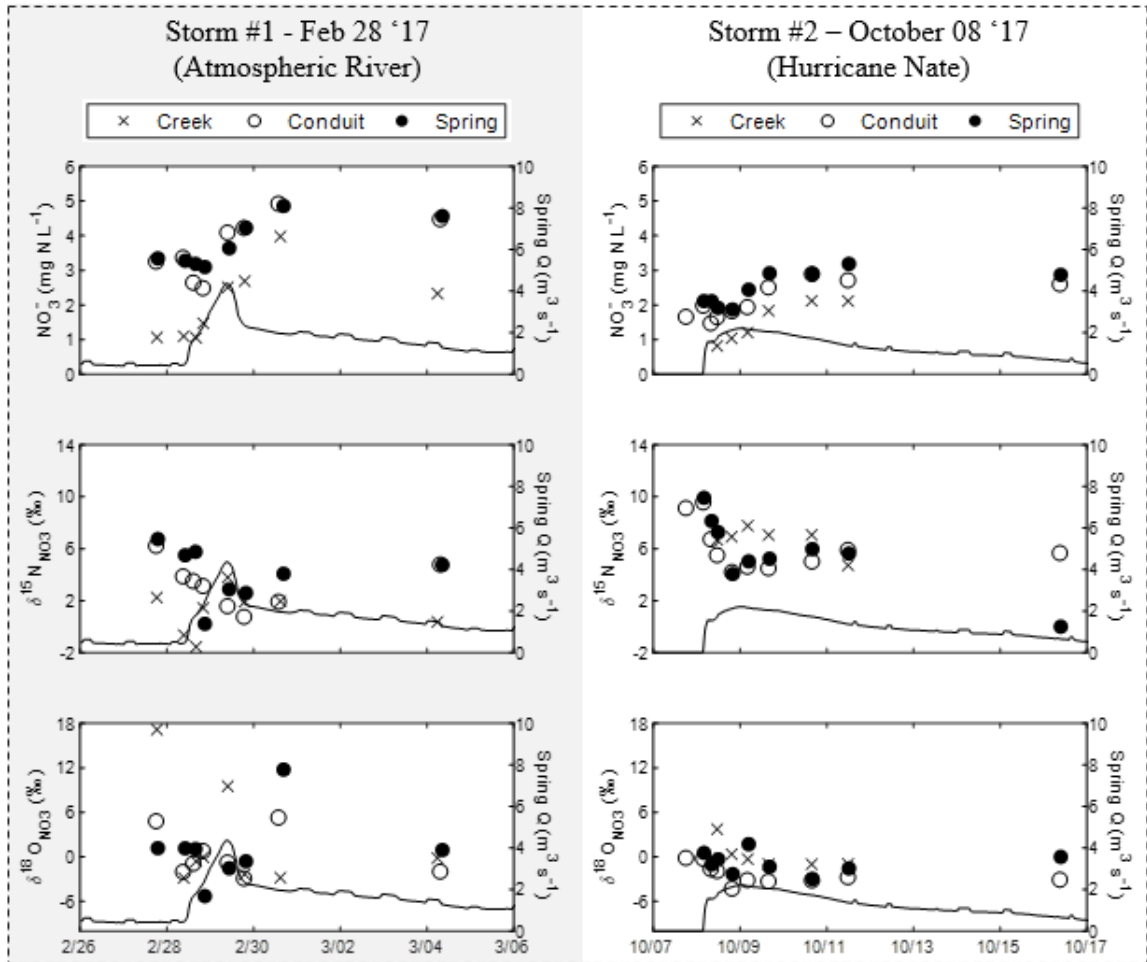


Figure 4.7 $\delta^2\text{H}_{\text{H}_2\text{O}}$, $\delta^{18}\text{O}_{\text{H}_2\text{O}}$, and $\delta^{13}\text{C}_{\text{DIC}}$ signatures of creek, conduit, and spring water during two extreme events. Variability is limited in the $\delta^2\text{H}_{\text{H}_2\text{O}}$ and $\delta^{18}\text{O}_{\text{H}_2\text{O}}$ signatures during Storms 1 and 2, but the fall event caused by Hurricane Nate delivered highly depleted rain water (close to that of sea surface water vapor $\delta^{18}\text{O}_{\text{H}_2\text{O}} \sim -12\text{‰}$). Likewise, $\delta^{13}\text{C}_{\text{DIC}}$ data indicate delivery of highly depleted DIC during Storm 2.

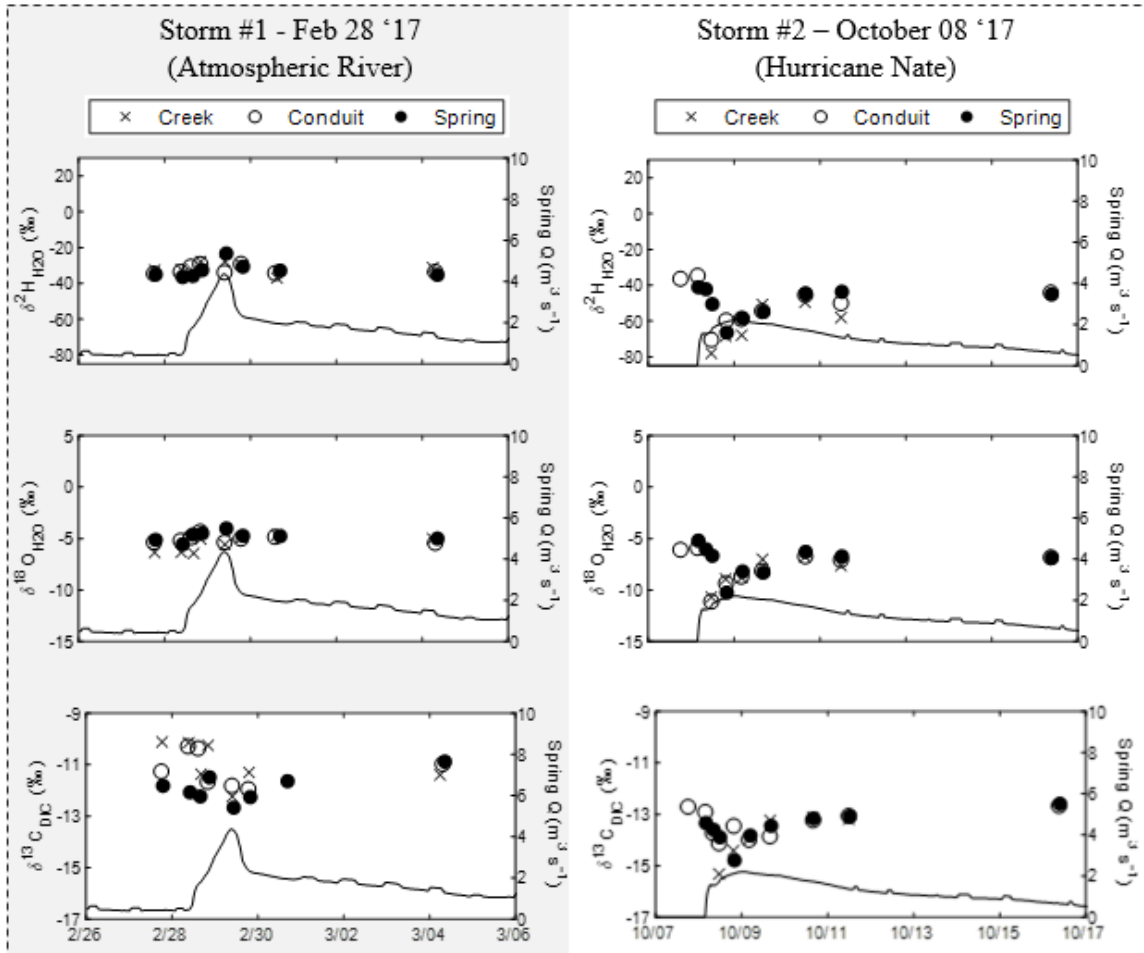


Figure 4.8 (a) $\delta^2\text{H}_{\text{H}_2\text{O}}$ and $\delta^{18}\text{O}_{\text{H}_2\text{O}}$ of all samples collected for the two storm events. (b) Sample sets collected from creek, conduit, and spring in relation to spring hydrograph. (c) Zoom-in on Storm #3 (Hurricane Nate). $\delta^2\text{H}_{\text{H}_2\text{O}}$ and $\delta^{18}\text{O}_{\text{H}_2\text{O}}$ signatures show an appreciable effect of coastal water delivery to inland Kentucky *via* the shift towards lighter isotopes of water during peak event activity. Numbers inset in gray circles in (c) indicate the approximate $\delta^2\text{H}_{\text{H}_2\text{O}}$ and $\delta^{18}\text{O}_{\text{H}_2\text{O}}$ average of creek, conduit, and spring samples in a set. GMWL = global mean water line.

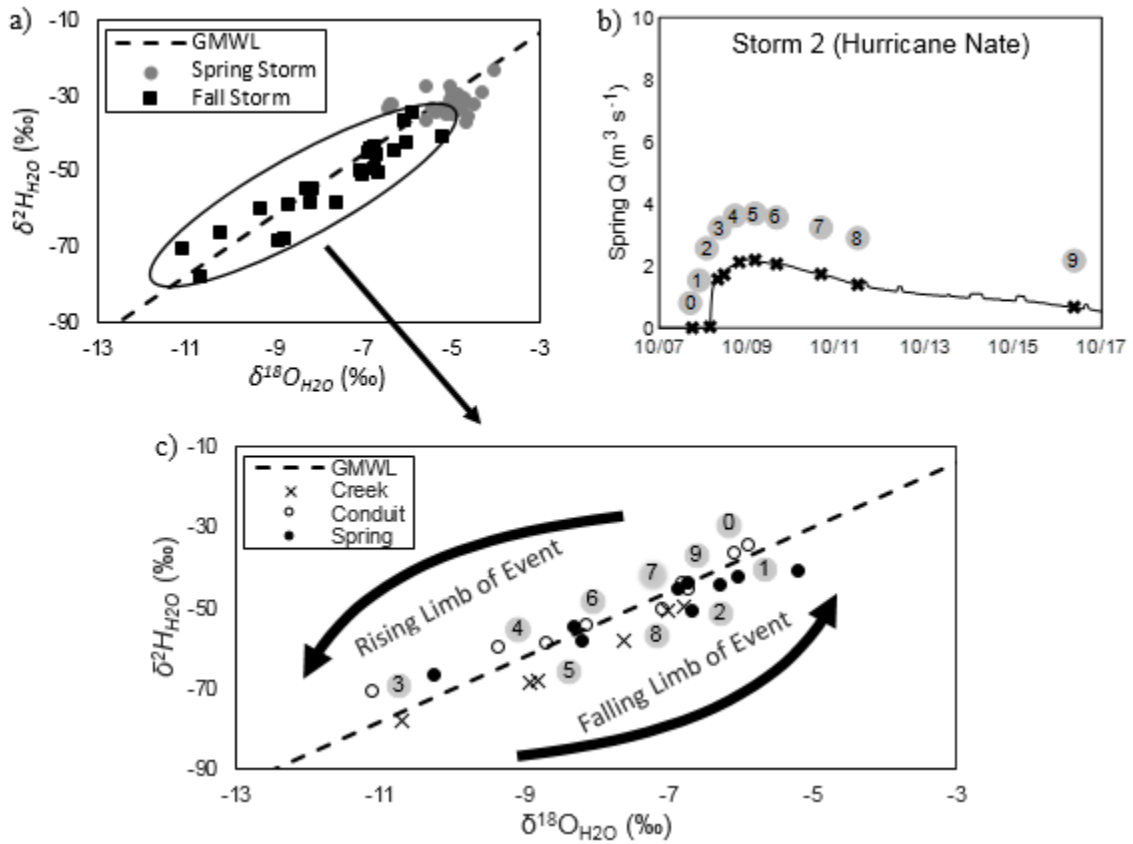
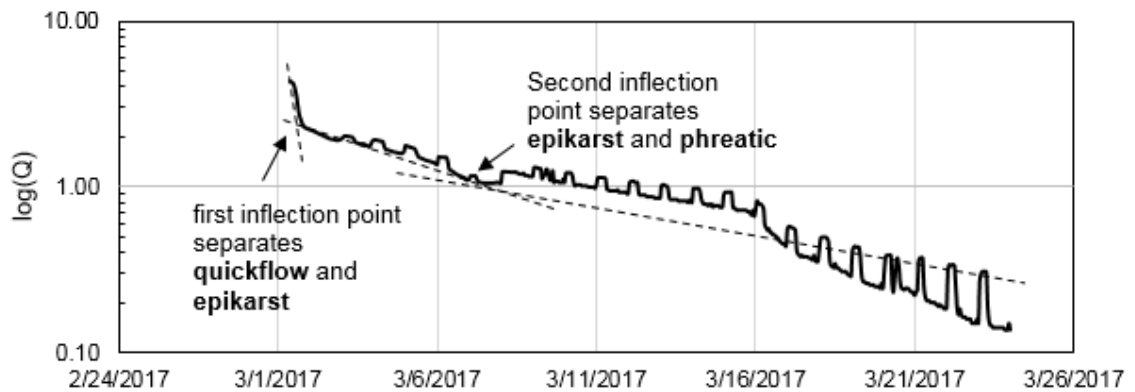


Figure 4.9 Method for hydrograph and loadograph recession analyses and separation of pathways. (a) During the spring event (atmospheric river), quickflow-epikarst and epikarst-phreatic inflection points occur 0.5 and 5.8 days, respectively, after peak of event. (b) During the fall event (tropical cyclone), quickflow-epikarst and epikarst-phreatic inflection points occur 2.5 and 6.3 days, respectively, after peak of event. Note: Abrupt spikes and drops in the recession hydrographs are the result of periodic pumping, by a water treatment plant, directly upstream of the v-notch weir where water depth is gaged. These abstractions were considered when estimating the recession lines.

a) Spring Storm Recession



b) Fall Storm Recession

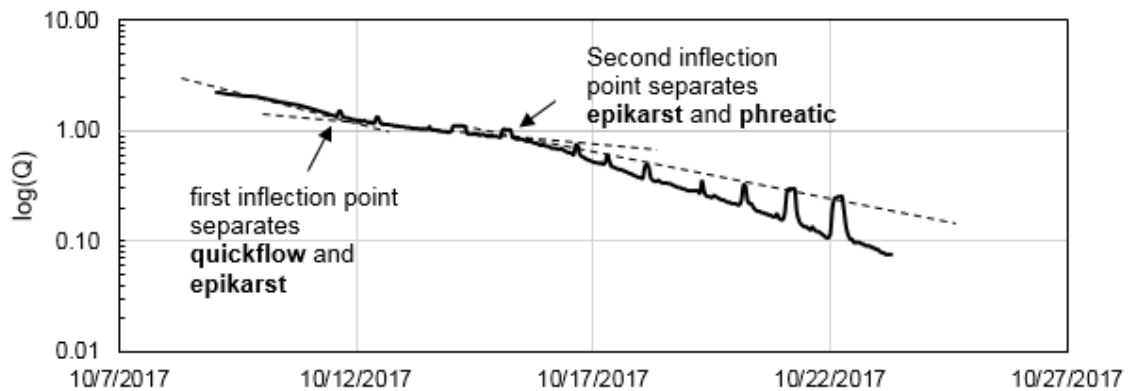


Figure 4.10 (a) Atmospheric river (spring storm) loadograph results separated into three separate pathways (quickflow, epikarst, and phreatic). The dashed lines direct to the inflection points (quickflow-epikarst and epikarst-phreatic) identified by the recession analysis. (b) Same as (a) but for the tropical cyclone event. (c) The fraction of the total event spring discharge and nitrate loading per pathway for the atmospheric river and tropical cyclone events. Note: Abrupt spikes and drops in the loadograph are the result of periodic pumping, by a water treatment plant, directly upstream of the v-notch weir where water depth is gaged.

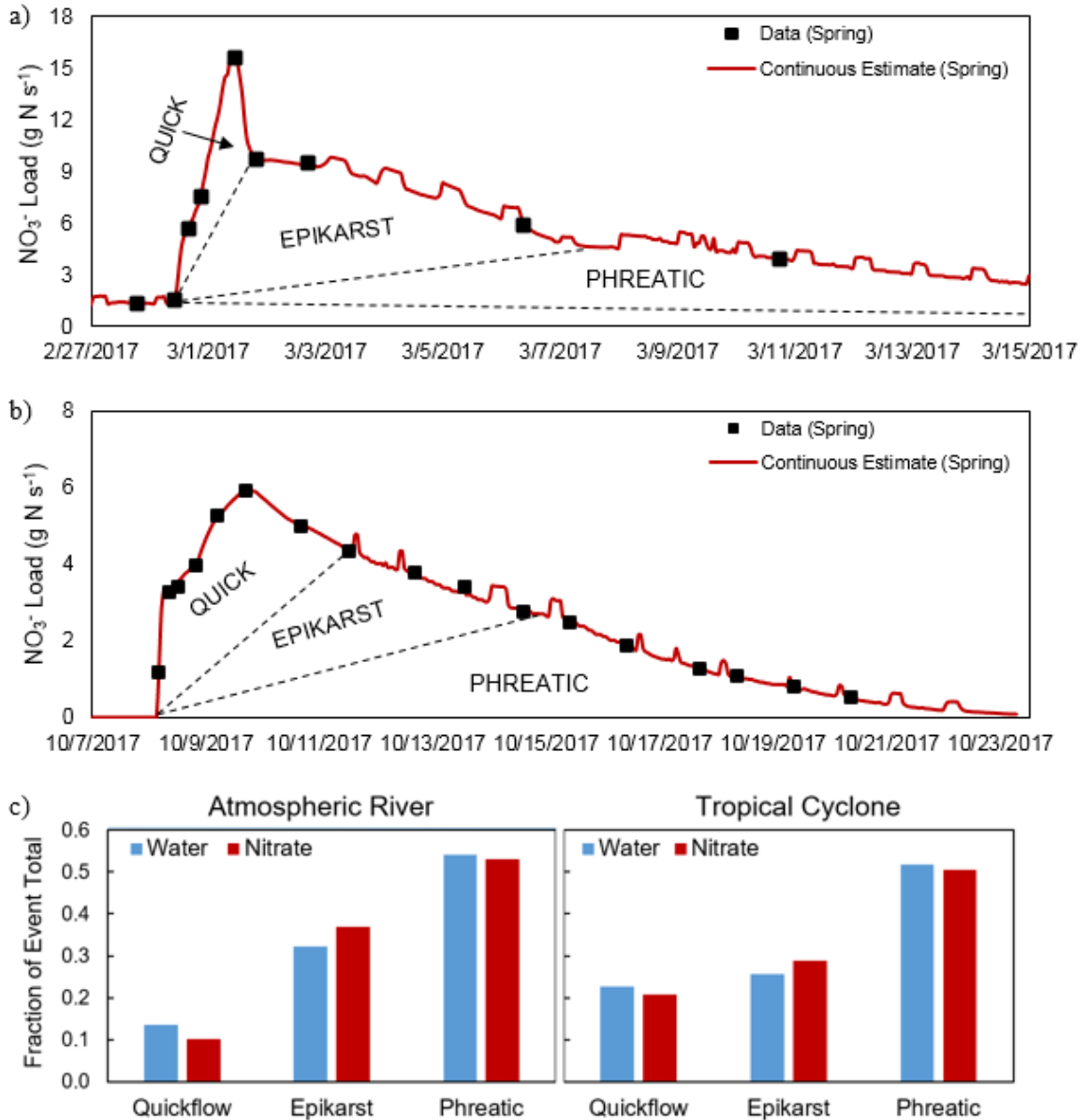


Figure 4.11 Temporal changes in water quality and isotopes plotted alongside the flow contribution of different pathways during the two extreme events. The left axis corresponds with samples collected at spring, conduit, and creek sites. The right axis is the discharge by each pathway.

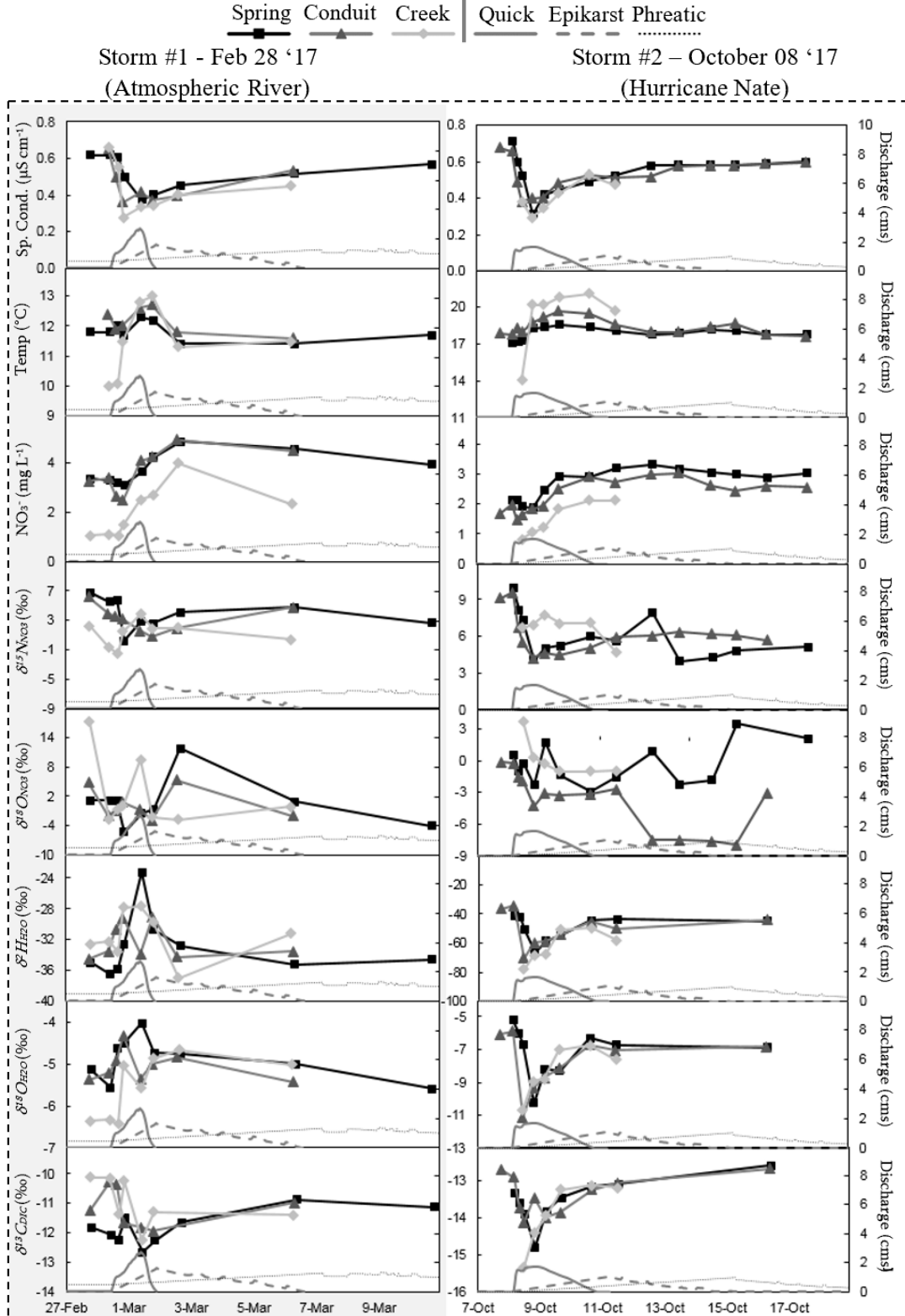
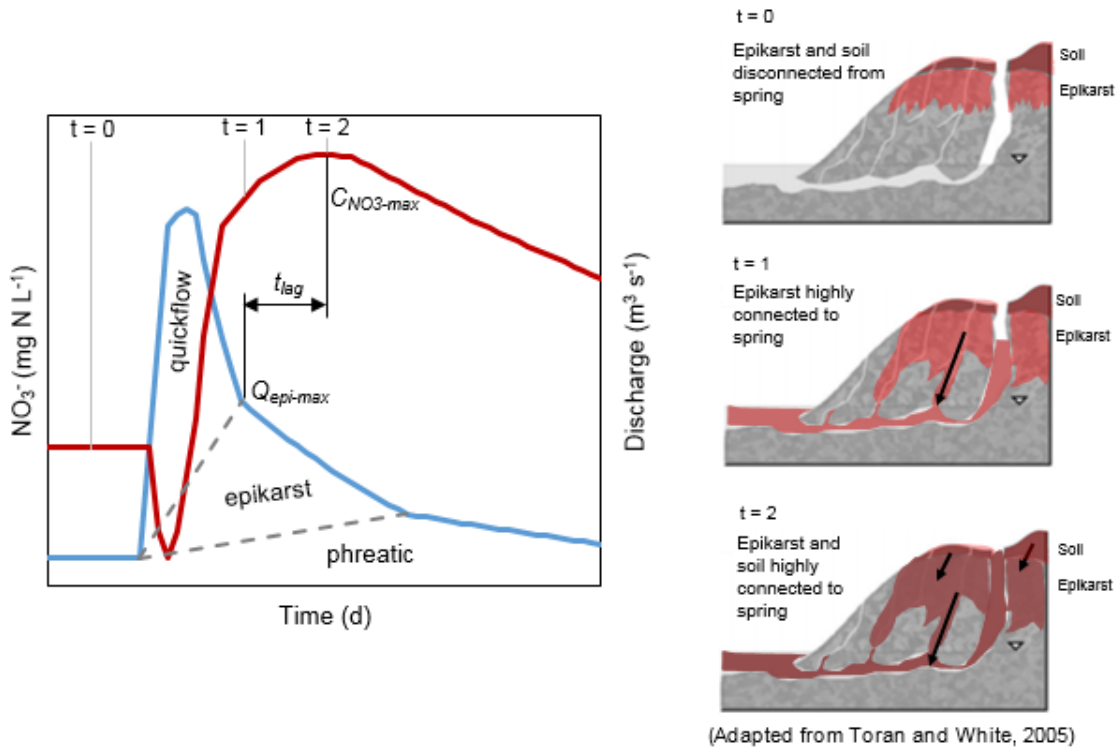


Figure 4.12 Conceptualized response of nitrate to extreme events in a mature karst watershed. Prior to a storm event, when the epikarst and soil are disconnected from the spring, nitrate concentrations are constant ($t = 0$). An initial decrease to the nitrate concentration (C_{NO_3}) is caused by dilute storm recharge. Nitrate concentration increases as epikarst flow (Q_{epi}) becomes more dominant ($t = 1$). There is a time lag between peak epikarst discharge and peak nitrate concentration (t_{lag}). This lag occurs as pre-storm epikarst water drains and is recharged by nitrate-rich soil water ($t = 2$). Lastly, as the hydrograph recedes, nitrate concentrations return to phreatic groundwater levels.



Chapter 5: Nitrogen stable isotopes and numerical modeling show hot moments, hot spots, and environmental drivers in a karst surficial fine-grained laminae

5.1 ABSTRACT

Nitrogen (N) transformation rates within subsurface karst can vary with time, space, and external forcing; however, the impact of these changes on altering downstream N flux is poorly understood. We collected one year of sediment N data and two years of nitrate data from inputs and outputs to a mature karst system and thereafter developed a numerical model of N interactions in the karst surficial fine-grained laminae (SFGL). The stable isotope composition of sediment N ($\delta^{15}\text{N}_{\text{Sed}}$) inputs ($5.07\pm 1.01\text{‰}$) and outputs ($6.45\pm 0.71\text{‰}$) were significantly different indicating in-conduit transformation. Dissolved N immobilization into the sediment biota and shifting of the SFGL to a recalcitrant N source are believed to drive observed enrichment of $\delta^{15}\text{N}_{\text{Sed}}$ outputs relative to inputs. Further, hydrologically wet conditions versus dry conditions controlled temporal variability of the karst SFGL behavior. Hot moments occurred during dry conditions when the ammonium pool was exhausted, resulting in the karst SFGL acting as a net sink for dissolved N. Hot spots for N removal in the karst SFGL occur close to the sinking stream's entrance into the karst cave because of the availability of labile organic matter deposits, which fuel denitrification. Environmental drivers such as changes to air and water temperature, discharge intensity, and land use are predicted to increase hot moments and hot spots in the karst SFGL in this wet, temperate region. Our results point to the karst SFGL as an active biogeochemical pathway that is influenced by internal hot moments and hot spots as well as external environmental drivers.

5.2 INTRODUCTION

Our premise is that sinking streams transport sediment and fuel sediment biogeochemistry in subsurface karst environments. Sinking streams are formed in karst terrain from carbonate dissolution of soluble bedrock (White, 2002). Sinking streams convey water and sediment from above-ground to below-ground pathways, and deposition of sediment and sediment carbon (C) is common in caves (Herman *et al.*, 2008; Husic *et al.*, 2017b). Deposited labile sediment C can then fuel nutrient transformation as well as decomposition in surficial cave sediment. We adopt sediment transport terminology (e.g., Droppo and Stone, 1994; Stone and Droppo, 1994; Russo and Fox, 2012) and call the thin sediment layers stored in subsurface karst the ‘surficial fine-grained laminae’, or SFGL. In rivers, the SFGL is a streambed layer with frequent bed erosion-deposition and active cycling of C and nutrients (Droppo *et al.*, 2001; Ford and Fox, 2014; Ford *et al.*, 2017). We conceptualize the karst SFGL similarly, which is supported by indirect study of karst phenomena (Simon *et al.*, 2003, 2007; Goldscheider *et al.*, 2006; Pronk *et al.*, 2009) and, more recently, direct study (Figure 1.1, Husic *et al.*, 2017a,b). Karst SFGL research shows a changing sediment layer consistent with the above description, albeit absent of light and the autotrophy it generates (Husic *et al.*, 2017a). However, studies have not represented the karst SFGL as a unique temporally and spatially dynamic entity, which represents a step change from traditional hydrologic models that represent stored sediment as a boundary condition. Our motivation is to explicitly represent the karst SFGL and its biogeochemistry using stable N isotopes to understand its hot moments, hot spots, and environmental drivers.

Our motivation is consistent with contemporary study that explicitly represents dynamic boundaries and their interacting hydrologic and biogeochemical processes. Representation of the SFGL, and its C and nutrient cycles, in non-karst streams, has highlighted the ability of the SFGL to control sediment source apportionment (Russo and Fox, 2012), accrue labile C for almost a decade (Ford *et al.*, 2015b), assimilate nutrients at rates higher than hyporheic conveyance (Orr *et al.*, 2009), and export a labile organic N load equaling that of phytoplankton N (Ford and Fox, 2017). More broadly, representing the SFGL as a dynamic entity at liquid-solid interfaces in waterways is consistent with emerging research that couples hydrology and biology (e.g., see discussion of

ecohydrological interfaces in Krause *et al.*, 2017 and Hupfer *et al.*, 2018). We draw on questions broadly relevant to contemporary study but uniquely posed for the karst SFGL in light-absent caves that drain agricultural landscapes.

One question we ask is, when and under what conditions does the karst SFGL experience hot moments and hot spots of N removal? Hot moments and spots are times and locations of enhanced activity that shift net system behavior (e.g., N source to N sink) and/or disproportionately alter the fluxes of water, energy, and matter (Lewandowski *et al.*, 2007; Bernhardt *et al.*, 2017). Similarly to surface streams, we expect the subsurface karst SFGL to exhibit temporal and spatial variability of its biogeochemistry. In nutrient-rich agricultural non-karst streams, temporal ‘hot moments’ cause late summer denitrification in spatial ‘hot spots’ where sediment accrual occurs (Baldwin and Mitchell, 2000; Inwood *et al.*, 2005; Arango *et al.*, 2007). The light-absent karst may show dependence on hydrologic patterns and the quality of C input from sinking streams.

A second question we ask is, how sensitive is the karst SFGL to environmental drivers? Environmental drivers, such as land use change and climate change, are predicted to shift ecosystem function in many freshwater systems (Janse *et al.*, 2015), albeit our representation of transitions is lacking (Krause *et al.*, 2017). For example, streamflow shifts resulting from land use change have been suggested to blanket SFGL in surface streams, shielding freshwater C from turnover (Russo, 2009; Russo and Fox, 2012). Changes in regional climate are suggested to cause non-monotonic shifts to benthic algae in the SFGL (Ford, 2014). We emphasize potential impacts of land use, temperature, and precipitation/discharge shifts to the subterranean karst SFGL function in a wet, temperate region.

One method advancement that allows us to represent the karst SFGL is the use of ambient stable N isotopes. Ambient isotope tracing of sediment N ($\delta^{15}\text{N}_{\text{Sed}}$)—not to be confused with ^{15}N stream injection—can provide insight to sediment provenance, autochthonous growth, and nutrient turnover in streams (Davis *et al.*, 2009; Ford *et al.*, 2017; Jensen *et al.*, 2018). Transported sediment acts as an integrator, and $\delta^{15}\text{N}_{\text{Sed}}$ has been shown to provide an integrated response of the SFGL in an agricultural stream (Ford *et al.*, 2015a). We hypothesized that any shifts in $\delta^{15}\text{N}_{\text{Sed}}$ when comparing sediments entering a karst cave through sinking streams to sediments exiting a cave at a spring might reflect

internal karst SFGL processes. Stable isotopes have been used to un-mix sources of water and dissolved N in karst (Lee and Krothe, 2001; Liu *et al.*, 2006; Knierim *et al.*, 2013), and recently stable C isotopes of sediment were used in karst (Husic *et al.*, 2017a). We introduce the existing $\delta^{15}\text{N}_{\text{Sed}}$ technology to the karst setting in this paper.

A second method advancement that allows us to represent and evaluate karst SFGL processes is the use of stable isotope subroutines within our numerical model. Stable isotope subroutines provide additional equations without additional unknowns to numerical simulations. In turn, stable isotope data provides an additional response variable for multi-objective calibration that may reduce model equifinality (Ford *et al.*, 2017). A growing number of studies have reported the effectiveness of including stable isotopes within stream and watershed numerical models (see discussion and citations in Jensen *et al.*, 2018). We extend this discussion to numerical modeling of the karst SFGL. Thereafter, numerical modeling provides an effective means to investigate continuous temporal and spatial anomalies (e.g., hot moments, hot spots) and to test the sensitivity of environmental drivers (Alexander *et al.*, 2009).

Our overall goal was to explicitly model the karst SFGL and its biogeochemistry to investigate its temporal and spatial behavior and assess its sensitivity. Our objectives were to (1) perform method advancements for karst research, including sampling ambient stable sediment N isotope data and using that isotope data to model the karst SFGL, (2) investigate hot moments and (3) hot spots in karst SFGL that reflect shifts in biogeochemical cycling, and (4) investigate the impact of environmental drivers on hot moments and hot spots within the karst SFGL. These objectives provide the structural sub-headings used in the methods, results and discussion sections of this chapter.

5.3 THEORETICAL BACKGROUND

The theoretical background provides the context behind our conceptual model of the karst SFGL (Figure 5.2). As previously mentioned, the karst SFGL is the thin surficial sediment layer that covers the cave bed (Figure 5.1). The karst SFGL is characterized by frequent sediment and organic matter erosion and deposition, exchange of matter between the water column and sediment layer, and internal cycling of C and N.

Our concept (Figure 5.2a) is consistent with recent studies reporting karst sediment transport and biogeochemistry (Drysdales *et al.*, 2001; Massei *et al.*, 2002; Simon *et al.*, 2003, 2008; Herman *et al.*, 2008; Husic *et al.*, 2017a, 2017b). Sediment transport occurs in mature karst when sediment enters and exits caves *via* sinkhole features (e.g., sinking streams, swallets, and sinkholes) and springheads, respectively. Biogeochemical reactions occur because the microbial pool responsible for C and N turnover resides in cave sediments. For example, Lehman *et al.* (2001) reported that 99% of cave microorganisms reside within fine sediments. Feedbacks between sediment transport and biogeochemical reactions in cave sediments are expected, albeit their presence in the literature is limited. One example, by Brannen-Donnelly and Engel (2015), indicated that sediment transport promotes biogeochemistry because deposition and resuspension homogenized the microbial pool in caves.

A sediment transport and biogeochemistry feedback we can visualize and simulate is through sediment exchange with the karst SFGL that leads to C and N turnover (Figure 5.2b). Physically, hydraulic controls have been shown to promote sediment deposition in caves during storms. Thereafter, net-erosion occurs during the recession when sediment-free water from epikarst fractures and matrix pores provides the primary recharge to the conduit (Husic *et al.*, 2017a). Biogeochemically, karst conduits preclude autotrophic growth (barring chemoautotrophy), therefore, delivery and deposition of allochthonous organic matter is the primary fuel for heterotrophic turnover in the karst SFGL—a concept that is consistent with theory of external energy inputs to karst (Graening and Brown, 2003; Simon *et al.*, 2003, 2007; Hancock *et al.*, 2005; Lee *et al.*, 2012). In terms of N transformations, nitrification, mineralization, denitrification, anammox, and immobilization have all been observed in karst caves and are influenced by shifts in organic C availability (e.g., Barton and Northup, 2007; Kumar *et al.*, 2017).

We designed our research to consider the karst SFGL conceptual model. We assumed active transport of water and sediment in and out of a karst cave *via* sinkholes and springheads, respectively. In this manner, our concepts are limited to karst systems with dominant allochthonous C control (i.e., mature topography with prominent tertiary porosity). We are inclusive of solid and gaseous phases undergoing transformation while in suspension or within the SFGL. We assumed the existence, or lack thereof, of several

processes compiled in Table 5.1. Past research within our study site supports these assumptions.

We investigate the karst SFGL conceptual model by collecting measurements at sinking streams and springheads to assess inputs and outputs. The measurements allow net change detection of sediment C and N within the conduit and assist with boundary conditions in numerical modeling. We then use the conceptual model to formulate a numerical model for continuously simulating transport and biogeochemistry in the SFGL. Hot moments and hot spots are analyzed within the model and the sensitivity of environmental drivers to affect forecasted hot moments and hot spots is also assessed.

5.4 STUDY SITE AND MATERIALS

The study site is the Cane Run watershed and Royal Spring groundwater basin in the Bluegrass Region of Kentucky, USA (Figure 5.3). Cane Run is a mixed-use watershed that drains urban (40%) and agricultural (60%) lands with temperate climate (MAT: $13.0 \pm 0.7^\circ\text{C}$; MAP: $1,170 \pm 200$ mm). The geology is characterized by highly karstic, well-developed Lexington Limestone of the Middle Ordovician period. Cane Run creek collects runoff and shallow subsurface flow but much of this water is pirated by in-stream karst features. Numerous sinkholes and swallets (> 50) exist in the stream corridor and convey water and sediment to the subsurface cave, and as a result the stream at the Cane Run watershed outlet runs dry for approximately 80% of the year. The karst conduit is generally aligned with Cane Run creek for much of its course and is located approximately 20 m below the ground surface (Figure 5.3). The conduit is phreatic and limited in its maximum discharge by a downstream hydraulic control (Husic *et al.*, 2017a). The conduit discharges at Royal Spring which supplies the municipal drinking water supply for the city of Georgetown, KY. The site has been a karst research site led by the Kentucky Geological Survey and the University of Kentucky the past 40 years (Spangler, 1982; Thrailkill *et al.*, 1991; Taylor, 1992; Paylor and Currens, 2004; Zhu *et al.*, 2011; Currens *et al.*, 2015; Husic *et al.* 2017a,b).

A number of recent sediment transport and C turnover findings from the study site are of importance in this study. Deposition and resuspension of sediment occur in the karst

conduit, and was observed through downhole videos (e.g., Figure 5.1) taken at different time periods and through data and modeling (Husic *et al.*, 2017a,b). The reason for the deposition and resuspension of sediment is the phreatic nature and hydraulic control of the conduit. During storm events, the surface stream recharges sediment to the conduit, but the sediment transport carrying capacity (i.e., the fluid's energy to carry sediment) is limited within the conduit because of a downstream hydraulic control (i.e., the elevation of the springhead). The limited energy forces deposition of surface-derived material. During hydrograph recession and baseflow, diffuse recharge is free of sediment and erodes previously deposited material from the karst SFGL. Data results show a 30% net loss of organic C in sediment exiting the conduit (Husic *et al.*, 2017a), which prompted the further modeling of N performed in this paper.

Materials for data collection included instrumented sampling stations (Figure 5.3). Two sampling stations were placed in tributaries (surface streams) upstream of swallets. One tributary sampling station isolated urban land use, and the second isolated agricultural land use. A sampling station was placed at the spring ("Royal Spring" in Figure 5.3) providing water and sediment outputs from the karst conduit and SFGL. A sampling station was placed at the Cane Run creek surface water overflow, which was activated during high-intensity rainfall events. A sampling station was located inside the conduit near its longitudinal midpoint (see "GW station" in Figure 5.3, Zhu *et al.*, 2011; Husic *et al.*, 2017a). Sampling stations were equipped with Telog 2109 water level recorders, YSI 6920v2 water quality sondes, Phillips et al. 2000 sediment samplers (surface tributary and spring stations), and Teledyne ISCO 6712 pump samplers (Husic *et al.*, 2017a). The United States Geological Survey (USGS) operates a flow gage at Royal Spring (USGS 03288110).

Materials for continuous numerical modeling included published results used as model inputs and supercomputing facilities. Water and sediment data collection and sediment transport modeling were previously published in Husic *et al.* (2017a,b). These results provide inputs to the karst SFGL numerical model in this study, including sediment exchange between the water column and karst SFGL, water and sediment flux into and out of the conduit, sediment particle size distributions entering and exiting the conduit, and the distribution of organic matter source material (i.e., soil, litter, and algae) entering the

conduit. Sediment C fate and transport modeling from Husic *et al.* (2017b) is used as an input for this study. Nutrient data collection and modeling were published in Chapter 3. These results provide inputs of nutrients (NO_3^- , NH_4^+ , DON) recharged to the conduit.

Materials for forecasting environmental drivers associated with climate change included climate change projections from publicly-available global climate modeling (GCM) results. Results from eight GCMs were included in this study. The GCM results were downscaled for our region as part of a number of climate change projects, including, statistical downscaling *via* the Coupled Model Inter-comparison Project phases three and five, or CMIP3 and CMIP5 (Brekke *et al.*, 2013), and dynamical downscaling *via* the North American Regional Climate Change Assessment Program, or NARCCAP (Mearns *et al.*, 2013). The GCMs included the Canadian Global Climate Model including CGCM3 from CMIP3 and CanESM2 from CMIP5 (Flato, 2005); the National Center for Atmospheric Research Community Climate Model including CCSM3 from CMIP3 and CCSM4 from CMIP5 (Collins *et al.*, 2006); the Geophysical Fluid Dynamics Laboratory including GFDL CM2.1 from CMIP3 and CM3 from CMIP5 (Delworth *et al.*, 2006); and the United Kingdom Hadley Centre Climate Model including HadCM3 from CMIP3 and HadGEM2-ES from CMIP5 (Gordon *et al.*, 2000). The statistical downscaling methods adopted in CMIP3 and CMIP5 were bias correction and spatial disaggregation or bias-correction and constructed analog (Brekke *et al.*, 2013). Six dynamical downscaling methods were adopted *via* regional climate models in NARCCAP, including, the Canadian Regional Climate Model (CRCM) (Plummer *et al.*, 2006), the Experimental Climate Prediction Center (ECPC) model (Juang *et al.*, 1997), the Hadley Regional Model 3 (HRM3) (Jones *et al.*, 2003), the MM5- PSU/NCAR mesoscale model (MM5I) (Chen and Dudhia, 2001), the Regional Climate Model version 3 (RCM3) (Giorgi *et al.*, 1993), and the Weather Research and Forecasting model (WRFP) (Skamarock *et al.*, 2005). GCM results from hindcast (1981-2000) and forecast (2046-2065) periods were applied in this study. Forecast results reflect a range of emission scenarios, including, the SRES type in CMIP3 (A1B, A2, and B1) and the RCPs type in CMIP5 (RCP2.6, RCP4.5, RCP6.0, and RCP8.5).

Materials for forecasting environmental drivers associated with land use change included land use change projections publicly-available from the United States Geological Survey (USGS EROS Land-cover modeling program). Results of the spatially explicit

simulation model known as forecasting scenarios of land cover change (FORE–SCE) (Sohl *et al.*, 2007; Sohl and Saylor, 2008) published by the USGS were input in this study. The FORE–SCE uses linkages with both external models and the inclusion of input data to project changes at different scales with driving-force variables (Zhu *et al.*, 2010). The land use land cover change results are freely available (<https://landcover-modeling.cr.usgs.gov/>) and are detailed in Zhu *et al.* (2010). The results include three sets of results for IPCC SRES future scenarios.

5.5 METHODS

5.5.1 Karst SFGL data collection and modeling using stable isotopes

Sediment N and $\delta^{15}\text{N}_{\text{Sed}}$ Collection and Processing

In-situ suspended sediment traps (Phillips *et al.*, 2000) were used to collect 9 months (December 2012 to August 2013) of data from urban and agricultural tributary inputs and spring outputs. The in-situ traps allow for spatially and temporally integrated sample collection (Phillips *et al.*, 2000). Samples were collected approximately every two weeks and samples that were clogged or without adequate sample weight were discarded. Samples were analyzed for elemental content and stable isotope composition of sediment N entering and exiting the karst conduit. Carbon elemental and isotope values were measured and discussed in Husic *et al.* (2017a) but are also presented herein alongside the N results.

In the lab, samples were dewatered and weighed, wet-sieved through a 53 μm sieve, dewatered and weighed again, ground to a fine powder, and acidified repeatedly using 6% sulfurous acid following the method of Verardo *et al.*, 1990 (Ford and Fox, 2014; Husic *et al.*, 2017a). Sediment C, N, $\delta^{13}\text{C}_{\text{Sed}}$, and $\delta^{15}\text{N}_{\text{Sed}}$ samples were analyzed by combusting samples at 980°C on a Costech 4010 Elemental Analyzer, passing the gas stream through a Gas Chromatograph (GC) column (3 m HS-Q), and finally to a Thermo Finnigan Delta-Plus XP Isotope Ratio Mass Spectrometer (IRMS) at the University of Arkansas Stable Isotope Lab (Ford *et al.*, 2015).

The C and N elemental compositions were reported as a percentage of the mass of the element relative the mass of sediment. Isotopic results were reported in delta notation (δ) as

$$\delta^{13}\text{C} = \left(\frac{R_{\text{C-Sample}}}{R_{\text{C-Standard}}} - 1 \right) * 1000, \quad (1)$$

$$\delta^{15}\text{N} = \left(\frac{R_{\text{N-Sample}}}{R_{\text{N-Standard}}} - 1 \right) * 1000, \quad (2)$$

where $R_{\text{C-Sample}}$ is the $^{13}\text{C}/^{12}\text{C}$ ratio of the samples and $R_{\text{C-Standard}}$ is the $^{13}\text{C}/^{12}\text{C}$ ratio of the universal standard, Vienna Pee Dee Belemnite (VPDB). The elemental reference was acetanilide (%C=71.09%, %N = 10.36%), and isotopic references were DORM ($\delta^{13}\text{C}=-19.59$, $\delta^{15}\text{N}=12.46$) and CCHIX ($\delta^{13}\text{C}=-16.4\text{‰}$, $\delta^{15}\text{N}=3.2\text{‰}$). Average standard deviations for elemental standards were 0.34 and 0.25% for C and N, respectively. Average standard deviations for isotopic standards were 0.20 and 0.20‰ for C and N, respectively. Average standard deviations of replicates were 0.10% and 0.08‰ for C concentration and $\delta^{13}\text{C}$, respectively, and 0.01% and 0.18‰ for N concentration and $\delta^{15}\text{N}$, respectively.

Bi-weekly water samples were collected and analyzed for the stable N isotope composition of nitrate within the conduit (see “Groundwater Station” in Figure 5.3). The water samples were used to provide justification of $\delta^{15}\text{N}$ of nitrate entering the karst SFGL substrate during microbial immobilization. Discrete sample collection of NO_3^- was conducted using sterile 1 L jars (I-Chem 312-0950BPC). Samples were extracted in the field from the 1 L jars using pre-cleaned 60 mL syringes and filtered through 0.45 μm syringe filters (Whatman 6780-2504) into sterile 40 mL borosilicate vials (I-Chem TB36-0040). Stable isotopic signatures of NO_3 ($\delta^{15}\text{N}_{\text{NO}}$) were measured using a bacterial denitrification method after Revesz and Casciotti (2007) and analyzed on a Thermo Gas Bench II interfaced to a Thermo Finnigan Delta-Plus IRMS. Reference standards for the analysis were USGS 32 ($\delta^{15}\text{N}=180\text{‰}$) and USGS 34 ($\delta^{15}\text{N}=-1.8\text{‰}$). Average standard deviations for reference material and replicates were 2.0‰ and 0.3‰ for $\delta^{15}\text{N}$, respectively. Duplicates of $\delta^{15}\text{N}_{\text{NO}_3}$ (n = 5) had a standard deviation of 0.28‰. Blanks of $\delta^{15}\text{N}_{\text{NO}_3}$ had less than 10% of the intensity of regular samples.

Sediment N Mass Balance Subroutine

The mass balance of sediment N with k source pools (i.e., soil, litter, and algae) was modeled as

$$S_{SN(i)}^{(j)} = S_{SN(i-1)}^{(j)} - E_{SN(i)}^{k(j)} + D_{SN(i)}^{k(j)} - R_{Sed(i)}^{k(j)} - X_{SN_{SFGL \rightarrow SS(i)}}^{k(j)} + X_{SN_{SS \rightarrow SFGL(i)}}^{k(j)}, \quad (3)$$

where, i and j are temporal and spatial steps, respectively, $S_{SN(i-1)}^{(j)}$ is the supply of sediment N from the previous time step (kg N), $E_{SN(i)}^{k(j)}$ is the amount of sediment N eroded (kg N), $D_{SN(i)}^{k(j)}$ is the amount of sediment N deposited (kg N), $R_{Sed(i)}^{k(j)}$ is net mass balance change of sediment N in response to biogeochemical processes (kg N), and $X_{SN_{SFGL \rightarrow SS(i)}}^{k(j)} + X_{SN_{SS \rightarrow SFGL(i)}}^{k(j)}$ is the equilibrium exchange of N between the suspended and bed sediment (kg N) (Husic *et al.*, 2017b). Quality of sediment N deposited to the karst SFGL was performed using the un-mixing results of C (soil, litter, and algae) from Husic *et al.* (2017b) and applying C:N ratios ($C:N_{soil}$, $C:N_{litter}$, $C:N_{algae}$) to estimate N quantity. Physical processes affecting C are the same for N and are explained in further detail in Chapter 2. The mass of sediment N transformed (kg N) was modeled as:

$$R_{Sed(i)}^{k(j)} = N_{min\ SN(i)}^{k(j)} - N_{imm(i)}^{k(j)}, \quad (4)$$

where $N_{min\ SN(i)}^{k(j)}$ is the amount of sediment N mineralized to NH_4^+ (kg N) and $N_{imm(i)}^{k(j)}$ is the mass of dissolved N immobilized into sediment N by biota (kg N). Mineralization and immobilization are both modeled using first-order rate constants for each respective pool (i.e., soil, litter, algae).

$\delta^{15}N_{Sed}$ Mass Balance Subroutine

The numerical model in this work simulates $\delta^{15}N_{Sed}$ mass balance with Rayleigh fractionation (Sharp, 2007) as

$$\delta^{15}N_{Sed(i)}^{(j)} = \delta^{15}N_{Sed(i-1)}^{(j)} X_{(i-1)}^{k(j)} + \sum \delta^{15}N_{Sed_{inputs(i)}}^{(j)} X_{inputs(i)}^{k(j)} - \sum \delta^{15}N_{Sed_{outputs(i)}}^{(j)} X_{outputs(i)}^{k(j)} - \sum \epsilon_{frac(i)}^{(j)} \ln \left(f_{frac(i)}^{(j)} \right) \quad (5)$$

where $\delta^{15}N_{Sed(i-1)}^{(j)}$ is the $\delta^{15}N_{Sed}$ of the sediment from the previous time step (‰), $X_{(i-1)}^{k(j)}$ is the fraction of N in a given (k) pool estimated by Equation (3), $\delta^{15}N_{Sed_{inputs(i)}}^{(j)}$ is the

$\delta^{15}N_{Sed}$ of sediment inputted to the bed (‰), $X^{k(j)}_{inputs(i)}$ is the fraction of inputs associated with k pool, $\delta^{15}N_{Sed_{outputs(i)}}^{(j)}$ is the $\delta^{15}N_{Sed}$ of sediment outputted from the bed (‰), $X^{k(j)}_{outputs(i)}$ is the fraction of outputs associated with k pool, $\epsilon_{frac(i)}^{(j)}$ is the enrichment factor during an isotopic process, and $f_{frac(i)}^{(j)}$ is the fraction of substrate remaining after a reaction. The NO_3^- isotope balance is beyond the scope of this model, instead an average $\delta^{15}N_{NO_3}$ value based on the average of all field measurements is used to represent the isotopic value of dissolved N immobilized into sediment.

Dissolved Nitrogen Mass Balance Subroutines

The mass balance of nitrate (NO_3^-), ammonium (NH_4^+), and dissolved organic N (DON) were modeled as

$$NO_3^-(i)^{(j)} = NO_3^-(i-1)^{(j)} + R_{NO_3(i)}^{(j)} + Q_{(i-1)}^{(j-1)} C_{NO_3(i-1)}^{(j-1)} \Delta t - Q_{(i)}^{(j)} C_{NO_3(i)}^{(j)} \Delta t, \quad (6)$$

and

$$NH_4^+(i)^{(j)} = NH_4^+(i-1)^{(j)} + R_{NH_4(i)}^{(j)} + Q_{(i-1)}^{(j-1)} C_{NH_4(i-1)}^{(j-1)} \Delta t - Q_{(i)}^{(j)} C_{NH_4(i)}^{(j)} \Delta t, \quad (7)$$

and

$$DON(i)^{(j)} = DON(i-1)^{(j)} + R_{DON(i)}^{(j)} + Q_{(i-1)}^{(j-1)} C_{DON(i-1)}^{(j-1)} \Delta t - Q_{(i)}^{(j)} C_{DON(i)}^{(j)} \Delta t, \quad (8)$$

where $NO_3^-(i)^{(j)}$, $NH_4^+(i)^{(j)}$, $DON(i)^{(j)}$ are the masses of NO_3^- , NH_4^+ , and DON from the previous time step, respectively (kg N), $R_{NO_3(i)}^{(j)}$ is the biogeochemical processing that contributes to or removes N from the NO_3^- phase (kg N), $R_{NH_4(i)}^{(j)}$ is the biogeochemical processing that contributes to or removes N from the NH_4^+ phase (kg N), $R_{DON(i)}^{(j)}$ is the biogeochemical processing that contributes to or removes N from the DON phase (kg N), $Q_{(i-1)}^{(j-1)}$ is the flow rate into a cell ($m^3 s^{-1}$), $C_{NO_3(i-1)}^{(j-1)}$, $C_{NH_4(i-1)}^{(j-1)}$, $C_{DON(i-1)}^{(j-1)}$ are the concentrations of NO_3^- , NH_4^+ , and DON coming into a cell ($mg N L^{-1}$), respectively, Δt is time step duration (s), $Q_{(i)}^{(j)}$ is the flow rate exiting a cell ($m^3 s^{-1}$), and $C_{NO_3(i)}^{(j)}$, $C_{NH_4(i)}^{(j)}$, and $C_{DON(i)}^{(j)}$ are the concentrations of NO_3^- , NH_4^+ , and DON exiting a cell ($mg N L^{-1}$), respectively.

The masses of NO_3^- , NH_4^+ , and DON transformed (kg N) were modeled as:

$$R_{\text{NO}_3(i)}^{(j)} = N_{\text{DEN}(i)}^{(j)} - N_{\text{IN}(i)}^{(j)} - N_{\text{directN}(i)}^{(j)} - \lambda \cdot N_{\text{imm}(i)}^{(j)}, \quad (9)$$

and

$$R_{\text{NH}_4(i)}^{(j)} = N_{\text{IN}(i)}^{(j)} + N_{\text{directN}(i)}^{(j)} + \lambda \cdot N_{\text{imm}(i)}^{(j)} + N_{\text{ANA}(i)}^{(j)} - N_{\text{minSN}(i)}^{(j)} - N_{\text{minDON}(i)}^{(j)}, \quad (10)$$

and

$$R_{\text{DON}(i)}^{(j)} = N_{\text{minDON}(i)}^{(j)}, \quad (11)$$

where $N_{\text{IN}(i)}^{(j)}$ is the mass of recently mineralized NH_4^+ indirectly nitrified to NO_3^- in the streambed (kg N), $N_{\text{directN}(i)}^{(j)}$ is the mass of NH_4^+ directly nitrified to NO_3^- in the water column (kg N), $N_{\text{DEN}(i)}^{(j)}$ is the mass of NO_3^- denitrified to N_2 (kg N), $N_{\text{minSN}(i)}^{(j)}$ is the amount of sediment N mineralized to NH_4^+ (kg N), $N_{\text{imm}(i)}^{(j)}$ is the mass of N immobilized by into sediment N by biota (kg N), $N_{\text{minDON}(i)}^{(j)}$ is the mass of DON mineralized to NH_4^+ (kg N), $N_{\text{ANA}(i)}^{(j)}$ is the mass of NH_4^+ directly removed as N_2 by anammox bacteria (kg N), and λ (either a “1” or a “0”) activates NO_3^- as the N immobilized by sediment biota if and only if the NH_4^+ pool is exhausted.

The rate of C decomposition and N mineralization are impacted by temperature and were modeled following Reichstein *et al.* (2000, 2005) with a temperature dependence as

$$r(T)_i = Q_{10}^{(T_i - T_{ref})/10}, \quad (12)$$

where Q_{10} is a measure of the rate of change of a biogeochemical reaction from increasing the temperature by 10 °C, T_i is the temperature within the conduit (°C), and T_{ref} is a reference temperature for the reaction (°C). Likewise, nearly all nutrient transformations are affected by temperature (Bowie *et al.*, 1985) and other reactions impacted by temperature are modeled using a modified Arrhenius expression (Veraart *et al.*, 2011). For example, rates were modeled as

$$k_T = k_{20} \theta^{T_i - T_{ref}}, \quad (13)$$

where k_{20} is the reaction rate at a temperature of 20 °C (d^{-1}), θ is a temperature adjustment coefficient. The equations for all N reactions (i.e., denitrification, indirect nitrification, anammox, direct nitrification, mineralization (DON), mineralization (PON or “Sed N”),

and immobilization) are shown in Table 5.2 (Equations 14 to 20) and their terms are defined therein.

Model Evaluation

A framework of model inputs, model simulation, parameter optimization, comparison to data, and statistical testing was developed (Figure 5.4). Model parameters were constrained by user-defined bounds derived from the literature or measured in the field (see Table 5.3 for inputs and parameters). Initial parameter values were selected from previous studies (Husic *et al.*, 2017a, Ford *et al.*, 2017) and then optimized to fit collected sediment N, $\delta^{15}\text{N}_{\text{Sed}}$, and NO_3^- data. Model results were compared to observed results of sediment N (C_{SN}), $\delta^{15}\text{N}_{\text{Sed}}$, and NO_3^- . First the model was calibrated to C_{SN} simultaneously with $\delta^{15}\text{N}_{\text{Sed}}$. Time-integrated samples of C_{SN} and $\delta^{15}\text{N}_{\text{Sed}}$ at the spring were used as the response variable for the sediment N model. Calibration of the sediment N model was performed utilizing manual calibration techniques of sensitive parameters to achieve statistically sufficient results ($\alpha = 0.05$). Prior uncertainty analysis of sediment C decomposition (Husic *et al.*, 2017b) was used to bound sediment N mineralization rates as the two processes are coupled (Ford *et al.*, 2017). Manual calibration was also performed to include as many of the data results within the modeled end-members as possible. The modeled end-members for this system are the SFGL as the more recalcitrant source and pirated sediment as the labile source of C and N. Lastly, the model was calibrated to discrete NO_3^- concentration data collected from within the conduit. The NO_3^- model was calibrated using the constrained nonlinear multivariate solver with the Interior-Point Algorithm (MATLAB™ optimization toolset).

C_{SN} and $\delta^{15}\text{N}_{\text{Sed}}$ data were collected at the spring from December 2012 to August 2013 and included 18 total time-integrated traps. Large datasets of C_{SN} and $\delta^{15}\text{N}_{\text{Sed}}$ can be investigated seasonally (Ford *et al.*, 2017), but given that our data range is less than a year, we apply a statistical t-test to compare mean model and measured results (see Husic *et al.*, 2017b). NO_3^- samples were collected from within the phreatic conduit from January 2012 to September 2013 and include 211 discrete samples. Given the larger size of the dataset, the discrete NO_3^- samples were compared at the hourly time-scale using the Nash-Sutcliffe

Efficiency (NSE). We calibrated the model with the last 70% of the NO_3^- dataset ($n = 148$) and validated with the first 30% ($n = 63$). The NSE was calculated as

$$NSE = 1 - \frac{\sum_{t=1}^T (Q_m^t - Q_o^t)^2}{\sum_{t=1}^T (Q_m^t - \overline{Q_o})^2}, \quad (21)$$

where T is the total number of observations, Q_o is the observed value at time t , Q_m is the modeled value at time t , and $\overline{Q_o}$ is the mean of observed values. The Nash Sutcliffe efficiency ranges from $-\infty$ to 1, with 1 indicating a perfect match of the model to data and 0 indicating the model performs no better than the mean of the data (Moriasi *et al.*, 2007).

5.5.2 Hot moments in the karst SFGL

We investigated moments of N turnover in the karst SFGL. Periods that regulate contaminant movement to downstream waters and mitigate upstream loading are termed “hot moments” (Vidon *et al.*, 2010). We continuously simulate sediment N and dissolved N (NO_3^- , NH_4^+ , and DON) dynamics in the subsurface karst conduit and identify periods of activity that mitigate elevated upstream loading. The net removal of N was a primary focus for identifying hot moments. Within the karst SFGL, N can be removed temporarily (immobilized into sediment) or it can be removed permanently (denitrified to dinitrogen gas, N_2). The removal of N can vary based on the size and availability of constituent pools. For example, NH_4^+ is continually nitrified (given appropriate field conditions) into NO_3^- until the NH_4^+ pool is exhausted. Thereafter, no reactions involving NH_4^+ can occur until the pool is either recharged by inflowing water or regenerated by mineralization of organic N in the karst SFGL. Pool sizes, reaction rates, temperatures, and exchanges vary temporally and identification of periods where removal is high are of interest.

5.5.3 Hot spots in the karst SFGL

We investigated spots of N turnover in the karst SFGL. Patches within an ecosystem that show enhanced removal rates can be conceptualized as “hot spots” (Kuzyakov and Blagodatskaya, 2015). Longitudinal variations in N transformations are influenced by the sediment trapping capability of the conduit, connectivity to labile surface inputs, in-conduit transport dynamics, and the bioavailability of C substrate to fuel reactions. We continuously simulate the factors and observe their net effect on sediment N and dissolved N (NO_3^- , NH_4^+ , and DON) dynamics. The spatial net removal of N was a

primary focus for identifying hot spots. By simulating longitudinal removal rates, locations of enhanced removal could be identified and the dynamics and transformations that lead to that enhanced removal could be investigated. Therefore, processes that vary longitudinally such as deposition of sediment, connectivity to the surface, and bioavailability of C in the karst SFGL were of high interest.

5.5.4 Environmental drivers impacting the karst SFGL

We investigated how environmental drivers may increase or decrease future hot moments and hot spots for N turnover in the karst SFGL. Environmental drivers due to climate change and land use change were investigated.

Downscaled GCM results were used to forecast relative shifts in mean monthly temperature and flowrate for the study site (Table 5.4a,c). Ensemble modeling of GCM results, including ± 1 standard deviation of forecasts, was performed in order to assess high and low bounds on forecasts. A balanced GCM design of ensemble forecasts (e.g., downscaling approach, emission scenario) was used, and the balanced design for this study region is reported in Al Aamery *et al.* (2016). Relative climate changes reflect the difference between forecast and hindcast GCM model runs. Monthly air temperature and flowrate shifts were included for results centered around 2057 (see Table 5.4). All air temperature inputs reflect a temperature increase. Flowrate differences showed increases and some decreases (-).

Karst conduit water temperature was needed to assess temperature shifts of climate change as opposed to air temperature shifts. Therefore, an empirical relationship was constructed between air temperature and conduit water temperature for current conditions. The empirical function was used to forecast the conduit water temperature for 2057. The subsurface dampens temperature variations in the conduit, and this idea is reflected in the forecasted temperature shifts (see Table 5.4b). Within modeling, temperature changes are reflected in all biogeochemical transformations (see Equations 14 to 20 in Table 5.2). Within modeling, flow rate changes are reflected in quantity of inputs, erosion and deposition dynamics, and bed evolution.

Environmental drivers from land use and land cover change for the groundwater basin were input from the USGS modeling results (Zhu *et al.*, 2010). The Royal Spring's

groundwater basin boundary (Paylor and Currens, 2004) was used to mask the USGS modeling results and showed a land use shift from agricultural to urban dominance for 2057. Depending on forecast scenario, USGS results were 84%, 93% and 88% urban land use for 2057, with the remainder of land use remaining as agricultural (Table 5.4d). Within modeling, land use changes are reflected in the quality of organic C and N supplied to the subsurface (see Chapter 2 equations for explicit formulation). Within the study area, urban sources of water are more heavily concentrated in C and N and as urbanization increases so does the quantity of C and N input to the conduit.

5.6 RESULTS AND DISCUSSION

5.6.1 Karst SFGL data collection and modeling using stable isotopes

Stable N isotope signatures of sediment were significantly different for karst inputs and outputs, which allowed inference as to the net function of the karst SFGL (Figure 5.5a). Collected data show that Royal Spring sediment N ($\delta^{15}\text{N}_{\text{Sed}}=6.45\pm 0.71\text{‰}$) was significantly heavier (i.e., higher $\delta^{15}\text{N}_{\text{Sed}}$ values) compared to the urban and agricultural tributary sediment ($\delta^{15}\text{N}_{\text{Sed}}=5.07\pm 1.01\text{‰}$) recharging the conduit ($p < 1\times 10^{-5}$). Time series comparison of the data showed that only one of the sediment samples from Royal Spring had a lower $\delta^{15}\text{N}_{\text{Sed}}$ than contemporaneously sampled tributary sediment (Figure 5.5a). Taken together, results suggest sediment becomes enriched in ^{15}N as it travels through the conduit and is temporarily stored in the karst SFGL.

Total sediment N showed a net decrease (i.e. reduced concentration) at Royal Spring relative to recharging tributary sediment (Figure 5.5b). On average, spring sediment N concentration ($0.36\pm 0.09 \text{ gN } 100\text{gSed}^{-1}$) was 16% lower than surface tributary sediment ($0.43\pm 0.07 \text{ gN } 100\text{gSed}^{-1}$). Likewise, earlier data results indicated that sediment organic C at the spring ($3.4\pm 0.5 \text{ gC } 100\text{gSed}^{-1}$) was 30% lower than tributary inputs ($4.8\pm 1.2 \text{ gC } 100\text{gSed}^{-1}$). Thus, data results indicate that transformations act to reduce the concentration of sediment C and N during fate and transport within the karst SFGL. Previous work has indicated the average sediment residence time in the karst SFGL to be approximately one year (Husic *et al.*, 2017b), which supports the idea of labile material being trapped and made available for turnover in the karst SFGL.

While the biologically-active components of the transported sediment underwent changes, other data-streams indicative of physical changes to the sediment (e.g., additional sources) varied less. One such data-stream, the stable carbon isotope of sediment ($\delta^{13}\text{C}_{\text{Sed}}$), indicated no significant differences between inputs ($\delta^{13}\text{C}_{\text{Sed}} = -26.64 \pm 0.80\text{‰}$) and outputs ($\delta^{13}\text{C}_{\text{Sed}} = -26.61 \pm 0.86\text{‰}$). As a further support for this idea, particle size distribution analysis of sediment collected at surface tributaries ($D_{50} = 29.8 \mu\text{m}$), the surface outlet ($D_{50} = 29.8 \mu\text{m}$), and the groundwater conduit ($D_{50} = 31.6 \mu\text{m}$) showed no significant differences (Husic *et al.*, 2017a).

Taken together, data suggests sediment enters the karst conduit, resides in the karst SFGL on average for one year, and exits the conduit at the spring. During temporary residence in the SFGL, sediment becomes enriched in ^{15}N by more than one per mil, and loses both sediment N and organic C. Nitrogen cycling of sediment N and microbial turnover of sediment C in the karst SFGL are suggested, as opposed to mixing with an external (i.e., missing) sediment source because $\delta^{13}\text{C}_{\text{Sed}}$ and particle size distributions of conduit inputs and outputs are identical. A lack of change in $\delta^{13}\text{C}_{\text{Sed}}$ is consistent with the fact that isotopic enrichment is small during sediment C turnover (i.e., the enrichment factor for sediment C turnover is $\sim 0\text{--}2\text{‰}$, Jacinthe *et al.*, 2009). This enrichment factor is small relative to other C transformations such as uptake (15-25‰) and methanogenesis (5-10‰) (Jensen *et al.*, 2018). Lack of change in the particle size distribution also suggests the same sediments are moving through the conduit, and recent results have suggested that temporary residence in the SFGL does not change the particle size distribution of sediments, at least in this temperate region (Fox *et al.*, 2014).

The stable N isotope composition of nitrate ($\delta^{15}\text{N}_{\text{NO}_3}$) collected from within the conduit ($6.94\text{‰} \pm 1.89\text{‰}$) was slightly heavier than the $\delta^{15}\text{N}_{\text{Sed}}$ leaving the conduit ($6.45 \pm 0.71\text{‰}$). For most of the year, the dissolved NO_3^- transported in the conduit is dominated by NO_3^- drained from the surrounding landscape rather than NO_3^- outgassed from the sediment bed. That is, transport of NO_3^- through karst systems is suggested to have a greater control on downstream NO_3^- concentration and loading than biochemical production (see Chapter 3). Therefore, we expect that one of the reasons for similarities in $\delta^{15}\text{N}_{\text{NO}_3}$ and $\delta^{15}\text{N}_{\text{Sed}}$ is heterotrophic microbe demand by the karst SFGL for isotopically heavier NO_3^- entrained in the water column. As the isotopically lighter, tributary-derived

sediment ($\delta^{15}\text{N}_{\text{Sed}}=5.07\pm 1.01\text{‰}$) is deposited to the bed, assimilation of the isotopically heavier nitrate ($\delta^{15}\text{N}_{\text{NO}_3}=6.94\pm 1.89\text{‰}$) by karst SFGL biota leads to an increase in $\delta^{15}\text{N}_{\text{Sed}}$ of sediment that eventually discharges at the spring ($\delta^{15}\text{N}_{\text{Sed}}=6.45\pm 0.71\text{‰}$). We do expect some fractionation during immobilization ($\epsilon = 1\text{-}13\text{‰}$, Jensen *et al.*, 2018), but microbial demand is one reason for the isotopically heavier $\delta^{15}\text{N}_{\text{Sed}}$, which is further discussed below.

The karst SFGL numerical model showed sensitivity during calibration for a number of different response variables, which in turn showed the utility of multi-objective calibration. Carbon and nitrogen concentration of sediment showed sensitivity to C and N turnover rates within the karst SFGL. Turnover rates were sensitive as C and N concentration of sediment significantly decreased from the entrance to the exit of the conduit. $\delta^{15}\text{N}_{\text{Sed}}$ provided a unique response variable for several reasons. Modeled $\delta^{15}\text{N}_{\text{Sed}}$ did exhibit some dependence on C and N turnover. This is primarily due to the loss of labile organic matter (i.e., algae and litter, $\delta^{15}\text{N}_{\text{algae}}=5.0\text{‰}$ and $\delta^{15}\text{N}_{\text{litter}}=3.9\text{‰}$) relative to recalcitrant organic matter (i.e., soil organic matter, $\delta^{15}\text{N}_{\text{SOM}}=6.9\text{‰}$) at the conduit entrance to the exit. Modeled $\delta^{15}\text{N}_{\text{Sed}}$ was also slightly sensitive to N turnover during mineralization (i.e., $\epsilon=\pm 1\text{‰}$ during mineralization, Jensen *et al.*, 2018). However, the sensitivity of $\delta^{15}\text{N}_{\text{Sed}}$ modelled to mineralization alone did not allow good comparison of modeled $\delta^{15}\text{N}_{\text{Sed}}$ with data $\delta^{15}\text{N}_{\text{Sed}}$ results. We found that the $\delta^{15}\text{N}_{\text{Sed}}$ response variable was sensitive to assimilatory immobilization by heterotrophs in microbial films of the karst SFGL. Immobilization of NO_3^- accounted for approximately a 0.20‰ increase in $\delta^{15}\text{N}_{\text{Sed}}$, which represented approximately 15% of the observed fractionation. Process justification for model calibration can be explained if relatively-enriched $\delta^{15}\text{N}$ is assimilated by the sediment microbial pool leading to the sediment organic N substrate becoming enriched in ^{15}N . The good agreement between $\delta^{15}\text{N}$ of nitrate and sediment (6.94 ± 1.89 and $6.45\pm 0.71\text{‰}$, respectively), as discussed above, further justifies adjusting immobilization rates to calibrate modeled $\delta^{15}\text{N}_{\text{Sed}}$ at the conduit outlet with observed $\delta^{15}\text{N}_{\text{Sed}}$ data.

Our model evaluation showed that modeled end-members, including pirated surface sediment and karst SFGL, bounded well the data results of transported sediment (Figure 5.6). Data results falling outside of the modeled end-members are likely due to high variability in the quality of source material. This material may be flushed directly through the conduit (without deposition) and thus is not transformed significantly within

the karst SFGL. Histograms of modeled SOC, TN, $\delta^{13}\text{C}_{\text{Sed}}$, and $\delta^{15}\text{N}_{\text{Sed}}$ compared well to data results, but modeled results tend to have less deviation as compared to data results (Figure 5.7). The sediment N model under predicts the range of variability seen in the data partly because the model is spatially discretized to one kilometer reaches and captures mean trend behavior (Husic *et al.*, 2017b).

In summary, our N isotope data and numerical model results showed the efficacy of the ambient isotope data to be sensitive to net N transformation in the karst SFGL. The utility for stable isotope data to assist with multi-objective calibration was also shown. The efficacy of N isotopes to reduce uncertainty for this application adds to an emerging body of literature that emphasizes the use of stable isotopes for watershed and water quality modeling (see Jensen *et al.*, 2018). The confidence gained from the data and model results allowed us to carry forward the model to investigate hot moments, hot spots, and environmental drivers.

5.6.2 Hot moments in the karst SFGL

Dissolved N model formulation and results were crucial to identifying temporal variability of the karst SFGL behavior. The dissolved N numerical model performed well for the bulk of samples collected from within the phreatic conduit (Figure 5.8). Nash Sutcliffe coefficients of 0.33 and 0.19 during the calibration and validation phases, respectively, indicate the utility of in-conduit modeling to improve dissolved N transformation estimates. In one instance during an event in January 2013, modelling was unable to capture a transient flushing of NO_3^- that accounted for the three largest NO_3^- concentrations of the 211 sample set. To this end, a closer inspection of N dynamics indicates that hydrologically active, or wet, conditions versus dry conditions control temporal variability of the karst SFGL behavior. We distinguish wet versus dry conditions in our figures based on seasonally dependent rainfall and, in turn, mean water discharge in the conduit. For the duration of this study (two years), the wet season (December through May) accounts for 75% of water discharge at the spring and the dry season accounts for the remaining 25%.

We found that hot moments of N turnover occur during dry conditions when temperatures are high, discharge is low, and nitrification is limited in the karst SFGL

(Figure 5.9a). During the wet season (Figure 5.9b), the NO_3^- concentration of outflowing water closely follows that of inflowing water due to its low residence time and lack of net exchange with the karst SFGL. During the dry season (Figure 5.9c), NO_3^- concentrations between inflowing and outflow water begin to diverge due to longer residence times, which allows for increased relative exchange with the SFGL.

Transformations of NH_4^+ and NO_3^- within the karst SFGL also vary temporally (Figure 5.10). NH_4^+ transformations such as mineralization, immobilization, and indirect nitrification are heavily reliant upon the size of the sediment N pool so they fluctuate seasonally based on trapping of surface-derived sediment and decomposition dynamics (Figure 5.10a). Typically, the sediment N pool is large enough to sustain reactions year-round. On the other hand, the dissolved NH_4^+ pool can be exhausted during dry periods of limited nutrient-laden recharge to the conduit. Processes dependent on the availability of NH_4^+ such as anammox and direct nitrification contribute negligibly to NH_4^+ transformation during these dry spells. NO_3^- transformations are tightly coupled to availability of NH_4^+ (for direct nitrification), sediment C (for denitrification), and sediment N (for indirect nitrification) (Figure 5.10b). Nitrification is the primary contributor to the NO_3^- load, but is dependent on NH_4^+ availability which, as shown previously, can be limited during dry spells. Thus, recharge of NH_4^+ and DON from concentrated and diffuse pathways are shown by the model to fuel nitrification (Figure 5.10a). On the other hand, denitrification is driven largely by the sediment community and thus transforms NO_3^- into N_2 during hydrologically active and inactive periods. Indirect nitrification varies temporally, but is sustained throughout the study period by the completion of sediment N mineralization (from organic N to NH_4^+ to NO_3^-). The relative stability of temperature within the conduit ($T_{avg} = 14.1 \pm 3.5$ °C) keeps nitrifying activity high and nitrification rates by bacteria at near constant levels throughout the year. Taken together, modeling results estimate that the karst SFGL acts as a net-nitrifier during wet conditions (Figure 5.9b).

Modeling results estimate that hot moments for N removal (i.e., net-denitrifying) occur during dry conditions when nitrification is limited in the karst SFGL. The dry conditions cause the karst SFGL to shift from a net N source to a net N sink (Figure 5.9c). Net DIN removal occurs as the denitrification and anammox fluxes exceed nitrification fluxes in the phreatic conduit (Figure 5.10a,b). Limited nitrification is reflected in the lack

of available NH_4^+ and DON input to the conduit given the low water recharge rates during the dry season. For example, the availability of reactive material on N transformation is reflected in the formulation for direct nitrification (Equation 17), which depends on NH_4^+ concentration in the conduit water. Other formulations, such as denitrification (Equation 14) are not dependent on reactive material concentration as our datasets justifies that NO_3^- was non-limiting (NO_3^- is on the order of 1 mg N L^{-1} or higher). Additionally, the stability of the karst SFGL bed provides year-long availability of sediment organic C to fuel the reaction (although the quality of sediment organic C does change bi-annually). At the same time, NO_3^- concentration data at the spring showed its lowest levels during these dry periods, which agrees with N removal (e.g., in Figure 5.9c, 60% NO_3^- removal in August 2012). Comparing the results of this conduit study to the results of the aquifer-scale study in Chapter 3, we see the impact of the conduit on NO_3^- concentration relative to other pathways (Table 5.5). The karst SFGL's impact on NO_3^- concentration is on the order of the soil reservoir. Net results are 8.9% reduction in NO_3^- concentration in the dry season and 3.6% increase in NO_3^- concentration in the wet season. Distributed across temporary and permanent N removal mechanisms, the proportions of reactive N in the water column removed by microbial immobilization, denitrification, and anammox are 18%, 47%, and 35%, respectively.

The subsurface karst SFGL shows similarities and differences with surface streams draining agricultural lands. Surface streams show high temperature dependence with low winter temperatures reducing production rates by orders of magnitude to near zero (White *et al.*, 1991; Thamdrup and Fleischer, 1998) and N transformation rates are near zero (Miller *et al.*, 2015). Light-absent karst obviously does not have light-dependent autotrophy and temperature dependence is relatively low due to the stability of temperature ($14.1 \pm 3.5 \text{ }^\circ\text{C}$) from the rock layers. The karst SFGL stability result contrasts with surface streams where high rainfall events have been shown to change the SFGL makeup and blanket the streambed with low-quality (recalcitrant) organic matter that would exhibit low nitrification from coupled C and N turnover (Arango and Tank, 2008; Ford *et al.*, 2015a). The net removal results during dry conditions are similar to nutrient dynamics in slow-moving surface waters with high nitrate concentration overlying agriculturally-derived

sediments, where denitrification dominates transformations (Birgand *et al.*, 2007; Arango and Tank, 2008; Zarnetske *et al.*, 2011).

In summary, results suggest that the karst SFGL's ability to act as a net N source or sink during hot moments is mostly controlled by water inputs. N dynamics in the wet season are heavily influenced by physical transport and hydrodynamic routing of surface-derived water through the subsurface conduit. The influence of physical factors on N dynamics during the dry season begins to wane and relative importance of biochemical drivers becomes more apparent. Thus, hot moment nutrient dynamics within karst SFGL are impacted by both hydrologic delivery and biochemical availability and turnover of material.

5.6.3 Hot spots in the karst SFGL

We find that hydrologic conditions also dictate spatial variability of the karst SFGL behavior. Hot spots for N turnover in the karst SFGL occur close to the sinking stream's entrance into the cave. That is, spatial variability, and in turn hot spots of NO_3^- turnover, are heavily influenced by longitudinal distribution of the C and N content of the karst SFGL (Figure 5.11). Peak N removal for most spatial cells occurs during the middle of summer in August (Figure 5.11a). During this time, the addition of NO_3^- by NH_4^+ oxidation is at its lowest due to dry season conditions, organic C has been deposited to the SFGL during the hydrologically wet spring and summer, conduit water temperatures are at their highest, and denitrification rates are also at their highest levels. However, N removal fluxes are higher in the upper sections of the conduit as compared to longitudinally downstream cells (Figure 5.11b). Within the upper reaches of the Cane Run watershed, the surface and subsurface are highly connected (~50 swallets per 10 km of stream) and intermittently recharge the karst SFGL with organic matter and nutrients from urban land. However, the downstream third of the karst SFGL is largely disconnected from the surface stream and relies on already-processed bed material (i.e., recalcitrant, low quality C) to be transported from upstream in the conduit. This low quality material provides less fuel for denitrification (Figure 5.11b,c). In summary, hot spots for N turnover in the karst SFGL occur close to the sinking stream's entrance into the karst cave. The reason is because the

fluid's energy to transport sediment is limited in phreatic karst, and therefore labile sediment C deposits after entering the cave and can fuel N turnover (Husic *et al.*, 2017a).

Hot spots for N turnover have not been discussed extensively for streams in caves, to our knowledge, but show parallels to surface streams and groundwater results. While agricultural surface streams are subject to quasi-seasonal C fluctuations based on autotrophy and heterotrophy (Arango and Tank, 2008; Ford *et al.*, 2015a), the karst SFGL behavior is more heavily influenced by hydrodynamic delivery of C diffused longitudinally across the conduit. Nonetheless, in both systems denitrification and anammox are influenced by organic C availability and anoxic conditions (Trimmer *et al.*, 2003; Rysgaard *et al.*, 2004) although some studies have shown less dependence of anammox on organic C availability (e.g., Kumar *et al.*, 2017). In a meltwater stream, spatial variability and the presence of benthic microbial mats highly influences potential denitrification rates (Gooseff *et al.*, 2004). Lastly, Hedin *et al.* (1998) showed hot spots of denitrification where two groundwater flow paths converge to form zones of high denitrification. Thus it is likely that spatial variability in the delivery and trapping of water, sediment C, and N largely influences the extent of N removal both in surface systems and in our subsurface cave.

One practical implication of explicitly representing the karst SFGL and its N hot moments and hot spots relates to field sampling agendas. The determination of locations to sample and the timing of data collection are important considerations for researchers as dissolved and particulate C and N can vary both spatially and temporally within a karst conduit. For example, when un-mixing sources of NO_3^- with stable isotopes ($^{15}\text{N}_{\text{NO}_3}$ and $^{18}\text{O}_{\text{NO}_3}$), researchers will often assume that baseflow water samples represent phreatic diffuse flow water. However, if samples are collected during a period of high N removal within the subsurface, source provenance results may be negatively affected.

Another implication of explicitly representing the karst SFGL and its hot moments and hot spots relates to the discussion of C, N and P limits in cave systems (Northup and Lavoie, 2001; Simon and Benfield, 2001), at least in the case of karst draining agricultural lands with high leaching of NO_3^- . In time, the non-dominant dissolved N (NH_4^+) limitation during low flow shifts the net behavior of the karst SFGL and cave overall from an N source to N sink. Spatially, available C becomes limited longitudinally downstream in the

cave due to microbial respiration and accumulation of recalcitrant C and therefore biological processes may favor N increases rather than removal (Figure 5.9). The latter point agrees with recent reports by others (Gallo *et al.*, 2014; Leigh *et al.*, 2016) that we need to do a better job to understand surficial inputs of C from rivers feeding karst systems.

5.6.4 Environmental drivers impacting the karst SFGL

Environmental drivers are predicted to increase hot moments and hot spots in karst SFGL in this wet temperate region (Figure 5.12). Peaks in NO_3^- removal will increase by an average of $16.7 \pm 18.6\%$ under 12 future scenarios that include conduit temperature, conduit flow rate, and land use changes to the watershed (Figure 5.12a). The trend for all scenarios above current base levels (Figure 5.12a) is a greater peak in the summer and a greater width to the length of time the karst conduit acts as a net-denitrifier. Increases are associated with greater temperatures (thus affecting reaction rates) and a shift towards a more labile C source (the urban sediment, in the case of the Cane Run Watershed). In particular, land use changes to the watershed will have the greatest impact on sediment C, N, and dissolved N processes (Figure 5.12b). Land use for the watershed is projected to approach 90% urban by 2057, a stark contrast to the current 40% urban land use. The quality of sediment entering the conduit will be most affected by this change. The sediment C content of urban sediment ($5.70 \text{ gC } 100\text{gSed}^{-1}$) is about 50% greater than agricultural sediment ($3.83 \text{ gC } 100\text{gSed}^{-1}$) in Cane Run thus providing more fuel to all reactions which rely on organic C.

Temperature has the smallest impact to the biogeochemistry of the subsurface karst SFGL (Figure 5.12b). Changes in air temperature over the next 30 years may be quite noticeable, but the effect that temperature has on karst conduit water is significantly dampened. As surface water enters the subsurface, it is cooled by the limestone bedrock. A significant change to the natural background temperature of the karst rock would have to occur for temperature effects on conduit N removal to have a significant effect. Thus, in the case of the karst SFGL, warming of the atmosphere and surface temperatures is not expected to significantly change hot spots and may slightly increase the intensity of hot moments when temperatures are highest (e.g., in August and September).

Changes to flow rate have some of the largest impacts to sediment delivery, N removal, and N turnover (or lack thereof) in the karst SFGL. Less mineralization of N and decomposition of C is projected to occur in the future, potentially due to eroding of the cave stream bed. Important to note is that the sediment transport model in this study was calibrated to current conditions (2011-2018) and as such was formulated to maintain long-term bed equilibrium. However, with an increasingly changing climate, this long-term bed equilibrium may shift towards net erosion or deposition. For this region, climate change is expected to generally increase flow rates (Al Aamery *et al.*, 2016), and a change in the amount volume of water discharged as baseflow, for example, could introduce clean water that has the energy to entrain sediment particles (Husic *et al.*, 2017). Projections of discharge change are difficult to constrain as they are derived from precipitation which is fraught with uncertainty (Hawkins and Sutton, 2011). While further work will need to be done to constrain results and potentially calibrate to future scenarios, projected changes in flow rate, land use, and temperature, will likely result in a net increase in NO_3^- removal.

5.7 CONCLUSIONS

The main conclusions of this chapter are the following:

- Stable nitrogen isotope signatures of sediments were significantly different for karst inputs and outputs, which allowed inference as to the net function of the karst SFGL. Stable isotopes were helpful in numerical model calibration, and coupling multi-objective calibration with stable isotope subroutines reduced uncertainty of N transformation rates.
- Hydrologically active (wet) conditions versus dry conditions controlled temporal variability of the karst SFGL behavior. Hot moments occur during dry conditions when nitrification is limited in the karst SFGL. The dry conditions cause the karst SFGL to shift from a net N source to a net N sink.
- Hydrologic conditions also dictate spatial variability of the karst SFGL behavior. Hot spots for N turnover in the karst SFGL occur close to the sinking stream's entrance into the cave. The reason is because the fluid's energy to transport sediment is limited in phreatic karst, and therefore labile sediment carbon deposits soon after entering the cave, fueling N turnover.

- Environmental drivers are predicted to increase hot moments and hot spots in karst SFGL in this wet temperate region. Climate change associated with temperature and land use change associated with urbanization will cause increases to the duration and intensity of hot moments. The effect of climate changes to precipitation is not clear, but may lead to greater denitrification and lower residence time of sediment.

5.8 TABLES AND FIGURES

Table 5.1 Summary of dominant processes in subsurface karst SFGL. Note: justification for excluding a process is noted by a parenthetical in the process description.

Process Name	Modeled in This Study?	Description of Process
Erosion	Yes	Detachment of sediment particles from the SFGL
Deposition	Yes	Sedimentation of suspended particles to the SFGL
Mixing	Yes	Mixing of suspended and C & N during net-zero erosion-deposition
Decomposition	Yes	Degassing of organic C as dissolved inorganic C
Mineralization	Yes	Conversion of organic N into mineral N
Immobilization	Yes	Incorporation of inorganic N into biomass by heterotrophs
Direct Nitrification	Yes	Oxidation of stream-water ammonium to nitrate
Indirect Nitrification	Yes	Oxidation of mineralized ammonium to nitrate
Denitrification	Yes	Anaerobic reduction of nitrate to nitrogen gas
Anammox	Yes	Anaerobic oxidation of ammonium to nitrogen gas
Plant Uptake	No	Assimilation of inorganic N by autotrophs (requires light)
Photoautotrophy	No	Assimilation of DIC for primary production (requires light)
Chemoautotrophy	No	Oxidation of electron donors not requiring light (abundant organic carbon present in conduit)
Fixation	No	Conversion of dissolved N gas to ammonium (not open to atmosphere)
Volatilization	No	Conversion of ammonia to ammonia gas (not open to atmosphere i.e. no air exchange)
DNRA	No	Dissimilatory nitrate reduction to ammonium (no NO ₂ ⁻ accumulation)
Sorption/Desorption	No	Abiotic attachment of ions to substrate (Relatively low mean NH ₄ ⁺ concentrations and well-mixed SFGL)

Table 5.2 Nitrogen transformations, equations, terms and units, and associated references.

Reaction	Equation	Terms and Units	Reference
Denitrification	$N_{DEN(i)}^{(j)} = \beta_{Den} \left(C_{SFGL(i)}^{(j)} \right)^{\alpha_{Den}} \times SA_{(i)}^{(j)} \times \theta_{DEN}^{(T_i - T_{ref})} \times \Delta t, \quad (14)$	β_{Den} = Coefficient for denitrification (kg N m ⁻² s ⁻¹) α_{Den} = exponent calibration coefficient (assumed equal to 1) C_{SFGL} = carbon content of bed SA = surface area of bed (kg) θ_{DEN} = temperature coef. for DEN	Arango and Tank, 2008 Ford et al., 2017 Veraart et al., 2011
Indirect Nitrification	$N_{IN(i)}^{(j)} = \beta_{IN} \left(C_{SFGL(i)}^{(j)} \right)^{\alpha_{IN}} \times SA_{(i)}^{(j)} \times \theta_{IN}^{(T_i - T_{ref})} \times \Delta t, \quad (15)$	β_{IN} = Coefficient for indirect nitrification (kg N m ⁻² s ⁻¹) α_{IN} = exponent calibration coefficient (assumed equal to 1) θ_{IN} = temperature coef. for IN	Arango and Tank, 2008 Ford et al., 2017 Bowie et al., 1985
Anammox	$N_{ANA(i)}^{(j)} = \beta_{ANA} \left(C_{SFGL(i)}^{(j)} \right)^{\alpha_{ANA}} \times SA_{(i)}^{(j)} \times \theta_{ANA}^{(T_i - T_{ref})} \times \Delta t, \quad (16)$	β_{ANA} = Coefficient for anammox (kg N m ⁻² s ⁻¹) α_{ANA} = exponent calibration coefficient (assumed equal to 1) θ_{ANA} = temperature coef. for ANA	Kumar et al., 2017 rates after Arango and Tank, 2008 formulation of other N reactions
Direct Nitrification	$N_{directN(i)}^{(j)} = k_{nitr} \times NH_4^+_{(i)}^{(j)} \times \theta_{directN}^{(T_i - T_{ref})} \times \Delta t, \quad (17)$	k_{nitr} = first order rate constant for nitrification (d ⁻¹) $\theta_{directN}$ = temperature coef. for direct	Bowie et al., 1985 Ryzhakov et al. 2010
Mineralization (DON)	$N_{min\ DON(i)}^{(j)} = k_{min\ DON} \times DON_{(i)}^{(j)} \times \theta_{min\ DON}^{(T_i - T_{ref})} \times \Delta t, \quad (18)$	k_{min} = first order rate constant for mineralization (d ⁻¹) $\theta_{min\ DON}$ = temperature coef. for min DON	Bowie et al., 1985 Ryzhakov et al. 2010
Mineralization (Sediment)	$N_{min\ Sed(i)}^{(j)} = \sum_{j=1}^{n_p} k_{min\ j} S_{N\ Sed\ j} \times r(T)_i \times \Delta t, \quad (19)$	p = index for nitrogen pool (i.e., litter, soil, algae) n_p = total number of pools $k_{min\ j}$ = mineralization rate of each pool (d ⁻¹) $S_{N\ Sed\ j}$ = supply of sediment N of each pool (kg N)	Ford et al., 2017 Reichstein et al., 2000
Immobilization	$N_{imm(i)}^{(j)} = \sum_{j=1}^{n_p} k_{imm\ j} S_{N\ Sed\ j} \times r(T)_i \times \Delta t, \quad (20)$	$k_{imm\ j}$ = immobilization rate of each pool (d ⁻¹)	Lin et al., 2017 Reichstein et al., 2000

Table 5.3 Model inputs, sediment nitrogen and $\delta^{15}\text{N}_{\text{sed}}$ model parameter ranges and calibrated values, and dissolved N model parameter ranges and calibrated values.

Symbol	Description	Value	Unit	Source	
L	Spatial step	1000	[m]		
Δ	Temporal step	3600	[s]		
Q_{10}	Temperature coefficient of biological activity	2.77	[-]	Reichstein et al., 2000, 2005	
T_{ref}	Reference temperature for reactions	20	[°C]	Bowie et al., 1985	
$C_{DON-rec}$	Concentration of DON recharge	0.30	[mg N L ⁻¹]	Measured on site	
$C_{NH4-rec}$	Concentration of NH ₄ ⁺ recharge	0.12	[mg N L ⁻¹]	Measured on site	
$C:N_{soil}$	Carbon to Nitrogen ratio of soil	12.4	[-]	Ford et al., 2015	
$C:N_{litter}$	Carbon to Nitrogen ratio of litter	12.0	[-]	Liao et al., 2006	
$C:N_{algae}$	Carbon to Nitrogen ratio of algae	10.3	[-]	Ford et al., 2015	
$\delta^{15}\text{N}_{immob\text{ile}}$	$\delta^{15}\text{N}$ value of N immobilized by sediment biota	7.22	[‰]	Measured on site	
$\delta^{15}\text{N}_{soil}$	$\delta^{15}\text{N}$ value of soil N	6.85	[‰]	Ford et al., 2015	
$\delta^{15}\text{N}_{litter}$	$\delta^{15}\text{N}$ value of litter N	3.90	[‰]	Kendall et al., 2001	
$\delta^{15}\text{N}_{algae}$	$\delta^{15}\text{N}$ value of algae N	4.95	[‰]	Ford et al., 2015	
Sediment Nitrogen and $\delta^{15}\text{N}_{\text{sed}}$ Model Parameters		Parameter Range	Calibrated Value	Unit	Source
$k_{min-soil}$	Soil mineralization rate	$2.6 \times 10^{-6} - 2.3 \times 10^{-4}$	3.6×10^{-4}	[d ⁻¹]	Ford et al., 2017; Lin et al., 2016
$k_{min-litter}$	Litter mineralization rate	$2.3 \times 10^{-4} - 8.0 \times 10^{-3}$	4.2×10^{-3}	[d ⁻¹]	Ford et al., 2017; Lin et al., 2016
$k_{min-algae}$	Algae mineralization rate	$2.3 \times 10^{-4} - 8.0 \times 10^{-3}$	5.2×10^{-3}	[d ⁻¹]	Ford et al., 2017; Lin et al., 2016
$k_{imm-soil}$	Soil immobilization rate	$2.6 \times 10^{-6} - 2.3 \times 10^{-4}$	2.7×10^{-4}	[d ⁻¹]	Lin et al., 2016
$k_{imm-litter}$	Litter immobilization rate	$2.3 \times 10^{-4} - 8.0 \times 10^{-3}$	3.2×10^{-3}	[d ⁻¹]	Lin et al., 2016
$k_{imm-algae}$	Algae immobilization rate	$2.3 \times 10^{-4} - 8.0 \times 10^{-3}$	3.9×10^{-3}	[d ⁻¹]	Lin et al., 2016
Dissolved Nitrogen Model Parameters		Parameter Range	Calibrated Value	Unit	Source
β_{IN}	Coefficient for indirect nitrification	$5 \times 10^{-10} - 5 \times 10^{-7}$	2.19×10^{-8}	[kg N m ⁻² s ⁻¹]	Mulholland et al, 2008; Ford et al. 2017
β_{DEN}	Coefficient for denitrification	$5 \times 10^{-10} - 5 \times 10^{-7}$	2.61×10^{-8}	[kg N m ⁻² s ⁻¹]	Mulholland et al, 2008; Ford et al. 2017
β_{ANA}	Coefficient for anammox	$5 \times 10^{-10} - 5 \times 10^{-7}$	2.34×10^{-8}	[kg N m ⁻² s ⁻¹]	Kumar et al., 2017
$k_{min-DON}$	First-order mineralization constant	0 – 0.04	0.01	[d ⁻¹]	Ryzhakov et al. 2010
k_{nitr}	First-order direct nitrification constant	0 – 0.68	0.25	[d ⁻¹]	Ryzhakov et al. 2010

Table 5.4 a) Relative air temperature shifts (all increases) for 2057 using GCM ensemble results. b) Relative conduit water temperature shifts (all increases) for 2057 using GCM ensemble results. c) Relative mean flow shifts for 2057 using GCM ensemble results. Results for ± 1 standard deviation (σ) from the projected mean are shown. d) Forecasted scenarios for land cover change for 2057.

Month	a) Air Temperature Changes			b) Conduit Temperature Changes		
	Mean ΔT ($^{\circ}C$)	$\Delta T+1\sigma$ ($^{\circ}C$)	$\Delta T-1\sigma$ ($^{\circ}C$)	Mean ΔT ($^{\circ}C$)	$\Delta T+1\sigma$ ($^{\circ}C$)	$\Delta T-1\sigma$ ($^{\circ}C$)
January	2.7	3.3	2.2	0.5	0.6	0.4
February	2.0	3.0	1.0	0.3	0.5	0.2
March	1.8	3.1	0.5	0.5	0.9	0.1
April	2.2	3.2	1.2	0.7	1.0	0.4
May	2.8	3.8	1.7	0.8	1.2	0.5
June	3.4	4.4	2.5	0.4	0.5	0.3
July	3.7	5.6	1.8	0.1	0.1	0.0
August	4.0	5.8	2.2	0.0	0.1	0.0
September	4.2	5.8	2.7	0.6	0.9	0.4
October	3.5	4.5	2.5	0.5	0.7	0.4
November	2.7	3.5	1.8	0.4	0.5	0.3
December	2.9	4.2	1.6	0.5	0.7	0.3
Month	c) Percent Change in Flow			d) Land Use Projections		
	Mean ΔQ (%)	$\Delta Q+1\sigma$ (%)	$\Delta Q-1\sigma$ (%)	Scenario	Urban (%)	Agriculture (%)
January	26.6	48.8	4.3	A2	84	16
February	21.1	38.1	4.2	A1B	93	7
March	14.8	38.6	-8.9	B1	88	12
April	24.9	50.8	-0.9			
May	-2.4	19.3	-24.1			
June	-11.0	11.8	-33.8			
July	1.8	36.5	-32.9			
August	10.0	44.0	-23.9			
September	17.3	52.4	-17.8			
October	-2.2	29.8	-34.3			
November	-0.4	23.8	-24.6			
December	33.8	53.4	14.3			

Table 5.5 Fate of NO_3^- during temporary residence within karst soil, epikarst, matrix, and conduit (SFGL) zones. Soil, epikarst, and matrix results are from Chapter 3. The SFGL zone is further subdivided to highlight seasonality of conduit N transformation. MRT = mean residence time (see Chapter 3 for MRT method and results).

	Soil	Epikarst	Matrix	SFGL (dry)	SFGL (wet)
Inflow (mg N L^{-1})	1.66	3.44	3.18	2.03	3.34
Outflow (mg N L^{-1})	3.09	3.21	2.79	1.90	3.39
MRT (d)	25.0	41.2	148.2		1.5
Change ($\Delta\text{N d}^{-1}$)	+5.7%	-0.6%	-0.3%	-8.9%	+3.6%

Figure 5.1 Lighted photograph of the karst SFGL from an underwater camera placed in a groundwater well that intersects a phreatic conduit 20 meters below the ground surface. SFGL = “surficial fine-grained laminae”.

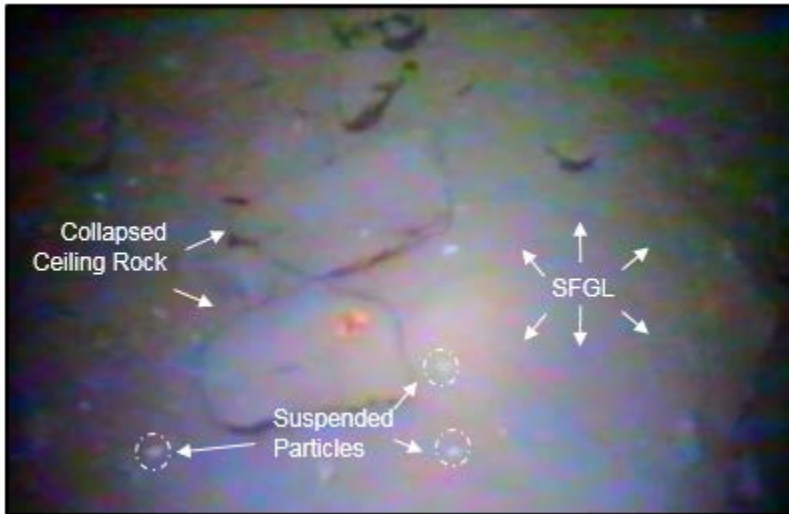


Figure 5.2 (a) Conceptual model of sediment carbon (SOC) and nitrogen (SN) delivery, trapping, and export in fluvio-karst system. Emboldened text indicates processes. (b) Transect of a phreatic conduit illustrating dominant processes. Inflow of SOC and SN is supplied by quickflow pathways and inflow of dissolved inorganic N and dissolved organic N is supplied by quickflow, fracture, and matrix pathways. Physical processes include deposition, erosion, and equilibrium mixing. Biochemical processes include N immobilization, mineralization, nitrification, denitrification, anammox, and C decomposition.

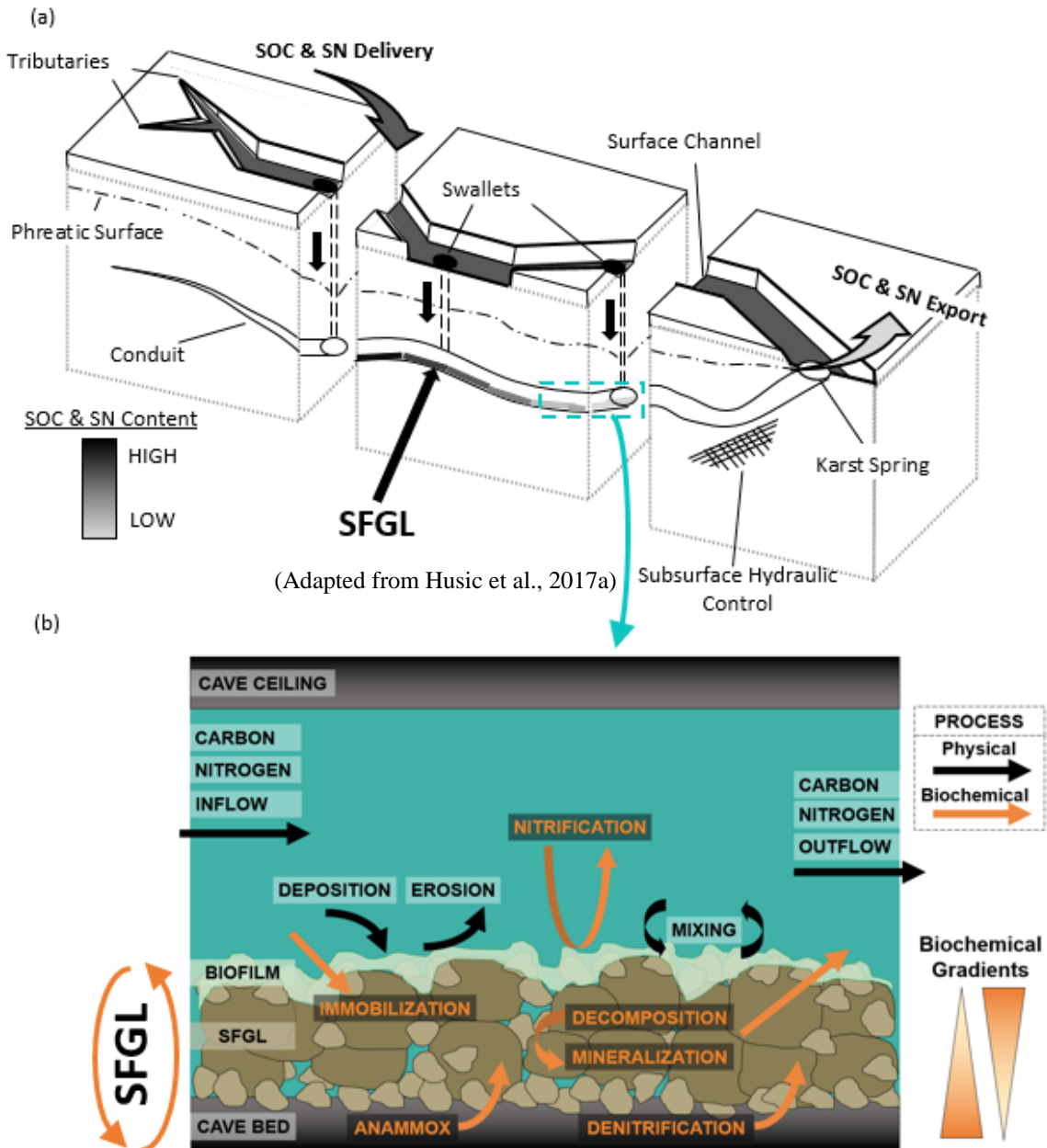
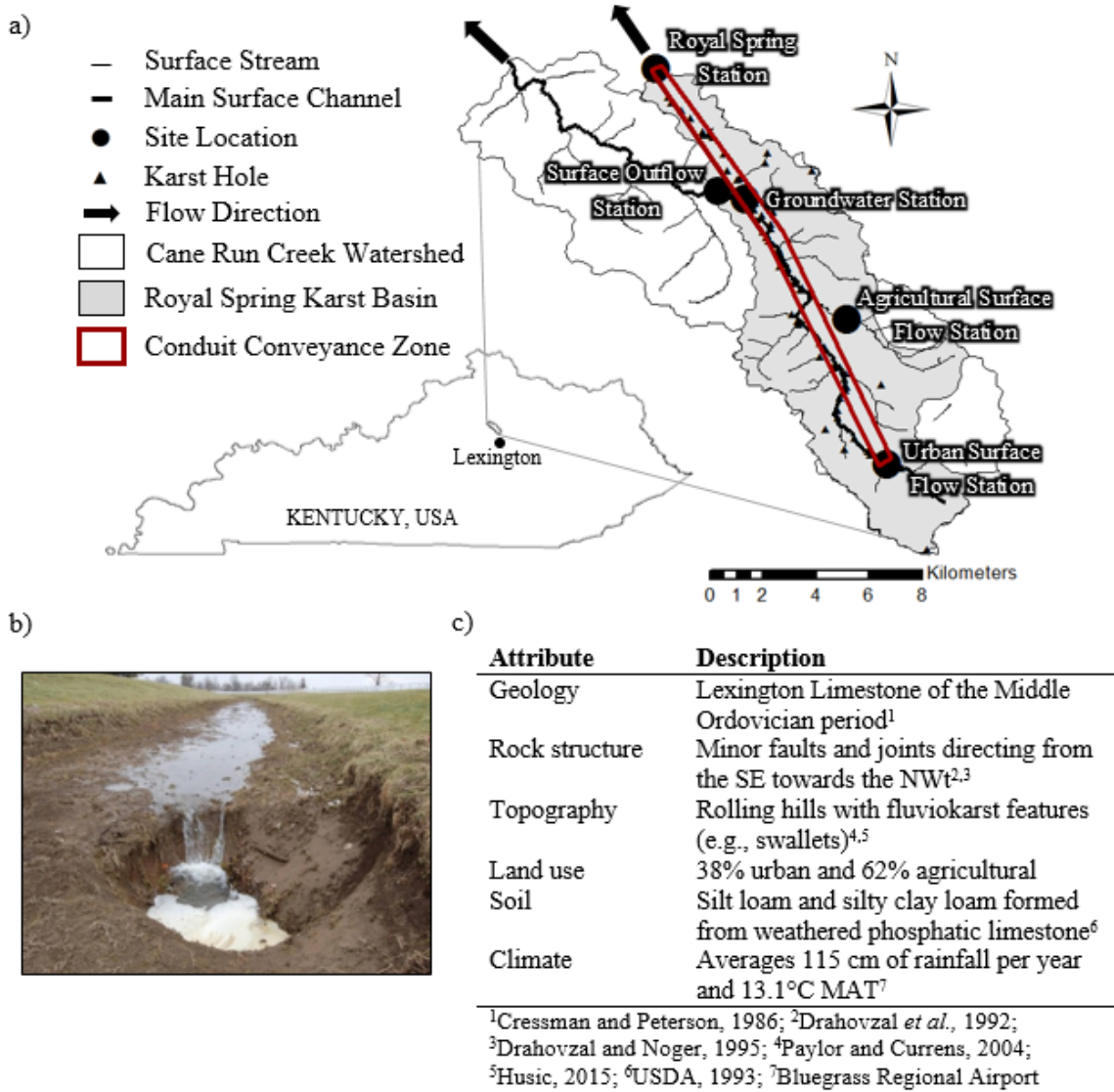


Figure 5.3 (a) Cane Run watershed and Royal Spring basin, (b) karst swallet pirating surface flow during low flow, and (c) watershed attributes



(Adapted from Husic *et al.*, 2017a)

Figure 5.4 Sediment N concentration (C_{SN}), sediment N isotope ($\delta^{15}N_{Sed}$), and nitrate (C_{NO_3}) modeling framework. STAGE 1: Model inputs from previously published water, sediment, and carbon (Husic *et al.*, 2017a,b), and NO_3^- pathway recharge (Chapter 3) results. STAGE 2: Sediment N and $\delta^{15}N_{Sed}$ modeling. Immobilization and mineralization rates (k_{imm} and k_{min}) of nitrogen pools (i.e., algae, litter, and soil) were calibrated and evaluated using a t-test. STAGE 3: Dissolved nitrogen (NO_3^- , NH_4^+ , and DON) modeling. Sensitive rates (β_{DEN} and k_{nitr}) were calibrated to match model results to C_{NO_3} data.

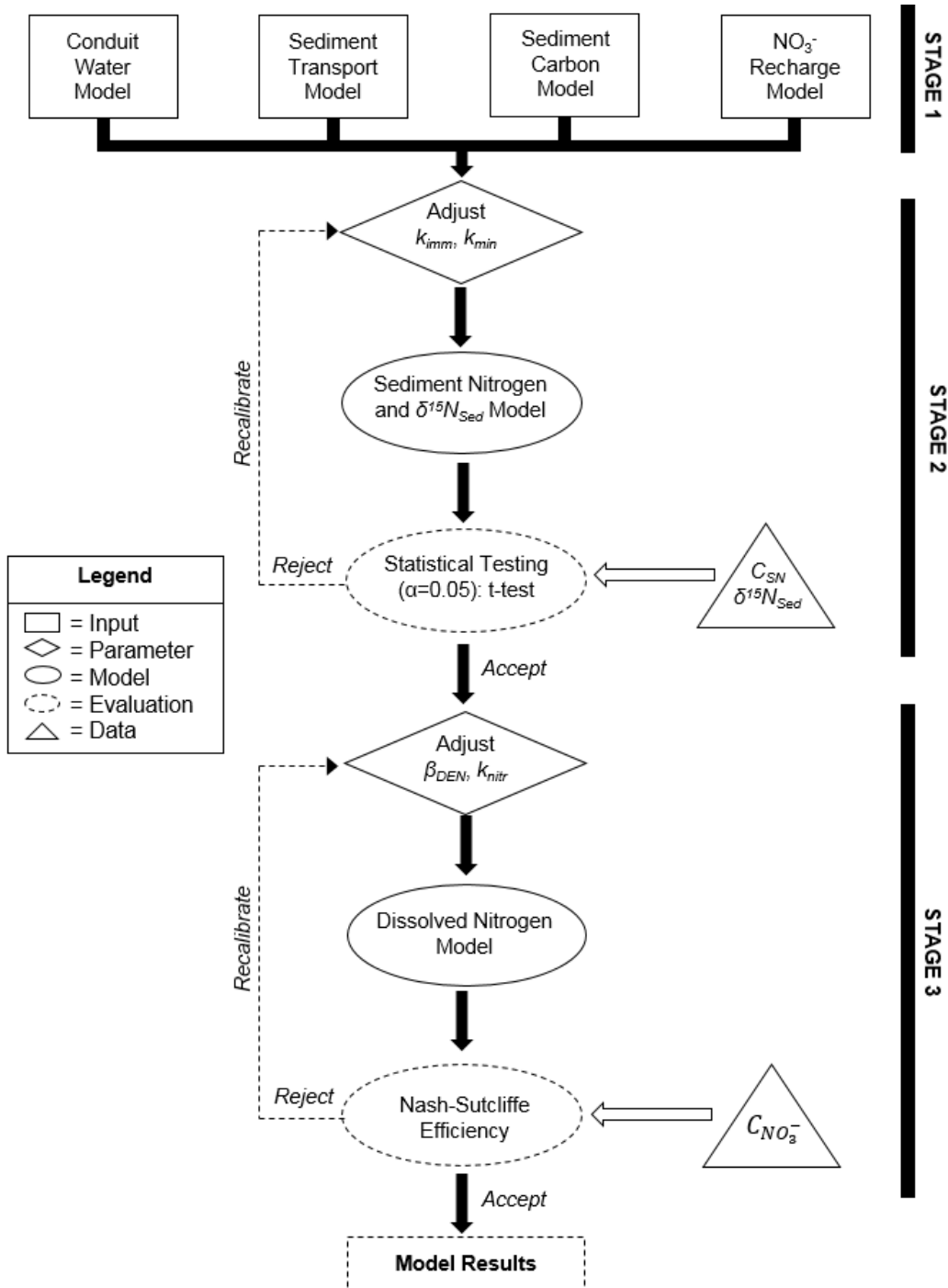


Figure 5.5 Elemental and isotopic data results for (a) stable nitrogen isotope of sediment ($\delta^{15}N_{Sed}$), and (b) sediment nitrogen (SN) at two surface tributaries (Spindletop and Lexmark) and the conduit discharge point (Royal Springs).

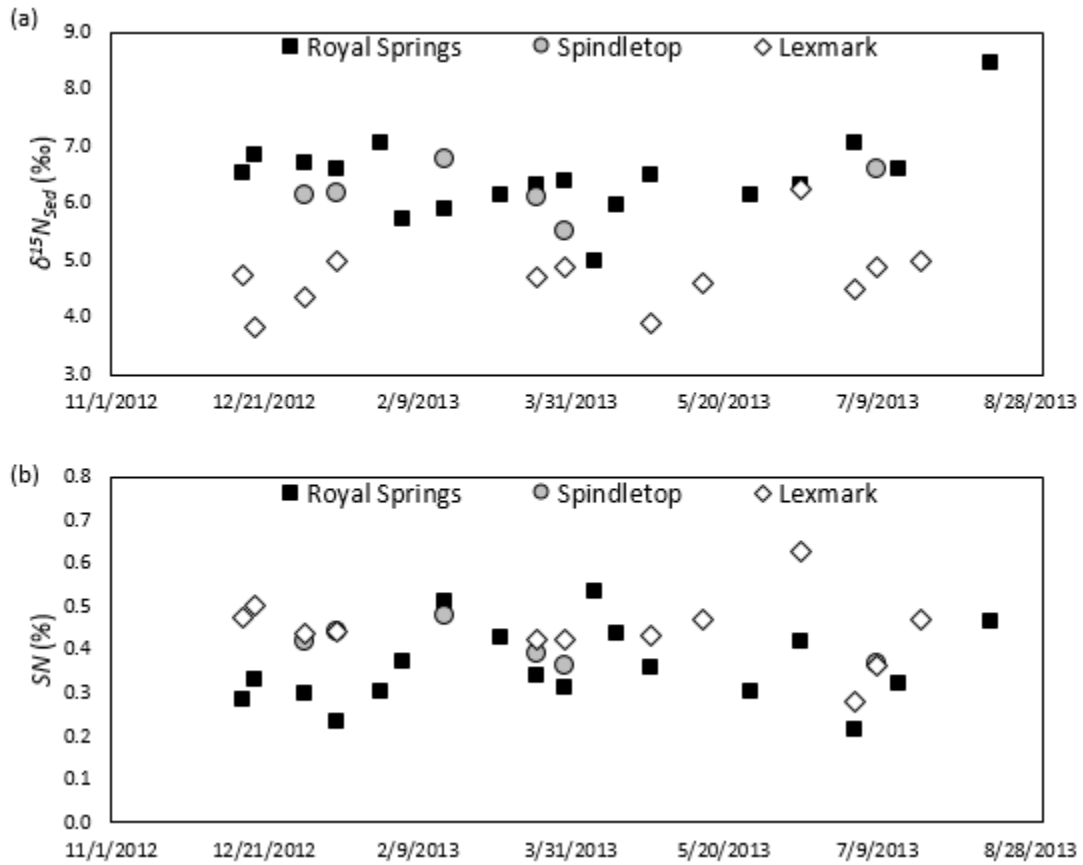


Figure 5.6 Modeled results of (a) SOC, (b) SN, (c) $\delta^{13}C_{Sed}$, and (d) $\delta^{15}N_{Sed}$ at Royal Spring. Legend: Blue line indicates composition of suspended sediment, solid black line indicates composition of the SFGL, and dashed black line indicates average composition of pirated surface sediment. Black and red bars represent data and model results with the width of each bar describing the deployment duration of the temporally-integrated sediment trap sample.

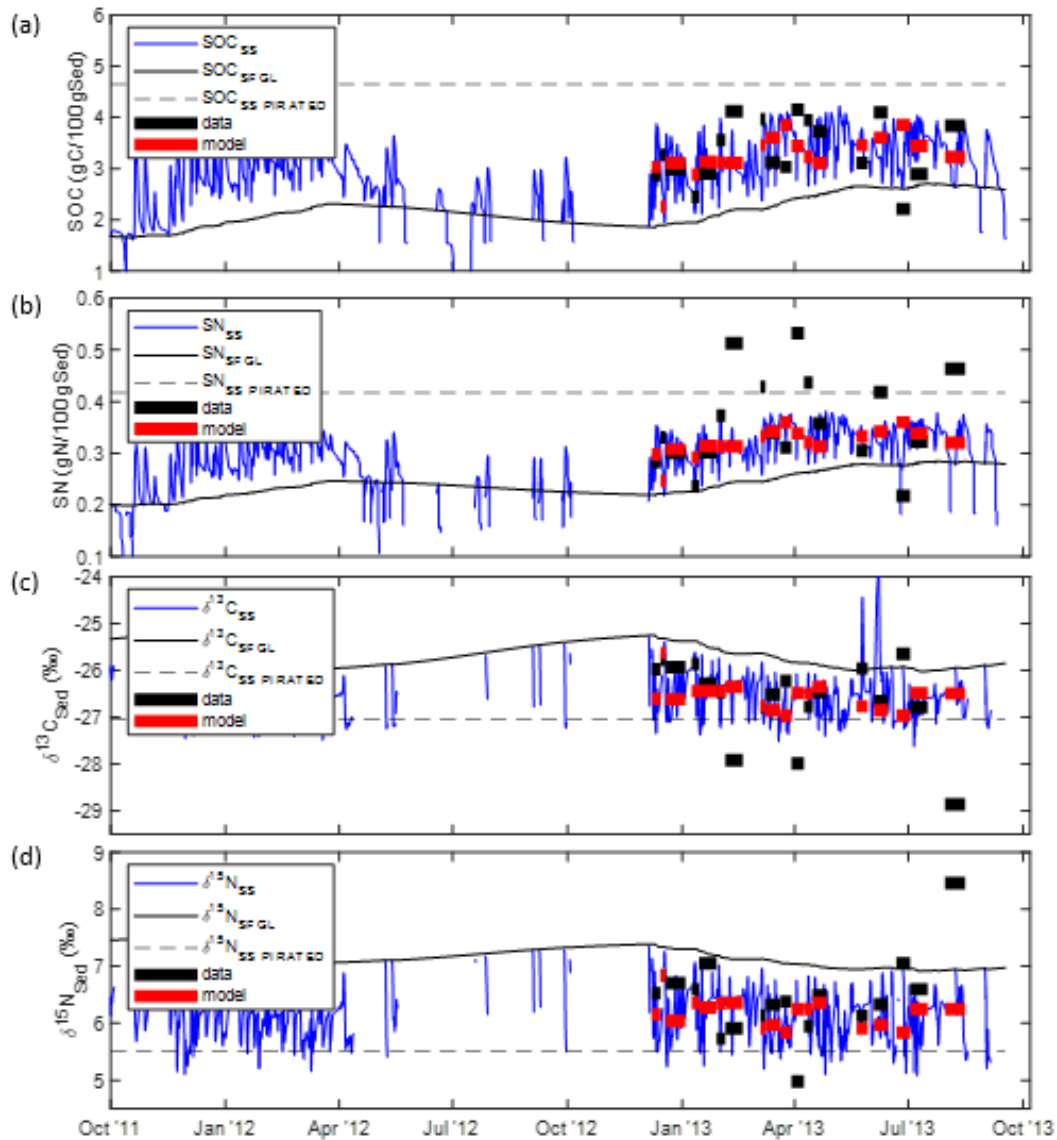


Figure 5.7 Histogram distribution of data and model results at Royal Spring (n = 18) for (a) SOC, (b) SN, (c) $\delta^{13}C_{Sed}$, and (d) $\delta^{15}N_{Sed}$.

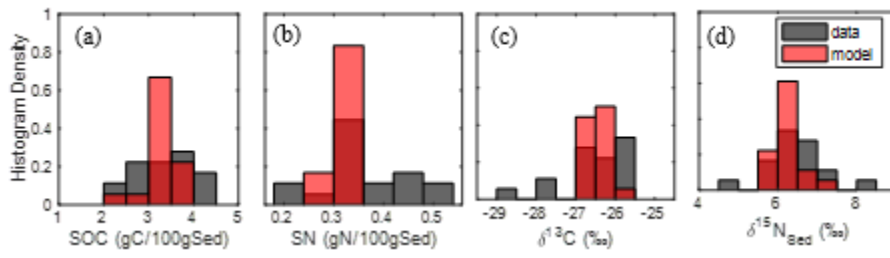


Figure 5.8 Measured vs modeled NO_3^- concentrations. The model simulates the typical range of observed NO_3^- (0 to 4 mg N L^{-1}) well. Three data points during disproportionately affect model statistics and are associated with a transient event of high NO_3^- flushing.

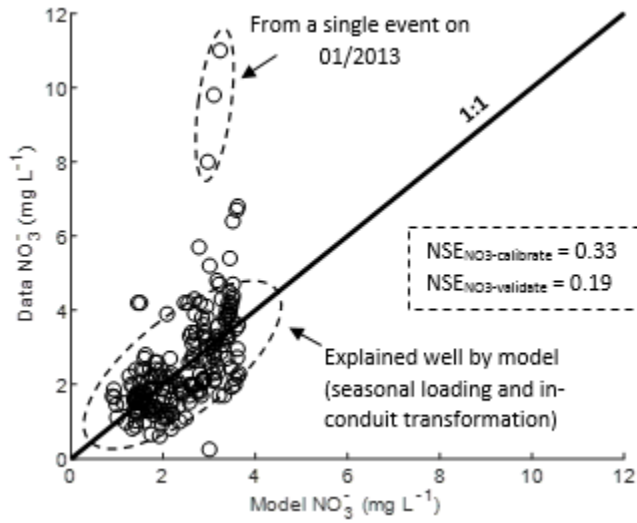


Figure 5.9 Time-series of modeled NO_3^- concentrations for water recharging the conduit (inflowing) and water discharging at KYHP (outflowing). (a) During the entire study period, (b) zoomed-in view a wet season (net-nitrifying), and (c) zoomed-in view of a dry season (net-denitrifying). Shaded regions indicate dry seasons.

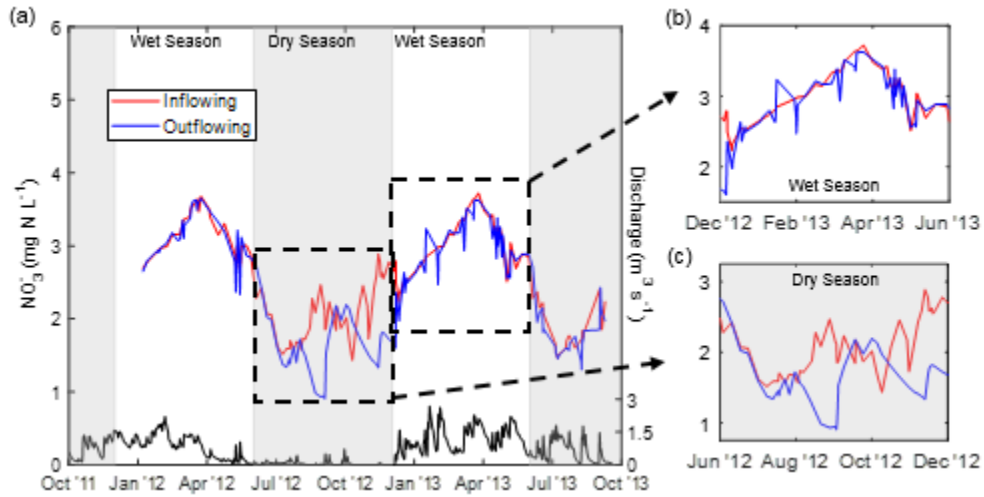


Figure 5.10 Mean (i.e. averaged over the entire conduit) transformations and removal of (a) NH_4^+ and (b) NO_3^- over the two-year study period. For example, positive NO_3^- removal values represent NO_3^- losses (e.g. denitrification) whereas negative removal values represent additions to the NO_3^- pool (e.g. nitrification). Spring discharge is shown on the secondary axis. Shaded regions indicate dry seasons.

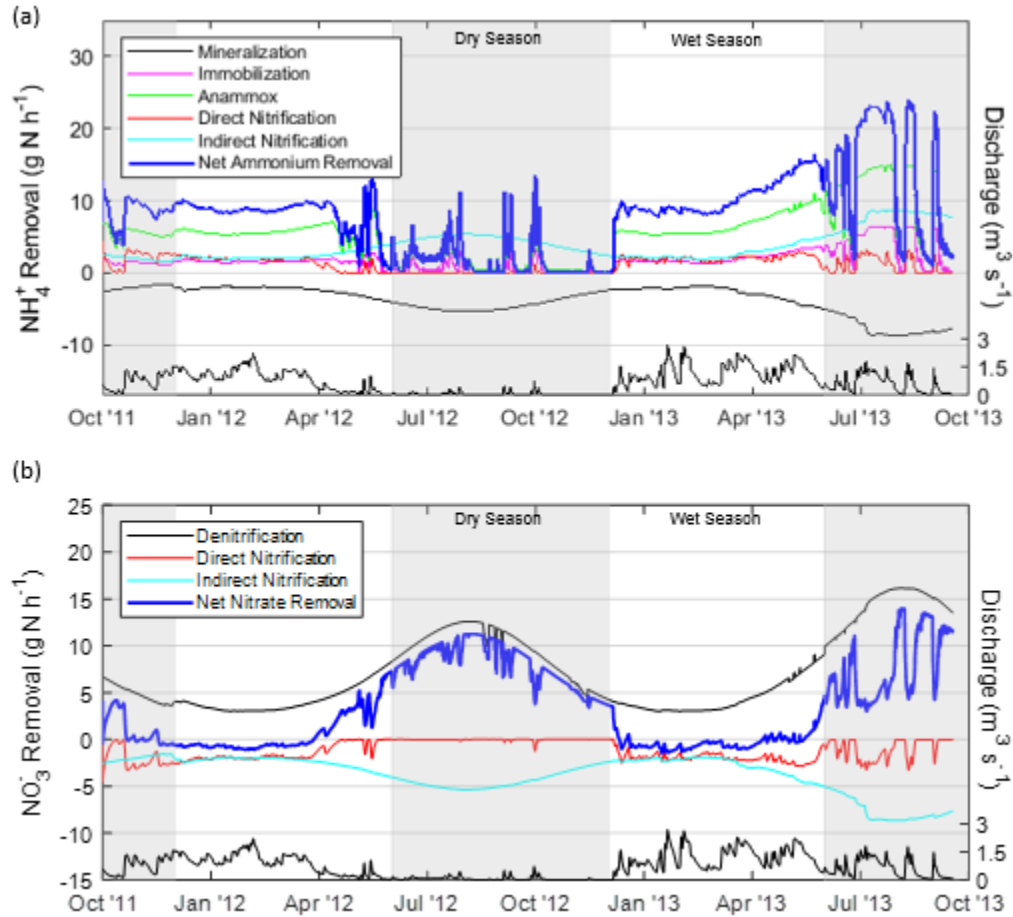


Figure 5.11 (a) Modeled NO_3^- removal and (b) modeled sediment carbon and (c) nitrogen content as they vary spatially within the karst SFGL over the course of the two year study period. Positive NO_3^- removal values represent aggregate NO_3^- losses (e.g. denitrification) whereas negative removal values represent additions to the NO_3^- pool (e.g. nitrification). Results indicate that cells with greater sediment carbon contents remove relatively more NO_3^- during the dry season and contribute relatively less NO_3^- during the wet season. Additionally, upstream cells (spatial steps 1 to 10) are more well-connected to labile organic inputs from the surface than are downstream cells (spatial step 11 to 16). Gaps in continuous modeling indicate that a substrate was exhausted (i.e. complete erosion of SFGL). Shaded regions indicate dry seasons.

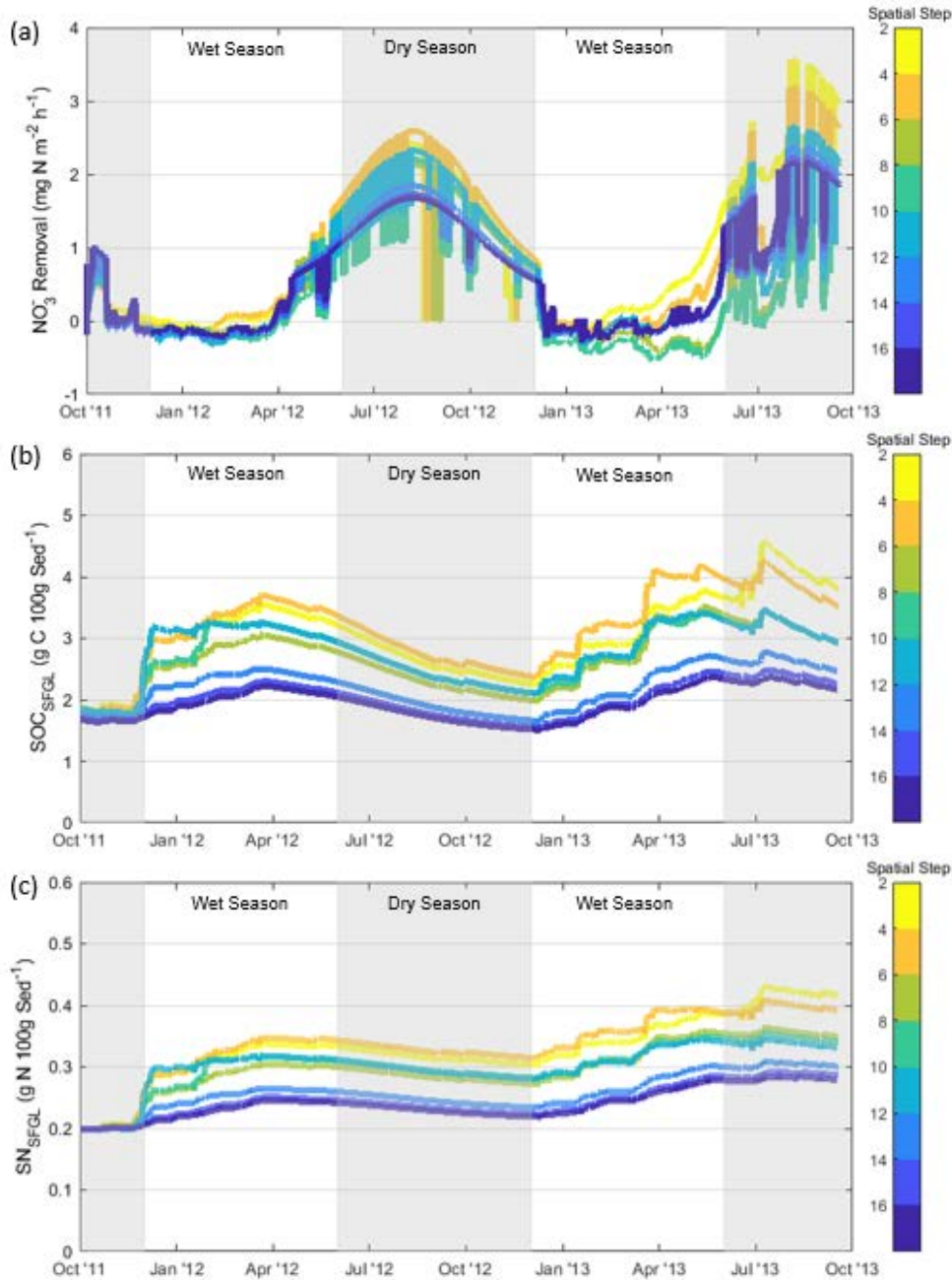
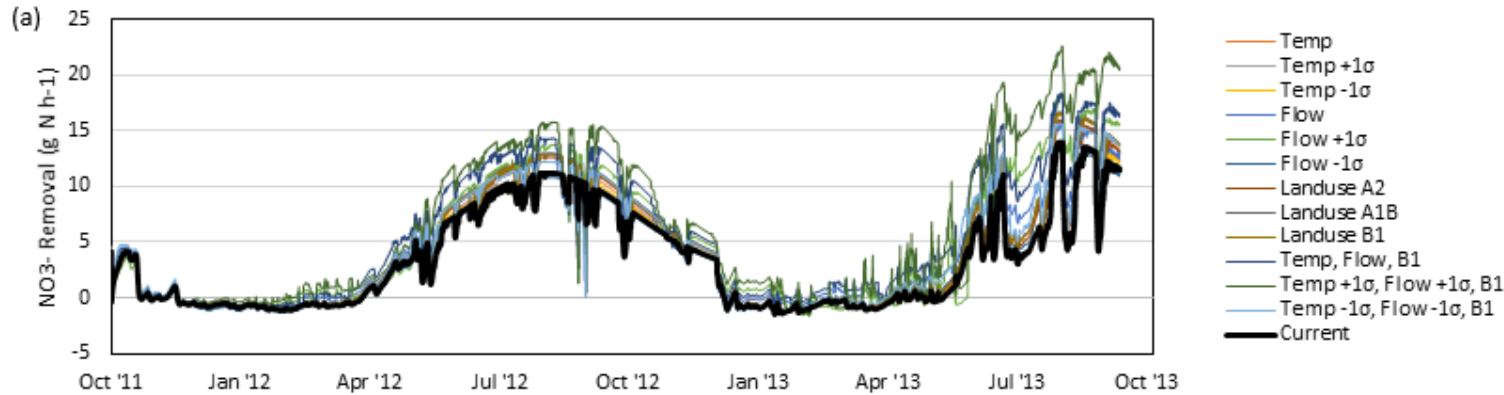


Figure 5.12 (a) Change in net-nitrate removal in karst SFGL under varying temperature, flow discharge, and land use 2057 scenarios. (b) Percent change in model yields and fluxes under varying temperature, flow discharge, and land use 2057 scenarios.



(b) Scenario	SOC _{in} (%)	SOC _{dec} (%)	TN _{in} (%)	TN _{min} (%)	TN _{imm} (%)	NO ₃ ⁻ Den (%)	NH ₄ ⁺ nitrit (%)	NH ₄ ⁺ ana (%)
Current	0.0	0.0	0.0	0.0	0.0	0.0	0.0	0.0
Temp	0.1	3.4	0.0	3.8	3.8	5.0	3.3	2.4
Temp +1σ	0.4	3.5	0.5	4.2	4.2	7.6	3.8	3.7
Temp -1σ	0.1	1.6	0.0	1.8	1.8	2.8	1.7	1.1
Flow	14.2	-20.4	14.2	-23.2	-23.2	7.5	-16.2	5.8
Flow +1σ	39.0	-50.1	39.2	-53.7	-53.7	7.0	-35.1	5.5
Flow -1σ	-10.1	0.8	-10.1	2.0	2.0	-2.3	-0.9	-7.5
Land use A2	17.5	11.1	17.8	11.1	11.1	12.0	7.4	8.7
Land use A1B	22.0	14.1	22.3	13.9	13.9	15.1	9.3	11.0
Land use B1	21.2	14.9	21.3	14.5	14.5	14.4	9.7	10.2
Temp, Flow, B1	36.4	-5.4	36.4	-8.6	-8.6	27.0	-5.7	18.7
Temp +1σ, Flow +1σ, B1	67.3	-40.0	67.7	-43.6	-43.6	31.3	-27.7	21.5
Temp -1σ, Flow -1σ, B1	7.6	16.1	7.8	17.2	17.2	13.6	9.8	1.8

Chapter 6: Nitrate removal in a phreatic karst conduit: estimating nitrification and denitrification rates by coupling stable isotope data with numerical modeling

6.1 ABSTRACT

Nitrate (NO_3^-) removal estimates in turbulent karst groundwater pathways are lacking due, in part, to the difficulty of accessing highly heterogeneous subsurface environments. To address this knowledge and methodological gap, we collected daily NO_3^- , $\delta^{15}\text{N}_{\text{NO}_3}$, and $\delta^{18}\text{O}_{\text{NO}_3}$ data for 65 consecutive days at a subsurface phreatic karst conduit and the spring it feeds, and we develop a numerical model of NO_3^- isotope dynamics to help provide closure of N transformation rates in the subsurface. The phreatic karst conduit in this study showed usefulness as a closed system experiment to investigate N transformation in karst. During the study period, the investigated portion of the karst sinking stream acts as a net source of NO_3^- via net nitrification, albeit with evidence of denitrification of soil organic nitrogen, fertilizer N, and manure N sources. The isotope-aided numerical model greatly reduced uncertainty (i.e., solution domain reduced by 99%) when estimating NO_3^- removal for the karst sinking stream. The karst sinking stream's NO_3^- removal ($16.8 \pm 21.5 \text{ mg N m}^{-2} \text{ d}^{-1}$) falls between the bounds of groundwater systems ($\sim 1 \text{ mg N m}^{-2} \text{ d}^{-1}$) and surface water systems ($\sim 100 \text{ mg N m}^{-2} \text{ d}^{-1}$). The areal extent of karst sinking streams, caves, and phreatic conduits may be limited, but results suggest they have disproportionately greater effects on NO_3^- removal relative to other groundwater pathways. This contribution shows the efficacy of ambient N isotope data to reflect N transformation in subsurface karst, highlights the usefulness of stable isotopes to assist with water quality numerical modelling in karst, and provides a rare, if not unique, reported estimate of N fate in karst conduits.

6.2 INTRODUCTION

Subsurface karst pathways including sinking streams, caves, fractures, and matrix pores have recently been reported to transform NO_3^- and ammonium (NH_4^+) (McCormack *et al.*, 2016; Orr *et al.*, 2016). Dissolved nitrogen in sinking streams may have shorter residence times relative to other groundwater stores, suggesting a decreased importance of N removal, especially during hydrologic events (McMahon, 2001; McCallum *et al.*, 2008; Jahangir *et al.*, 2013; Orr *et al.*, 2016). However, unlike matrix and fracture pathways, the availability of sediment organic carbon in karst conduits, by way of sinking streams, can fuel heterotrophic denitrifiers, analogous to sediments in surface streams (Chapter 5). This process occurs in the cave bed, and we adopt sediment transport terminology and call the thin sediment layers stored in subsurface karst the ‘surficial fine-grained laminae’, or SFGL (Droppo and Stone, 1994; Stone and Droppo, 1994; Russo and Fox, 2012). The bioavailable carbon entering the subsurface via sinking streams suggests that karst conduits could have disproportionate effects on NO_3^- transformation and removal relative to other groundwater pathways over the same time period.

At the watershed scale, karst basins have been shown to turn over N through analysis of surface soil N inputs and springhead NO_3^- loads (McCormack *et al.*, 2016). However, few, if any studies report N transformations, including denitrification, for sinking streams and phreatic conduits (Yue *et al.*, 2018). One major reason for the lack of reporting is access. Subsurface karst conduits are often difficult to locate even with a variety of geophysical methods (Zhu *et al.*, 2011). Additionally, if located, they are difficult to access in such a way that net upstream-to-downstream N fate analysis can be performed. One possible solution is that subsurface sediment discharged by karst springs (Reed *et al.*, 2010; Husic *et al.*, 2017a) could be collected and investigated via lab incubation studies. However, past review has shown lab incubations, and fundamental investigation of N turnover, show an order-of-magnitude higher difference relative to apparent N turnover rates derived from field assessments (Birgand *et al.*, 2007). Therefore, our motivation was to estimate N transformation and turnover from within a karst conduit using field assessment methods.

A number of method advances are needed to estimate N turnover in a phreatic karst conduits. One method advancement needed is to intersect a conduit. The probability of

randomly drilling into a karst conduit is incredibly low (Zhu *et al.*, 2011). In addition to being improbable, indiscriminate drilling is also incredibly resource intensive and intrusive (Zhu *et al.*, 2011). Conventional geophysical methods such as electrical sounding and electrical profiling cannot adequately identify subsurface voids in areas of high karst geologic complexity (Chalikakis *et al.*, 2011). On the other hand, electrical resistivity has shown success in karst (Roth and Nyquist, 2003; Chalikakis *et al.*, 2011; Zhu *et al.*, 2011). Electrical resistivity lines identify low resistivity areas (water-filled voids) and high resistivity areas (solid bedrock) (Denahan and Smith, 1984) and inform subsequent drilling. Therefore, adoption of an appropriate geophysical method that provides significant differences in void and bedrock characterization is an important precursor to investigating in-conduit longitudinal fate.

Another method advancement is use of ambient stable N isotopes. Stable N isotopes can be used to separate allochthonous and autochthonous sources (Ford and Fox, 2014; Husic *et al.*, 2017a), elucidate denitrification processes (Clément *et al.*, 2003; Xue *et al.*, 2009), and assist with reducing equifinality in numerical modeling (Ford *et al.*, 2017). Further, the oxygen isotope within NO_3^- is an additional tracer and can be used to delineate NO_3^- sources (Xue *et al.*, 2009; Jensen *et al.*, 2018). Nitrogen transformation and fractionation typically occurs through biologically mediated pathways (Kendall *et al.*, 2007; Sharp *et al.*, 2007). Stable N isotope fractionation of NH_4^+ varies from relatively little to significant depending on NH_4^+ pool size (Kendall *et al.*, 2007; Jensen *et al.*, 2018) while fractionation of the organic N pool is small (Kendall *et al.*, 2007). The extent to which denitrification enriches N and O isotopes also varies from very little to a significant amount depending on the site of denitrification (e.g., water or sediment) (Lehmann *et al.*, 2004; Sigman *et al.*, 2005). As stable N isotopes can be indicative of subsurface transformations, we apply this methodology within the intersected conduit to infer biogeochemical fate processes in karst.

Another method advancement is to use numerical modeling of stable isotopes. Characterizing flow and contaminant transport in karst is a non-trivial task. Extensive spatial heterogeneity in the subsurface makes it difficult to physically monitor fluxes and adequately constrain unknowns (Heffernan *et al.*, 2012). A cost-effective alternative to high-resolution data collection is numerical modeling (Jensen *et al.*, 2018). Numerical

modeling can provide a continuous estimate of integrated processes within a study section provided inputs and outputs are measured and knowledge of hydrodynamic behavior in the testbed is known (Husic *et al.*, 2017b). Literature exists for models of karst hydrology (Jeannin, 2001; Palanisamy and Workman, 2015), sediment transport (Nerantzaki *et al.*, 2015; Husic *et al.*, 2017b), particulate carbon and nitrogen fate (Chapter 5), and NO_3^- concentration (Yoshimoto *et al.*, 2013; Hartmann *et al.*, 2016; Chapter 3). Though applied as a data-driven approach, the isotopes of NO_3^- ($\delta^{15}\text{N}_{\text{NO}_3}$ and $\delta^{18}\text{O}_{\text{NO}_3}$) have been used to study N cycling within forested stream ecosystems (Sebestyen *et al.*, 2014) and to apportion NO_3^- sources using a decision tree informed by isotopes (Xue *et al.*, 2013). However, no studies to our knowledge have focused on numerical modeling of $\delta^{15}\text{N}_{\text{NO}_3}$ and $\delta^{18}\text{O}_{\text{NO}_3}$ fate in karst.

Our objectives were (1) set up an experiment to assess N turnover in karst conduits by collecting NO_3^- concentration and stable isotope ($\delta^{15}\text{N}_{\text{NO}_3}$ and $\delta^{18}\text{O}_{\text{NO}_3}$) data from within a longitudinal section of conduit, (2) develop a number model capable of simulating N stable isotope transformation in the karst SFGL, and (3) estimate karst N turnover relative to groundwater and surface water N removal. These objectives provide the structural subheadings for the methods and results of this chapter.

6.3 THEORETICAL BACKGROUND

The theoretical background provides the context behind our conceptual model of the N transformations, turnover, and isotopic changes that occur in the karst SFGL (Figure 6.1). The theoretical development from Chapter 5 is relevant to this chapter as dissolved and particulate phases of N are highly coupled. As previously mentioned, the karst SFGL is the thin surficial sediment layer that covers the cave bed. The karst SFGL receives dissolved inputs (e.g., dissolved organic carbon and nitrogen) from the bedrock matrix, epikarst, sinkholes, and sinking streams. On the other hand, the karst SFGL receives inputs particulate inputs (sediment organic carbon and nitrogen) only from tertiary porosity pathways (e.g., sinkholes, swallets, and sinking streams). Together, these inputs provide the necessary conditions for microbially induced N transformation the subsurface karst SFGL.

Our concept (Figure 6.1) is consistent with recent studies reporting karst sediment transport and biogeochemistry (Drysdale *et al.*, 2001; Dussart-Baptista *et al.*, 2003; Simon *et al.*, 2003, 2008; Herman *et al.*, 2008; Husic *et al.*, 2017a, 2017b). Suspended sediment is deposited, mixed, and eroded by shear forces at the sediment surface (Husic *et al.*, 2017a). Biogeochemical reactions occur because the microbial pool responsible for C and N turnover resides in cave sediments, e.g., Lehman *et al.* (2001) reported that 99% of cave microorganisms reside within fine sediments.

In terms of N transformations, nitrification, mineralization, denitrification, anammox, and immobilization have all been observed in karst caves and are influenced by shifts in organic carbon availability (Barton and Northup, 2007; Kumar *et al.*, 2017). The stable isotopic signature of NO_3^- can be tied to these physical and biochemical processes, which in turn are impacted by biogenic or anthropogenic activity (Ford *et al.*, 2017) (Figure 6.1). The isotopic ratio (δ) represents the relative abundance of heavy to light isotopes in a sample to that of a standard (e.g., $\delta^{15}\text{N} = [((^{15}\text{N}/^{14}\text{N})_{\text{sample}}/(^{15}\text{N}/^{14}\text{N})_{\text{air}})-1] \times 1000$) and is reported in units of per mil (‰). During transit and storage, many N transformations occur and impact the N-fingerprint: mineralization converts organic N to NH_4^+ or NO_3^- (Peterson *et al.*, 2001; Lin *et al.*, 2016); assimilation/immobilization biologically incorporates NH_4^+ and NO_3^- into organic N (Manzoni and Porporato, 2009; Wilhartz *et al.*, 2009); nitrification oxidizes NH_4^+ to NO_3^- (Peterson *et al.*, 2001; Fox *et al.*, 2017); anammox reduces NH_4^+ directly to dinitrogen gas (N_2) (Smith *et al.*, 2015; Kumar *et al.*, 2017); and denitrification anaerobically reduces NO_3^- to N_2 (Birgand *et al.*, 2007; Findlay *et al.*, 2011).

The usefulness of stable N isotopes to N transformation studies is realized because each of the aforementioned biogeochemical processes isotopically discriminates towards the energetically favorable light isotopes (Kendall *et al.*, 2007; Granger and Wankel, 2016). An enrichment factor (ϵ) is used to quantify these isotopic discrimination effects (e.g., $\epsilon_{\text{NO}_3-\text{NH}_4} = [((^{15}\text{N}/^{14}\text{N})_{\text{NO}_3}/(^{15}\text{N}/^{14}\text{N})_{\text{NH}_4})-1] \times 1000$). In some instances, parallel enrichment of different elements of the same compound (e.g., N and O of NO_3^-) can follow an identifiable trajectory. For example, during denitrification O is fractionated at approximately half the rate of N, providing a useful indication of the presence of denitrification when plotting $\delta^{18}\text{O}_{\text{NO}_3}$ against $\delta^{15}\text{N}_{\text{NO}_3}$ (Kendall and Aravena, 2000, Lehmann *et al.*, 2003). With the

above conceptual model in mind, we set up an experiment where changes in N concentrations and isotopic signatures could be used to help estimate N transformation with numerical modeling.

We implement the experiment within a fairly well-understood section of karst conduit that acts as a “conveyor belt” of water and sediment (Husic *et al.*, 2017a). During low flows, external (i.e., surface or near-surface) inputs of water and NO_3^- are limited to the study section, thus allowing for in-conduit estimation of longitudinal NO_3^- fate. NO_3^- concentration, $\delta^{15}\text{N}_{\text{NO}_3}$, and $\delta^{18}\text{O}_{\text{NO}_3}$ data were collected due to their ability to provide insight to N cycling. Thereafter, a numerical model was developed and applied to simulate the longitudinal fate and transport of NO_3^- , the interaction of bed sediment and conduit water, and the fractionation $\delta^{15}\text{N}_{\text{NO}_3}$ and $\delta^{18}\text{O}_{\text{NO}_3}$.

6.4 STUDY SITE AND MATERIALS

The study site is the Cane Run watershed and Royal Spring groundwater basin in the Bluegrass Region of Kentucky, USA (Figure 6.2). Cane Run is a mixed-use watershed that drains urban (40%) and agricultural (60%) lands with temperate climate (MAT: $13.0 \pm 0.7^\circ\text{C}$; MAP: $1,170 \pm 200$ mm). The geology is characterized by highly karstic, well-developed Lexington Limestone of the Middle Ordovician period. Cane Run creek collects runoff and shallow subsurface flow but much of this water is pirated by in-stream karst features. Numerous sinkholes and swallets (> 50) exist in the stream corridor and convey water and sediment to the cave, and as a result the stream at the Cane Run watershed outlet runs dry for approximately 80% of the year. The karst conduit is generally aligned with Cane Run creek for much of its course and is located approximately 20 m below the ground surface (Figure 6.2). The conduit is phreatic and limited in its maximum discharge by a downstream hydraulic control (Husic *et al.*, 2017a). The conduit discharges at a surface location termed Royal Spring where the water is used as a municipal drinking source for the city of Georgetown, Kentucky. The site has been a karst research site led by the Kentucky Geological Survey and the University of Kentucky the past 40 years (Spangler, 1982; Thrailkill *et al.*, 1991; Taylor, 1992; Paylor and Currens, 2004; Zhu *et al.*, 2011; Currens *et al.*, 2015; Husic *et al.* 2017a,b).

A number of recent sediment transport and C turnover findings from the study site are of importance in this study. Deposition and resuspension of sediment occur in the karst conduit, and was observed through downhole videos (e.g., Figure 6.1) taken inside the conduit at different time periods and through data and modeling (Husic *et al.*, 2017a,b). The reason for the deposition and resuspension of sediment is the phreatic nature and hydraulic control of the conduit. During storm events, the surface stream recharges sediment to the conduit, but the sediment transport carrying capacity (i.e., the fluid's energy to carry sediment) is limited within the conduit because of a downstream hydraulic control (i.e., the elevation of the springhead). The limited energy forces deposition of surface-derived material. During hydrograph recession and baseflow, diffuse recharge is free of sediment and erodes previously deposited material from the karst SFGL. Results show a 30% net loss of organic C in sediment exiting the conduit which is consistent with the idea of a biogeochemically active karst SFGL (Husic *et al.*, 2017a), thus prompting the detailed modeling in this paper.

Materials for data collection included instrumented sampling stations. A sampling station was placed at the spring (Royal Spring in Figure 6.2) providing water and sediment outputs from the karst conduit and SFGL. A second sampling station was a groundwater well directly intersecting the primary phreatic conduit (see Phreatic Conduit in Figure 6.2, Zhu *et al.*, 2011; Husic *et al.*, 2017a). The longitudinal distance between these two sampling stations is approximately 5 km. Given an average velocity of $0.12 \pm 0.11 \text{ m s}^{-1}$ (Husic *et al.*, 2017a), fluid starting at the Phreatic Conduit reaches Royal Spring within 10 ± 9 hours, on average, providing ample time for downgradient changes at the scale observed with daily sampling.

Materials for continuous numerical modeling included published results used as model inputs and supercomputing facilities. Water and sediment data collection and sediment transport modeling were previously published in Husic *et al.* (2017a,b). These results provide inputs to the karst SFGL numerical model in this study, including sediment exchange between the water column and karst SFGL, water and sediment fluxes into and out of the conduit, sediment particle size distributions entering and exiting the conduit, and the distribution of organic matter source material (i.e., soil, litter, and algae) entering the conduit. Sediment C and N fate and transport modeling from Husic *et al.* (2017b) and

Chapter 5, respectively, are used as inputs for this study. Numerical modeling uncertainty analysis was performed on an institutionally shared high performance computing cluster (DLX2/3) with 4800 processor cores, 18TB of RAM, and 1PB of high-speed disk storage.

6.5 METHODS

6.5.1 Collection of ambient stable N isotope data:

Paired sample collection at the entrance (Phreatic Conduit) and the exit (Royal Spring) of the study section was performed daily for 65 consecutive days (see dashed box in Figure 6.3). During this dry spell, three low-flow periods, defined as 10 or more consecutive days with little to no discharge at the spring, were identified. Grab samples of NO_3^- were collected at the mouth of Royal Spring using sterile 1 L jars (I-Chem 312-0950BPC). At the conduit site, samples were collected using a deep well pump (Hallmark Industries MA0414X-7) submerged directly into the phreatic conduit. Water depth in the same well as the pump was measured with a well-level indicator (Slope 113583). A multi-parameter probe (Horiba U-10) was used to record temperature and specific conductivity data at both sites.

The Kentucky Geological Survey (KGS) laboratory analyzed NO_3^- samples following US EPA Method 300.0. Analysis was performed using a Dionex ICS-3000 Ion Chromatography System featuring a carbonate-bicarbonate eluent generator and Dionex AS4A analytical column. The NO_3^- anion was identified by retention time and the peak area was compared to a calibration curve generated from known standards. Lab duplicates had a standard deviation of $\pm 0.02 \text{ mg N L}^{-1}$. Duplicate field samples of NO_3^- showed little variability ($\pm 0.07 \text{ mg N L}^{-1}$, $n = 8$). No lab, field, or equipment blanks registered above the method detection limit (MDL).

Samples for $\delta^{15}\text{N}_{\text{NO}_3}$ and $\delta^{18}\text{O}_{\text{NO}_3}$ analysis were extracted in the field from the aforementioned 1 L jars using clean 60 mL syringes and filtered through 0.45 μm syringe filters (Whatman 6780-2504) into sterile 40 mL borosilicate vials with a permeable 1.5 mm septum (I-Chem TB36-0040). Samples were stored in a refrigerated environment without the use of preservatives prior to delivery to the University of Arkansas Stable Isotope Lab (UASIL) for analysis. Isotopic data for NO_3^- were produced using the bacterial denitrifier

method with a Thermo Scientific GasBench II (Sigman *et al.*, 2001; Casciotti *et al.*, 2002). The references used for the analysis of N and O are related to AIR and Vienna Standard Ocean Water (VSMOW), respectively. The isotopic reference materials for NO_3^- were USGS32 ($\delta^{15}\text{N}_{\text{NO}_3}=+180\text{‰}$), USGS34 ($\delta^{15}\text{N}_{\text{NO}_3}=-1.8\text{‰}$, $\delta^{18}\text{O}_{\text{NO}_3}=-27.9\text{‰}$), and USGS35 ($\delta^{18}\text{O}_{\text{NO}_3}=+57.5\text{‰}$). Average standard deviations for the NO_3^- isotopic standards were 2.03‰ for USGS32 for $\delta^{15}\text{N}$; 0.34 and 0.70‰ for USGS34 for $\delta^{15}\text{N}$ and $\delta^{18}\text{O}$, respectively; and 1.00‰ for USGS35 for $\delta^{18}\text{O}$. Duplicates of $\delta^{15}\text{N}_{\text{NO}_3}$ and $\delta^{18}\text{O}_{\text{NO}_3}$ ($n = 5$) had standard deviations of $\pm 0.28\text{‰}$ and $\pm 0.45\text{‰}$, respectively. All detection was accomplished through interfacing with a Thermo Scientific Delta Plus or Delta V Advantage IRMS.

6.5.2 Isotope-aided numerical modeling of nitrate removal:

A model was developed to simulate transport and transformations of N phases (i.e., NO_3^- , NH_4^+ , and DON) between the Phreatic Conduit and Royal Spring sites (Figure 6.4). This model builds upon the sediment C and N transport models (Husic *et al.*, 2017b; Chapter 5). NO_3^- , $\delta^{15}\text{N}_{\text{NO}_3}$, and $\delta^{18}\text{O}_{\text{NO}_3}$ measurements at the Phreatic Conduit site were used as upstream model input conditions. The model runs at an hourly time step and interpolation between daily collected samples is performed to provide a continuous input record of NO_3^- , $\delta^{15}\text{N}_{\text{NO}_3}$, and $\delta^{18}\text{O}_{\text{NO}_3}$.

Many physical and biogeochemical processes impact NO_3^- concentration, $\delta^{15}\text{N}_{\text{NO}_3}$, and $\delta^{18}\text{O}_{\text{NO}_3}$. Masses of N advect with streamflow and interact with the streambed during transport. Flow in the conduit is estimated using a data-driven approach where velocity in the study section is determined by flow rate at the spring and cross-sectional area measured at the Phreatic Conduit site. Flow peaks at the Phreatic Conduit and Royal Spring are similar in magnitude ($Q_{\text{RS}} = 0.99Q_{\text{PC}}$, $R^2 = 0.77$; Husic, 2016) and we assumed this relationship holds for low flows as well.

The mass balance of NO_3^- (kg N) within a model cell of conduit water is a function of upstream inflow, downstream outflow, and the reaction of NO_3^- with bed sediment. This balance was modeled as

$$NO_3^-(i)^{(j)} = NO_3^-(i-1)^{(j)} + R_{(i)}^{(j)} + Q_{(i-1)}^{(j-1)} C_{NO_3}^{(j-1)} \Delta t - Q_{(i)}^{(j)} C_{NO_3}^{(j)} \Delta t, \quad (1)$$

where i is the model time step, and j is the model spatial step, $NO_3^-(i)^{(j)}$ is the mass of NO_3^- from the previous time step (kg N), $R_{(i)}^{(j)}$ is the biogeochemical processing of N that can

contribute to or remove from an N phase (e.g., NH_4^+ , NO_3^- , and DON), $Q_{(i-1)}^{(j-1)}$ is the flow rate coming into a cell ($\text{m}^3 \text{s}^{-1}$), $C_{\text{NO}_3}(i-1)^{(j-1)}$ is the concentration of NO_3^- coming into a cell (mg N L^{-1}), Δt is time step duration (s), $Q_{(i)}^{(j)}$ is the flow rate exiting a cell ($\text{m}^3 \text{s}^{-1}$), and $C_{\text{NO}_3}(i)^{(j)}$ is the concentration of NO_3^- exiting a cell (mg N L^{-1}). The NH_4^+ and DON mass balances are constructed in the same way as NO_3^- in Equation (1).

The suspended pool of N can interact with the sediment N pool. The sediment N (kg N) pool was modeled as:

$$S_{TN(i)}^{(j)} = S_{TN(i-1)}^{(j)} - E_{TN(i)}^{(j)} + D_{TN(i)}^{(j)} - R_{(i)}^{(j)} - X_{SFGL \rightarrow SS(i)}^{(j)} + X_{SS \rightarrow SFGL(i)}^{(j)}, \quad (2)$$

where $S_{TN(i-1)}^{(j)}$ is the supply of sediment nitrogen from the previous time step (kg N), $E_{TN(i)}^{(j)}$ is the amount of sediment nitrogen eroded (kg N), $D_{TN(i)}^{(j)}$ is the amount of sediment nitrogen deposited (kg N), and $X_{SFGL \rightarrow SS(i)}^{(j)} + X_{SS \rightarrow SFGL(i)}^{(j)}$ is the equilibrium exchange of N between the suspended and bed sediment (kg N) (Husic *et al.*, 2017b). Physical processes affecting carbon are the same for nitrogen and are explained in further detail in Chapter 2.

The mass of N exchanged between all pools (kg N) was modeled as:

$$R_{(i)}^{(j)} = \pm N_{IN(i)}^{(j)} \pm N_{directN(i)}^{(j)} - N_{DEN(i)}^{(j)} \pm N_{minSed(i)}^{(j)} \pm N_{imm(i)}^{(j)} \pm N_{minDON(i)}^{(j)} \pm N_{ANA(i)}^{(j)}, \quad (3)$$

where $N_{IN(i)}^{(j)}$ is the mass of recently mineralized NH_4^+ indirectly nitrified to NO_3^- in the streambed (kg N), $N_{directN(i)}^{(j)}$ is the mass of NH_4^+ directly nitrified to NO_3^- in the water column (kg N), $N_{DEN(i)}^{(j)}$ is the mass of NO_3^- denitrified to N_2 (kg N), $N_{minSed(i)}^{(j)}$ is the amount of particulate N mineralized to NH_4^+ (kg N), $N_{imm(i)}^{(j)}$ is the mass of N immobilized into sediment N by biota (kg N), $N_{minDON(i)}^{(j)}$ is the mass of DON mineralized to NH_4^+ (kg N), and $N_{ANA(i)}^{(j)}$ is the mass of NH_4^+ directly removed as N_2 by anammox bacteria (kg N). Sorption is not considered as low flows are unlikely to agitate the conduit bed and release stored NH_4^+ or NO_3^- . Equations for each of these reactions are shown in Table 6.2 and their respective terms are defined therein. Further details on the effects of temperature on transformation rates is explained in Chapter 5. Finally, only the relevant transformations, enumerated in Equation (3), are applied to each N pool. For example, if considering mass

balance changes to the DON pool, the denitrification and nitrification terms would effectively equal “0” as they don’t impact the mass of DON.

The cycling of N between oxidation states is recognized to discriminate in favor of lighter isotopes in a process known as fractionation (Kendall *et al.*, 2007; Jensen *et al.*, 2018). The isotope mass balance accounting for mixing of sources and many different biogeochemical processes through space and time was described as

$$\delta_{(i)}^{(j)} = \delta_{(i-1)}^{(j)} X_{(i-1)}^{(j)} + \sum \delta_{inputs(i)}^{(j)} X_{inputs(i)}^{(j)} - \sum \delta_{outputs(i)}^{(j)} X_{outputs(i)}^{(j)} - \sum \varepsilon \ln \left(f_{(i)}^{(j)} \right), \quad (4)$$

where i is the time step, j is the spatial step; δ is the isotopic signature of a given pool (‰); X is the fraction of an element in a given pool; δ_{inputs} is the isotopic signature of an input (‰) and X_{inputs} is the fraction of an element in the inflowing material; $\delta_{outputs}$ is the isotopic signature of an output (‰) and $X_{outputs}$ is the fraction of an element in the outflowing material; ε is the enrichment factor for a process (and is simulated using a Rayleigh-type model, Sharp *et al.*, 2007) (‰); and f is the fraction remaining of a reactant after the process occurs. Applying this formulation to NO_3^- yields:

$$\begin{aligned} \delta^{15}\text{N}_{\text{NO}_3(i)}^{(j)} = & \delta^{15}\text{N}_{\text{NO}_3(i-1)}^{(j)} X_{\text{NO}_3(i-1)}^{(j)} + \delta^{15}\text{N}_{\text{NO}_3-in(i)}^{(j)} X_{\text{NO}_3-in(i)}^{(j)} - \delta^{15}\text{N}_{\text{NO}_3-out(i)}^{(j)} X_{\text{NO}_3-out(i)}^{(j)} \\ & + \delta^{15}\text{N}_{directN(i)}^{(j)} X_{directN(i)}^{(j)} + \delta^{15}\text{N}_{IN(i)}^{(j)} X_{IN(i)}^{(j)} - \varepsilon_{DEN-N} \ln \left(f_{DEN-N(i)}^{(j)} \right), \end{aligned} \quad (5)$$

This same formulation is applied to the O isotope of NO_3^- , and also to the N isotope of TN, DON, and NH_4^+ .

Model Inputs, Parameterization, Evaluation, and Uncertainty

Inputs and parameters to the sediment, sediment C, and sediment N sub-models are defined in Chapters 2 and 5. Inputs and parameters to the NO_3^- , $\delta^{15}\text{N}_{\text{NO}_3}$, and $\delta^{18}\text{O}_{\text{NO}_3}$ model developed in this chapter are shown in Table 6.1. Parameters and inputs are bound by values collected in the field or reported in the literature. We parameterize unique values for NH_4^+ concentration (C_{NH_4}) and NH_4^+ -N stable isotope ($\delta^{15}\text{N}_{\text{NH}_4}$) of recharging water for each of the three events in the low-flow period to reflect the varying mobilization of N from different sources. NH_4^+ concentrations collected at the spring by the local municipality (Georgetown Municipal Water and Sewer Service), in the months prior to and during the low-flow sampling period, include values ranging from ~0 to 1.2 mg N L⁻¹. Of the 65 paired samples, 44 occur during periods we define as low flow and those 44 were

used for statistical evaluation of the model. We evaluate model performance using the Nash-Sutcliffe efficiency (*NSE*):

$$NSE = 1 - \frac{\sum_{t=1}^T (Q_m^t - Q_o^t)^2}{\sum_{t=1}^T (Q_m^t - \overline{Q_o})^2}, \quad (6)$$

where T is the total number of observations, Q_o is the observed value at time t , Q_m is the modeled value at time t , and $\overline{Q_o}$ is the mean of observed values. The Nash-Sutcliffe efficiency ranges from $-\infty$ to 1, with 1 indicating a perfect match of the model to data and 0 indicating the model performs no better than the mean of the data (Moriassi *et al.*, 2007). A multi-objective calibration (MOC) approach was used to calibrate the numerical model, where NSE_{NO_3} and $NSE_{\delta^{15}N_{NO_3}}$ are the NSE statistics for the NO_3^- and $\delta^{15}N_{NO_3}$ sub-models, respectively. $NSE_{\delta^{18}O}$ was not considered as the data do not show a trend. Model uncertainty and parameter sensitivity was assessed using the generalized likelihood uncertainty estimation (GLUE) method (Beven and Freer, 2001; Ford *et al.*, 2017) (Figure 6.4). The GLUE methodology is initiated by assuming a prior distribution for model parameters and retaining parameter sets that satisfy evaluation metrics defined as $NSE_{NO_3} > 0$ and $NSE_{\delta^{15}N} > 0$. A posterior distribution was then constructed from the set of acceptable evaluations. An uncertainty bound was generated for NO_3^- , $\delta^{15}N_{NO_3}$, and $\delta^{18}O_{NO_3}$ model predictions and contains 95% of acceptable solution sets.

6.5.3 Nitrate removal in sinking streams:

In order to provide comparison of the karst sinking stream's NO_3^- removal rates, we compiled denitrification and nitrification rates reported in the literature. Studies included other karst aquifers (Heffernan *et al.*, 2012), karst lakes (McCormack *et al.*, 2016), non-karst lakes (Reddy and DeLaune, 2008), global estimates for groundwater (Seitzinger *et al.*, 2006), rivers and stream sediment (Seitzinger, 1988). The Heffernan *et al.* (2012) study investigated 61 springs in the Upper Floridian Aquifer (USA) and estimated that, despite relatively low rates, denitrification accounted for removing a large percentage of N inputs to the aquifer. McCormack *et al.* (2016) calculated denitrification in karst turloughs (disappearing lakes) by a mass-balance calculation. Likewise, nitrification rates can vary significantly based on ecological setting and lentic or lotic conditions. Studies of nitrification considered here include prairie and agriculture-impacted streams (Kemp and Dodds, 2002a, 2002b), coastal shelf sediment (Henriksen *et al.*, 1993), and in streams of

varying use (e.g., urban, forest, agriculture) (Arango *et al.*, 2007). The aforementioned studies cover a range of land uses, hydrology, and residence times and may provide a useful comparison for the present karst conduit. The studies by Seitzinger *et al.* (1988, 2006) and Reddy and DeLaune (2008) provide a comparison for our study to N removal rates in more typical surface and subsurface pathways, while studies by Arango *et al.* (2008) and Kemp and Dodds (2002a,b) provide a comparison to nitrification rates across different land uses in non-karst landscapes. While the authors find no estimates of nitrification in karst, prior studies suggest its potential importance in the saturated zone (Einsiedl and Mayer, 2006; Musgrove *et al.*, 2016). The similarities and differences in NO_3^- removal in the present study with the various studies above may be a point of interest and an indicator of the net role of karst conduits in N cycling.

6.6 RESULTS AND DISCUSSION

6.6.1 Collection of ambient stable N isotope data:

Data results reinforce the closed-system assumption of the experimental set up and show that the karst conduits acts as a net source of NO_3^- from the upstream (conduit) to downstream (spring) sampling locations. Likewise, longitudinal changes in $\delta^{15}\text{N}_{\text{NO}_3}$ reflect N transformations that occur within the conduit, and $\delta^{15}\text{N}_{\text{NO}_3}$ results suggest that N loading to the spring is derived from soil organic nitrogen, fertilizer, and manure sources.

Results from water, temperature, and conductivity data gives us confidence in our experimental design and provide support for assessing in-conduit NO_3^- fate. Low-flow periods were defined as 10 or more days with discharge less than $0.3 \text{ m}^3 \text{ s}^{-1}$, and three such periods occurred during the 65-day consecutive sampling routine (Figure 6.5). The water height above the conduit was only slightly ($<0.5 \text{ m}$) above the spring elevation for most of the two-month period apart from days with storm activity. Temperature in the conduit decreased downstream due to the low background temperature of the aquifer ($\sim 13^\circ\text{C}$). The differences in temperature are statistically significant ($p < 0.001$), and can be accounted for by thermal convection at the conduit wall ($T_{\text{WALL}} - T_{\text{H}_2\text{O}} \approx 4^\circ\text{C}$). For example, in a recent modeling study, longitudinal temperature changes in a 3.2-km-long phreatic conduit varied by as much as 3°C during periods of diffuse-flow recharge (Long and Gilcrease, 2009). In terms of specific conductance, water became slightly more conductive as it is transported

downstream due to dissolution of karst bedrock, but the difference is not significant during low-flows. This result is not surprising as other modeling studies indicate conductivity responds to changes half as slowly as temperature during downstream transport (Winston and Criss, 2004). We have confidence in our experimental design because the temperature and conductivity results reinforce the idea that this section of the phreatic conduit can be treated as a closed system.

Nitrate data show the karst conduit acts as a net source of NO_3^- from the upstream (conduit) to downstream (spring) sampling locations, and is therefore, on average, dominated by nitrification over denitrification. NO_3^- concentration increased with longitudinal distance downstream (Figure 6.6a). The mean NO_3^- concentration showed an average increase of 4% ($p < 0.05$) during low-flow events. $\delta^{15}\text{N}_{\text{NO}_3}$ decreased from the upstream (conduit) to downstream (spring) sampling locations (Figure 6.6b). The observed longitudinal decrease in $\delta^{15}\text{N}_{\text{NO}_3}$ coupled with an increase in NO_3^- concentration suggests biological transformation. The reason for the longitudinal shift in $\delta^{15}\text{N}_{\text{NO}_3}$ during low-flow periods could be due to net mineralization of organic N or nitrification of NH_4^+ that are isotopically lighter than the $\delta^{15}\text{N}_{\text{NO}_3}$ of the NO_3^- pool. That is because the speciation of NO_3^- from isotopically lighter $\delta^{15}\text{N}_{\text{DON}}$ and $\delta^{15}\text{N}_{\text{NH}_4}$ likely offsets ^{14}N losses from enrichment by denitrification of the NO_3^- pool. Direct and indirect nitrification will decrease $\delta^{15}\text{N}_{\text{NO}_3}$ because the isotopic signatures of NH_4^+ ($\delta^{15}\text{N}_{\text{NH}_4} = -3 \pm 7\text{‰}$) and a number of labile organic N pools ($\delta^{15}\text{N}_{\text{algae}} = 5 \pm 2\text{‰}$ and $\delta^{15}\text{N}_{\text{detritus}} = 5 \pm 2\text{‰}$) are lower than the observed conduit NO_3^- signature (typically $\sim 6\text{‰}$) (Kendall *et al.*, 2007; Ford *et al.*, 2015). On the other hand, denitrification will increase the $\delta^{15}\text{N}_{\text{NO}_3}$ of the remaining NO_3^- pool. The net decreases in $\delta^{15}\text{N}_{\text{NO}_3}$ by organic N and NH_4^+ pools work simultaneously with increases in $\delta^{15}\text{N}_{\text{NO}_3}$ by denitrification. The final $\delta^{15}\text{N}_{\text{NO}_3}$ signature at the spring reflects the imprint of these competing reactions.

The $\delta^{18}\text{O}_{\text{NO}_3}$ data results were variable, and comparison of $\delta^{18}\text{O}_{\text{NO}_3}$ at upstream and downstream sites did not provide statistically significant results (Figure 6.6c). The lack of an apparent trend in $\delta^{18}\text{O}_{\text{NO}_3}$ doesn't necessarily imply $\delta^{18}\text{O}$ is not involved in reactions, but rather the imprint of any one reaction may be masked by many other simultaneous reactions.

The ambient stable N isotope of NO_3^- for the basin overall suggests N sources of soil organic N, fertilizer and manure (Figure 6.7). Overall data collected for $\delta^{15}\text{N}_{\text{NO}_3}$ ($\sim 7 \pm 1.5\text{‰}$) reflects soil organic nitrogen ($\delta^{15}\text{N}_{\text{SOM}} = 7 \pm 0.5\text{‰}$), and likely a mixture of fertilizer and manure ($\delta^{15}\text{N}_{\text{NH}_4 \text{ fert}} = \sim 0\text{‰}$ and $\delta^{15}\text{N}_{\text{manure}} = \sim 10\text{‰}$) (Kendall *et al.*, 2007; Ford *et al.*, 2015). $\delta^{18}\text{O}_{\text{NO}_3}$ ($0 \pm 2.12\text{‰}$) also generally centers on these sources, but does not agree with the isotopic value of NO_3^- fertilizer ($\sim 22.5\text{‰}$), however it does agree with NH_4^+ fertilizer ($\sim 0\text{‰}$). One potential reason that we did not see an increase in $\delta^{18}\text{O}_{\text{NO}_3}$ that is consistent with NO_3^- fertilizer input ($+22\text{‰}$, Kendall *et al.*, 2007), is that the immobilization and remineralization that likely occurs in the cave bed and overlying soils resets the $\delta^{18}\text{O}_{\text{NO}_3}$ value of newly formed NO_3^- . Expected values for $\delta^{18}\text{O}_{\text{NO}_3}$ formed from nitrification are around 1‰ (Amberger and Schmidt, 1987), which is very close to observed spring values of $0 \pm 2.12\text{‰}$.

We also characterize the potential for denitrification in the groundwater basin based on all of the $\delta^{15}\text{N}_{\text{NO}_3}$ and $\delta^{18}\text{O}_{\text{NO}_3}$ data collected (see Figure 6.7). The 1:2 denitrification trend observed in stable isotope data of NO_3^- (Xue *et al.*, 2009) reflects that denitrification is generally occurring in the groundwater basin upstream of the conduit site. The material that arrives at the conduit could originate from the soil, epikarst, phreatic matrix, or further upstream within the conduit. These overlapping denitrification processes and pathways are also suggested by the NO_3^- concentration decrease (Figure 6.6a) and $\delta^{15}\text{N}_{\text{NO}_3}$ increase over time at a single location (Figure 6.6b). For example, during low-flows 1, 2, and 3, the concentration at the Phreatic Conduit site decreased an average of 1 to 5% per day indicating either a change in source material or upstream removal.

Results show that ambient stable N isotope data help to reflect N transformation. The sensitivity of ambient $\delta^{15}\text{N}_{\text{NO}_3}$ results, as distinct from ^{15}N labeling studies, is possible due to the high NO_3^- concentration of water in the agriculturally impacted basin. The result adds to the body of emerging literature that use ambient N isotope signatures of NO_3^- and sediment N to estimate nitrogen transformation (Fox *et al.*, 2010; Sebestyen *et al.*, 2014; Ford *et al.*, 2017; Jensen *et al.*, 2018).

6.6.2 Isotope-aided numerical modeling of nitrate removal:

The isotope-aided numerical model helped us reduce uncertainty when estimating NO_3^- removal for the karst sinking stream. The NO_3^- modeling alone (i.e., without isotopes) allowed initial parameterization of rates for the experimental reach because NO_3^- and NH_4^+ pool size from data allow initial constraints to net reactions. However, the response of NO_3^- at the downstream (spring) location was not very sensitive to nitrification and denitrification rates. Adding the second set of equations via the isotopes without adding a second set of unknowns helped constrain the problem. Nitrification decreased the $^{15}\text{N}:^{14}\text{N}$ ratio of NO_3^- because the $\delta^{15}\text{N}$ of NH_4^+ is considerably lower than that of NO_3^- (see Figure 6.7), and the NH_4^+ pool size limits the extent of $\delta^{15}\text{N}$ decrease of NO_3^- . In turn, coefficients controlling denitrification could be calibrated because denitrification causes the $\delta^{15}\text{N}$ increase of $\delta^{15}\text{N}_{\text{NO}_3}$ back towards the downstream boundary condition matched to the observations.

The size of acceptable parameter sets was greatly reduced when calibrating to $\delta^{15}\text{N}_{\text{NO}_3}$ in addition to NO_3^- concentration. During the initial calibration phase (i.e., $NSE_{\text{NO}_3} > 0$), 20,958 of the total 42,000 model simulations met the model criteria. We also checked DON and NH_4^+ inflowing and outflowing concentrations to ensure that the acceptable set of parameters produced behavior consistent with field data. Then, we calibrated to an additional response variable (i.e., $NSE_{\text{NO}_3} > 0$ and $NSE_{\delta^{15}\text{N}} > 0$). Ambient isotopes of N reduced the acceptable parameter space to 15 solutions. The multi-objective calibration of dissolved N concentration and stable N isotopes reduced the acceptable parameter space and thus equifinality by ~99%. Equifinality is the condition by which many different parameter sets reproduce observed behavior (Beven and Freer, 2001). Ambient N isotopes have shown success when applied to constrain NO_3^- transformations in an agriculturally dominated surface stream (Ford *et al.*, 2017). Our results show the potential of ambient N stable isotopes to assist with N modeling in karst groundwater.

After performing the isotope-aided calibration procedure, we evaluated the modelling results. The NO_3^- and $\delta^{15}\text{N}_{\text{NO}_3}$ calibrated using the multi-objective function (i.e. NSE_{NO_3} and $NSE_{\delta^{15}\text{N}}$) show agreement between modeled and measured results (Figure 6.8). Consistent with the data results, numerical modeling results for NO_3^- and $\delta^{15}\text{N}_{\text{NO}_3}$, during the three low-flow periods, agrees well with field observations (i.e., downstream increase

in NO_3^- and decrease in $\delta^{15}\text{N}_{\text{NO}_3}$), albeit with some exceptions (Figure 6.8a,b). Some disagreement between the model and data occurs when the model overestimates $\delta^{15}\text{N}_{\text{NO}_3}$ data at the beginning of low-flow period 3, immediately after the storm event lasting between August 23 and September 6. A reason could be due to a process not included in the modelling. For example, this overestimation could be because NH_4^+ or NO_3^- was released from the SFGL or a ‘hot spot’ of activity in the karst SFGL existed and was activated. The explanation is plausible because storm flow can disturb the SFGL (Ford *et al.*, 2015) and cause sediment exchange between the SFGL and water column, even in absence of net deposition/erosion (Husic *et al.*, 2017b). Another example of process not explicitly modeled could be the deposition of highly labile carbon during hydrologic activity. Sometimes after long dry periods there is a crust on the ephemeral pathways from hot-drying-cracking that then can easily get washed/eroded off the surface soil/streams (Cui and Caldwell, 1997). Our sediment transport model probably would not pick up on this transient process as our model is calibrated to mean loading conditions. As an additional check, the $\delta^{18}\text{O}_{\text{NO}_3}$ model simulations approximate a considerable number of samples, but the lack of a trend and sporadic changes in $\delta^{18}\text{O}_{\text{NO}_3}$ caused the model to not closely approximate the full range of $\delta^{18}\text{O}_{\text{NO}_3}$ data points (Figure 6.8c).

Uncertainty and sensitivity analysis of modeled inputs and parameters show that a few parameters have a very strong influence on model results while many parameters have a lesser or no influence (Figure 6.9). For example, parameters such as the enrichment factor of nitrification (ϵ_{nitr}) and recharge signature of $\delta^{15}\text{N}_{\text{NH}_4}$ for event 3 ($\delta^{15}\text{N}_{\text{NH}_4\text{-rec}(3)}$) are sensitive, while others such as the enrichment factor of immobilization (ϵ_{imm}) and the reaction coefficient for indirect nitrification (β_{IN}) are not sensitive. The relative sensitivity of NH_4^+ recharge concentrations ($C_{\text{NH}_4\text{-rec}(1)}$, $C_{\text{NH}_4\text{-rec}(2)}$, and $C_{\text{NH}_4\text{-rec}(3)}$) and isotopic ratios ($\delta^{15}\text{N}_{\text{NH}_4\text{-rec}(1)}$, $\delta^{15}\text{N}_{\text{NH}_4\text{-rec}(2)}$, and $\delta^{15}\text{N}_{\text{NH}_4\text{-rec}(3)}$) for the three events indicates the importance of NH_4^+ recharge and nitrification on altering the downstream quality of NO_3^- .

The success of the isotope-aided modeling provides more evidence of the usefulness of stable isotopes to assist with stream and watershed water quality modelling. In the present study, nitrification and denitrification parameterization is improved by adding additional equations to help constrain the rates. Other studies have also shown recent usefulness of coupling stable isotopes with stream and watershed water quality modelling

(Kaown *et al.*, 2009; Young *et al.*, 2009; Jensen *et al.*, 2018), and we compliment this growing body of literature with insights from a karst watershed.

6.6.3 Nitrate removal in sinking streams:

The karst sinking stream's NO_3^- removal falls between the bounds of groundwater systems and surface water systems. Denitrification results for the karst sinking stream for the duration of the experiment were $16.8 (\pm 21.5) \text{ mg N m}^{-2} \text{ d}^{-1}$ of NO_3^- , on average, between the upstream (conduit) and downstream (spring) sites. In comparison, the average areal rate for 61 springs in a karst aquifer was $0.33 \text{ mg N m}^{-2} \text{ d}^{-1}$ (Heffernan *et al.*, 2012). The global estimated average for groundwater denitrification is $0.96 \text{ mg N m}^{-2} \text{ d}^{-1}$ (Seitzinger *et al.*, 2006). In surface systems, 18 to $170 \text{ mg N m}^{-2} \text{ d}^{-1}$ is denitrified in river and stream sediment based on field estimates (Seitzinger *et al.*, 1988). Karst and non-karst lakes fall within the ranges of river and stream denitrification rates. A karst lake showed $44 \text{ mg N m}^{-2} \text{ d}^{-1}$ (McCormack *et al.*, 2016) while a range for non-karst lakes was reported equal 34 to $57 \text{ mg N m}^{-2} \text{ d}^{-1}$ (Reddy and DeLaune, 2008). Our results point towards elucidating the non-conservative nature of NO_3^- in karst conduits.

Taken together, the karst sinking stream has denitrification rates an order of magnitude greater than groundwater systems but an order of magnitude lower than surface freshwater systems. The results seem reasonable when considering inputs controlling bioavailable carbon. The sinking stream receives terrestrial and aquatic derived sediment organic carbon (i.e., detritus, soil carbon, and sloughed benthic algae from tributaries). The particulate carbon inputs and presence of carbon in the SFGL are expected to be higher overall than groundwater systems receiving dissolved carbon but little particulate carbon. The sinking stream lacks photo-autotrophy along its length, therefore, lack of this additional labile carbon source places denitrification rates lower than surface systems where benthic algae in streams and phytoplankton in lakes/large rivers can be a major contributor of carbon (Ford and Fox, 2017).

Nitrification in the sinking stream was on the higher end of rates reported in the literature, which is consistent with periods of high NH_4^+ levels observed in our system. Mean nitrification between the upstream conduit and downstream spring sites was $37 (\pm 13) \text{ mg N m}^{-2} \text{ d}^{-1}$. Our results are consistent with other studies of agriculture-impacted

watersheds where maximum rates of nitrification can be up to tenfold greater than denitrification (Kemp and Dodds, 2002) and net-nitrifying streams are associated with higher NO_3^- concentrations (Peterson *et al.*, 2001). In comparison, nitrification rates in surface streams vary greatly, from 0 to $10 \text{ mg N m}^{-2} \text{ d}^{-1}$ in urban, forest, and agricultural watersheds (Arango *et al.*, 2008) to 60 to $120 \text{ mg N m}^{-2} \text{ d}^{-1}$ in a watershed draining prairie and agricultural fields (Kemp and Dodds, 2002a,b). In coastal shelf sediments, nitrification areal rates range from 4 to $25 \text{ mg N m}^{-2} \text{ d}^{-1}$ (Henriksen *et al.*, 1993). Prior studies have suggested the importance of nitrification within the phreatic karst zone (Einsiedl and Mayer, 2006; Musgrove *et al.*, 2016), and our study provides a quantification of its importance.

In the sinking stream, NH_4^+ is high, on average, and very high for some point samples. Our relatively high nitrification rates are potentially the result of elevated concentrations during the sampling period of this study. In the Royal Spring basin, the long-term average concentration of NH_4^+ recharging the subsurface is 0.12 mg N L^{-1} and the NH_4^+ concentration of spring discharge is 0.07 mg N L^{-1} (Chapter 3). However, shortly prior to and during the study period, high concentrations of NH_4^+ were detected at Royal Spring (e.g., May 5, 1.2 mg N L^{-1} ; June 12, 0.38 mg N L^{-1} , and Sept. 15, 0.40 mg N L^{-1}), and in some instances such as May 5 and June 1 the water treatment plant at Royal Spring shut down operations due to high NH_4^+ concentrations.

The areal extent of karst sinking streams, caves, and phreatic conduits may be limited, but results suggest that they have disproportionate effects on NO_3^- removal relative to other groundwater pathways. The result might be considered when assessing removal in karst drainages and in life cycle assessments. We suggest that our isotope approach can be used in other studies to provide complimentary results to the present study for comparison of denitrification in sinking streams.

6.7 CONCLUSIONS

The conclusions of this chapter are as follows:

- A karst phreatic conduit showed usefulness as a closed-system experiment to investigate N transformations in subsurface karst. N concentration and isotope data results show that the karst sinking stream acts as a net source of NO_3^- via net

nitrification, notwithstanding evidence of denitrification of soil organic N, fertilizer, and manure sources in the groundwater basin. Our results add to the emerging body of literature on the usefulness of ambient N isotope signatures of NO_3^- and sediment N to estimate nitrogen transformation.

- The isotope-aided numerical model helped us reduce uncertainty when estimating NO_3^- removal for the karst sinking stream. The success of the isotope-aided modeling provides another study in the usefulness of stable isotopes to assist with stream and watershed water-quality modelling.
- The karst sinking stream's NO_3^- removal falls between the bounds of groundwater systems and surface water systems, and results provide a rare, if not unique, reported estimate of denitrification in karst conduits. The karst sinking stream has denitrification rates an order of magnitude higher than groundwater systems but an order of magnitude lower than surface freshwater systems. Results reflect bioavailable carbon in comparison of the different systems. The areal extent of karst sinking streams, caves and phreatic conduits may be limited, but results suggest they have disproportionately greater effects on NO_3^- removal relative to other groundwater pathways.

6.8 TABLES AND FIGURES

Table 6.1 Inputs and calibration parameters for NO_3^- , $\delta^{15}\text{N}_{\text{NO}_3}$, and $\delta^{18}\text{O}_{\text{NO}_3}$ fate and transport model. Input and parameter descriptions, ranges, calibrated values, and units are presented.

Parameter	Description	Range Simulated in Model	Units	Reference
ϵ_{min}	Mineralization (DON) enrichment factor	1 – 3	[-]	Kendall et al. 2007, Ford et al. 2017
ϵ_{nitr}	Direct nitrification (NH_4^+) enrichment factor	1 – 26	[-]	
ϵ_{IN}	Indirect nitrification (NH_4^+) enrichment factor	1 – 26	[-]	
ϵ_{ANA}	Anammox (NH_4^+) enrichment factor	1 – 26	[-]	
ϵ_{imm}	Immobilization (NH_4^+) enrichment factor	1 – 13	[-]	
ϵ_{DEN-N}	Denitrification (N) (NO_3^-) enrichment factor	1 – 18	[-]	
ϵ_{DEN-O}	Denitrification (O) (NO_3^-) enrichment factor	1 – 18	[-]	
β_{IN}	Coefficient for indirect nitrification reaction	5×10^{-10} – 5×10^{-7}	$[\text{kg N m}^{-2} \text{ s}^{-1}]$	Mulholland et al, 2008, Ford et al. 2017
β_{DEN}	Coefficient for denitrification reaction	5×10^{-10} – 5×10^{-7}	$[\text{kg N m}^{-2} \text{ s}^{-1}]$	
β_{ANA}	Coefficient for anammox reaction	5×10^{-10} – 5×10^{-7}	$[\text{kg N m}^{-2} \text{ s}^{-1}]$	Kumar et al. 2017
k_{min}	First-order mineralization constant	0 – 0.04	$[\text{d}^{-1}]$	Ryzhakov et al. 2010
k_{nitr}	First-order direct nitrification constant	0 – 0.68	$[\text{d}^{-1}]$	
$C_{DON-rec}$	DON concentration of recharge	0.20 – 0.50	$[\text{mg N L}^{-1}]$	Measured at site
$C_{\text{NH}_4-rec(1)}$	NH_4^+ concentration of recharge (initial)	0 – 0.60	$[\text{mg N L}^{-1}]$	
$C_{\text{NH}_4-rec(2)}$	NH_4^+ concentration of recharge (Aug. 7 event)	0 – 0.60	$[\text{mg N L}^{-1}]$	
$C_{\text{NH}_4-rec(3)}$	NH_4^+ concentration of recharge (Aug. 21 event)	0 – 0.60	$[\text{mg N L}^{-1}]$	
$\delta^{15}\text{N}_{\text{DON-rec}}$	$\delta^{15}\text{N}_{\text{DON}}$ recharge	2 – 9	[‰]	Husic et al. 2018b
$\delta^{15}\text{N}_{\text{NH}_4-rec(1)}$	$\delta^{15}\text{N}_{\text{NH}_4}$ of recharge (initial)	-10 – 5	[‰]	Kendall et al. 2007
$\delta^{15}\text{N}_{\text{NH}_4-rec(2)}$	$\delta^{15}\text{N}_{\text{NH}_4}$ of recharge (Aug. 7 event)	-10 – 5	[‰]	
$\delta^{15}\text{N}_{\text{NH}_4-rec(3)}$	$\delta^{15}\text{N}_{\text{NH}_4}$ of recharge (Aug. 21 event)	-10 – 5	[‰]	

Table 6.2 Nitrogen transformations, equations, terms and units, and associated references.

Reaction	Equation	Terms and Units	Reference
Denitrification	$N_{DEN(i)}^{(j)} = \beta_{Den} \left(C_{SFGL(i)}^{(j)} \right)^{\alpha_{Den}} \times SA_{(i)}^{(j)} \times \theta_{DEN}^{(T_i - T_{ref})} \times \Delta t,$	β_{Den} = Coefficient for denitrification (kg N m ⁻² s ⁻¹) α_{Den} = exponent calibration coefficient (assumed equal to 1) C_{SFGL} = carbon content of bed SA = surface area of bed (kg) θ_{DEN} = temperature coef. for DEN	Arango and Tank, 2008 Ford et al., 2017 Veraart et al., 2011
Indirect Nitrification	$N_{IN(i)}^{(j)} = \beta_{IN} \left(C_{SFGL(i)}^{(j)} \right)^{\alpha_{IN}} \times SA_{(i)}^{(j)} \times \theta_{IN}^{(T_i - T_{ref})} \times \Delta t,$	β_{IN} = Coefficient for indirect nitrification (kg N m ⁻² s ⁻¹) α_{IN} = exponent calibration coefficient (assumed equal to 1) θ_{IN} = temperature coef. for IN	Arango and Tank, 2008 Ford et al., 2017 Bowie et al., 1985
Anammox	$N_{ANA(i)}^{(j)} = \beta_{ANA} \left(C_{SFGL(i)}^{(j)} \right)^{\alpha_{ANA}} \times SA_{(i)}^{(j)} \times \theta_{ANA}^{(T_i - T_{ref})} \times \Delta t,$	β_{ANA} = Coefficient for anammox (kg N m ⁻² s ⁻¹) α_{ANA} = exponent calibration coefficient (assumed equal to 1) θ_{ANA} = temperature coef. for ANA	Kumar et al., 2017 rates after Arango and Tank, 2008 formulation of other N reactions
Direct Nitrification	$N_{directN(i)}^{(j)} = k_{nitr} \times NH_4^+{}_{(i)}^{(j)} \times \theta_{directN}^{(T_i - T_{ref})} \times \Delta t,$	k_{nitr} = first order rate constant for nitrification (d ⁻¹) $\theta_{directN}$ = temperature coef. for direct	Bowie et al., 1985 Ryzhakov et al. 2010
Mineralization (DON)	$N_{minDON(i)}^{(j)} = k_{minDON} \times DON_{(i)}^{(j)} \times \theta_{minDON}^{(T_i - T_{ref})} \times \Delta t,$	k_{min} = first order rate constant for mineralization (d ⁻¹) θ_{minDON} = temperature coef. for min DON	Bowie et al., 1985 Ryzhakov et al. 2010
Mineralization (Sediment)	$N_{minSed(i)}^{(j)} = \sum_{j=1}^{n_p} k_{minj} S_{N Sed j} \times r(T)_i \times \Delta t,$	p = index for nitrogen pool (i.e., litter, soil, algae) n_p = total number of pools k_{minp} = mineralization rate of each pool (d ⁻¹) $S_{N Sed p}$ = supply of sediment N of each pool (kg N) $r(T)_i$ = temperature dependence function	Ford et al., 2017 Reichstein et al., 2000
Immobilization	$N_{imm(i)}^{(j)} = \sum_{j=1}^{n_p} k_{immj} S_{N Sed j} \times r(T)_i \times \Delta t,$	$k_{imm p}$ = immobilization rate of each pool (d ⁻¹)	Lin et al., 2017 Reichstein et al., 2000

Figure 6.1 Conceptual model of physical and biogeochemical carbon and nitrogen processes in a subsurface conduit. Physical processes are shown in black arrows. Biogeochemical processes are shown in orange arrows. Fractionations for each transformation are also identified.

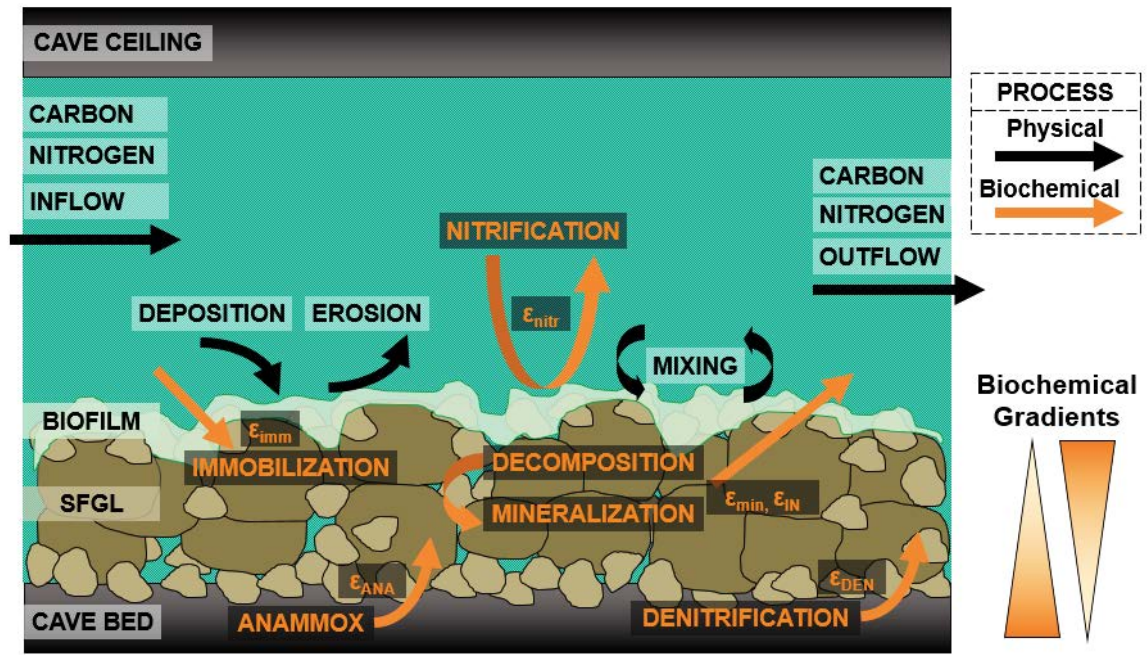


Figure 6.2 Cane Run Watershed and Royal Spring Basin indicating the Phreatic Conduit and Royal Spring sites. During low-flow periods, flow between these two points is believed to consist of the same material. Also shown is the location of the surface Cane Run Creek that is activated during moderate to large events.

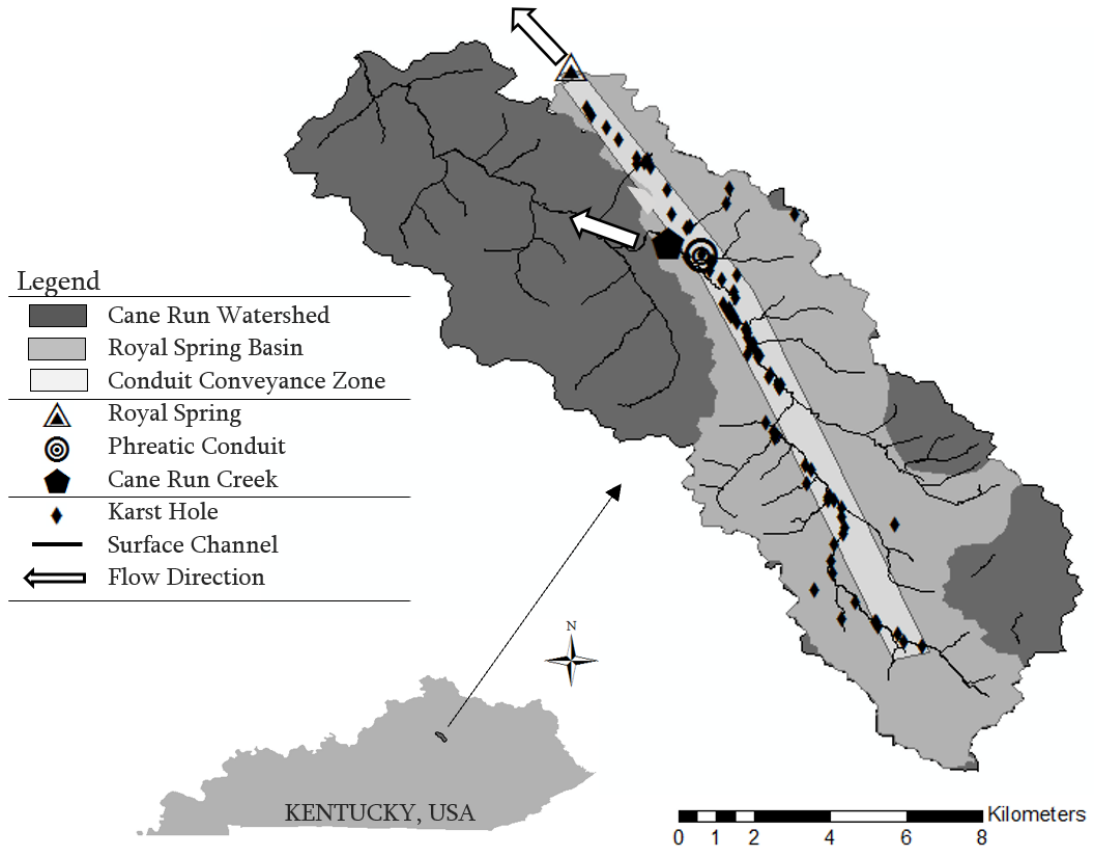


Figure 6.3 Daily average air temperature, spring discharge, and precipitation intensity for the 2017 year. High air temperatures coincide with a low spring discharge and limited recharge to the conduit. One such period is identified with a dashed box and serves as the focus of this study. The numbers inset in the dashed box enumerate the low-flow periods of 10 or more consecutive days.

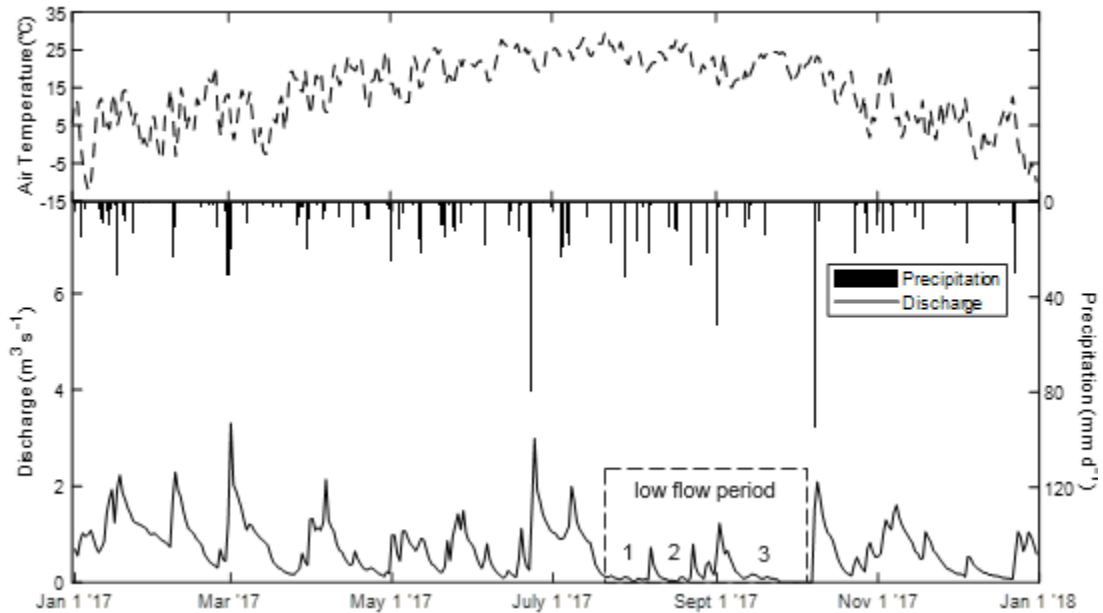


Figure 6.4 Model calibration and uncertainty framework for evaluating NO_3^- and $\delta^{15}\text{N}_{\text{NO}_3}$, NH_4^+ , and DON model results. R_{NH_4} represents the ratio of average NH_4^+ into vs out of the conduit. R_{DON} is calculated the same way as R_{NH_4} , but for DON. Modeled R_{NH_4} and R_{DON} were compared to data R_{NH_4} and R_{DON} to constrain uncertainty in NH_4^+ and DON inputs. For a definition of other terms see Table 6.1.

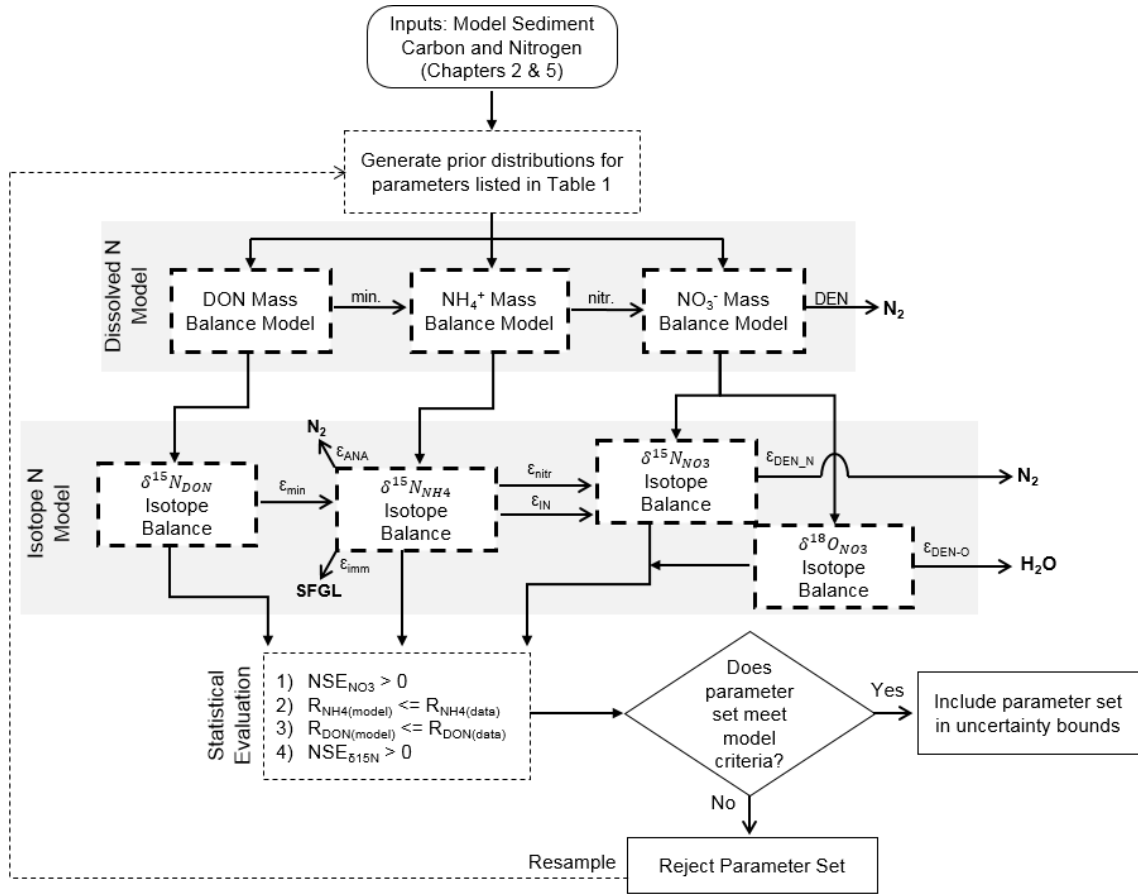


Figure 6.5 Water quality data collected at the subsurface conduit and the primary spring. The top plot shows groundwater elevation (above mean sea level) at the conduit and discharge at the spring. The dashed horizontal line represents the spring elevation. In the bottom plot, water temperature (solid lines) and specific conductivity (dashed lines) at the conduit (black) and spring (blue) sites are shown. Environmental data show that water is cooled and becomes more conductive during transport within the conduit. Areas shaded in gray indicate low-flow periods (defined as 10 or more days with less than $0.3 \text{ m}^3 \text{ s}^{-1}$).

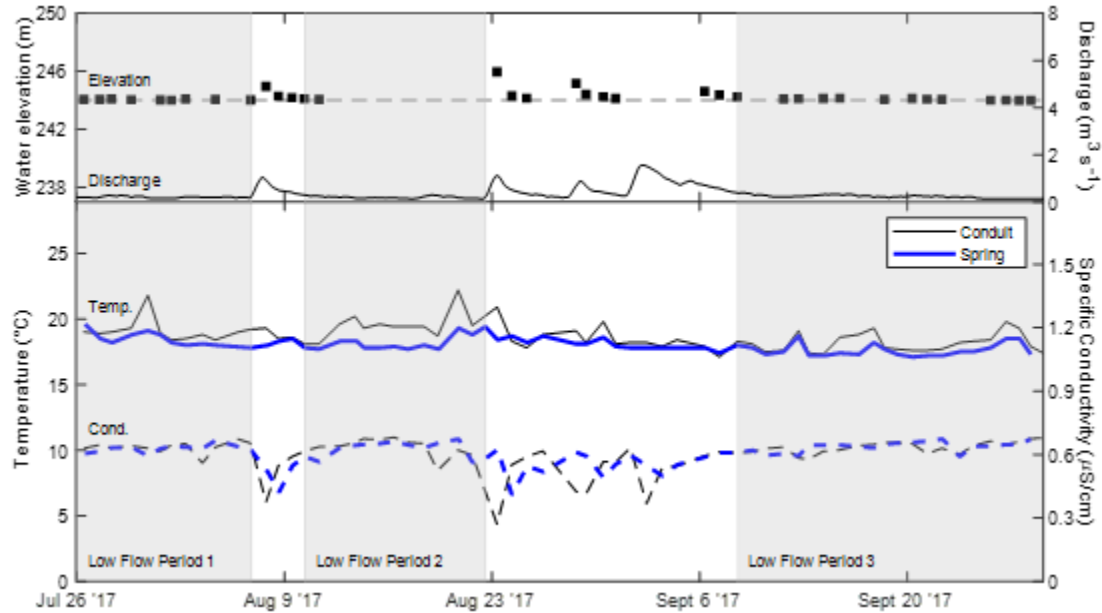


Figure 6.6 Elemental and isotopic data collected at the subsurface conduit and the spring. (a) NO_3^- concentration decreases temporally during dry periods, but tends to increase longitudinally from conduit to spring. (b) $\delta^{15}\text{N}_{\text{NO}_3}$ increases temporally, indicating enrichment of NO_3^- , but tends to decrease longitudinally, suggesting an additional mineralization or nitrification source. (c) $\delta^{18}\text{O}_{\text{NO}_3}$ at the two sites is not significantly different ($p = 0.66$), is highly variable, and does not show any discernable trends. Areas shaded in gray indicate low-flow periods (defined as 10 or more days with less than $0.3 \text{ m}^3 \text{ s}^{-1}$).

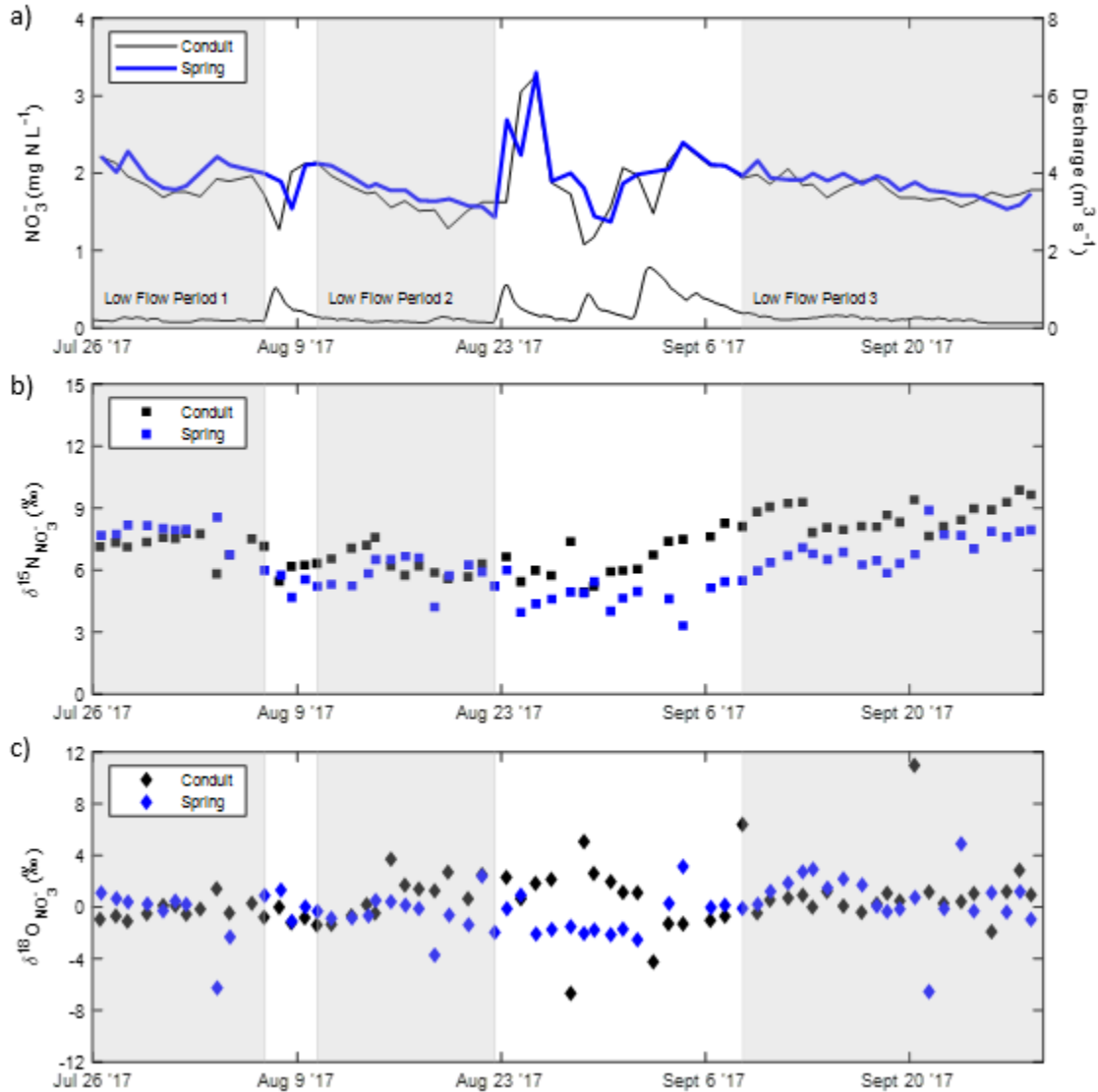


Figure 6.7 $\delta^{18}\text{O}_{\text{NO}_3}$ and $\delta^{15}\text{N}_{\text{NO}_3}$ of collected samples from conduit and spring locations. At first observation, samples collected at the spring outlet could ostensibly indicate denitrification, but the observed longitudinal trend shows a relatively depleted spring $\delta^{15}\text{N}_{\text{NO}_3}$ relative to the intermediate conduit location, suggesting additional in-conduit biogeochemical cycling (i.e., nitrification). We note a statistically significant ($p < 10^{-5}$) difference in $\delta^{15}\text{N}$ means (spring: $6.48 \pm 1.17\text{‰}$ vs conduit: $7.80 \pm 1.41\text{‰}$), but not in $\delta^{18}\text{O}$ signatures ($p = 0.66$) of the two sites. Approximate NO_3^- sources and their ranges are demarcated (adapted from Kendall *et al.*, 2008). The “Denitrification Trend” is manually drawn through the data with a 1:2 slope (Kendall *et al.*, 2008).

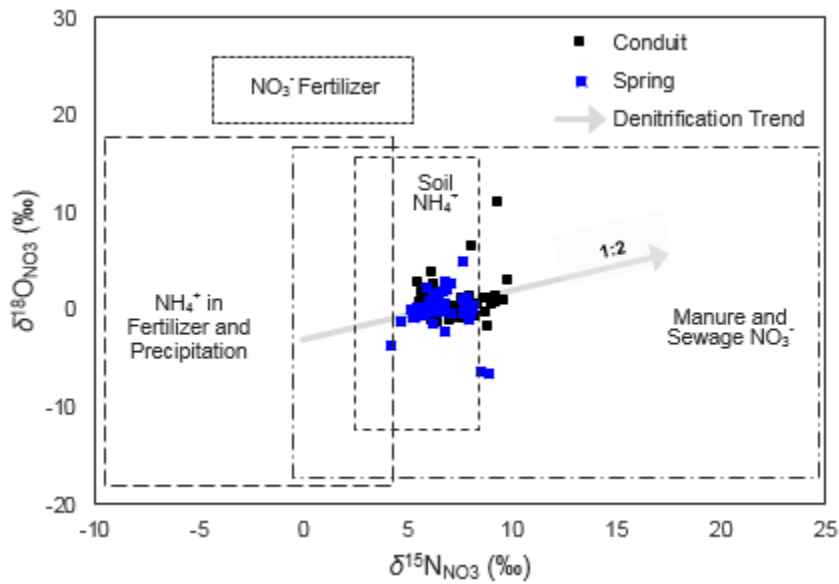


Figure 6.8 Modeling results of (a) NO_3^- , (b) $\delta^{15}\text{N}_{\text{NO}_3}$, and (c) $\delta^{18}\text{O}_{\text{NO}_3}$ for three low-flow periods contained within the sampling duration. Input concentrations to the study section (gray lines) are interpolated from data (see Figure 6.4) while outflowing concentrations at the spring (shaded blue area) are continuously simulated. Spring output is presented as the 95% prediction bound from the set of acceptable model simulations. Blue dots represent discrete data points collected at the primary spring. Sub-models were evaluated using the Nash-Sutcliffe Efficiency and the resulting value for the best cumulative run is shown on each graph. Areas shaded in gray indicate low-flow periods (defined as 10 or more days with less than $0.3 \text{ m}^3 \text{ s}^{-1}$).

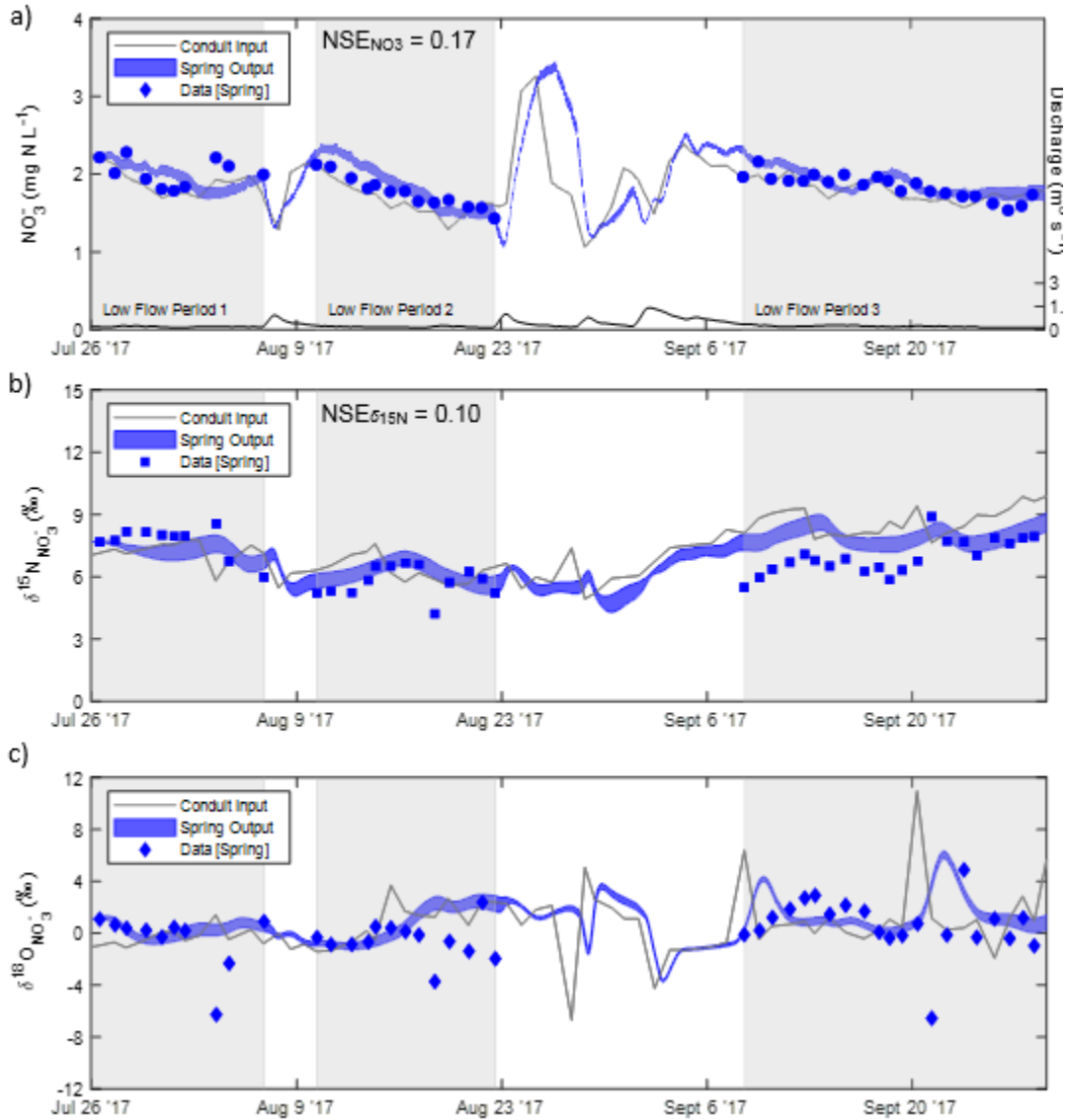
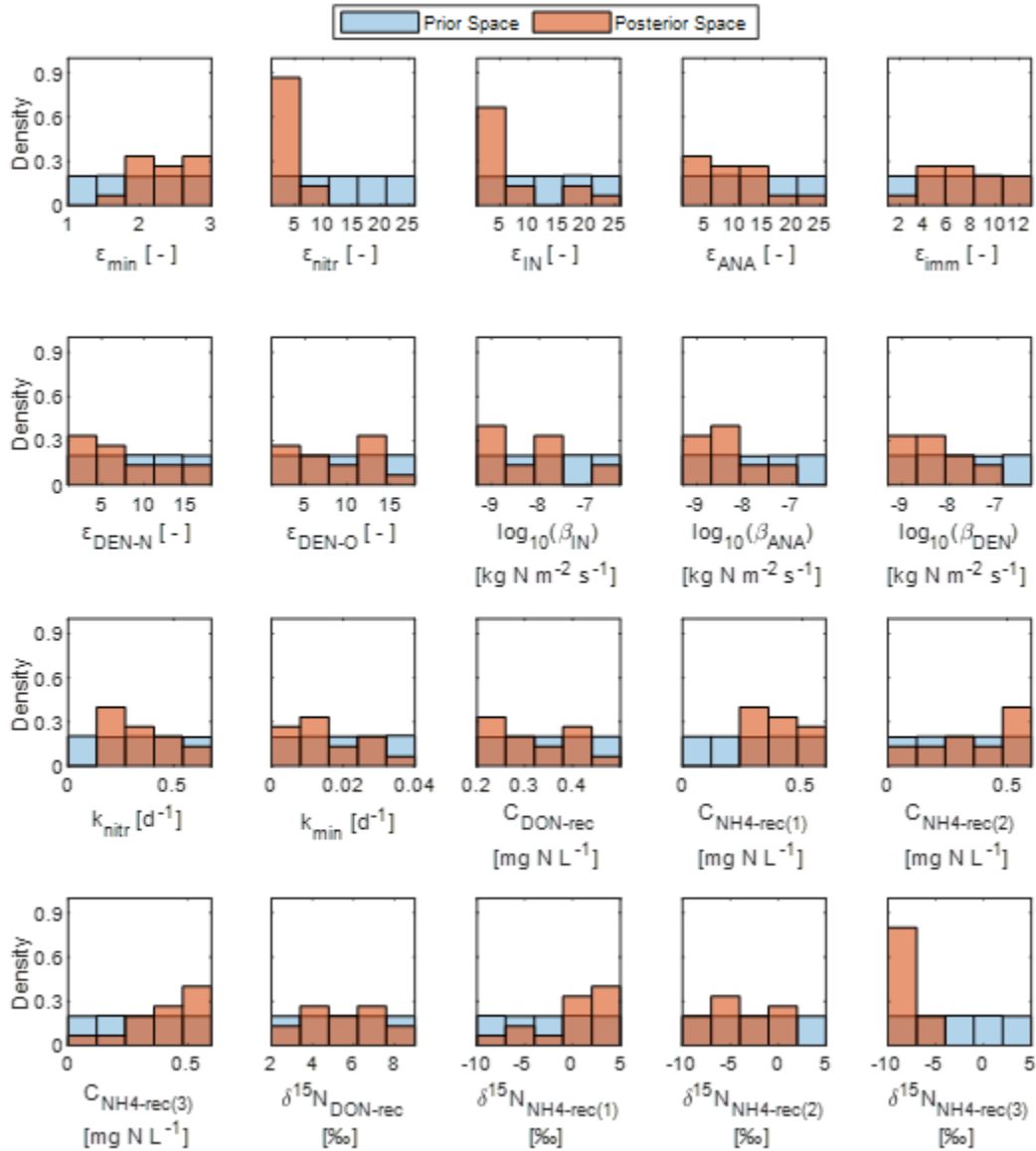


Figure 6.9 Prior (uniform) and posterior histogram densities of model parameters and inputs. Parameters such as the enrichment factors of nitrification (ϵ_{nitr} and ϵ_{IN}) and the recharge concentration of NH_4^+ and signature of $\delta^{15}\text{N}_{\text{NH}_4}$ during event 3 are sensitive while others such as enrichment factor of immobilization (ϵ_{imm}), reaction coefficient for indirect nitrification (β_{IN}), and the recharge signature of $\delta^{15}\text{N}_{\text{DON}}$ are not sensitive.



APPENDIX

Quality Assurance Project Plan (QAPP)

Project Title: Cane Run & Royal Spring Water Quality Research

River Basin: Kentucky River

Sub-Catchment: Cane Run Creek

Organization: University of Kentucky

Project Co-Managers:

Admin Husic

Signature

Date

Jimmy Fox (Primary)

Signature

Date

Project Laboratory Manager

Jason Backus (KGS)

Signature

Date

Erik Pollock (UASIL)

Signature

Date

Section A: Project Management and Objectives

A.1) Distribution List

Admin Husic
Graduate Associate Department of Civil Engineering
University of Kentucky
161 O.H. Raymond Bldg
Lexington, Kentucky 40506
Phone: 859-218-1543
admin.husic@uky.edu

Dr. Jimmy Fox
Department of Civil Engineering
University of Kentucky
161 O.H. Raymond Bldg
Lexington, Kentucky 40506
Phone: 859-257-8668
james.fox@uky.edu

Jason Backus
Kentucky Geological Survey
University of Kentucky
366 Mining and Minerals Building
Lexington, Kentucky 40506
Phone: 859-257-5500
jbackus@uky.edu

Erik Pollock
University of Arkansas Stable Isotope Laboratory
University of Arkansas
850 W Dickson Street
Fayetteville, Arkansas 72701
Phone: 479-575-4506
epolloc@uark.edu

A.2) Project Organization

A.2.1) Roles and Responsibilities, Communication Pathways, and Organizational Chart

The roles and responsibility of the participating parties are outlined below. The project organizational chart detailing participant roles and the propagation of information between party members is shown in Figure 1. Parts of this QAPP are adapted from the South Elkhorn QAPP (Ford, 2014).

Admin Husic

Graduate Assistant Department of Civil Engineering
University of Kentucky
Role: Graduate Research Associate and Co-Principal Investigator
Responsibilities: Manager of the project, QAPP Development, Transport data to KGS lab, Ensure data meets all quality requirements, Analyze sediment elemental and stable isotope samples, Perform post-analysis and work to publish dataset

Dr. Jimmy Fox

Department of Civil Engineering
University of Kentucky
Role: Co-Principal Investigator, Primary advisor to the graduate student
Responsibility: Co-manager of the project, Advisor to graduate student and assists with post-analysis and publication of data

Jason Backus

Kentucky Geological Survey
University of Kentucky
Role: Lab manager at the Kentucky Geological Survey Laboratory
Responsibility: Performs analysis of ground water and surface water samples, Insure proper quality control measures are taken and all protocol are met

Erik Pollock

University of Kentucky Stable Isotope Laboratory (UASIL)
University of Arkansas
Role: Lab Manager of Arkansas Stable Isotope Lab
Responsibility: Performs analysis of stream water $\delta^{15}\text{N}_{\text{NO}_3}$, Insure proper quality control measures are taken and all protocol are met

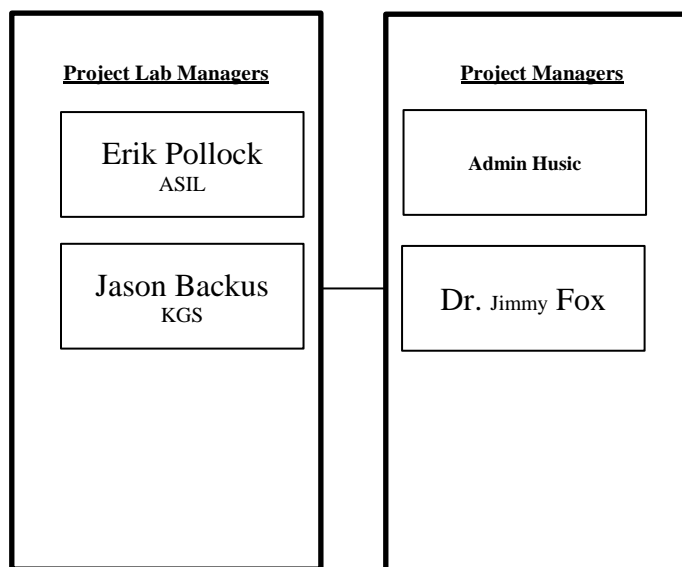


Figure 1) Project Organizational Chart

A.2.2) Special Training Requirements and Certification

No special training requirements are required to perform the procedures outlined in this QAPP. The project/data manager has been trained by advisors and laboratory personnel on all of the procedures he will perform, and the project manager will oversee undergraduate students that collect probe data and sediment trap samples. The project manager will visit and learn all laboratory procedures performed in KGS lab that lab work is to be contracted out to.

A.3) Project Planning / Problem Definition

A.3.1) Project Definition

Fluviokarst landscapes are solutionally dissolved landforms dominated by secondary and tertiary porosity (Thraillkill, 1974; Smart and Hobbs, 1986). As a result of the high connectivity, karst aquifers are typically very susceptible to anthropogenic contaminant loading from surface sources such as agricultural farms, wastewater treatment plants, and combined storm sewers (Mahler *et al.*, 2000; Pronk *et al.*, 2006; Heinz *et al.*, 2009). Pathogens, nutrients, and other contaminants are quickly transported through large karst conduits without adequate bioremediation (Mahler *et al.*, 2000). In conduit-dominated karst systems, the transport and proliferation of bacteria can be exacerbated by particulate sediment transport which provides protection against predators that graze on free-floating bacteria (Harvey *et al.*, 1984), resistance against chemical attack (Rittman, 1993), and an energy source from sediment-bound organic material (Husic *et al.*, 2016). Karst aquifers can serve as drinking water sources for municipalities and individual homeowners, and understanding contaminant source and fate within aquifers can answer questions about the potability of karst waters.

There exists a significant potential for contamination of karst waterways as a result of agricultural land practices and the continued urbanization of metropolitan areas. Agricultural horse farms are abundant in the Inner Bluegrass Region of Kentucky and serve both a recreational and competitive purpose to the community. Intense hydrologic events create surface runoff that can inundate horse stables and fields facilitating the transport of fecal matter downgradient towards swallow holes and estavelles. In addition, agricultural lands in the Inner Bluegrass are also commonly used for animal grazing and crop production (e.g., tobacco). Crop agriculture requires the spreading of fertilizer and nutrients over the soil surface in order to promote plant growth while animal grazing promotes erosion of soil surfaces. Combined storm sewers are still commonly used and have the potential to overflow after excessive precipitation. As a result, organic waste is washed off into streams where it can be diverted to the subsurface karst aquifer. By coupling stable isotope analysis to collected samples within the watershed, relative contribution of sediment and contaminants can be traced back to land types and practices.

Contaminants affecting the water quality of karst systems in the Inner Bluegrass include total suspended and dissolved solids, nitrate, phosphorous, and fecal coliform bacteria. Previous research performed by the Kentucky Water Resources Research Institute (KWRRRI) show that the Cane Run Watershed exceeds the criteria of fecal coliform contamination for primary recreational contact (Cane Run and Royal Spring Watershed-Based Plan UKCAFE 2012). In addition, Kentucky is one of the largest contributors of nutrients (i.e., nitrogen and phosphorous) to the Mississippi River (Alexander *et al.*, 2008). Nitrogen occurs primarily as dissolved inorganic nitrogen (DIN) or particulate nitrogen (PN). The dissolved inorganic forms commonly include nitrate (NO₃) and ammonium (NH₄⁺). Nitrogen is cycled through its various forms via fixation, ammonification, nitrification, assimilation, and denitrification. Nitrogen cycling is a naturally occurring phenomena that has been accelerated due to human influence (Vitousek *et al.*, 1997). Phosphorous occurs primarily from the application of organic fertilizer to the soil system, and, along with nitrogen, is the nutrient most responsible for plant growth (e.g., algae blooms). Fecal coliform bacteria are the most common type of microbial contamination and are used as an indicator species to identify the presence of other harmful pathogens.

Investigating the transformation and flux of sediment, carbon, nitrogen, phosphorous, and fecal coliform bacteria is necessary in order to assure aquifer health and assess the bioremediation capabilities of karst conduits. Karst caverns are turbulent mixing conduits governed by complicated hydrodynamic and biogeochemical processes that act as an intersection between open channel flows and traditional porous media ground water flows with the potential for temporary trapping of surface-derived sediment and organic turnover

(Herman *et al.*, 2008; Husic *et al.*, 2016). A dataset comprising of several years of sediment, carbon, nitrogen, phosphorous, and fecal coliform samples will provide extensive insight into the capabilities of fluviokarst systems to not only transport - but also transform - water quality constituents from watershed headwaters to depositional zones. As a result of the complex nature of karst hydrogeology, constructing numerical models can often times prove difficult. Large datasets which include high temporal frequency sampling and multiple sampling locations are often times necessary to reinforce conceptual and numerical models by providing a large range of water quality results for various conditions (e.g., flow, temperature, and moisture.) In particular, the role of the karst conduit surface fine-grained laminae (SFGL) with regards to assimilating and interacting with surface contaminants is an area of great importance as well as uncertainty. The SFGL is the biologically active top-layer of bed sediment with high overlap of physical and biological processes in which water-sediment interactions are greatly coupled (Battin *et al.*, 2008; Russo and Fox, 2012). Understanding the source, fate, and transport of contaminants related to water quality will allow for implementation of appropriate treatment and mitigation strategies. Additionally, water chemistry variability in the subsurface can influence not only biological activity but also dissolution and precipitation of calcium carbonate (White, 2002).

The objective of this project is to amass a dataset by collecting a suite of elemental and isotopic measurements from the surface waters and subsurface waters of the fluviokarst system. Samples are to be collected during storm events, low flow periods, and on a biweekly sampling routine. Sediment, water, and nitrate samples will be analyzed to determine the elemental concentration of carbon and nitrogen, as well as isotopic ratios of oxygen, deuterium, nitrogen, and carbon in order to (1) estimate the contribution of water and nitrate from various sources of karstic waters, (2) investigate the role of physical and biogeochemical processes in transforming nitrogen and carbon within karst storage zones, (3) and estimate the net flux of nitrate from subsurface pathways relative to surface pathways.

With regards to objective 1, the nitrogen and oxygen isotopes of nitrate can be used to unmix the sources of nitrate contributing to spring discharge (Einsiedl and Mayer, 2006; Katz *et al.*, 2010; Zhang *et al.*, 2015). Towards objective 2, this study will incorporate a greater focus into the fractionation process of nitrate isotopes by modeling the different karst storage reservoirs thus increasing provenance determination accuracy. Additionally, to aid in estimating transformation rates, a “convey-belt” portion of the conduit will be used as an experimental testbed during low-flow periods where inputs and outputs to the section can be constrained. Finally, pertaining to objective 3, the flux of water quality constituents is of paramount interest to watershed shareholders such as farmers and municipalities. The biweekly sampling of nutrients will shed light on the variance in concentrations over time.). Given that 50% of the land area in the state of Kentucky shows karst potential, it is vital to estimate fluviokarst contaminant loading to downstream surface water. Previous and on-going research by Husic *et al.*, (2017) has identified two tributaries, one surface outflow location, a subsurface conduit location, and primary springhead as important watershed sampling locations (Figure 2). These locations including new sites encompass the watershed domain for the new sampling design.

Table 1) Summary of Project Data Needs

Name	Description	Sample Frequency	Location	No. of Samples
TDS	A measure of the total dissolved solids	Biweekly	K,C	N/A
TSS	A measure of the total suspended solids	B/S	K,C	N/A
DO	A measure of the amount of oxygen dissolved in the water	B/S	K,C,R	N/A
pH	A measure of the acidic/basic level of water	B/S	K,C,R	N/A
Temp	A measure of the temperature in the water	B/S	K,C,R	N/A
Cond	A measure of ease of the ionic activity in the water	B/S	K,C,R	N/A
H	A measure of the stream flow and well depth/stage	C	K,C,R	N/A
Q	A volumetric means of representing discharge	C	R	N/A
NO ₃	A measure of Nitrate concentrations in the water	B/S	K,C,R	116
P	A measure of Phosphorous concentrations in the water	B	K,C	116
POC	A measure of the Particulate Organic Carbon within a sediment sample	B/S	R,L,D,S	158
PN	A measure of total nitrate-nitrogen, nitrite-nitrogen, and organic nitrogen in a sediment sample	B/S	R,L,D,S	158
δ ¹³ C _{sed}	A measure of the Carbon isotope ratio in a sediment sample	B/S	R,L,D,S	158
δ ¹⁵ N _{sed}	A measure of the Nitrogen isotope ratio in a sediment sample	B/S	R,L,D,S	158
δ ¹⁵ N _{NO₃}	A measure of the Nitrogen isotope ratio in a nitrate sample	B/S	K(S),C(S), W(S), R	172
δ ¹⁸ O _{NO₃}	A measure of the Nitrogen isotope ratio in a nitrate sample	B/S	K(S),C(S), W(S), R	172
δ ¹³ C _{DIC}	A measure of the Carbon isotope ratio in a water sample	B/S	K(S),C(S), W(S), R	117
δ ² H _{H₂O}	A measure of the Hydrogen isotope ratio in a water sample	S	K,C,W,R	85
δ ¹⁸ O _{H₂O}	A measure of the Oxygen isotope ratio in a water sample	S	K,CW,R	85
Prcp	A measure of the precipitation	C	*	N/A

K=Kentucky Horse Park (Conduit), C=Cane Run Creek, W=Well 21, R=Royal Spring, L=Lexmark (Urban Tributary), D=Dairy Road, S=Spindletop (Ag Tributary)

C=Continuous, B=Biweekly, S=Storm

*Precipitation measurements will be obtained from NOAA at the Lexington Airport Station, obtained from USGS stations located in the watershed outlet and the adjacent system, and average rainfall depths will be determined using NOAA protocols for the sub-watersheds upstream from the sampling locations.

A.3.2) Sampling Plan and Budget

Storm Sampling Plan: The sampling detailed below is for one storm event. Data will be collected from three to five storm events, which is summed up in the total budget. Samples will be collected at four locations throughout the storm. The timing of sample collection is shown below. Samples will be collected from Royal Spring, Groundwater Station, Cane Run Creek, and a groundwater well. Sediment samples will be collected only at Royal Spring. Storm samples total 71 per event (24 nitrate, 17 DIC, 17 water, 6 sediment and 7 elemental).

Table 2) Storm Sampling Overview

Hour	Solute Samples (RYSP, CRCK, KYHP)			Water Samples (RYSP, CRCK)		Groundwater Well Samples (WELL)		Sediment Samples (RYSP)		Elemental Samples (RYSP, CRCK, KYHP)		
	$\delta^{15}\text{N}_{\text{NO}_3}$	$\delta^{18}\text{O}_{\text{NO}_3}$	$\delta^{13}\text{C}_{\text{DIC}}$	$\delta^2\text{H}_{\text{H}_2\text{O}}$	$\delta^{18}\text{O}_{\text{H}_2\text{O}}$	$\delta^{15}\text{N}_{\text{NO}_3}$ $\delta^{13}\text{C}_{\text{DIC}}$	$\delta^{18}\text{O}_{\text{H}_2\text{O}}$ $\delta^{18}\text{O}_{\text{NO}_3}$	$\delta^{15}\text{N}_{\text{Sed}}$ $\delta^{13}\text{C}_{\text{Sed}}$	PN POC	NO_3^-		
-3	x	x	x	x	x	x	x				x	
6	x	x	x	x	x			x	x		x	
12	x	x	x	x	x			x	x		x	
24	x	x	x	x	x	x	x	x	x		x	
48	x	x	x	x	x			x	x		x	
72	x	x	x	x	x			x	x		x	
96	x	x	x	x	x	x	x	x	x		x	
Locations Sampled	3	3	2	2	2	1	1	1	1		3	
Total Nitrate Samples	24	Total DIC Samples	17	Water Samples	14	Well Water Samples	3	Total Sediment Samples	6		Total Elemental Samples	21
Total Number of Samples Per Storm:					85							

Low Flow Sampling Plan: Samples will be collected for three “low flow events”. Below is the samples that will be collected for one low flow event. Samples will be collected from both the Groundwater Station at the mid-point of the karst conduit and at Royal Spring. The samples will be collected every day for 10 days for each event, equaling a total of 40 samples. The costs are summed up at the end of the document.

Table 3) Low Flow Sampling Overview

Location	Solute Samples		Elemental Samples	
	$\delta^{15}\text{N}_{\text{NO}_3}$	$\delta^{18}\text{O}_{\text{NO}_3}$	NO_3^-	
Royal Spring	x	x	x	
Groundwater Station	x	x	x	

Biweekly Sampling: Samples will be collected every two weeks from Royal Spring, Groundwater Station, and Cane Run Creek. Biweekly sampling will take place over the next 16 months. A total of 32 events will be sampled.

Table 4) Biweekly Sampling Overview

Location	Solute Samples			Sediment Samples				Elemental Samples
	$\delta^{15}\text{N}_{\text{NO}_3}$	$\delta^{18}\text{O}_{\text{NO}_3}$	$\delta^{13}\text{C}_{\text{DIC}}$	$\delta^{13}\text{C}_{\text{Sed}}$	$\delta^{15}\text{N}_{\text{Sed}}$	PN	POC	NO_3^-
Cane Run Creek								x
Groundwater Station								x
Royal Spring	x	x	x	x	x	x	x	x
Lexmark				x	x	x	x	
Spindletop				x	x	x	x	
Dairy Rd				x	x	x	x	

Table 5) Total Sampling Costs

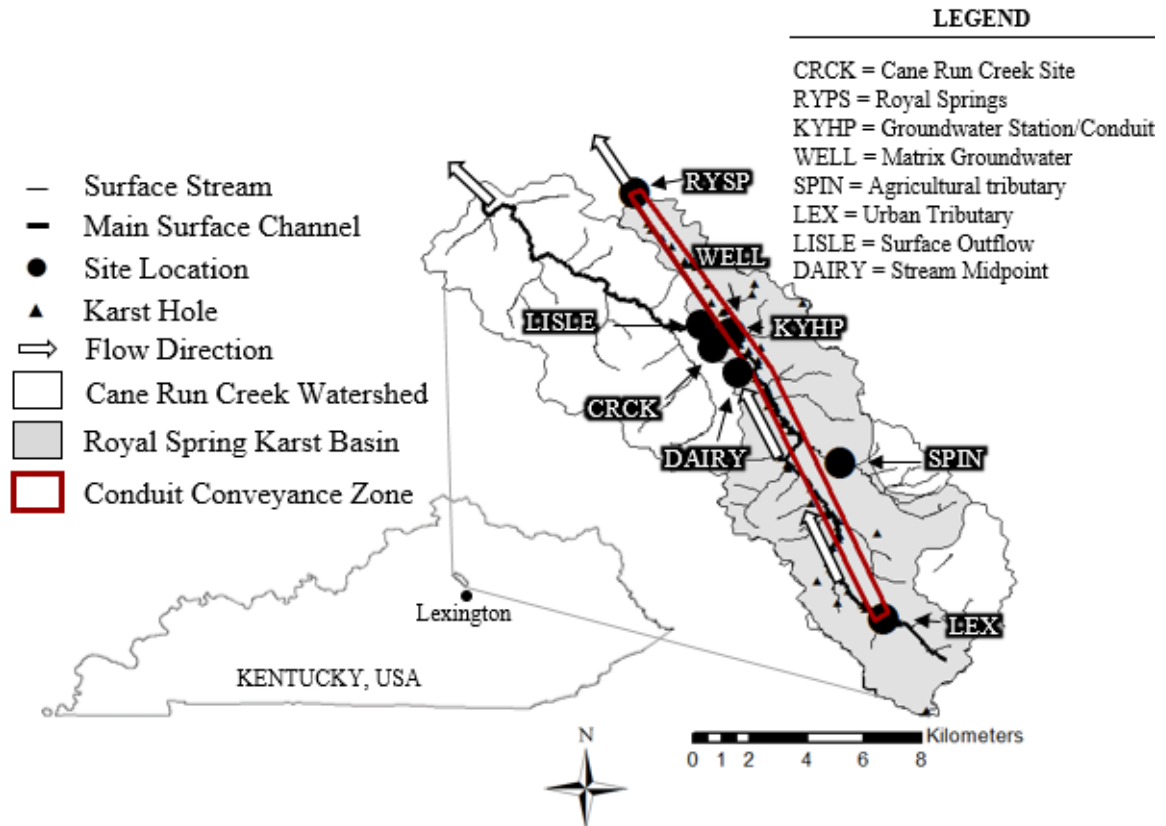
	# samples per event	# of events	Cost per event	Sampling cost
Storm Sampling	85	5	\$ 1,896	\$ 9,480
Low Flow Sampling	40	3	\$ 1,060	\$ 3,180
Biweekly Sampling	9	32	\$ 146	\$ 4,672
			Total Cost	\$ 17,332

A.3.3) Watershed Overview

Study Watershed

The Cane Run watershed is a mixed-use, fluviokarst watershed located in the Inner Bluegrass Region of central Kentucky contained within Fayette and Scott Counties. The underlying Royal Spring karst groundwater basin surfaces in Georgetown, Kentucky, where it serves as a municipal drinking water source for the city and has the largest base flow discharge of any spring in the region (Currens *et al.*, 2015). This portion of the coupled surface-subsurface network has a drainage area of 58 km² and is characterized by mature karst topography. The headwaters of Cane Run creek are located in the southernmost portion of the watershed near downtown Lexington. Within the drainage area, the investigated portion of the watershed is 38% urban/suburban and 62% agricultural, primarily of which is the horse farms. The Cane Run watershed has high connectivity between the surface stream channel and the primary subsurface phreatic conduit. Fifty seven karst holes (e.g., swallets and estavelles) have been mapped primarily in and around the main stream corridor (Paylor and Currens, 2004). Many of these features connect to a primary subsurface karst corridor, located 20 m below the ground surface, which conveys water to Royal Spring in Georgetown (Taylor, 1992). The underlying bedrock in the Cane Run watershed is composed of Lexington Limestone of the Middle Ordovician period (Cressman and Peterson, 1986). The rock structures in the region are a result of a tectonic stress-field which initiated a pattern of an echelon minor faults and joints directing from the southeast towards the northwest (Drahovzal *et al.*, 1992; Drahovzal and Noger, 1995). The landscape of the watershed is typified karst and rolling hills in nature with well vegetated grass and trees. The area is comprised of deep, well-drained series of soils (e.g., Maury, McAfee, and Lowell) that are formed from weathered phosphatic limestone (USDA, 1993). These soil series are characterized by moderately low to moderately rapid permeability (USDA, 1993). Both the subsurface conduit and Cane Run creek are active during winter periods when soil moisture conditions are high and rainfall activity is prolonged. During the summer months, seasonal creeks are activated by hydrologic events and run dry during subsequent inactive periods of rainfall.

Figure 2) Geographic Location of the Cane Run Watershed



Attribute	Description
Geology	Lexington Limestone of the Middle Ordovician period ¹
Rock structure	En echelon minor faults and joints directing from the southeast towards the northwest ^{2,3}
Landscape	Rolling hills with fluviokarst features, e.g., swallets, over the 58 km ² drainage area ^{4,5}
Land uses	38% urban/suburban and 62% agricultural, primarily of which is horse farm pasture ⁵
Soils	Silt loam and silty clay loam formed from weathered phosphatic limestone ⁶
Climate	Averages 115 cm of rainfall per year and 13.1°C MAT ⁷

¹Cressman and Peterson, 1986; ²Drahovzal *et al.*, 1992; ³Drahovzal and Noger, 1995; ⁴Paylor and Currens, 2004; ⁵Husic, 2015; ⁶USDA, 1993; ⁷Bluegrass Regional Airport historic data

Previous Monitoring

The Cane Run watershed has been monitored since the late 1960's. The Lexington Fayette Urban County Government (LFUCG) has been performing pathogen sampling in Cane Run since 1993. In 2007, the United States Environmental Protection Agency (USEPA) and the LFUCG entered into a consent decree over violations of the Federal Water Pollution Control Act. Subsequently, the University of Kentucky Department of Biosystems and Agricultural Engineering began developing a watershed based plan which was completed in 2012. The Biosystems and Agricultural Engineering Department began monitoring the surface water component of the dual drainage system. Results showed that surface streams are intermittent and are activated primarily by rainfall. The report emphasized that the single greatest challenge to water quality in the system is the coupling of karst hydrogeologic pathways with surface streams. In response to this challenge, in conjunction with the Kentucky Geological Survey (KGS), an investigation into the ground water component of the system was initiated.

Over the last decade, the KGS located the primary karst conduit: electrical resistivity tests and well drilling were used to map the phreatic conduit that serves as the primary subterranean pathway for the karst drainage from the headwaters to Royal Spring (Zhu *et al.*, 2011). Over a two year period (2011 – 2013), water and sediment fluxes were continuously monitored at surface and subsurface sites while carbon inflows and outflows were measured using time-integrated samples (Husic *et al.*, 2016). Figure X details the previously collected data for the Cane Run watershed. Flow rate, turbidity, temperature, dissolved, conductivity, and pH were collected

using continuous probes when available during the study. Sediment carbon, nitrate, and phosphorous samples were collected on a biweekly to monthly basis. Fecal coliform bacteria samples were collected intermittently depending on field conditions. Additionally, a sediment and sediment carbon transport model including isotope source un-mixing was developed by Husic et al. (2016) for the Cane Run and Royal Springs watershed. As further research is completed, the system inner workings become less obfuscated as shown by successful modeling of sediment transport in the subsurface karst conduit. Sediment modeling in karst is rare, and the work by Husic et al. (2016) is the only known publication by the authors to model the physical and biogeochemical processes affecting sediment transport and SFGL transformation. A historical summary of studies performed in the Cane Run/Royal Springs Watershed can be found in Table 6.

Primarily, the limited, yet sustained, transport carrying capacity of the conduit promotes the deposition of labile carbon to the conduit bed followed by later resuspension of the deposited sediment. Perennial flow within the conduit coupled with the subsequent deposition and resuspension of sediment provide conditions for heterotrophic bacteria to oxidize labile sediment carbon and in turn provide a mechanism for particulate carbon loss, likely as a result of CO₂ production, in the fluviokarst system. The existence of loosely compacted surficial fine grained laminae at the floor of the conduit within oxygenated water further supports the phreatic conduits as a biologically-active pathway for sediment organic carbon. The results suggest karst pathways as biologically active conveyors of sediment carbon that temporarily store sediment, turnover carbon at higher rates than would be considered otherwise, and recharge relatively depleted organic carbon back to the surface stream within the fluvial system.

The preliminary water quality results of the project show:

1. The geometric means of the fecal coliform count at the surface stream (605) and at the karst conduit (369) exceed the 200 cfu/100mL criteria for primary recreational contact.
2. The fecal coliform dataset shows that the conduit and surface stream are highly coupled and both have peaks and troughs coinciding with one another.
3. $\delta^{15}\text{N}$ of sediment does not vary much over time, but it does vary longitudinally (more enriched as it is transported downstream). There may be potential for denitrification to occur in the conduit.
4. Nitrate concentrations decrease with temperature perhaps due to phytoplankton production in the surface and later diverting of water experiencing a high uptake of nutrients.
5. Nitrate levels in the subsurface are almost greater than nitrate levels in Cane Run creek, but both are very similar.
6. Fecal coliform peaks seem to coincide with low levels of nitrate; nitrate peaks seem to coincide with low levels of coliform.
7. Nitrate leaching is a prominent feature of the Cane Run agricultural fluviokarst system.

Table 6) Previous Research

Project Name/ Organization	Data Collected	Sampling Frequency	Sampling Duration	Sampling Locations
Cane Run Research (UK Sediment Team)	$\delta^{13}\text{C}$, $\delta^{15}\text{N}$, POC, PN	Biweekly	2011 - 2013, 2017 - Current	LEX, SPIN, LISLE, RYSP
Royal Spring Aquifer Study (KGS)	Dye traces, geological formations, conduit profile, water levels, turbidity, conduit velocity	(50 total wells), continuous sampling	2007 - Current	KYHP, Numerous groundwater wells
Cane Run 271B (KGS)	NO ₃ , TP, TDS, TSS, Chlorine, Fecal Col.	Biweekly	2012 - Current	KYHP, CRCK
Cane Run WBP (UKCAFE)	Nutrients, Fecal counts	NA	2008 - 2010	12 sub-basins
Surface stream study (UK CAFE)	Stream flow rate, turbidity, temperature, stream profiles	Continuous	2011 - 2013	LEX, SPIN, LISLE
303(d) study (KDOW)	DO, Bacteria	NA	1998 - 2010	All 17.4 miles of Cane Run
Cane Run/Royal Spring Study (Third Rock Consulting)	CBOD, NO ₂ , NH ₃ , Ortho P, TSS, E. Coli, Fecal	Monthly, storm-event	2016 - Current	13 locations
Bacteria study (KWERRI)	Fecal swimming/wading	Weekly to monthly	2002	8 surface locations
Water quality study (LFUCG)	E. coli/Fecal swimming/wading, NO ₂ , NH ₃ , Macro counts	NA	1999 - 2011	6 surface locations
Water treatment data (GMWSS)	Turbidity	Daily	2011 - Current	RYSP

A.3.4) Project Planning and Expected Measurements

The objective of this project is to collect constituents of sediment, carbon, nitrogen and phosphorous in order to (1) estimate the contribution of water and nitrate from various sources of karstic waters, (2) investigate the role of physical and biogeochemical processes in transforming nitrogen and carbon within karst storage zones, (3) and estimate the net flux of nitrate from subsurface pathways relative to surface pathways. The samples will be tested for $\delta^2\text{H}_{\text{H}_2\text{O}}$, $\delta^{18}\text{O}_{\text{H}_2\text{O}}$, $\delta^{15}\text{N}_{\text{NO}_3}$, $\delta^{18}\text{O}_{\text{NO}_3}$, $\delta^{13}\text{C}_{\text{DIC}}$, NO_3^- , P, $\delta^{15}\text{N}_{\text{Sed}}$, $\delta^{13}\text{C}_{\text{Sed}}$, PN, and POC. The project quality objectives are outlined in section A.4. Sampling, analytical and data review activities are discussed briefly in the following subsections, but are detailed in Part B, with Table 1 summarizing the data collection needs defined during the planning process between the project manager and the primary advisor. Additional, non-analytical, inputs are discussed in section A.4.1.3. Final products and deliverables from the project are outlined in section C.5.

1) Sediment Concentration (TSS)

Suspended sediment samples will be collected at a specified point using Teledyne ISCOs for storm events at the watershed outlet and two tributaries. Depth integrated sediment samples will be collected during weekly (sediment trap) field sampling and during monthly (grab) field sampling. Samples will be brought back to the lab and analyzed for Total Suspended Solids. Refer to section A.6.2 for sampling schedules. Refer to section B for sample analysis and acquisition methodology. A relationship will also be established between TSS and Turbidity to simulate continuous estimates of sediment concentration.

2) Field Parameters (DO, pH, Temp, Cond)

Four different field parameters will be measured at the Groundwater Station. These include temperature, pH, dissolved oxygen, and specific conductance. These parameters will be measured using a YSI 6920v2 sonde will be utilized to generate 5 minute measurements. For other locations, these parameters will be measured manually using the Horiba Water Quality Checker U-10.

3) Stage (H)

Stage data will be collected at all sediment trap sites during field visits using a meter stick. The measurements will be made at repeatable locations (e.g. on the front left side of a t-post that is embedded in the streambed) and will measure the distance from the streambed to the water surface. Stage data will also be collected from USGS staff gauges. Additionally, well stage will be measured using a piezometer at Well 21 and KYHP.

4) Flowrate (Q)

Flowrate will be obtained from a USGS gauging station at Royal Spring and several surface locations. Refer to section A.5 for treatment of secondary data.

5) Nitrate (NO_3^-)

Grab samples will be collected at each of the surface water data acquisition stations and groundwater station. These samples will be analyzed for Nitrate. Refer to Section A.6.2 for sampling schedules. Refer to Section B for sample analysis and acquisition methodology.

6) Total Recoverable Phosphorus (P)

Grab samples will be collected at each of the surface water data acquisition stations and groundwater station. These samples will be analyzed for Dissolved Phosphorus. Refer to Section A.6.2 for sampling schedules. Refer to Section B for sample analysis and acquisition methodology.

7) $\delta^{13}\text{C}$, $\delta^{15}\text{N}$, POC, and PN of Transported Sediment

Sediment traps will be placed at two tributaries (one urban, one ag), at the longitudinal midpoint of the main surface channel, and at Royal Spring to gather spatially and temporally integrated sediment samples. These samples will be analyzed for $\delta^{15}\text{N}$ and $\delta^{13}\text{C}$ of Transported Sediment, POC, and PN using an elemental analyzer that is interfaced with an Isotope Ratio Mass Spectrometer.

8) $\delta^{18}\text{O}_{\text{NO}_3}$ and $\delta^{15}\text{N}_{\text{NO}_3}$ of Transported Water

Water samples will be collected at Royal Spring, Cane Run Creek, a groundwater well, and at the Groundwater Station to gather spatially and temporally integrated water samples. These samples will be analyzed for $\delta^{18}\text{O}_{\text{NO}_3}$ and $\delta^{15}\text{N}_{\text{NO}_3}$ using an Isotope Ratio Mass Spectrometer.

9) $\delta^{13}\text{C}_{\text{DIC}}$ of Transported Water

Water samples will be collected at Royal Spring, Cane Run Creek, a groundwater well, and at the Groundwater Station to gather spatially and temporally integrated water samples. These samples will be analyzed for $\delta^{13}\text{C}_{\text{DIC}}$ using an Isotope Ratio Mass Spectrometer.

10) $\delta^{18}\text{O}_{\text{H}_2\text{O}}$ and $\delta\text{D}_{\text{H}_2\text{O}}$ of Transported Water

Water samples will be collected at Royal Spring, Cane Run Creek, a groundwater well, and at the Groundwater Station to gather spatially and temporally integrated water samples. These samples will be analyzed for $\delta^{18}\text{O}_{\text{H}_2\text{O}}$ and $\delta\text{D}_{\text{H}_2\text{O}}$ using an Isotope Ratio Mass Spectrometer.

11) Precipitation (PRCP)

Precipitation data will be obtained continuously at hour intervals using rainfall records available from NOAA for the Lexington Airport. Average rainfall depths for the sub-watersheds upstream of each sampling locations will be determined using standard NOAA protocols. No approved EPA method exists for the measurement of precipitation data. Precipitation data will also be obtained from 2 USGS gauging stations (located at the watershed outlet and in an adjacent system). Refer to section A.5 for treatment of secondary data.

A.4) Project Quality Objectives and Measurement Performance Criteria

All data collected in support of the project will follow standard operating procedures, EPA protocols for *Quality Assurance Project Plans*, EPA-505-B-04-900A, 2005 and the *Kentucky Ambient/Watershed Water Quality Monitoring Standard Operating Procedure Manual*, 2005. The latter document provides both quality objectives and criteria (e.g Appendix F – Quality Control Design) which are applicable to both field parameters (i.e. specific conductance, pH, and dissolved oxygen) as well as phosphorus grab samples (i.e. nutrients) that will be collected as part of this study. Further, analysis of isotope samples will follow *EPA-Sip/OP.1* which outlines the quality objectives criteria for carbon and nitrogen elemental/isotopic analysis.

A.4.1) Development of Project Quality Objectives Using the Systematic Planning Process

A.4.1.1) Problem Statement

The problem statement is outlined in section A.3.1.

A.4.1.2) Goals of the Study

The primary hypothesis of the study is that the surface fine-grained laminae of the karst conduit bed provides the potential for bioremediation of surface-derived nutrients and bacteria. Alternatively we hypothesize that the surface fine-grained laminae does not have any significant bioremediation capabilities, however improving numerical modeling of nutrient and bacteria transport in karst conduits will improve fluvio-karst nutrient budgets. Additional goals of the study include estimating nitrogen and phosphorus transformation rates and estimating karst water contribution from various sources with isotopic data.

A.4.1.3) Information Inputs

See section A.3.2 for the analytical inputs needed to fill gaps missing in the Problem Statement. Additional inputs needed for the study includes geospatial data for the watershed including land cover maps, stream-conduit connectivity, and topography.

A.4.1.4) Study Boundaries

The proposed dataset will be collected over a 16 month timeframe within a 58 km² study basin. Sediment transport and water quality inputs will be collected at the 5 km² scale to understand tributary inputs. Intermediate tributaries and main stem sites will be collected to understand spatial variability in the watershed. Sampling was designed around current knowledge and data gaps. See section A.3.1 for justification of the sampling design and timing found in section A.6.

A.4.1.5) Analytical Approach

Samples collected from sample sites in Figure 2 will represent integrated measurements of all upstream surface and subsurface activity, respectively. Samples collected from Urban Trib (~5 km²) will represent mean urban tributaries in the watershed and Ag Trib (~5 km²) will represent predominantly agricultural watersheds. The parameters of interest and their use are outlined in Table 1.

A.4.1.6) Performance or Acceptance Criteria

Detailed information on data quality indicators, performance activities and performance criteria of each analyte can be found in section A.4.2.

A.4.1.7) Detailed Plan for Obtaining Data

See section B.1 for the detailed tasks of collecting data and the attached appendices for data collection methods and analytical procedures.

A.4.2) Measurement Performance Criteria

Measurement Performance Criteria (MPC) are quantified for each analytical process in the below tables in order to address issues associated with (1) precision, (2) accuracy and bias, (3) sensitivity and quantitation limits, (4) representativeness, (5) comparability and (6) completeness (see EPA-505-B-04-900A). The first 4 MPCs are addressed in Tables 7 and 8. Completeness is addressed using the checklist found in Table 9. The completeness form is a tool that provides project managers with a comprehensive checklist of deliverables used to verify the quality of the data through rigorous documentation of the sample collection and analytical procedures. With regard to comparability, samples will be taken from the exact same location each time by staking sampling locations with t-posts that are driven into the streambed. Although Method Detection Limits (MDL) and Quantitation limits (QL) are not clearly defined here, they are defined for each analysis in section A.6.1.

Table 7) QC Sample or Measurement Performance Activity

Analyte	Lab Precision	Overall Precision	Lab Accuracy/ Bias	Overall Accuracy/ Bias	Sensitivity
Nitrate	Standard Duplicates	Sample Duplicates	Standards/ Blanks	Equipment Blank	Based on Instrument
Phosphorus	Standard Duplicates	Sample Duplicates	Standards/ Blanks	Equipment Blank	Based on Instrument
Sediment Concentration	Balance/ Analytical Standard	Sample Duplicates	Standards/ Blanks	Equipment Blank	N/A
POC of Transported Sediment	Standard Duplicates	Sample Triplicates	Calibrate standard to	Blanks	See SIP/OP.01 EPA
PN of Transported Sediment	Standard Duplicates	Sample Triplicates	Calibrate standard to	Blanks	See SIP/OP.01 EPA
δ ¹³ C of Transported Sediment	Standard Duplicates	Sample Triplicates	Calibrate standard to	Blanks	See SIP/OP.01 EPA
δ ¹⁵ N of Transported Sediment	Standard Duplicates	Sample Triplicates	Calibrate standard to	Blanks	See SIP/OP.01 EPA
δ ¹⁵ N of Nitrate	Standard Duplicates	Sample Triplicates	Calibrate standard to	Blanks	Based on Standards
δ ¹⁸ O of Nitrate	Standard Duplicates	Sample Triplicates	Calibrate standard to	Blanks	Based on Standards
δ ¹³ C of DIC	Standard Duplicates	Sample Triplicates	Calibrate standard to	Blanks	See SIP/OP.01 EPA
δ ¹⁸ O of Water	Standard Duplicates	Sample Triplicates	Calibrate standard to	Blanks	See SIP/OP.01 EPA
δ ² H of Water	Standard Duplicates	Sample Triplicates	Calibrate standard to	Blanks	See SIP/OP.01 EPA

Table 8) Measurement Performance Criteria

Analyte	Lab Precision	Overall Precision	Lab Accuracy/ Bias	Overall Bias	Accuracy/ Sensitivity
Nitrate	RPD ≤10%	RPD ≤10%	Standard ±10% Blank <MDL	<MDL	0-40mg/L
Total Recoverable Phosphorous	RPD ≤10%	RPD ≤10%	Standard ±10% Blank <MDL	<MDL	0.05-1mg/L
Sediment Concentration	Balance <0.5mg Standard ±15%	>50mg/L RPD<20% <50mg/L ±10mg/L	Standard ±10% Blank <10mg/L	<10mg/L	>10mg/L
δ ¹⁵ N of Transported Sediment	±0.5‰	±0.5‰	Standard ±0.5‰ Blank No peak	No peak	0.5-10 Volts
δ ¹³ C of Transported Sediment					
POC of Transported Sediment	SD ±10%	SD ±10%	Standard ±10% Blank No peak	No peak	0-50%
PN of Transported Sediment	SD ±10%	SD ±10%	Standard ±10% Blank No peak	No peak	0-10%
δ ¹⁵ N of Nitrate					
δ ¹⁸ O of Nitrate					
δ ¹³ C of DIC					
δ ¹⁸ O of Water					
δ ² H of Water					

Table 9) Completeness Checklist (from EPA-505-B-04-900A)

Item	Description	Verification (completeness)	Validation (conformance specifications) to
Planning Documents/Records			
1	Approved QAPP		
2	Contract		
4	Field SOPs		
5	Laboratory SOPs		
Field Records			
6	Field logbooks		
7	Equipment calibration records		
8	Chain-of-Custody Forms		
9	Sampling diagrams/surveys		
10	Geophysics reports		
11	Relevant Correspondence		
12	Change orders/deviations		
13	Field audit reports		
14	Field corrective action reports		
Analytical Data Package			
15	Cover sheet (laboratory identifying information)		
16	Case narrative		
17	Internal laboratory chain-of-custody		
18	Sample receipt records		
19	Sample chronology (i.e. dates and times of receipt, preparation, & analysis)		
20	Communication records		
21	Project-specific PT sample results		
22	LOD/LOQ establishment and verification		
23	Standards Traceability		
24	Instrument calibration records		
25	Definition of laboratory qualifiers		
26	Results reporting forms		
27	QC sample results		
28	Corrective action reports		
29	Raw data		
30	Electronic data deliverable		

A.5) Secondary Data Evaluation

The secondary data, sources, uses, and limitations are summarized in Table 10. Flowrate at the spring outlet (USGS station) will be used to aid in calibration of the sediment transport model. The USGS gauging station is located downstream of Groundwater Station and is used as a surrogate when Groundwater Station equipment is inactive. The estimates are collected continuously at a five minute interval. Geospatial USGS data including National Land Cover Datasets (NLCD) will be used for the sub-basin in question. A potential limitation exists in the resolution of the data needing to match the resolution of the model.

Previously published transported sediment (Fox *et al.*, 2010; Russo and Fox, 2012; Ford and Fox, 2012; Husic *et al.*, 2016) and bank sediment (Fox *et al.*, 2010) data will be used to assist in model parameterization. Elemental and isotopic signatures of transported sediments were collected using integrated sediment trap samplers. The data was analyzed using appropriate QC as discussed in this QAPP.

Table 10) Secondary data sources, use, and limitations

Data type	Source	Data uses relative to current project	Factors affecting the reliability of data and limitations on data use
Flowrate at watershed outlet	USGS	Calibration of hydrologic model.	Downstream of Groundwater Station calibration point. Used as a surrogate.
Land Cover Data	USGS-NLCD	Determine the % land use of each sub-basin. Inputs into the hydrologic model	No known limitations.
Carbon Model	Husic <i>et al.</i> , 2016	Used as an input for the nitrogen model.	Only calibrated to suspended sediment carbon, no calibration for bed sediment carbon.
Sediment Transport Model	Russo and Fox, 2012; Husic <i>et al.</i> , 2016	Used as an input for the nitrogen model.	Spatial sediment influx to subsurface is an uncertainty.
Sediment trap data	Fox <i>et al.</i> , 2010	Used as tributary input for the sediment, carbon, nitrogen and nitrogen isotope models	Data collected from a surface-dominated watershed.
Bank Sediment data	Fox <i>et al.</i> , 2010	Used as input for the sediment, carbon, nitrogen and nitrogen isotope models	Data collected from a surface-dominated watershed.

A.6) Project Overview and Schedule

A.6.1) Project Overview (Outcome of Project Scoping Activities)

Table 11 provides a detailed overview of the project data needs, the laboratory method detection limit (MDL) and the quantitation limit (QL). The MDL is a statistically derived detection limit that represents a 99% confidence level that the reported signal is different from a blank sample and the QL is the minimum concentration of an analyte that can be routinely identified and quantified above the method detection limit. The QL is optimally defined as 10*MDL but can be as low as 3*MDL (see EPA-505-B-04-900A). The analytical procedures and labs were chosen as a result of proximity, temporal and economic feasibility balanced with the desired project quality criteria discussed in section A.4.

Table 11) Overview of project data needs, quantitation limits and method detection limits.

Analyte	Quantitation Limit (QL)	Method Detection Limit (MDL)
Nitrate	0 mg/L	0 mg/L
Total Recoverable Phosphorous	0.06 mg/L	0.02 mg/L
Sediment Concentration	30 mg/L	10 mg/L
$\delta^{15}\text{N}$ of Transported Sediment	0.5 Volts	0 Volts
$\delta^{13}\text{C}$ of Transported Sediment	0.5 Volts	0 Volts
POC of Transported Sediment	N/A	N/A
PN of Transported Sediment	N/A	N/A
$\delta^{13}\text{C}$ of DIC		
$\delta^{15}\text{N}$ of Nitrate		
$\delta^{18}\text{O}$ of Nitrate		
$\delta^{18}\text{O}$ of Water		
$\delta^2\text{H}$ of Water		
Fecal Coliform	2 cfu/100mL	0 cfu/100mL

A.6.2) Project Schedule

The below project schedule addresses particular tasks needed to satisfy the sampling procedure described in Task B.1.1. Generally, samples will be collected over 16 months (Feb 2017-June 2018) and analysis and subsequent data implementation will be conducted the following 3 months (June 2018-Aug 2018). The project schedule activities, responsible parties, timeframe of the proposed activity, deliverables and deliverable due dates are addressed in Table 12.

Table 12) Project Scheduling Summary

Activity	Responsible parties	Activity Timeframe	Deliverable(s)	Deliverable due date
Sample collection-Surface Water	Admin Husic	Feb 2017- June 2018	Field notes	June 2018
Sample collection-Sediment Traps	Admin Husic/ Undergraduate Researchers	Feb 2017- June 2018	Field notes	June 2018
Sample collection- Sediment Load	Admin Husic/ Undergraduate Researchers	Feb 2017- June 2018	Field notes	June 2018
Surface Water Sample Analysis	Jason Backus/ Erik Pollock/ Admin Husic	Feb 2017- June 2018	Report of Analyses for each sample run	June 2018
Sediment Trap Sample Preparation	Admin Husic/ Undergraduate Researchers	Feb 2017- June 2018	Laboratory Procedure Spreadsheet	June 2018
Sediment Trap Elemental/Isotope Analysis	Admin Husic/ Dr. Romanek	Feb 2017- June 2018	Report of Analyses for each sample run	June 2018
Sediment Load Sample Analysis	Undergraduate Researchers/ Admin Husic	Feb 2017- June 2018	Report of Analyses for each sample run	June 2018
Data Validation	Admin Husic	Feb 2017- June 2018	QAQC Report	June 2018
Incorporation into modeling Framework	Admin Husic	Feb 2017- June 2018	Dissertation Research	June 2018

Section B: Measurement/ Data Acquisition

B.1) Sampling Tasks

B.1.1) Sampling Process Design and Rationale

B.1.1.1) Location of Environmental Samples

To generate the desired spatial variability and to assess the importance of watershed scale, samples will be obtained from the sites depicted in Figure 2 in section A.3.1. Two tributary streams with drainage areas on the order of 5 km² will be monitored. Site selection was motivated by understanding nutrient and carbon inputs from urban and agricultural lands *via* the small tributaries and to assess how alterations occur during downstream transport under various flow conditions.

Sites on the order of 5 km² were chosen since they produced representative quantities of other sub-basins within the watershed (Husic *et al.*, 2016). Finally, the main stem site offer integration of the two prominent land uses, and a conduit site offers a representation of mixed surface/subsurface flows and processes.

Site selection was determined based on the following criteria which was obtained from the Kentucky Ambient/Watershed Water Quality Monitoring SOP Manual

- **Sampler Safety**- Expensive sampling equipment will be used to sample sediment load (i.e. the turbidity and ISCO samplers), hence safety of samplers is of the utmost importance. Sites were generally located in 'out of sight' secluded areas and lines will be buried.
- **Accessibility**- Sites selected were generally easily accessible from a nearby road in which a parking spot is readily available.
- **Proximity to a current hydrological Station**- The Cane Run watershed was partially chosen as the test bed for this study as it has a USGS gauging station and a KGS gauging station on the main stem.
- **Transport time to laboratories**- The Cane Run watershed is a short drive (approximately 10 miles) from the University of Kentucky Hydrosystems and KGS labs.
- **Conformation of stream reach sampled**- Stream reaches of sampling sites were generally straight riffle sections. This also allows for wading during higher flows to obtain grab samples.
- **Reach mixing**- Monitored stream sections appeared to be well mixed with homogenous pH, DO, and temperature readings in the area surrounding the sampling site.
- **Backwater effect**- Sampling locations were setup upstream of major tributaries (or upstream of the main stem for the small tributaries) to avoid backwater effects.
- **Other factors**- Site safety and authorization to sample from landowners were considered during the site selection process.

B.1.1.2) Scheduling, Number of Samples and Sampling Design Rationale

To meet the desired objectives of the project, the samples mentioned in Table 1 will be collected. Note, that within a given season the order of sampling can be rearranged since hydrologic conditions are highly unpredictable. Therefore, 16-month sampling routine is proposed. The following subsections detail the scheduling, number of samples and design rationale (e.g. why the sample design was selected for each data type). Table 13 displays a summary schedule for water and sediment samples collected throughout the project.

1) Sediment Concentration (TSS)

Suspended sediment samples will be collected at a specified point using Teledyne ISCOs for storm events at the watershed outlet and two tributaries. Depth integrated sediment samples will be collected during sediment trap field sampling and during grab field sampling.

Samples will be brought back to the lab and analyzed for Total Suspended Solids. Refer to section A.6.2 for sampling schedules. Refer to section B for sample analysis and acquisition methodology. A relationship will also be established between TSS and Turbidity to simulate continuous estimates of sediment concentration.

2) Field Parameters (DO, pH, Temp, Cond)

Four different field parameters will be measured at the Groundwater Station. These include temperature, pH, dissolved oxygen, and specific conductance. These parameters will be measured using a YSI 6920v2 sonde will be utilized to generate 5 minute measurements. For other locations, these parameters will be measured manually using the Horiba Water Quality Checker U-10.

3) Stage (H)

Stage data will be collected at all wadable sites during field visits using a meter stick. The measurements will be made at repeatable locations (e.g. on the front left side of a t-post that is embedded in the streambed) and will measure the distance from the streambed to the water surface. Stage data will also be collected from USGS staff gauges. Additionally, well stage will be measured using a piezometer at Well 21 and KYHP.

4) Flowrate Measurements (Q)

Flowrate will be obtained from a USGS gauging station at Royal Spring and several surface locations. Flowrates are needed for calibration of the hydrologic model. Refer to section A.5 for treatment of secondary data.

5) Nitrate (NO_3^-)

Nitrate samples will be collected biweekly and during storm events at KYHP, CRCK, RYSP, and Well 21 (Storm Only). Preliminary samples suggest that nitrate is abundant during all seasons and that both seasonal and spatial variability may be important in governing nitrate transport and removal. Likewise, storm events need to be closely monitored since the majority of transported nitrogen occurs during these periods. A total of 116 samples will be collected.

6) Total Recoverable Phosphorus (P)

DP samples will be collected biweekly at KYHP, CRCK, and RYSP. Collection of DP will help to constrain the stream carbon cycle since it can provide rate limiting conditions for carbon growth, which will ultimately assist in parameterization of the nitrogen model. Preliminary results suggest that the tributaries represent DP end members with the main stem site falling somewhere in between depending on flow conditions. A total number of 116 samples will be collected.

7) $\delta^{15}\text{N}$, $\delta^{13}\text{C}$, PN, and POC of Transported Sediment

Sediment traps will be placed at two tributaries (one urban, one ag), at the longitudinal midpoint of the main surface channel, and at Royal Spring to gather spatially and temporally integrated sediment samples. These samples will be analyzed for $\delta^{15}\text{N}$ and $\delta^{13}\text{C}$ of Transported Sediment, POC and PN using an elemental analyzer that is interfaced with an Isotope Ratio Mass Spectrometer. A total number of 158 samples will be analyzed.

8) $\delta^{15}\text{N}_{\text{NO}_3}$ and $\delta^{18}\text{O}_{\text{NO}_3}$ of Transported Water

Water samples will be collected at RYSP during biweekly sampling, KYHP and RYSP during low flow sampling, and at KYHP, CRCK, Well 21, and RYSP during storm events in order to gather spatially and temporally integrated water samples. These samples will be analyzed for $\delta^{18}\text{O}_{\text{H}_2\text{O}}$ and $\delta\text{D}_{\text{H}_2\text{O}}$ using an Isotope Ratio Mass Spectrometer. A total number of 172 samples will be analyzed

9) $\delta^{13}\text{C}_{\text{DIC}}$ of Transported Water

Water samples will be collected at RYSP during biweekly sampling and at KYHP, CRCK, Well 21, and RYSP during storm events to gather spatially and temporally integrated water samples. These samples will be analyzed for $\delta^{18}\text{O}_{\text{H}_2\text{O}}$ and $\delta\text{D}_{\text{H}_2\text{O}}$ using an Isotope Ratio Mass Spectrometer. A total number of 117 samples will be analyzed

10) $\delta^{18}\text{O}_{\text{H}_2\text{O}}$ and $\delta\text{D}_{\text{H}_2\text{O}}$ of Transported Water

Water samples will be collected at KYHP, CRCK, Well 21, and RYSP during storm events to gather spatially and temporally integrated water samples. These samples will be analyzed for $\delta^{18}\text{O}_{\text{H}_2\text{O}}$ and $\delta\text{D}_{\text{H}_2\text{O}}$ using an Isotope Ratio Mass Spectrometer. A total number of 85 samples will be analyzed

11) Precipitation (PRCP)

Precipitation data will be obtained continuously at hour intervals using rainfall records available from NOAA for the Lexington Airport. Average rainfall depths for the sub-watersheds upstream of each sampling locations will be determined using standard NOAA protocols. No approved EPA method exists for the measurement of precipitation data. Precipitation data will also be obtained from 2 USGS gauging stations (located at the watershed outlet and in an adjacent system). Refer to section A.5 for treatment of secondary data.

Table 13) Summary of the monthly sampling routine.

Constituent	Event	Feb 2017	Mar 2017	Apr 2017	May 2017	June 2017	July 2017	Aug 2017	Sept 2017	Oct 2017	Nov 2017	Dec 2017	Jan 2018	Feb 2018	Mar 2018	April 2018	May 2018	June 2018
NO ₃ ⁻	Biweekly	KYHP, RYSP, CRCK	KYHP, RYSP, CRCK	KYHP, RYSP, CRCK	KYHP, RYSP, CRCK	KYHP, RYSP, CRCK	KYHP, RYSP, CRCK	KYHP, RYSP, CRCK	KYHP, RYSP, CRCK	KYHP, RYSP, CRCK	KYHP, RYSP, CRCK	KYHP, RYSP, CRCK	KYHP, RYSP, CRCK	KYHP, RYSP, CRCK	KYHP, RYSP, CRCK	KYHP, RYSP, CRCK	KYHP, RYSP, CRCK	KYHP, RYSP, CRCK
	Storm	KYHP, RYSP, CRCK, WELL		KYHP, RYSP, CRCK, WELL			KYHP, RYSP, CRCK, WELL			KYHP, RYSP, CRCK, WELL				KYHP, RYSP, CRCK, WELL				
	Low																	
δ ¹⁵ N _{NO3} & δ ¹⁵ N _{NO3}	Biweekly	RYSP	RYSP	RYSP	RYSP	RYSP	RYSP	RYSP	RYSP	RYSP	RYSP	RYSP	RYSP	RYSP	RYSP	RYSP	RYSP	RYSP
	Storm	KYHP, RYSP, CRCK, WELL		KYHP, RYSP, CRCK, WELL			KYHP, RYSP, CRCK, WELL			KYHP, RYSP, CRCK, WELL				KYHP, RYSP, CRCK, WELL				
	Low			KYHP, RYSP			KYHP, RYSP									KYHP, RYSP		
δ ¹³ C _{DIC}	Biweekly	RYSP	RYSP	RYSP	RYSP	RYSP	RYSP	RYSP	RYSP	RYSP	RYSP	RYSP	RYSP	RYSP	RYSP	RYSP	RYSP	RYSP
	Storm	KYHP, RYSP, CRCK, WELL		KYHP, RYSP, CRCK, WELL			KYHP, RYSP, CRCK, WELL			KYHP, RYSP, CRCK, WELL				KYHP, RYSP, CRCK, WELL				
	Low																	
δ ¹⁸ O _{H2O} & δ ² H _{H2O}	Biweekly																	
	Storm	KYHP, RYSP, CRCK, WELL		KYHP, RYSP, CRCK, WELL			KYHP, RYSP, CRCK, WELL			KYHP, RYSP, CRCK, WELL				KYHP, RYSP, CRCK, WELL				
	Low																	
δ ¹⁵ N _{sed} , δ ¹³ C _{sed} , POC _{sed} , PN _{sed}	Biweekly	LEX, SPIN, DAIRY, RYSP	LEX, SPIN, DAIRY, RYSP	LEX, SPIN, DAIRY, RYSP	LEX, SPIN, DAIRY, RYSP	LEX, SPIN, DAIRY, RYSP	LEX, SPIN, DAIRY, RYSP	LEX, SPIN, DAIRY, RYSP	LEX, SPIN, DAIRY, RYSP	LEX, SPIN, DAIRY, RYSP	LEX, SPIN, DAIRY, RYSP	LEX, SPIN, DAIRY, RYSP	LEX, SPIN, DAIRY, RYSP	LEX, SPIN, DAIRY, RYSP	LEX, SPIN, DAIRY, RYSP	LEX, SPIN, DAIRY, RYSP	LEX, SPIN, DAIRY, RYSP	LEX, SPIN, DAIRY, RYSP
	Storm	RYSP	RYSP	RYSP	RYSP	RYSP	RYSP	RYSP	RYSP	RYSP	RYSP	RYSP	RYSP	RYSP	RYSP	RYSP	RYSP	RYSP
	Low																	

Locations: KYHP-Kentucky Horse Park (Conduit), CRCK-Cane Run Creek, WELL-Well 21, RYSP-Royal Spring, LEX-Urban Tributary at Lexmark, SPIN-Agricultural Tributary at Spindletop, DAIRY-Dairy Road

Table 14) Monthly Schedule/Checklist

Month	Sampling			Data Review/Validation	Database Incorporation	Quarterly QA Report	Data Implementation	Final Report
Feb-17	Biweekly x2	Storm		End of Month	End of Month			
Mar-17	Biweekly x2			End of Month	End of Month			
Apr-17	Biweekly x2	Storm	Low Flow	End of Month	End of Month	End of Month		
May-17	Biweekly x2			End of Month	End of Month			
Jun-17	Biweekly x2			End of Month	End of Month			
Jul-17	Biweekly x2	Storm	Low Flow	End of Month	End of Month	End of Month		
Aug-17	Biweekly x2			End of Month	End of Month			
Sep-17	Biweekly x2			End of Month	End of Month			
Oct-17	Biweekly x2	Storm		End of Month	End of Month	End of Month		
Nov-17	Biweekly x2			End of Month	End of Month			
Dec-17	Biweekly x2			End of Month	End of Month			
Jan-18	Biweekly x2			End of Month	End of Month	End of Month		
Feb-18	Biweekly x2	Storm		End of Month	End of Month			
Mar-18	Biweekly x2			End of Month	End of Month			
Apr-18	Biweekly x2	Low Flow		End of Month	End of Month			
May-18	Biweekly x2			End of Month	End of Month	End of Month		
Jun-18							Progress Report	
Jul-18							Progress Report	
Aug-18							Progress Report	Finished

Table 15) Weekly Schedule/Checklist Excerpt

Week		Prepare for Sampling	Biweekly Sample	Nutrient Sample to KGS	Sediment Sample to Freeze Dry	Mail Isotope Samples	Backup Unclejonny	Monthly Data Review/Validation	Database Incorporation	Quarterly QA Report	Data Implementation	Final Report
2/13/2017	2/19/2017											
2/20/2017	2/26/2017	D/I	D/I	D/I								
2/27/2017	3/5/2017				D/I	D/I		D/I	D/I			
3/6/2017	3/12/2017	D/I	D/I	D/I			D/I					
3/13/2017	3/19/2017				D/I	D/I	D/I					
3/20/2017	3/26/2017	D/I	D/I	D/I			D/I					
3/27/2017	4/2/2017				D/I	D/I	D/I	D/I	D/I			
4/3/2017	4/9/2017	D/I	D/I	D/I			D/I					
4/10/2017	4/16/2017				D/I	D/I	D/I					
4/17/2017	4/23/2017	D/I	D/I	D/I			D/I					
4/24/2017	4/30/2017				D/I	D/I	D/I	D/I	D/I			
5/1/2017	5/7/2017	D/I	D/I	D/I			D/I					
5/8/2017	5/14/2017				D/I	D/I	D/I					
5/15/2017	5/21/2017	D/I	D/I	D/I			D/I					
5/22/2017	5/28/2017				D/I	D/I	D/I					
5/29/2017	6/4/2017	D/I	D/I	D/I			D/I	D/I	D/I			
6/5/2017	6/11/2017				D/I	D/I	D/I					
6/12/2017	6/18/2017	D/I	D/I	D/I			D/I					

Table 17 Low Flow Schedule Checklist Template

Low Flow Schedule Checklist		Event Number:		Sampled By:		
Day	KYHP			RYSP		
	Analyte	Date	Time	Sample	Date	Time
1	NO ₃			NO ₃		
	$\delta^{15}\text{N}/\delta^{18}\text{O}_{\text{NO}_3}$			$\delta^{15}\text{N}/\delta^{18}\text{O}_{\text{NO}_3}$		
2	NO ₃			NO ₃		
	$\delta^{15}\text{N}/\delta^{18}\text{O}_{\text{NO}_3}$			$\delta^{15}\text{N}/\delta^{18}\text{O}_{\text{NO}_3}$		
3	NO ₃			NO ₃		
	$\delta^{15}\text{N}/\delta^{18}\text{O}_{\text{NO}_3}$			$\delta^{15}\text{N}/\delta^{18}\text{O}_{\text{NO}_3}$		
4	NO ₃			NO ₃		
	$\delta^{15}\text{N}/\delta^{18}\text{O}_{\text{NO}_3}$			$\delta^{15}\text{N}/\delta^{18}\text{O}_{\text{NO}_3}$		
5	NO ₃			NO ₃		
	$\delta^{15}\text{N}/\delta^{18}\text{O}_{\text{NO}_3}$			$\delta^{15}\text{N}/\delta^{18}\text{O}_{\text{NO}_3}$		
6	NO ₃			NO ₃		
	$\delta^{15}\text{N}/\delta^{18}\text{O}_{\text{NO}_3}$			$\delta^{15}\text{N}/\delta^{18}\text{O}_{\text{NO}_3}$		
7	NO ₃			NO ₃		
	$\delta^{15}\text{N}/\delta^{18}\text{O}_{\text{NO}_3}$			$\delta^{15}\text{N}/\delta^{18}\text{O}_{\text{NO}_3}$		
8	NO ₃			NO ₃		
	$\delta^{15}\text{N}/\delta^{18}\text{O}_{\text{NO}_3}$			$\delta^{15}\text{N}/\delta^{18}\text{O}_{\text{NO}_3}$		
9	NO ₃			NO ₃		
	$\delta^{15}\text{N}/\delta^{18}\text{O}_{\text{NO}_3}$			$\delta^{15}\text{N}/\delta^{18}\text{O}_{\text{NO}_3}$		
10	NO ₃			NO ₃		
	$\delta^{15}\text{N}/\delta^{18}\text{O}_{\text{NO}_3}$			$\delta^{15}\text{N}/\delta^{18}\text{O}_{\text{NO}_3}$		

B.1.1.3) Design Assumptions

The following assumptions are associated with the selected sample design.

- 7 Selected tributaries are representative of their respective land use across the watershed.
- 8 Since urban and agriculture practices are fairly homogenous across the watershed, this is justifiable.
- 9 It's assumed that the sampling design frequency is sufficient to capture seasonal variation in key constituents.
- 10 Based on results of Ford and Fox, *in progress* monthly sampling frequency is adequate to capture the distribution of the population.
- 11 It is assumed that the detailed sampling of the 3 storm events will be sufficient for providing a representative range of flow conditions and that each storm event sampled is representative of storm events occurring in the season.
- 12 Assumes that no significant land use changes will occur over the sampling duration.
- 13 We will monitor for development or changing land use practices.
- 14 By sampling using grab sample methods, it is assumed dissolved constituents are uniformly distributed in the water column.
- 15 Diffusion and well mixed streamwater promote uniformity with depth.

B.1.1.4) Validation of Nonstandard Methods

No nonstandard methods are required for this project.

B.1.2) Sampling Procedures and Requirements

The following sections describe the procedures and requirements to collect samples in the field and deliver them to the laboratory. Standard operating procedures (SOPs) and reference material can be found in the Reference and Appendix sections.

B.1.2.1) Sample Collection Procedures

The following subsections outline the procedures used to collect samples used in this project.

Nitrate, Dissolved Phosphorus, $\delta^{15}\text{N}$ and $\delta^{18}\text{O}$ of Nitrate, $\delta^2\text{H}$ and $\delta^{18}\text{O}$ of Water, $\delta^{13}\text{C}$ of DIC - The direct method for streams (EPA #EH-01) will be utilized to sample NO₃, DP, $\delta^{15}\text{N}_{\text{NO}_3}$, $\delta^{18}\text{O}_{\text{NO}_3}$, $\delta^2\text{H}_{\text{H}_2\text{O}}$, $\delta^{18}\text{O}_{\text{H}_2\text{O}}$, and $\delta^{13}\text{C}_{\text{DIC}}$ at CRCK and RYSP. After the bottle is rinsed in the stream water, the sample is collected by placing the bottle under the water surface with the opening pointing upstream. The sampler will remain downstream of the container and the sample will be collected in a downstream to upstream motion without

disturbing the substrate. At KYHP the conduit well will be sampled with a bailer or water pump lowered 62 feet to the conduit. Water will be pumped or bailed into sampling container. At WELL, the well will be purged three times to 60 feet. The purging ensures the phreatic water is being sampled. After the second purge the conductivity of the water will be tested using the Hach or Horiba probe and checked against the third purging. If the difference between the tested values is insignificant then the third purging will be used for the sample. If there is a large variance, the well will be purged consecutively and checked as needed to obtain a correct sample.

Precipitation- Data will be collected from the NOAA website monthly and stored in an appropriate database (discussed in section B.5).

Fluid Velocity- In-stream vertical velocity profiles will be measured for a range of flows at quarter, half and three quarter stations in the stream cross-section using a Gurley Pigmy propeller meter. Operation of the Gurley meter will follow manufacturer specifications (Gurley, 2004).

Flowrate Measurements- Data will be collected from the NOAA website monthly and stored in an appropriate database (discussed in section B.5).

Sediment Concentration- Sediment concentration will be collected using an automated pump sampler to collect dense concentration data during storm events. Methods for probe measurement, i.e., programming and operation, will follow manufacturer specifications (Teledyne, 2009). Further, an isokinetic-depth integrated sampler will be used to estimate sediment concentrations at fixed stations using accepted USGS methods for sample collection (USGS, 2003).

Stage- Stage will be measured at quarter, half and three quarter stations in the stream cross-section and average stage will be reported for each site. Stage is collected continuously at T1, F1 and F2 using Teledyne ISCO Bubbler Modules (see Teledyne-Bubbler Document in the Appendix).

Turbidity and Temperature- Turbidity and temperature will be sampled in the field using a YSI 600 OMS Multiparameter Sonde with a 6136 Turbidity probe. Methods for probe measurement and calibration will follow manufacturer specifications (YSI, 2011). The probe will be maintained weekly in the field and calibrated once per month in the lab.

$\delta^{15}\text{N}$ of Transported Sediment, POC and PN- Sediment trap samplers will be left in the field for a week at a time to generate a spatially and temporally integrated measure of $\delta^{15}\text{N}$ of Transported Sediment, POC and PN. Briefly, at the front of the trap (inlet) a 4mm diameter inlet tube allows acceleration of fluid into a 98mm diameter test section. The increase in area results in sedimentation, and subsequent trapping of fine sediments. The fluid exits the test section through another 4mm tube. This method was originally published in Phillips et al. (2000) and has been utilized for published studies in the watershed selected for this project (Fox et al., 2010; Ford and Fox, 2012).

Field Parameters- DO, conductivity, pH and water temperature will be sampled in the field using a Hach handheld meter or a Horiba U-10 Water Quality Checker with the appropriate probes. Methods for probe measurement and calibration will follow manufacturer specifications (Hach, 2006, Horiba). The probes will be calibrated prior to and after sampling.

B.1.2.2) Sample Containers, Volume and Preservation

In the field, bulk samples will be collected for the suite of water quality parameters (NO_3 , DP, $\delta^{15}\text{N}_{\text{NO}_3}$, $\delta^{15}\text{N}_{\text{NO}_3}$, $\delta^{18}\text{O}_{\text{NO}_3}$, $\delta^2\text{H}_{\text{H}_2\text{O}}$, $\delta^{18}\text{O}_{\text{H}_2\text{O}}$, $\delta^{13}\text{C}_{\text{DIC}}$) in pre-cleaned wide mouth, 1000 mL, HDPE, plastic bottles or ISCO bottles (which are EPA approved for water quality sample collection). For collection containers of sediment and sediment trap samples see the following sub-headings. Differing trains of thought are present on whether samples should be filtered in the field or in the lab. Field conditions are uncontrollable; hence there are numerous routes in which the sample can become contaminated. For this study, samples will be collected (unfiltered) in the field and filtered immediately after using a 60 ml syringe with filter. Based on the sample collection guide from the USDA (Turk, 2003) samples that are most susceptible to degradation are ones that have high suspended solids (which are relatively low based on previous TSS analysis at baseflow) or samples analyzed for trace constituents. Samples will be filtered using Whatman Glass Fiber 0.45 μm , 47mm filters and then separated into their respective splits for analysis (see the following subheadings). The total require volume of samples (see below) is 815 mL, hence the 1000 mL bottle will provide plenty of extra sample in case of a spill. During transport of water quality samples back to the lab, the samples are placed in zip lock bags to avoid contamination and then placed in a cooler to refrigerate the sample to 4°C.

Nitrate, Dissolved Inorganic Carbon, Dissolved Phosphorus- Filtered nitrate and DP samples remain in the 1000mL HDPE I-CHEM bottles or ISCO bottles without acid preservation (see KGS 9056 and KGS D515/ASTM D515). Samples are then refrigerated to 4°C and have a holding time of 28 days. For the NO_3 and DP split, a minimum of 150 mL of sample is needed.

Sediment Concentration- Depth integrated suspended sediment samples will be collected in pint, plastic containers, of which about $\frac{3}{4}$ is filled with sample. Automated samplers will collect 750 mL of sample in 1000 mL plastic bottles (see Teledyne ISCO manual). The samples will be stored in coolers at 4°C until they can be refrigerated at 4°C in the UK hydraulics lab. Holding times are up to 7 days as per EPA 160.2.

$\delta^{15}\text{N}/\delta^{13}\text{C}$ of Nitrate- Filtered Nitrate samples are poured into pre-cleaned 40 mL VOC Sterile Septum Vials without acid preservation (USGS RSIL, 2003a). Samples are then refrigerated to 4°C and have a holding time of 4 weeks.

$\delta^{18}\text{O}/\delta^2\text{H}$ of Water- Filtered Water samples are poured into pre-cleaned 40 mL VOC Sterile Septum Vials without acid preservation (USGS RSIL, 2003a). Samples are then refrigerated to 4°C and have a holding time of 4 weeks.

$\delta^{13}\text{C}$ of DIC- Filtered DIC samples are poured into pre-cleaned 40 mL VOC Sterile Septum Vials without acid preservation (USGS RSIL, 2003a). Samples are then refrigerated to 4°C and have a holding time of 4 weeks.

$\delta^{15}N$ of Transported Sediment, POC and PN- Samples are collected in a sediment trap as described in Phillips et al. (2000). Approximately 8L of a sediment/water mixture is poured into clean 5 gallon buckets. The samples are preserved by refrigerating at 4 C to minimize microbial transformations. The samples are allowed to settle in the buckets for a minimum of two days. After, water in the bucket is removed through siphoning until a disturbance in the sediment is noted. The remaining mixture is poured into 750 ml bottles and put into the centrifuge to spin down the samples. Again water is removed and the mixture placed on the centrifuge until approximately 100 ml or less of water remains. Samples are then frozen overnight and subsequently freeze-dried to convert the frozen sample into only sediment.

B.1.2.3) Equipment/Sample Containers Cleaning and Decontamination Procedures

All sample containers for water quality and sediment analysis will be new, pre-cleaned, disposable equipment and does not require decontamination. For bottles, and containers used to collect sediments and for the filtration apparatus in the KGS and UK hydraulics lab, standard decontamination procedures for equipment cleaning and decontamination (KDOW, 2005) will be followed.

B.1.2.4) Field Equipment Calibration, Maintenance, Testing and Inspection Procedures

Equipment Calibration- The only non-analytical equipment that needs calibration is the Teledyne ISCO automated grab sampler. Procedures outlined in the manufacturer's manual will be followed. The date of line replacement and calibration will be denoted in the "Cane Run Fieldbook" discussed in B.1.2.6.

Maintenance, Testing and Inspection-Before sampling all equipment will be inspected to ensure it has been cleaned and is in proper working condition. Sampling will be done on an event-by-event basis (this includes baseflow sampling) and will be somewhat unpredictable with regard to timing. Sampling failure can only be ascertained after an event, and as such, any opportunity for capturing samples from a particular event will have passed. Therefore, after each event, all equipment will be thoroughly inspected to ascertain if failure occurred, and if so, the nature of the failure. Information concerning the failure will be recorded in the Equipment Maintenance/Failure Log (which stems from the corrective actions response log--Figure 5. Steps will then be taken to repair or replace the equipment. Additional monitoring equipment will be available for replacement if any equipment fails in the UK Hydraulics Laboratory.

Responsible person- Admin Husic, Graduate Student, University of Kentucky.

B.1.2.5) Sampling Supply Inspection and Acceptance Procedures

B.1.2.5.1) Supplies for cleaning equipment

- Simple Green All-Purpose Cleaner (Phosphate free)---Lowe's/Home Depot
 - Special precaution will be taken not to contaminate the cleaner by using designated bottles for the cleaner.
- Acetone Optima* or Klean Strip, High purity mobile phase for HPLC and/or extraction solvent for GC applications---Fischer Scientific
 - Reagent lot numbers will be recorded for their use duration in a laboratory notebook.
 - Special precaution will be taken not to contaminate the reagent by using designated bottles for the reagent.

Note: If any supplies are known to have become contaminated they will be removed and new supplies will be utilized. Any such incident will be documented accordingly.

B.1.2.5.2) Responsible persons for checking supplies and implementing protocol

- Admin Husic, Graduate Student, University of Kentucky.
- Undergraduate Students, University of Kentucky

B.1.2.6) Field Documentation Procedures

Water Samples- For collection of water samples a notebook titled "Cane Run Streamwater Sampling/Nutrient Sampling Fieldbook" will be utilized. Each collection site will get its own section of the notebook and will denote the following characteristics.

- A visual schematic of the sampling site including significant objects and the sampling location
- Further columns in the notebook will be used to denote the following stream and well measurements.
 - Sample Date/Time
 - Site ID
 - pH
 - DO
 - Temp
 - Conductivity
 - Well Depth (if applicable)
 - Comments (e.g. site conditions, any problems or abnormalities)
 -

Sediment Concentration- To keep up with sediment concentration sampling in the field, a notebook called "Cane Run TSS and Turbidity Sampling Fieldbook" will be used. Sediment concentrations will be collected using two methods as discussed before, and each will have their own section of the notebook.

Stage- Stream stage measurements are actively updated using USGS water data website.

Sediment Trap Samples- For collection of sediment trap samples a notebook titled "Cane Run Weekly Sediment Trap Fieldbook" will be utilized. Each collection site will get its own section of the notebook and will denote the following characteristics.

- A visual schematic of the sampling site including significant objects and the sampling location
- Further columns in the notebook will be used to denote the following stream measurements.
 - Sample Date/Time
 - Site ID (Carried throughout the Analysis Procedure)

- o Condition of the tube (e.g. clogged, clear, rotated, raised off bed)
- o Depth of the tube after installation
- o pH
- o DO
- o Temp
- o Conductivity
- o Comments (e.g. site conditions, any problems or abnormalities)

B.2) Analytical Tasks

B.2.1) Sample Preparation for Analysis

Methods used to prepare samples for analytical procedures need to be documented to understand potential sources of error. For preparation procedures see the Appendix section the SOPs in the Appendix section.

B.2.2) Analytical SOPs

The following table provides a summary of the analytical SOPs used in this document. For more detailed information on how to perform any of the analytical procedures, please refer to the Appendix or Reference sections.

Table 18) Analytical Standard Operating Procedure Summary

Analyte	SOP Ref.	Title and Date	Definitive Screening Data or	Modified for Project? Y/N
Nitrate	KGS 9056/ ASTM vol. 11.01 D4327	KGS- Ion Chromatography of Water, January 2009 (Derived from "Standard Test Method for Anions in Water by Chemically Suppressed Ion Chromatography", 1996)	Definitive	N
Dissolved Phosphorus	KGS D515/ ASTM vol. 11.01 D515	KGS- Total Phosphorus in Water, April 2011. (Derived from "Standard Methods for the Examination of Water and Wastewater", 1998, pg. 24)	Definitive	N
Sediment Concentration	EPA 160.2	Residue, Non-Filterable (Gravimetric, Dried at 103-105°C), 1971.	Definitive	N
Stage	Teledyne (2011)	730 Bubbler Module Installation and Operation Guide, 2011	Definitive	N
Turbidity	YSI (2006)	6-series Multiparameter Water Quality Sondes, 2006	Definitive	N
Temperature	YSI (2006)	6-series Multiparameter Water Quality Sondes, 2006	Definitive	N
$\delta^{18}\text{O}$ of Water	Coplen et al. (2008)	Determination of the $\delta^{18}\text{O}$ of water; RSIL lab code 489, chap. 2 of Stable isotope-ratio methods. Revised in 2008	Definitive	***
$\delta^2\text{H}$ of Water	Coplen et al. (2008)	Determination of the $\delta^2\text{H}$ of water; RSIL lab code 1574, chap. 1 of Stable isotope-ratio methods. Revised in 2008	Definitive	***
$\delta^{13}\text{C}$ of DIC	Coplen et al. (2012)	Determination of the $\delta^{13}\text{C}$ of dissolved inorganic carbon in water; RSIL lab code 1710, chap. 18 of Stable isotope-ratio methods. Revised in 2012	Definitive	***
$\delta^{15}\text{N}$ / $\delta^{18}\text{O}$ of Nitrate	Coplen et al. (2012)	Determination of the $\delta^{15}\text{N}$ and $\delta^{18}\text{O}$ of nitrate in water; RSIL lab code 2900, chap. 17 of Stable isotope-ratio methods. Revised in 2012	Definitive	Y-See revised analytical SOP in Appendix 11
$\delta^{15}\text{N}/^{13}\text{C}$ of Transported Sediment	EPA SIP/OP.01	Analysis of Environmental Samples Using Continuous Flow Gas Isotope Ratio Mass Spectrometry, January 1999.	Definitive	Y-See revised analytical SOP in Appendix 13
POC, PN of Transported Sediment	EPA SIP/OP.01	Analysis of Environmental Samples Using Continuous Flow Gas Isotope Ratio Mass Spectrometry, January 1999.	Definitive	Y-See revised analytical SOP in Appendix 13
Temp, pH, DO, Conductivity	Hach (2006)	HACH HQ Series Portable Meters User Manual, Edition 5, 2006	Definitive	N

***Awaiting confirmation from Erik

B.2.3) Field Analytical Instrument Calibration Procedures

B.2.3.1) Instruments Requiring Calibration

YSI turbidity probe

The YSI 600 OMS Sonde with a 6136 Turbidity probe will be used to determine turbidity continuously in the streamwater. Sonde calibration is site dependent and will likely be an iterative process. Preliminarily the plan is to calibrate the probe monthly, but maintain on a weekly basis and check for deviation from the calibrated values bimonthly using a field meter.

Hach ph, DO, and conductivity probes/Horiba U-10 Water Quality Checker

The Hach sension156 Portable Multiparameter Meter/ Horiba U-10 Water Quality Checker will be used to determine conductivity, dissolved oxygen, and pH content. The meter will be calibrated in the laboratory before and after each series of field testing. The meter will be calibrated approximately halfway through each sampling event. All post-calibration measurements will be recorded in the calibration log for that instrument. Initial and post-calibration values will be compared and any substantial discrepancies in both the calibration log and on the appropriate field data sheet will be notes.

B.2.3.2) Instrument Calibration Methods

Turbidity probe calibration

Standard for Turbidity probe is 126 NTU created in lab using Fox method detailed in appendix. Two point calibration is used in which the zero point is Deionized organic free water and the second point is the 126 NTU standard. Calibration steps are:

- Open up the Ecowatch software to perform the calibration.
- Select the 2-point option to calibrate the turbidity probe using only two calibration standards (One clear water-0 NTU, One Turbidity Solution 126 NTU).
- Immerse the sonde in the 0 NTU standard and press enter.
- The screen will display real-time readings that will allow determination of reading stabilization.
- Pressing enter will confirm the first calibration.
- Place the sonde in the second turbidity standard and input the correct turbidity value in NTU and press enter.
- After the readings have stabilized press enter to confirm the calibration (make sure to record the value that the probe stabilized at for both calibration points).

Conductivity probe calibration

Hach and Horiba Conductivity probe uses a 1000 $\mu\text{S}/\text{cm}$ (at 25 °C) NaCl standard solution. For typical applications with conductivity of 0–10,000 μS (10 mS/cm), calibrate with this standard to achieve the accuracy specified for the meter. Calibration steps are:

1. Make sure the meter is in Conductivity Reading mode.
2. Place the probe in the conductivity standard. Agitate the probe to dislodge bubbles in the cell. Avoid resting the probe on the bottom or side of the container.
3. Press CAL. Icons that represent the active navigation keys will appear in the lower part of the display. The meter will recall the most recent type of calibration. Look at the units field to see what kind of calibration is active.
4. Scroll to the preferred units using the UP or DOWN ARROWS.
5. Use the number keys to change the numeric value, if desired. The value entered must be the standard's conductivity value at a reference temperature of 25 °C. (Note: All Hach standards have the conductivity value corresponding to the 25 °C reference temperature printed on their labels. It is not necessary to fill up the numeric entry screen before moving on. To clear the numeric display, press CE.)
6. When the value and units are correct, press ENTER to calibrate on the standard. The meter automatically corrects the calibration measurement to the 25 °C reference temperature using the NaCl-based, non-linear temperature coefficient.
7. The meter will return to Conductivity Reading mode when the calibration is finished.

pH and temperature probe calibration

1. Prepare three pH buffers according to the electrode instruction manual. Choose from 1.68, 4.01, 7.00 (or 6.86), 10.01, and 12.45 pH buffers. (Note: Use a 6.86 or 7.0 pH buffer for the mid-range buffer.)
2. Turn the instrument on. From the pH Reading mode, press CAL. CAL and flashing ? will appear in the upper display area, along with Standard and 1.
3. Place the pH electrode in one of the buffers.
4. Press READ. The instrument will automatically recognize the calibration buffer value. The temperature and pH values will be updated until a stable reading is reached. [(Note: The pH values for the buffers are given for 25 °C. If the calibration buffer temperature is not 25 °C, the pH values displayed for the buffers will reflect the correct pH value for the calibration buffer temperature.) (Note: If the meter is measuring in pH mode, it automatically moves to the next calibration step when the reading stabilizes (indicated by three beeps). If measuring in mV mode, the meter beeps three times when the reading stabilizes. Press ENTER to accept the reading.)]
5. When the reading has stabilized or been accepted, the standard number will change to 2.
6. Remove the probe from the first buffer and rinse with deionized water. Place the probe in the second buffer.
7. Press READ. The temperature and pH values will be updated until a stable reading is reached.
8. When the reading has stabilized or been accepted, the standard number will change to 3. (To accept this calibration after two points, press EXIT. Press ENTER to accept the calibration or EXIT to cancel the calibration without saving it.)
9. Remove the probe from the second buffer and rinse with deionized water. Place the probe in the third buffer.
10. Press READ. The temperature and pH values will be updated until a stable reading is reached.
11. When the reading has stabilized or been accepted, the slope value and the Store and ? icons will appear.
12. To save the calibration and return to the reading mode, press ENTER. To exit the calibration without saving it and return to the reading mode, press EXIT.

DO probe calibration

1. Secure the probe cable to the calibration and storage chamber by wrapping cable through the bottom of the chamber lid before filling with water. (Note: Avoid completely filling the lower part of the calibration chamber with water.)
2. Prepare the calibration and storage chamber by holding it under water and squeezing it a couple of times to pull a small amount of water into the lower chamber through the inlet. Alternately, open the bottom of the chamber and insert a water-soaked sponge.

3. Insert the DO probe into the calibration and storage chamber. The tip of the probe must not be flooded with water or be holding a drop of water on the membrane.
4. Allow at least ten minutes for the atmosphere in the chamber to reach a steady state. [(Note: Gently squeezing the lower chamber a couple of times to force water-saturated air into the probe chamber will speed up stabilization. Avoid squeezing liquid water into the chamber.) (Note: Keep the DO probe at a uniform temperature. When holding the probe, do not touch the metallic button on the side of the probe. The button is a thermistor that senses temperature. An inaccurate calibration will result if the temperature of the thermistor is different from the probe membrane.)]
5. Press the DO key to put the meter in DO Reading mode.
6. Press the CAL key located in the lower left corner of the keypad.
7. The display will show 100%. Press the ENTER key. The stabilizing icon will appear while the meter completes the calibration.
8. When the calibration is complete, the meter will return to the reading mode. Press the EXIT key during the calibration sequence to back out of the calibration routine, one screen at a time, without completing a calibration. (Note: If the CAL and ? icons flash after calibration, the calibration failed and needs to be repeated.)

B.2.3.3) Calibration Apparatus

Calibration for the YSI meter will be conducted in manufacturer provided calibration containers. For the Hach and Horiba probes the calibration apparatus includes the containers for the calibration standards that are supplied by the manufacturer.

B.2.3.4) Calibration Standards

Turbidity Standard

126 NTU Formazin polymer-based standard created in lab

Conductivity standard

1000 $\mu\text{S}/\text{cm}$ (at 25 °C) NaCl standard solution

pH and temperature probe calibration

1.68, 4.01, 7.00 (or 6.86), 10.01, and 12.45 pH buffers

DO probe calibration

De-ionized, organic free water within the calibration storage chamber.

B.2.3.5) Calibration Frequency

The YSI turbidity probe will be calibrated every two weeks. In addition, every other week the probe will be tested against standards in the field to check if the probe has undergone extensive drift or fouling. The Hach or Horiba multimeter probes will be calibrated prior to and after each sampling trip. No midpoint calibration will be performed due to time constraints of bringing samples back to the lab for filtration and preservation.

B.2.3.6. Personnel Responsible for Calibration and Inspection

Admin Husic and Undergraduate Students at the University of Kentucky Hydraulics Lab will be responsible for calibration and inspection procedures.

B.2.3.7. Documentation of Calibration Procedures

The YSI turbidity meter calibration and maintenance procedure will be documented in the “Cane Run TSS and Turbidity Fieldbook”. Calibration dates, readings during bimonthly field checks, condition of the YSI meter, and readings during calibration process will be recorded in the fieldbook. Calibration procedures will similarly be documented in the “Cane Run Weekly Sediment Trap Fieldbook”.

B.2.4) Lab Analytical Instrument Calibration Procedures

All laboratory analytical instrument calibration procedures are detailed in the SOP references found in the Appendix. All analytical instruments were chosen in order that they meet the required QLs specified in this QAPP.

B.2.5) Analytical Instrument and Equipment Maintenance, Testing and Inspection Procedures

For maintenance, testing and inspection procedures for all laboratory instruments please refer to the analytical SOPs referenced in Table 18 and subsequently found in the Appendix section. For field based analytical instruments, the manufacturers manual was used to insure the instruments were maintained, tested and inspected properly before and after measurements were taken. Any problems with the instrumentation will be clearly noted in the field notebooks associated with the specific instrument (section B.2.3.7). The instrumentation will be secured in the UK Hydraulics laboratory. Spare parts are available in case of probe failure.

B.2.6) Analytical Supply Inspection and Acceptance Procedures

B.2.6.1) Supplies for Analytical Procedures

The following discusses the supplies and acceptance procedures for analytical equipment in the three laboratories. For the KGS and ASIL labs protocol provided in the Appendix section and outlined in Table 18 will provide the supply Inspection and Acceptance Procedures.

- Kentucky Geological Survey Analytical Procedures

- Refer to Table 18/Appendices for the Nitrate and DP SOPs for all supplies, reagents and laboratory procedures to ensure availability and freedom from target analytes and interferences.
- Arkansas Stable Isotope Lab Analytical Procedures
 - Refer to Table 18/Appendices for the $\delta^{15}\text{N}$ and $\delta^{18}\text{O}$ of Nitrate, $\delta^2\text{H}$ and $\delta^{18}\text{O}$ of Water, and $\delta^{13}\text{C}$ of DIC SOPs for all supplies, reagents and laboratory procedures to ensure availability of supplies and cleanliness.
- Hydraulics Lab Analytical Procedures
 - TSS Analysis
 - Forceps
 - Graduated Cylinder
 - Filtration Apparatus
 - Sediment Trap Sample Preparation Procedure
 - Plastic Pitcher
 - Siphon
 - HDPE 125 mL bottles
 - 750 mL plastic centrifuge bottles
 - 250 mL centrifuge bottles
 - <53 micron mesh sieves
 - Sample grinding
 - Metal Spatula
 - NO_3 , DP, $\delta^{15}\text{N}_{\text{NO}_3}$, $\delta^{18}\text{O}_{\text{NO}_3}$, $\delta^2\text{H}_{\text{H}_2\text{O}}$, $\delta^{18}\text{O}_{\text{H}_2\text{O}}$, and $\delta^{13}\text{C}_{\text{DIC}}$
 - HDPE 1-L bottles
 - 60 ml Syringe
 - 0.45 Micron Whatman Filter
 - 40 mL VOC Sterile Septum Vial
- UK Stable Isotope Lab Analytical Procedures
 - Sediment Trap Sample Analysis
 - Metal Spatula
 - Forceps

Note: If any supplies are known to have become contaminated they will be removed and new supplies will be utilized or decontaminated appropriately. Any such incident will be documented accordingly.

B.2.6.2) Responsible persons for checking supplies and implementing protocol

- Admin Husic, Graduate Student, University of Kentucky.
- Jason Backus, KGS Lab, University of Kentucky.
- Erik Pollock, ASIL, University of Arkansas.
- Undergraduate Students, University of Kentucky
-

B.3) Sample Collection Documentation, Handling, Tracking, and Custody Procedures

B.3.1) Sample Collection Documentation

On-site and off-site analytical documentation procedures are discussed in section B.5. Further, refer to section B.1.2.6 for information about field documentation. This section addresses container identification labels, the required sample identification information and an example.

B.3.1.1) Sample Identification

Measurements requiring labeled containers include nitrate, DP, $\delta^{15}\text{N}_{\text{NO}_3}$, $\delta^{18}\text{O}_{\text{NO}_3}$, $\delta^2\text{H}_{\text{H}_2\text{O}}$, $\delta^{18}\text{O}_{\text{H}_2\text{O}}$, and $\delta^{13}\text{C}_{\text{DIC}}$, and sediment trap samples.

Field Container Labeling-During field sampling, the following information will be filled out and placed on each sample container used.

Site _____
 Analysis _____
 Collector _____
 Date/Time _____

Laboratory Labels- Upon returning to the laboratory each sample brought in needs to be logged in (section 3.2) and given an appropriate, traceable Sample ID. New sample containers, or field sampling containers (depending on the analyte) will be labeled using the following.

Site _____
 Sample ID _____
 Analysis _____
 Collector _____
 Date/Time _____
 Grab/Composite _____
 Preservation _____

B.3.1.2) Sample Label Protection

To protect the sample labels, clear, waterproof tape will cover all labels to prevent bleeding of ink, or tearing of the label.

B.3.2) Sample Handling and Tracking System

Samples will be entered into a log book whenever they come into the UK Hydraulics lab and will be given a unique sample identification number. The sampling number system will denote the analytical run, the site, the sample number associated with that site, and information about the sample matrix (e.g. filtered, ground, bulk sample etc.). For example, a sample that was collected from CRCK during March that is a field duplicate and is filtered for DIC would be labeled "CRCK 3-6-17 DIC". Further information about the samples, such as the analysis being conducted, can be found on the analyte specific sample container (see section B.3.1). A key will be kept in the lab book to help identify what each component means.

Procedures used for internal laboratory tracking are discussed in the SOPs found in the Appendix section. Typically the sample ID provided upon arrival at the UK hydraulics lab will be used throughout analytical procedure in order to minimize confusion. Further, specific laboratory storage procedures for each analyte are discussed in the SOPs found in the Appendix.

B.3.2.1) Sample Handling

Sampling Organization: University of Kentucky, Department of Civil Engineering

Laboratory: UK Hydraulics Lab, UKSIL, KGS Lab, ASIL

Method of sample delivery (shipper/carrier): Carried /Shipped (UPS overnight)

Number of days from reporting until sample disposal: Maximum Holding Time/Project duration

Table 19) Sample Handling Process

Activity	Organization and title or position of person responsible for the activity
Sample labeling	Admin Husic/Undergraduate students- University of Kentucky, Department of Civil Engineering.
COC form completion	Admin Husic- University of Kentucky, Department of Civil Engineering
Packaging	Admin Husic- University of Kentucky, Department of Civil Engineering
Shipping coordination	Admin Husic- University of Kentucky, Department of Civil Engineering
Sample receipt, inspection, & log-in	Jason Backus- Kentucky Geological Survey Erik Pollock- University of Arkansas Stable Isotope Lab Admin Husic- University of Kentucky, Department of Civil Engineering
Sample custody and storage	Jason Backus- Kentucky Geological Survey Erik Pollock- University of Arkansas Stable Isotope Lab
Sample disposal	Jason Backus- Kentucky Geological Survey (SOPs state retention time) Erik Pollock- University of Arkansas Stable Isotope Lab (SOPs states retention time)

B.3.2.2) Sample Delivery

Samples analyzed at the Kentucky Geological Survey or UK Stable Isotope Lab will be carried by Admin Husic, or an undergraduate assistant. Samples sent to the Arkansas Stable Isotope Lab, water samples will be shipped in insulated containers with ice packs (to keep samples cooled to 4°C) each month after sample collection. If storm events are sampled, the samples won't be shipped until all samples from a given event are obtained. Samples will be shipped overnight using UPS. Sample delivery groups (SDGs) of 20 or less will be used (EPA-505-B-04-900A). Chain of custody forms will be used to denote when samples are shipped and received (see section B.3.3). No hazardous materials will be shipped during the course of this project.

B.3.3) Sample Custody

To document sample handling, the following procedure will be used for chain of custody.

1. Person collecting samples will complete the respective Fieldbook log.
2. Person relinquishing packaged samples to carrier will sign Chain-of-Custody form and obtain signature of the representative of the carrier.
3. Transported package will include a copy of the Samples Collection Log, Equipment Maintenance/Failure Log (if necessary) and the Chain-of-Custody form.
4. Person receiving transported samples will obtain signature of representative of carrier and sign Chain-of-Custody form.
5. Laboratory personnel will sign Chain-of-Custody form to acknowledge receipt of samples.
6. Laboratory personnel will sign Chain-of-Custody form when samples are disposed.
7. The Database Manager will keep a copy of the Chain-of-Custody form.

The forms used for Chain of Custody are seen in Figure 3 and 4. This form is applicable to all analysis performed in this project.

B.4) Quality Control Samples

B.4.1) Sampling Quality Control Samples

B.4.1.1.) Water Quality Parameters and DIN Stable Isotope Parameters

To ensure QC of field based methods, field blanks and field duplicates will be collected every other sample run (e.g. approximately 1/16 samples) which adheres to the suggestion of 5% (KDOW, 2006). Blanks will consist of De-ionized water and will be carried to each site and will be processed identically to the other samples. Duplicate samples will be collected from each sampling site at least once during the sampling routine. For confidentiality purposes blanks and duplicates will not be explicitly labeled as that,

instead the sample identification number will be used as identification and the sample log in book, which links the sample to the sample identification number, will not be available to off-site lab managers.

B.4.1.2) Sediment Concentration

Blanks and replicates of sediment concentration samples in the field are not feasible due to the nature of the sampling regime (e.g. sediment concentrations can change rapidly thus both depth integrated and automated sampling would not be unable to collect a “duplicate” sample).

B.4.1.3) $\delta^{15}\text{N}$, $\delta^{13}\text{C}$ of Transported Sediment, POC and PN

Sediment trap samples are integrated samples and are collected at a fixed point the stream. It's not feasible to collect duplicates and impossible to collect blanks for these samples.

B.4.2) Analytical Quality Control Samples

Analytical control samples for KGS Lab procedures are well defined and have been fine-tuned by the lab operator. The QC procedures are found in the Appendix SOPs. Analytical QC samples for tasks performed at the UKSIL, UK hydraulics lab, and ASIL are outlined in the following subsections.

B.4.2.1) Sediment Concentration

Blanks will be established by running a known volume of deionized water through the filtration device and measuring the resulting TSS. This measurement is performed to ensure that no contamination occurs during the analytical procedure and that the scale is working properly. If the blank is greater than the MDL then the test will be rerun and all equipment will be checked accordingly. Sample splits will be conducted 1/10 samples. During this process a homogenized sample will be split into two equal volumes and if the resultant TSS concentration is greater than 10% different the test will be rerun with the next sample, the previous data will be red flagged in the database and lab notebooks.

B.4.2.2) $\delta^{15}\text{N}/\delta^{18}\text{O}$ of Nitrate

Deionized water was utilized as a Blank. Standards for the analysis were 20 μM KNO_3 , IAEA (International Atomic Energy Agency) N3 (19.975 μM N- KNO_3 , $\delta^{15}\text{N}=4.7\text{‰}$ and $\delta^{18}\text{O}=25.6\text{‰}$), USGS 32 (19.7 μM KNO_3 , $\delta^{15}\text{N}=180\text{‰}$ and $\delta^{18}\text{O}=25\text{‰}$), USGS 34 (20 μM KNO_3 , $\delta^{15}\text{N}=-1.8\text{‰}$ and $\delta^{18}\text{O}=-27.9\text{‰}$), USGS 35 (20 μM KNO_3 , $\delta^{15}\text{N}=2.7\text{‰}$ and $\delta^{18}\text{O}=57.5\text{‰}$). Duplicates and blanks were taken bimonthly from the field. For isotope analysis, splits are taken for ten percent of the samples.

B.4.2.3) $\delta^2\text{H}/\delta^{18}\text{O}$ of Water

Vienna Standard Mean Ocean Water (Coplen 1996)

B.4.2.4) $\delta^{13}\text{C}$ of DIC

Vienna Peedee Belemnite (Coplen 1996)

B.4.2.5) $\delta^{15}\text{N}$, $\delta^{13}\text{C}$ of Transported Sediment, POC and PN

Standard deviations of the instrument are established by injecting a reference gas for carbon and nitrogen. Further, linearity is established by injecting the reference gas at different concentrations and calculating the change in the isotopic signature over the change in voltage. Since a single sample is used to obtain all 4 parameters and a range of isotopic values needs to be established, two isotopic standards and one elemental standard will be used. A template has been established (see Section 3.5) for a typical sample run. The instrument is warmed up by running equipment blanks to ensure background concentrations are low and a set of standards to ensure that the instrument is working appropriately. During the analysis, around 1/4th of the run is standards. One out of every ten samples is run in triplicate to establish a standard deviation of the data and to test homogeneity and processing of the samples.

B.5) Data Management Tasks

B.5.1) Project Documentation and Records

The purpose of this section is to detail all records that will be generated encompassing all aspects of the project. Section B.5.1 details lists the documents and records that will be generated in this project. Section B.5.2 will detail package deliverable documents for sample collection and field measurement, on-site analytical, and off-site analytical data deliverable documents. Section B.5.3 will discuss procedures for manual and electronic data recording and storage and provide templates for the appropriate forms. Section B.5.4 describes handling and management of data from generation to its final use and storage. Section B.5.5 discusses the procedures for tracking, control, storage, archival, retrieval and security of the data.

B.5.1.1) Sample Collection and Field Measurements

The following provides a comprehensive list of records and documents that will be generated for the sample collection and field measurements

1. Field data collection (Section B.1.2.6)
2. Chain of custody records (Section B.3.3)
3. Sampling instrument calibration/maintenance logs (Section B.2.3.2)
4. Sampling locations and their associated schematic (Section B.1)
5. Sampling plan (Section B.1)
 1. Sampling notes (See Field book discussion in section B.1.2.6)
 2. Corrective action/ Failure reports (Figure 5)
 3. Data Exclusion Reports (See section D.2 for reasons to exclude data)
 4. Documentation of methods deviations (See section D.2 for occurrence of deviations from QAPP methods)
 5. Electronic Data Deliverables (Section B.5.3)

6. Meteorological Data from field (Section A.5)
7. Continuous Stream Data (Section A.5 and A.3.2)
8. Sampling Instrument Maintenance and Calibration Logs (See Field book discussion in section B.1.2.6, calibration in section B.2.3 and maintenance in section B.2.5)

B.5.1.2) Analytical Records

The following provides a comprehensive list of records and documents that will be generated for analytical records.

- Chain of Custody records (Section B.3.3)
- Preparation and Analysis forms (logbooks) (For field logbooks see previous section, for analytical logbooks see section B.5.3).
- Raw data and tabulated data summary forms, standard QC checks, QC samples (See section B.5.3 for raw analytical data forms, see Data review section D for tabulate data summary information).
- Sample Chronology (Section B.5.3).
- Corrective action/ Failure reports (Figure 5)
- Documentation of methods deviations (See section D.2 for occurrence of deviations from QAPP methods)
- Electronic Data deliverables (Section B.5.3).
- Instrument Calibration Records (Section B.2.3)
- Laboratory Sample Identification Number (Section B.3.1.1)
- Reporting Forms, completed with actual results (Section B.5.2)
- Signatures for laboratory sign-off (COC forms)

B.5.1.3) Project Data Assessment Records

- Field Sampling Audit Checks (Section C.1.1)
- Analytical Audit Checks (Section C.1.1)
- Data Review Reports (Section D)
- Corrective action/Failure reports (Figure 5)

B.5.2) Data Package Deliverables

B.5.2.1) Sample Collection and Field Measurements Data Package Deliverables

Grab samples shall be logged into the specified field manual along with analytical data including, pH, DO, temp and conductivity. Data should be input electronically into a database immediately after returning from the field (Section B.5.3).

B.5.2.2) On-site Analysis Data Package Deliverables

All raw data generated from on-site analysis shall be recorded manually on the lab analysis or logbook sheets (see section B.5.3). The data will be uploaded to a spreadsheet electronically for storage.

B.5.2.3) Off-site Laboratory Package Deliverables

Laboratory Records shall consist of the monthly analysis reports as prepared by the Kentucky Geological Survey laboratory and the Arkansas Stable Isotope laboratory. Analysis of samples should be completed and reported within one month of receipt of the samples.

B.5.3) Data Reporting Formats

B.5.3.1) Sample Collection and Field Measurements

Data collected in the field will be recorded manually into fieldbooks or onto data sheets. If data needs to be corrected, it shall be marked out with a straight line and written above the marked out section (room permitting). All original data and corrections need to be initialed by the sampler. Collected data will be transformed from raw forms into usable data forms by transcribing the data into an EXCEL spreadsheet via electronic import. Chain of Custody forms (Figure 3) will be filled out in concert with fieldbooks and will be uploaded to the electronic database upon receipt of the completed form.

B.5.3.2) Procedural alterations and data exclusions

Raw forms for corrective actions, data exclusion and method deviations forms (Figures 3-7) should be filled out during the collection and analytical process. Thereafter, the template will be used to import a soft copy of the reports.

B.5.3.3) Analytical instrument maintenance and calibration

Raw fieldbook data for instrument maintenance and calibration will be electronically transcribed into an EXCEL spreadsheet using the template in Figure 8. The spreadsheet will be emailed to co-managers immediately after entering the data and stored on a UK engineering server.

B.5.3.4) Secondary Data

Continuous data will be collected electronically from the NOAA Lexington Bluegrass airport using the template in Figure 9. Turbidity, flow, stage, precipitation and temperature will be collected continuously in the stream channel at three sites and logged using the template found in Figure 10.

B.5.3.5) On-site laboratory analytical procedures

Upon entry into the lab, each sample will be logged in using Figure 11. For samples sent to other labs, the Chain of custody forms will be used to track their location after the carrier takes them out of the lab. For samples analyzed by Admin Husic and the undergraduate researchers the samples progress will be tracked with the form in Figure 14. On-site laboratory analysis will be recorded using raw data forms found in Figures 12-16. This includes the TSS analysis (Figure 19), preparation work for $\delta^{15}\text{N}$, $\delta^{13}\text{C}$, TOC, PN and C:N of the sediment traps (Figures 20-21) and the associated EA/IRMS analysis templates (Figure 15-16), and preparatory work for $\delta^{15}\text{N}_{\text{NO}_3}$, $\delta^{18}\text{O}_{\text{NO}_3}$, $\delta^2\text{H}_{\text{H}_2\text{O}}$, $\delta^{18}\text{O}_{\text{H}_2\text{O}}$, and $\delta^{13}\text{C}_{\text{DIC}}$. All forms will be transcribed in their associated template and saved in separate folders for organizational purposes

Cane Run Watershed Project

CHAIN OF CUSTODY RECORD

REQUEST ID:

SAMPLING LOCATION:

Date/Time	SAMPLE IDENTIFICATION	MATRIX	NUMBER of CONTAINERS	PRESERVATION TREATMENT	ANALYSIS A- Add D- Delete X- Select	REQUESTED	LAB USE ONLY
Date: ___/___/___ Time: ___:___ MILITARY	ID# _____	<input type="checkbox"/> WATER <input type="checkbox"/> SOIL <input type="checkbox"/> SEDIMENT <input type="checkbox"/> OTHER Other:	<input type="checkbox"/> Glass, 1000 mL <input type="checkbox"/> Plastic, 1000 mL <input type="checkbox"/> Glass, 250 mL <input type="checkbox"/> Plastic, 250 mL <input type="checkbox"/> Plastic, 125 mL <input type="checkbox"/> ISCO <input type="checkbox"/> Glass, 60 mL <input type="checkbox"/> Vial, 40 mL <input type="checkbox"/> Vacutainer	<input type="checkbox"/> ICE <input type="checkbox"/> H2SO4 <input type="checkbox"/> HNO3 <input type="checkbox"/> HCl <input type="checkbox"/> H3PO4 <input type="checkbox"/> RAW <input type="checkbox"/> FILTERED <input type="checkbox"/> GROUND	<input type="checkbox"/> NO3 <input type="checkbox"/> DP <input type="checkbox"/> $\delta^{15}N$ Sed, $\delta^{13}C$ Sed <input type="checkbox"/> $\delta^{15}N_{NO_3^-}$, $\delta^{18}O_{NO_3^-}$ <input type="checkbox"/> $\delta^2H_{H_2O}$, $\delta^{18}O_{H_2O}$ <input type="checkbox"/> $\delta^{13}C_{DIC}$	<input type="checkbox"/> POC <input type="checkbox"/> PN OTHER	LAB ID: COMMENTS:
Date: ___/___/___ Time: ___:___ MILITARY	ID# _____	<input type="checkbox"/> WATER <input type="checkbox"/> SOIL <input type="checkbox"/> SEDIMENT <input type="checkbox"/> OTHER Other:	<input type="checkbox"/> Glass, 1000 mL <input type="checkbox"/> Plastic, 1000 mL <input type="checkbox"/> Glass, 250 mL <input type="checkbox"/> Plastic, 250 mL <input type="checkbox"/> Plastic, 125 mL <input type="checkbox"/> ISCO <input type="checkbox"/> Glass, 60 mL <input type="checkbox"/> Vial, 40 mL <input type="checkbox"/> Vacutainer	<input type="checkbox"/> ICE <input type="checkbox"/> H2SO4 <input type="checkbox"/> HNO3 <input type="checkbox"/> HCl <input type="checkbox"/> H3PO4 <input type="checkbox"/> RAW <input type="checkbox"/> FILTERED <input type="checkbox"/> GROUND	<input type="checkbox"/> NH4 <input type="checkbox"/> NO3 <input type="checkbox"/> DIC <input type="checkbox"/> DOC <input type="checkbox"/> DP <input type="checkbox"/> $\delta^{15}N$ NH4 <input type="checkbox"/> $\delta^{15}N$ NO3 <input type="checkbox"/> $\delta^{15}N$ Sediment <input type="checkbox"/> $\delta^{13}C$ Sediment	<input type="checkbox"/> POC <input type="checkbox"/> PN OTHER	LAB ID: COMMENTS:
Date: ___/___/___ Time: ___:___ MILITARY	ID# _____	<input type="checkbox"/> WATER <input type="checkbox"/> SOIL <input type="checkbox"/> SEDIMENT <input type="checkbox"/> OTHER Other:	<input type="checkbox"/> Glass, 1000 mL <input type="checkbox"/> Plastic, 1000 mL <input type="checkbox"/> Glass, 250 mL <input type="checkbox"/> Plastic, 250 mL <input type="checkbox"/> Plastic, 125 mL <input type="checkbox"/> ISCO <input type="checkbox"/> Glass, 60 mL <input type="checkbox"/> Vial, 40 mL <input type="checkbox"/> Vacutainer	<input type="checkbox"/> ICE <input type="checkbox"/> H2SO4 <input type="checkbox"/> HNO3 <input type="checkbox"/> HCl <input type="checkbox"/> H3PO4 <input type="checkbox"/> RAW <input type="checkbox"/> FILTERED <input type="checkbox"/> GROUND	<input type="checkbox"/> NH4 <input type="checkbox"/> NO3 <input type="checkbox"/> DIC <input type="checkbox"/> DOC <input type="checkbox"/> DP <input type="checkbox"/> $\delta^{15}N$ NH4 <input type="checkbox"/> $\delta^{15}N$ NO3 <input type="checkbox"/> $\delta^{15}N$ Sediment <input type="checkbox"/> $\delta^{13}C$ Sediment	<input type="checkbox"/> POC <input type="checkbox"/> PN OTHER	LAB ID: COMMENTS:

Sampler's Signature:

Relinquished by:	Date:	Received by:	Date:
Representing:	Time:	Laboratory:	Time:
Archiving/Disposal (Notes/Dates):			
Signature			

Figure 3) Chain of Custody Form (Cover)

EA/IRMS Analysis Template Design

A	1	2	3	4	5	6	7	8	9	10	11	12
	Blank	Cond. Int. std1	Cond. Int. std1	Cond. Int. std1	%Std 1	%Std 2	Int. Std1.1	Int. Std1.2				
B	13	14	15	16	17	18	19	20	21	22	23	24
		Int. Std1.3	Int. Std2.1					Int. Std1.4				
C	25	26	27	28	29	30	31	32	33	34	35	36
		Int. Std1.5						Int. Std1.6				
D	37	38	39	40	41	42	43	44	45	46	47	48
		Int. Std1.7	Int. Std2.2									Int. Std1.8
E	49											
	%Std 3											

*Template design includes the timing of the standards (two for isotopes and one for concentration) during the automated run.
Figure 16) Template Design for EA/IRMS procedure

B.5.4) Data Handling and Management

B.5.4.1) Data Recording

Data will be entered electronically in excel spreadsheets. Data will be crosschecked with COC forms and with fieldbooks to ensure that transcription errors are minimized. Data will be entered into the database using the templates depicted in the preceding section. Database entries will be logged on the Database Entry Log sheet depicted in Figure 17.

B.5.4.2) Data Transformations and Data Reduction

B.5.4.2.1) Discharge Data

Storm runoff rates for each sample site will be obtained using the existing USGS gauging station at the watershed outlet. Discharge at each site will be determined by using a weighted area basis by applying an appropriate factor to the discharge from the USGS gauging stations. Discharges from the area weighted method will be cross checked against measured discharges in the tributaries.

B.5.4.2.2) Sediment, Carbon, Nitrogen and Phosphorus Fluxes

Constituent fluxes are determined using the discharge rate at the time the sediment samples were collected and multiplying the discharge rate by the sample constituent concentration (e.g. TSS, NO₃, TP, DIC).

Any data conversions that occur will be recorded in the Data transformations log (Figure 18). *At this time no data reduction procedures are planned.*

B.5.4.3) Data Transfer and Transmittal

All electronic data will be transmitted *via* email. All data will be emailed to co-managers. Backup copies of all data will be maintained at all times to insure data is not lost. The person transmitting the data should include a metadata file that includes the names, sizes, and descriptions of each of the files in the transmittal. Data recorded on paper will be transmitted by fax or scanned and converted to Adobe Acrobat format and transmitted as detailed above. An example of the electronic data transfer form used on this project is found in Figure 19. This form is used if electronic data is requested by project personnel.

B.5.4.4) Data Analysis

Microsoft EXCEL will be used to process and analyze data. The data will be used primarily for parameterizing and calibration/validation of a numerical model that is still under development but stems from work performed by Husic et al. (2017), Russo and Fox (2012), and Fox et al. (2010).

B.5.4.5) Data Review

Data Request and Transfer Form

Data Requested:	(Please describe the requested and explain why it is being requested)
------------------------	---

Requested by: _____ (Signature)

Request Date: _____

Date Needed: _____

- Data Format:**
- Graph
 - Table
 - Spreadsheet
 - Other (please specify format) _____

Figure 19) Data Transfer Request Form

B.5.5) Data Tracking and Control

B.5.5.1) Data Tracking

A Data Tracking Log (Figures 21 and 22) will be utilized to keep track of data through various stages. The project manager/database manager will be in charge of updating the data tracking logs.

B.5.5.2) Data Storage, Archiving, Retrieval

The project data will be stored on a password-protected computer and backed up on the UncleJonny database. The Database Manager, the primary advisor, and others working on the project are authorized to access and retrieve data within the database. In order to correct, enter, or change project data within the database, the appropriate documentation is to be filled out and checked by the Database Manager or primary advisor before it is finalized.

The UncleJonny database will also contain historical data, project documentation (forms, logs, schedules, etc.), and the QAPP itself. All project workers are authorized to view and download these documents as the need arises.

The database manager shall archive a hardcopy of the QAPP, all project logs, schedules, forms, records, and reports. Hardcopy documents shall be available to all project personnel upon request. Hardcopies of all logs, forms, records, and reports shall be made available to the Project Quality Assurance Officer on a quarterly basis. Additional hardcopies are present in the project binder.

In order to better understand the organization of the UncleJonny database, a network nesting and description is available in Figure 20.

B.5.5.3) Data Security

All data will be stored on the Database Manager's computer, which is password protected, and backed up on the UncleJonny database. Data will be backed up and archived on a weekly basis on UncleJonny. The Database Manager will be responsible for querying the database and exporting desired data in Microsoft EXCEL format to produce data reports.

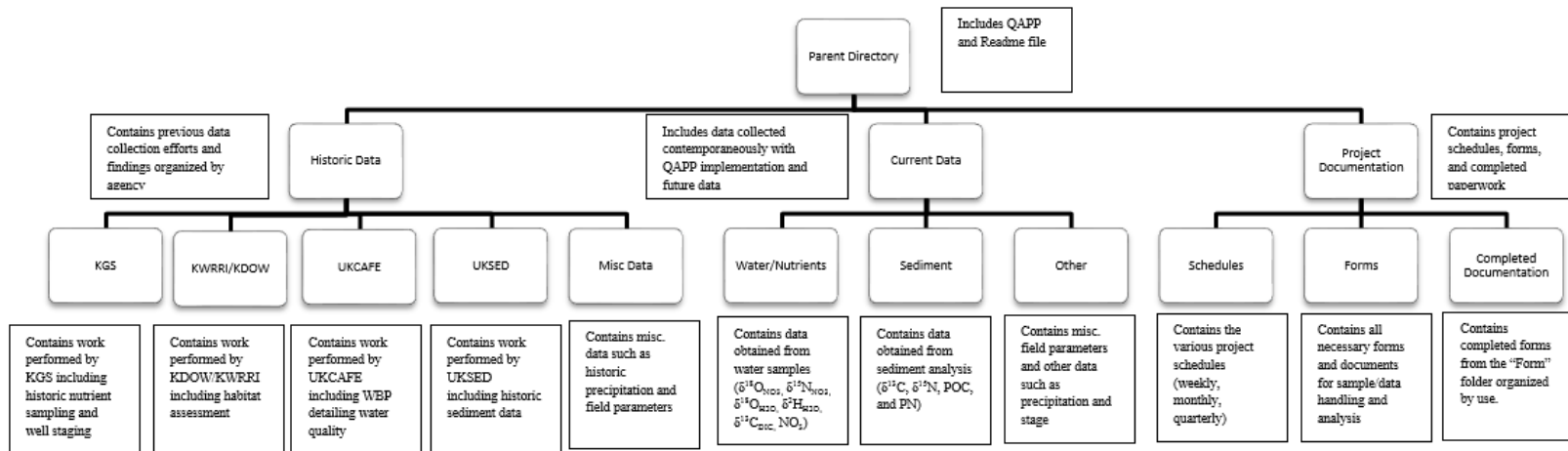


Figure 20) UncleJonny Database Nesting Example

Section C: Assessment/Oversight

C.1) Assessments and Response Actions

C.1.1) Planned Assessments

Internal assessment activities will consist of reviewing monthly data for completeness and representativeness. If the data fails to be complete and representative, a review of the data's history will be performed by Admin Husic to determine if any errors were committed in the logging, entry, transforming, and calculation processes. If logging, entry, transforming, or calculation errors come to light, the data will be flagged for exclusion from use in the statistical analysis. Admin Husic will also perform a Field Sampling, on-site analytical and off-site analytical TSA at the beginning of the sampling routine to ensure that all methods are conforming to the information displayed in this QAPP.

C.1.2) Assessment Findings and Corrective Action Responses

With regard to the internal audit process at the initiation of the project, any deficiencies will be documented using a corrective action response form (Figure 5), and stored in the project database. Thereafter corrective actions will be taken to ensure that the method corresponds with the criteria outlined in this QAPP. The parties involved (for example lab managers and the primary advisor) will be notified upon audit completion. The person in charge of sampling or the analytical procedures shall be the one in charged with receiving and addressing the corrective action report.

Data not meeting requirements for completeness or representativeness will be excluded from the data set, although included in the database and flagged for exclusion from statistical analyses. All data not meeting the Data Quality Objectives will be logged on the Data Exclusion Report sheet (Figure 6). The Data Exclusion Report will be archived by Admin Husic and will be available to all project personnel. After comment from project personnel, Admin Husic will render the decision to include or exclude the data from further use. If the data has been excluded, the data will be flagged within the database as excluded from analyses.

C.2) QA Management Report

QA management reports will be generated quarterly by Admin Husic and distributed to all personnel involved with the project. As well, a final project report will include all QA management reports. In general these reports will address the following.

- A summary of the project status and scheduled delays.
- Conformance of project activities to QAPP requirements and procedures.
- Deviations from the approved QAPP and approved amendments to the QAPP.
- Data reports of all data available for publishing.
- A complete copy of the Equipment Maintenance/Failure Log.
- A complete copy of the Data Tracking Log.
- A complete copy of the Database Correction Log.
- A complete set of all Data Exclusion Reports.
- A complete set of Chain-of-Custody Records.
- All Data Quality Assessment Reports to date.
- Data usability in terms of accuracy, precision, representativeness, completeness, comparability, and sensitivity.
- Any limitations on the generated data.
- A summary of tasks yet to be completed.

C.3) Final Project Report

The final Project report will address the above concerns as well as additional QA concerns such as:

1. Narrative and timeline of project activities
2. Summary of PQO Development
3. Reconciliation of PQO Development
4. Summary of major problems encountered and their resolution
5. Data summary, including tables, charts, and graphs with appropriate sample identification or station location numbers, concentration units, and data quality flags.
6. Conclusions and recommendations

Section D: Data Review

D.1) Overview

The data review process is outlined in the QAPP as a three step procedure. The following outlines these processes and the appropriate review steps and outputs. This will be performed quarterly to ensure the research remains viable.

Table 20) Requirements for Data Review (EPA-505-B-04-900A)

Process Term	Objective	Scope	Data Review Step	Output
Verification	Review to see if data required for the project are available.	– Sampling* – Analysis	I. Completeness check	Verification Report – May be checklist form – Package includes all documentation
Validation	– Assess and document the performance of the field sample collection process. – Assess and document the performance of the analytical process.	– Sampling* – Analysis	IIa. Check compliance with method, procedure, and contract requirements IIb. Compare with measurement performance criteria from the QAPP*	Validation Report – Includes qualified data – May be part of other report such as RI/FS
Usability Assessment*	Assess and document usability to meet project quality objectives.	- Sampling - Analysis	III. Assess usability of data by considering project quality objectives and the decision to be made*	Usability Report – May be part of other report such as RI/FS

*The scope of the term or the step involved is an expansion of current practice.

The following sections will detail the procedures associated with data review and will address how these procedures will be completed for the Cane Run project.

D.2) Data Review Steps

D.2.1) Step I: Verification

D.2.1.1) Responsible Personnel and Documentation

All data verification procedures will be handled by Admin Husic for sampling/handling and analytical procedures at the UK hydraulics lab and UKSIL. Jason Backus will assist with verification (as needed) at the KGS Lab and Erik Pollock will assist (as needed) with verification at the ASIL. All verification procedures need to be documented and included in quarterly reports.

D.2.1.2) Sample Collection

Sample collection procedures will be verified by checking that the field book data is consistent with the data loaded onto the electronic database. If inconsistencies are observed, appropriate changes will be made and the corrective action log will be filled out (Figure 5). If data from the field appears erroneous or in error, the QC manager will consult the sampler and mitigative actions will take place. Identification of the sampler will come from sampler signatures in the fieldbook. If no signature is present or if the sampler is unsure about the erroneous data/metadata in the field book the information will be flagged in both the field book and the database and a Data Exclusion Report will be filled out. If the error is recognized by the sampler and can be mitigated, a Corrective Action Log will be filled out and appropriate database corrections will be made.

Analytes	Ensure that required lists of analytes were reported as specified in governing documents
Chain of custody	Examine traceability throughout project and examine COC records against method or procedural requirements.
Holding Times	Confirm/document if holding times were met. Ensure samples were analyzed within holding times. If not, ensure documentation of deviations.
Sample Handling	Ensure all appropriate procedures were followed and any deviations documented
Sampling Methods and Procedures	Establish that required sampling methods were used and that deviations were documented. Ensure performance criteria were met.
Field Transcription	Authenticate transcription accuracy of sampling data
Analytical Methods and Procedures	Establish that required analytical methods were used and that deviations were noted. Ensure QC samples met performance criteria and that deviations were documented.
Laboratory Transcription	Authenticate accuracy of the transcription of analytical data
Standards	Determine that standards are traceable and meet contract, method or procedural requirements
Communication	Establish that required communication procedures were followed by field or lab personnel
Audits	Review field and lab audit reports and accreditation and certification records the labs performance on specific methods
Step IIa Validation Report	Summarize deviations from methods or procedures. Include qualified data and explanation of all data qualifiers.

D.2.2.2) Step IIb Validation Activities

This portion of the validation procedure ensures that all data fulfill the requirements of the measurement performance criteria. The following table outlines procedures for this.

Table 22) Comparison with Measurement Performance Criteria (Modified from Table 11 of EPA-505-B-04-900A)

Project Component	Validation Activity
Data Deliverables and QAPP	Ensure that the data report from Step IIa was provided
Deviations	Determine the impacts of deviations. If deviations significantly impact the results determine the effectiveness of corrective actions
Sampling Plan	Determine if all components of sampling plan was executed as specified
Sampling Procedures	Determine whether all sampling procedures were conducted according to the specified methods (e.g. techniques, equipment, decontamination, volumes, and preservation techniques).
Field Duplicates	Compare results of field duplicates with established criteria
Project QLs	Determine that quantitation limits were achieved, as outlined in the QAPP and that the lab successfully analyzed a standard at the QL.
Confirmatory Analysis	Evaluate agreement of lab results if split samples are analyzed in different labs
Performance Criteria	Evaluate QC data against project-specific performance criteria in the QAPP
Step IIb Validation Report	Summarize outcome of comparison of data to MPC in the QAPP. Include qualified data and explanation of all data qualifiers.

D.2.3) Step III: Usability Assessment

Table 21 documents the usability assessment procedure for the Cane Run Project.

Table 23) Usability Assessment Procedure

Step 1	Review the project's objectives and sampling design <i>Review the key outputs defined during systematic planning (i.e., POCs or DQOs and MPCs) to make sure they are still applicable. Review the sampling design for consistency with stated objectives. This provides the context for interpreting the data in subsequent steps.</i>
Step 2	Review the data verification and data validation outputs <i>Review available QA reports, including the data verification and data validation reports. Perform basic calculations and summarize the data (using graphs, maps, tables, etc.). Look for patterns, trends, and anomalies (i.e., unexpected results). Review deviations from planned activities (e.g., number and locations of samples, holding time exceedances, damaged samples, non-compliant PT sample results, and SOP deviations) and determine their impacts on the data usability. Evaluate implications of unacceptable QC sample results.</i>
Step 3	Verify the assumptions of the selected statistical method <i>Verify whether underlying assumptions for selected statistical methods are valid. Common assumptions include the distributional form of the data, independence of the data, dispersion characteristics, homogeneity, etc. Depending on the robustness of the statistical method, minor deviations from assumptions usually are not critical to statistical analysis and data interpretation. If serious deviations from assumptions are discovered, then another statistical method may need to be selected.</i>
Step 4	Implement the statistical method <i>Implement the specified statistical procedures for analyzing the data and review underlying assumptions. For decision projects that involve hypothesis testing consider the consequences for selecting the incorrect alternative; for estimation projects, consider the tolerance for uncertainty in measurements.</i>
Step 5	Document data usability and draw conclusions <i>Determine if the data can be used as intended, considering implications of deviations and corrective actions. Discuss data quality indicators. Assess the performance of the sampling design and Identify limitations on data use. Update the conceptual site model and document conclusions. Prepare the data usability summary report which can be in the form of text and/or a table.</i>

D.2.3.1) Data Limitations and Action from Usability Assessment

Usability assessment will consider data quality indicators including precision, accuracy/bias, representativeness, comparability, sensitivity and quantitation limits, and completeness.

D.2.3.2) Activities

The project team (primarily Husic and Fox) will perform the usability assessment once data validation and verification procedures have concluded on the project.

D.3) Streamlining Data Review

Since the dataset is not extremely dense, streamlining of data review is not necessary and all data will be verified and validated.

References

- Alexander R.B., Smith, R.A., Schwarz G.E., Boyer, E.W., Nolan J.V., Brakebill, J.W. (2008) "Differences in Phosphorus and Nitrogen Delivery to The Gulf of Mexico from the Mississippi River Basin" *Environ. Sci. Technol.* 42, 822-830
- Arango, C.P., and Tank, J.L. (2008). "Land use influences the spatiotemporal controls on nitrification and denitrification in headwater streams." *Journal of the North American Benthological Society*, 27, 90–107.
- Conley, D.J., Paerl, H.W., Howarth, R.W., Boesch, D.F., Seitzinger, S.P., Havens, K.E., Lancelot, C., and Likens, G.E. (2009). "Controlling Eutrophication: Nitrogen and Phosphorus." *Science*, 323, 1014-1015.
- Diaz, R. J., and Rosenberg, R. (1995). "Marine benthic hypoxia: a review of its ecological effects and the behavioural responses of benthic macrofauna." *Oceanography and Marine Biology- an Annual Review*, 33, 245–303.
- Findlay, S.E.G., Mulholland P.J., Hamilton, S.K., Tank, J.L., Bernot, M.J., Burgin A.J., Crenshaw, C.L., Dodds, W.K., Grimm, N.B., McDowell, W.H., Potter, J.D., Sobota, D.J. (2011) "Cross-stream comparison of substrate-specific denitrification potential." *Biogeochemistry* 104, 381-392.
- Ford W.L., Fox, J.F. (2012) "Model of particulate organic carbon transport in an agriculturally impacted watershed" *Hydrological Processes* accepted.
- Fox, J.F., Davis, C.M., and Martin, D.K. (2010). "Sediment source assessment in a lowland watershed using nitrogen stable isotopes." *Journal of the American Water Resources Association*, 46, 1192–1204.
- Galloway, J.N. et al. (2008). "Transformation of the nitrogen cycle: recent trends, questions, and potential solutions." *Science*, 320, 889-892.
- Kendall, C. (1998). "Tracing Nitrogen Sources and Cycling in Catchments." In: C. Kendall and J.J. McDonnell (Eds.), *Isotope Tracers in Catchment Hydrology*, Elsevier, Amsterdam, 519-576.
- National Academy of Engineers (NAE) (2008). Grand Challenges of Engineering, Feb 16, 2008, Online at: <http://www.engineeringchallenges.org/cms/8996/9221.aspx>, last visited March 3, 2011.
- Newcomer, T.A., Kaushal, S.S., Mayer, P.M., Shields, A.R., Canuel, E.A., Groffman, P.M., Gold, A.J. (2012) "Influence of natural and novel organic carbon sources on denitrification in forest, degraded urban, and restored streams." *Ecological Monographs* 82(4) 449-466.
- Peterson, B.J., Wollheim, W.M., Mulholland, P.J., Webster, J.R., Meyer, J.L., Tank, J.L., Martõ, E., Bowden, W.B., Valett, H.M., Hershey, A.E., McDowell, W.H., Dodds, W.K., Hamilton, S.K., Gregory, S., and Morrall, D.D. (2001). "Control of Nitrogen Export from Watersheds by Headwater Streams." *Science*, 292, 86-90.
- Rabalais, N.N., Turner, R.E., et al. (1996). "Nutrient changes in the Mississippi River and system responses on the adjacent continental shelf." *Estuaries*, 19, 386–407.
- Russo, J.P. and Fox, J.F. (2012). "The role of the surface fine-grained laminae in a lowland watershed: a model approach." *Geomorphology*.
- Seitzinger S. 2008. "Out of reach." *Nature*, 452:162-163.
- Turner, R. E., and Rabalais, N. N. (1991). "Changes in Mississippi River water quality this century: implications for coastal food webs." *Bioscience*, 41, 140–147.
- Turner, R. E., and Rabalais, N. N. (1994). "Coastal eutrophication near the Mississippi river delta." *Nature*, 368, 619–621.
- Vitousek, P.M., Aber, J.B., Howarth, R.W., Likens, G.E., Matson, P.A., Schindler, D.W., Schlesinger, W.H., and Tilman, G.D. (1997). "Human alteration of the global nitrogen cycle: sources and consequences." *Ecological Applications*, 7, 737–750.
- Zhou, X.; Helmers, M. J.; Asbjornsen, H.; Kolka, R.; Tomer, M. D. (2010) "Perennial filter strips reduce nitrate levels in soil and shallow groundwater after grassland-to-cropland conversion." *Journal of Environmental Quality*. 39, 2006-2015.

Appendices

In the following Appendices, Standard Operating Procedures (SOPs) and reference material are provided for (1) standard water quality parameters (i.e. nitrate, DIC, DOC, DP, and Sediment concentration) that have well established methods and collection procedures, (2) analytical field instrumentation and techniques (i.e. Fluid velocity, Stage, Turbidity, Temperature, DO, pH, and Conductivity) and (3) methods that involve some project specific alterations to accepted methods (i.e. $\delta^{15}\text{N}/\delta^{18}\text{O}$ of nitrate, $\delta^2\text{H}/\delta^{18}\text{O}$ of water, $\delta^{13}\text{C}$ of DIC, and $\delta^{15}\text{N}/\delta^{13}\text{C}$ of Transported sediment, POC and PN). For the latter, SOPs developed for this project are provided to ensure QA.

A1) Nitrate

A1.1) Field SOP

See section A15.1

A1.2) Laboratory SOP- Ion Chromatography of Water --KGS 9056

Ion Chromatography of Water

1. Discussion

Principle

This method addresses the sequential determination of the following inorganic anions: *bromide, chloride, fluoride, nitrate, Kjeldahl nitrogen, total nitrogen and sulfate*. A small volume of water sample is injected into an ion chromatograph to flush and fill a constant volume sample loop. The sample is then injected into a stream of carbonate-bicarbonate eluent. The sample is pumped through three different ion exchange columns and into a conductivity detector. The first two columns, a precolumn (or guard column), and a separator column, are packed with low-capacity, strongly basic anion exchanger. Ions are separated into discrete bands based on their affinity for the exchange sites of the resin. The last column is a suppressor column that reduces the background conductivity of the eluent to a low or negligible level and converts the anions in the sample to their corresponding acids. The separated anions in their acid form are measured using an electrical conductivity cell. Anions are identified based on their retention times compared to known standards. Quantitation is accomplished by measuring the peak area and comparing it to a calibration curve generated from known standards.

Sensitivity

Ion Chromatography values for anions ranging from 0 to approximately 40 mg/L can be measured and greater concentrations of anions can be determined with the appropriate dilution of sample with deionized water to place the sample concentration within the working range of the calibration curve.

Interferences

Any species with retention time similar to that of the desired ion will interfere. Large quantities of ions eluting close to the ion of interest will also result in interference. Separation can be improved by adjusting the eluent concentration and/or flow rate. Sample dilution and/or the use of the method of Standard Additions can also be used. For example, high levels of organic acids may be present in industrial wastes, which may interfere with inorganic anion analysis. Two common species, formate and acetate, elute between fluoride and chloride. The water dip, or negative peak, that elutes near, and can interfere with, the fluoride peak can usually be eliminated by the addition of the equivalent of 1 mL of concentrated eluent (100X) to 100 mL of each standard and sample. Alternatively, 0.05 mL of 100X eluent can be added to 5 mL of each standard and sample.

Because bromide and nitrate elute very close together, they can potentially interfere with each other. It is advisable not to have Br-/NO₃- ratios higher than 1:10 or 10:1 if both anions are to be quantified. If nitrate is observed to be an interference with bromide, use of an alternate detector (e.g., electrochemical detector) is recommended.

Method Interferences may be caused by contaminants in the reagent water, reagents, glassware, and other sample processing apparatus that lead to discrete artifacts or elevated baseline in ion chromatograms. Samples that contain particles larger than 0.45 micrometers and reagent solutions that contain particles larger than 0.20 micrometers require filtration to prevent damage to instrument columns and flow systems. If a packed bed suppressor column is used, it will be slowly consumed during analysis and, therefore, will need to be regenerated. Use of either an anion fiber suppressor or an anion micro-membrane suppressor eliminates the time-consuming regeneration step by using a continuous flow of regenerant.

Because of the possibility of contamination, do not allow the nitrogen cylinder to run until it is empty. Once the regulator gauge reads 100 kPa, switch the cylinder out for a full one. The old cylinder should then be returned to room #19 for storage until the gas company can pick it up. Make sure that the status tag marks the cylinder as "EMPTY".

Sample Handling and Preservation

Samples should be collected in glass or plastic bottles that have been thoroughly cleaned and rinsed with reagent water. The volume collected should be sufficient to ensure a representative sample and allow for replicate analysis, if required. Most analytes have a 28 day holding time, with no preservative and cooled to 4°C. Nitrite, nitrate, and orthophosphate have a holding time of 48 hours. Combined nitrate/nitrite samples preserved with H₂SO₄ to a pH ≤2 can be held for 28 days; however, pH ≤2 and pH ≥12 can be harmful to the columns. It is recommended that the pH be adjusted to pH ≥2 and pH ≤12 just prior to analysis.

Note: Prior to analysis, the refrigerated samples should be allowed to equilibrate to room temperature for a stable analysis.

2. Apparatus

Dionex DX500
Dionex CD20 Conductivity Detector
Dionex GP50 Gradient Pump
Dionex Eluent Organizer
Dionex AS40 Automated Sampler
Dionex ASRS-Ultra Self-Regenerating Suppressor
Dionex Ionpac Guard Column (AG4A, AG9A, or AG14A)
Dionex Ionpac Analytical Column (AS4A, AS9A, or AS14A)
Dionex Chromeleon 6.8 Software Package
Dionex 5 mL Sample Polyvials and Filter Caps
2 L Regenerant Bottles
5 mL Adjustable Pipettor and Pipettor Tips
1 mL Adjustable Pipettor and Pipettor Tips
A Supply of Volumetric Flasks ranging in size from 25 mL to 2 L
A Supply of 45 micrometer pore size Cellulose Acetate Filtration Membranes
A Supply of 25x150 mm Test Tubes
Test Tube Racks for the above 25x150 mm Test Tubes

3. Reagents

Purity of Reagents—HPLC grade chemicals (where available) shall be used in all reagents for Ion Chromatography, due to the vulnerability of the resin in the columns to organic and trace metal contamination of active sites. The use of lesser purity chemicals will degrade the columns.

Purity of Water—Unless otherwise indicated, references to water shall be understood to mean Type I reagent grade water (Milli Q Water System) conforming to the requirements in ASTM Specification D1193.

Eluent Preparation for SYSTEM2 NITRATE Methods, including Bromides (using AG4, AG4 and AS4 columns)—All chemicals are predried at 105° C for 2 hrs then stored in the desiccator. Weigh out 0.191 g of sodium carbonate (Na₂CO₃) and 0.286 g of sodium bicarbonate (NaHCO₃) and dissolve in water. System 2 (the chromatography module that contains the AG4, AG4, and AS4 Dionex columns) to be sparged, using helium, of all dissolved gases before operation.

Eluent Preparation for SYSTEM2 NITRATE (F) Method (using AG14 and AS14 columns)—Weigh out 0.3696 g of sodium carbonate (Na₂CO₃) and 0.080 g of sodium bicarbonate (NaHCO₃) and dissolve in water. Bring the volume to 1000 mL and place the eluent in the System 1 bottle marked for this eluent concentration. The eluent must be sparged using helium as in the above reagent for System 2.

Eluent Preparation for SYSTEM2 TKN (TKN) Methods, including Total Nitrogen (using AG4A, AG4A, and AS4A columns)—Weigh out 0.191 g of sodium carbonate (Na₂CO₃) and 0.143 g of sodium bicarbonate (NaHCO₃) and dissolve in water. Bring the volume up to 1000 ml and place in the System 2 bottle labeled “IC-TKN 0.191/0.143”. Sparge the eluent as in the above reagent for System 2.

100X Sample Spiking Eluent—prepared by using the above carbonate/bicarbonate ratios, but increasing the concentration 100X. Weigh out 1.91 g of Na₂CO₃ and 2.86 g of NaHCO₃ into a 100 mL volumetric flask. 0.05 mL of this solution is added to 5 mL of all samples and standards to resolve the water dip associated with the fluoride peak.

Stock standard solutions, 1000 mg/L (1 mg/mL): Stock standard solutions may be purchased (SPEX) as certified solutions or prepared from ACS reagent grade materials (dried at 105° C for 30 minutes)

Calibration Standards—for the SYSTEM2 NITRATE (except Bromide) methods are prepared as follows:

- *Calibration Standard 1*: Pipette 0.1 mL of 1000 mg/L NaNO₃ stock standard, 0.1 mL of 1000 mg/L NaF stock standard, 2 mL of 1000 mg/L NaCl stock standard, and 10 mL of 1000 mg/L K₂SO₄ stock standard into a 1000 mL volumetric flask partially filled with water, then fill to volume.
- *Calibration Standard 2*: Pipette 0.5 mL of 1000 mg/L NaNO₃ stock standard, 0.5 mL of 1000 mg/L NaF stock standard, 5 mL of 1000 mg/L NaCl stock standard, and 20 mL of 1000 mg/L K₂SO₄ stock standard into a 1000 mL volumetric flask, partially filled with water, then fill to volume.
- *Calibration Standard 3*: Pipette 2.5 mL of 1000 mg/mL NaNO₃ stock standard, 2.5 mL of 1000 mg/L NaF stock standard, 10 mL of 1000 mg/L NaCl stock standard, and 40 mL of 1000 mg/L K₂SO₄ stock standard into a 1000 mL volumetric flask partially filled with deionized water, then fill to volume.
- *Quality Control Sample*: Pipette 1.0 mL of 1000 mg/L NaNO₃ stock solution, 1.0 mL of 1000 mg/L NaF stock solution, 8 mL of 1000 mg/L NaCl stock solution, and 30 mL of mg/L K₂SO₄ stock standard into a 1000 mL volumetric flask, partially filled with water, then fill to volume.

Calibration Standards—for the SYSTEM2 NITRATE (Fluoride) method are prepared as follows:

- A. *Calibration Standard 1*: Pipette 0.01 mL of 1000 mg/L NaF stock standard into a 1000 mL volumetric flask partially filled with water, then fill to volume.
- B. *Calibration Standard 2*: Pipette 0.05 mL of 1000 mg/L NaF stock standard into a 1000 mL volumetric flask partially filled with water, then fill to volume.
- C. *Calibration Standard 3*: Pipette 0.1 mL of 1000 mg/mL NaF stock standard into a 1000 mL volumetric flask partially filled with water, then fill to volume.
- D. *Calibration Standard 4*: Pipette 0.5 mL of 1000 µg/mL NaF stock standard into a 1000 mL volumetric flask partially filled with water, then fill to volume.
- E. *Calibration Standard 5*: Pipette 1.0 mL of 1000 mg/L 1000 stock standard into a 1000 mL volumetric flask partially filled with water, then fill to volume.
- F. *Quality Control Standard*: Pipette 0.1 mL of 1000 mg/L NaF from a separate source stock standard into a 1000 mL volumetric flask partially filled with water, then fill to volume.
- G. *Quality Control Standard*: Pipette 0.4 mL of 1000 mg/L NaF from a separate source stock standard into a 1000 mL volumetric flask partially filled with water, then fill to volume.
- H. *Quality Control Standard*: Pipette 1.0 mL of 1000 mg/L NaF from a separate source stock standard into a 1000 mL volumetric flask partially filled with water, then fill to volume.

Calibration Standards—for the SYSTEM2 NITRATE (Bromide) method are prepared as follows:

1. *Calibration Standard 1*: Pipette 2 mL of 1000 mg/L NaBr stock standard into a 1000 mL volumetric flask partially filled with water, then fill to volume.

1. Calibration Standard 2: Pipette 5 mL of 1000 mg/L NaBr stock standard into a 1000 mL volumetric flask partially filled with water, then fill to volume.
2. Calibration Standard 3: Pipette 10 mL of 1000 mg/L NaBr stock standard into a 1000 mL volumetric flask partially filled with water, then fill to volume.
3. Quality Control Standard: Pipette 8 mL of 1000 mg/L NaBr stock standard into a 1000 mL volumetric flask partially filled with water, then fill to volume.

Outside Source Certified Quality Control Sample—ERA

4. Procedure

A. Instrument Preparation

1. Before turning on the Dionex Ion Chromatography System:
 1. Fill the eluent reservoir(s) with fresh eluent.
 2. Make certain the waste reservoir is empty of all waste.
 3. Turn on the helium. The system pressure should be between 7 - 15psi. The system pressure can be regulated with the knob on the back of the Eluent Organizer.
 4. Connecting a piece of tubing to the gas line going into the eluent bottle and putting the tubing into the eluent degasses the eluent reservoir(s). The gas knob on the Eluent Organizer that corresponds to the eluent bottle should be slowly opened until a constant bubbling stream can be seen in the eluent bottle.
 5. The eluent should be degassed with helium, for a minimum of 30 minutes, before operation of the instrument.
 6. After the eluent has been degassed, remove the tube from the eluent and tightly seal the eluent bottle. The eluent is now ready to introduce into the system.
2. Whether using the IP25 for Fluorides or the GP50 for everything else, turn off the browser, scroll to **REMOTE** on the screen, select **LOCAL** and **ENTER**.
3. Scroll to mL/min., change to 0 mL/min., and hit **ENTER**. If using the IP25 pump, skip to step #5.
4. Hit **MENU** and select **1**, then **ENTER**.
5. Insert syringe into the Priming Block, open the gas valve on the Eluent Organizer, turn the valve on the Priming Block counterclockwise, and turn on the pump that corresponds with the method to be ran by pushing the **OFF/ON** button.
6. If the syringe does not fill freely, assist by gently pulling back on the plunger of the syringe. Make certain that all of the air bubbles are removed from the eluent line to the pumps.
7. Press **OFF/ON** on the pump to turn it off.
8. Turn the valve on the Priming Block clockwise, remove the syringe and expel the air bubbles from the syringe.
9. Reinsert the syringe filled with eluent into the Priming Block.
10. Open the valve on the Pressure Transducer and the valve on the Priming Block with the eluent filled syringe still attached. This is accomplished by turning both counterclockwise.
11. Press **PRIME** on the pump and push the contents of the syringe into the Priming Block. After the eluent has been injected into the Priming Block, press **OFF/ON** to turn the prime pump off and to close the valves on the Pressure Transducer and Priming Block.
12. Remove the syringe from the Priming Block.
13. Scroll to the mL/min. on the screen for the pump. For the GP50, type 2 mL/min., and press **ENTER**. For the IP25, type 1.2 mL/min., and press **ENTER**.
14. Press **OFF/ON** to turn on the pump at the appropriate rate. The pressure should soon stabilize between both pumpheads after two minutes of pumping time.
15. If the pressure between pumpheads has a difference >20 psi, then shut down the pump and repeat steps 2-14 to remove air bubbles and prime the pumps.
16. Once the pump has a pumping pressure difference between pumpheads of <20 psi, then go to the computer and enter PeakNet.
17. On the computer, **turn on the Chromelon 6.8 browser**, then choose either **System 1** (Fluoride) or **System 2** (all other anions including Bromide and TKN).
18. Go to **last run sequence, click to highlight and go to file, click save as..** This will load the method of interest and a template for the current sequence run.
19. The sequence is edited to reflect the method and samples that are to be run.
 2. **SYSTEM2 NITRATE** for Fluoride
 3. **SYSTEM2 NITRATE** for Bromides
 4. **SYSTEM2 TKN** for TKN and Total Nitrogen

Note: Data is reprocessed in the section of Chromelon 6.8 called *Sequence integration editor*. Only operators with a minimum of three months experience in Ion Chromatography should attempt to reprocess data for this analysis. Once data is optimized, then the nitrogen values from nitrate and nitrite analysis can be subtracted from this value for the TKN nitrogen value. If only Total Nitrogen is needed then use the optimized data value without the correction for nitrite and nitrate nitrogen.

5. **SYSTEM 2 NITRATE** for all other anions,
 20. Observe the reading on the screen of the CD20 Conductivity Detector. A conductivity rate change of <0.03 μ S over a 30 second time span is considered stable for analysis.
 21. If using the GP50 pump, it will take about 15-30 minutes for the CD20 system to stabilize. If using the IP25, it will take between 30 minutes to 2 hours for stabilization.
 22. Once the CD20 is stabilized, the Dionex DX500 Ion Chromatography System is ready to start standardization.

6. Quality Control

A quality control sample obtained from an outside source must first be used for the initial verification of the calibration standards. A fresh portion of this sample should be analyzed every week to monitor stability. If the results are not within +/- 10 % of the true value listed for the control sample, prepare a new calibration standard and recalibrate the instrument. If this does not correct the problem, prepare a new standard and repeat the calibration. A quality control sample should be run at the beginning and end of each sample delivery group (SDG) or at the frequency of one per every ten samples. The QC's value should fall between ± 10 % of its theoretical concentration.

A duplicate should be run for each SDG or at the frequency of one per every twenty samples, whichever is greater. The RPD (Relative Percent Difference) should be less than 10%. If this difference is exceeded, the duplicate must be reanalyzed.

From each pair of duplicate analytes (X_1 and X_2), calculate their RPD value:

$$\% RPD = 2 \bullet \left(\frac{X_1 - X_2}{X_1 + X_2} \right) \times 100$$

where: ($X_1 - X_2$) means the absolute difference between X_1 and X_2 .

7. Method Performance

The method detection limit (MDL) should be established by determining seven replicates that are 2 to 5 times the instrument detection limit. The MDL is defined as the minimum concentration that can be measured and reported with 99% confidence that the analyte concentration is greater than zero and is determined from analysis of a sample in a given matrix containing the analyte.

$$MDL = t_{(n-1, 1-\alpha=99)} (S)$$

where: **t** = the t statistic for n number of replicates used (for n=7, t=3.143)

n = number of replicates

S = standard deviation of replicates

8. Reference

EPA SW 846-9056, Chapter 5, September 1994

U.S. EPA Method 300.0, March 1984

ASTM vol. 11.01 (1996), D 4327, "Standard Test Method for Anions in Water by Chemically Suppressed Ion Chromatography".

0/2010 addendum to 01/2009 Ion Chromatography of Water

a. Discussion

1. Principle and iodine.

2. Reagents

Calibration Standards

1. Calibration Standard 1: Pipette 0.1 mL of 1000 mg/L I stock standard into a 1000 mL volumetric flask partially filled with water, then fill to volume.
2. Calibration Standard 2: Pipette 0.5 mL of 1000 mg/L I stock standard into a 1000 mL volumetric flask partially filled with water, then fill to volume.
3. Calibration Standard 3: Pipette 1.0 mL of 1000 mg/L I stock standard into a 1000 mL volumetric flask partially filled with water, then fill to volume.
4. Calibration Standard 4: Pipette 5.0 mL of 1000 mg/L I stock standard into a 1000 mL volumetric flask partially filled with water, then fill to volume.
5. Calibration Standard 5: Pipette 10.0 mL of 1000 mg/L I stock standard into a 1000 mL volumetric flask partially filled with water, then fill to volume.
6. Quality Control Sample: Pipette 5.0 mL of 1000 mg/L I stock standard into a 1000 mL volumetric flask partially filled with water, then fill to volume.

A2) Dissolved Phosphorus (DP)

A2.1) Field SOP

See section A15.1

A2.2) Analytical SOP- Total Phosphorus (TP) --KGS D515

Total Phosphorus in Water

1. Discussion

Principle

MDL= 0.02 as of 5/2002

Separation into total dissolved and total recoverable forms of phosphorus depends on filtration of the water sample through a 0.45 µm membrane filter. Total recoverable phosphorus includes all phosphorus forms when the unfiltered, shaken sample is heated in the presence of sulfuric acid and ammonium peroxydisulfate. Total dissolved phosphorus includes all phosphorus forms when the filtered, shaken sample is heated in the presence of sulfuric acid and ammonium peroxydisulfate. Phosphorus is converted to orthophosphate by digesting the water sample with ammonium persulfate and diluted sulfuric acid. Ammonium molybdate and antimony potassium tartrate can then react in an acid medium with dilute solutions of orthophosphate to form an antimony-phosphate-molybdate complex. This complex is reduced to an intensely blue-colored complex by ascorbic acid. The color intensity is proportional to the phosphorus concentration.

Sensitivity

The range of determination for this method is 0.05 mg/L to 1.00 mg/L P.

Interferences

Ferric iron must exceed 50 mg/L, copper 10 mg/L, or silica 10 mg/L, before causing an interference. Higher silica concentrations cause positive interferences over the range of the test, as follows: results are high by 0.005 mg/L of phosphorus for 20 mg/L of SiO₂, 0.015 mg/L of phosphorus for 50 mg/L, and 0.025 mg/L of phosphorus for 100 mg/L. Because arsenic and phosphorus are analyzed similarly, arsenic can cause an interference if its concentration is higher than that of phosphorus.

Sample Handling and Preparation

Samples should be preserved only by refrigeration at 4 °C. A raw sample should be used in the analysis. The holding time for this analysis is 28 days.

2. Safety

Safety glasses, gloves, and a lab coat should be worn while performing this analysis due to the use of, and possible exposure to, strong acids and bases.

3. Apparatus

Varion 50 Spectroscopy system

Filtration Apparatus

Coors 60242 Büchner funnels.

Suction flasks, connected in series to a vacuum system.

Reservoir for the filtrate, 500 mL.

Trap which prevents liquid from entering the vacuum system, 1000 mL

Paper filters—7.5 cm, 1 µm. (VWR Cat. # 28321-005)

Analytical balance, capable of weighing to the nearest 0.0001 g.

Drying oven.

Desiccator.

Thermix Stirring Hot Plate—Model 610T

HCl Acid washed glassware—Refer to the “Total P” section of the Glassware GLP for further details. Commercial detergents should never be used. Glassware should be dedicated for Total P use only.

6 ½ oz. Disposable polystyrene specimen cups—Cups should be rinsed three times with DI water.

4. Reagents

Purity of Reagents—Reagent grade chemicals shall be used in all tests. Unless otherwise indicated, all reagents shall conform to the specifications of the Committee on Analytical Reagents of the American Chemical Society. Other grades may be used, provided it is first ascertained that the reagent is sufficiently high in purity to permit its use without lessening the accuracy of the determinations.

Purity of Water—Unless otherwise indicated, references to water shall be understood to mean Type I reagent grade water (Milli Q Water System) conforming to the requirements in ASTM Specification D1193.

Ammonium Peroxydisulfate—Place 20 g of ammonium peroxydisulfate in a 50 mL volumetric flask. Dilute with water to volume. Add a magnetic stirrer to the flask and let the solution stir until all the crystals have dissolved (minimum of 20 minutes). Prepare daily. (enough for 30 beakers total)

Solution Mixture—Dissolve 0.13 g of antimony potassium tartrate and 5.6 g of ammonium molybdate in approximately 700 mL of water. Cautiously add 70 mL of concentrated sulfuric acid. Allow the solution to cool and dilute to 1 liter. The solution must be kept in a polyethylene bottle away from heat. This solution is stable for one year.

Combined Reagent—Dissolve 0.50 g solid ascorbic acid in 100 mL of solution mixture. Prepare daily.

Phenolphthalein indicator solution—Dissolve 0.5 g of phenolphthalein in a mixture of 50 mL isopropyl alcohol and 50 mL water.

Sulfuric acid (31 + 69)—Slowly add 310 mL of concentrated H₂SO₄ to approximately 600 mL of water. Allow solution to cool and dilute to 1 liter.

Sodium Hydroxide, 10 N—Dissolve 400 g of NaOH in approximately 800 mL of water. Allow solution to cool and dilute to 1 liter.

Sodium Hydroxide, 1 N—Dissolve 40 g of NaOH in approximately 800 mL of water. Allow solution to cool and dilute to 1 liter.

Phosphorus stock solution (50 mg/L)—Dissolve 0.2197 g of predried (105 °C for one hour) KH_2PO_4 in water and dilute to 1 liter. Prepare daily.

Phosphorus standard solution (2.5 mg/L)—Dilute 50 mL of the stock solution to exactly 1 liter of water. Prepare daily.

Blank—reagent grade water.

Total phosphorus stock QC solution—Using a commercially available Quality Control solution, dilute to desired range and record manufactures name, lot #, and date.

Quality control sample—Dilute total P stock solution so that QC value falls midway in analysis working range (0.05-1.00 ppm). Using 6.11 ppm QC stock solution, dilute 25 mL of Total Phosphorous stock solution to 500 mL resulting in a concentration of 0.306 ppm.

Acid for glassware—Carefully add 250 mL of concentrated hydrochloric acid to approximately 600 ml of water. Dilute to 1 liter.

1. Procedure

5. Prepare the spectrophotometer by turning on the lamp and allowing it to warm up for at least one hour. See the Spectrophotometer GLP for a detailed listing of necessary computer commands.

A. B. Standards Prep

Prepare a series of phosphorus standards from the 2.5 mg/L phosphorus standard solution according to the following table. Dilute each to 50 mL with water.

<u>Volume of phosphorus standard, mL</u>	<u>Standard concentration, ppm</u>
1. 0.05	
2. 0.10	
4	0.20
10	0.50
15	0.75
20	1.00
1	0.35

2. Prepare all standards daily.

2. C. Sample Prep

Pour 50 mL of each of the two blanks, standards, samples, duplicates, and Total P QC's into 100 mL glass beakers. Add 3 - 6 glass boiling beads to each beaker.

Mark beakers at top of liquid with a Sharpie.

Add 1 mL of ammonium peroxydisulfate solution and 1 mL of H_2SO_4 (31+69) to each marked beaker.

Place beakers on the large hot plates that are located in the hood.

Turn the Temp. knob on the hot plates to "HI."

Let each sample (blank, standard, duplicate, or QC) stay on the hot plate until its volume decreases to 10 mL. This process takes approximately 1 to 1 ½ hours. Do **not** allow the samples to completely evaporate.

Allow each sample to cool in the hood.

Add a drop of phenolphthalein indicator solution to each sample.

Add 1 mL of 10 N NaOH to each sample.

Continue adjusting the pH's by adding 1 N NaOH until each sample becomes faint pink in color. The pH is approximately 10 at this point.

Bring samples back to colorless by adding 1 N H_2SO_4 to each sample. The pH is approximately 4 at this point.

Bring each sample's volume back up to the mark with water.

Filter each of the samples using the acid washed ceramic funnels and 1 µm paper filters.

3. 14. Pour 25 mL of each sample into its corresponding 4 ½ oz. plastic beaker.
4. 15. Add 5 mL of combined reagent to the sample and mix thoroughly.
5. 16. After a minimum of 10 minutes, but no longer than 30 minutes, measure
6. the absorbance of the blue color at **880** nm with the spectrophotometer.

7. D. Sample Analysis

1. The computer, by comparing the concentration of each calibration standard against its absorbance, can plot a calibration curve. The correlation coefficient must be ≥ 0.994 to be acceptable. If above criteria is not met the standards may need to be remade and rerun.
2. Once the spectrophotometer is standardized properly, the samples may be analyzed.
3. Once the analysis is completed, print out a copy of the standard values, plotted curve, and the sample values. Copy the relevant data onto the Total Phosphorous Data Sheet.

E. Clean Up

1. Turn off the spectrophotometer lamp.
2. The waste must be placed in the acid waste container.
3. For glassware clean up, refer to the "Total P" section of the Glassware GLP.

6. Quality Control

A quality control sample should be run at the beginning and end of each sample delivery group (SDG) or at the frequency of one per every ten samples. The QC's value should fall between $\pm 10\%$ of its theoretical concentration.

A duplicate analysis should be run for each SDG or at the frequency of one per every twenty samples, whichever is greater. The RPD (Relative Percent Difference) should be less than 10%. If this difference is exceeded, the duplicate must be reanalyzed.

From each pair of duplicate analytes (X_1 and X_2), calculate their RPD value:

$$\% RPD = 2 \cdot \left(\frac{X_1 - X_2}{X_1 + X_2} \right) \times 100$$

where: ($X_1 - X_2$) means the absolute difference between X_1 and X_2 .

7. Method Performance

The method detection limit (MDL) should be established by determining seven replicates that are 2 to 5 times the instrument detection limit. The MDL is defined as the minimum concentration that can be measured and reported with 99% confidence that the analyte concentration is greater than zero and is determined from analysis of a sample in a given matrix containing the analyte.

$$MDL = t_{(n-1, 1-\alpha=99)} (S)$$

where:

t = the t statistic for n number of replicates used (for n=7, t=3.143)

n = number of replicates

S = standard deviation of replicates

8. References

ASTM vol. 11.01 (1996), D 515, "Standard Test Methods for Phosphorus in Water", pg. 24

ASTM vol. 11.01 (1996), D 1193, "Specification for Water", pg. 116

EPA 365.2 Phosphorous, All Forms (Colorimetric, Ascorbic Acid)

A3) Sediment Concentration

A3.1) Field SOP-

See section A15.2

A3.2) Laboratory SOP- Standard Methods for Total Suspended Solids EPA 160.2

METHOD #: 160.2 Approved for NPDES (Issued 1971)

TITLE: Residue, Non-Filterable (Gravimetric, Dried at 103-105°C)

ANALYTE: Residue, Non-Filterable

INSTRUMENTATION: Drying Oven

STORET No. 00076

1.0 Scope and Application

- 1.1 This method is applicable to drinking, surface, and saline waters, domestic and industrial wastes.
- 1.2 The practical range of the determination is 4 mg/L to 20,000 mg/L.

2.0 Summary of Method

- 2.1 A well-mixed sample is filtered through a glass fiber filter and the residue retained on the filter is dried to constant weight at 103-105°C.
- 2.2 The filtrate from this method may be used for Residue, Filterable.

3.0 Definitions

- 3.1 Residue, non-filterable, is defined as those solids which are retained by a glass fiber filter and dried to constant weight at 103-105°C.

4.0 Sample Handling and Preservation

- 4.1 Non-representative particulates such as leaves, sticks, fish, and lumps of fecal matter should be excluded from the sample if it is determined that their inclusion is not desired in the final result.
- 4.2 Preservation of the sample is not practical; analysis should begin as soon as possible. Refrigeration or icing to 4°C, to minimize microbiological decomposition of solids, is recommended.

5.0 Interferences

- 5.1 Filtration apparatus, filter material, pre-washing, post-washing, and drying temperature are specified because these variables have been shown to affect the results.
- 5.2 Samples high in Filterable Residue (dissolved solids), such as saline waters, brines and some wastes, may be subject to a positive interference. Care must be taken in selecting the filtering apparatus so that washing of the filter and any dissolved solids in the filter (7.5) minimizes this potential interference.

6.0 Apparatus

- 6.1 Glass fiber filter discs, without organic binder, such as Millipore AP-40, Reeves Angel 934-AH, Gelman type A/E, or equivalent.

NOTE: Because of the physical nature of glass fiber filters, the absolute pore size cannot be controlled or measured. Terms such as "pore size," collection efficiencies and effective retention are used to define this property in glass fiber filters. Values for these parameters vary for the filters listed above.

- 6.2 Filter support: filtering apparatus with reservoir and a coarse (40-60 microns) fritted disc as a filter support.

NOTE: many funnel designs are available in glass or porcelain. Some of the most common are Hirsch or Buchner funnels, membrane filter holders and Gooch crucibles. All are available with coarse fritted disc.

- 6.3 Suction flask.
- 6.4 Drying oven, 103-105°C.
- 6.5 Desiccator.
- 6.6 Analytical balance, capable of weighing to 0.1 mg.

7.0 Procedure

7.1 Preparation of glass fiber filter disc: Place the glass fiber filter on the membrane filter apparatus or insert into bottom of a suitable Gooch crucible with wrinkled surface up. While vacuum is applied, wash the disc with three successive 20 mL volumes of distilled water. Remove all traces of water by continuing to apply vacuum after water has passed through. Remove filter from membrane filter apparatus or both crucible and filter if Gooch crucible is used, and dry in an oven at 103-105°C for one hour. Remove to desiccator and store until needed. Repeat the drying cycle until a constant weight is obtained (weight loss is less than 0.5 mg). Weigh immediately before use. After weighing, handle the filter or crucible/filter with forceps or tongs only.

7.2 Selection of Sample Volume for a 4.7 cm diameter filter, filter 100 mL of sample. If weight of captured residue is less than 1.0 mg, the sample volume must be increased to provide 1.0 mg least 1.0 mg of residue. If other filter diameters are used, start with a sample volume equal to 7 mL/cm² of filter area and collect at least a weight of residue proportional to the 1.0 mg stated above.

NOTE: If during filtration of this initial volume the filtration rate drops rapidly or if filtration time exceeds 5 to 10 minutes, the following scheme is recommended: Use an unweighed glass fiber filter of choice affixed in the filter assembly. Add a known volume of sample to the filter funnel and record the time elapsed after selected volumes have passed through the filter. Twenty-five mL increments for timing are suggested. Continue to record the time and volume increments until filtration rate drops rapidly. Add additional sample if the filter funnel volume is inadequate to reach a reduced rate. Plot the observed time versus volume filtered. Select the proper filtration volume as that just short of the time a significant change in filtration rate occurred.

7.3 Assemble the filtering apparatus and begin suction. Wet the filter with a small volume of distilled water to seat it against the fritted support.

○ Shake the sample vigorously and quantitatively transfer the predetermined sample volume selected in 7.2 to the filter using a graduated cylinder. Remove all traces of water by continuing to apply vacuum after sample has passed through.

7.5 With suction on, wash the graduated cylinder, filter, non-filterable residue and filter funnel wall with three portions of distilled water allowing complete drainage between washing. Remove all traces of water by continuing to apply vacuum after water has passed through.

NOTE: Total volume of wash water used should equal approximately 2 mL per cm². For a 4.7 cm filter the total volume is 30 mL.

7.6 Carefully remove the filter from the filter support. Alternatively, remove crucible and filter from crucible adapter. Dry at least one hour at 103-105°C. Cool in a desiccator and weigh. Repeat the drying cycle until a constant weight is obtained (weight loss is less than 0.5 mg).

8.0 Calculations

- 8.1 Calculate non-filterable residue as follows:
A = weight of filter (or filter and crucible) + residue in mg
B = weight of filter (or filter and crucible) in mg
C = mL of sample filtered

9.0 Precision and Accuracy

- 9.1 Precision data are not available at this time.
- 9.2 Accuracy data on actual samples cannot be obtained.

Bibliography

1. NCASI Technical Bulletin No. 291, March 1977. National Council of the Paper Industry for Air and Stream Improvement, Inc., 260 Madison Ave., NY

A4) Turbidity

Calibration, operation, inspection, maintenance, storage and other analytical needs are covered in the YSI manual for the 6136 Turbidity probe. The manual can be obtained from the YSI company at www.foundriest.com. The citation for the manual is: YSI (2006) 6-Series Multiparameter Water Quality Sondes. YSI, Yellow Springs, OH, User Manual 069300 Revision D.

A5) Temperature

Calibration, operation, inspection, maintenance, storage and other analytical needs are covered in the YSI manual for the Temperature probe. The manual can be obtained from the YSI company at www.foundriest.com. The citation for the manual is: YSI (2006) 6-Series Multiparameter Water Quality Sondes. YSI, Yellow Springs, OH, User Manual 069300 Revision D.

A6) $\delta^{15}\text{N}/\delta^{18}\text{O}$ of Nitrate

A6.1) Field SOP

See section A15.1

A6.2) Analytical SOP

SOP for determining $\delta^{15}\text{N}$ / $\delta^{18}\text{O}$ of Nitrate
UK Dept. of Civil Engineering
2-1-17

1. Overview

The SOP for analyzing the stable nitrogen isotope signature of streamwater nitrate is derived from the methods published by the USGS Reston Stable Isotope Lab (Coplen, 2012). $\delta^{15}\text{N}$ will be analyzed in each sample to determine seasonal and hydrologic variability of streamwater inputs and the impacts of biological uptake on $\delta^{15}\text{N}$. Denitrification of streamwater nitrate is conducted using *Pseudomonas* (*P.*) *chlororaphis* or *P. aureofaciens* to convert nitrate (NO_3^-) to nitrous oxide (N_2O). These bacteria lack the ability to further reduce the compound to dinitrogen gas (N_2) making it ideal to study both the oxygen and nitrogen isotopes. The nitrate gas will be trapped in a small-volume trap and immersed in liquid nitrogen. The analyte was cleaned on a gas chromatograph and analyzed on a continuous flow IRMS.

2. Safety

The analysis will incorporate culturing of bacteria. Thus, safety gloves, lab coats, and protective eye wear should be used during the analysis.

3. Equipment, Reagents and Consumable Supplies

A. Lab Instrumentation

- Centrifuge
- Reciprocal Shaker
- Analytical Balance
- -80 Degrees Celsius freezer
- Bunsen Burner
- Autoclave
- Sterile Hood
- Finnigan Delta^{Plus} CF-IRMS
- ISODAT 2.0
-

B. Reagents and Consumable Supplies

- *P. chlororaphis*, *P. aureofaciens*
- Tryptic Soy Agar
- Tryptic Soy Broth
- 1-mL plastic vials
- 1000-mL Pyrex Flask
- 2000-mL Culture media flask with screw top
- Petri dishes, 100mm
- Crimp tops-aluminum with silicone septa
- Decrimper
- Crimper-crimping jaw and crimp mate unit
- 20-mL glass sample vials
- 250-mL Centrifuge tubes
- 500-mL Pyrex Plus coated media bottle
- Glycerol
- Antifoam B Emulsion
- KNO_3
- $(\text{NH}_4)_2\text{SO}_4$
- Reagent Grade Alcohol
- Autoclave bags
- Needles: 25 G 5/8inch
- Needles: 25 G 1.5 inch
- 1-mL glass syringe
- 22s gauge needle
- Helium gas
- Dry ice
- Liquid Nitrogen

4. Sample Preparation

A. Bacteria Preparation

- Samples are collected in the field using proper collection protocol and are immediately preserved by cooling the samples to 4 degrees Celsius. The samples are shipped to the appropriate lab (ASIL) immediately.
- Plate media shall be made using a mix of 20 grams of tryptic soy agar, .505g KNO_3 , .06607g $(\text{NH}_4)_2\text{SO}_4$ and 500-mL of deionized water. Ingredients are mixed and stirred on a hot plate using a magnetic stirrer. The flask will be autoclaved at 250 °F for 15 minutes. The media will be poured into 2 bags of sterile plates and dried under the hood for 15 minutes.
- The plates are stored at 4 °C for 15 minutes. 1-L batches of culture media shall be made by mixing 40g of tryptic soy broth, 1.01 g KNO_3 , 0.1321g $(\text{NH}_4)_2\text{SO}_4$ and 1000-mL of deionized water into a 2000-mL Pyrex flask, stirred

as with the plate media. 412-416 mL of the media is poured into 500mL Pyrex media bottles and autoclaved. 500 mL of nitrate free media (20g soy broth, 500mL of deionized water) is then autoclaved and cooled similar to the plate and batch culture media.

- 250-mL centrifuge tubes and caps are autoclaved for sterilization purposes, and 32 sample vials are acid washed and placed in a muffle furnace at 500 °C for 4 hours.
- A flamed loop will be used to streak bacteria onto two of the 500-mL media bottles. The bottles are placed on a shaker, allowing bacteria to grow for 4-6 days at ambient light and room temperatures.
- The bacteria/media mixture in the 500-mL bottles are dispersed into four 250-mL centrifuge bottles and centrifuged at 2800 RPM for 15 minutes. The supernatant is poured off and 25-mL of nitrate free media is added to each bottle.
- The bottles were consolidated into one bottle and centrifuged again pouring off the supernatant afterwards. The process was repeated 4 times, adding 100-mL of the nitrate free media after each cycle.
- After the fourth time 110-mL of nitrate free media are added and the sample is homogenized and poured into a large, sterile glass-beaker.
- Ten drops of anit-foam (sigma A6707-500ML) are added and mixed accordingly. Thereafter, 3-mL of samples is pipetted into 20 ml crimp top vials for IRMS analysis.

5. Analytical Procedures

A. Arkansas IRMS Analysis

- Each of the vials was purged with helium gas for an hour to remove any air from the samples. The samples were diluted so that nitrate concentrations were around 20µM. One mL of the sample was added to a vial using a syringe. The process is repeated for each sample and standard, ensuring two duplicates of each. The 32 samples were placed on an automated sampler which extracted the sample by pumping helium into the sample through one needle and removing the He and N₂O mixture with an extraction needle. For each sample the mixture was sent through a water removal unit (Nafion dryer), a CO₂ removal unit (Mg(ClO₄)₂/Ascarite trap), a cryogenic trap, a GC column, a second water removal unit, and an open split.
- A Finnigan Delta^{Plus} CF-IRMS was used to generate the δ¹⁵N and δ¹⁸O of the samples. This was accomplished by ionizing the gas/helium mixture with an electron emitting hot filament, accelerating the ions into the analyzer and separating the ion beams in the analyzer using a magnet. Thereafter the beams were collected in faraday cups and the intensity of the beams were measured. ISODAT 2.0 computer software was used to setup, calibrate the system and calculate the “δ” values.

6. QC and Calibration

Deionized water was utilized as a “Blank”. Standards for the analysis were 20µM KNO₃, IAEA (International Atomic Energy Agency) N3 (19.975 µM N-KNO₃, δ¹⁵N=4.7‰ and δ¹⁸O=25.6‰), USGS 32 (19.7 µM KNO₃, δ¹⁵N=180 ‰ and δ¹⁸O=25‰), USGS 34 (20 µM KNO₃, δ¹⁵N=-1.8 ‰ and δ¹⁸O=-27.9‰), USGS 35 (20 µM KNO₃, δ¹⁵N=2.7‰ and δ¹⁸O=57.5‰). Duplicates and blanks were taken bimonthly from the field. For isotope analysis, splits are taken for ten percent of the samples.

7. Calculations

$$\delta = \left[\frac{R_{sample}}{R_{standard}} - 1 \right] * 1000$$

where R denotes the isotopic ratio of a given constituent.

$$\sigma = \sqrt{\left[\frac{\sum(xbar - x)^2}{n - 1} \right]}$$

where, *xbar* is the mean of the data and σ is the standard deviation of the data.

8. Data Quality Objectives

Based on Coplen et al. (2012), reference materials have been observed to have reproducibility of approximately + or - 0.25‰ given a range of values between -1.8-180‰ which encompasses the range found in nature. Blanks should not register a peak.

9. References

Coplen, T.B., Qi, Haiping, Révész, Kinga, Casciotti, Karen, and Hannon, J.E., 2012, Determination of the δ¹⁵N and δ¹⁸O of nitrate in water; RSIL lab code 2900, chap. 17 of Stable isotope-ratio methods, sec. C of Révész, Kinga, and Coplen, T.B. eds., Methods of the Reston Stable Isotope Laboratory (slightly revised from version 1.0 released in 2007): U.S. Geological Survey Techniques and Methods, book 10, 35 p., available only at <http://pubs.usgs.gov/tm/2006/tm10c17/>. (Supersedes version 1.0 released in 2007.)

A7) δ¹⁵N and δ¹³C of Transported Sediment, POC and PN

A7.1) Field SOP

Refer to section A15.3

A7.2) Analytical SOP-UKSIL EA/IRMS

SOP for determining δ¹⁵N, δ¹³C, TOC and PN of Sediment Samples
UK Dept. of Civil Engineering
2-1-17

1. Overview

Measurement of elemental composition and stable isotopic abundance of carbon and nitrogen in fluvial sediments has important implications for carbon and nitrogen cycling in streams and rivers. The following SOP details the necessary procedures, QC sampling and calculations necessary to analytically estimate carbon and nitrogen elemental compositions and stable isotopic abundance utilizing a Finnigan Delta Plus isotope ratio mass spectrometer which is interfaced with a Costech elemental analyzer. Operating

Procedures for analyzing elemental and stable isotope signatures (carbon and nitrogen) for sediments are covered in the EPA SIP/OP.01 (Griffis, 1999). The following will outline the procedures used to analyze the samples collected for this project.

2. Safety

Since a corrosive acid is to be used during the procedure, gloves, protective eye wear and an apron should be used during any procedures using strong or corrosive acids.

3. Equipment, Reagents and Consumable Supplies

A. Lab Instrumentation

- Finnigan Delta Plus mass spectrometer
- Costech Elemental Analyzer
- Hewlett-Packard Model 689- high resolution gas chromatograph
- ISODAT Software
- Microbalance
- DHAUS Scout pro Balance
- Dupont Sorvall RC-5B Refrigerated Superspeed Centrifuge
- OHAUS 2kg-5klb capacity Balance
- OHAUS Scout Pro Electronic Balance
- Thermo Modulyod Freeze Drier with Thermo Savant VLP 200 ValuPump
- QL Model 30 GC Lab Oven
- Rinn Crescent Wig-L-Bug Grinder
- Pyrex Dessicator
- Thermo Sorvall Legend RT+ Centrifuge

B. Reagents and Consumable Supplies

- Deionized Ultra-Pure Water
- Siphon line
- Magnesium Chloride Hexahydrate
- Drierite # 24001 Dessicating Agent
- Metal Spatula
- Grinder Vials with Steel Balls
- Forceps
- Number 200, 53µm U.S.A Standard Test Sieve
- Accumax Pro Micropipette 10-100 µL with pipette tips
- Fisher A307-1 Sulfurous Acid Certified ACS Grade 1L
- 750mL centrifuge bottles
- 250mL centrifuge bottles
- 125mL HDPE bottles
- Small vials for ground samples
- Costech #41067 Silver Capsules
- Costech #080016 Sample Trays
- Costech #011001 Chromium Oxide or equivalent
- Costech #021022 Magnesium Perchlorate or Equivalent
- Costech #011009 Tungsten Oxide on Aluminum or Equivalent
- Costech #021025 Quartz turnings or equivalent
- Costech #021020 Carbon Dioxide Absorbent or Equivalent
- Costech #021026 Quartz Wool or Equivalent
- Fisons #33821710 Cupric Oxide Wires or Equivalent
- Costech #011005 Reduced Copper, Pure or Equivalent
- Costech #061105 Opaque Quartz Reaction Tube or Equivalent
- Finnigan #M0000-56911 Gasket or Equivalent
- Finnigan #M00-1027920 Filament Assembly
- Finnigan #M0000-69322 Gasket or Equivalent
- Finnigan #00950-00911 Lubricant Cartridge for Turbo Molecular Drag Pump
- Finnigan #00950-01116 Lubricant Cartridge for Turbo Molecular Drag Pump
- Oxygen, Zero Grade, for Costech Elemental Analyzer
- Helium, Ultra High Purity 99.999%, for Costech Elemental Analyzer
- Nitrogen, Ultra High Purity, 99.999%, Delta Plus Reference Gas.
- Carbon Dioxide, Coleman Grade, 99.99%, Delta Plus Reference Gas.

4. Sample Preparation

A. Settling/Decanting Field Samples

- A. Bring sediment samples back to lab after collection in the field.
- B. Leave samples undisturbed in buckets/appropriately-sized containers for 48 hours in refrigerator (Hydrolab basement Floor Raymond Bldg.) set to 4°C.
- C. 48 hours is a relative time that usually allows all of the sediment contained in the sample to settle to the bottom of the bucket/container. **If all sediment has not settled to the bottom of the bucket, allow more time for settling.**
- D. Gently pour water off the top of settled sediment samples. If a large volume of water is present, may use small rubber tubing as siphon. This is up to the technician's preference.
- E. Pour/siphon water from the bucket until either (a) the sediment nearly flows out of the bucket if pouring or (b) the sample has a manageable amount of water to allow for centrifugation.

B. Centrifuging (Bulk Sample)

- Agitate decanted sample in bucket to encourage homogeneous mixture.

- Pour sample into a clean (4 DI/DO rinses) 750 mL Nalgene pitcher until the pitcher is nearly full.
- Place bucket, bottle (in bucket), and bottle cap for a sample on each side of balance.
- Slowly fill one bottle with sample until nearly full (almost to neck).
- Slowly fill opposing tube with sample until nearly balanced.
- Using plastic pipette, delicately balance both bottles with DI/DO H₂O (see “DI/DO H₂O” procedure) until the two sides are the same weight.
- Place cap on tube.
- Align these two balanced bottles across from one another in centrifuge.
- Repeat steps 1-7 with remaining two bottles so opposing tubes are well balanced.
- Settings on centrifuge should be set as follows:
 - *Rotational Velocity:* 4.25 on knob or 4250 rpm
 - *Time:* 4-7 minutes
 - *Temperature:* room temp (20 degrees Celsius)
 - *Rotor:* SH-3000
- Close top (will click).
- Press start button (Play button located to the right of the temperature).
- If vibration is severe upon spinning, samples are not well balanced. Press the stop button (square), inspect tube balance, add DI/DO H₂O, etc.
- After centrifuge is **completely** stopped, centrifuge door light will come on open top by pressing door button.
- Remove adapters/bottles two at a time, decant, and add additional sample from the Nalgene pitcher to each bottle, balancing opposing bottle as necessary.
- Repeat previous steps until the sample is completely centrifuged into four bottle.
- Consolidate entire sample into 1 labeled centrifuge tube (may need to use two centrifuge tubes if the sample contains a large amount of sediment).
- After consolidation, bottle may have a large amount of supernatant above the sediment. If this occurs, place the single centrifuge bottle back into the cooler until another sample is centrifuged and contains a large amount of supernatant as well. These two separate samples can be balanced, centrifuged, and decanted to remove excess supernatant.
- Place bottles in freezer (-40°C) after removing as much supernatant as possible.

Notes:

- If, after spinning, sample has a large amount of fine sediment still in suspension (murky color), add ~10mL Magnesium Chloride Hexahydrate (MgCl₂-6H₂O) prepared at 0.5M (see “Magnesium Chloride” procedure).
- Once the entire sample is poured into the Nalgene pitcher, spray off any sediment remaining on the inside of the bucket using DI/DO H₂O.
- Once the entire sample is poured into the centrifuge tubes, spray off any sediment remaining on the inside of the Nalgene pitcher using DI/DO H₂O.

C. Freeze Drying

- Check to make sure there is enough oil in the machine. (Look in the front at the tube).
- Turn on the refrigeration unit by pressing the button that says “Fridge”. (It is preferred to do this a little before the samples are put in so that the atmosphere will cool faster.)
- This procedure differs depending on the size of the bottle. If the sample bottle fits in the glass jars, refer to section 1. If the sample bottle does not fit in the glass jars refer to section 2.

Section 1:

- Be sure that the sample bottle is covered with cheesecloth and held with a rubber band.
- Start the vacuum, by pressing the button on the front of the Freeze drier that says, “Pump”. (don’t turn on pump until fridge temperature <-41C)
- Place a sample bottle into the glass jar and seal the jar with the rubber cap.
- Push the cap firmly into the vacuum chamber and ensure that it is on tightly so that the glass jar does not fall off.
- Turn the valve on the manifold from “Vent” to “Vac” to allow a vacuum to reach the sample.
- Make sure the drain hose is removed and that all the pressure releases are closed.

Section 2:

- Be sure that the sample bottle is covered with cheesecloth and held with a rubber band.
- Remove the top glass piece from the vacuum chamber.
- Place the sample bottles inside the chamber around the edge so that they are stable. (put samples with the most ice on top)
- Put the top glass piece into its proper position. Be sure that there is a good seal.
- Make sure the drain hose is removed and that all the pressure releases are closed.
- Start the vacuum, by pressing the button on the front of the Freeze drier that says, “Pump”. (don’t turn on pump until fridge temperature < -41C)

Once the samples are dry:

- Once samples are completely dry, turn off the vacuum by pressing the “Pump” button on the freeze drying unit.
- Slightly turn a pressure release so that pressure is slowly restored to atmospheric pressure.
- Remove glass piece or the jars to remove the samples.
- Recap the samples.

- a) If samples are going to be put on to the freeze dryer right away and the condenser does not have a lot of ice on it, leave the condenser on. Repeat the previous steps for more samples.
 - b) If not, turn the condenser off by pressing the same button that was used to turn it on. Be sure drain valve is open. Let the condenser drain until all of the ice is off the side wall.
- D. Consolidation and Weighing
- This is a dry procedure so all equipment used must be washed and acetone used to ensure dryness.
 - Weigh an empty Nalgene bottle and record the empty weight.
 - Using the spatula, break large soil particles into smaller particles so that they can be wet sieved easier.
 - Tip the centrifuge bottle into the Nalgene bottle (a funnel may be needed).
 - Using the spatula, scrape the side of the centrifuge tube so all soil particles fall to the bottom.
 - Tip the centrifuge bottle into the Nalgene bottle.
 - Using the spatula strongly tap the centrifuge bottle so that all of the soil gets knocked into the Nalgene bottle.
 - Repeat the three previous steps until all of the sediment is in the Nalgene bottle.
 - Weigh the Nalgene bottle with the sample and record the weight.
 - Label the Nalgene bottle with the appropriate name and number.
- E. Wet Sieving
- Use DIDO water to fill the Nalgene bottle and shake the bottle to break up particles.
 - Pour sediment solution through 3" diameter 53 micron sieve. Flush through sieve with DIDO water into sieve pan. (It helps to shake the sieve as you spray the sieve.)
 - Rinse bottom of 53 micron sieve with DIDO water into sieve pan. Repeat these two steps until water on top and bottom while washing remains clear.
 - Rinse fine solids retained on 53 micron sieve through plastic funnel leading to centrifuge tube (labeled w/sample #).
 - Pour contents of pan through funnel into separate centrifuge tube (labeled w/sample #).
 - Rinse funnel (4 DI/DO, 1 acetone) between each sample.
 - Each sample should now be split into two parts ($>53\mu\text{m}$, $<53\mu\text{m}$) and labeled accordingly.
 - Keep samples in labeled bucket in ERTL refrigerator (3rd Floor) until centrifugation.
- F. Centrifuging (Wet Sieved Sample)
- Agitate decanted sample in bucket to encourage homogeneous mixture.
 - Pour sample into a clean (4 DI/DO rinses) 250 mL Nalgene pitcher until the pitcher is nearly full.
 - Place bucket, tube (in bucket), and tube cap on each side of balance.
 - Slowly fill one tube with sample until nearly full (almost to neck) Avoid any liquid on outside of tube or on insert (use pipette if necessary) if any fluid is on side of tube or insert dry before placing in centrifuge.
 - Slowly fill opposing tube with sample until nearly balanced.
 - Using plastic pipette, delicately balance both tubes with DI/DO H₂O (see "DI/DO H₂O" procedure) until the two sides are the same weight.
 - Place cap on tube.
 - Align these two balanced tubes across from one another in centrifuge.
 - Repeat steps 1-7 with remaining two tubes so opposing tubes are well balanced.
 - Settings on centrifuge should be set as follows:
 - i. *Rotational Velocity:* 3200 * g
 - ii. *Time:* 4 minutes 0.04 = 4 minutes 4.00 = 4 hours
 - iii. *Temperature:* room temp (20 degrees Celsius)
 - iv. *Motor:* 243 – Rotor
 - v. *Acceleration (on left):* 3
 - vi. *Brake (on right):* 2
 - Close top gently will self set (will click).
 - Press start button (Play button located to the right of the temperature).
 - If vibration is severe upon spinning, samples are not well balanced. Press the stop button (square), inspect tube balance, add DI/DO H₂O, etc.
 - After centrifuge is **completely** stopped (0*g, centrifuge will beep and say "end"), open top by pressing appropriate button.
 - Remove adapters/tubes two at a time, decant, and add additional sample from the Nalgene pitcher to each tube, balancing opposing tubes as necessary.
 - Repeat previous steps until the sample is completely centrifuged into four tubes.
 - Consolidate entire sample into 1 labeled centrifuge tube (may need to use two centrifuge tubes if the sample contains a large amount of sediment).
 - After consolidation, tubes may have a large amount of supernatant above the sediment. If this occurs, place the single centrifuge tube back into the cooler until another sample is centrifuged and contains a large amount of supernatant as well. These two separate samples can be balanced, centrifuged, and decanted to remove excess supernatant.
 - Place tubes in freezer (-40°C) after removing as much supernatant as possible.
- G. Consolidation and Weighing
- Samples are again consolidated and weighed as in Step D
- H. Grinding

- Place the steel ball into the vial with.
- Fill the stainless steel vial for the Wig-L-Bug grinder roughly halfway with sample using the funnel with the small opening. Be sure to scrape the funnel to ensure all the soil is in the vial. For soils, this volume is approximately equal to 1 gram of sample. For organics, this weight is much less. Place the cap on.
- Secure the vial in the arms of the grinder. Make sure that the top of the vial is facing the rear of the grinder (towards the brass nut). Tighten the front screw using the provided allen wrench (two turns past hand tight is sufficient).
- Run the Wig-L-Bug for 30 seconds.
- Once the grinder has stopped, loosen the front screw and remove the vial.
- Place the ground sample into the desired container.
- Using a magnetic-tipped screwdriver, remove the steel ball from the vial.
- If more ground sample is required, repeat steps 1-8.
- Be sure to clean the equipment thoroughly between each sample. Consecutive runs of the same sample do not require cleaning the equipment. Follow the procedure below for each instrument:
 - i. Tap water rinse/wire brush scrub
 - ii. 4 DI/DO rinses
 - iii. 1 100% ethanol rinse or acetone
 - iv. Dry with Kim-wipes

I. Weighing Subsamples and Acid Digestion

- Clean tweezers/small spoon by wiping thoroughly with Kim-Wipes.
- Calibrate scale (precision of 1 μ m) using 2g sample.
 - a. Hold Tare button until 'Busy' shows on screen.
 - b. Add 2g calibration weight using tweezers.
 - c. After 'Busy' is gone once again, gently remove calibration weight. If screen says 'H', start over.
- Using tweezers, gently place molded silver caps in the plastic sample tray. Widen the tops of the caps by pressing on edges with tweezers/spoon.
- Place the cap onto the scale. Tare the scale.
- Using the spoon, add sample to the cap until desired amount is reached.
- ** If sample spilled onto weighing pan, remove cap, pick up pan w/tweezers and blow off **
- Place cap w/sample back in plastic mass spec tray in the appropriate position.
- ** For each sample, record weight of sample tested + position in plastic tray **
- Add 10,30,50 then 100 μ L of sulfurous acid to each sample (in silver cap). This will remove carbonates from sample and leave only organic carbons.
- Place plastic tray w/caps in an oven at 60 degrees Celsius. Repeat 100 μ L once/hour until there is no reaction (gaseous bubbling) when adding acid.
- Once the samples no longer react with the sulfurous acid, the samples can be prepared to run through the mass spectrometer. Perform the following steps for this preparation:
 - a. Remove the polyethylene block containing the samples from the oven.
 - b. Wipe the brass rod thoroughly with Kim-wipes.
 - c. Close the silver caps by squaring off the silver caps to form a small square pellet.

5. Analytical Procedures

Samples will be loaded into a Costech Elemental Analyzer in an automated sampler and combusted. All organic material contained in the sample is oxidized and ashes are left in the oxidation column. The helium stream in the EA carries the gas through a reduction column, a water trap and then through a Conflo IV interface to separate the gasses. The sample are ionized and

- Costech Elemental Analyzer
 - The Costech EA is set up to run sediment samples under the following conditions
 - Oxygen Pressure = 100psi
 - Helium Pressure = 100psi
 - Helium Flow Rate = 90-92 cfs
 - Oxidation Furnace Temperature = 980 Degrees C
 - Reduction Furnace Temperature = 650 Degrees C
 - Actuator Compressed Air Pressure = 70 psi
 - Standby Conditions of the Costech EA are the following:
 - Oxygen Pressure= OFF
 - Helium Flow Rate=15-19cfs
 - Oxidation Furnace Temperature = 820 Degrees C
 - Reduction Furnace Temperature = 520 Degrees C
 - Since large sample masses are used for the present analysis, ashes must be removed, and the Quartz insert changed in the oxidation column after each sample run. The oxidation tube must be replaced approximately every 1000 analysis, the reduction tube every 500 analysis and the water trap every 300 analysis.
 - Samples are loaded into a 49 well automated sampler. Load samples using forceps, ensuring that each sample goes into the appropriate slot.
 - Make sure the EA is in work mode, check the flow rate.
 - After samples are loaded, close the lid of the automated sampler and hand tighten the screws that hold the lid down. Use clamps to help tighten the lid and finish hand tightening the screws. Make sure that the middle bolt is unscrewed and turn on the helium stream to remove any air from the autosampler. After 8 minutes simultaneously shut off the helium and close the screw such that are can't get into or out of the autosampler

- Check the autosampler for helium leaks using the helium detector.
- Open up the door that leads from the autosampler into the oxidation column
- Check the autosampler again for helium leaks.
- Conflo IV Interface
 - Reduces the speed of the helium stream
 - Introduces the CO₂ and N₂ reference gases that are used to ensure the IRMS instrument linearity and precision.
 - Isotopic signatures of reference gases are quantified relative to universal reference standards
 - Vienna Pee Dee Belemnite (VPDB)
 - Atmospheric nitrogen
 - Dilutes the CO₂ sample
 - Since carbon concentrations for large samples create voltages outside of the IRMS sensitivity range samples need to be diluted. The Conflo IV will automatically dilute each sample by a specified percentage using the Helium Diluent. For this project an 80% dilution was found to place the samples in their optimum voltage range. Thereafter the ISODAT software will automatically correct for the dilution.
 - Pressure settings for the Conflo IV interface are as follows:
 - CO₂ Reference Gas = 1.5 bar
 - N₂ Reference Gas = 1.5 bar
 - Helium Diluent Gas = 2 bar
- Finnigan Delta Plus IRMS
 - Refer to the Finnigan Delta Plus Operating manual (Finnigan MAT, 1997a) and the ISODAT software operating manual (Finnigan, 1996) for exhaustive information on the instrument operations
 - Samples are ionized and accelerated into a curved flight tube
 - A .75 Tesla electromagnet is located on the outside of the flight tube
 - Ions are focused into appropriate Faraday Cup detectors based on the ion beam momentum.
 - Three cups pick up masses 28, 29, and 30 for nitrogen and masses 44,45 and 46 for carbon dioxide.
 - The voltages measured from these beams are delivered to the ISODAT software and are converted to δ notation (see section 8).
 - Enter the appropriate information (e.g. sample identification number and weight of the sample) into the isodat software.
 - Run a sequence of nitrogen gas reference additions. If the standard deviation (see section 8) of the 11 reference additions is >0.1‰ rerun the sequence. Perform at least 4 sequences with 2-3 consecutive ones with standard deviations <0.1‰.
 - Air in the line could cause potential interferences as air contains ~70% nitrogen.
 - Perform a series of nitrogen linearity tests in which additions result in a reference peak between 0.5-10 volts. Check the linearity (denoted by the Diff/volt equation in section 8) and ensure that it is <0.1. If it's not working properly, perform an autocalibration (see the Finnigan operation manual).
 - Repeat the standard deviation and linearity tests for carbon using the carbon reference gas.
 - Once the instrument is tuned and functioning properly turn the remote setting on the elemental analyzer on.
 - Select all the samples in the desired sequence run, save the template and then click the run button.
 - Check the samples periodically to ensure that blanks aren't providing any peaks, samples are dropping properly into the EA and that the standards are giving appropriate results.

6. QC and Calibration

QC samples for the analysis include blanks (which are empty silver capsules that), two isotopic standards (DORM and CCHIX) and one concentration standard, acetanilide (ACE). Generating a field blank, or a blank that is taken through the preparation procedure isn't feasible. The DORM and ACE standards are used to calibrate each sample run. The following outlines the usage of the each of the QC standard types.

- A. Blanks
 - One blank will be analyzed at the beginning of each sample run to ensure nothing is leaking into the system (e.g. background concentrations are low)
- B. DORM
 - Dorm is the primary isotopic standard and it's carbon and nitrogen isotopic signature in nature is well defined ($\delta^{13}\text{C} = -19.59\text{‰}$, $\delta^{15}\text{N} = 12.46\text{‰}$)
 - After each sample run the all samples are calibrated to the average Dorm value
 - Out of the 49 samples analyzed during a run the 7,8,14, 20,26,32,38 and 48th samples are DORMs.
 - The standard deviations of the standards are checked against performance criteria.
- C. CCHIX
 - CCHIX is a secondary isotopic standard that also has well defined carbon and nitrogen isotopic compositions.
 - If standard deviations of the DORMS do not meet performance criteria, the standard deviations of the secondary isotopic standards are checked.
- D. ACE
 - ACE is an elemental standard with known concentrations of carbon and nitrogen (C=71.09% and N=10.36%)
 - The average value of ACEs are used to calibrate the concentrations for the run
 - Out of the 49 samples analyzed during a run the 5,6,49th samples are ACEs.
- E. Split Samples
 - 1 out of 10 samples will be analyzed in triplicate to generate a standard deviation of the sample. The standard deviation of the samples will be checked against the performance criteria.

If samples do not meet performance criteria, then the samples analyzed will be reanalyzed until the standard performance criteria are satisfied.

7. Calculations

$$\delta = \left[\frac{R_{\text{sample}}}{R_{\text{standard}}} - 1 \right] * 1000$$

where R denotes the isotopic ratio of a given constituent.

$$\sigma = \sqrt{\frac{\sum(xbar - x)^2}{n - 1}}$$

where, $xbar$ is the mean of the data and σ is the standard deviation of the data.

$$\frac{Diff}{volt} = \frac{\delta_{\text{Last}} - \delta_{\text{first}}}{v_{\text{Last}} - v_{\text{first}}}$$

where, v is the voltage reading

8. Data Quality Objectives

The data quality objectives are best described using a table (seen below). These are based off EPA SIP/OP.01 (Griffis, 1999) data quality objectives and are consistent with that of the instrument to be used on this project. Sample runs analyzed for elemental and isotopic signatures need to meet the following specifications in order to be considered acceptable data.

Analysis	Range	Accuracy	Precision	Completeness
$\delta^{13}\text{C}$	1-10 Volts	$\pm 0.5\%$	Stdev<0.5‰	N/A
$\delta^{15}\text{N}$	0.5-10 Volts	$\pm 0.5\%$	Stdev<0.5‰	N/A
% Carbon	0-50%	90-110%	Stdev<10%	N/A
% Nitrogen	0-10%	90-110%	Stdev<10%	N/A

9. References

Griffis, W.L. 1999. Analysis of Environmental Samples Using Continuous Flow Gas Isotope Ratio Mass Spectrometry. EPA SIP/OP.01. Integrated Stable Isotope Research Facility.

A8) Field Parameters

Calibration, operation, inspection, maintenance, storage and other needed analytical needs are covered in the Hach manual for the pH, Conductivity, DO and Temperature probes. The manual can be obtained from the Hach company at www.hach.com. The citation for the manual is:

Hach Company. HACH HQ Series Portable Meters User Manual, September 2006, Edition 5. Catalog Number HG40d18. Hach Company, PO Box 389, Loveland, Colorado.

A9) Field Standard Operating Procedures

A9.1) Water Quality Parameters

Method

The direct method for streams (EPA #EH-01) will be utilized to sample NH_4^+ , NO_3 , DIC, DOC, DP, $\delta^{15}\text{N}_{\text{NO}_3}$, $\delta^{18}\text{O}_{\text{NO}_3}$, $\delta^{18}\text{O}_{\text{NO}_3}$, $\delta^2\text{H}_{\text{NO}_3}$, $\delta^{13}\text{C}_{\text{DIC}}$ at each site. Bulk samples will be collected for the suite of water quality parameters in pre-cleaned wide mouth, 1000 mL, HDPE, plastic bottles, which are EPA approved for water quality sample collection (KDOW, 2005). The total required volume of samples is 815 mL, hence the 1000 mL bottle will provide a sample subset for archiving. After the bottle is rinsed 3 times in the stream water, the sample is collected by placing the bottle under the water surface with the opening pointing upstream. The sampler will remain downstream of the container and the sample will be collected in a downstream to upstream motion without disturbing the substrate. For this study, samples will be collected (unfiltered) in the field and filtered immediately after using a 60 ml syringe with filter. Based on the sample collection guide from the USDA (Turk, 2003) samples that are most susceptible to degradation are ones that have high suspended solids (which are relatively low in this watershed during low-flow conditions based on previous TSS analysis at baseflow) or samples analyzed for trace constituents. Samples will be filtered using Whatman Glass Fiber 0.45 μm , 47mm filters and separated into their respective splits for analysis (see Analytical SOPs for sample preparation and preservation needs). During transport of water quality samples back to the lab, the samples are placed in zip lock bags to avoid contamination and then placed in a cooler to refrigerate the sample to 4°C to assist in minimizing microbial activity. All split sample containers for water quality and sediment analysis will be new, pre-cleaned, disposable equipment and does not require decontamination. Standard decontamination procedures will be used for decontamination of the syringes (KDOW, 2005).

References

EPA, 2003, SOP # EH-01 Surface Water Collection, Adapted from ERT/REAC SOP 2013 Rev 1.0. East Helena Site, Montana.
 Turk, J.T., 2001. Field Guide for Surface Water Sample Data Collection, USDA Forest Program, Washington, DC, 20250-9410.
 KDOW, 2005. Kentucky Ambient/Watershed Water Quality Monitoring Standard Operating Procedure Manual. Frankfort, Kentucky, 40601.

A9.2) Sediment Concentration Samples

A9.2.1) Depth Integrated Sediment Samples

Method

Sediment concentration will be collected using an isokinetic-depth integrated sampler to estimate sediment concentrations at fixed stations using accepted USGS methods for sample collection (USGS, 2003). Depth integrated suspended sediment samples will be collected in pint sized, plastic containers, of which about ¾ of the bottle shall be filled with sample. The samples will be stored in coolers at 4°C until they can be refrigerated at 4°C in the UK hydraulics lab. Holding times are up to 7 days as per EPA 160.2. Standard decontamination procedures for equipment cleaning and decontamination (KDOW, 2005) will be followed.

References

USGS, 2003. National Field Manual for the Collection of Water-Quality Data, Chapter A2. Selection of Equipment for Water Sampling. Reston, VA, 20192.
KDOW, 2005. Kentucky Ambient/Watershed Water Quality Monitoring Standard Operating Procedure Manual. Frankfort, Kentucky, 40601.

A10.2.2) Fixed Point Automated Samples

Method

Sediment concentration will be collected using an automated pump sampler to collect dense concentration data during storm events. Methods for probe measurement, i.e., programming and operation, will follow manufacturer specifications (Teledyne, 2009). Automated samplers will collect 750 mL of sample in 1000 mL plastic bottles (see Teledyne ISCO manual). The samples will be stored in coolers at 4°C until they can be refrigerated at 4°C in the UK hydraulics lab. Holding times are up to 7 days as per EPA 160.2. Standard decontamination procedures for equipment cleaning and decontamination (KDOW, 2005) will be followed.

References

Teledyne, 2009. 6712 Portable Sampler Installation and Operation Guide. Revision Z. Lincoln, NE, 68501-2531.
KDOW, 2005. Kentucky Ambient/Watershed Water Quality Monitoring Standard Operating Procedure Manual. Frankfort, Kentucky, 40601.

A9.3) Sediment Trap Samples

Method

Sediment trap samplers will be placed in the field for a specified time interval to generate a spatially and temporally integrated measure of $\delta^{15}\text{N}$ and $\delta^{13}\text{C}$ of Transported Sediment, POC and PN. Briefly, at the front of the trap (inlet) a 4mm diameter inlet tube allows acceleration of fluid into a 98mm diameter test section. The increase in area results in sedimentation, and subsequent trapping of fine sediments. The fluid exits the test section through another 4mm outlet tube. This method was originally published in Phillips et al. (2000). Samples are collected in a sediment trap as described in Phillips et al. (2000). Approximately 8L of a sediment/water mixture is poured into clean 5 gallon buckets. The samples are preserved by refrigerating at 4°C to minimize microbial transformations. Samples are spun down and de-watered to a steady state as quickly as possible. Standard decontamination procedures for equipment cleaning and decontamination (KDOW, 2005) will be followed.

References

Phillips J, Russell M, Walling D. 2000. Time-integrated sampling of fluvial suspended sediment: a simple methodology for small catchments. *Hydrological Processes* 14: 2589–2602.

REFERENCES

- Acton, P. M., Fox, J. F., Campbell, J. E., Rowe, H., & Wilkinson, M. (2013). Carbon isotopes for estimating soil decomposition and physical mixing in well-drained forest soils. *Journal of Geophysical Research: Biogeosciences*, *118*(4), 1532–1545.
- Ahmadi, S. H., Amin, S., Reza Keshavarzi, A., & Mirzamostafa, N. (2006). Simulating Watershed Outlet Sediment Concentration using the ANSWERS Model by applying Two Sediment Transport Capacity Equations. *Biosystems Engineering*, *94*(4), 615–626.
- Al Aamery, N., Fox, J. F., & Snyder, M. (2016). Evaluation of climate modeling factors impacting the variance of streamflow. *Journal of Hydrology*, *542*, 125–142.
- Al Aamery, N., Fox, J. F., Snyder, M., & Chandramouli, C. V. (2018). Variance analysis of forecasted streamflow maxima in a wet temperate climate. *Journal of Hydrology*, *560*, 364–381.
- Albéric, P., & Lepiller, M. (1998). Oxidation of organic matter in a karstic hydrologic unit supplied through stream sinks (Loiret, France). *Water Research*, *32*, 2051–2064.
- Albertin, A. R., Sickman, J. O., Pinowska, A., & Stevenson, R. J. (2012). Identification of nitrogen sources and transformations within karst springs using isotope tracers of nitrogen. *Biogeochemistry*, *108*(1–3), 219–232.
- Alexander, R. B., Böhlke, J. K., Boyer, E. W., David, M. B., Harvey, J. W., Mulholland, P. J., ... Wollheim, W. M. (2009). Dynamic modeling of nitrogen losses in river networks unravels the coupled effects of hydrological and biogeochemical processes. *Biogeochemistry*, *93*(1–2), 91–116.
- Allen, J. J., Shockling, M. A., Kunkel, G. J., & Smits, A. J. (2007). Turbulent flow in smooth and rough pipes. *Philosophical Transactions of the Royal Society A: Mathematical, Physical and Engineering Sciences*, *365*, 699–714.
- Álvarez, S., & Guerrero, M. (2000). Enzymatic activities associated with decomposition of particulate organic matter in two shallow ponds. *Soil Biology and Biochemistry*, *32*, 1941–1951.
- Amberger, A., & Schmidt, H. L. (1987). Natürliche Isotopengehalte von Nitrat als Indikatoren für dessen Herkunft. *Geochimica et Cosmochimica Acta*, *51*(10), 2699–2705.
- Aquilina, L., Ladouche, B., & Dörfliker, N. (2006). Water storage and transfer in the epikarst of karstic systems during high flow periods. *Journal of Hydrology*, *327*(3–4), 472–485.
- Arango, C. P., & Tank, J. L. (2008). Land use influences the spatiotemporal controls on nitrification and denitrification in headwater streams. *Journal of the North American Benthological Society*, *27*(1), 90–107.
- Arango, C. P., Tank, J. L., Schaller, J. L., Royer, T. V., Bernot, M. J., & David, M. B. (2007). Benthic organic carbon influences denitrification in streams with high nitrate concentration. *Freshwater Biology*, *52*(7), 1210–1222.
- Atkinson, T. C. (1977). Diffuse flow and conduit flow in limestone terrain in the Mendip Hills, Somerset (Great Britain). *Journal of Hydrology*, *35*(1–2), 93–110.
- Baffaut, C., & Benson, V. W. (2009). Modeling flow and pollutant transport in a karst watershed with SWAT. *Transactions of the American Society of Agricultural and Biological Engineers*, *52*(2), 469–479.
- Bakalowicz, M., El Hakim, M., & El-Hajj, A. (2008). Karst groundwater resources in the

- countries of eastern Mediterranean: The example of Lebanon. *Environmental Geology*, 54(3), 597–604.
- Baldini, J. U. L., Baldini, L. M., McDermott, F., & Clipson, N. (2006). Carbon dioxide sources, sinks, and spatial variability in shallow temperate zone caves: Evidence from Ballynamintra Cave, Ireland. *Journal of Cave and Karst Studies*, 68(1), 4–11.
- Baldwin, D. S., & Mitchell, A. M. (2000). The effects of drying and re-flooding on the sediment and soil nutrient dynamics of lowland river–floodplain systems: a synthesis. *Regulated Rivers: Research & Management*, 16(5), 457–467.
- Barbieri, M., Boschetti, T., Petitta, M., & Tallini, M. (2005). Stable isotope (^2H , ^{18}O and $^{87}\text{Sr}/^{86}\text{Sr}$) and hydrochemistry monitoring for groundwater hydrodynamics analysis in a karst aquifer (Gran Sasso, Central Italy). *Applied Geochemistry*, 20(11), 2063–2081.
- Barton, H. A., & Northup, D. E. (2007). Geomicrobiology in cave environments: Past, current and future perspectives. *Journal of Cave and Karst Studies*, 69(1), 163–178.
- Battin, T. J., Kaplan, L. A., Findlay, S., Hopkinson, C. S., Marti, E., Packman, A. I., ... Sabater, F. (2008). Biophysical controls on organic carbon fluxes in fluvial networks. *Nature Geoscience*, 1(2), 95–100.
- Battin, T. J., Kaplan, L. A., Newbold, J. D., & Hansen, C. M. E. (2003). Contributions of microbial biofilms to ecosystem processes in stream mesocosms. *Nature*, 426, 439–442.
- Bauwe, A., Tiemeyer, B., Kahle, P., & Lennartz, B. (2015). Classifying hydrological events to quantify their impact on nitrate leaching across three spatial scales. *Journal of Hydrology*, 531, 589–601.
- Bellanger, B., Huon, S., Velasquez, F., Vallès, V., Girardin, C., & Mariotti, A. (2004). Monitoring soil organic carbon erosion with $\delta^{13}\text{C}$ and $\delta^{15}\text{N}$ on experimental field plots in the Venezuelan Andes. *Catena*, 58(2), 125–150.
- Bernhardt, E. S., Blaszcak, J. R., Ficken, C. D., Fork, M. L., Kaiser, K. E., & Seybold, E. C. (2017). Control Points in Ecosystems: Moving Beyond the Hot Spot Hot Moment Concept. *Ecosystems*, 20(4), 665–682.
- Beven, K. (2006). A manifesto for the equifinality thesis. *Journal of Hydrology*, 320(1–2), 18–36.
- Beven, K., & Binley, A. (1992). The Future of Distributed model: Calibration and Uncertainty Prediction. *Hydrological Processes*, 6, 279–298.
- Beven, K., & Freer, J. (2001). Equifinality, data assimilation, and uncertainty estimation in mechanistic modelling of complex environmental systems using the GLUE methodology. *Journal of Hydrology*, 249(1–4), 11–29.
- Birgand, F., Skaggs, R. W., Chescheir, G. M., & Gilliam, J. W. (2007). Nitrogen removal in streams of agricultural catchments - A literature review. *Critical Reviews in Environmental Science and Technology*, 37(5), 381–487.
- Bonacci, O. (2001). Analysis of the maximum discharge of karst springs. *Hydrogeology Journal*, 9(4), 328–338.
- Bottrel, S. H., & Atkinson, T. C. (1992). Tracer study of flow and storage in the unsaturated zone of a karstic limestone aquifer. In H. Hotzl & A. Werner (Eds.), *Tracer Hydrology* (pp. 207–211). Rotterdam: Balkema.
- Bowie, G. L., Mills, W. B., Porcella, D. B., Campbell, C. L., Pagenkopf, J. R., Rupp, G. L., ... Gherini, S. A. (1985). *Rates, Constants, and Kinetics Formulations in Surface*

- Water Quality Modeling. EPA 600 (Vol. 1).*
- Boyer, D. G., & Alloush, G. A. (2001). Spatial distribution of nitrogen on grazed karst landscapes. *TheScientificWorldJOURNAL*, 1, 809–813.
- Boyer, D. G., & Pasquarell, G. C. (1995). Nitrate Concentrations in Karst Springs in an Extenswely Grazed Area. *Journal of the American Water Resources Association*, 31(4), 729–736.
- Brannen-Donnelly, K., & Engel, A. S. (2015). Bacterial diversity differences along an epigenic cave stream reveal evidence of community dynamics, succession, and stability. *Frontiers in Microbiology*, 6, 729.
- Brekke, L., Thrasher, B., Maurer, E. P., & Pruitt, T. (2013). *Downscaled CMIP3 and CMIP5 Climate Projections: Release of Downscaled CMIP5 Climate Projections, Comparison with Preceding Information, and Summary of User Needs*. Denver, CO.
- Buda, A. R., & DeWalle, D. R. (2009). Dynamics of stream nitrate sources and flow pathways during stormflows on urban, forest and agricultural watersheds in central Pennsylvania, USA. *Hydrological Processes*, 23, 3292–3305.
- Burns, D. A., Miller, M. P., Pellerin, B. A., & Capel, P. D. (2016). Patterns of diel variation in nitrate concentrations in the Potomac River. *Freshwater Science*, 35(4), 1117–1132.
- Butman, D., & Raymond, P. A. (2011). Significant efflux of carbon dioxide from streams and rivers in the United States. *Nature Geoscience*, 4(12), 839–842.
- Cambardella, C. A., & Elliott, E. T. (1992). Particulate Soil Organic-Matter Changes across a Grassland Cultivation Sequence. *Soil Science Society of America Journal*, 56(3), 777–783.
- Cánovas, C. R., Hubbard, C. G., Olías, M., Nieto, J. M., Black, S., & Coleman, M. L. (2008). Hydrochemical variations and contaminant load in the Río Tinto (Spain) during flood events. *Journal of Hydrology*, 350(1–2), 25–40.
- Carvalhais, N., Reichstein, M., Ciais, P., Collatz, G. J., Mahecha, M. D., Montagnani, L., ... Seixas, J. (2010). Identification of vegetation and soil carbon pools out of equilibrium in a process model via eddy covariance and biometric constraints. *Global Change Biology*, 16(10), 2813–2829.
- Casciotti, K. L., Sigman, D. M., Hastings, M. G., Böhlke, J. K., & Hilkert, A. (2002). Measurement of the oxygen isotopic composition of nitrate in seawater and freshwater using the denitrifier method. *Analytical Chemistry*, 74(19), 4905–4912.
- Cellino, M., & Lemmin, U. (2004). Influence of Coherent Flow Structures on the Dynamics of Suspended Sediment Transport in Open-Channel Flow. *Journal of Hydraulic Engineering*, 130(11), 1077–1088.
- Chalikakis, K., Plagnes, V., Guerin, R., Valois, R., & Bosch, F. P. (2011). Contribution of geophysical methods to karst-system exploration: An overview. *Hydrogeology Journal*, 19(6), 1169–1180.
- Chang, H. H. (1988). *Fluvial Processes in River Engineering*. Malabar, Florida: Krieger Publishing Company.
- Chang, Y., Wu, J., Jiang, G., & Kang, Z. (2017). Identification of the dominant hydrological process and appropriate model structure of a karst catchment through stepwise simplification of a complex conceptual model. *Journal of Hydrology*, 548, 75–87.
- Chapelle, F. H. (2001). *Groundwater Microbiology and Geochemistry*. New York City,

- New York: Wiley.
- Chen, F., & Dudhia, J. (2001). Coupling an Advanced Land Surface – Hydrology Model with the Penn State – NCAR MM5 Modeling System. Part II: Preliminary Model Validation. *Monthly Weather Review*, *129*(4), 587–604.
- Christopher, S. F., Mitchell, M. J., McHale, M. R., Boyer, E. W., Douglas, B. A., & Kendall, C. (2008). Factors controlling nitrogen release from two forested catchments with contrasting hydrochemical responses. *Hydrological Processes*, *22*, 46–62.
- Clare, E. (2018). Spatial and Temporal Variations of In-Stream Nutrient Concentrations in Similar Mixed-Use Watersheds. In *Kentucky Water Resources Research Institute Annual Symposium*. Lexington, KY.
- Clément, J. C., Holmes, R. M., Peterson, B. J., & Pinay, G. (2003). Isotopic investigation of denitrification in a riparian ecosystem in western France. *Journal of Applied Ecology*, *40*(6), 1035–1048.
- Cole, J. J., Prairie, Y. T., Caraco, N. F., McDowell, W. H., Tranvik, L. J., Striegl, R. G., ... Melack, J. (2007). Plumbing the global carbon cycle: Integrating inland waters into the terrestrial carbon budget. *Ecosystems*, *10*(1), 171–184.
- Collins, W. D., Bitz, C. M., Blackmon, M. L., Bonan, G. B., Bretherton, C. S., Carton, J. A., ... Smith, R. D. (2006). The Community Climate System Model Version 3 (CCSM3). *Journal of Climate*, *19*(11), 2122–2143.
- Cressman, E. R., & Peterson, W. L. (1986). Ordovician System. In *The Geology of Kentucky: A Text to Accompany The Geologic Map of Kentucky*.
- Croll, B. T., & Hayes, C. R. (1988). Nitrate and water supplies in the United Kingdom. *Environmental Pollution*, *50*(1–2), 163–187.
- Cui, M., & Caldwell, M. M. (1997). A large ephemeral release of nitrogen upon wetting of dry soil and corresponding root responses in the field. *Plant and Soil*, *191*(2), 291–299.
- Currens, J. C., Taylor, C. J., Webb, S., Zhu, J., Workman, S. R., Agouridis, C., ... Husic, A. (2015). Initial Findings from the Karst Water Instrumentation System Station, Royal Spring Groundwater Basin, Kentucky Horse Park 2010-2014. In *Proceedings Kentucky Water Resources Annual Symposium, Kentucky Water Resources Research Institute* (pp. 9–10). Lexington, KY.
- Daly, D., Dassargues, A., Drew, D., Dunne, S., Goldscheider, N., Neale, S., ... Zwahlen, F. (2002). Main concepts of the “European approach” to karst-groundwater-vulnerability assessment and mapping. *Hydrogeology Journal*, *10*(2), 340–345.
- Danovaro, R., Dell’Anno, A., & Fabiano, M. (2001). Bioavailability of organic matter in the sediments of the Porcupine Abyssal Plain, northeastern Atlantic. *Marine Ecology Progress Series*, *220*, 25–32.
- Davis, C. M., & Fox, J. F. (2009). Sediment Fingerprinting : Review of the Method and Future Improvements for Allocating Nonpoint Source Pollution. *Journal of Environmental Engineering*, *135*, 490–504.
- Davis, J. V., Petersen, J. C., Adamski, J. C., & Freiwald, D. A. (1995). *Water-quality assessment of the Ozark Plateaus study unit, Arkansas, Kansas, Missouri, and Oklahoma-analysis of information on nutrients, suspended sediment, and suspended solids, 1970-92. Water-Resources Investigations Report*. Retrieved from <http://pubs.er.usgs.gov/publication/wri954042>
- De Chant, L. J. (2005). The venerable 1/7th power law turbulent velocity profile: A

- classical nonlinear boundary value problem solution and its relationship to stochastic processes. *Applied Mathematics and Computation*, 161(2), 463–474.
- Dean, S., Freer, J., Beven, K., Wade, A. J., & Butterfield, D. (2009). Uncertainty assessment of a process-based integrated catchment model of phosphorus. *Stochastic Environmental Research and Risk Assessment*, 23(7), 991–1010.
- Debbage, N., Miller, P., Poore, S., Morano, K., Mote, T., & Marshall Shepherd, J. (2017). A climatology of atmospheric river interactions with the southeastern United States coastline. *International Journal of Climatology*, 37(11), 4077–4091.
- Delworth, T. L., Broccoli, A. J., Rosati, A., Stouffer, R. J., Balaji, V., Beesley, J. A., ... Zhang, R. (2006). GFDL's CM2 global coupled climate models. Part I: Formulation and simulation characteristics. *Journal of Climate*, 19(5), 643–674.
- Denahan, B., & Smith, D. L. (1984). Electrical Resistivity Investigation of Potential Cavities Underlying a Proposed Ash Disposal Area. *Environmental Geology and Water Sciences*, 6(1), 45–49.
- Derickson, R. ., & Long, a. . (1999). Linear systems analysis in a karst aquifer. *Journal of Hydrology*, 219, 206–217.
- Di, H. J., & Cameron, K. C. (2002). Nitrate leaching in temperate agroecosystems: Sources, factors and mitigating strategies. *Nutrient Cycling in Agroecosystems*, 64(3), 237–256.
- Dirnböck, T., Kobler, J., Kraus, D., Grote, R., & Kiese, R. (2016). Impacts of management and climate change on nitrate leaching in a forested karst area. *Journal of Environmental Management*, 165, 243–252.
- Dodds, W. K., & Smith, V. H. (2016). Nitrogen, phosphorus, and eutrophication in streams. *Inland Waters*, 6(2), 155–164.
- Dogwiler, T., & Wicks, C. M. (2004). Sediment entrainment and transport in fluviokarst systems. *Journal of Hydrology*, 295(1–4), 163–172.
- Dou, G. R. (1974). Similarity theory and its application to the design of total sediment transport model. In *Research Bulletin of Nanjing Hydraulic Research Institute*. Nanjing, China.
- Drahovzal, J. A., Harris, D. C., Wickstrom, L. H., Walker, D., Baranoski, M. T., Keith, B., & Furer, L. C. (1992). *The east continent rift basin: a new discovery*. Lexington, KY.
- Drahovzal, J. A., & Noger, M. C. (1995). *Preliminary map of the structure of the Precambrian surface in eastern Kentucky*. Lexington, KY.
- Droppo, I. G., & Amos, C. L. (2001). Structure, stability, and transformation of contaminated lacustrine surface fine-grained laminae. *Journal of Sedimentary Research*, 71(5), 717–726.
- Droppo, I. G., Lau, Y. L., & Mitchell, C. (2001). The effect of depositional history on contaminated bed sediment stability. *Science of The Total Environment*, 266(1–3), 7–13.
- Droppo, I. G., & Stone, M. (1994). In-channel surficial fine-grained sediment laminae. Part I: Physical characteristics and formational processes. *Hydrological Processes*, 8(2), 101–111.
- Drysdale, R., Pierotti, L., Piccini, L., & Baldacci, F. (2001). Suspended sediments in karst spring waters near Massa (Tuscany), Italy. *Environmental Geology*, 40(8), 1037–1050.
- Dussart-Baptista, L., Massei, N., Dupont, J. P., & Jouenne, T. (2003). Transfer of bacteria-

- contaminated particles in a karst aquifer: Evolution of contaminated materials from a sinkhole to a spring. *Journal of Hydrology*, 284(1–4), 285–295.
- Einsiedl, F., & Mayer, B. (2006). Hydrodynamic and microbial processes controlling nitrate in a fissured-porous karst aquifer of the Franconian Alb, Southern Germany. *Environmental Science and Technology*, 40(21), 6697–6702.
- Ekmekci, M. (2005). Pesticide and nutrient contamination in the Kestel polje-Kirkgoz karst springs, Southern Turkey. *Environmental Geology*, 49(1), 19–29.
- Farnleitner, A. H., Wilhartitz, I., Ryzinska, G., Kirschner, A. K. T., Stadler, H., Burtscher, M. M., ... Mach, R. L. (2005). Bacterial dynamics in spring water of alpine karst aquifers indicates the presence of stable autochthonous microbial endokarst communities. *Environmental Microbiology*, 7(8), 1248–1259.
- Fenton, O., Mellander, P. E., Daly, K., Wall, D. P., Jahangir, M. M. R., Jordan, P., ... Richards, K. G. (2017). Integrated assessment of agricultural nutrient pressures and legacies in karst landscapes. *Agriculture, Ecosystems and Environment*, 239, 246–256.
- Ferguson, R. I. (1981). Channel forms and channel changes. In J. Lewin (Ed.), *British Rivers* (pp. 90–125). London: Allen and Unwin.
- Findlay, S. E. G., Mulholland, P. J., Hamilton, S. K., Tank, J. L., Bernot, M. J., Burgin, A. J., ... Sobota, D. J. (2011). Cross-stream comparison of substrate-specific denitrification potential. *Biogeochemistry*, 104(1–3), 381–392.
- Fiorillo, F. (2014). The Recession of Spring Hydrographs, Focused on Karst Aquifers. *Water Resources Management*, 28(7), 1781–1805.
- Flato, G. M. (2005). The Third Generation Coupled Global Climate Model (CGCM3). Retrieved from <http://www.ec.gc.ca/ccmac-cccma/default.asp?n=1299529F-1>
- Fleury, P., Ladouche, B., Conroux, Y., Jourde, H., & Dörfliger, N. (2009). Modelling the hydrologic functions of a karst aquifer under active water management - The Lez spring. *Journal of Hydrology*, 365(3–4), 235–243.
- Fleury, P., Maréchal, J. C., & Ladouche, B. (2013). Karst flash-flood forecasting in the city of Nîmes (southern France). *Engineering Geology*, 164, 26–35.
- Fleury, P., Plagnes, V., & Bakalowicz, M. (2007). Modelling of the functioning of karst aquifers with a reservoir model: Application to Fontaine de Vaucluse (South of France). *Journal of Hydrology*, 345(1–2), 38–49.
- Ford, D. C., & Williams, P. (2007). *Karst hydrogeology and geomorphology*. Chichester: John Wiley & Sons Ltd.
- Ford, W. I., & Fox, J. F. (2014). Model of particulate organic carbon transport in an agriculturally impacted stream. *Hydrological Processes*, 28(3), 662–675.
- Ford, W. I., & Fox, J. F. (2015). Isotope-based Fluvial Organic Carbon (ISOFLOC) Model: Model formulation, sensitivity, and evaluation. *Water Resources Research*, 51(6), 4046–4064.
- Ford, W. I., & Fox, J. F. (2017). Stabilization of benthic algal biomass in a temperate stream draining agroecosystems. *Water Research*, 108, 432–443.
- Ford, W. I., Fox, J. F., & Pollock, E. (2017). Reducing equifinality using isotopes in a process-based stream nitrogen model highlights the flux of algal nitrogen from agricultural streams. *Water Resources Research*, 53(8), 6539–6561.
- Ford, W. I., Fox, J. F., Pollock, E., Rowe, H., & Chakraborty, S. (2015a). Testing assumptions for nitrogen transformation in a low-gradient agricultural stream. *Journal*

- of Hydrology*, 527, 908–922.
- Ford, W. I., Fox, J. F., & Rowe, H. (2015b). Impact of extreme hydrologic disturbance upon the sediment carbon quality in agriculturally impacted temperate streams. *Ecohydrology*, 8(3), 438–449.
- Ford, W. I., King, K., & Williams, M. R. (2018a). Upland and in-stream controls on baseflow nutrient dynamics in tile-drained agroecosystem watersheds. *Journal of Hydrology*, 556(3), 800–812.
- Ford, W. I., Williams, M. R., Young, M. B., King, K. W., & Fischer, E. (2018b). Assessing Intra-Event Phosphorus Dynamics in Drainage Water Using Phosphate Stable Oxygen Isotopes. *Transactions of the American Society of Agricultural and Biological Engineers*, (in press).
- Fournier, M., Massei, N., Bakalowicz, M., Dussart-Baptista, L., Rodet, J., & Dupont, J. P. (2007). Using turbidity dynamics and geochemical variability as a tool for understanding the behavior and vulnerability of a karst aquifer. *Hydrogeology Journal*, 15(4), 689–704.
- Fox, J. F. (2005). *Fingerprinting Using Biogeochemical Tracers to Investigate Watershed Processes*. University of Iowa.
- Fox, J. F. (2009). Identification of Sediment Sources in Forested Watersheds With Surface Coal Mining Disturbance Using Carbon and Nitrogen Isotopes. *Journal of the American Water Resources Association*, 45(5), 1273–1289.
- Fox, J. F., Davis, C. M., & Martin, D. K. (2010). Sediment Source Assessment in a Lowland Watershed Using Nitrogen Stable Isotopes. *Journal of the American Water Resources Association*, 46(6), 1192–1204.
- Fox, J. F., & Ford, W. I. (2016). Impact of landscape disturbance on the quality of terrestrial sediment carbon in temperate streams. *Journal of Hydrology*, 540, 1030–1042.
- Fox, J. F., Ford, W. I., Strom, K., Villarini, G., & Meehan, M. (2014). Benthic control upon the morphology of transported fine sediments in a low-gradient stream. *Hydrological Processes*, 28(11), 3776–3788.
- Fox, J. F., & Martin, D. K. (2014). Sediment fingerprinting for calibrating a soil erosion and sediment-yield model in mixed land-use watersheds. *Journal of Hydrologic Engineering*, 20(6), C4014002.
- Fox, J. F., & Papanicolaou, A. N. (2007). The use of carbon and nitrogen isotopes to study watershed erosion processes. *Journal of the American Water Resources Association*, 43(4), 1047–1064.
- Fox, J. F., & Papanicolaou, A. N. (2008). An un-mixing model to study watershed erosion processes. *Advances in Water Resources*, 31(1), 96–108.
- Franklin, P., Dunbar, M., & Whitehead, P. (2008). Flow controls on lowland river macrophytes: A review. *Science of the Total Environment*, 400(1–3), 369–378.
- Fretwell, B. A., Burgess, W. G., Barker, J. A., & Jefferies, N. L. (2005). Redistribution of contaminants by a fluctuating water table in a micro-porous, double-porosity aquifer: Field observations and model simulations. *Journal of Contaminant Hydrology*, 78(1–2), 27–52.
- Gallo, E. L., Lohse, K. A., Ferlin, C. M., Meixner, T., & Brooks, P. D. (2014). Physical and biological controls on trace gas fluxes in semi-arid urban ephemeral waterways. *Biogeochemistry*, 121(1), 189–207.
- Gao, Y., Fu, J. S., Drake, J. B., Liu, Y., & Lamarque, J. F. (2012). Projected changes of

- extreme weather events in the eastern United States based on a high resolution climate modeling system. *Environmental Research Letters*, 7(4).
- Garcia-Anton, E., Cuezva, S., Fernandez-Cortes, A., Benavente, D., & Sanchez-Moral, S. (2014). Main drivers of diffusive and advective processes of CO₂-gas exchange between a shallow vadose zone and the atmosphere. *International Journal of Greenhouse Gas Control*, 21, 113–129.
- Gehre, M., Geilmann, H., Richter, J., Werner, R. A., & Brand, W. A. (2004). Continuous flow 2H/1H and 18O/16O analysis of water samples with dual inlet precision. *Rapid Communications in Mass Spectrometry*, 18(22), 2650–2660.
- Geyer, T., Birk, S., Licha, T., Liedl, R., & Sauter, M. (2007). Multitracer test approach to characterize reactive transport in karst aquifers. *Ground Water*, 45(1), 36–45.
- Ghasemizadeh, R., Hellweger, F., Butscher, C., Padilla, I., Vesper, D., Field, M. S., & Alshawabkeh, A. (2012). Review: Groundwater flow and transport modeling of karst aquifers, with particular reference to the North Coast Limestone aquifer system of Puerto Rico. *Hydrogeology Journal*, 20(8), 1441–1461.
- Gillieson, D. (1986). Cave sedimentation in the New Guinea highlands. *Earth Surface Processes and Landforms*, 11(5), 533–543.
- Giorgi, F., Marinucci, M. R., & Bates, G. T. (1993). Development of a Second-Generation Regional Climate Model (RegCM2). Part I: Boundary-Layer and Radiative Transfer Processes. *Monthly Weather Review*.
- Goldscheider, N., Hunkeler, D., & Rossi, P. (2006). Review: Microbial biocenoses in pristine aquifers and an assessment of investigative methods. *Hydrogeology Journal*, 14(6), 926–941.
- Gong, Y., Shen, Z., Hong, Q., Liu, R., & Liao, Q. (2011). Parameter uncertainty analysis in watershed total phosphorus modeling using the GLUE methodology. *Agriculture, Ecosystems and Environment*, 142(3–4), 246–255.
- Gooseff, M. N., McKnight, D. M., Runkel, R. L., & Duff, J. H. (2004). Denitrification and hydrologic transient storage in a glacial meltwater stream, McMurdo Dry Valleys, Antarctica. *Limnology and Oceanography*, 49(5), 1884–1895.
- Goovaerts, P. (2000). Geostatistical approaches for incorporating elevation into the spatial interpolation of rainfall. *Journal of Hydrology*, 228(1–2), 113–129.
- Gordon, C., Cooper, C., Senior, C. A., Banks, H., Gregory, J. M., Johns, T. C., ... Wood, R. A. (2000). The simulation of SST, sea ice extents and ocean heat transports in a version of the Hadley Centre coupled model without flux adjustments. *Climate Dynamics*, 16(2–3), 147–168.
- Gouzie, D., Berglund, J., & Mickus, K. L. (2015). The application of quantitative fluorescent dye tracing to evaluate karst hydrogeologic response to varying recharge conditions in an urban area. *Environmental Earth Sciences*, 74(4), 3099–3111.
- Graening, G. O., & Brown, A. V. (2003). Ecosystem Dynamics and Pollution Effects in an Ozark Cave Stream. *Journal of the American Water Resources Association*, 39(6), 1497–1507.
- Granger, J., & Wankel, S. D. (2016). Isotopic overprinting of nitrification on denitrification as a ubiquitous and unifying feature of environmental nitrogen cycling. *Proceedings of the National Academy of Sciences*, 113(42), E6391–E6400.
- Griffiths, N. A., Tank, J. L., Royer, T. V., Warner, T. J., Frauendorf, T. C., Rosi-Marshall, E. J., & Whiles, M. R. (2012). Temporal variation in organic carbon spiraling in

- Midwestern agricultural streams. *Biogeochemistry*, 108(1–3), 149–169.
- Guo, Q., Wang, Y., Ma, T., & Li, L. (2005). Variation of karst spring discharge in the recent five decades as an indicator of global climate change: A case study at Shanxi, northern China. *Science in China Earth Sciences*, 48(11), 2001.
- Guy, B. T., Dickenson, W. T., Sohrabi, T. M., & Rudra, R. P. (2009). Development of an empirical model for calculating sediment-transport capacity in shallow overland flows: Model calibration. *Biosystems Engineering*, 103(2), 245–255.
- Hancock, P. J., Boulton, A. J., & Humphreys, W. F. (2005). Aquifers and hyporheic zones: Towards an ecological understanding of groundwater. *Hydrogeology Journal*, 13(1), 98–111.
- Hanson, G. J., & Simon, A. (2001). Erodibility of cohesive streambeds in the loess area of the Midwestern USA. *Hydrological Processes*, 15(1), 23–38.
- Hanson, R. L. (1991). Evapotranspiration and Droughts. In R. W. Paulson, E. B. CHase, R. S. Roberts, & D. W. Moody (Eds.), *U.S. Geological Survey Water-Supply Paper* (pp. 99–104). Retrieved from <http://geochange.er.usgs.gov/sw/changes/natural/et/>
- Hart, E. A., & Schurger, S. G. (2005). Sediment storage and yield in an urbanized karst watershed. *Geomorphology*, 70(1–2), 85–96.
- Hartmann, A. (2017). Experiences in calibrating and evaluating lumped karst hydrological models. In M. Parise, F. Gabrovšek, G. Kaufmann, & N. Ravbar (Eds.), *Advances in Karst Research: Theory, Fieldwork and Applications*. (pp. 331–340). London: Geological Society, London, Special Publications.
- Hartmann, A., Goldscheider, N., Wagener, T., Lange, J., & Weiler, M. (2014a). Karst water resources in a changing world: Approaches, of hydrological modeling. *Review of Geophysics*, (1), 1–25.
- Hartmann, A., Kobler, J., Kralik, M., Dirnböck, T., Humer, F., & Weiler, M. (2016). Model-aided quantification of dissolved carbon and nitrogen release after windthrow disturbance in an Austrian karst system. *Biogeosciences*, 13(1), 159–174.
- Hartmann, A., Mudarra, M., Andreo, B., Marin, A., Wagener, T., & Lange, J. (2014b). Modelling spatiotemporal impacts of hydroclimatic extremes on groundwater recharge at a Mediterranean karst aquifer. *Water Resources Research*, 50, 6507–6521.
- Hawkins, E., & Sutton, R. (2011). The potential to narrow uncertainty in projections of regional precipitation change. *Climate Dynamics*, 37(1), 407–418.
- He, Q., Yang, P., Yuan, W., Jiang, Y., Pu, J., Yuan, D., & Kuang, Y. (2010). The use of nitrate, bacteria and fluorescent tracers to characterize groundwater recharge and contamination in a karst catchment, Chongqing, China. *Hydrogeology Journal*, 18(5), 1281–1289.
- Hedin, L. O., Fischer, J. C. Von, Ostrom, N. E., Kennedy, B. P., Brown, M. G., Robertson, G. P., ... Mar, N. (1998). Thermodynamic Constraints on Nitrogen Transformations and Other Biogeochemical Processes at Soil-Stream Interfaces. *Ecology*, 79(2), 684–703.
- Heffernan, J. B., Albertin, A. R., Fork, M. L., Katz, B. G., & Cohen, M. J. (2012). Denitrification and inference of nitrogen sources in the karstic Floridan Aquifer. *Biogeosciences*, 9, 1671–1690.
- Henriksen, K., Blackburn, T. H., Lomstein, B. A., & McRoy, C. P. (1993). Rates of nitrification, distribution of nitrifying bacteria and inorganic N fluxes in northern Bering-Chukchi shelf sediments. *Continental Shelf Research*, 13(5–6), 629–651.

- Herman, E. K., Toran, L., & White, W. B. (2008). Threshold events in spring discharge: Evidence from sediment and continuous water level measurement. *Journal of Hydrology*, 351(1–2), 98–106.
- Hessel, R., & Jetten, V. (2007). Suitability of transport equations in modelling soil erosion for a small Loess Plateau catchment. *Engineering Geology*, 91(1), 56–71.
- Hirsch, R. M. (2014). Large Biases in Regression-Based Constituent Flux Estimates: Causes and Diagnostic Tools. *Journal of the American Water Resources Association*, 50(6), 1401–1424.
- Hossain, S., Eyre, B., & McConchie, D. (2002). Spatial and temporal variations of suspended sediment responses from the subtropical Richmond River catchment, NSW, Australia. *Australian Journal of Soil Research*, 40(3), 419–432.
- Hotchkiss, E. R., & Hall, R. O. (2015). Whole-stream ¹³C tracer addition reveals distinct fates of newly fixed carbon. *Ecology*, 96(2), 403–416.
- Huang, T., Pang, Z., & Yuan, L. (2013). Nitrate in groundwater and the unsaturated zone in (semi)arid northern China: Baseline and factors controlling its transport and fate. *Environmental Earth Sciences*, 70(1), 145–156.
- Huebsch, M., Fenton, O., Horan, B., Hennessy, D., Richards, K. G., Jordan, P., ... Blum, P. (2014). Mobilisation or dilution? Nitrate response of karst springs to high rainfall events. *Hydrology and Earth System Sciences*, 18(11), 4423–4435.
- Humphreys, W. F. (2006). Aquifers: The ultimate groundwater-dependent ecosystems. *Australian Journal of Botany*, 54(2), 115–132.
- Hupfer, M., Engesgaard, P., Jensen, H., Krause, S., & Nützmann, G. (2018). Aquatic interfaces and linkages: An emerging topic of interdisciplinary research. *Limnologica*, 68, 1–4.
- Husic, A. (2015). *Sediment Organic Carbon Fate and Transport in a Fluviokarst*. University of Kentucky.
- Husic, A., Fox, J. F., Agouridis, C., Currens, J. C., Ford, W. I., & Taylor, C. J. (2017a). Sediment carbon fate in phreatic karst (Part 1): Conceptual model development. *Journal of Hydrology*, 549, 179–193.
- Husic, A., Fox, J. F., Ford, W. I., Agouridis, C., Currens, J. C., & Taylor, C. J. (2017b). Sediment carbon fate in phreatic karst (Part 2): Numerical model development and application. *Journal of Hydrology*, 549, 208–219.
- Imberger, S. J., Cook, P. L. M., Grace, M. R., & Thompson, R. M. (2014). Tracing carbon sources in small urbanising streams: Catchment-scale stormwater drainage overwhelms the effects of reach-scale riparian vegetation. *Freshwater Biology*, 59(1), 168–186.
- Inamdar, S. P., Christopher, S. F., & Mitchell, M. J. (2004). Export mechanisms for dissolved organic carbon and nitrate during summer storm events in a glaciated forested catchment in New York, USA. *Hydrological Processes*, 18(14), 2651–2661.
- Inwood, S. E., Tank, J. L., & Bernot, M. J. (2005). Patterns of denitrification associated with land use in 9 midwestern headwater streams. *Journal of the North American Benthological Society*, 24(2), 227–245.
- Jacinte, P. A., Lal, R., & Owens, L. B. (2009). Application of stable isotope analysis to quantify the retention of eroded carbon in grass filters at the North Appalachian experimental watersheds. *Geoderma*, 148(3–4), 405–412.
- Jackson, C. R., & Vallaire, S. C. (2007). Microbial activity and decomposition of fine

- particulate organic matter in a Louisiana cypress swamp. *Journal of the North American Benthological Society*, 26(4), 743–753.
- Jahangir, M. M. R., Johnston, P., Addy, K., Khalil, M. I., Groffman, P. M., & Richards, K. G. (2013). Quantification of in situ denitrification rates in groundwater below an arable and a grassland system. *Water, Air, and Soil Pollution*, 224(9).
- Jarsjö, J., Chalov, S. R., Pietroń, J., Alekseenko, A. V., & Thorslund, J. (2017). Patterns of soil contamination, erosion and river loading of metals in a gold mining region of northern Mongolia. *Regional Environmental Change*, 17(7), 1991–2005.
- Jarvie, H. P., Sharpley, A. N., Brahana, V., Simmons, T., Price, A., Neal, C., ... Haggard, B. E. (2014). Phosphorus Retention and Remobilization along Hydrological Pathways in Karst Terrain. *Environmental Science & Technology*, 48(9), 4860–4868.
- Jeannin, P.-Y. (2001). Modeling flow in phreatic and epiphreatic karst conduits in the Holloch cave (Muotatal, Switzerland). *Water Resources Research*, 37(2), 191–200.
- Jensen, A., Ford, W. I., Fox, J. F., & Husic, A. (2018). Improving in-stream nutrient routines in water quality models using stable isotope tracers: A review and synthesis. *Transactions of the American Society of Agricultural and Biological Engineers*, 61(1), 139–157.
- Jones, A. L., & Smart, P. L. (2005). Spatial and temporal changes in the structure of groundwater nitrate concentration time series (1935-1999) as demonstrated by autoregressive modelling. *Journal of Hydrology*, 310(1–4), 201–215.
- Jones, R., Hassell, D., Hudson, D., Wilson, S., Jenkins, G., & Mitchell, J. (2003). *Generating High Resolution Climate Change Scenarios Using PRECIS*.
- Juang, H. M. H., Hong, S. Y., & Kanamitsu, M. (1997). The NCEP Regional Spectral Model: An Update. *Bulletin of the American Meteorological Society*, 78(10), 2125–2143.
- Julien, P. Y., & Simons, D. B. (1985). Sediment Transport Capacity of Overland Flow. *American Society of Agricultural Engineers*.
- Kaown, D., Koh, D. C., Mayer, B., & Lee, K. K. (2009). Identification of nitrate and sulfate sources in groundwater using dual stable isotope approaches for an agricultural area with different land use (Chuncheon, mid-eastern Korea). *Agriculture, Ecosystems and Environment*, 132(3–4), 223–231.
- Katz, B. G., Catches, J. S., Bullen, T. D., & Michel, R. L. (1998). Changes in the isotopic and chemical composition of ground water resulting from a recharge pulse from a sinking stream. *Journal of Hydrology*, 211(1–4), 178–207.
- Katz, B. G., Chelette, A. R., & Pratt, T. R. (2004). Use of chemical and isotopic tracers to assess nitrate contamination and ground-water age, Woodville Karst Plain, USA. *Journal of Hydrology*, 289(1–4), 36–61.
- Katz, B. G., Coplen, T. B., Bullen, T. D., & Hal Davis, J. (1997). Use of chemical and isotopic tracers to characterize the interactions between ground water and surface water in mantled karst. *Groundwater*.
- Katz, B. G., Griffin, D. W., McMahon, P. B., Harden, H. S., Wade, E., Hicks, R. W., & Chanton, J. P. (2010). Fate of Effluent-Borne Contaminants beneath Septic Tank Drainfields Overlying a Karst Aquifer. *Journal of Environment Quality*, 39(4), 1181.
- Kemp, M. J., & Dodds, W. K. (2002a). Comparisons of nitrification and denitrification in prairie and agriculturally influenced streams. *Ecological Applications*, 12(4), 998–1009.

- Kemp, M. J., & Dodds, W. K. (2002b). The influence of ammonium, nitrate, and dissolved oxygen concentrations on uptake, nitrification, and denitrification rates associated with prairie stream substrata. *Limnology and Oceanography*, *47*(5), 1380–1393.
- Kendall, C., & Aravena, R. (2000). Nitrate Isotopes in Groundwater Systems. In P. G. Cook & A. L. Herceg (Eds.), *Environmental Tracers in Subsurface Hydrology, 2000* (pp. 261–297). Springer US.
- Kendall, C., Elliott, E. M., & Wankel, S. D. (2007). Tracing anthropogenic inputs of nitrogen to ecosystems. In R. H. Michener & K. Lajtha (Eds.), *Stable Isotopes in Ecology and Environmental Science (2007)* (2nd ed., pp. 375–449). Blackwell Publishing.
- KGS (Kentucky Geological Survey). (2018). Groundwater information Via the Kentucky Groundwater Data Repository. Retrieved from <https://kgs.uky.edu/kgsweb/DataSearching/watersearch.asp>
- Klaus, J., Zehe, E., Elsner, M., Külls, C., & McDonnell, J. J. (2013). Macropore flow of old water revisited: Experimental insights from a tile-drained hillslope. *Hydrology and Earth System Sciences*, *17*(1), 103–118.
- Knierim, K. J., Pollock, E., & Hays, P. D. (2013). Using Isotopes of Dissolved Inorganic Carbon Species and Water To Separate Sources of Recharge in a Cave Spring, Northwestern Arkansas, Usa. *Acta Carsologica*, *42*(2–3), 261–276.
- Knight, D. B., & Davis, R. E. (2009). Contribution of tropical cyclones to extreme rainfall events in the southeastern United States. *Journal of Geophysical Research Atmospheres*, *114*(23), 1–17.
- Koenig, L. E., Shattuck, M. D., Snyder, L. E., Potter, J. D., & McDowell, W. H. (2017). Deconstructing the Effects of Flow on DOC, Nitrate, and Major Ion Interactions Using a High-Frequency Aquatic Sensor Network. *Water Resources Research*, *53*(12), 10655–10673.
- Kovačič, G. (2010). Hydrogeological Study of the Malencica Karst Spring (SW Slovenia) by Means of A time Series Analysis. *Acta Carsologica*, *39*(2), 201–215.
- Krause, S., Lewandowski, J., Grimm, N. B., Hannah, D. M., Pinay, G., McDonald, K., ... Turk, V. (2017). Ecohydrological interfaces as hot spots of ecosystem processes. *Water Resources Research*, *53*(8), 6359–6376.
- Kumar, S., Herrmann, M., Thamdrup, B., Schwab, V. F., Geesink, P., Trumbore, S. E., ... Küsel, K. (2017). Nitrogen loss from pristine carbonate-rock aquifers of the hainich critical zone exploratory (Germany) is primarily driven by chemolithoautotrophic anammox processes. *Frontiers in Microbiology*, *8*, 1–13.
- Kuzyakov, Y., & Blagodatskaya, E. (2015). Microbial hotspots and hot moments in soil: Concept & review. *Soil Biology and Biochemistry*, *83*, 184–199.
- KWW (Kentucky Water Watch). (2016). Volunteers protecting Kentucky Waterways. Retrieved from <http://water.ky.gov/ww/Pages/default.aspx>
- Lal, R., Delgado, J. A., Groffman, P. M., Millar, N., Dell, C., & Rotz, A. (2011). Management to mitigate and adapt to climate change. *Journal of Soil and Water Conservation*, *66*(4), 276–285.
- Lane, C. S., Lyon, D. R., & Ziegler, S. E. (2013). Cycling of two carbon substrates of contrasting lability by heterotrophic biofilms across a nutrient gradient of headwater streams. *Aquatic Sciences*, *75*(2), 235–250.
- Larson, J., Zhou, Y., & Higgins, R. W. (2005). Characteristics of landfalling tropical

- cyclones in the United States and Mexico: Climatology and interannual variability. *Journal of Climate*, 18(8), 1247–1262.
- Lavers, D. A., & Villarini, G. (2013). Atmospheric rivers and flooding over the central United States. *Journal of Climate*, 26(20), 7829–7836.
- Lavers, D. A., Villarini, G., Allan, R. P., Wood, E. F., & Wade, A. J. (2012). The detection of atmospheric rivers in atmospheric reanalyses and their links to British winter floods and the large-scale climatic circulation. *Journal of Geophysical Research Atmospheres*, 117(20), 1–13.
- Lawrence, J. R., & Gedzelman, S. D. (1996). Low stable isotope ratios of tropical cyclone rains. *Geophysical Research Letters*, 23(5), 527–530.
- Lee, E. S., & Krothe, N. C. (2001). A four-component mixing model for water in a karst terrain in south-central Indiana, USA. Using solute concentration and stable isotopes as tracers. *Chemical Geology*, 179(1–4), 129–143.
- Lee, N. M., Meisinger, D. B., Aubrecht, R., Kovacik, L., Saiz-jimenez, C., Baskar, S., ... Engel, A. S. (2012). Caves and Karst Environments. In E. M. Bell (Ed.), *Life at Extremes: Environments, Organisms and Strategies for Survival* (pp. 320–344). UK: CAB International.
- Lehman, R. M., Colwell, F. S., & Bala, G. A. (2001). Attached and unattached microbial communities in a simulated basalt aquifer under fracture- and porous-flow conditions. *Applied and Environmental Microbiology*, 67(6), 2799–2809.
- Lehmann, M. F., Bernasconi, S. M., Barbieri, A., Simona, M., & McKenzie, J. A. (2004). Interannual variation of the isotopic composition of sedimenting organic carbon and nitrogen in Lake Lugano: A long-term sediment trap study. *Limnology and Oceanography*, 49(3), 839–849.
- Leigh, C., Boulton, A. J., Courtwright, J. L., Fritz, K., May, C. L., Walker, R. H., & Datry, T. (2016). Ecological research and management of intermittent rivers: an historical review and future directions. *Freshwater Biology*, 61(8), 1181–1199.
- Lewandowski, J., Laskov, C., & Hupfer, M. (2007). The relationship between Chironomus plumosus burrows and the spatial distribution of pore-water phosphate, iron and ammonium in lake sediments. *Freshwater Biology*, 52(2), 331–343.
- Li, S. L., Liu, C. Q., Lang, Y. C., Zhao, Z. Q., & Zhou, Z. H. (2010). Tracing the sources of nitrate in karstic groundwater in Zunyi, Southwest China: A combined nitrogen isotope and water chemistry approach. *Environmental Earth Sciences*, 60(7), 1415–1423.
- Lin, X., Hou, L., Liu, M., Li, X., Zheng, Y., Yin, G., ... Jiang, X. (2016). Nitrogen mineralization and immobilization in sediments of the East China Sea: Spatiotemporal variations and environmental implications. *Journal of Geophysical Research: Biogeosciences*, 121(11), 2842–2855.
- Liu, C.-Q., Li, S.-L., Lang, Y.-C., & Xiao, H.-Y. (2006). Using $\delta^{15}\text{N}$ and $\delta^{18}\text{O}$ values to identify nitrate sources in karst groundwater, Guiyang, Southwest China. *Enviro Sci Technol.*, 40(22), 6925–6933.
- Liu, D., Guo, S., Wang, Z., Liu, P., Yu, X., Zhai, Q., & Zou, H. (2018). Statistics for sample splitting for the calibration and validation of hydrological models. *Stochastic Environmental Research and Risk Assessment*, 1–18.
- Liu, H., He, Q., Wang, Z., Weltje, G. J., & Zhang, J. (2010). Dynamics and spatial variability of near-bottom sediment exchange in the Yangtze Estuary, China.

- Estuarine, Coastal and Shelf Science*, 86(3), 322–330.
- Liu, Y., Yao, T., Gleixner, G., Claus, P., & Conrad, R. (2013). Methanogenic pathways, ^{13}C isotope fractionation, and archaeal community composition in lake sediments and wetland soils on the Tibetan Plateau. *Journal of Geophysical Research: Biogeosciences*, 118(2), 650–664.
- Long, A. J. (2009). Hydrograph separation for karst watersheds using a two-domain rainfall-discharge model. *Journal of Hydrology*, 364(3–4), 249–256.
- Long, A. J., & Gilcrease, P. C. (2009). A one-dimensional heat-transport model for conduit flow in karst aquifers. *Journal of Hydrology*, 378(3–4), 230–239.
- Long, A. J., Sawyer, J. F., & Putnam, L. D. (2008). Environmental tracers as indicators of karst conduits in groundwater in South Dakota, USA. *Hydrogeology Journal*, 16(2), 263–280.
- Luhmann, A. J., Covington, M. D., Alexander, S. C., Chai, S. Y., Schwartz, B. F., Groten, J. T., & Alexander, E. C. (2012). Comparing conservative and nonconservative tracers in karst and using them to estimate flow path geometry. *Journal of Hydrology*, 448–449, 201–211.
- Madej, M. A., Sutherland, D. G., Lisle, T. E., & Pryor, B. (2009). Channel responses to varying sediment input: A flume experiment modeled after Redwood Creek, California. *Geomorphology*, 103(4), 507–519.
- Maggi, F., & Riley, W. J. (2009). Transient competitive complexation in biological kinetic isotope fractionation explains nonsteady isotopic effects: Theory and application to denitrification in soils. *Journal of Geophysical Research: Biogeosciences*, 114(4), 1–13.
- Mahler, B. J., Bennett, P. C., & Zimmerman, M. (1998). Lanthanide-labeled clay: A new method for tracing sediment transport in karst. *Ground Water*.
- Mahler, B. J., & Garner, B. D. (2009). Using nitrate to quantify quick flow in a karst aquifer. *Ground Water*, 47(3), 350–360.
- Mahler, B. J., & Lynch, F. L. (1999). Muddy waters: Temporal variation in sediment discharging from a karst spring. *Journal of Hydrology*, 214(1–4), 165–178.
- Mahler, B. J., Lynch, F. L., & Bennett, P. C. (1999). Mobile sediment in an urbanizing karst aquifer: implications for contaminant transport. *Environmental Geology*, 39(1), 25–38.
- Mahler, B. J., Valdes, D., Musgrove, M., & Massei, N. (2008). Nutrient dynamics as indicators of karst processes: Comparison of the Chalk aquifer (Normandy, France) and the Edwards aquifer (Texas, U.S.A.). *Journal of Contaminant Hydrology*, 98(1–2), 36–49.
- Mahoney, D. T., Fox, J. F., & Al Aamery, N. (2018). Watershed erosion modeling using the probability of sediment connectivity in a gently rolling system. *Journal of Hydrology*, 561, 862–883.
- Malík, P., & Vojtková, S. (2012). Use of recession-curve analysis for estimation of karstification degree and its application in assessing overflow/underflow conditions in closely spaced karstic springs. *Environmental Earth Sciences*, 65(8), 2245–2257.
- Mangin, A. (1984). The use of autocorrelation and spectral analyses to obtain a better understanding of hydrological systems. *Journal of Hydrology*, 67, 25–43.
- Manzoni, S., & Porporato, A. (2009). Soil carbon and nitrogen mineralization: Theory and models across scales. *Soil Biology and Biochemistry*, 41(7), 1355–1379.

- Marín-Spiotta, E., Gruley, K. E., Crawford, J., Atkinson, E. E., Miesel, J. R., Greene, S., ... Spencer, R. G. M. (2014). Paradigm shifts in soil organic matter research affect interpretations of aquatic carbon cycling: Transcending disciplinary and ecosystem boundaries. *Biogeochemistry*, 117(2–3), 279–297.
- Markovic, T., Miko, S., Kapelj, S., Buljan, R., Larva, O., & Peh, Z. (2006). Behaviour of metals and nutrients in soils and groundwater of a karst polje. *Journal of Geochemical Exploration*, 88(1–3 SPEC. ISS.), 124–129.
- Martin, J. B., & Dean, R. W. (2001). Exchange of water between conduits and matrix in the Floridan aquifer. *Chemical Geology*, 179(1–4), 145–165.
- Martinotti, W., Camusso, M., Guzzi, L., Patrolecco, L., & Pettine, M. (1997). C, N and their stable isotopes in suspended and sedimented matter from the PO estuary (Italy). *Water, Air, and Soil Pollution*, 99(1–4), 325–332.
- Marwick, T. R., Tamoo, F., Teodoru, C. R., Borges, A. V., Darchambeau, F., & Boillon, S. (2015). The age of river-transported carbon: A global perspective. *Global Biogeochemical Cycles*, 29(2), 122–137.
- Massei, N., Lacroix, M., Wang, H. Q., Mahler, B. J., & Dupont, J. P. (2002). Transport of suspended solids from a karstic to an alluvial aquifer: The role of the karst/alluvium interface. *Journal of Hydrology*, 260(1–4), 88–101.
- Massei, N., Wang, H. Q., Dupont, J. P., Rodet, J., & Laignel, B. (2003). Assessment of direct transfer and resuspension of particles during turbid floods at a karstic spring. *Journal of Hydrology*, 275(1–2), 109–121.
- Massei, N., Wang, H. Q., Field, M. S., Dupont, J. P., Bakalowicz, M., & Rodet, J. (2006). Interpreting tracer breakthrough tailing in a conduit-dominated karstic aquifer. *Hydrogeology Journal*, 14(6), 849–858.
- Mazzilli, N., Guinot, V., & Jourde, H. (2012). Sensitivity analysis of conceptual model calibration to initialisation bias. Application to karst spring discharge models. *Advances in Water Resources*, 42, 1–16.
- McCallum, J. E., Ryan, M. C., Mayer, B., & Rodvang, S. J. (2008). Mixing-induced groundwater denitrification beneath a manured field in southern Alberta, Canada. *Applied Geochemistry*, 23(8), 2146–2155.
- McCormack, T., Naughton, O., Johnston, P. M., & Gill, L. W. (2016). Quantifying the influence of surface water-groundwater interaction on nutrient flux in a lowland karst catchment. *Hydrology and Earth System Sciences*, 20(5), 2119–2133.
- McMahon, P. B. (2001). Aquifer/aquitard interfaces: Mixing zones that enhance biogeochemical reactions. *Hydrogeology Journal*, 9(1), 34–43.
- Mearns, L. O., Sain, S., Leung, L. R., Bukovsky, M. S., McGinnis, S., Biner, S., ... Sloan, L. (2013). Climate change projections of the North American Regional Climate Change Assessment Program (NARCCAP). *Climatic Change*, 120(4), 965–975.
- Mellander, P.-E., Melland, A. R., Jordan, P., Wall, D. P., Murphy, P. N. C., & Shortle, G. (2012). Quantifying nutrient transfer pathways in agricultural catchments using high temporal resolution data. *Environmental Science & Policy*, 24, 44–57.
- Miller, M. P., Tesoriero, A. J., Hood, K., Terziotti, S., & Wolock, D. M. (2017). Estimating Discharge and Nonpoint Source Nitrate Loading to Streams From Three End-Member Pathways Using High-Frequency Water Quality Data. *Water Resources Research*, 53(12), 10201–10216.
- Moatar, F., Abbott, B. W., Minaudo, C., Curie, F., & Pinay, G. (2017). Elemental

- properties, hydrology, and biology interact to shape concentration-discharge curves for carbon, nutrients, sediment, and major ions. *Water Resources Research*, 53(2), 1270–1287.
- Molson, J., Pehme, P., Cherry, J., & Parker, B. (2007). Numerical analysis of heat transport within fractured sedimentary rock: implications for temperature probes. In *Proceedings of the NGWA/US EPA Fractured Rock Conference*.
- Mooers, H. D., & Alexander, E. C. (1994). Contribution of spray irrigation of wastewater to groundwater contamination in the Karst of Southeastern Minnesota, USA. *Applied Hydrogeology*, 2(1), 34–44.
- Moore, B. J., Neiman, P. J., Ralph, F. M., & Barthold, F. E. (2012). Physical Processes Associated with Heavy Flooding Rainfall in Nashville, Tennessee, and Vicinity during 1–2 May 2010: The Role of an Atmospheric River and Mesoscale Convective Systems*. *Monthly Weather Review*, 140(2), 358–378.
- Moore, J. C., Berlow, E. L., Coleman, D. C., De Suiter, P. C., Dong, Q., Hastings, A., ... Wall, D. H. (2004). Detritus, trophic dynamics and biodiversity. *Ecology Letters*, 7(7), 584–600.
- Moriasi, D. N., Arnold, J. G., Liew, M. W. Van, Bingner, R. L., Harmel, R. D., & Veith, T. L. (2007). Model Evaluation Guidelines for Systematic Quantification of Accuracy in Watershed Simulations. *Transactions of the American Society of Agricultural and Biological Engineers*, 50(3), 885–900.
- Mudarra, M., Andreo, B., Barberá, J. A., & Mudry, J. (2014). Hydrochemical dynamics of TOC and NO₃–contents as natural tracers of infiltration in karst aquifers. *Environmental Earth Sciences*, 71(2), 507–523.
- Mukundan, R., Radcliffe, D. E., Ritchie, J. C., Risse, L. M., & McKinley, R. A. (2010). Sediment Fingerprinting to Determine the Source of Suspended Sediment in a Southern Piedmont Stream. *Journal of Environment Quality*, 39(4), 1328.
- Musgrove, M., Opsahl, S. P., Mahler, B. J., Herrington, C., Sample, T. L., & Banta, J. R. (2016). Source, variability, and transformation of nitrate in a regional karst aquifer: Edwards aquifer, central Texas. *Science of the Total Environment*, 568, 457–469.
- Nerantzaki, S. D., Giannakis, G. V., Efstathiou, D., Nikolaidis, N. P., Sibetheros, I. A., Karatzas, G. P., & Zacharias, I. (2015). Modeling suspended sediment transport and assessing the impacts of climate change in a karstic Mediterranean watershed. *Science of the Total Environment*, 538, 288–297.
- NHC NOAA (National Hurricane Center). (2017). Hurricane NATE Advisory Archive. Retrieved from www.nhc.noaa.gov/archive/2017/NATE.shtml?
- Nikolaidis, N. P., Bouraoui, F., & Bidoglio, G. (2013). Hydrologic and geochemical modeling of a karstic Mediterranean watershed. *Journal of Hydrology*, 477, 129–138.
- NOAA (National Oceanic and Atmospheric Organization). (2017). Billion-Dollar Weather and Climate Disasters: Overview. Retrieved from www.ncdc.noaa.gov/billions
- Northup, D. E., & Lavoie, K. H. (2001). Geomicrobiology of caves: A review. *Geomicrobiology Journal*, 18(3), 199–222.
- Obeidat, M. M., Ahmad, F. Y., Hamouri, N. A., Massadeh, A. M., & Athamneh, F. S. (2008). Assessment of nitrate contamination of karst springs, Bani Kanana, northern Jordan. *Revista Mexicana de Ciencias Geológicas*, 25(3), 426–437.
- Opsahl, S. P., Musgrove, M., & Slattery, R. N. (2017). New insights into nitrate dynamics in a karst groundwater system gained from in situ high-frequency optical sensor

- measurements. *Journal of Hydrology*, 546, 179–188.
- Orr, A., Nitsche, J., Archbold, M., Deakin, J., Ofterdinger, U., & Flynn, R. (2016). The influence of bedrock hydrogeology on catchment-scale nitrate fate and transport in fractured aquifers. *Science of the Total Environment*, 569–570, 1040–1052.
- Orr, C. H., Clark, J. J., Wilcock, P. R., Finlay, J. C., & Doyle, M. W. (2009). Comparison of morphological and biological control of exchange with transient storage zones in a field-scale flume. *Journal of Geophysical Research: Biogeosciences*, 114(2), 1–10.
- Padilla, I. Y., & Vesper, D. (2018). *Karst Groundwater Contamination and Public Health*. (W. B. White, J. S. Herman, E. K. Herman, & M. Rutigliano, Eds.). Springer International Publishing.
- Paerl, H. W., Hall, N. S., & Calandrino, E. S. (2011). Controlling harmful cyanobacterial blooms in a world experiencing anthropogenic and climatic-induced change. *Science of the Total Environment*, 409(10), 1739–1745.
- Palanisamy, B., & Workman, S. R. (2014). Hydrologic Modeling of Flow through Sinkholes Located in Streambeds of Cane Run Stream, Kentucky. *Journal of Hydrologic Engineering*, 20(5), 04014066.
- Panagopoulos, G. (2012). Application of MODFLOW for simulating groundwater flow in the Trifilia karst aquifer, Greece. *Environmental Earth Sciences*, 67(7), 1877–1889.
- Panno, S. V., Hackley, K. C., Hwang, H. H., & Kelly, W. R. (2001). Determination of the sources of nitrate contamination in karst springs using isotopic and chemical indicators. *Chemical Geology*, 179(1–4), 113–128.
- Papanicolaou, A., Fox, J., & Marshall, J. (2003). Soil fingerprinting in the Palouse Basin, USA, using stable carbon and nitrogen isotopes. *International Journal of Sediment Research*.
- Paylor, R., & Currens, J. C. (2004). *Royal Springs Karst Groundwater Travel Time Investigation*. Lexington, KY.
- Perrin, J., Jeannin, P.-Y., & Zwahlen, F. (2003). Epikarst storage in a karst aquifer: A conceptual model based on isotopic data, Milandre test site, Switzerland. *Journal of Hydrology*, 279(1–4), 106–124.
- Peterson, B. J., Wollheim, W. M., Mulholland, P. J., Webster, J. R., Meyer, J. L., Tank, J. L., ... Morrall, D. D. (2001). Control of nitrogen export from headwaters by headwater streams. *Science*, 292, 86–90.
- Peterson, E. W., Davis, R. K., Brahana, J. V., & Orndorff, H. A. (2002). Movement of nitrate through regolith covered karst terrane, northwest arkansas. *Journal of Hydrology*, 256(1–2), 35–47.
- Phillips, J. D. (2015). Karstification at Bowman's Bend. Retrieved from <https://geography.as.uky.edu/blogs/jdp/karstification-bowmans-bend>
- Phillips, J. D., Martin, L. L., Nordberg, V. G., & Andrews, W. A. (2004). Divergent evolution in fluviokarst landscapes of central Kentucky. *Earth Surface Processes and Landforms*, 29(7), 799–819.
- Phillips, J. M., Russell, M. A., & Walling, D. E. (2000). Time-integrated sampling of fluvial suspended sediment: A simple methodology for small catchments. *Hydrological Processes*, 14(14), 2589–2602.
- Plummer, D. A., Caya, D., Frigon, A., Côté, H., Giguère, M., Paquin, D., ... De Elia, R. (2006). Climate and climate change over North America as simulated by the Canadian RCM. *Journal of Climate*, 19(13), 3112–3132.

- Pronk, M., Goldscheider, N., & Zopfi, J. (2006). Dynamics and interaction of organic carbon, turbidity and bacteria in a karst aquifer system. *Hydrogeology Journal*, 14(4), 473–484.
- Pronk, M., Goldscheider, N., & Zopfi, J. (2009a). Microbial communities in karst groundwater and their potential use for biomonitoring. *Hydrogeology Journal*, 17(1), 37–48.
- Pronk, M., Goldscheider, N., Zopfi, J., & Zwahlen, F. (2009b). Percolation and particle transport in the unsaturated zone of a karst aquifer. *Ground Water*, 47(3), 361–369.
- Ralph, F. M., & Dettinger, M. D. (2012). Historical and national perspectives on extreme west coast precipitation associated with atmospheric rivers during december 2010. *Bulletin of the American Meteorological Society*, 93(6), 783–790.
- Rashidul Islam, M., & Hanif Chaudhry, M. (1997). Numerical solution of transport equation for applications in environmental hydraulics and hydrology. *Journal of Hydrology*, 191(1–4), 106–121.
- Raymond, P. A., Hartmann, J., Lauerwald, R., Sobek, S., McDonald, C., Hoover, M., ... Guth, P. (2013). Global carbon dioxide emissions from inland waters. *Nature*, 503(7476), 355–359.
- Reddy, K. R., & DeLaune, R. D. (2008). *Biogeochemistry of Wetlands: Science and Applications*. Boca Raton, FL: CRC Press.
- Reed, T. M., Fryar, A. E., Brion, G. M., & Ward, J. W. (2011). Differences in pathogen indicators between proximal urban and rural karst springs, Central Kentucky, USA. *Environmental Earth Sciences*, 64(1), 47–55.
- Reed, T. M., Todd McFarland, J., Fryar, A. E., Fogle, A. W., & Taraba, J. L. (2010). Sediment discharges during storm flow from proximal urban and rural karst springs, central Kentucky, USA. *Journal of Hydrology*, 383(3–4), 280–290.
- Regnier, P., Friedlingstein, P., Ciais, P., Mackenzie, F. T., Gruber, N., Janssens, I. A., ... Thullner, M. (2013). Anthropogenic perturbation of the carbon fluxes from land to ocean. *Nature Geoscience*, 6(8), 597–607.
- Reichstein, M., Bednorz, F., Broll, G., & Kätterer, T. (2000). Temperature dependence of carbon mineralisation: Conclusions from a long-term incubation of subalpine soil samples. *Soil Biology and Biochemistry*, 32(7), 947–958.
- Rier, S. T., Francoeur, S. N., Kuehn, K. A., & Francoeur, S. N. (2007). Algal regulation of extracellular enzyme activity in stream microbial communities associated with inert substrata and detritus. *Journal of the North American Benthological Society*, 26, 439–449.
- Roth, M. J. S., & Nyquist, J. E. (2003). Evaluation of multi-electrode Earth resistivity testing in karst. *Geotechnical Testing Journal*, 26(2), 167–178.
- Rowden, R. D., Libra, R. D., & Liu, H. (1998). *Shallow Groundwater and Surface Water Monitoring of the Silver Creek Sub-Basin within the Big Spring Basin 1986-1995: A Summary Review*. Des Moines, IA.
- Rowden, R. D., Liu, H., & Libra, R. D. (2001). Results from the Big Spring basin water quality monitoring and demonstration projects, Iowa, USA. *Hydrogeology Journal*, 9(5), 487–497.
- Royer, T. V., David, M. B., & Gentry, L. E. (2006). Timing of riverine export of nitrate and phosphorus from agricultural watersheds in Illinois: Implications for reducing nutrient loading to the Mississippi River. *Environmental Science and Technology*,

- 40(13), 4126–4131.
- Rusjan, S., Brilly, M., & Mikoš, M. (2008). Flushing of nitrate from a forested watershed: An insight into hydrological nitrate mobilization mechanisms through seasonal high-frequency stream nitrate dynamics. *Journal of Hydrology*, 354(1–4), 187–202.
- Russo, J., & Fox, J. F. (2012). The role of the surface fine-grained laminae in low-gradient streams: A model approach. *Geomorphology*, 171–172, 127–138.
- Russo, J. P. (2009). *Investigation of Surface Fine Grained Laminae, Streambed, and Streambank Processes Using a Watershed Scale Hydrologic and Sediment Transport Model*. University of Kentucky.
- Rutz, J. J., Steenburgh, W. J., & Ralph, F. M. (2014). Climatological Characteristics of Atmospheric Rivers and Their Inland Penetration over the Western United States. *Monthly Weather Review*, 142(2), 905–921.
- Ryan, M., & Meiman, J. (1996). An examination of short-term variations in water quality at a karst spring in Kentucky. *Groundwater*, 34(1), 23–30.
- Rysgaard, S., Glud, R. N., Risgaard-Petersen, N., & Dalsgaard, T. (2004). Denitrification and anammox activity in Arctic marine sediments. *Limnology and Oceanography*, 49(5), 1493–1502.
- Sanford, L. P., & Maa, J. P. Y. (2001). A unified erosion formulation for fine sediments. *Marine Geology*, 179(1–2), 9–23.
- Scanlon, B. R., Mace, R. E., Barrett, M. E., & Smith, B. (2003). Can we simulate regional groundwater flow in a karst system using equivalent porous media models? Case study, Barton Springs Edwards aquifer, USA. *Journal of Hydrology*, 276(1–4), 137–158.
- Schilling, K. E., & Helmers, M. (2008). Tile drainage as karst: Conduit flow and diffuse flow in a tile-drained watershed. *Journal of Hydrology*, 349(3–4), 291–301.
- Sebestyen, S., Shanley, J., Boyer, E., Kendall, C., & Doctor, D. (2014). Coupled hydrological and biogeochemical processes controlling variability of nitrogen species in streamflow during autumn in an upland forest. *Water Resources Research*, 50, 1569–1591.
- Seitzinger, S., Harrison, J., Bohlke, J., Bouwman, A., Lowrance, R., Peterson, B., ... Van Drecht, G. (2006). Denitrification across landscapes and waterscapes: a synthesis. *Ecological Applications*, 16(6), 2064–2090.
- Seitzinger, S. P. (1988). Denitrification in freshwater and coastal marine ecosystems: Ecological and geochemical significance. *Limnology and Oceanography*, 33(4part2), 702–724.
- Sharp, Z. (2007). *Principles of stable isotope geochemistry*. Upper Saddle River, NJ: Pearson Education.
- Shepherd, J. M., Grundstein, A., & Mote, T. L. (2007). Quantifying the contribution of tropical cyclones to extreme rainfall along the coastal southeastern United States. *Geophysical Research Letters*, 34(23), 1–5.
- Shih, J.-S., Alexander, R. B., Smith, R. A., Boyer, E. W., Schwarz, G. E., & Chung, S. (2010). *An Initial SPARROW Model of Land Use and In-Stream Controls on Total Organic Carbon in Streams of the Conterminous United States*. U.S. Geological Survey Open-File Report 2010-1276. <https://doi.org/10.3133/ofr20101276>
- Sigman, D. M., Casciotti, K. L., Andreani, M., Barford, C., Galanter, M., & Böhlke, J. K. (2001). A bacterial method for the nitrogen isotopic analysis of nitrate in seawater and

- freshwater. *Analytical Chemistry*, 73(17), 4145–4153.
- Sigman, D. M., Granger, J., DiFiore, P. J., Lehmann, M. M., Ho, R., Cane, G., & van Geen, A. (2005). Coupled nitrogen and oxygen isotope measurements of nitrate along the eastern North Pacific margin. *Global Biogeochemical Cycles*, 19(4), 1–14.
- Silvestro, F., Gabellani, S., Rudari, R., Delogu, F., Laiolo, P., & Boni, G. (2015). Uncertainty reduction and parameter estimation of a distributed hydrological model with ground and remote-sensing data. *Hydrology and Earth System Sciences*, 19(4), 1727–1751.
- Simon, A., Pollen-Bankhead, N., Mahacek, V., & Langendoen, E. (2009). Quantifying reductions of mass-failure frequency and sediment loadings from streambanks using toe protection and other means: Lake Tahoe, United States. *Journal of the American Water Resources Association*, 45(1), 170–186.
- Simon, A., & Thomas, R. E. (2002). Processes and forms of an unstable alluvial system with resistant, cohesive streambeds. *Earth Surface Processes and Landforms*, 27(7), 699–718.
- Simon, K. S., & Benfield, E. F. (2001). Leaf and wood breakdown in cave streams. *Journal of the North American Benthological Society*, 20(4), 550–563.
- Simon, K. S., Benfield, E. F., & Macko, S. A. (2003). Food Web Structure and the Role of Epilithic Biofilms in Cave Streams. *Ecology*, 84(9), 2395–2406.
- Simon, K. S., Fong, D., Hinderstein, L., Maloney, B., Payn, R., Vernarsky, Mi., & Wilhelm, F. (2008). Focus Group on Ecosystem Function. In J. B. Martin & W. B. White (Eds.), *Frontiers of Karst Research* (pp. 90–95). San Antonio: Karst Waters Institute.
- Simon, K. S., Pipan, T., & Culver, D. C. (2007). A conceptual model of the flow and distribution of organic carbon in caves. *Journal Of Cave And Karst Studies*, 69(2), 279–284.
- Sinha, E., & Michalak, A. M. (2016). Precipitation Dominates Interannual Variability of Riverine Nitrogen Loading across the Continental United States. *Environmental Science & Technology*, 50(23), 12874–12884.
- Six, J., & Jastrow, J. D. (2002). Organic Matter Turnover. In *Encyclopedia of Soil Science* (pp. 936–942). New York City, NY: Marcel Dekker.
- Skamarock, W. C., Klemp, J. B., Dudhi, J., Gill, D. O., Barker, D. M., Duda, M. G., ... Powers, J. G. (2008). *A Description of the Advanced Research WRF Version 3. NCAR Technical Report*. Boulder, CO. <https://doi.org/10.5065/D6DZ069T>
- Smart, P. L., & Hobbs, S. L. (1986). Characterisation of carbonate aquifers: a conceptual base. In *Proceedings of the Environmental Problems in Karst Terranes and Their Solutions Conference. National Water Well Association* (pp. 1–14). Dublin, OH.
- Smith, R. L., Böhlke, J. K., Song, B., & Tobias, C. R. (2015). Role of Anaerobic Ammonium Oxidation (Anammox) in Nitrogen Removal from a Freshwater Aquifer. *Environmental Science and Technology*, 49(20), 12169–12177.
- Sohl, T. L., Sayler, K. L., Drummond, M. A., & Loveland, T. R. (2007). The FORE-SCE model: A practical approach for projecting land cover change using scenario-based modeling. *Journal of Land Use Science*, 2(2), 103–126.
- Sohl, T., & Sayler, K. (2008). Using the FORE-SCE model to project land-cover change in the southeastern United States. *Ecological Modelling*, 219(1–2), 49–65.
- Spangler, L. E. (1982). *Karst hydrogeology of northern Fayette and southern Scott*

- counties, Kentucky. University of Kentucky.
- St-Jean, G. (2003). Automated quantitative and isotopic (^{13}C) analysis of dissolved inorganic carbon and dissolved organic carbon in continuous-flow using a total organic carbon analyser. *Rapid Communications in Mass Spectrometry*, 17(5), 419–428.
- Stone, M., & Droppo, I. G. (1994). In-channel surficial fine-grained sediment laminae. Part II: Chemical characteristics and implications for contaminant transport in fluvial systems. *Hydrological Processes*, 8, 113–124.
- Stueber, A. M., & Criss, R. E. (2005). Origin and Transport of Dissolved Chemicals in a Karst Watershed, Southwestern Illinois. *Journal of the American Water Resources Association*, 41(2), 267–290.
- Swanson, E. (2004). *Analysis of phosphorus in Spring Creek and Sheridan Lake in the Black Hills of South Dakota*. South Dakota School of Mines and Technology.
- Swift, M. J., Heal, O. W., & Anderson, J. M. (1979). *Decomposition in terrestrial ecosystems (Vol. 5)*. University of California Press.
- Taylor, C. J. (1992). *Ground-water occurrence and movement associated with sinkhole alignments in the Inner Bluegrass Karst Region of central Kentucky*. University of Kentucky.
- Tesoriero, A. J., Duff, J. H., Saad, D. A., Spahr, N. E., & Wolock, D. M. (2013). Vulnerability of streams to legacy nitrate sources. *Environmental Science and Technology*, 47(8), 3623–3629.
- Tesoriero, A. J., & Puckett, L. J. (2011). O_2 reduction and denitrification rates in shallow aquifers. *Water Resources Research*, 47(12), 1–17.
- Thamdrup, B., & Fleischer, S. (1998). Temperature dependence of oxygen respiration, nitrogen mineralization, and nitrification in Arctic sediments. *Aquatic Microbial Ecology*, 15(2), 191–199.
- Thorp, J. H., & Delong, M. D. (2002). Dominance of autochthonous autotrophic carbon in food webs of heterotrophic rivers. *Oikos*, 96(3), 543–550.
- Thraillkill, J. (1974). Pipe flow models of a Kentucky limestone aquifer. *Groundwater*, 12(4), 202–205.
- Thraillkill, J., Sullivan, S. B., & Gouzie, D. R. (1991). Flow parameters in a shallow conduit-flow carbonate aquifer, Inner Bluegrass Karst Region, Kentucky, USA. *Journal of Hydrology*, 129(1–4), 87–108.
- Tomer, M. D., & Schilling, K. E. (2009). A simple approach to distinguish land-use and climate-change effects on watershed hydrology. *Journal of Hydrology*, 376(1–2), 24–33.
- Toran, L., & White, W. B. (2005). Variation in nitrate and calcium as indicators of recharge pathways in Nolte Spring, PA. *Environmental Geology*, 48(7), 854–860.
- Trimmer, M., Grey, J., Heppell, C. M., Hildrew, A. G., Lansdown, K., Stahl, H., & Yvon-Durocher, G. (2012). River bed carbon and nitrogen cycling: State of play and some new directions. *Science of the Total Environment*, 434, 143–158.
- Trimmer, M., Nicholls, J. C., & Deflandre, B. (2003). Anaerobic Ammonium Oxidation Measured in Sediments along the Thames Estuary, United Kingdom. *Applied and Environmental Microbiology*, 69(11), 6447–6454.
- Tritz, S., Guinot, V., & Jourde, H. (2011). Modelling the behaviour of a karst system

- catchment using non-linear hysteretic conceptual model. *Journal of Hydrology*, 397(3–4), 250–262.
- Tzoraki, O., & Nikolaidis, N. P. (2007). A generalized framework for modeling the hydrologic and biogeochemical response of a Mediterranean temporary river basin. *Journal of Hydrology*, 346(3–4), 112–121.
- UKAg (University of Kentucky Agriculture Weather Center). (2007). Research Farm Climate Data. Retrieved from http://www.wagwx.ca.uky.edu/ky/data.php#Spindletop_Farm_Data
- UKCAFE (University of Kentucky College of Agriculture Food and the Environment). (2011). Cane Run and Royal Spring watershed based plan, Version 5. EPA Project Number C9994861-06. Retrieved from www.bae.uky.edu/CaneRun/PDFs/Cane_Run_WBP_2011.pdf
- USDA (United States Department of Agriculture). (1993). *Soil Survey Manual. Revised Edition. United States Department of Agriculture Handbook No. 18*. Washington, DC.
- Vaute, L., Drogue, C., Garrelly, L., & Ghelfenstein, M. (1997). Relations between the structure of storage and the transport of chemical compounds in karstic aquifers. *Journal of Hydrology*, 199(3–4), 221–238.
- Venarsky, M. P., Benstead, J. P., & Huryn, A. D. (2012). Effects of organic matter and season on leaf litter colonisation and breakdown in cave streams. *Freshwater Biology*, 57(4), 773–786.
- Veraart, A. J., de Klein, J. J. M., & Scheffer, M. (2011). Warming can boost denitrification disproportionately due to altered oxygen dynamics. *PLoS ONE*, 6(3), 2–7.
- Verardo, D. J., Froelich, P. N., & McIntyre, A. (1990). Determination of organic carbon and nitrogen in marine sediments using the Carlo Erba NA-1500 analyzer. *Deep Sea Research*, 37(1), 157–165.
- Vesper, D. J., & White, W. B. (2004). Storm pulse chemographs of saturation index and carbon dioxide pressure: Implications for shifting recharge sources during storm events in the karst aquifer at Fort Campbell, Kentucky/Tennessee, USA. *Hydrogeology Journal*, 12(2), 135–143.
- Vidon, P., Allan, C., Burns, D., Duval, T. P., Gurwick, N., Inamdar, S., ... Sebestyen, S. (2010). Hot spots and hot moments in riparian zones: Potential for improved water quality management. *Journal of the American Water Resources Association*, 46(2), 278–298.
- Vieira, A. A., & Myklestad, S. (1986). Production of extracellular carbohydrate in cultures of *Ankistrodesmus densus* Kors. (Chlorophyceae). *Journal of Plankton Research*, 8(5), 985–994.
- Waite, A. M., Olson, R. J., Dam, H. G., & Passow, U. (1995). Sugar-Containing Compounds on the Cell Surfaces of Marine Diatoms Measured Using Concanavalin a and Flow Cytometry. *Journal of Phycology*, 31(6), 925–933.
- Walling, D. E., Collins, A. L., Jones, P. A., Leeks, G. J. L., & Old, G. (2006). Establishing fine-grained sediment budgets for the Pang and Lambourn LOCAR catchments, UK. *Journal of Hydrology*, 330(1–2), 126–141.
- Walling, D. E., & Webb, B. W. (1982). Sediment availability and the prediction of storm-period sediment yields. In *Recent Developments in the Explanation and Prediction of Erosion and Sediment Yield (Proceedings of the Exeter Symposium)* (Vol. 137, pp. 327–337).

- Waltham, A. C., & Fookes, P. G. (2003). Engineering classification of karst ground conditions. *Quarterly Journal of Engineering Geology and Hydrogeology*, 36(2), 101–118.
- Webster, J. R., Benfield, E. F., Ehrman, T. P., Schaeffer, M. A., Tank, J. L., Hutchens, J. J., & D'Angelo, D. J. (1999). What happens to allochthonous material that falls into streams? A synthesis of new and published information from Coweeta. *Freshwater Biology*, 41(4), 687–705.
- Wells, E. R., & Krothe, N. C. (1989). Seasonal fluctuation in $\delta^{15}\text{N}$ of groundwater nitrate in a mantled karst aquifer due to macropore transport of fertilizer-derived nitrate. *Journal of Hydrology*, 112(1–2), 191–201.
- Whitaker, F. F., & Smart, P. L. (2007). Geochemistry of meteoric diagenesis in carbonate islands of the northern Bahamas: 1. Evidence from field studies. *Hydrological Processes*, 21, 949–966.
- White, P. A., Kalff, J., Rasmussen, J. B., & Gasol, J. M. (1991). The effect of temperature and algal biomass on bacterial production and specific growth rate in freshwater and marine habitats. *Microbial Ecology*, 21, 99–118.
- White, W. B. (2002). Karst hydrology: Recent developments and open questions. *Engineering Geology*, 65(2–3), 85–105.
- Wilhartitz, I. C., Kirschner, A. K. T., Stadler, H., Herndl, G. J., Dietzel, M., Latal, C., ... Farnleitner, A. H. (2009). Heterotrophic prokaryotic production in ultraoligotrophic alpine karst aquifers and ecological implications. *FEMS Microbiology Ecology*, 68(3), 287–299.
- Williams, P. W. (2008). The role of the epikarst in karst and cave hydrogeology: A review. *International Journal of Speleology*, 37(1), 1–10.
- Wilson, J. F., Cobb, E. D., & Kilpatrick, F. A. (1986). *Fluorometric procedures for dye tracing: U.S. Geological Survey Techniques of Water Resources Investigations*.
- Winston, W. E., & Criss, R. E. (2004). Dynamic hydrologic and geochemical response in a perennial karst spring. *Water Resources Research*, 40(5), 1–11.
- Wynn, T. M., Henderson, M. B., & Vaughan, D. H. (2008). Changes in streambank erodibility and critical shear stress due to subaerial processes along a headwater stream, southwestern Virginia, USA. *Geomorphology*, 97(3–4), 260–273.
- Xue, D., Botte, J., De Baets, B., Accoe, F., Nestler, A., Taylor, P., ... Boeckx, P. (2009). Present limitations and future prospects of stable isotope methods for nitrate source identification in surface- and groundwater. *Water Research*, 43(5), 1159–1170.
- Xue, D., De Baets, B., Van Cleemput, O., Hennessy, C., Berglund, M., & Boeckx, P. (2013). Classification of Nitrate Polluting Activities through Clustering of Isotope Mixing Model Outputs. *Journal of Environment Quality*, 42(5), 1486.
- Yan, L. J., Yu, X. X., Lei, T. W., Zhang, Q. W., & Qu, L. Q. (2008). Effects of transport capacity and erodibility on rill erosion processes: A model study using the Finite Element method. *Geoderma*, 146(1–2), 114–120.
- Yoshimoto, S., Tsuchihara, T., Ishida, S., & Imaizumi, M. (2013). Development of a numerical model for nitrates in groundwater in the reservoir area of the Komesu subsurface dam, Okinawa, Japan. *Environmental Earth Sciences*, 70(5), 2061–2077.
- Yoshimura, C., Gessner, M. O., Tockner, K., & Furumai, H. (2008). Chemical properties, microbial respiration, and decomposition of coarse and fine particulate organic matter. *Journal of the North American Benthological Society*, 27(3), 664–673.

- Young, M. B., McLaughlin, K., Kendall, C., Stringfellow, W., Rollog, M., Elsbury, K., ... Paytan, A. (2009). Characterizing the oxygen isotopic composition of phosphate sources to aquatic ecosystems. *Environmental Science and Technology*, 43(14), 5190–5196.
- Yuan, L., Pang, Z., & Huang, T. (2012). Integrated assessment on groundwater nitrate by unsaturated zone probing and aquifer sampling with environmental tracers. *Environmental Pollution*, 171, 226–233.
- Yuan, Y., Bingner, R. L., & Rebach, R. A. (2001). Evaluation of AnnAGNPS on Mississippi Delta MSEA Watersheds. *Transactions of the ASAE*, 44(5), 1183–1190.
- Yue, F.-J., Li, S.-L., Zhong, J., & Liu, J. (2017). Evaluation of factors driving seasonal nitrate variations in surface and underground systems of a karst catchment. *Vadose Zone Journal*, 17(1).
- Yue, F. J., Li, S. L., Liu, C. Q., Lang, Y. C., & Ding, H. (2015). Sources and transport of nitrate constrained by the isotopic technique in a karst catchment: An example from Southwest China. *Hydrological Processes*, 29(8), 1883–1893.
- Zak, D. R., Grigal, D. F., & Ohmanri, L. F. (1993). Kinetics of microbial respiration and nitrogen mineralization in Great Lakes forests. *Soil Science Society of America Journal*, 57, 1100–1106.
- Zarnetske, J. P., Haggerty, R., Wondzell, S. M., & Baker, M. A. (2011). Dynamics of nitrate production and removal as a function of residence time in the hyporheic zone. *Journal of Geophysical Research: Biogeosciences*, 116(1), 1–12.
- Zhu, J., Currens, J. C., & Dinger, J. S. (2011). Challenges of using electrical resistivity method to locate karst conduits-A field case in the Inner Bluegrass Region, Kentucky. *Journal of Applied Geophysics*, 75(3), 523–530.
- Zhu, Z.-L., Bergamaschi, B. A., Bernknopf, R., Clow, D., Dye, D., Faulkner, S., ... Wein, A. (2010). *A method for assessing carbon stocks, carbon sequestration, and greenhouse-gas fluxes in ecosystems of the United States under present conditions and future scenarios.* (Z.-L. Zhu, Ed.), *Scientific Investigations Report*. Reston, VA. Retrieved from <http://pubs.er.usgs.gov/publication/sir20105233>

VITA

Admin Husic

EDUCATION

Master of Science in Civil Engineering University of Kentucky	Degree Date: Dec, 2015
Bachelor of Science in Civil Engineering University of Kentucky	Degree Date: May, 2014

RESEARCH EXPERIENCE

Graduate Research Assistant – Research Advisor: Dr. James Fox (Aug. 2014 – Present)
Hydrosystems Lab at the University of Kentucky, Lexington, KY

1. Developed numerical and conceptual models of water, sediment, carbon, and nitrogen fate and transport in karst watersheds.
2. Assessed controlling dynamics of organic matter fate in phreatic caves by coupling novel sediment data streams in karst with hydraulic and biochemical numerical modeling.
3. Investigated leaching of nitrate from agro-karst landscapes by using pathway modeling to identify dominant processes leading to relative enrichment of subsurface nitrate.
4. Constructed an experiment to elucidate mixing and fractionation processes that complicate the use of tracer isotopes in identifying contaminant provenance.
5. Conducted turbulence experiments in two laboratory flumes to investigate energy and timescales of macroturbulent structures using acoustic Doppler velocimetry.

GRADUATE TEACHING

Teaching Assistant (Aug. 2014 – Present)
Department of Civil Engineering, University of Kentucky, Lexington, KY

1. Served as a teaching assistant for three courses: *Watershed Sedimentation*, *Engineering Exploration II*, and *Fundamentals of Engineering Computing*.
2. Led lab and field segments of *Watershed Sedimentation*, lectured in *Fundamentals of Engineering Computing*, and assisted with project design in *Engineering Exploration II*.

Graduate Mentor & Advisor (Aug. 2014 – Present)
Department of Civil Engineering, University of Kentucky, Lexington, KY

1. Co-advised four undergraduate students including: Ethan Adams, Zack Galusha, Joshua Bobak, and Jeremy Puckett.
2. Assisted students with designing and implementing a research plan as well as drafting a project report of results.

SOCIETY MEMBERSHIPS

Member of the American Society of Civil Engineers (ASCE)

Member of the American Geophysical Union (AGU)

Member of the American Water Works Association (AWWA)

Member of the Water Environment Federation (WEF)

Member of the Tau Beta Pi Engineering Honor Society (TBP)

Member of the Chi Epsilon Civil Engineering Honor Society (XE)

Member of the Omicron Delta Kappa Leadership Society (ODK)

HONORS & AWARDS

National Ground Water Association Past President's Award (2017)

Burton E. Heard Graduate Fellowship (2017)

KY-TN American Water Works Association Fellowship (2017)

Graduate Student Travel Funding Award (2015-17)

Burton E. Heard Graduate Fellowship (2016)

Great Lakes National Scholarship (2016)

USGS KY Water Resources Research Institute Research Enhancement (2015)

ASCE J. Waldo Smith Hydraulic Fellowship (2015)

Robert Eugene Fish Hydraulic Fellowship (2014)

PUBLICATIONS

Submitted

- **Husic, A. et al.**, (2018). Nitrate leaching and pathways in an agricultural fluviokarst system: evidence from a multi-year dataset and model development. *Submitted*.
- **Husic, A. et al.**, (2018). Inland impacts of atmospheric river and tropical cyclone extremes on nitrate transport and stable isotope measurements. *Submitted*.

In Preparation

- **Husic, A. et al.**, (approx. 2018). Development of hydraulic and sediment transport model of a coupled surface water and phreatic fluviokarst system. *In prep*.
- Ghesemi, A., Fox, J., **Husic, A.**, and Stewart, R. (2018). Evaluation of the energy and timescales of macroturbulence within flow over a gravel bed: a spectral approach. *In prep*.
- **Husic, A. et al.**, (approx. 2018). Application of isotopic and elemental data streams for estimating source and transformation processes of dissolved nitrogen in a phreatic karst system. *In prep*.

- **Husic, A. et al.**, (approx. 2018). Development of a multi-isotope numerical model for simulating water quality in a phreatic karst watershed. *In prep.*

Published

- Jensen, A., Ford, W., Fox, J., and **Husic, A.** (2017). Improving water quality models using stable isotope tracers: a review and synthesis. *Transactions of the ASABE. In press.* (doi: 10.13031/trans.12545)
- **Husic, A. et al.**, (2017). Sediment carbon source, fate, and transport in a fluviokarst watershed (Part 1): conceptual model development. *Journal of Hydrology*, 549, 179-193.
- **Husic, A. et al.**, (2017). Sediment carbon source, fate, and transport in a fluviokarst watershed (Part 2): numerical model development and application. *Journal of Hydrology*, 549, 208-219.

Other Writings

- **Husic, A.** (2015). Sediment organic carbon fate and transport in a fluviokarst watershed in the Bluegrass Region. *Theses and Dissertations*, University of Kentucky, Lexington, Kentucky.
- **Husic, A.** (2014). Heat as a tracer to monitor groundwater-surfacewater interactions at estavelles. *Univ. of Kentucky Journal of Undergraduate Scholarship, Kaleidoscope*, 12.

CONFERENCE PROCEEDINGS

- **Husic, A. et al.**, (2018, June). Application of isotopic and elemental data streams for estimating source and transformation processes in an agricultural karst system. Oral Presentation. World Environmental and Water Resources Congress. Minneapolis, MN.
- **Husic, A. et al.**, (2017, December). Nitrogen fate in a phreatic fluviokarst watershed: a stable isotope, sediment tracing, and numerical modeling approach. Poster Presentation. American Geophysical Union Fall Meeting. New Orleans, LA.
- **Husic, A. et al.**, (2017, May). Nitrate leaching and pathways in agricultural fluviokarst systems. Oral Presentation. World Environmental & Water Resources Congress. Sacramento, CA.
- Ford, W., Fox, J., and **Husic, A.** (2017, May). Role of non-conservative sediment stable isotope tracers in watershed modeling. Oral Presentation. World Environmental & Water Resources Congress. Sacramento, CA.
- **Husic, A. et al.**, (2017, March). Nitrate leaching in an agricultural fluviokarst system in the Bluegrass Region. Oral Presentation. Kentucky Water Resources Research Institute Symposium. Lexington, KY.

- **Husic, A. et al.**, (2016, March). Data and model investigation of a fluviokarst system in the Bluegrass Region: water, sediment, and carbon interactions. Oral Presentation. Kentucky Water Resources Research Institute Symposium. Lexington, KY.
- **Husic, A. et al.**, (2015, December). Sediment organic carbon fate and transport in a fluviokarst watershed in the Bluegrass Region. Poster Presentation. American Geophysical Union Fall Meeting. San Francisco, CA.
- **Husic, A. et al.**, (2015, December). Sediment carbon fate in a fluviokarst watershed in the Bluegrass Region. Poster Presentation. 5th Annual Sustainability Forum. Lexington, KY.
- **Husic, A. et al.**, (2015, May). Investigation of source, fate, and transport of sediments in a karst dominated watershed. Oral Presentation. World Environmental & Water Resources Congress. Austin, TX.
- **Husic, A. et al.**, (2015, March). Sediment transport mechanisms in a fluvial karst system in Bluegrass Region. Oral Presentation. Kentucky Water Resources Research Institute Annual Symposium. Lexington, KY.
- **Husic, A. et al.**, (2015, February). Sediment organic carbon fate and transport mechanisms in a fluvial karst system in the Bluegrass Region. Poster Presentation. Posters-at-the-Capitol. Frankfort, KY.

SERVICE & PROFESSIONAL ACTIVITIES

Peer Reviewer for the *Journal of Hydrology*, *Journal of Hydraulic Engineering*, and the *Transactions of the ASABE* (2017-Present)

Member of Review Committee for Civil Engineering Department Chair (2017-Present)

Volunteer Tutor in Mathematics at the Carnegie Center for Literacy (2016-Present)

Civil Engineering Representative to the UK Graduate Student Congress (2016-17)

Graduate Student Representative to the Dept. of Civil Engineering Education Team (2015-17)

Engineer in Training (EIT) Professional Designation (2014)

President (2013-14)/Vice-President (2012-13) of the American Society of Civil Engineers UK Student Chapter.

Ambassador for the UK College of Engineering (2013-14).

Co-captain of the Univ. of Kentucky Concrete Canoe Club (2012-14).